Title
Perturbation Theory Models for Precision Cosmology with Large-Scale Structure Surveys

Author
Chen, Shi-Fan Stephen

Publication Date
2022

Peer reviewed|Thesis/dissertation

Perturbation Theory Models for Precision Cosmology with Large-Scale Structure Surveys

by

Shi-Fan Stephen Chen

A dissertation submitted in partial satisfaction of the

requirements for the degree of

Doctor of Philosophy

in

Physics

in the

Graduate Division

of the

University of California, Berkeley

Committee in charge:

Professor Martin White, Chair
Professor Uroš Seljak
Professor Chung-Pei Ma

Summer 2022

Perturbation Theory Models for Precision Cosmology with Large-Scale Structure Surveys

Abstract

Perturbation Theory Models for Precision Cosmology with Large-Scale Structure Surveys

by

Shi-Fan Stephen Chen

Doctor of Philosophy in Physics

University of California, Berkeley

Professor Martin White, Chair

The next generation of cosmological surveys will measure the large-scale structure (LSS) of the universe with unprecedented statistical power, covering large cosmological volumes and yielding constraints on cosmological parameters competitive with the cosmic microwave background (CMB), letting us test the standard model of cosmology at percent levels or below across cosmic history, from the recombination era to the present. Unlike CMB experiments, which probe the early universe in the linear regime, these new surveys will map the distribution of matter and galaxies at late times where the effects of nonlinearities are significant. To reliably extract fundamental physics information from this data will require theoretical models that can make accurate predictions on large, cosmological scales while being robust against the effects of nonlinear physics of small scales, due not just to gravitational collapse but also the astrophysics of galaxy formation whose precision modeling currently eludes us.

In this dissertation we develop perturbation theory (PT) models for two key observables in upcoming surveys: the redshift-space clustering of galaxies in spectroscopic surveys and the cross correlation of galaxy clustering with weak gravitational lensing. Perturbation theory at the linear level has an indispensable role in CMB analyses, and the past decade has seen rapid developments in *nonlinear* perturbation theories of large-scale structure, in part due to a reinterpretation of PT through the lens of effective field theories that has allowed for a robust and theoretically consistent treatment of the effects of non-perturbative small-scale physics on large-scale clustering. We review these developments in Chapter 1 before diving into the study of galaxy velocities and redshift-space distortions in Eulerian and Lagrangian perturbation theory (LPT) in Chapter 2. We use this knowledge to construct a model of the redshift-space galaxy 2-point function at 1-loop in perturbation theory featuring a full infrared (IR) resummation of large-scale displacements and velocities in Chapter 3. In Chapter 4, we use the same mathematical techniques to model density-field reconstruction, a technique used to sharpen the baryon acoustic oscillations (BAO) signal in spectroscopic surveys.

The PT techniques described above are quite versatile and, in Chapter 5 and 6, we use

them "out-of-the-box" to study non-standard features in galaxy clustering due to relative perturbations between dark matter and baryons after recombination as well as exotic early-universe scenarios such as non-standard inflation and early dark energy, with a particular focus on IR resummation in LPT. In Chapter 7 we exploit this same resummation of displacements for a different purpose: by combining the perturbative Lagrangian bias expansion with exact displacements solved-for in N-body simulations we construct a model for galaxy-matter cross correlations in weak lensing surveys that significantly extend the reach of PT models without requiring any additional assumptions about the galaxy-halo connection.

To complete this dissertation, we apply the LPT models constructed in the preceding chapters to existing data in Chapters 8 and 9. In the former, we use the predictions of LPT to jointly model the "full shape" of pre- and post-reconstruction galaxy 2-point functions in the Baryon Oscillation Spectroscopic Survey (BOSS), showing that this combined analysis can be performed directly at the data level as opposed to the ex post facto approach of earlier analyses. In the latter, we further add in cross correlations with the weak lensing of the CMB from the Planck satellite, and, by modeling the cross correlation with the same LPT formalism as the galaxy power spectrum, do so within a consistent dynamical framework and with minimal additional parameters. Together, these pilot analyses demonstrate that the LPT formalism developed in this dissertation, and more generally perturbation theory, can offer a robust and pragmatic choice for future analyses of cosmological data, modeling the large-scale structure of the universe on cosmologically interesting scales to well within the statistical requirements set by future surveys.

To my grandfather An Chi (安祺)

Contents

List of Figures

List of Tables

Acknowledgments

When I started five years ago it's safe to say I had very little idea what I was doing. The scientific community at Berkeley presents an embarrassment of riches for a budding cosmologist and I am sad to have to leave it right when I had almost found my bearings, but overall quite happy for having had the opportunity to meet so many wonderful people. I would be remiss not to express my thanks to all of them.

First and foremost I would like to thank my advisor Martin White, who has taught me just about everything I know about cosmology and being a cosmologist. Martin's deep physical intuition and common-sense approach to science have been invaluable in shaping my own scientific outlook. I continue to be inspired by the scope and depth of his knowledge. Working with Martin is like trying to catch a train on a bicycle if the train were also juggling and performing administrative duties, and I am sure Martin would've been much more productive in the past five years were it not for our long, meandering conversations, but for me this wild ride has been all the more rewarding for it. Martin and Joanne have been a constant source of warmth and support throughout my time at Berkeley, particularly during the tumultuous COVID years, and for that I am immensely grateful.

I would like to thank Uroš Seljak for often offering incisive viewpoints that have challenged my preconceptions, as well as introducing me to the world of Slovenian skin-contact wines. I would also like to especially thank Chung-Pei Ma for her mentorship and good advice since well before my Berkeley days. I feel very privileged to have her and Uroš on my dissertation committee. I would also like to thank Bill Holzapfel for being a life-saving addition to my qualifying exam committee after a previous member was found to be at the South Pole. I want to give special thanks to my undergraduate research mentors Rob Simcoe and Paul Torrey who first set me on this journey.

In addition to Martin I have been extremely lucky to have had two excellent scientific mentors and LPT co-conspirators in my time at Berkeley. Emanuele Castorina took me on as a fledgling graduate student and patiently showed me the lay of the land. Zvonimir Vlah—who's analytical prowess never ceases to amaze me—has been my most frequent collaborator, and I have learned much of what I know of the techniques of perturbation theory from him. Our weekly Skypes have entered the territory of ritual, and a visit to CERN to collaborate on redshift-space distortions at his invitation, right before COVID shut everything down in the winter of 2019, was a turning point in my career.

Nick Kokron and Joe DeRose appear as my coauthors only once in this dissertation—it is fair to say that this belies the frequency of our collaboration, which has been rewarding, enjoyable and, I hope, ongoing. I would also like to thank Nick for being a close confidante and for keeping me up to date on many of the more practical (e.g. how to sign up for job talks) aspects of being a cosmologist. Nick and I met briefly at several grad-school open houses more than five years ago and quasi-miraculously reconnected partway through the COVID years; I am immensely grateful for his friendship.

Several people at Berkeley have played important roles shaping my time here for the better. Chirag Modi taught me the ways of `nbodykit` while working on what would eventually turn

into Chapter 7 and, no less importantly, sent me his thesis template, without which this dissertation would have never compiled. Byeonghee Yu has been extremely generous to me throughout my time at Berkeley, starting all the way back with helping me with my CMB lensing code when I was too embarrassed to ask anyone else my first year here. Exchanging packets of tea and snacks provided much-needed breaks during long days at work. Jamie Sullivan brightened my days by humoring my cynical takes on everything. I would also like to thank Martin's other students Noah Sailer and Alex Krolewski for their scientific help and camaraderie. I want to especially thank Pat McDonald and Simone Ferraro for frequent and enlightening conversations that have often helped me re-center my perspectives on the big picture.

My time at Berkeley has also been greatly enriched by many outside colleagues and collaborators. Many of these have come from within the DESI collaboration, which I am sad to leave. I would like to especially thank Hee-Jong Seo and Nikhil Padmanabhan for keeping me in the loop of all things BAO even while I was delinquent, and Mariana Vargas Magaña for invaluable help with using the BOSS correlation functions and covariances. Outside of DESI I would like to thank Massimo Pietroni for the invitation to work on the asymptotic limit of large-scale structure and showing me that sometimes calculations can just be done for the fun of it. I would also like to thank Sergey Sibiryakov for helping set up my CERN visit in 2019, during which critical parts of my dissertation work were done.

I spent much of my first year at Berkeley aimlessly wondering what I was going to do with my life. During that time I am grateful for having had the support of Mike DeWeese and Dibyendu Mandal, who helped me learn many cool things about nonequilibrium statistical mechanics during a project I lazily never finished. I would like to than Adam Frim and Adrianne Zhong for finishing that project.

I would also like to thank all of my non-cosmology friends—yes they exist—who have accompanied me throughout my time in grad school. James Rowan agreed to become housemates on the sole basis of having learned of our mutual love of Herman Melville at a frat party back at MIT—it has been a pleasure helming Forecastle, a ship perhaps slightly overstocked with alcoholic beverages, with him. Jiapei Chen, who I have known since that first math class at Exeter, has been a constant companion in exploring the culinary landscapes first of tiny Exeter, NH, then Boston, and now San Francisco over many memorable nights. Vincent Su's Taiwanese beef noodle soup game continues to reach new heights—I am sad to have to make my own again when I move! Vincent and I became fast friends during grad school visits, wound up being office mates our first year at Berkeley and, together with Mia Kanzawa, have gone on multiple adventures and shared more food and wine than I can recall. They have been real friends. Finally, I want to thank my dear friend Tomo Soejima who incredibly, after all these years, still shares with me a love of *shonen* comics, action movies and video games. I knew Tomo and I would be friends the moment we started talking about quantum decoherence the week before freshman year at MIT and, in addition to all the stupid stuff, I still learn new things whenever I talk to him, sometimes at the expense of losing Smash games for hours at a time. I feel very fortunate our academic paths crossed again in grad school.

Above all, I would like to thank my parents—it is a cliché to say that they have always supported me no matter what I wanted to do, but that is exactly what they have done time and again—and my sister Jill, who has been and will always be my best friend. I love you guys. Finally, I would like to thank my partner Samuel Stubblefield, who has been my indispensable companion for the past five years. Berkeley would simply not have been *Berkeley* without you.

Conventions

In this dissertation we will follow the convention for Fourier transforms

$$\tilde{f}(\mathbf{k}) = \int d^3\mathbf{x}\; e^{-i\mathbf{k}\cdot\mathbf{x}}\; f(\mathbf{x}), \quad f(\mathbf{x}) = \int \frac{d^3\mathbf{k}}{(2\pi)^3}\; e^{i\mathbf{k}\cdot\mathbf{x}}\tilde{f}(\mathbf{k}). \tag{1}$$

Except in places where it is ambiguous we will typically forego the tilde's on Fourier transformed quantities, so that $\tilde{f}(\mathbf{k}) \leftrightarrow f(\mathbf{k})$. Throughtout this work we will use the letters $\mathbf{k}, \mathbf{p}$ to refer to wavenumbers in Fourier space and the $\mathbf{x}, \mathbf{q}, \mathbf{s}$ to refer to (Eulerian, Lagrangian and redshift-space) configuration space coordinates; their magnitudes will be uniformly denoted with un-bolded letter (e.g. k, r) and their components by subscripts (e.g. k_i). We will sometimes use the shorthand

$$\int_{\mathbf{k}} = \int \frac{d^3\mathbf{k}}{(2\pi)^3} \tag{2}$$

for the Fourier-space integral. In order to avoid confusion with overdensities δ we will write Dirac delta functions as $\delta_D(\mathbf{x})$.

We will deal extensively with N-point correlation functions in this dissertation. Due to translation invariance they will typically take the Fourier-space form

$$\langle f_1(\mathbf{k}_1) f_2(\mathbf{k}_2) ... f_n(\mathbf{k}_n)\rangle = C(\mathbf{k}_1, \mathbf{k}_2, ..., \mathbf{k}_n)\; (2\pi)^3 \delta_D\Big(\sum_{i=1}^{n} \mathbf{k}_i\Big).$$

In order to avoid writing extraneous delta functions we will sometimes use the notation

$$\langle f_1(\mathbf{k}_1) f_2(\mathbf{k}_2) ... f_n(\mathbf{k}_n)\rangle' = C(\mathbf{k}_1, \mathbf{k}_2, ..., \mathbf{k}_n). \tag{3}$$

Chapter 1

Introduction

We are entering a golden age of cosmological data. As this dissertation was being written the Dark Energy Spectroscopic Instrument (DESI) [108] observed its 12.8 millionth galaxy spectrum, dwarfing previous spectroscopic galaxy surveys like the Baryon Oscillation Spectroscopic Survey (BOSS, 1.5 million, $z < 0.7$) [101] and mapping the three-dimensional distribution of galaxies deeper into cosmic history past $z = 1.0$ just one year into its planned five-year run.[1] The coming years will further see complementary advances in space-based galaxy surveys in Euclid, SPHEREx and Roman [12, 116, 117], imaging surveys in the Rubin Observatory [224] and ground-based cosmic microwave background (CMB) experiments like Simons Observatory and CMB-S4 [141, 1], each of which will significantly advance our observational reach of the large-scale structure (LSS) of the universe. The wealth of expected data in the coming years presents the burgeoning field of *precision cosmology* with both a unique opportunity to learn about fundamental physics and a theoretical challenge to model the formation of cosmic structure robustly at the (sub-)percent level.

An important feature of the coming era of precision cosmology is that the new data will primarily involve structure formation in the *nonlinear* regime. Precision cosmology had its birth in CMB experiments like the WMAP and Planck satellites [175, 285] which mapped fluctuations in the primordial universe ($z \approx 1100$) at the 10^{-5} level. The smallness of these CMB fluctuations meant that they could be modeled highly accurately—minus small changes due to intervening matter between us and the CMB such as lensing—using linear theory, with a clean separation of scales and robust features in the angular two-point function that could be used to cleanly extract cosmological and fundamental physics parameters (see e.g. ref. [114]). In contrast, in the universe today matter density fluctuations on typical ($\approx 8h^{-1}$ Mpc) scales are of order $\sigma_8 \approx 0.8$ and the main objects of interest, galaxies, are formed via gravitational collapse in dark-matter halos that are even-denser still. In this regime nonlinearities due to gravity and astrophysical processes couple modes on large and small scales, complicating the required modeling and de-correlating observables from the early-universe initial conditions we wish to probe. On the other hand, properly leveraging these effects can yield new information

[1] *One Year and 12.8 Million Galaxy Redshifts*, David Schlegel, May 14 (2022). https://www.desi.lbl.gov/2022/05/14/one-year-and-12-8-million-galaxy-redshifts/.

about the early universe and general relativity beyond what can be derived in the primary CMB. Upcoming surveys like DESI promise to rise up to the gold-standard set by the CMB and even existing ones like BOSS (see e.g. ref. [186]) and the Dark Energy Survey (DES) [2] place constraints on some cosmological parameters that are competitive, and often in mild statistical tension, with Planck.

It is against this backdrop that this dissertation has been written. While many innovative and predominantly simulations-based methods to analyze LSS data have been proposed, we will take a more conservative approach and approach structure formation analytically within the formalism of perturbation theory (PT) using techniques from effective field theory (EFT). In what follows, our focus will be to show that models of matter and galaxy clustering can be rigorously and robustly built from fundamental principles using this approach and meet the stringent requirements set by future experiments without making undue assumptions about the small-scale astrophysics of galaxy formation, using current surveys like BOSS and weak lensing from Planck as demonstrative examples. As we will see, these models will also tell us about where the information lives in cosmological data and the limits of LSS analyses. In the rest of this Introduction I will provide a concise overview of large-scale structure phenomenology and perturbation theory, before moving on to develop models of galaxy clustering in the rest of this dissertation.

1.1 The Standard Model of Cosmology

Culminating with measurement of fluctuations in the CMB and of cosmic acceleration from Type IA supernovae [305, 281], accumulating evidence in the last several decades (see e.g. ref. [263]) has painted a remarkable picture wherein the universe as we see it—ranging from the observed abundance of light elements and the age of the oldest stars to the CMB to the observed counts and clustering of galaxies—can be parsimoniously explained within one cosmological model with only a few ingredients. This "Standard Model" of cosmology is also known as the ΛCDM model and posits that we live in an approximately isotropic, uniform and flat spacetime with an energy density dominated by two invisible components: a cosmological constant or dark energy component (Λ) with an unevolving density making up about 70% and cold, nonrelativistic dark matter (CDM) making up most of the rest, with small contributions from baryonic matter, neutrinos and photons, in that order. Within General Relativity this system is described by a flat Friedmann-Lemaître-Robertson-Walker (FLRW) metric[2]

$$ds^2 = -dt^2 + a^2(t)\, d\mathbf{x}^2. \tag{1.1}$$

The scale factor $a(t)$ describes the expansion of the universe and it is conventional to set its present value to one. Photons emitted at earlier times $a < 1$ will receive a redshift z related to the scale factor by $a = (1+z)^{-1}$. It is also conventional to define the conformal time

[2]Much of the material in this section is derived from the excellent textbook by Dodelson [114], to which we direct readers of this dissertation looking for more than just definitions to.

$\tau = dt/a$ such that the metric is instead given by $ds^2 = a^2(-d\tau^2 + d\mathbf{x}^2)$, with its associated conformal Hubble parameter $\mathcal{H} = Ha$. Throughout this dissertation we will use t, τ, a and z interchangeably as the time coordinate.

As the universe expands different species evolve according to their equations of state, e.g. matter dilutes trivially so that $\rho_m \propto a^{-3}$, radiations both dilutes *and* Doppler shifts such that $\rho_r \propto a^{-4}$ and $\rho_\Lambda \propto$ const. The evolution of the scale factor is entirely determined by these relations together with the first Friedmann equation $H(a)^2 = 8\pi G\rho/3$, where the Hubble parameter at each time is given by $H(a) = \dot{a}/a$. It is conventional to define fractional densities in terms of the present-day critical densities $\rho_{\rm crit} = 3H_0^2/8\pi G$, such that the Hubble parameter in a flat universe dominated by CDM and Λ is governed by

$$\frac{H(a)}{H_0} = \sqrt{\Omega_m a^{-3} + (1 - \Omega_m)}, \quad \Omega_m = \frac{\rho_{m,0}}{\rho_{\rm crit}}. \tag{1.2}$$

Beyond the cosmic energy census another key ingredient of the Standard Model is a rapid period of exponential expansion $a(t) \sim e^{Ht}$ in the early universe known as *inflation*.[3] Proposed in the 1980's, inflation provides a simple mechanism to explain (at least) three apparent puzzles of the standard Big Bang model: the uniformity of the CMB at the 10^{-5} level at separations that should be causally disconnected (horizon problem), the apparent flatness of the universe in a setup where flatness is unstable (flatness problem) and the lack of magnetic monopoles and other topological defects that should generically appear in Grand Unified Theories (monopole problem).[4] These problems are generically resolved by a rapid expansion in $a(t)$ and drop in the comoving Hubble radius $(aH)^{-1}$.

Perhaps most significant for our purposes here, though, is that inflation provides a simple and testable mechanism through which the initial fluctuations that grow into CMB anisotropies and large-scale structure are seeded. In the most straightforward models of inflation, the rapid expansion is driven by a single scalar field ϕ with action

$$S_\phi = \int d^4x\sqrt{-R}\left(\frac{1}{2}\partial^2\phi - V(\phi)\right) \tag{1.3}$$

where R is the Ricci scalar coupling ϕ to the metric. When ϕ dominates its equation of motion the Friedman equations are given by

$$\ddot{\phi} + 3H\dot{\phi} + \frac{dV}{d\phi} = 0, \quad H^2 = \frac{8\pi G}{3}\Big(\frac{1}{2}\dot{\phi}^2 + V(\phi)\Big). \tag{1.4}$$

The conditions for inflation are met if the potential energy $V(\phi)$ dominates over the kinetic $\dot{\phi}^2$ term, and for a sufficiently long period implying that $\ddot{\phi}$ is subdominant in the equation of

[3]The following paragraphs represent a lightning summary of the key aspects of cosmological inflation for our purposes in this dissertation—for further details the reader is encouraged to consult e.g. Daniel Baumann's excellent TASI lectures on the topic [26].

[4]The flatness problem is arguably a prediction of inflation, since constraints of spatial curvature using e.g. the CMB and galaxy clustering in e.g. [175, 285] post-date the development of inflationary theory.

motion; these conditions for *slow roll* inflation can be summarized in terms of the parameters[5]

$$\epsilon, |\eta| \ll 1; \quad \epsilon = \frac{1}{16\pi G}\left(\frac{V'}{V}\right)^2, \ \eta = \frac{1}{8\pi G}\left(\frac{V''}{V}\right). \tag{1.5}$$

The preceding discussion focused on the classical dynamics of the ϕ background. However, the inflaton is a quantum field, and it is its quantum fluctuations that form the seeds of structure formation we will study in the rest of this thesis. Inflation generically predicts adiabatic scalar fluctuations generated by a single degree of freedom ϕ. Indeed, slow roll inflation tends to enhance the scalar curvature perturbations ζ: roughly speaking, sub-horizon quantum fluctuations in ϕ are stretched by inflation and exit the comoving Hubble radius ($k = aH$) where they become frozen in as commuting classical fluctuations in ζ with power spectrum given by

$$P_\zeta(k) = \left[\left(\frac{H}{\dot\phi}\right)^2\left(\frac{H}{2\pi}\right)^2\right]_{k=aH} = 2\pi^2 k^{-3} A_s \left(\frac{k}{k_0}\right)^{n_s - 1 + \frac{1}{2}(dn_s/d\ln k)\ln(k/k_0)}. \tag{1.6}$$

In the second equality we have adopted the parametrization used in CMB analyses (e.g. ref. [285]) where A_s is the amplitude of the dimensionless power spectrum at some chosen pivot scale k_0 and n_s is the spectral tilt; a characteristic prediction of inflation is a nearly-scale invariant power spectrum with neglible running at second order in the slow-roll parameters

$$n_s - 1 = 2\eta - 6\epsilon, \quad \frac{dn_s}{d\ln k} = \mathcal{O}(\epsilon^2). \tag{1.7}$$

The resulting fluctuations would be mostly Gaussian, with any detections of non-Gaussianities shedding light on inflaton interactions and deviations from single-field inflation. Inflation also predicts tensor (gravitational-wave) fluctuations $P_t = 64\pi G(H/2\pi)^2_{k=aH}$ without the slow-roll enhancement and with a slight redward tilt $n_t = -2\epsilon$ and tensor-to-scalar ratio $r = 16\epsilon$. While these tensor perturbations will not concern us in the following their detection would yield a direct measurement of the energy scale of inflation and test of the slow-roll predictions for n_t and r, and indeed are one of the main drivers of next-generation CMB experiments.

With ingredients assembled from subfields of physics ranging from galactic rotation curves (dark matter) to supernovae (dark energy) to magnetic monopoles (inflation), the standard model of cosmology as laid out above makes very particular predictions for large scale structure which have been remarkably confirmed over the past two decades. After the end of inflation, the growth of the comoving Hubble radius resumes and the large-scale fluctuations generated become unfrozen as they enter the horizon in the radiation-dominated era. These unfrozen fluctuations then cause acoustic oscillations in the tightly-coupled photon-baryon fluid which, due to their starting from rest "in-phase", yield a coherent series of troughs and peaks in the power spectrum (e.g. [183, 329, 113]). Under the Friedmann equations the universe continues to expand and cool until the first hydrogen atoms form (recombination)

[5] We follow the conventions of the 2020 Particle Data Group Review [271].

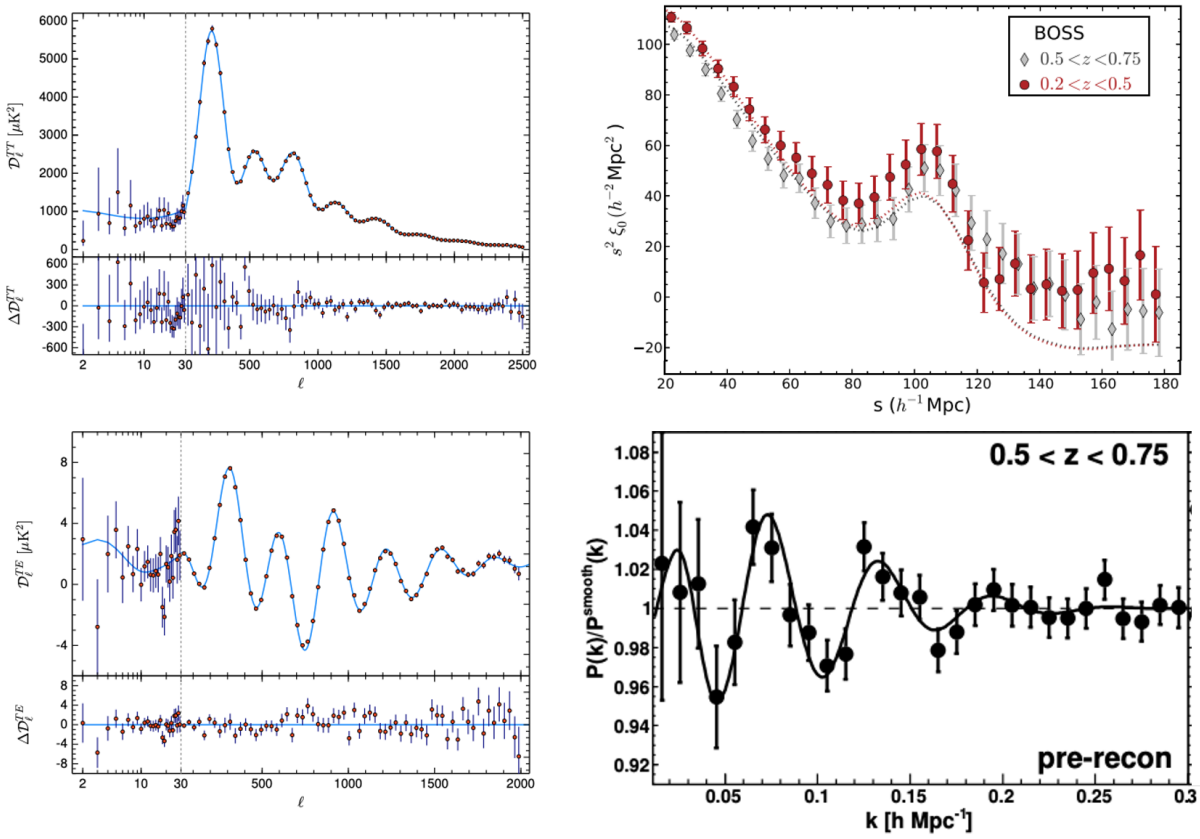

Figure 1.1: Evidence for acoustic oscillations in the primordial plasma. (Left) Angular power spectra of temperature and temperature-polarization cross correlations in the CMB as observed by the Planck satellite. The data are well-described by the standard cosmological model and broadly support the inflationary paradigm. Adapted from ref. [288]. (Right) Baryon acoustic oscillations imprinted in galaxy clustering, seen as an isolated peak at $r_{\rm BAO} \approx 100\,h^{-1}\,{\rm Mpc}$ in the correlation function monopole (top), or as wiggles with wavelengh $\approx 0.06\,h\,{\rm Mpc}^{-1}$ in the power spectrum (bottom), both measured from the BOSS survey. Together with the CMB these data are very suggestive of a flat ΛCDM cosmology. Figure adapted from refs. [307, 45].

and photons sufficiently decouple from baryons to free-stream. These free-streaming photons became the CMB we see today, with the observation of acoustic features in the CMB serving as dramatic confirmation of the predictions of the standard model and inflation. Indeed, high-precision measurements of the CMB temperature and polarization spectra (Fig. 1.1) reveal a universe at decoupling well-described by a flat universe and just six parameters—the physical baryon and cold dark matter densities $\Omega_{b,c}h^2$, the angular scale of the observed acoustic oscillations, the amplitude A_s and spectral tilt n_s of the scalar fluctuations, and the astrophysical optical depth to reionization τ—on which tight, (sub)percent level constraints can be obtained. The present-day Hubble parameter $H_0 = 100h$ km/s/Mpc and other commonly-defined parameters such as the amplitude of linear matter fluctuations on 8 h^{-1} Mpc scales σ_8 are deriveable from this set. Perhaps most remarkably, the CMB measures superhorizon fluctuations at multipoles $\ell \lesssim 200$, the spectral tilt to be close to but not equal to one ($n_s = 0.9649 \pm 0.0043$ from ref. [285]), the universe is flat to within errors, and the initial fluctuations to be essentially adiabatic and Gaussian, in dramatic confirmation of the inflationary paradigm.

The predictions of standard model do not end at the CMB. Post decoupling the acoustic oscillations seen in the CMB are frozen in, and their imprints in the observed clustering of galaxies, known as baryon acoustic oscillations (BAO) have been observed in galaxy surveys like BOSS [7]. Given that their physical scales $r_{\rm BAO} \approx 100h^{-1}$ Mpc are well-understood from CMB physics, BAO serve also as a standard ruler test of ΛCDM cosmology (Fig. 1.1). Beyond acoustic oscillations the growth of structure connecting the primordial curvature amplitude to the size of cosmic velocities and weak lensing observed in galaxy redshift and imaging surveys also paint a picture that is overall consistent with the standard model.

Despite its successes, however, in the past decade a growing number of cosmological surveys and analyses have begun to reveal potential cracks in the ΛCDM model. Probably the most well-known of these is the so-called Hubble tension, wherein the Hubble constant determined from supernovae measurements disagree with those from the CMB by 5σ [304]. Perhaps even more relevant for the purposes of this dissertation is the S_8-tension, wherein the measured clustering from weak lensing and redshift surveys seems to be weaker by around $2-3\sigma$ than implied from the CMB (see e.g. Section V in ref. [3] as well as Fig. 9.11 in Chapter 9). This tension is currently at less statistical significance than the Hubble tension but is notable for its encompassing of multiple LSS probes, all with different systematics, and its resolution or clarification on the theory side will have to rely squarely on the types of analytical methods we will develop in the following chapters. In parallel to homing in on tensions between different cosmological data sets it is also possible to investigate deviations from ΛCDM by constraining extensions to the base model such as deviations from dark energy away from a cosmological constant (e.g. [94]), early dark energy (e.g. [291]), features in the primordial spectrum due to inflation beyond slow roll [44], etc. While no conclusive detections of these extensions, or solutions to the above tensions, have been found to date, in order to robustly investigate these topics in light of the sharpened constraints upcoming surveys will offer it will be important to systematically build and test our models of structure formation in the most general way possible–this will be our task for the remainder of this

work.

1.2 Theory of Structure Formation

We begin by discussing the equations governing structure formation, treating dark matter and baryons as one dark matter fluid for now.[6] Throughout the rest of this dissertation we will limit our discussion to non-relativistic structure formation in the weak-field limit well within the horizon in the matter era, which is the regime where the late-time LSS observables we will consider reside; the linear theory of structure formation at earlier times as relevant for e.g. the CMB is a rich, well-studied subject and we will not quantitatively address it in any detail.[7] We will work in the conformal Newtonian gauge with only scalar perturbations on top of the FLRW background given by

$$ds^2 = -(1+2\Phi)dt^2 + a^2(t)(1-2\Psi)d\mathbf{x}^2, \quad \Phi = \Psi, \tag{1.8}$$

where the equality between the two potentials follows from the fact that we operate strictly in the non-relativistic regime, though we keep them separate in anticipation of applications to weak gravitational lensing.

1.2.1 From Vlasov to Fluid Equations

In the regime of interest the dynamics of collisionless dark matter are governed by the Vlasov equation

$$\frac{\mathrm{d}f(\mathbf{x},\mathbf{p})}{\mathrm{d}\tau} = \frac{\partial f}{\partial \tau} + \frac{\partial f}{\partial x_i}\frac{dx_i}{d\tau} + \frac{\partial f}{\partial p_i}\frac{dp_i}{d\tau} = 0 \tag{1.9}$$

where $f(\mathbf{x},\mathbf{p})$ denotes the phase-space distribution function of dark matter particles, such that e.g. the matter distribution is given by

$$\rho(\mathbf{x},\tau) = ma^{-3}\int d^3\mathbf{p}\; f(\mathbf{x},\mathbf{p}) \equiv \bar{\rho}(t)\;(1+\delta_m(\mathbf{x},\tau)). \tag{1.10}$$

and the gravitational potential Φ is given by Poisson's equation $\nabla^2_{\mathbf{x}}\Phi = 4\pi G a^2 \bar{\rho}\delta_m$. Here $p_i = ma\mathbf{v}$ is the *canonical* momentum and $\mathbf{v} = a\; dx/dt = dx/d\tau$ is the physical peculiar velocity, such that the particle equations of motion in phase space are given by

$$\frac{d\mathbf{x}}{d\tau} = \frac{\mathbf{p}}{ma}, \quad \frac{d\mathbf{p}}{d\tau} = -ma\nabla_{\mathbf{x}}\Phi. \tag{1.11}$$

We can set the initial conditions at early times when the dynamics are still linear, in which case the *single-stream* limit is valid

$$f(\mathbf{x},\mathbf{p}) = \frac{\rho(\mathbf{x})}{ma^{-3}}\;\delta_D\big(\mathbf{p} - ma\mathbf{v}(\mathbf{x})\big) \tag{1.12}$$

[6] The notation and much of the standard development in this section follows the excellent review in ref. [40].

[7] That dissertation has already been written by another Berkeley graduate.

where δ_D is the Dirac-delta function. In this regime particle velocities at a single point $\mathbf{x}$ are coherent, though as we will see this limit is broken by the onset of nonlinearities.

The Vlasov and Poisson equations fully describe structure formation in a dark-matter universe but are in general very hard to solve analytically. In order to make some traction it is customary to work instead in terms of the velocity moments of the distribution function, including the mean (comoving) number density n, the mean velocity $\mathbf{v}$ and the velocity dispersion σ_{ij}

$$\begin{aligned} n(\mathbf{x}) &= \int d^3\mathbf{p}\ f(\mathbf{x},\mathbf{p}) \equiv ma^{-3}\rho(\mathbf{x}), \\ n(\mathbf{x})\mathbf{v}(\mathbf{x}) &= \int d^3\mathbf{p}\ \frac{\mathbf{p}}{ma} f(\mathbf{x},\mathbf{p}), \\ n(\mathbf{x})\big(v_i v_j + \sigma_{ij}(\mathbf{x})\big) &= \int d^3\mathbf{p}\ \frac{p_i p_j}{m^2 a^2} f(\mathbf{x},\mathbf{p}), \end{aligned} \tag{1.13}$$

and so on. The moments of Equation 1.9 give the continuity and Euler equations of fluid mechanics

$$\begin{aligned} &\frac{\partial n}{\partial \tau} + \nabla_{\mathbf{x}} \cdot \big(n\mathbf{v}\big) = 0 \\ &\frac{dv_i}{d\tau} + \mathcal{H} v_i + v_j \nabla_{\mathbf{x},j} v_i = -\nabla_{\mathbf{x},i}\Phi - \frac{1}{n}\nabla_{\mathbf{x},j}\big(n\sigma_{ij}\big). \end{aligned} \tag{1.14}$$

At this point it seems impossible to continue without knowledge of the evolution of the stress tensor $n\sigma_{ij}$, which would involve taking the third moment of the Vlasov equation, which would involve the fourth moment... and so on. Alternatively, it is possible to "close" the hierarchy by assuming an ansatz for $n\sigma_{ij} = c_0\delta\delta_{ij} + c_1(\partial_i v_j + \partial_j v_i) + c_2\delta_{ij}\partial_i v_i + ...$ where the coefficients c_n correspond to pressure and viscosity [40]. We will return to the physical origin of these coefficients shortly, but for now we note that in the single-stream limit (Eqn. 1.12) the velocity dispersion vanishes and we have, swapping in δ for n,

$$\begin{aligned} &\frac{\partial \delta}{\partial \tau} + \nabla_{\mathbf{x}} \cdot \big((1+\delta)\mathbf{v}\big) = 0 \\ &\frac{dv_i}{d\tau} + \mathcal{H} v_i + v_j \nabla_{\mathbf{x},j} v_i = -\nabla_{\mathbf{x},i}\Phi. \end{aligned} \tag{1.15}$$

These are the fundamental equations governing Eulerian perturbation theory (EPT), also commonly known as "standard" perturbation theory (SPT).

Alternatively to the Eulerian picture presented above it is possible to solve the Vlasov equation within the Lagrangian formalism of fluid mechanics, where the dynamics are described in terms of the displacements of infinitesimal fluid elements. When the initial conditions are single-stream (Eqn. 1.12) they can be characterized entirely by fluid elements at initially uniform Lagrangian positions $\mathbf{q}$ with displacements Ψ such that their positions at conformal time τ are given by

$$\mathbf{x}(\mathbf{q},\tau) = \mathbf{q} + \Psi(\mathbf{q},\tau). \tag{1.16}$$

In this case the equation of motion equivalent to Equations 1.11 are simply given by

$$\frac{d^2\Psi}{d\tau^2} + \mathcal{H}\frac{d\Psi}{d\tau} = -\nabla_{\mathbf{x}}\Phi. \tag{1.17}$$

The overdensity sourcing the potential is given by number conservation to be [231]

$$1 + \delta(\mathbf{x}, \tau) = \int d^3\mathbf{q}\ \delta_D\big(\mathbf{x} - \mathbf{q} - \Psi(\mathbf{q}, \tau)\big) = \frac{1}{|\det\big[\delta_{ij} + \Psi_{i,j}\big]|}. \tag{1.18}$$

These are the governing equations of Lagrangian perturbation theory (LPT). It is important to note that, unlike those for EPT, the equations above are valid beyond the single-stream regime, save for the last equality in Equation 1.18 which would have to be summed over any solutions of the delta function. Stream crossing in the Lagrangian picture simply corresponds to instances where the map $\mathbf{q} \to \mathbf{x}$ is many-to-one, so that the dynamics at at a given point $\mathbf{x}$ no longer corresponds to a single $\mathbf{q}$ and it is no longer possible to do perturbation theory about a single point. Nonetheless, even beyond stream crossing the Vlasov equation and Equation 1.17 are completely equivalent and analytic solutions for Ψ beyond shell crossing show excellent agreement with numerical solutions to the Vlasov Equations [365, 297].

The equations of motion above admit a simple symmetry due to the diffeomorphism invariance of general relativity called *generalized Galilean invariance* [198, 277, 91]. This symmetry is especially simple in Lagrangian coordinates [179]: given a time-dependent but spatially constant vector field $\mathbf{n}(\tau)$, the transformation

$$\Psi(\tau) \to \Psi(\tau) + \mathbf{n}(\tau), \quad \Phi \to \Phi - \left(\frac{d^2\mathbf{n}}{d\tau^2} + \mathcal{H}\frac{d\mathbf{n}}{d\tau}\right) \cdot \mathbf{x}. \tag{1.19}$$

This symmetry naturally includes the normal Galilean transformations of translations and boosts. As we will see, a nice feature of LPT is that it will be easy to compute N-point functions in a way that explicitly satisfies this symmetry. It is worth noting that if the vector $\mathbf{n}$ satisfies the linearized equation of motion (see subsection below)

$$\frac{d^2\mathbf{n}}{d\tau^2} + \mathcal{H}\frac{d\mathbf{n}}{d\tau} = 4\pi G a^2 \bar{\rho}_m \mathbf{n} \tag{1.20}$$

then the generalized Galilean transformation it generates is equivalent to the dynamical effect of an evolving long-wavelength mode in the background [180]; this fact can be used to derive consistency relations for LSS in inflationary universes with adiabatic initial conditions [91].

1.2.2 Linear Theory

Let us first consider the dynamics at linear order, that is to say at first order in the perturbations from uniformity $(\delta, \mathbf{v}, \Phi, \Psi)$. Dropping the nonlinear quantities including the

stress tensor in Equation 1.15 we obtain

$$\frac{\partial \delta}{\partial \tau} + \theta = 0,$$
$$\frac{dv_i}{d\tau} + \mathcal{H} v_i = -\nabla_{\mathbf{x},i}\Phi, \quad \nabla^2_{\mathbf{x}}\Phi = \frac{3}{2}\mathcal{H}^2\Omega_m(\tau)\delta$$

where we have defined the matter density fraction at τ by $\Omega_m(\tau) = \rho_m(\tau)/\rho_{\rm crit}(\tau)$. It is convenient to work in terms of the divergence $\theta = \nabla_{\mathbf{x}} \cdot \mathbf{v}$ and curl $\mathbf{w} = \nabla_{\mathbf{x}} \times \mathbf{v}$. It is straightforward to show that the latter decays as a function of time, and more generally from Equation 1.15 that irrotational initial conditions as in our case do not generate $\mathbf{w}$ when $\sigma_{ij} = 0$.

To isolate the dynamics of longtitudinal part we take the divergence of the Euler equation and use the continuity equations to give

$$\frac{d^2\delta}{d\tau^2} + \mathcal{H}\frac{d\delta}{d\tau} = \frac{3}{2}\mathcal{H}^2\Omega_m(\tau)\delta. \tag{1.21}$$

This second-order differential equation admits a growing and a decaying mode $\delta_{\rm lin}(\tau) = D(\tau)\delta_+ + D_-(\tau)\delta_-$, where in a flat ΛCDM cosmology the growing and decay modes are given respectively by

$$D(\tau) = H(a)\int_0^a \frac{da'}{a'^3 H(a')}, \; D_-(\tau) = H(a). \tag{1.22}$$

It is conventional to normalize the growth factor such that it is equal to unity at the present. In what follows we will drop the decaying mode, which is negligible at the times we will work in. In this case the velocity divergence is given by

$$\theta_{\rm lin}(\tau) = -f(a)\mathcal{H}\ \delta_{\rm lin}(\tau) \tag{1.23}$$

where the linear growth rate is defined to be $f(a) = d\ln D/d\ln a$. Within matter domination the growth factor and rate admit the simple forms $D(a) = a$ and $f(a) = 1$.

We can also perform the same analysis in Lagrangian space. To leading order we have $\nabla_{\mathbf{q}} = \nabla_{\mathbf{x}}$, so Equation 1.18 implies that $\delta = -\nabla \cdot \Psi$, from which it is straightforward to see that the divergence and curl of Ψ in $\mathbf{q}$-space satisfies the same linear equation as δ and $\mathbf{w}$.[8] Discarding the curl and decaying mode we get $\Psi = -\nabla^{-1}\delta$, or in Fourier space

$$\Psi(\mathbf{k}, \tau) = \frac{i\mathbf{k}}{k^2} D(\tau)\delta_0(\mathbf{k}) \tag{1.24}$$

where δ_0 is the linear overdensity evaluated at $D = 1$. This first-order solution is known as the Zeldovich approximation. It is exact in one dimension until shell crossing, as can be seen in Figure 1.2. Unlike linear theory in EPT, which simply scales the linear density field

[8]Note, however, that displacements Ψ will generically develop vorticity in $\mathbf{q}$ space [230] even if the flow in Eulerian $\mathbf{x}$ space remains irrotational.

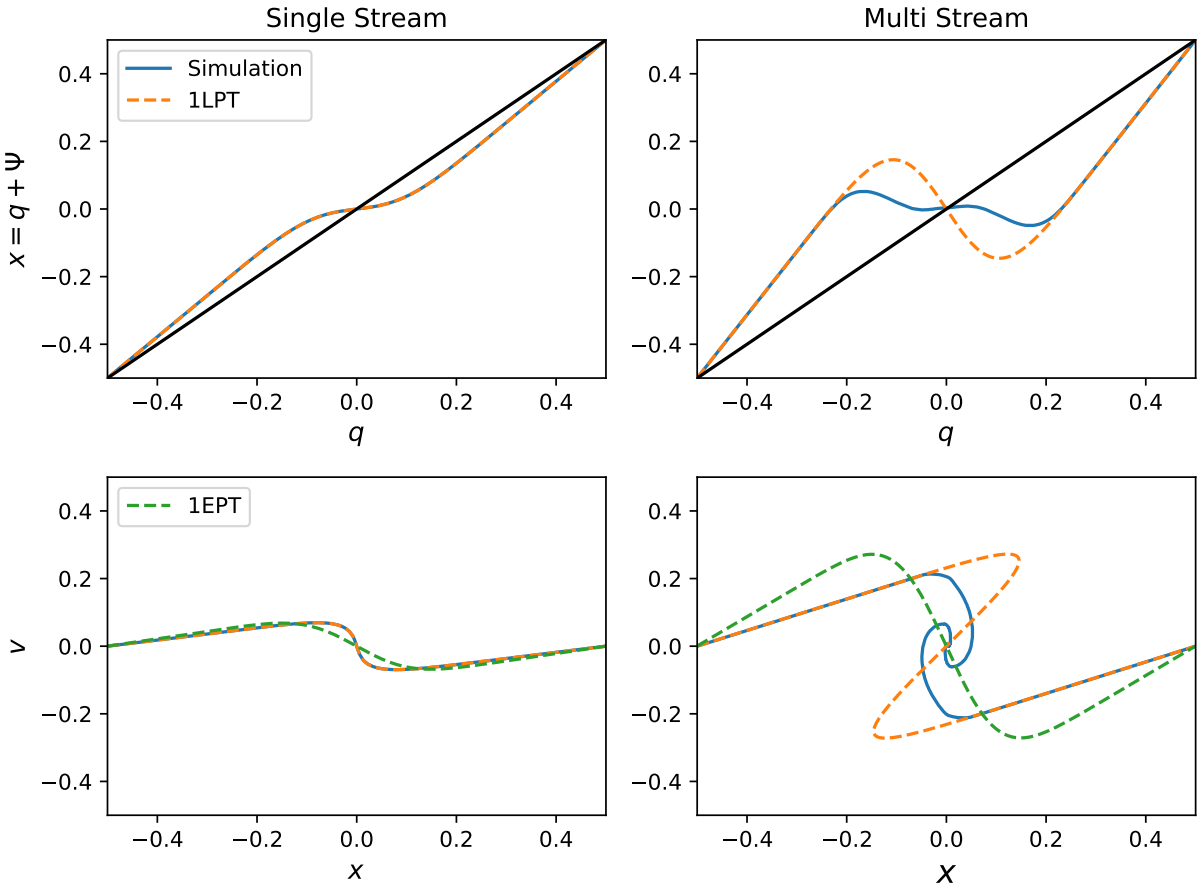

Figure 1.2: Results of an N-body simulation of the Vlasov equation in one dimension compared to linear-theory predictions using Lagrangian (orange) and Eulerian (green) perturbation theory. The top row shows the mapping from initial $\mathbf{q}$ to final $\mathbf{x}$ positions in the N-body simulation and LPT, while the bottom row shows the phase space distribution. In the single-stream regime (left), the Zeldovich approximation (1LPT) is exact, but once stream crossing occurs (right) the Zeldovich particles simply stream past each other, unlike in the N-body simulation where they turn around and gravitationally collapse.

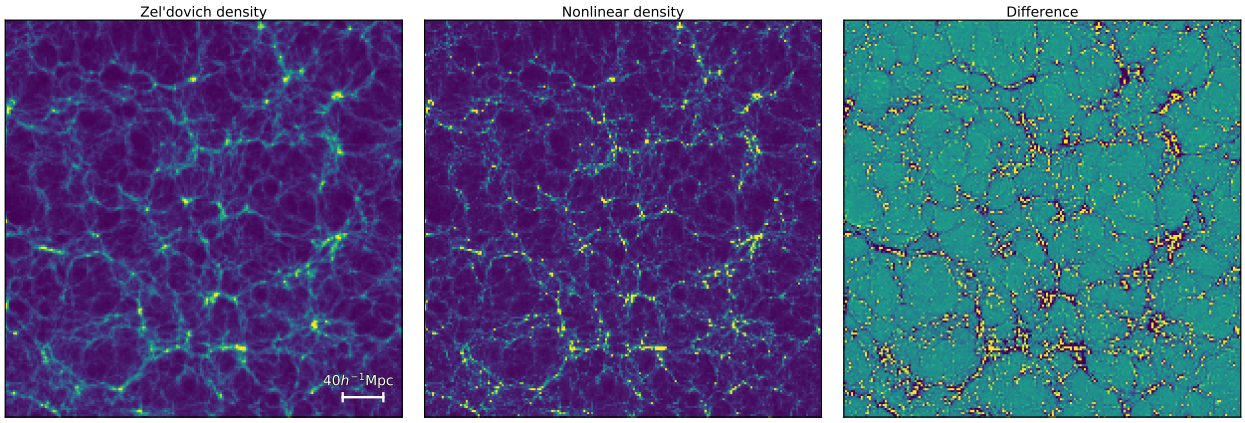

Figure 1.3: Comparison of the Zeldovich approximation vs. the full solution of the Vlasov equations by N-body simulations. The Zeldovich approximation makes qualitatively excellent predictions of the structure of the cosmic web but, as expected, fails to capture the formation of halos and nonlinear collapse. Figure based on data from the Quijote simulations [394] taken from ref. [205].

over time by a scale-independent factor D, the Zeldovich approximation predicts nontrivial distortions $J_{ij} = dx_i/dq_j = \delta_{ij} + \Psi_{i,j}$ that qualitatively explain the filamentary structure of LSS known as the "cosmic web" seen in more exact solutions to the Vlasov problem (Fig 1.3), though it tends to generate puffier structures due to particles moving in a straight line even after shell crossing instead of turning around and collapsing, as can be seen in Figure 1.2.

1.2.3 Beyond Linear Theory: Perturbation Theory Kernels

We are now in a position to formulate the perturbation theory of structure formation. Within PT the formation of structure is computed order-by-order in the initial conditions, e.g. $\delta(\mathbf{x},\tau) = \delta^{(1)} + \delta^{(2)} + \delta^{(3)} + ...$ where the superscripts denote the perturbative order. Separating the linear and nonlinear parts of Equation 1.15 we get in Fourier space

$$\frac{\partial\delta(\mathbf{k},\tau)}{\partial\tau} + \theta(\mathbf{k},\tau) = -\int \frac{d^3\mathbf{p}}{(2\pi)^3}\ \alpha(\mathbf{p},\mathbf{k}-\mathbf{p})\ \theta(\mathbf{p})\delta(\mathbf{k}-\mathbf{p})$$
$$\frac{\partial\theta(\mathbf{k},\tau)}{\partial\tau} + \mathcal{H}\theta(\mathbf{k},\tau) + \frac{3}{2}\mathcal{H}^2\Omega_m(\tau)\delta(\mathbf{k},\tau) = -\int \frac{d^3\mathbf{p}}{(2\pi)^3}\ \beta(\mathbf{p},\mathbf{k}-\mathbf{p})\ \theta(\mathbf{p})\theta(\mathbf{k}-\mathbf{p})$$

where the kernels are defined as

$$\alpha(\mathbf{k}_1,\mathbf{k}_2) = \frac{\mathbf{k}_{12}\cdot\mathbf{k}_1}{k_1^2},\ \beta(\mathbf{k}_1,\mathbf{k}_2) = \frac{k_{12}^2(\mathbf{k}_1\cdot\mathbf{k}_2)}{2k_1^2k_2^2},\ \mathbf{k}_{12} = \mathbf{k}_1 + \mathbf{k}_2. \tag{1.25}$$

From the above we can see that the n$^{\text{th}}$ order solutions $\delta^{(n)}, \theta^{(n)}$ are simply governed by non-homogeneous differential equations whose homogeneous counterpart is given by the linear

equations of motion we already derived, with products of lower-order solutions acting as sources. In this way solving the linear equations of motion gives you the ones at quadratic order, which gives you the cubic ones, etc. Indeed, we can pull the same trick as we did in the linear case and substitute θ for the time derivative of δ to get

$$\frac{\partial^2\delta^{(n)}(\mathbf{k},\tau)}{\partial\tau^2} + \mathcal{H}\frac{\partial\delta^{(n)}(\mathbf{k},\tau)}{\partial\tau} - \frac{3}{2}\mathcal{H}^2\Omega_m(\tau)\delta^{(n)}(\mathbf{k},\tau) = F\left[\delta^{(m<n)}, \theta^{(m<n)}\right]$$

where F is a time-dependent source term due to lower-order solutions. This equation can be straightforwardly solved by a retarded Green's function given in terms of the linear solutions found earlier [60, 230, 128] (see Appendix A.2 for an example calculation).

We can similarly derive the equations of motion for LPT. Again, we can take the (Eulerian) divergence and curl of the displacement field to get

$$\nabla_{\mathbf{x}} \cdot \left(\frac{\partial^2\Psi(\mathbf{q},\tau)}{\partial\tau^2} + \mathcal{H}\frac{\partial\Psi(\mathbf{q},\tau)}{\partial\tau}\right) = -\frac{3}{2}\mathcal{H}^2\Omega_m(\tau)\delta(\mathbf{x})$$
$$\nabla_{\mathbf{x}} \times \left(\frac{\partial^2\Psi(\mathbf{q},\tau)}{\partial\tau^2} + \mathcal{H}\frac{\partial\Psi(\mathbf{q},\tau)}{\partial\tau}\right) = 0.$$

To make further progress we need to write these equations solely in terms of the Lagrangian coordinate $\mathbf{q}$ using $\nabla_{\mathbf{x}_i} = (\partial\mathbf{x}_i/\partial\mathbf{q}_j)^{-1}\nabla_{\mathbf{q}_j} = (\delta_{ij} + \Psi_{i,j})^{-1}\nabla_{\mathbf{q}_j}$. This gives equations of the form [230]

$$\frac{\partial^2\Psi_{i,i}}{\partial\tau^2} + \mathcal{H}\frac{\partial\Psi_{i,i}}{\partial\tau} - \frac{3}{2}\mathcal{H}^2\Omega_m(\tau)\Psi_{i,i} = F\left[\nabla\Psi\otimes\nabla\Psi, \nabla\Psi\otimes\nabla\Psi\otimes\nabla\Psi\right]$$
$$\frac{\partial^2(\nabla\times\Psi)}{\partial\tau^2} + \mathcal{H}\frac{\partial(\nabla\times\Psi)}{\partial\tau} = \left(\nabla\Psi_i\right)\times\nabla\left(\frac{\partial^2\Psi_i}{\partial\tau^2} + \mathcal{H}\frac{\partial\Psi_i}{\partial\tau}\right) \tag{1.26}$$

where all partial derivatives are with respect to $\mathbf{q}$. From this we can immediately draw two lessons: (a) the equation for the divergence $\Psi_{i,i}$ can be solved for order-by-order using the same Green's function as in the Eulerian case and (b) the vorticity can be dynamically generated at higher order even for irrotational initial conditions, unlike in Euclidean space, though no vorticity is generated at second order.[9] The second order solution is derived as an example in Appendix A.2.

In the above we have laid out the construction of perturbative solutions of structure formation in fairly general terms. However, for the case of a matter dominated, i.e. Einstein-de Sitter (EdS) universe the equations of motion admit a particularly simple solution. In particular, in such a universe we have $D \propto a$ and, writing the equations of motion of LPT or EPT in terms of $\ln(D)$ we find that the coefficients of the differential equation become time-independent and admit solutions which are series expansions in the growth factor, i.e.

[9] Note that this does not mean that the fluid flow itself is not irrotational once we convert to $\mathbf{x}$ coordinates, and in fact the dominant growing mode we will discuss next is given by a potential flow as shown in ref. [230].

for EPT

$$\delta^{(n)}(\mathbf{k},\tau) = \int \frac{d^3\mathbf{p}_1}{(2\pi)^2}...\frac{d^3\mathbf{p}_1}{(2\pi)^2}\ F_n(\mathbf{p}_1,...,\mathbf{p}_n)\ \delta_{\rm lin}(\mathbf{p}_1)...\delta_{\rm lin}(\mathbf{p}_n)\ \delta_D(\mathbf{k}-\sum_i \mathbf{p}_i)$$
$$\theta^{(n)}(\mathbf{k},\tau) = -f\mathcal{H}\int \frac{d^3\mathbf{p}_1}{(2\pi)^2}...\frac{d^3\mathbf{p}_1}{(2\pi)^2}\ G_n(\mathbf{p}_1,...,\mathbf{p}_n)\ \delta_{\rm lin}(\mathbf{p}_1)...\delta_{\rm lin}(\mathbf{p}_n)\ \delta_D(\mathbf{k}-\sum_i \mathbf{p}_i) \quad (1.27)$$

and similarly for LPT

$$\Psi_i^{(n)} = \frac{i}{n!}\int \frac{d^3\mathbf{p}_1}{(2\pi)^2}...\frac{d^3\mathbf{p}_1}{(2\pi)^2}\ L_i^{(n)}(\mathbf{p}_1,...,\mathbf{p}_n)\ \delta_{\rm lin}(\mathbf{p}_1)...\delta_{\rm lin}(\mathbf{p}_n)\ \delta_D(\mathbf{k}-\sum_i \mathbf{p}_i), \quad (1.28)$$

as long as the initial conditions are decaying-mode free. Here we have used the abbreviation for the linear overdensity at time τ: $\delta_{\rm lin}(\mathbf{p}) = D(\tau)\delta_0(\mathbf{p})$ where δ_0 is the initial linear overdensity normalized so that the present-day growth factor is equal to unity. Remarkably, within an EdS universe perturbative solutions to the growth factor can be found using the linearly evolved overdensity at the same time $\delta_{\rm lin}(\mathbf{p})$ alone. The EdS approximation turns out to be an excellent one even in our (at least approximately) ΛCDM universe—our universe has spent a large portion of its lifetime in matter domination, so that deviations from EdS in the late universe only produce small deviations from the EdS ansatz, well within the precision required by current or future cosmlogical surveys [128, 115]. In fact, the EdS approximation can be thought of as an expansion in $\Omega_m(\tau)/f^2(\tau) - 1$, which is well-justified since $f \approx \Omega_m^{0.55}$ in our universe [40, 230, 114]. We list the EPT and LPT kernels up to third order in Appendix A.1 and show how to relate the EdS and Green's functions approaches in Appendix A.2.

1.2.4 Beyond Linear Theory: N-Body Simulations

The focus of this section has been to develop the perturbative solution of structure formation within the Eulerian and Lagrangian frameworks. However, it is important to emphasize that these are approximate solutions that are only valid in the single-stream limit where $\sigma_{ij} = 0$ and the mapping $\mathbf{x}(\mathbf{q})$ is one-to-one. In §1.3 we will discuss ways in which this incompleteness can be analytically addressed, but before we move on it is worth briefly discussing how how the Vlasov system can be solved to arbitrary precision *numerically* using N-body simulations.

The Vlasov equation (Eqn. 1.9) is essentially an expression of number conservation in phase space. The strategy of N-body simulations is thus to sample the phase space $(\mathbf{x},\mathbf{p})$ with N particles or phase-space elements according to the initial conditions and evolve them under the Hamiltonian equations of motion (Eqn. 1.11). In fact, since the initial conditions are single-stream it is sufficient to initialize the system at a grid of initial positions $\mathbf{q}$ with small initial displacements $\Psi(\mathbf{q})$ and velocities $\dot{\Psi}(\mathbf{q})$, i.e. the initial distribution occupies a 3-dimensional surface in phase-space (see ref. [295] for further discussion). Since the initial conditions are set up on a grid they can possess anomalous structure at the resolution scale—in general it is thus desirable to set up initial conditions when sufficient structure

has formed to make this anomalous contribution subdominant, though sufficiently early that the initial conditions, typically set up using LPT, are still valid. On this front there has been much fruitful cross-pollination between the PT and numerical communities, not just in setting up higher-order PT initial conditions [92, 157] but also extending them to multiple fluids [298] (see also Chapter 5) and neutrinos [124].

N-body simulations thus solve the same dynamical system as the equations of LPT; the difference between the two approaches lies in the fact that perturbative approaches typically assume a 1-to-1 mapping between initial and final positions. As discussed earlier, it is not impossible to construct solutions to LPT beyond stream crossing by summing over multiples solutions to $\mathbf{x} = \mathbf{x}(\mathbf{q})$, but as we go deeper into the multi-streaming regime this becomes increasingly cumbersome. On the other hand, within N-body simulations the solution is quite straightforward: at each particle position $\mathbf{x} = \mathbf{q} + \Psi(\mathbf{q})$ one can simply compute the gravitational force by summing over the inverse square law contributions from each particle in the simulation. This operation naively scales as N^2 and is quite expensive for large numbers of particles, but various numerical techniques, such as Tree or Particle-Mesh codes, have been developed which significantly speed up the force evaluations. Since the purpose of this dissertation is mainly to explore analytical models of structure formation, with N-body simulations used mostly for theory validation, we will not try to describe the details of N-body simulations in any further detail. For a recent comparison of various N-body techniques and demonstration of the impressive accuracy they can achieve, the reader is directed to ref. [152].

1.3 From Fields to Statistics

The standard model of cosmology as laid out in § 1.1 describes the initial conditions of the early universe statistically as a Gaussian random field seeded by inflationary quantum fluctuations. For this reason, by necessity most cosmological analyses study not the particular configuration of LSS we observe but rather its statistics.

In this dissertation we are primarily interested in analyzing structure formation on large, quasilinear scales. In this regime deviations from Gaussianity are relatively small and most of the cosmological signal is encoded in the 2-point, or correlation, function

$$\xi(\mathbf{r}) = \langle \delta(\mathbf{r}_1)\delta(\mathbf{r}_2)\rangle_{\mathbf{r}=\mathbf{r}_1-\mathbf{r}_2}. \tag{1.29}$$

The fact that ξ is only a function of the separation $\mathbf{r}$ is a consequence of translation invariance. In the absence of observational effects cosmological correlations are also rotationally invariant, so that $\xi(\mathbf{r}) = \xi(r)$; in Chapter 2 we will discuss the 2-pt function observed in spectroscopic surveys wherein line-of-sight velocities break isotropy along the line-of-sight. The 2-pt function in Fourier space is called the power spectrum, defined as

$$\langle \delta(\mathbf{k}_1)\delta(\mathbf{k}_2)\rangle = P(\mathbf{k}_1)\ (2\pi)^3\delta_D(\mathbf{k}_1 + \mathbf{k}_2). \tag{1.30}$$

Here translational invariance is enforced by the delta function and rotational invariance implies $P(\mathbf{k}) = P(k)$. The power spectrum and correlation function are Fourier transforms of

each other, $\xi(\mathbf{r}) = \int d^3\mathbf{x}\ P(\mathbf{k})\ e^{i\mathbf{k}\cdot\mathbf{r}}$. Beyond the 2-pt functions many higher-order statistics have been investigated as potential sources of additional information. A chief example is the 3-point function, or bispectrum, defined as

$$\langle\delta(\mathbf{k}_1)\delta(\mathbf{k}_2)\delta(\mathbf{k}_3)\rangle = B(\mathbf{k}_1,\mathbf{k}_2)\ (2\pi)^3\delta_D(\mathbf{k}_1+\mathbf{k}_2+\mathbf{k}_3). \tag{1.31}$$

The galaxy bispectrum was recently shown to yield modest improvements when combined with the power spectrum in ref. [282].

In the rest of this section our goal will be to sketch out the basic technology required to compute the matter two-point function within perturbation theory. This will lead the way to more detailed calculations for galaxies in the following chapters, in particular the computation of real-space density and velocity spectra in Chapter 2.

1.3.1 The 1-loop Matter Power Spectrum

Let us first consider the linear-theory prediction for the matter power spectrum as a warm-up. Within linear theory each Fourier mode $\delta(\mathbf{k})$ evolves independently and can be connected to the primordial curvature perturbation due to inflation ζ by a multiplicative factor called the transfer function $T_m(\mathbf{k},\tau)$. This transfer function characterizes the growth of structure both during and before the period of matter domination we have focused on so far; for our purposes we can think of the transfer function as setting the initial conditions for structure formation after radiation domination and decoupling at some time τ_i when linear growth becomes scale-independent such that

$$\delta^{(1)}(\mathbf{k},\tau) = T_m(\mathbf{k},\tau)\zeta(\mathbf{k}) = \frac{D(\tau)}{D(\tau_i)}\delta_m^{(1)}(\mathbf{k},\tau_i) = D(\tau)\delta_{m,0}^{(1)}(\mathbf{k}) \tag{1.32}$$

where $\delta_{m,0}^{(1)}$ is the present-day linear matter overdensity. The above equalities assume that any decaying modes can be neglected. Of course, structure formation is not truly scale independent even at the present epoch due to the presence of free-streaming massive neutrinos— in order to match our linear theory prediction to solutions of the linearized Boltzmann equation we use the full transfer function obtained from Boltzmann codes such as CAMB [220] or CLASS [48] to compute $\delta_{\rm lin}(\mathbf{p})$ in the perturbative expansions in Equations 1.27 and 1.28. In any case, since linear evolution amounts to a simple, if scale-dependent, rescaling of a Gaussian field (Eqn.1.6), the linear-theory prediction for the matter power spectrum is simply

$$\langle\delta^{(1)}(\mathbf{k})\delta^{(1)}(\mathbf{k}')\rangle = T_m(k,\tau)^2P_\zeta(k)(2\pi)^3\delta_D(\mathbf{k}+\mathbf{k}') \equiv P_{\rm lin}(k,\tau)(2\pi)^3\delta_D(\mathbf{k}+\mathbf{k}'). \tag{1.33}$$

In what follows we will drop the conformal time argument since we will always be operating at equal times.

In order to make further progress we need to make use of Wick's theorem for Gaussian random fields, which states that the expectation value of the product of n Gaussian fields with zero mean f_i is equal to the sum of the products of all possible pairs, i.e.

$$\langle f_{i_1}f_{i_2}...f_{i_n}\rangle = \sum_{p_\alpha\in P}\prod_{(i_a,i_b)\in p_\alpha} C_{i_ai_b}, \quad C_{ij} = \langle f_if_j\rangle, \tag{1.34}$$

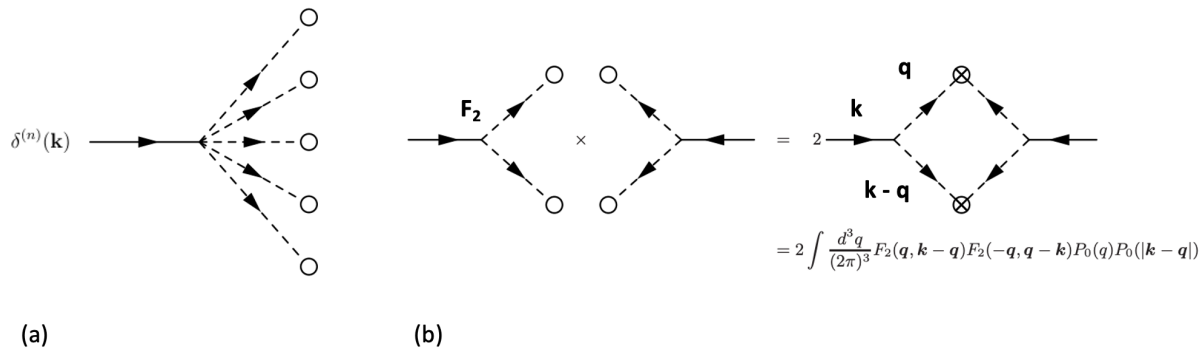

Figure 1.4: Feynman diagram representations of perturbation theory solutions. (a) The n$^{\text{th}}$ order solution to the matter overdensity represented as a vertex where the incoming mode $\mathbf{k}$ is sourced by n (in this case five) outgoing linear modes $\mathbf{q}_i$ denoted with open circles. (b) The (22) contribution to the 1-loop power spectrum. Each linear mode can be contracted with another to yield a factor of the linear power spectrum, here denoted P_0. Figure adapted from ref. [59].

where P is the set of all partitions of $i_1, ..., i_n$ into pairs and p_α is a particular partition. The expectation value is zero for odd numbers of fields.[10]

From the above statement of Wick's theorem we can see that the next-to-leading contribution to the power spectrum after linear theory has to come from two pairs of linear fields $\delta_{\rm lin}(\mathbf{p})$. There are exactly two such contributions

$$\langle \delta(\mathbf{k})\delta(\mathbf{k}')\rangle \ni 2\langle \delta^{(1)}\delta^{(3)}\rangle, \langle \delta^{(2)}\delta^{(2)}\rangle. \tag{1.36}$$

These can be diagrammatically represented as Feynman diagrams, as shown in Figure 1.4. The important feature is that fields linked by Wick contraction have their momenta forced to sum to zero by the delta function in Equation 1.33.

The matter power spectrum up to 1-loop order in EPT, then, is given by $P(k) = P_{\rm lin}(k) + 2P^{(13)}(k) + P^{(22)}(k)$ where we have defined

$$\begin{aligned} P^{(13)}(k) &= 3P(k)\int \frac{d^3\mathbf{p}}{(2\pi)^3}\, F_3(\mathbf{p}, -\mathbf{p}, \mathbf{k}) P_{\rm lin}(\mathbf{p}) \\ P^{(22)}(k) &= 2\int \frac{d^3\mathbf{p}}{(2\pi)^3}\, F_2(\mathbf{p}, \mathbf{k}-\mathbf{p})^2 P_{\rm lin}(\mathbf{p}) P_{\rm lin}(\mathbf{k}-\mathbf{p}) \end{aligned} \tag{1.37}$$

[10] Wick's theorem is straightforward to prove by considering the generating function for an N-dimensional Gaussian variable

$$F(J) = \frac{1}{\mathcal{N}}\int d^N\mathbf{f}\, e^{-\frac{1}{2}f_i f_j C_{ij}^{-1} + f_i J_i} = e^{J_i J_j C_{ij}/2}. \tag{1.35}$$

The expectation value of n fields can be obtained by taking partial derivatives $\partial/\partial J_i$. Taylor expanding $F(J) = \sum_{m=0}^{\infty}(J_i J_j C_{ij})^m/2^m m!$ we see that the combinatorial factors exactly account for the number of degeneracies with unordered sets of m unordered pairs. As a byproduct we also get the cumulant theorem for Gaussian fields, i.e. $\langle e^{f_i}\rangle = e^{C_{ii}/2}$.

where the numbers in brackets indicate the orders of solutions that each contribution is combined from. The mulitplicative factors of 2 and 3 come from the numbers of distinct Wick contractions. We will return to the physical interpretation of these expressions in the following two subsections.

The equivalent expression in Lagrangian perturbation theory only requires a little more work. Fourier transforming Equation 1.18 we have that

$$\delta(\mathbf{k}) = \int d^3\mathbf{q}\; e^{i\mathbf{k}\cdot\mathbf{q}}\Big(e^{i\mathbf{k}\cdot\Psi(\mathbf{q})} - 1\Big), \tag{1.38}$$

implying that the power spectrum is given by

$$P(k) = \int d^3\mathbf{q}\; e^{i\mathbf{k}\cdot\mathbf{q}}\Big(\langle e^{i\mathbf{k}\cdot\Delta}\rangle_{\mathbf{q}=\mathbf{q}_1-\mathbf{q}_2} - 1\Big), \quad \Delta = \Psi(\mathbf{q}_1) - \Psi(\mathbf{q}_2). \tag{1.39}$$

A nice feature of this equation is that, phrased in this way, the power spectrum is manifestly invariant under generalized Galilean transformations (Eqn. 1.19). This feature is much more subtle in EPT, as we will see.

Let us begin once again with the prediction of linear theory, i.e. the Zeldovich approximation (ZA). Within ZA the pairwise displacement Δ is Gaussian, and we can use the cumulant theorem (see footnote 10) to evaluate the power spectrum exactly

$$P_{\rm Zel}(k) = \int d^3\mathbf{q}\; e^{i\mathbf{k}\cdot\mathbf{q}}\Big(e^{-\frac{1}{2}k_ik_jA^{\rm lin}_{ij}(\mathbf{q})} - 1\Big), \quad A^{\rm lin}_{ij}(\mathbf{q}) = \langle\Delta^{(1)}_i\Delta^{(1)}_j\rangle. \tag{1.40}$$

While this expression reduces to $P_{\rm lin}(k)$ for sufficiently small k, as can be straightforwardly shown by expanding the exponential to first order, unlike in the case of EPT at first order it is not linear in initial conditions and carries significant information about nonlinear processes in structure formation, a point we will return to soon.

Going beyond linear theory, we have that

$$\langle e^{i\mathbf{k}\cdot\Delta}\rangle = \exp\Big[-\frac{1}{2}k_ik_jA_{ij}(\mathbf{q}) - \frac{i}{6}k_ik_jk_kW_{ijk}(\mathbf{q}) + ...\Big] \tag{1.41}$$

where we have generally defined [58] $\mathbf{A} = \langle\Delta\Delta\rangle$ and $\mathbf{W} = \langle\Delta\Delta\Delta\rangle$. At one-loop order these moments of the pairwise displacement Δ receive contributions

$$\begin{aligned} A_{ij}(\mathbf{q}) &= A^{\rm lin}_{ij}(\mathbf{q}) + A^{\text{1-loop}}_{ij}(\mathbf{q}),\; A^{\text{1-loop}}_{ij}(\mathbf{q}) = 2A^{(13)}_{ij}(\mathbf{q}) + A^{(22)}_{ij}(\mathbf{q}) \\ W_{ijk}(\mathbf{q}) &= W^{(112)}_{ijk} + W^{(121)}_{ijk} + W^{(211)}_{ijk}. \end{aligned} \tag{1.42}$$

Explicit expressions for these quantities are given in Appendix A.3. From the above we have that the power spectrum is given up to this order by

$$P(k) = \int d^3\mathbf{q}\; e^{i\mathbf{k}\cdot\mathbf{q}-\frac{1}{2}k_ik_jA^{\rm lin}_{ij}(\mathbf{q})}\Big(1 - \frac{1}{2}k_ik_jA^{\text{1-loop}}_{ij}(\mathbf{q}) - \frac{i}{6}k_ik_jk_kW_{ijk}(\mathbf{q})\Big). \tag{1.43}$$

In the above we have kept the linear displacements $A_{ij}^{\rm lin}$ exponentiated while Taylor-expanding the higher order terms. The former choice keeps the effects of these displacements to all orders in perturbation theory and is known as "convolutional" LPT, or CLPT [58]; this prescription is not obvious and we will discuss various possible choices in some detail in Chapters 2 and 3. For example, expanding the exponent to second order and Fourier transforming recovers the 1-loop matter power spectrum in EPT derived above [231, 397].

1.3.2 Interlude: Construction of Effective Theories

Equations 1.37 and 1.43 are about as far as we can go within the traditional assumptions of perturbation theory, but they are not complete. This is because the fluid approximations we have worked with thus far (single-stream, vanishing velocity dispersion) is not a consistent description of structure formation at all scales even for the CDM Vlasov system we have been developing. The 1-loop integrals in these equations run to arbitarily small scales, i.e. high $\mathbf{k}$, where these assumptions break down; alternatively, one may assume a *regularization* scheme to control the small-scale dependence of these integrals, i.e. by instituting a hard cutoff $k < \Lambda$, but it is unlikely that this scheme corresponds to actual small-scale physics, so any dependence on the regularization scheme is undesirable. Practically, while it may be possible to model structure formation in a purely CDM universe on all scales using N-body simulations[11], in practice on small scales we have to contend with additional effects on small scales due to baryons, galaxy formation, or more exotic scenarios such as interacting dark matter.

The effective-theory solution to these issues is to split the system into a smoothed "long-wavelength" and a small-scale "short-wavelength" part, i.e. for the density

$$\delta(\mathbf{x}) = \int d^3\mathbf{x}\; W_\Lambda(\mathbf{x}-\mathbf{x}')\;\delta(\mathbf{x}') + \delta_s(\mathbf{x}) \equiv \delta_l(\mathbf{x}) + \delta_s(\mathbf{x}) \tag{1.44}$$

where W_Λ is a filter smoothing out scales above Λ. Performing this split renders the remaining smoothed modes δ_l to be sufficiently close to linearity that they can be perturbatively modeled. In the below we will drop the label l and refer to only the long contributions to various fields unless otherwise specified. The Gaussianity of initial conditions implies that the long and short modes are uncorrelated absent dynamics coupling them.

Of course, the effect of the short modes cannot simply be ignored. Within the EPT language it can be shown [28, 60] that their presence induces a nonzero stress tensor $\tau_{ij} = n\sigma_{ij}$ in the Euler equation. At each spacetime point the short modes will evolve even in the absence of long modes, i.e. $\tau_{ij} = \tau_{0,ij}(\mathbf{x},\tau)$, but in general we also need to account for the

[11] It is important to note, however, that the finite resolution of N-body simulations corresponds to a particular regularization scheme of the Vlasov system, with numerical results which may be strongly sensitive to given some classes of initial conditions.

presence of long-wavelength backgrounds, i.e. schematically[12]

$$\tau_{ij}(\mathbf{x},\tau) = \tau_{0,ij}(\mathbf{x},\tau) + \int d\tau'\ K_0(\tau,\tau')\ \partial_i\partial_j\phi\big(\mathbf{x}(\tau')\big) + K_1(\tau,\tau')\ \delta\big(\mathbf{x}(\tau')\big)\delta_{ij} + K_2(\tau,\tau')\ \partial_k v_k\big(\mathbf{x}(\tau')\big)\delta_{ij} + K_3(\tau,\tau')\ \Big(\partial_i v_j + \partial_j v_i\Big)\big(\mathbf{x}(\tau')\big) + \ \ldots \qquad (1.45)$$

where the K_n are (unknown) kernels characterizing the response of the stress tensor to long-wavelength perturbations in the tidal tensor $\partial^2\phi$, density δ and velocity gradient ∂v (potentials and their gradients ϕ, $\partial\phi$ and velocities v cannot appear due to the symmetries of general relativity). These kernels are in principle actually dependent on the small-scale structure at $\mathbf{x}$ and therefore random variables themselves; however, since our interest will be in correlations at long distances where the short modes will be uncorrelated we can write $\langle K_n(\mathbf{x})K_m(\mathbf{0})\rangle = \langle K_n\rangle\langle K_m\rangle$ and, since the expectation values at different points must be the same due to translation invariance, we can regard them as regular numbers.

The above expression is the equivalent of closing the Boltzmann hierarchy via pressure and viscosity discussed below Equation 1.14. The difference is that the long-wavelenght response here is nonlocal in time—since all structures evolve on times $\sim H^{-1}$—but local in space, since $v/H \ll c/H$. This integral is carried out along the trajectory $\mathbf{x}(\tau)$ of a fluid element since the short modes can only depend on their local environment at each time. The purely short contribution τ_0 is uncorrelated with long modes by construction. Finally, if working to only linear order in the long modes we can use that all of the fields in Equation 1.45 are related to the linear overdensity such that the stress-tensor gradient can be written as $\partial_i\tau_{ij} = A(\tau)\ \partial_i\delta$.[13] Integrating the equations of motions gives a *counterterm* contribution to the density

$$\delta^{\text{c.t.}}(\mathbf{k},\tau) = \frac{1}{2}\alpha k^2\delta^{(1)}(\mathbf{k},\tau). \qquad (1.46)$$

where α is again a free-parameter depending on the smoothing scheme (Λ) and not determined by the theory. It can be shown that additional contributions due to e.g. baryonic physics also take this form to lowest order [217]. Similarly the purely short-mode, i.e. stochastic, contribution from τ_0 contributions a term to the density $\epsilon \sim \partial^2\tau_0$.

A similar strategy can be pursued within LPT. Here it is helpful to think of the effective theory as one where the structureless, infinitesimal fluid elements of LPT are replaced by extended objects with sufficient size to smooth out scales where stream crossing occurs [290]. Both the dynamics and gravitational fields of these objects then depend not only on their centers of mass but the multipole moments of their density distributions.[14] As with EPT we

[12]For brevity of presentation we will write $\nabla_{\mathbf{x}} = \partial$ in this section, leaving $\nabla = \partial_{\mathbf{q}}$.

[13]Note that we can essentially neglect the time dependence of $\partial^2\phi, \delta, \partial v$ since, while they do grow like $D(\tau)$, since K_n cannot be known *a priori* neither can $A_n = \int d\tau' K_n(\tau,\tau')D(\tau')$, i.e. we are left with simply defining new free parameters α_n.

[14]This is the same treatment as multipoles in classical electromagnetism, essentially a long-distance effective theory where objects of size R interacting on large distances $r \gg R$ can be characterized purely in terms of the multipoles without requiring further knowledge of their charge distributions.

again need to write out the possible contributions of short modes and their responses to long modes; at 1-loop order we need to enumerate up to the quadrupole, i.e. the second moment of the displacements [399, 290]

$$\begin{aligned}\Psi_i^{\text{c.t.}}(\mathbf{q}) &= \mathcal{S}_i + \frac{1}{2}\alpha_0\nabla_i\delta^{(1)}(\mathbf{q}) \\ \Big(\Psi_i(\mathbf{q})\Psi_j(\mathbf{q})\Big)^{\text{c.t.}} &= \frac{1}{3}\alpha_0\delta_{ij} + \alpha_2\delta_{ij}\nabla\cdot\Psi^{(1)} + \alpha_3\big(\nabla_i\Psi_j^{(1)} + \nabla_j\Psi_i^{(1)}\big).\end{aligned} \tag{1.47}$$

where $\mathcal{S}$ represents small-scale forces not correlated with large scales like τ_0 in EPT. The second equation contains a novel feature of the Lagrangian EFT: the presence of *composite* operators composed of products of displacements evaluated at a single point which require their own counterterms. This is because the density itself is a (infinite-order) composite operator, such that e.g. the presence of terms like $\Psi(\mathbf{q}_1)\Psi(\mathbf{q}_1)\Psi(\mathbf{q}_2)$ in W_{ijk} (Eqn 1.43) requires these additions. We will see more examples of composite operators when computing the moments of pairwise velocities in Chapter 2. It is straightforward to show, however, that as in the case of EPT when these terms all contribute identically to each other in the 1-loop power spectrum, and indeed to the EPT counterterm derived above, and for this reason we will not put much work into distinguishing them in the rest of the text.

1.3.3 Interpretation of 1-loop Results and Expansion Parameters

The effective-theory considerations in the previous subsection complete the development of the perturbative formulation of structure formation as a cosmological fluid. Let us consider what the contributions to matter 2-point clustering at $\mathbf{k}$ are from modes at scales p smaller, larger and about equal to k within this formalism. Since the perturbative structure of EPT and LPT are extremely similar, except for the modes larger than $\mathbf{k}$ as we will see, we will stick with the former below for the sake of brevity.

Let us first consider modes for which $p \gg k$ in Equation 1.37. For this we need to use the short-wavelength, or ultraviolet (UV), limit of the PT kernels F_n: in the limit that the sum (i.e. $\mathbf{k}$) of the arguments of F_n remains fixed, but two of the momenta $\mathbf{p}$ become large, $F_n \propto k^2/p^2$ [148, 40]. This suppression of the dependence on small-scale densities reflects that gravity on large scales doesn't depend on small-scale structure [114] except for derivative-suppressed contributions from multipoles as discussed in the construction of the Lagrangian EFT. From this we get that the leading UV contributions to the power spectrum go as

$$\begin{aligned}P_{UV}^{(13)} &\sim k^2 P(k)\left[\int_{\Lambda>p\gg k}\frac{d^3\mathbf{p}}{(2\pi)^3}\,\frac{P_{\rm lin}(\mathbf{p})}{p^2}\right] \sim k^2\Sigma^2_>P(k) \\ P_{UV}^{(22)} &\sim k^4\left[\int_{\Lambda>p\gg k}\frac{d^3\mathbf{p}}{(2\pi)^3}\,\frac{P_{\rm lin}(\mathbf{p})^2}{p^4}\right]\end{aligned} \tag{1.48}$$

where $\Sigma_>$ is the Zeldovich displacement due to small-scale modes. While these contributions are suppressed by inverse powers of p they are still unphysically dependent on the cutoff Λ. Indeed, for power spectra that scale with wavenumber as k^n, the (13) and (22) components will diverge if $n > -1$ and $n > \frac{1}{2}$. It is worth noting two consequences of this discussion: (1) the UV sensitivity of $P^{(22)}$ is subdominant and (2) within ΛCDM we have $P_{\rm lin} \propto k^{-1.5}$ on scales of interest, so no divergences occur, but Λ-dependent convergence is not an indicator of correctness.

Thankfully, we have not exhausted the list of contributions at 1-loop order. In particular, we still need to account for the stochastic contributions due to $\tau_{0,ij}$ and counterterms, which we can think of as second and third-order contributions to the matter density that lead to 1-loop contributions

$$P^{\rm EFT}(k) = \alpha k^2 P_{\rm lin}(k) + \langle \epsilon\epsilon \rangle'. \tag{1.49}$$

Since we have $\epsilon \sim \partial^2 \tau$ we have to lowest order $P_\epsilon \propto k^4$. Equation 1.49 is exactly the form of the UV contributions in Equation 1.48 and, in order for the final result to be physical, the Λ-dependence between the two must cancel. Focusing on the (13) contribution for example we have that the sum is

$$k^2(\Sigma_>^2 + \alpha) P_{\rm lin}(k) \equiv \left(\frac{k}{k_{nl}}\right)^2 P_{\rm lin}(k). \tag{1.50}$$

The parameter k_{nl} controls the size of nonlocality caused by nonlinearities , such that the system ceases to be perturbative on scales $k \sim k_{nl}$. Note that what matters is the *sum* contribution, which can only be measured from data or fully nonlinear simulations, and not the linear small-scale displacement $\Sigma_>^2$, though their size may be similar in ΛCDM universes.

Let us turn to modes $p \approx k$. In this regime the F_n are roughly of order unity with very mild scale dependence. We then have very approximately [114, 268]

$$\frac{k^3 P_{\text{1-loop}}^{p\approx k}(k)}{2\pi^2} \sim \left(\frac{k^3 P_{\rm lin}(k)}{2\pi^2}\right)^2 \tag{1.51}$$

where we have written our results in terms of the dimensionless power spectrum $\Delta(k) = k^3 P(k)/2\pi^2$ characterizing the typical amplitude of density fluctuations at scale $\mathbf{k}$. In order for the dynamics to be perturbative we must have $\Delta < 1$; this is irrespective of any additional EFT contributions since the expansion in Δ is based on the smallness of density fluctuations in the smoothed density field in the regime of interest near $\mathbf{k}$.

1.3.4 IR Resummation and the BAO Peak

Finally, let us comment on the role of long, i.e. infrared (IR), modes with $p \ll k$. If an argument $\mathbf{p}$ of F_n goes to zero, an infrared divergence $\propto p_i/p^2$ appears. This leads to contributions to the (13) and (22) terms proportional to long displacements

$$P_{\rm IR}^{(13)}, P_{\rm IR}^{(22)} \sim k^2 \Sigma_<^2 P(k), \quad \Sigma_<^2 = \int_{p<k} \frac{d^3\mathbf{p}}{(2\pi)^3} \frac{P_{\rm lin}(\mathbf{p})}{p^2}. \tag{1.52}$$

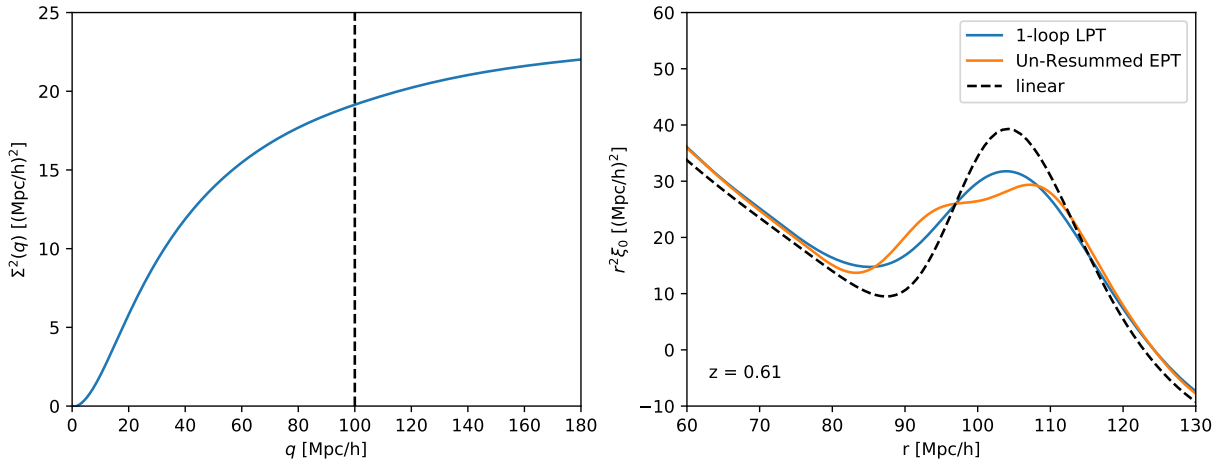

Figure 1.5: (Left) The mean square pairwise displacement at $z = 0.61$ for points separated by q. The damping of the BAO is determined by the parameter $k^2\Sigma^2(q = r_{\rm BAO})$ (black dashed), which is of order unity on scales $k \lesssim 0.2\,h\,{\rm Mpc}^{-1}$ where the BAO has support. (Right) Predictions for the galaxy correlation function monopole using LPT, 1-loop unresummed EPT and linear theory. Within LPT the BAO peak is properly damped compared to linear theory, but in unresummed EPT spurious features appear since $k^2\Sigma^2_{\rm BAO}$ is no longer small. Fits to the power spectrum based on the analysis in Chapter 8.

Remarkably, however, an exact calculation shows that these contributions cancel exactly [40], i.e. $2P^{(13)}_{\rm IR} + P^{(22)}_{\rm IR} = 0$. In fact, the cancellation of contributions due to $\Sigma_<$ occurs to all orders and is a consequence of generalized Galilean invariance [326]—displacements that are coherent on scales larger than $\mathbf{k}$ will simply translate pairs of points contributing to $P(\mathbf{k})$ by the same amount, leading to no change in the 2-point function. Indeed, within LPT all contributions to the power spectrum are written in terms of the pairwise displacement Δ, so the parameter $\Sigma_<$ explicitly cancels by construction. In the appendices to Chapter 2 we derive expressions for EPT power spectrum that are IR-safe, i.e. do not rely on numerical cancellations of contributions from long modes, using this observation.

The above considerations have a loophole, however. If the power spectrum and correlation function are smooth, Fourier modes $\mathbf{k}$ roughly translate to configuration space separation $r \sim 2\pi/k$; if, on the other hand, there is a sharp feature in the correlation function, its Fourier transform will *not* be well-localized in the power spectrum due to the uncertainty principle. A particularly relevant example is the BAO feature, which manifests either as a series of oscillatory peaks and troughs in Fourier space or a well-isolated peak in configuration space (Fig 1.1). The presence of a feature like the BAO peak introduces a new, potentially large parameter $\Sigma^2_{\rm BAO}$ whose effect needs to be resummed [335, 402, 50].

This effect can be most easily seen in the Lagrangian picture.[15] A sharp feature in the

[15]The following discussion follows that in Ref. [402]

correlation function is equivalent to oscillatory wiggles in the power spectrum, which we can therefore smooth into a wiggly and a smooth part

$$P_{\rm lin}(k) = P_{nw}(k) + P_w(k). \tag{1.53}$$

Within the Zeldovich approximation we can compute the 2-point function of pairwise displacements due to each part

$$A_{ij}^{\rm lin}(\mathbf{q}) = A_{ij}^{nw}(\mathbf{q}) + A_{ij}^{w}(\mathbf{q}), \quad A_{ij}^{nw,w}(\mathbf{q}) = 2\int \frac{d^3\mathbf{p}}{(2\pi)^3}\, e^{i\mathbf{k}\cdot\mathbf{q}} \left(1 - \frac{k_i k_j}{k^2}\right) P^{w,nw}(k) \tag{1.54}$$

where the nw piece will contain most of the power but the small w piece will contain the BAO feature at $q = r_{\rm BAO}$. Then, plugging in Equation 1.40 we get

$$\int d^3\mathbf{q}\; e^{i\mathbf{k}\cdot\mathbf{q} - \frac{1}{2}k_i k_j A_{ij}^{nw}(\mathbf{q})}\Big(1 - \frac{1}{2}k_i k_j A_{ij}^{w}(\mathbf{q}) + \dots\Big) \approx P_{\rm Zel}^{nw}(k) + e^{-\frac{1}{2}k^2\Sigma^2_{\rm BAO}} P^{w}(k), \tag{1.55}$$

where we have defined the angular-averaged pairwise displacement amplitude

$$\Sigma^2_{\rm BAO} = \langle A_{ij}^{nw}(\mathbf{q})\rangle_{q=r_{\rm BAO}} = \frac{1}{3}\int \frac{dk}{2\pi^2}\Big(1 - j_0(k r_{\rm BAO})\Big) P^{nw}(k). \tag{1.56}$$

Equation 1.55 relies on the saddle-point approximation—since A_{ij}^{w} has a sharp feature at $r_{\rm BAO}$ it will pick out the value of the exponentiated A_{ij}^{nw} at that scale.

The above is the well-known result that the BAO peak in large-scale structure is damped by long-wavelength (IR) displacements. Since the spherical Bessel function $j_0(x)$ approaches unity for small x, we see that $\Sigma^2_{\rm BAO}$ picks up Zeldovich displacements on scales larger than $r_{\rm BAO}$. This makes sense, since displacements larger than this will move the BAO feature coherently without distorting it, but, more importantly, the BAO wiggles at $\mathbf{k}$ can be influenced by displacements from modes $p < k$ as long as $p \gtrsim \pi/r_{\rm BAO}$. Within EPT it is possible to show that when the oscillatory BAO signal exists in addition to an otherwise smooth linear power spectrum, the cancellation in Equation 1.52 only occurs for wavelengths larger than the BAO scale.

The above significant because, while Equation 1.55 is exact in the limit that the BAO peak is infinitely narrow, 1-loop perturbation theory only predicts the contribution $P^{w}_{\text{1-loop}} = -\frac{1}{2}k^2\Sigma^2_{\rm BAO}P(k)$, which is unsatisfactory given that $k^2\Sigma^2_{\rm BAO}$ can be greater than unity on scales where the BAO wiggles have support in Fourier space, leading to spurious features in the correlation function (Fig. 1.5). In order to amend this problem *in EPT* it is necessary to *resum* damping effects due to long displacements exponentially, i.e.

$$P_{\rm resummed} = P_{\rm lin}^{nw} + P^{\text{1-loop}}\left[P_{\rm lin}^{nw}\right] + e^{-\frac{1}{2}k^2\Sigma^2_{\rm BAO}}\Big(\big(1 + \frac{1}{2}k^2\Sigma^2_{\rm BAO}\big)P_w + \Delta P_w^{\text{1-loop}}\Big) \tag{1.57}$$

where we have defined $\Delta P_w^{\text{1-loop}} = P^{\text{1-loop}}\left[P_{\rm lin}\right] - P^{\text{1-loop}}\left[P_{\rm lin}^{nw}\right]$ to be the difference in the 1-loop power spectrum evaluated with and without the wiggly component.[16] On the other

[16]The extra factor of $\frac{1}{2}k^2\Sigma^2_{\rm BAO}$ multiplying P_w nulls the contribution from $P^{w}_{\text{1-loop}}$.

hand, as is clear from our derivation, this nonlinear damping effect is naturally captured by the exponentiated Zeldovich displacements within LPT. We discuss IR resummation in perturbation greater detail and generality in Chapter 6.

1.4 The Bias Expansion

In this introduction our focus has been on developing the effective theory of matter clustering in EPT and LPT to demonstrate the general philosophy and techniques of perturbation theory. In order to progress to modeling data from upcoming galaxy surveys however, we will need to take one additional step and address the clustering of galaxies. Within the perturbation theory language galaxies are treated as *biased tracers*, objects which do not exactly trace the underlying matter field but whose large-scale distribution depends on structure formation in nontrivial ways. While we will leave the actual calculation of galaxy density and velocity statistics for Chapter 2, in this final section we will set up the tools and lay out the perturbation theory of biased tracers. But first, let us take a qualitative look at the kinds of physical effects we wish to capture by looking at the halo model.

1.4.1 Dark Matter Halos and Gravitational Collapse

One of the most striking predictions of N-body simulations of structure formation is the existence of dark matter *halos*: dense, discrete objects formed by gravitational collapse. Halos are highly nonlinear, completely decoupled from the background expansion and deep into the multi-streaming regime, i.e. well beyond the reach of perturbation theory. Even smaller are galaxies, many of which can inhabit a single halo in the modern understanding of galaxy formation. There are now a plethora of ways to make this galaxy-halo connection and, within these formalisms, the clustering of dark matter halos from N-body simulations can be directly translated into predictions of galaxy clustering. A comprehensive summary of the state-of-the-art can be found in ref. [408]. While there is no fundamental guarantee that the empirical relations of galaxy properties (e.g. masses, luminosities, colors) are good to the sub-percent levels that will be required by upcoming experiments[17], these models are undoubtedly each *possible* galaxy-halo connections. Our goal in the following subsections is to analytically study the simplest *halo models* to develop intuition for what a perturbative model of galaxy clustering requires.

[17] I respectfully note that this is not a universally held opinion, and many analyses of cosmological data using these techniques exist. The reader is referred to e.g. refs. [255, 210, 434] for examples of the state-of-the-art[18] at the time this dissertation was written.

[18] Though, in some sense, the ever-improving galaxy-halo connection models illustrate a fundamental problem: unlike in PT models, where free parameters are dictated by fundamental symmetries and measured deviations from linearity provide a self-contained measure for their validity, it is far less clear what set of parameters and prescriptions "complete" such a model and how to establish the regime of validity for such models.

The physics of halos concerns scales close to the Lagrangian halo radius R_h, the size of a sphere in comoving coordinates whose volume encloses enough matter to form a halo of mass M, i.e.

$$R_h = \left(\frac{3M}{4\pi\Omega_m\rho_{\rm crit}}\right)^{1/3} = 1.42\times\left(\frac{M}{10^{12}h^{-1}M_\odot}\right)^{1/3}\left(\frac{\Omega_m}{0.3}\right)^{-1/3} h^{-1}\,{\rm Mpc} \tag{1.58}$$

where $M_\odot$ denotes a solar mass, with $10^{12}{\rm M}_\odot$ being a ballpark reference for the halos and galaxies we will consider in this dissertation. The gravitational collapse of halos draws in matter from distance scales $\sim R_h$, which therefore controls the size of nonlocalities having to do with halo clustering.

A particularly simple model of halo formation is the *spherical tophat* model (see e.g. [89]). In this model, an initially slightly overdense sphere of mass M in an otherwise homogeneous FLRW universe slowly pulls away from the background expansion before eventually turning around and collapsing into a halo in virial equilibrium. Within an EdS universe this system can be straightforwardly solved to show that gravitational collapse completes by the time that the *linear* overdensity $\delta^{(1)}_{R_h}(\tau) > \delta_{\rm crit} = 1.686$ and that the halo is virialized when it reaches roughly 200 times the background density. These results are rather insensitive to deviations from EdS and are the basis to e.g. the common definitions of the halo mass and radius (M_{200}, R_{200}) to be where this condition is satisfied [412]. The implicit relation between the the halo mass and radius in this definition also allows us to estimate typical virial velocities within halos $v\sim\sqrt{GM_{200}/R_{200}}$, corresponding to velocities of about 150 km/s for a present-day $10^{12}h^{-1}M_\odot$ halo, with weak cosmology and redshift dependence. While obviously an extreme simplification, the spherical tophat model provides useful intuition for the physical scales associated with halos and galaxies due to nonlinear gravitational collapse.

In fact we can take this simple toy model even further into the realm of large-scale structure. In studies of LSS we are primarily interested not in the precise dynamics of halos but rather their statistical properties. The simplest such statistic is the *mass function* dn/dM describing the mean number density of halos per mass. The mass function depends on physics in the nonlinear regime and must be measured from simulations, with well-known fitting functions on the market (see e.g. ref. [375]) though analytically motivated versions [292, 341] exist. In the simplest version, known as the Press-Schechter formalism [292], one uses the spherical-collapse ansatz that halos are formed when $\delta^{(1)} = \delta_{\rm crit}$ to associate regions halos with mass greater than M with regions where the overdensity smoothed by a tophat filter of radius R_h is greater than this threshold. Since the linear-theory overdensity is Gaussian the probability that this threshold is crossed is simply given by[19]

$$P_{\rm PS}(M,z) = 2\times\frac{1}{\sqrt{2\pi}\sigma_{R_h}(z)}\int_{\delta_{\rm crit}}^{\infty}\exp\Big(-\frac{\delta^2}{2\sigma^2_{R_h}(z)}\Big),\ \sigma^2_{R_h}(z) = \int\frac{d^3\mathbf{p}}{(2\pi)^3}\,P_{\rm lin}(\mathbf{k},z)\tilde{W}^2_{R_h}(k). \tag{1.59}$$

[19]The factor of two was introduced by Press and Schechter to ensure that all dark matter is "collapsed" when small enough scales are considered. It was eventually justified by ref. [52] within the excursion-set formalism.

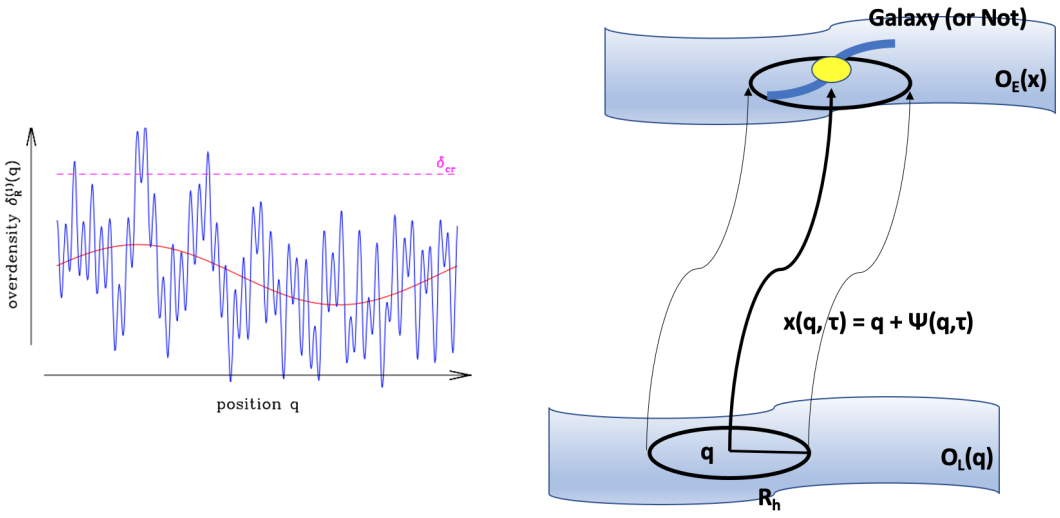

Figure 1.6: (Left) The peak background split: for a given density peak threshold $\delta_{\rm cr}$ required to form a halo, adding a background long-wavelength background mode (pink) is equivalent to locally decreasing the threshold by $\delta_l(\mathbf{q})$, making it easier to form a halo and thereby leading to halo bias. Figure taken from ref. [109] (Right) In general halo and galaxy formation is sensitive not just to the initial density field but to all symmetry-allowed operators O sampled in a neighborhood of order the halo radius R_h along its trajectory. However, this time evoltuion can be perturbatively factored and expressed in terms of bias operators evaluated either at initial Lagrangian positions $\mathbf{q}$ or at the evolved Eulerian position $\mathbf{x}$.

where we have defined $\sigma^2_{R_h}$ to be the variance of the density field smoothed by a spherical-top hat filter with radius R_h. The mass function is related to this probability by $dn/dM = (\rho_{m,0}/M)|dP/dM|$. While simple, the Press-Schechter formalism gives good qualitative predictions for mass function. The halo mass function thus probes the growth of structure on scales associated with the halo radius—this is the basis, for example, of cosmological constraints based on the observed abundances of galaxy clusters [10], which are thought to reside in extremely massive halos, though these abundances are subject to numerous theoretical and observational systematics that we will not further address in this introduction.

1.4.2 The Large-Scale Clustering of Halos and the Bias Expansion

We can also investigate the large-scale distribution of halos within the Press-Schechter formalism. Within the vicinity of a collapsing halo, a long-wavelength mode δ_l with $k \ll 1/R_h$ will appear as a scale-independent increase in the mean density, equivalent to lowering the threshold of collapse for short modes $\delta_{\rm crit} \to \delta_{\rm crit} - \delta_l$ (Fig. 1.6). This separation of the long and short modes is known as the Peak-Background split (PBS). Note that this is a *local* modulation in halo formation; the value of δ_l far away doesn't enter. Assuming that halos are

otherwise uniformly distributed on large scales we can Taylor-expand in the long mode to get

$$\delta_h(\mathbf{q}) = b_1\delta_l(\mathbf{q}) + \mathcal{O}(\delta^2), \quad b_1(M,z) = -\frac{1}{dn/dM}\left(\frac{d}{d\delta_{\rm crit}}\frac{dn}{dM}\right). \tag{1.60}$$

Intuitively, a positive local modulation in the background density makes it easier to form halos, with a proportionality constant equal to the linear *Lagrangian bias* b_1. Equation 1.60 was written in terms of the Lagrangian coordinate $\mathbf{q}$ where the linear overdensities are modified; in order to translate them to observed Eulerian positions we need to advect them as in Equation 1.18, i.e.

$$1 + \delta_h(\mathbf{x}) = \big(1 + \delta_h(\mathbf{q})\big)\big(1 + \delta_m(\mathbf{x})\big) \approx 1 + b_1^E\delta_{\rm lin}(\mathbf{x}) \tag{1.61}$$

where the Eulerian bias $b_1^E = 1 + b_1$, reflecting additional clustering due to motion induced by the long mode. It is straightforward to extend this analysis to higher-order biases such that $\delta_h(\mathbf{q}) = \sum_n b_n\delta_{\rm lin}^n(\mathbf{q})$ in order to capture clustering beyond linear theory.

The above treatment of halo clustering using the PBS illustrates a general principle—that the large-scale clustering of objects like halos and galaxies formed through highly nonlinear gravitational collapse can be captured by their response to large-scale modes—but is not complete. Let us note some of the missing pieces before we move on to the more general theory. Since we were operating within the parameters set by the spherical tophat model, the bias expansion derived above was only sensitive to spherically symmetric perturbations in the initial density field; in general, collapse need not be spherical and taking this into account in PBS-type arguments [67] leads to a bias quadratic in the shear field $s^2 = s_{ij}s_{ij}$ where the shear tensor is defined as

$$s_{ij}(\mathbf{x}) = \left(\frac{\partial_i\partial_j}{\partial^2} - \frac{1}{3}\delta_{ij}\right)\delta(\mathbf{x}). \tag{1.62}$$

While the trace of the tidal tensor $\partial_i\partial_j\Phi$ is given by the density, the shear denotes its traceless component, and at the linear level is also related to traceless components of the gradient of the velocity $\partial_i v_j$ and Lagrangian displacement $\nabla_i\Psi_j$.

We also need to account for the fact that, in general, we will need to study galaxy and halo clustering on scales where the Lagrangian radius R_h is perturbatively but not vanishingly small. In the PBS argument we implicitly assumed that the valude of the long mode at a point $\delta_l(\mathbf{q})$ could be substituted for its spherical average. This is true in the limit where its wavelength is infinite, but we can also compute its leading correction in the spherical tophat model $\langle\delta_l(\mathbf{q})\rangle_{R_h} = \delta_l(\mathbf{q}) + \frac{1}{10}R_h^2\nabla^2\delta_l(\mathbf{q}) + \ldots$. The bias expansion is thus only quasilocal, with *derivative bias* corrections

$$\delta_h(\mathbf{q}) \ni b_\nabla\nabla^2\delta_{\rm lin}(\mathbf{q}) \tag{1.63}$$

scaling with the finite size of the halo. We also need to account for statistics of modes with wavelength similar or smaller than R_h much like we dealt with them in the case of matter clustering in Equation 1.49. This generates a residual *stochastic* term

$$\delta_h(\mathbf{q}) \ni \epsilon(\mathbf{q}), \quad \langle\epsilon(\mathbf{q})\epsilon(\mathbf{q}')\rangle \sim R_h^3\delta_D(\mathbf{q}-\mathbf{q}') \tag{1.64}$$

which only correlates with itself in a neighborhood defined by R_h by construction and can therefore be approximated by a delta function on large scales. This form Fourier transforms into a flat contribution in Fourier space and is a catch-all that includes any small-scale correlations not captured by the large scale expansion; for example, a Poisson-sampled set of point particles will have a flat power spectrum $1/\bar{n}$ due to shot noise, halos excluding others from forming within their Lagrangian region induce a negative contribution $-V_{\rm excl}$ equal to the exclusion volume [23], etc. If the stochastic contribution is significant it may in addition be necessary to include higher derivatives of the delta function, e.g. $\sim R_h^5 \nabla^2 \delta_D(\mathbf{q}-\mathbf{q}')$.

Finally let us briefly comment on the clustering of galaxies *within* halos. In the simplest realization of the halo model, galaxies are Poisson sampled in halos of mass M with some mean $N(M)$ and distributed according to some (normalized) profile $u(\mathbf{x}|M)$. We can write the galaxy power spectrum as a sum $P_{gg} = P^{1h} + P^{2h}$ of a "1-halo" component due to correlations of galaxies occupying the same halo and a "2-halo" component due to correlations of position between halos, which are then [89]

$$P^{1h}(k) = \frac{1}{\bar{n}_g^2} \int dM \, \frac{dn}{dM} \, N(M)^2 \, |\tilde{u}(k|M)|^2$$
$$P^{2h}(k) = \frac{1}{\bar{n}_g^2} \int dM_1 dM_2 \, \frac{dn}{dM_1}\frac{dn}{dM_2} \, N(M_1)N(M_2) \, \tilde{u}(k|M_1)\tilde{u}^*(k|M_2) \, P_{M_1,M_2}(k) \qquad (1.65)$$

where $P_{M_1,M_2}(k)$ is the (cross) power spectrum of halos of mass M_1 and M_2, dn/dM is the average halo density per mass and $\bar{n}_g$ is the mean galaxy density. From Equation 1.65 we see that qualitatively the galaxy-halo connection introduces (1) an additional flat stochastic contribution due to the 1-halo term from the Poisson sampling of galaxies within each halo and (2) additional nonlocality due to the smearing out of the galaxy field by the profile $u(\mathbf{x}|M)$. Both of these properties are already included in the derivative bias and stochastic terms discussed above and indeed, if as may be expected the typical scale of the (collapsed) galaxy profile u is smaller than that of the (comoving) Lagrangian radius R_h, these additions should also be subleading to the halo ones. While it doesn't feature the full generality of the bias expansions we will discuss next, the halo model qualitatively ties clustering at large and small scales, and for this reason has been seen uses beyond galaxies such as intensity mapping [313] and used to constrain cosmological parameters with galaxy clusters using the thermal Sunyaev-Zeldovich effect [181]—essentially the pressure content—and cross correlations of cluster abundances and densities with weak lensing [376].

1.4.3 Bias Expansion: Formal Developments

Let us complete our discussion of the bias expansion by discussing the general case.[20] The density of a biased tracer (e.g. galaxy or halo) at a point $\mathbf{x}$ and conformal time τ can depend on any physical fluid observable O sampled in a neighborhood of size $\sim R_h$ along its past trajectory $\mathbf{x}(\tau)$ (Fig. 1.6) as long as its effect on the tracer density is allowed by rotational

[20] The reader is referred to ref. [109] for a more comprehensive treatment.

symmetry, Galilean invariance, the equivalence principle etc. Schematically, we can write the equivalent of Equation 1.45 for halos bias [332]

$$\delta_h(\mathbf{x}) \ni \int^{\tau} d\tau' K_{h,O}(\tau,\tau')\; O(\mathbf{x}(\tau'),\tau') = b_{O^{(1)}} O^{(1)} + b_{O^{(2)}} O^{(2)} + b_{O^{(2)}} O^{(3)} + ... \tag{1.66}$$

where $O(\mathbf{x}(\tau),\tau) = \sum_n O^{(n)}$ is the sum of its components at each order. The time dependence of the kernel $K_{h,O}$ cannot be known *a priori*, so as with Equation 1.45 we in general have to write its integrals with the time-dependence of $O^{(n)}$ as free bias parameters $b_{O^{(n)}}$. In the below we will focus on operators which can be related to tidal tensor $\partial_i\partial_j\Phi$ and its trace, the matter overdensity, without introducing additional physical scales, e.g. the velocity gradient $\partial\mathbf{v} \sim \mathcal{H}\delta$ which is $\mathcal{O}(\delta)$ when integrated over $\sim H_0^{-1}$—additional spatial derivatives $\nabla^2 O$ are necessarily suppressed by the halo scale R_h, though they along with the stochastic term are essential in properly accounting for the effects of short modes [233, 16] much like in the case of the matter power spectrum calculation in the previous section (Eqn 1.49).

In fact, many of the operators generated by the above procedure turn out to be linearly dependent, leading to simplified bias expansions that can be entirely constructed out of operators at either final (Eulerian) or initial (Lagrangian) times [241, 140, 139]. This can be shown to result from the structure of the perturbative solutions out of which we have constructed them, though ref. [139] recently showed that these irreducible sets of bias operators can be more generally derived from equivalence-principle considerations. In the case of the Eulerian bias expansion [234] we have up to third order[21]

$$\delta_h(\mathbf{x}) = b_1^E\delta(\mathbf{x}) + \frac{1}{2}b_2^E\delta^2(\mathbf{x}) + b_s^E s^2(\mathbf{x}) + \frac{1}{6}b_3^E\delta^3(\mathbf{x}) + b_{st}^E s_{ij}t_{ij}(\mathbf{x}) + b_{\delta s}^E\delta s^2(\mathbf{x}) + b_{s^3}^E s^3(\mathbf{x}), \tag{1.67}$$

where we have defined $s^3 = s_{ij}s_{jk}s_{ki}$ along with the second order operator

$$t_{ij} = \Big(\frac{\partial_i\partial_j}{\partial^2} - \frac{1}{3}\delta_{ij}\Big)(\theta-\delta), \quad t_{ij}^{(2)} = \frac{2}{7}\Big(\frac{\partial_i\partial_j}{\partial^2} - \frac{1}{3}\delta_{ij}\Big)\Big(s_{ij}^{(1)}s_{ij}^{(1)} - \frac{2}{3}\big(\delta^{(1)}\big)^2\Big). \tag{1.68}$$

It is conventional to "normal order" bias operators so that UV-sensitive contributions proportional to lower order operators are removed, e.g. for the density biases:

$$:\delta_{\rm lin}^2 := \delta_{\rm lin}^2 - \langle\delta_{\rm lin}^2\rangle, \quad :\delta_{\rm lin}^3 := \delta_{\rm lin}^3 - 3\langle\delta_{\rm lin}^2\rangle\delta_{\rm lin}. \tag{1.69}$$

Without normal ordering the cubic bias operator contains a contribution degenerate with linear bias, but proportional to the highly UV-sensitive expectation value of δ^2 at a point; by removing this contribution we can ensure the bias coefficients accurately capture the physical size of the response to each operator [233, 16], and we will adopt this convention throughout this dissertation.[22]

[21] In the path-breaking work of ref. [234] there was an additional operator ψ at third order; this operator turns out to be degenerate with the four other cubic operators listed here, so we have not included it.

[22] In the literature this operation is also often called bias *renormalization*, though aficionados of quantum field theory will see that it is more akin to normal ordering, i.e. subtracting out all nonzero contractions of a field.

We can also write the same expansion in a Lagrangian basis. Here the object of interest is the density of halos or galaxies in $\mathbf{q}$ coordinates, which are not clustered like $\mathbf{x}$. In particular, we can define $F(\mathbf{q},\tau)$ to be the number density of tracers at time τ that formed in a Lagrangian region $d^3\mathbf{q}$, so that the number density in Eulerian space is [229]

$$1+\delta_h(\mathbf{x},\tau) = \int d^3\mathbf{q}\; F(\mathbf{q})\; \delta_D\big(\mathbf{x}-\mathbf{q}-\Psi(\mathbf{q},\tau)\big) = F(\mathbf{q})\; \big(1+\delta(\mathbf{x},\tau)\big). \tag{1.70}$$

Note that the first equality in Equation 1.70 is in principle valid even beyond the single-stream limit; in the second equality we have assumed the $\mathbf{q}$-to-$\mathbf{x}$ mapping is 1-to-1 and used Equation 1.18 for the matter overdensity. A nice feature of the Lagrangian approach is that clustering due to dynamics $(1+\delta(\mathbf{x}))$ is explicitly separated out. Conceptually, we can think of $F(\mathbf{q})$ as the density of *protohalos*, i.e. regions which will eventually collapse into discrete tracers, written as a function of the initial density field at unadvected positions $\mathbf{q}$ [229, 414, 58, 396, 4, 74]

$$\begin{aligned} F(\mathbf{q}) &= 1 + b_1\delta_{\rm lin}(\mathbf{q}) + \frac{1}{2}b_2\delta^2_{\rm lin}(\mathbf{q}) + b_s s^2_{\rm lin}(\mathbf{q}) + \frac{1}{6}b_3\delta^3_{\rm lin}(\mathbf{q}) + b_{st}\big[s_{ij}t_{ij}\big]_{\rm lin}(\mathbf{q}) \\ &\quad + b_{\delta s}\delta_{\rm lin}s^2_{\rm lin}(\mathbf{q}) + b_{s^3}s^3_{\rm lin}(\mathbf{q}), \quad t^{\rm lin}_{ij}(\mathbf{q}) = \frac{2}{7}\Big(\frac{\nabla_i\nabla_j}{\nabla^2} - \frac{1}{3}\delta_{ij}\Big)\Big(s^2_{\rm lin}(\mathbf{q}) - \frac{2}{3}\delta^2_{\rm lin}(\mathbf{q})\Big). \end{aligned} \tag{1.71}$$

This expansion does not contain any references to nonlinearly evolved fields $\delta^{(n)}$, though perhaps at the expense of introducing unexpected terms like $t^{\rm lin}_{ij}$, which in the Eulerian basis could be understood as a difference between the density and velocity divergence. Of course, this is eliding the fact that both the Eulerian and Lagrangian bases capture the full time dependence of the integral in Equation 1.66.

In fact, it is easy to see that the Eulerian and Lagrangian bases are equivalent by writing the EPT kernels (Eqn. 1.27) in configuration space [241], which reveals

$$\begin{aligned} \delta(\mathbf{x},\tau) = \delta_{\rm lin}(\mathbf{q}) &+ \left(\frac{17}{21}\delta^2_{\rm lin}(\mathbf{q}) + \frac{2}{7}s^2_{\rm lin}(\mathbf{q})\right) \\ &+ \left(\frac{341}{567}\delta_{\rm lin}(\mathbf{q})^3 + \frac{11}{21}\delta_{\rm lin}s^2_{\rm lin}(\mathbf{q}) + \frac{2}{9}s^3_{\rm lin}(\mathbf{q}) - \frac{1}{3}\big(s_{ij}t_{ij}\big)_{\rm lin}(\mathbf{q})\right) + \;\ldots \end{aligned} \tag{1.72}$$

from which it is easy to read off the correspondence between Eulerian and Lagrangian bias parameters by enforcing $1+\delta_h(\mathbf{x}) = F(\mathbf{q})(1+\delta(\mathbf{x}))$. This expression also makes manifest why we do not need to include separate biases for e.g. $\delta^{(2)}, \delta^{(3)}$, since they are combinations of operators already in the bias expansion.

1.5 Outline

So far in this Introduction we have conducted a lightning review of how to rigorously construct perturbation theories describing the large-scale clustering of matter and biased tracers in

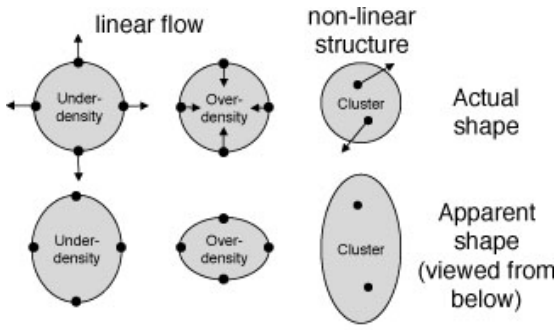

Figure 1.7: Redshift-space distortions lead to galaxies being observed at line-of-sight positions they *would* be at if they continued to stream at their present velocities for a Hubble time. On large scales, where densities and velocities are coherent, this leads to a increase (decrease) of structure along the LOS for over (under) densities. On small scales where velocities are dominated by nonlinear virial motions in halos RSD instead tend to smear out structure, leading to apparent elongated structures along the LOS called "fingers-of-god." Figure taken from ref. [279].

a FLRW universe with Gaussian initial conditions seeded by inflation. These perturbation theories represent a fully-general treatment of large-scale structure: all possible clustering contributions at a given order are systematically enumerated, and dependences on small-scale astrophysics where the theory breaks down are parametrically included as free counterterms and stochastic terms, with effects on large scales that are suppressed by the smallness of the nonlinear k_{nl}^{-1} and halo R_h scales. What remains to be done is to connect the predictions of this formalism to cosmological observables.

In the remainder of this dissertation our goal will be to develop perturbation theory models for galaxy surveys and their cross-correlations with weak lensing. Weak lensing describes the deflection of light due to the gravitational potential of intervening matter; in the Born approximation this angular deflection is given by $\Delta\theta_i = \nabla_\theta \Phi_L$ where the lensing potential is given by

$$\Phi_L(\hat{n}) = -2 \int \frac{d\chi}{\chi}\, \Phi_W(\chi\hat{n}) \left(\frac{\chi_s - \chi}{\chi}\right) \tag{1.73}$$

where $\Phi_W = (\Phi + \Psi)/2$ is the Weyl potential, equal to the Newtonian potential in the non-relativistic limit, $\hat{n}$ is the unit vector towards the line of sight (LOS), and χ is the comoving distance such that χ_s is the distance to the source. In this way we can think of weak lensing essentially as a projection of the matter density along the LOS weighted by the lensing kernel, and cross-correlating it with galaxies serves to isolate contributions localized at particular redshifts.

A major theme in our study of galaxy clustering will be *redshift-space distortions* (RSD): in spectroscopic surveys, distances to galaxies are typically inferred from their measured redshifts, which in addition to the Hubble expansion also receive a contribution due to their peculiar velocities, equivalent to boosting their positions by $\mathbf{u} = \hat{n}(\hat{n} \cdot \mathbf{v})/\mathcal{H}$. On large scales, where galaxies stream towards overdensities, RSD result in an anisotropic boost in power along

the LOS coherent with large-scale densities while, on small scales, virial velocities of galaxies in halos on the order of hundereds of kilometers per second (see discussion below Eqn. 1.58) smear out the observed positions of galaxies in halos, a phenomenon often called "Fingers of God" (Fig. 1.7). We study the statistics of these velocities in depth in Chapter 2 in both Eulerian and Lagrangian perturbation theory and relate them to the observed redshift-space clustering of galaxies. The large-scale velocities that contribute to RSD have a similar effect to the large-scale displacements that must be resummed to properly account for the damping of the BAO signal; in Chapter 3 we build upon this work and present a complete model of RSD within LPT with a full IR resummation of displacements and velocities, showing that it can accurately predict galaxy power spectra and correlation functions and be used to constrain cosmological parameters with data with error bars an order of magnitude smaller than an near term experiments.

The resummation of displacements in Lagrangian perturbation theory has applications beyond the standard galaxy 2-point function. In Chapter 4 use this resummation to model a standard technique to sharpen the BAO signal in galaxy surveys known as reconstruction [122] which seeks to reconstruct the Zeldovich displacement from the observed galaxy density field and thereby cancel some of the damping to the BAO peak. In the process, we show how to improve upon common empirical models of the post-reconstruction 2-point function using a saddle-point approximation. In Chapters 5 and 6, we investigate potential features in the 2-pt function beyond BAO including oscillatory features (1) due to residual baryon-dark matter differences post-recombination that can introduce additional terms to galaxy bias and (2) imprinted in the primordial power spectrum by exotic inflationary scenarios. In the latter case we compare the many IR resummation prescriptions on the market to investigate our ability to constrain the amplitude of these primordial features in redshift surveys using perturbation theory. Finally, as discussed earlier the Lagrangian advection in Equation 1.70 is in principle general beyond stream crossing, and in Chapter 7 we propose a new model for modeling galaxy-matter cross correlation in real space by using the fully nonlinear displacements computed from N-body simulations, significantly extending the reach of the Lagrangian perturbative bias expansion for use in galaxy-lensing cross correlations.

We put these models to use in the final two chapters of this dissertation. In Chapter 8, we combine our models for the reshift-space power spectrum and post-reconstruction correlation function to perform a ΛCDM fit. This analysis is followed-up in Chapter 9 where we further combine these data with cross-correlations with CMB lensing from the Planck satellite.

Chapter 2

Redshift-Space Galaxy Clustering I: Perturbative Modeling of Density and Velocity Statistics

This chapter was originally published as

> Shi-Fan Chen, Zvonimir Vlah, and Martin White. "Consistent modeling of velocity statistics and redshift-space distortions in one-loop perturbation theory". In: *JCAP* 2020.7, 062 (July 2020), p. 062. DOI: 10.1088/1475-7516/2020/07/062. arXiv: 2005.00523 [astro-ph.CO]

In the Introduction above we saw how to systematically construct perturbation theories of large-scale structure including the clustering of discrete tracers like galaxies. The purpose of this chapter is to connect this theory with observables from galaxy surveys. In particular, in spectroscopic surveys of galaxies the line-of-sight distance is inferred from the measured galaxy redshift, wherein the effect of the Hubble expansion and peculiar velocities are degenerate. Modeling the results of spectroscopic surveys thus requires properly accounting for the anisotropy generated by this real-to-redshift space mapping and the statistics of galaxy velocities. In turn, the peculiar velocities of biased tracers of the cosmic density field contain important information about the growth of large scale structure.

Using N-body data, we show that velocity expansions for halo redshift-space power spectra are converged at the percent-level at perturbative scales for most line-of-sight angles μ when the first three pairwise velocity moments are included, and that the third moment is well-approximated by a counterterm-like contribution. We compute these pairwise-velocity statistics in Fourier space using both Eulerian and Lagrangian one-loop perturbation theory using the previously described cubic bias scheme and a complete set of counterterms and stochastic contributions. We compare the models and show that our models fit both real-space velocity statistics and redshift-space power spectra for both halos and a mock sample of galaxies at sub-percent level on perturbative scales using consistent sets of parameters,

making them appealing choices for the upcoming era of spectroscopic, peculiar-velocity and kSZ surveys.

2.1 Introduction

The large-scale structure (LSS) of the Universe contains a trove of information relevant to astrophysics, cosmology and fundamental physics, including the initial conditions from the early universe and constraints on cosmological parameters and gravity [410, 364, 12]. As cosmological distances are typically inferred through redshifts, a common theme in LSS observations is the necessity to operate in redshift space, where the peculiar velocities of observed targets lead to structure beyond what exists in real space [196, 158]. These so-called redshift-space distortions (RSD) present both a modeling challenge and additional information by encoding information about cosmic velocities in observed densities, for example allowing us to measure the derivative of the linear growth factor $fD = \mathrm{d}D/\mathrm{d}\ln a$, where $f(a)$ and $D(a)$ are the linear-theory growth rate and growth factor (see e.g. refs. [410, 364] for recent reviews). Current and upcoming spectroscopic surveys such as DESI [108] and EUCLID [12] will test these measurements at unprecedented precision. At the same time, the rise of next-generation ground-based CMB experiments [141, 1] as well as renewed interest in low-redshift peculiar velocity surveys [182, 200, 150] in recent years makes it likely that direct measurements of the peculiar velocity statistics underlying redshift space distortions will become available in the near future, offering complementary probes for theories of structure formation. These developments make it timely to revisit our understanding of velocities in large scale structure and their link to redshift space distortions.

The evolution of the LSS at high redshifts and large scales is well modeled by linear perturbation theory [276, 275, 114], and the reach of the perturbation theory can be extended to intermediate scales by including higher order terms in the equations of motion [39]. In this chapter we shall consider 1-loop perturbation theory in both the Eulerian (EPT; [195, 395, 148, 225, 191, 39, 28, 60, 234, 280, 109, 239]) and Lagrangian (LPT; [54, 250, 177, 369, 231, 229, 58, 415, 440, 230, 397, 399]) formulations, and their extensions as an effective field theories [290, 399, 235]. EPT has been extensively employed in the analysis of large-scale structure surveys, with the most recent incarnation being refs. [96, 186, 88]. LPT provides a natural means of modeling biased tracers in redshift space [231, 229], including resummation of the advection terms which is important for modeling features in the clustering signal, and deals directly with the displacement vectors of the cosmic fluid, making it an ideal framework within which to understand their derivatives, i.e. cosmological velocities.

The goal of this chapter is to develop a consistent Fourier-space model of both peculiar-velocity and redshift-space statistics. Our strategy is twofold: first, since the redshift-space power spectrum of galaxies can be understood in terms of series expansions of their velocity statistics, we explore the convergence of these expansions to understand their requirements and limitations. Our analysis of these expansions for halo power spectra uses nonlinear velocity spectra measured directly from simulations, which include nonlinear bias and fingers-

of-god [190], and is a continuation of that in ref. [402], who explored these convergence properties within the Zeldovich approximation, and refs. [261, 260], who explored them in the context of matter and halo power spectra. Similar expansions using velocity statistics from N-body data have also been studied in configuration space for the Gaussian and Edgeworth streaming models [301, 405, 396, 381]. Second, we use one-loop perturbation theory with effective corrections for small scale effects to model the requisite velocity statistics. Our work builds naturally on previous work in configuration space combining velocity statistics and the correlation function in LPT, particularly within the context of the Gaussian streaming model [276, 137, 301, 303, 405, 396], though modeling these statistics in Fourier space enables us to more effectively extend the reach of perturbation theory. We compare and contrast the behavior of these velocity statistics in both EPT and LPT.

This work is organized as follows. We begin in Section 2.2 by describing the N-body simulations that we use throughout the paper. In Section 2.3 we briefly review two methods of expanding velocity statistics in the redshift-space power spectrum (the moment expansion approach and the Fourier streaming model) and study their convergence at the level of velocity statistics measured from N-body simulations. We describe the modeling of these velocity statistics in perturbation theory in Section 2.4 providing a comparison of and translation between the two approaches. Finally, in Section 2.5 the velocity expansions and PT modeling of velocities are combined to yield a consistent model for the power spectrum within one-loop perturbation theory. We conclude with a discussion of our results in Section 2.6. In Appendices, we compare our work to existing models (B.2, B.3), discuss differences between power spectrum wedges and multipoles (B.4) and provide details of our numerical calculations (B.5,B.6,B.7,B.8).

2.2 N-Body Simulations

In this chapter we will use N-body data for two purposes: (1) to test the convergence of various velocity-based expansions for redshift space distortions using exact velocity statistics extracted from simulations and (2) to investigate the extent to which these velocity statistics can be modeled within 1-loop perturbation theory and combined to model the redshift-space power spectrum for biased tracers. To this end we make use of the halo catalogs[1] from the simulations described in ref. [359]. These were the same simulations used in ref. [396], to which the reader is referred for further discussion. Briefly, there were 4 realizations of a ΛCDM ($\Omega_m = 0.2648$, $\Omega_b h^2 = 0.02258$, $h = 0.71$, $n_s = 0.963$, $\sigma_8 = 0.8$) cosmology simulated with 4096^3 particles in a $4\,h^{-1}$Gpc box. We measured the halo power spectrum in two mass bins ($12.5 < \lg M < 13.0$ and $13.0 < \lg M < 13.5$; all masses in $h^{-1}M_\odot$) at $z = 0.8$ and 0.55, in both real and redshift space. We compute the power spectra in bins of width $0.0031\,h\,\mathrm{Mpc}^{-1}$, which is small enough that effects due to binning are $\mathcal{O}(0.1\%)$ for the theories we wish to test. We additionally computed the Fourier-space pairwise velocity statistics up to fourth

[1]The data are available at http://www.hep.anl.gov/cosmology/mock.html. Of the 5 realizations, the data for the first were corrupted so we used only the last 4.

lg$M$	Redshift	$\bar{n}$	b
$12.5 - 13.0$	0.55	0.61	1.45
$13.0 - 13.5$	0.55	0.19	1.93
$12.5 - 13.0$	0.8	0.53	1.72
$13.0 - 13.5$	0.8	0.15	2.32
'Galaxies'	0.8	0.80	1.97

Table 2.1: Number densities and bias values for the samples we use. Halo masses are $\log_{10}$ of the mass in $h^{-1}M_\odot$, number densities are times $10^{-3}\,h^3\,\mathrm{Mpc}^{-3}$. The last row, labeled 'Galaxies', refers to the mock galaxy sample drawn from the halo occupation distribution described in the text.

order in real space. The aforementioned quantities were all computed using the publically available `nbodykit` software [163]. The number densities and rough estimates for the linear biases of the halo samples we consider are given in Table 2.1.

The total volume simulated, $256\,h^{-3}\mathrm{Gpc}^3$, is equivalent to > 40 and > 25 full-sky surveys for redshift slices $0.5 < z < 0.6$ and $0.75 < z < 0.85$, respectively. The statistical errors from the simulations should thus be much smaller than those of any future survey confined to a narrow redshift slice and are dominated by systematic errors in the algorithms or physics missing from the simulations themselves. In fact, the simulations were run with "derated" time steps and halo masses were adjusted to match the halo abundance of a simulation with finer time steps [359]. As detailed in ref. [396], tests of halo catalogs produced with and without derated time steps lead us to assign a systematic error of several percent to the clustering statistics measured in these simulations. Of direct relevance to redshift-space statistics, by comparing the mean-infall velocity and pairwise velocity dispersion on very large scales with linear theory predictions we see evidence that the velocities are underpredicted by about 1-2% by $z = 0.55$. In particular we note that agreement with theory can be improved on all scales if we increase N-body velocities by such a constant factor. To keep the measured redshift-space power spectrum and velocity statistics consistent, we do not apply this correction. Rather, we choose to focus our analysis primarily on the redshift bin $z = 0.8$, relevant in the near term for spectroscopic surveys such as DESI [108] and where the accumulated effects of this systematic are less severe, noting that a few percent error is well within the error budget for simulations of this form.

Finally we construct a mock galaxy sample at $z \simeq 0.8$ using a simple HOD applied to the dark matter halo catalogs. Since it is not our goal to match any particular sample, but rather to investigate how well our model performs on a sample covering a wide range of halo masses and with satellite galaxies, we simply populate all halos above $M_{\rm cut} = 10^{12.5}\,h^{-1}M_\odot$ with a "central" galaxy taken to be comoving with the halo and at the halo center. We also draw a Poisson number of satellites with

$$\langle N_{\rm sat}\rangle = \Theta\left(M - M_{\rm cut}\right)\left(\frac{M}{M_1}\right) \qquad , \quad M_1 = 10^{14}\,h^{-1}M_\odot \tag{2.1}$$

and arrange them following a spherically symmetric NFW profile [253] scaled by the halo concentration and virial radius. In addition to the halo velocity, the satellites have a random, line-of-sight velocity drawn from a Gaussian with width equal to the halo velocity dispersion. This sample has complex, scale-dependent bias and finger-of-god velocity dispersion on small scales providing a test of the ability of our model to fit observed galaxy samples which exhibit both properties.

2.3 Redshift Space Distortions: Velocity Expansions and Convergence

2.3.1 Formalism

In large-scale surveys, line-of-sight positions are typically inferred by measuring redshifts. Since redshifts are affected by the peculiar motions of the observed objects, these inferred redshift-space positions $\mathbf{s}$ will be shifted from the "true" positions $\mathbf{x}$ of these objects according to $\mathbf{s} = \mathbf{x} + \hat{n}(\hat{n} \cdot \mathbf{v})/\mathcal{H}$, where $\hat{n}$ is the unit vector along the line-of-sight and $\mathcal{H} = aH$ is the conformal Hubble parameter [275, 114]. Overdensities in redshift space are thus related to their real space counterparts via number conservation as

$$\begin{aligned} 1 + \delta_s(\mathbf{s}, \tau) &= \int d^3\mathbf{x} \, \left(1 + \delta_g(\mathbf{x}, \tau)\right) \, \delta_D(\mathbf{s} - \mathbf{x} - \mathbf{u}) \\ (2\pi)^3 \delta_D(\mathbf{k}) + \delta_s(\mathbf{k}) &= \int d^3\mathbf{x} \, \left(1 + \delta_g(\mathbf{x}, \tau)\right) \, e^{i\mathbf{k}\cdot(\mathbf{x}+\mathbf{u}(\mathbf{x}))}, \end{aligned} \tag{2.2}$$

where we have defined the shorthand $\mathbf{u} = \hat{n}(\hat{n} \cdot \mathbf{v})/\mathcal{H}$. From the above, the redshift space power spectrum can be written as a special case of the (Fourier transformed) velocity moment-generating function [398]

$$\tilde{M}(\mathbf{J}, \mathbf{k}) = \frac{k^3}{2\pi^2} \int d^3r \; e^{i\mathbf{k}\cdot\mathbf{r}} \; \left\langle (1 + \delta_g(\mathbf{x}_1))(1 + \delta_g(\mathbf{x}_2)) e^{i\mathbf{J}\cdot\Delta\mathbf{u}} \right\rangle_{\mathbf{x}_1 - \mathbf{x}_2 = \mathbf{r}} , \tag{2.3}$$

where we have defined the pairwise velocity $\Delta\mathbf{u} = \mathbf{u}_1 - \mathbf{u}_2$ and the $k^3/(2\pi^2)$ in inserted for convenience. Specifically, we have

$$\frac{k^3}{2\pi^2} P_s(\mathbf{k}) = \tilde{M}(\mathbf{J} = \mathbf{k}, \mathbf{k}) = \frac{k^3}{2\pi^2} \int d^3r \; e^{i\mathbf{k}\cdot\mathbf{r}} \; \left\langle (1 + \delta_g(\mathbf{x}_1))(1 + \delta_g(\mathbf{x}_2)) e^{i\mathbf{k}\cdot\Delta\mathbf{u}} \right\rangle_{\mathbf{x}_1 - \mathbf{x}_2 = \mathbf{r}} . \tag{2.4}$$

Note that the moment generating function with $\mathbf{J} = 0$ is directly proportional to the real space power spectrum, i.e. $\tilde{M}_0 = k^3 P(k)/(2\pi^2) = \Delta^2(k)$, where $\Delta^2(k)$ is the power per log interval in wavenumber in real space.

There exist many approaches to model the redshift space power spectrum (see e.g. refs. [418, 142, 398] for recent reviews). Roughly speaking, these techniques can be understood as different series expansions of the exponential in Equation 2.4 (see e.g. the discussion in ref. [398];

a related discussion on the correlation function and velocity expansions in configuration space can be found in ref. [93]). Our main objective here is to explore the effectiveness of two Fourier-space based approaches: the moment expansion (ME), or "distribution function approach" [328], and the recently proposed Fourier Streaming Model (FSM) [398].

In the moment expansion approach the redshift-space power spectrum is derived by expanding the exponential in Equation 2.4 such that

$$\frac{k^3}{2\pi^2}P_s(\mathbf{k}) = \tilde{M}(\mathbf{J}=\mathbf{k}) = \frac{k^3}{2\pi^2}\sum_{n=0}^{\infty}\frac{i^n}{n!}k_{i_1}\cdots k_{i_n}\tilde{\Xi}^{(n)}_{i_1\cdots i_n}(\mathbf{k}) \tag{2.5}$$

where the density-weighted pairwise velocity moments are defined to be the Fourier transforms of $\Xi^{(n)}_{i_1\cdots i_n} = \langle(1+\delta_1)(1+\delta_2)\Delta\mathbf{u}_{i_1}\cdots\Delta\mathbf{u}_{i_n}\rangle$. For example, the first and second moments are the mean pairwise velocity between halos separated by distance $\mathbf{r}$, $\Xi^{(1)}_i = v_{12,i}(\mathbf{r})$, and the pairwise velocity dispersion, $\Xi^{(2)}_{ij} = \sigma_{12,ij}(\mathbf{r})$[2].

In the Fourier Streaming Model, the redshift-space power spectrum is evaluated by applying the cumulant theorem to the logarithm

$$\ln\left[1+\Delta(k)\right] = \ln\left[1+\tilde{M}(\mathbf{J}=0,\mathbf{k})\right] + iJ_i\tilde{C}^{(1)}_i(\mathbf{k}) - \frac{1}{2}J_iJ_j\tilde{C}^{(2)}_{ij} + ... \tag{2.7}$$

The first few cumulants are related to the Fourier pairwise velocity moments by

$$\begin{aligned}
\tilde{C}^{(1)}_i(\mathbf{k}) &= \frac{k^3}{2\pi^2}\frac{\tilde{\Xi}_i(\mathbf{k})}{1+\Delta^2}\\
\tilde{C}^{(2)}_{ij}(\mathbf{k}) &= \frac{k^3}{2\pi^2}\frac{\tilde{\Xi}_{ij}(\mathbf{k})}{1+\Delta^2} - \tilde{C}^{(1)}_i\tilde{C}^{(1)}_j\\
\tilde{C}^{(3)}_{ijk}(\mathbf{k}) &= \frac{k^3}{2\pi^2}\frac{\tilde{\Xi}_{ijk}(\mathbf{k})}{1+\Delta^2} - \tilde{C}^{(2)}_{\{ij}\tilde{C}^{(1)}_{k\}} - \tilde{C}^{(1)}_i\tilde{C}^{(1)}_j\tilde{C}^{(1)}_k\\
\tilde{C}^{(4)}_{ijkl}(\mathbf{k}) &= \frac{k^3}{2\pi^2}\frac{\tilde{\Xi}_{ijkl}(\mathbf{k})}{1+\Delta^2} - \tilde{C}^{(3)}_{\{ijk}\tilde{C}^{(1)}_{l\}} - \tilde{C}^{(2)}_{\{ij}\tilde{C}^{(2)}_{kl\}} - \tilde{C}^{(1)}_i\tilde{C}^{(1)}_j\tilde{C}^{(1)}_k\tilde{C}^{(1)}_l,
\end{aligned} \tag{2.8}$$

The redshift-space power spectrum is then

$$1+\frac{k^3}{2\pi^2}P_s(\mathbf{k}) = \left(1+\Delta^2(k)\right)\exp\left[\sum_{n=1}^{\infty}\frac{i^n}{n!}k_{i_1}...k_{i_n}\tilde{C}^{(n)}_{i_1\ldots i_n}(\mathbf{k})\right]. \tag{2.9}$$

[2]Since redshift-space distortions depend only on line-of-sight velocities the only nonzero contributions in Equation 2.5 are those due to $k_{\hat{n}} = k\mu$, where μ is the cosine of the angle between the line-of-sight (LOS) and wave vector, which in turn multiplies only velocity statistics projected along the LOS $\hat{n}$. However, models of large-scale structure naturally predict not only the LOS component but the full tensorial quantity

$$\Xi'^{(n)}_{i_1\ldots i_n} = \mathcal{H}^{-n}\left\langle(1+\delta_1)(1+\delta_2)\Delta\mathbf{v}_{i_1}\cdots\Delta\mathbf{v}_{i_n}\right\rangle, \tag{2.6}$$

where $\Delta\mathbf{v} = \mathbf{v}_1 - \mathbf{v}_2$, along with its Fourier transform $\tilde{\Xi}'$, such that the statistics of $\mathbf{u}$ are given by the e.g. $\tilde{\Xi}^{(1)}_i = \tilde{\Xi}'^{(1)}_{\hat{n}}\hat{n}_i$. However, due to the symmetric structure of these velocity moments, the tensor components of Ξ' can be mapped 1-1 to the multipole moments of Ξ, and for this reason we will refer to them interchangeably throughout the text.

At any order the nonlinearity of the exponential in the FSM will produce a resummation of select terms when compared to the moment expansion. Indeed, ref. [398] found distinct differences in the rate of convergence for the case of Zeldovich matter dynamics. However, the two expansions are necessarily equivalent order-by-order in the Taylor-series expanded pairwise velocities, and on scales where $\Delta^2 \lesssim 1$, they will tend to behave similarly. Evaluating whether the differences between the two expansions are significant for halos and galaxies with nonlinear bias and dynamics will be one of the goals of the following sections.

2.3.2 Comparison of methods using simulated data

The Fourier-space velocity expansions described in the previous subsection can be tested by comparing the redshift-space power spectra measured in N-body simulations to velocity power spectra measured from the same simulations. Our aim in this subsection is to use this comparison to test the convergence of each expansion at $n^{\rm th}$ order in both the moment expansion and Fourier streaming approaches. Since the velocity expansions are effectively expansions in both k and μ we will focus on their convergence in terms of power spectrum wedges, sufficiently finely binned such that their values are equivalent to $P(k, \mu_i)$ where μ_i is the central value of each angular bin, but comment on the extension to power spectrum multipoles where appropriate.

Figure 2.1 shows the convergence of the moment expansion and Fourier streaming model for halos of mass $12.5 < \log M < 13.0$ in units of $h^{-1}M_\odot$ at $z = 0.8$ at orders $n = 2$, 3, 4 in each method using velocity spectra $\tilde{\Xi}^{(n)}(\mathbf{k})$ from simulations. The dots show power spectrum wedges (arranged by color in μ) extracted from simulations, while the curves show predictions for each model when keeping velocity statistics up to n^{th} order. The top two rows show the wedges expressed as $kP(k, \mu)$ and the ratio $\ln([1 + \Delta_s^2]/[1 + \Delta_r^2])$, while the bottom row shows the fractional difference between the data and models. The ME and FSM behave very similarly, except at high k and μ where they diverge. This can be understood from the fact that the redshift-to-real-space logarithm shown in the middle row is significantly below unity for most of the angles and scales shown, except for the $\mu = 0.9$ wedge where it reaches 30% and where the ME seems to have somewhat better convergence properties at high k. In both models, going from $n = 2$ to $n = 3$ dramatically improves the broadband shape predictions at $k > 0.05\,h\,{\rm Mpc}^{-1}$, especially in the highest μ bins where the improvement can be in the tens of percents. As a further test, we compute the multipoles predicted by the moment expansion at $n = 2$ and 3 and compare them to the data in the right panel of Figure 2.2. Once again, while staying at $n = 2$ grossly mis-estimates the power spectrum quadrupole, going to $n = 3$ yields excellent agreement on these scales. A similar improvement when incorporating third-order velocity statistics extracted from simulations was seen by refs. [381, 93] in configuration space in the context of correlation function multipoles (see Appendix B.3 for further discussion of configuration space). Interestingly, the fractional error on the quadrupole in both cases grows slightly faster than the fractional error in the highest μ bin in Figure 2.1 (rather than the fractional error of some intermediate wedge), while the fractional error on the hexadecapole far exceeds that of any wedge. We comment

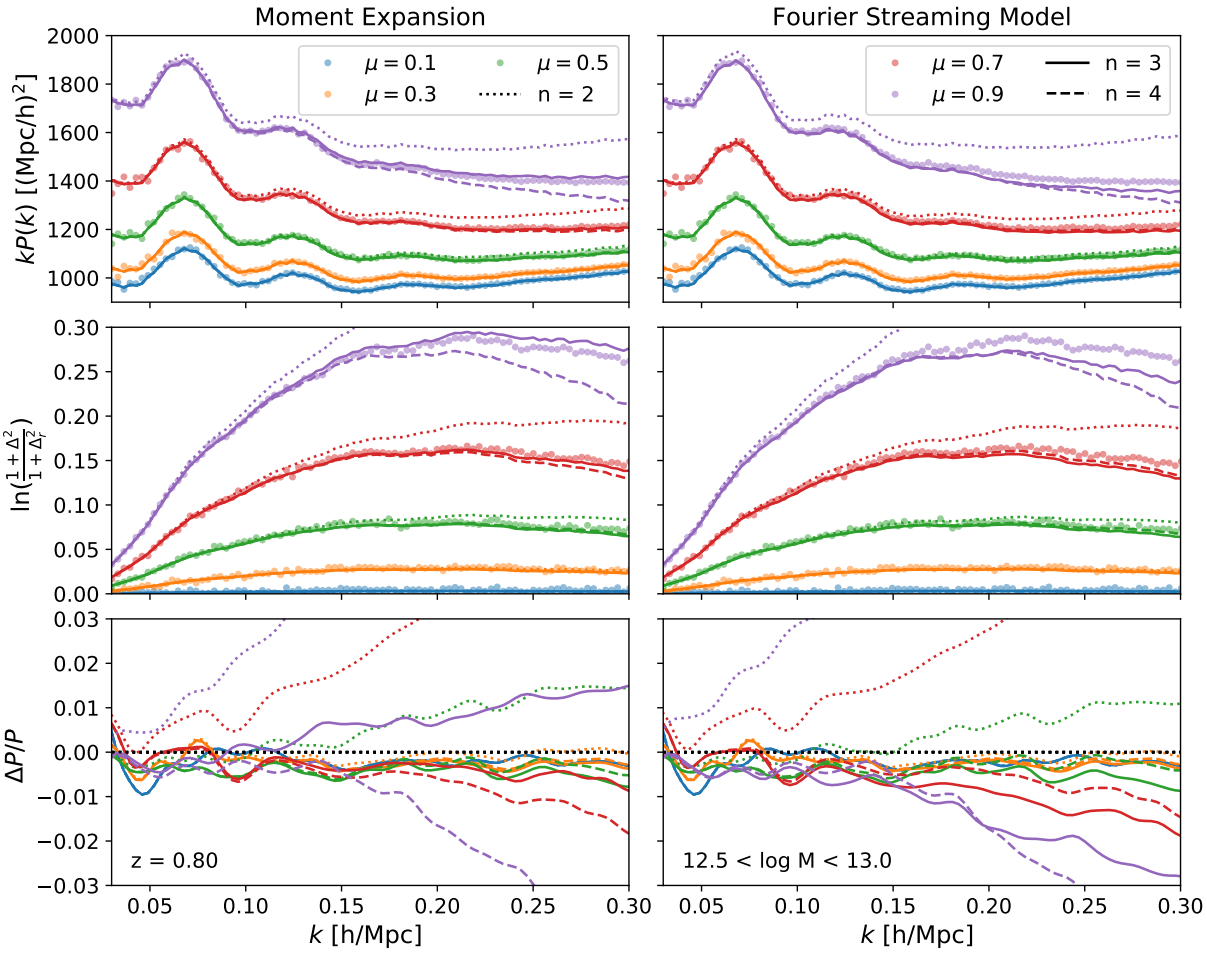

Figure 2.1: Convergence for the moment expansion (left) and Fourier streaming model (right) at each order in velocity statistics – using inputs extracted from simulation data – for halos of mass $12.5 < \log M < 13.0$ (in $h^{-1}M_\odot$) and $z = 0.8$. The top, middle, and bottom columns show five wedges $P(k, \mu)$ represented as $kP(k)$, the log ratio of $1 + \Delta$ in real and redshift space, and the error of each method (smoothed for presentation) and order compared to N-body data. While going from $n = 2$ to $n = 3$ dramatically improves agreement at essentially all scales, especially for large μ, going to $n = 4$ mostly only improves the asymptotic convergence at low k and μ at the mostly subpercent level without significant improvement at higher k and μ.

on these counter-intuitively large errors for multipoles and implications for data analyses in Appendix B.4.

Going to $n = 4$ improves the behavior at low k and μ, but it does not improve – indeed somewhat worsens – the recovery of the broadband shape over the scales smaller than $k \sim 0.15\,h\,\mathrm{Mpc}^{-1}$. This suggests that the reach of both the ME and FSM are limited to perturbative scales, $k|\Delta\mathbf{u}| \lesssim 1$, by the magnitude of the halo velocities and $n = 3$ almost saturates this reach. Indeed, at the scale where the virial velocities of halos become important one might expect that all velocity moments and cumulants contribute significantly to the redshift-space power, slowing the convergence of the velocity expansions. The fact that the inclusion of higher velocity moments does not obviously improve convergence suggests that extending treatments of RSD beyond industry-standard 1-loop order for extended reach in k might give meager returns beyond those generated from overfitting with more parameters. We have chosen to focus on this mass bin and redshift for ease of presentation but note that the other samples discussed in Section 2.2 exhibit qualitatively similar behavior; however, we caution that halos at even higher redshifts — relevant to futuristic galaxy surveys [135, 314, 373, 125] or 21-cm surveys [352] for example — might behave differently due both to the diminishing magnitude of large-scale velocities and differences in virial motions at high redshifts.

The above results suggest that in order to reproduce the broadband shape of $P(k,\mu)$ at the percent level on perturbative scales ($\mathrm{k} \sim 0.25\,h\,\mathrm{Mpc}^{-1}$) it should be sufficient to model velocity statistics up to third order. However, as we have already discussed we can expect that the higher velocity statistics will be dominated by stochastic contributions, i.e. the small scale virial motions of galaxies or halos. In this limit, neglecting the connected contributions to the correlator (see refs. [400, 401] for similar decomposition), we have

$$\Xi^{(3)}_{ijk}(\mathbf{r}) = \langle(1+\delta_1)(1+\delta_2)\Delta\mathbf{u}_i\Delta\mathbf{u}_j\Delta\mathbf{u}_k\rangle \approx \left\langle\Delta\mathbf{u}_{\{i}\Delta\mathbf{u}_j\right\rangle \Xi^{(1)}_{k\}}(\mathbf{r}) \approx \sigma_v^2\delta_{\{ij}\Xi^{(1)}_{k\}}(\mathbf{r})$$

where the curly brackets indicate a sum over symmetric combinations of i, j, k. At leading order in the moment expansion this is equivalent to a counterterm-like contribution

$$P_s(\mathbf{k}) \ni \frac{1}{2}k_\parallel^3\sigma_v^2\,\tilde{\Xi}^{(1)}_\parallel(\mathbf{k}) \approx \frac{1}{2}\sigma_v^2k^2\mu^4P_{\rm L}(k), \tag{2.10}$$

where $P_{\rm L}$ stands for the linear theory prediction with appropriate factors of bias. The predictions for using the moment expansion at $n = 2$ combined with this contribution are shown in dashed lines in Figure 2.2. In addition to providing excellent agreement in the monopole and quadrupole, the counterterm also gives a good fit to the hexadecapole. This supports the assumption we made above of keeping only the disconnected piece of the $n = 3$ velocity moment, indicating that due to the relativly large contribution of the small-scale part of the velocity dispersion, σ_v^2, this term dominates over the connected contributions on the scales of interest. We anticipate that this conclusion would only be strengthened by considering small-scale virial motions of satellite galaxies. This suggests that we focus our modeling efforts on the first two velocity moments, and in the next two sections we shall discuss the modeling of these moments in 1-loop perturbation theory.

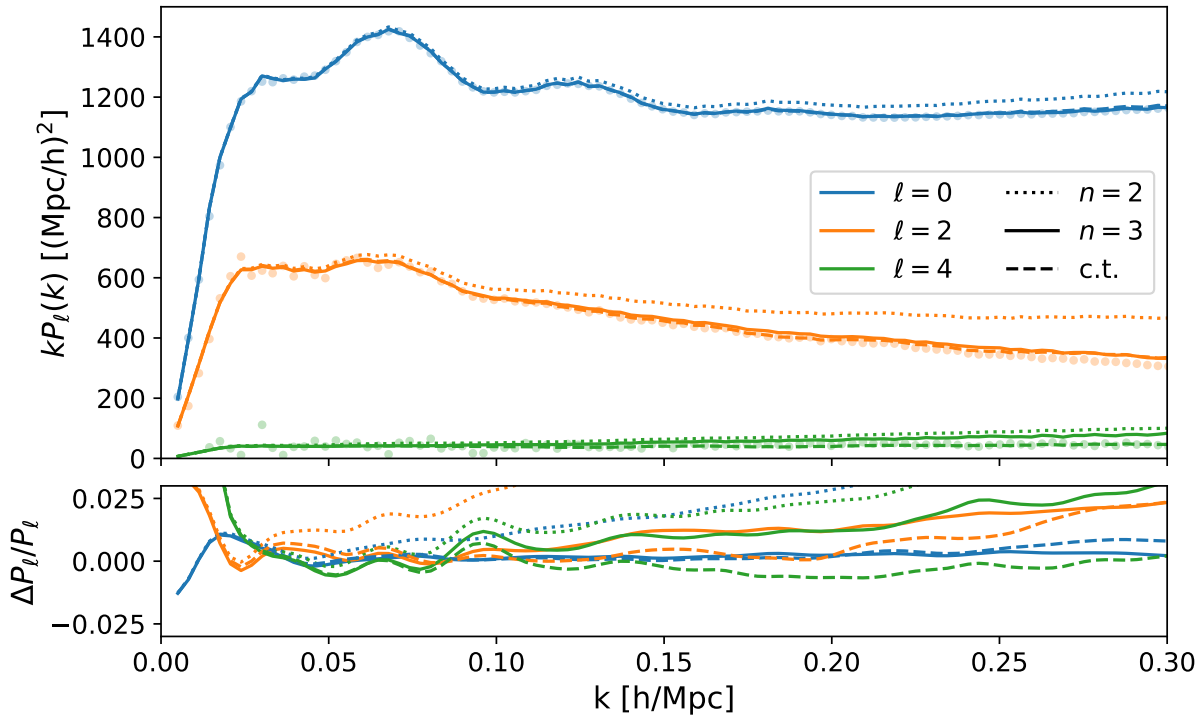

Figure 2.2: Convergence of the moment expansion at $z = 0.8$ for the first three multipoles of the redshift space power spectrum. The top panel shows kP_ℓ while the bottom panel shows the fractional error in each expansion, smoothed to highlight systematic trends. Similarly to the wedges, going from $n = 2$ to $n = 3$ presents substantial improvements in all three multipoles, with the agreeement in the quadrupole going from worse than 50 percent for $n = 2$ to a few percent at perturbative scales ($k < 0.25\,h\,\mathrm{Mpc}^{-1}$). In interpreting these differences it is important to bear in mind that for any observation the error on the quadrupole and hexadecapole are dominated by the monopole contribution and are therefore fractionally much larger than for the monopole.

Finally, it is instructive to consider the relative roles played by the multipole moments of the velocity moments in the redshift-space power spectrum. By symmetry we can write each line-of-sight velocity moment as

$$\tilde{\Xi}^{(n)}_{\mathrm{LOS}}(\mathbf{k}) = \sum_{\ell=0}^{n} \tilde{\Xi}^{(n)}_{\ell}(k)\mathcal{L}_\ell(\mu), \tag{2.11}$$

where $\mathcal{L}_\ell(\mu)$ are Legendre polynomials of the line-of-sight angle; since each moment $\tilde{\Xi}^{(n)}$ gets multiplied by $(k\mu)^n$ in the moment expansion, the components $\tilde{\Xi}^{(n)}_\ell$ contribute with the angular structure $\mu^n\mathcal{L}_\ell(\mu)$. As an example, in Figure 2.3 we have plotted the thus-enumerated contributions to $P_s(k,\mu)$ at three representative wavenumbers as a fraction of

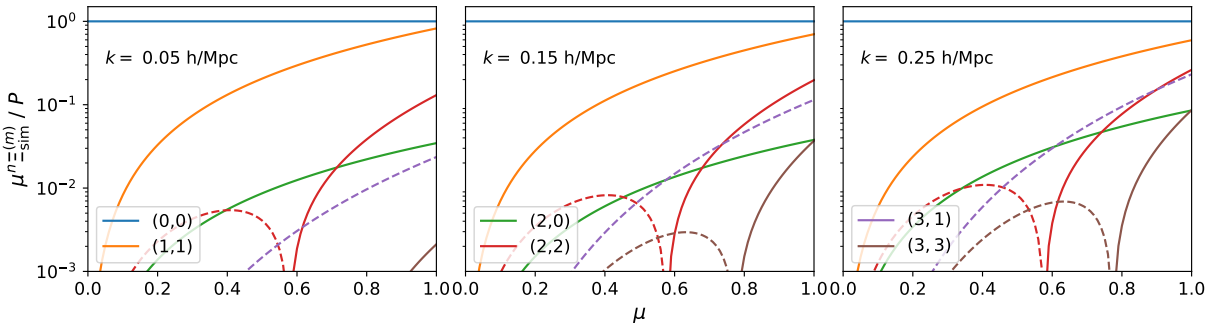

Figure 2.3: Angular contributions (n, m) to the redshift-space power spectrum from the m^{th} multipole of the n^{th} velocity moment at three wavenumbers $k = 0.05,\ 0.15,\ 0.25\,h\,\mathrm{Mpc}^{-1}$ as a fraction of the real-space power spectrum. The anisotropic signal is dominated by the first moment at all scales. For higher multipole moments, for example the quadrupole of the second moment, the absolute magnitude of the contribution to $P_s(k, \mu)$ is small at intermediate μ due to the occurence of zeros in $\mathcal{L}_\ell$.

the real-space power spectrum at that wavenumber. At all of these scales, which cover the reach of perturbation theory at low redshifts, the anisotropic signal is dominated by the first moment, which contributes proportionally to $\mu\mathcal{L}_1$, with the relative importance of higher moments roughly increasing with LOS angle μ. Moreover, the root structure of Legendre polynomials with $\ell > 0$ plays an interesting role in the relative prominence of each contribution–for example, while the quadrupole moment of $\Xi^{(2)}$ is typically larger in absolute magnitude than the monopole, its relative importance at intermediate μ can be comparatively suppressed due to proximity to the root of $\mathcal{L}_2(\mu)$ at $\mu = 1/\sqrt{3}$, and similarly for the octopole moment of $\Xi^{(3)}$. On the other hand, beyond these intermediate μ we expect the contamination of the cosmological signal by small scale (FoG) effects, as well as the importance higher velocity moments, to be increasingly large. Indeed, as we will see for realistic (galaxy) samples the monopole of $\Xi^{(2)}$ will tend to contain a large, constant small-scale contribution, further increasing its relative importance over the quadrupole. Roughly speaking, then, the contributions to the redshift-space power spectrum rank in importane as $\tilde{\Xi}^{(0)}_0$, $\tilde{\Xi}^{(1)}_1$, $\tilde{\Xi}^{(2)}_0$, $\tilde{\Xi}^{(2)}_2$, $\tilde{\Xi}^{(3)}_1$, and so on.

2.4 Pairwise Velocity Spectra in Perturbation Theory

In this section we present formulae for the real-space pairwise velocity spectra required for both the ME and FSM in Lagrangian and Eulerian perturbation theory. These quantities live naturally in configuration space, where they can be directly interpreted as density-weighted pairwise velocities, while in Fourier space they must be broken down into components to be measured. While we shall primarily employ the velocity spectra for computation of the

redshift-space power spectrum, we emphasize that pairwise velocity statistics are well-defined, Galilean invariant quantities and have the potential to be measured (in redshift space) by future kSZ and peculiar velocity surveys [358, 182, 200]. They are therefore interesting in their own right. Our results for the zeroth, first and second moments of the pairwise velocity in LPT are the Fourier-space analogues of the results presented in ref. [396], though we differ slightly in the treatment of counterterms in the velocity dispersion, include stochastic contributions to both densities and velocities and a superset of the density-bias expressions given in ref. [398]. We organize the expressions so that they can be efficiently evaluated numerically by converting the angular integrals into sums over spherical Bessel functions, then treating the resulting tower of Hankel transforms via the FFTLog algorithm [159, 397, 396]. The explicit form of these Hankel transforms is given in Appendix B.6. Throughout this section and the next we will compare our theoretical predictions to velocity statistics of the same halos studied in Section 2.3 (i.e. $12.5 < \log M < 13.0$ at $z = 0.8$). Results for the other mass bins and redshifts are qualitatively similar, though the potential for even higher systematics in the N-body data at lower z are an important caveat. We shall consider our mock galaxy catalogs when we combine the ingredients into the redshift-space power spectrum.

2.4.1 Background

Lagrangian and Eulerian Perturbation Theory

The two conventional frameworks within which to perturbatively model cosmological structure formation are Eulerian and Lagrangian perturbation theory (see the references in the introduction). Lagrangian perturbation theory models cosmological structure formation by tracking the trajectories $\mathbf{x}(\mathbf{q}, t) = \mathbf{q} + \mathbf{\Psi}(\mathbf{q}, t)$ of infinitesimal fluid elements originating at Lagrangian positions $\mathbf{q}$. These fluid elements cluster under the influence of gravity and their displacements obey the equation of motion $\ddot{\mathbf{\Psi}} + \mathcal{H}\dot{\mathbf{\Psi}} = -\nabla\Phi(\mathbf{x})$ — where the dotted derivatives are with respect to conformal time τ, $\mathcal{H} = aH$ is the conformal Hubble parameter and Φ is the gravitational potential — which we solve for order-by-order in terms of the linear density contrast $\delta_{\rm lin}$ as $\mathbf{\Psi} = \mathbf{\Psi}^{(1)} + \mathbf{\Psi}^{(2)} + \cdots$, where

$$\mathbf{\Psi}_i^{(n)}(\mathbf{q}) = \frac{i}{n!}\int_{\mathbf{k},\ \mathbf{p}_1\cdots\mathbf{p}_n} e^{i\mathbf{k}\cdot\mathbf{q}}\ \delta^D_{\mathbf{k}-\mathbf{p}}\ L_i^{(n)}(\mathbf{p}_1, ..., \mathbf{p}_n)\ \delta_{\rm lin}(\mathbf{p}_1)...\delta_{\rm lin}(\mathbf{p}_n), \tag{2.12}$$

were we use the shorthands $\mathbf{p} = \sum_i \mathbf{p}_i$ and $\delta^D_{\mathbf{k}-\mathbf{p}} = (2\pi)^3\delta^{(D)}(\mathbf{k}-\mathbf{p})$. Expressions for the n$^{\rm th}$ order kernels can be found in, for example, ref. [231]. By contrast, Eulerian perturbation theory (EPT, often also called standard perturbation theory: SPT), solves perturbatively for

the density and velocity at the observed, Eulerian position $\mathbf{x}$ (see e.g. ref. [39]), i.e.

$$\delta(\mathbf{k}) = \sum_n \int_{\mathbf{p}_1\cdots\mathbf{p}_n} \delta^D_{\mathbf{k}-\mathbf{p}_{1n}} F_n(\mathbf{p}_1,\ldots,\mathbf{p}_n)\delta_{\rm lin}(\mathbf{p}_1)...\delta_{\rm lin}(\mathbf{p}_n), \tag{2.13}$$
$$v_i(\mathbf{k}) = -if\mathcal{H}\frac{k_i}{k^2}\sum_n \int_{\mathbf{p}_1\cdots\mathbf{p}_n} \delta^D_{\mathbf{k}-\mathbf{p}_{1n}} G_n(\mathbf{p}_1,\ldots,\mathbf{p}_n)\delta_{\rm lin}(\mathbf{p}_1)...\delta_{\rm lin}(\mathbf{p}_n).$$

However, despite the apparent differences LPT and EPT are formally equivalent (see e.g. the discussion in ref. [235]). In particular, by solving for the observed matter overdensity

$$1+\delta(\mathbf{x}) = \int d^3\mathbf{q}\ \delta_D(\mathbf{x}-\mathbf{q}-\mathbf{\Psi}), \quad (2\pi)^3\delta_D(\mathbf{k})+\delta(\mathbf{k}) = \int d^3\mathbf{q}\ e^{-i\mathbf{k}\cdot(\mathbf{q}+\mathbf{\Psi})}, \tag{2.14}$$

order-by-order in the linear initial conditions, one recovers the expressions of EPT, and similarly for velocity statistics by weighting the integral above by appropriate functions of the velocity $\dot{\mathbf{\Psi}}(\mathbf{q})$. Nonetheless, the exponentiated displacements in Equation 2.14 can be used to motivate resummations of particular contributions to the nonlinear density due to long-wavelength (IR) displacements [335, 399], which can lead to dramatic differences with the predictions of (pure) EPT, as we will see later. A proper treatment of these IR displacements is important for cosmological inference.

Modeling biased tracers

The fact that cosmological surveys generally do not observe the underlying matter distribution but rather tracers of the nonlinear density field such as halos and galaxies presents an additional complication in mapping theory to observations. In PT one approaches this problem by perturbatively expanding the large-scale component of the galaxy and halo field that responds to the short-wavelength (UV) galaxy and halo formation physics via the so-called bias coefficients (see e.g. ref. [109] for a review, and recent ref. [139] for a direct construction based on the equivalence principle). Once again the treatment of bias in LPT and EPT, though ultimately equivalent, are subtly different; we will now describe them in turn.

In the Lagrangian approach the positions of discrete tracers like galaxies and halos are assumed to be drawn according to a distribution depending on local initial conditions such that their overdensities in their initial (Lagrangian) coordinates are given by

$$\begin{aligned} F[\delta_{\rm lin}(\mathbf{q}), s_{{\rm lin},ij}(\mathbf{q}), ..., \nabla\delta_{\rm lin}(\mathbf{q})] &= 1+\delta_g(\mathbf{q},\tau_0) \\ &= 1 + b_1\delta_{\rm lin}(\mathbf{q}) + \frac{1}{2}b_2\big(\delta^2_{\rm lin}(\mathbf{q}) - \langle\delta^2_{\rm lin}\rangle\big) + b_s\big(s^2_{\rm lin}(\mathbf{q}) - \langle s^2_{\rm lin}\rangle\big) \\ &\quad + b_3\ O_3(\mathbf{q}) + \cdots + b_\nabla\nabla^2\delta_{\rm lin}(\mathbf{q}) + \epsilon(\mathbf{q}), \end{aligned} \tag{2.15}$$

where s_0 is the initial shear field[3] and we have included a representative third-order operator O_3 to account for the various degenerate contributions to the power spectrum at one-loop

[3]The inclusion of the initial shear and Laplacian information, in addition to the initial density, improves the ability to model assembly bias to the extent that this is encoded in the peak statistics (e.g. ref. [99]).

order [234]. Definitions for these quantities are given in Appendix B.2. Given this bias functional, these initial overdensities can then be mapped to the evolved overdensities of biased tracers via number conservation much like the nonlinear matter density:

$$\begin{aligned} 1+\delta_g(\mathbf{x},\tau) &= \int d^3\mathbf{q}\; F(\mathbf{q})\; \delta_D(\mathbf{x}-\mathbf{q}-\mathbf{\Psi}(\mathbf{q},\tau)) \\ (2\pi)^3\delta_D(\mathbf{k})+\delta_g(\mathbf{k}) &= \int d^3\mathbf{q}\; e^{i\mathbf{k}\cdot(\mathbf{q}+\mathbf{\Psi}(\mathbf{q}))}F(\mathbf{q}). \end{aligned} \tag{2.16}$$

In this way, within LPT we have the apparent separation of clustering due to initial biasing in $F(\mathbf{q})$ and clustering due to nonlinear dynamics enforced by the equality $\mathbf{x}=\mathbf{q}+\mathbf{\Psi}$.

In the Eulerian approach, on the other hand, the galaxy overdensity is expressed in terms of a bias expansion based on present-day operators such as the nonlinear density $\delta(\mathbf{x})$. Here we adopt the biasing scheme of ref. [234], where up to third order a biased tracer field is expanded in terms of the nonlinear Eulerian fields as[4]

$$\delta_h = c_1\delta + \frac{c_2}{2}\delta^2 + c_s s^2 + \frac{c_3}{6}\delta^3 + c_{1s}\delta s^2 + c_{st}st + c_{s3}s^3 + c_\psi\psi, \tag{2.17}$$

where $s^2 = s_{ij}s_{ij}$, $s^3 = s_{ij}s_{jl}s_{li}$ and $st = s_{ij}t_{ij}$, and the shear operators are defined as

$$\psi = \eta - \frac{2}{7}s^2 + \frac{4}{21}\delta^2, \quad s_{ij} = \left(\frac{\partial_i\partial_j}{\partial^2} - \frac{1}{3}\delta_{ij}\right)\delta, \quad t_{ij} = \left(\frac{\partial_i\partial_j}{\partial^2} - \frac{1}{3}\delta_{ij}\right)\eta, \quad \eta = \theta - \delta. \tag{2.18}$$

In the above bias expansion we also implicitly assume subtraction of mean field values like $\langle\delta^2\rangle$.

Despite formal differences, the bias schemes in LPT and EPT can in fact be mapped to one another via the appropriate linear transformations of the bias parameters (see e.g. refs. [69, 310]). Indeed, these two approaches are a subset of a more general scenario in which the response of tracer formation to the large-scale structure is local in space but not in time, requiring us to take into account the evolution of the density field in the neighborhood around a tracer's trajectory; fortunately, these time-dependent responses have been shown to be perturbatively factorizable and equivalent to either LPT or EPT [332, 109, 4]. For our purposes, at one loop we have that the rotation[5] between the Lagrangian and Eulerian bases can be accomplished by (see e.g. ref. [109])

$$\begin{aligned} c_1 &= 1 + b_1 \\ c_2 &= b_2 + \frac{8}{21}b_1, \quad c_s = b_s - \frac{2}{7}b_1 \\ c_3 &= b_3 + ab_1 \end{aligned} \tag{2.19}$$

[4]Throughout this chapter we will adopt the notation c_n for Eulerian bias coefficients b_n^E.

[5]In performing this rotation we have implicitly assumed that the contributions from c_3 and b_3 degenerate with linear bias have been removed.

where we have used b and c to distinguish between the Lagrangian and Eulerian bias parameters, respectively, and a is a constant depending on which third-order bias parameter one chooses. For instance, choosing the third order operator to be $st = s_{ij}t_{ij}$ we obtain $c_{st} = b_{st} + \frac{1}{3}b_1$. Beyond being necessary to complete the correspondence between LPT and EPT, these bias mappings can also be of practical use; for example there is some evidence that higher order Lagrangian bias is small for halos in N-body simulations and the higher-order Eulerian bias parameters are generated primarily by evolution [4, 322]. The Eulerian c_n thus tend towards those predicted by "local" Lagrangian bias, allowing us to set useful restrictions on the Eulerian biases in EPT analyses.

Derivative Corrections and Stochastic Contributions

In addition to the bias operators discussed in the previous subsection, one also needs to consider terms from the derivative expansion and contributions arising purely from the coupling of short modes (stochastic contributions). In this chapter, we follow the standard approach in the literature (see, e.g., ref. [109] for a review) and add the leading order derivative contributions in the galaxy field of the form $(\partial/k_\star)\delta$ (in the appropriate coordinates for LPT and EPT). In the power spectrum, these terms generically result in contributions of the form $(k^2/k_\star^2)P_{\rm lin}$ (or $(k^2/k_\star^2)P_{\rm Zel}$ in case of LPT). In most of the velocity moment power spectra, these terms are degenerate with the counterterm contributions at one-loop order. We explicitly account for these in each of the moments discussed below and finally combine them in the redshift space power spectrum.

Stochastic contributions, in the RSD power spectrum as well as velocity moments, can come in two forms. First, we should add the pure noise field ϵ to our density expansion, which captures the galaxy field component uncorrelated with the long density fields and is characterized by scale-independent autocorrelations (shot noise). The second type of stochastic contributions appear as small-scale counterterms of the contact velocity correlators of the form $\langle v^n(x)\rangle$ that feature prominently in the higher velocity moments. These terms are traditionally labeled as "Finger of God" terms [190]. They reflect the non-linear structure of the redshift space mapping, encapsulating the feedback of small-scale (non-perturbative) velocity modes on the correlators on large scales.

It is important to note that 'perturbative' operators carry the bulk of the cosmological dependence, while stochastic terms mostly parameterize the part of the signal that is decorrelated with the linear density fluctuations and consequently with the initial conditions. Thus, once stochastic parameters dominate, it can be taken as an indication that little cosmological signal is left to be extracted from these scales. However, it is important to distinguish between pure stochastic terms, such as shot noise, and FoG-like contributions due to stochastic velocities; the latter behave like counterterms with shapes that depend nontrivially on large-scale modes. Similarly, higher derivative terms can show a significant correlation with long-wavelength fluctuations and thus, in principle, can also carry cosmological information. However, heavy reliance on these terms can, in practice, lead to many approximate degeneracies and thus can quickly reduce the amount of information available

from the scale dependence of the correlations of interest. In the rest of this section, we shall see how velocity moments exhibit this behavior, with higher moments displaying stronger reliance on stochastic and derivative contributions.

2.4.2 Velocity Correlators in LPT and EPT

Having reviewed the essential ingredients of LPT and EPT, our goal in this subsection is to provide expressions for the pairwise velocity moments at one loop in both formalisms. In LPT, these can be naturally computed as derivatives of the generating functional in Equation 2.3, which can be written as

$$M(\mathbf{J},\mathbf{k}) = \frac{k^3}{2\pi^2}\int d^3\mathbf{q}\; e^{i\mathbf{k}\cdot\mathbf{q}}\; \langle F(\mathbf{q}_1)F(\mathbf{q}_2)\; e^{i\mathbf{k}\cdot\Delta + i\mathbf{J}\cdot\dot{\Delta}}\rangle_{\mathbf{q}=\mathbf{q}_1-\mathbf{q}_2}, \tag{2.20}$$

where $\Delta = \mathbf{\Psi}_1 - \mathbf{\Psi}_2$ and $\dot{\Delta}$ is its time derivative, and which has the additional benefit that derivatives with respect to $\mathbf{J}$ are automatically Galilean invariant. In EPT, on the other hand, the pairwise velocity moments are most straightforwardly computed by decomposing them into density-velocity correlators

$$P_{LL'}(k,\mu) \equiv \left\langle \big(1+\delta\big) * u^L_{\hat{n}} \middle| \big(1+\delta\big) * u^{L'}_{\hat{n}} \right\rangle', \tag{2.21}$$

where, for brevity, we introduce the primed expectation values to denote expectation values with Dirac delta function dropped and a bar notation to indicate the arguments, i.e. $\langle A|B\rangle \equiv \langle A(\mathbf{k})B(\mathbf{k}')\rangle = (2\pi)^3\delta_D(\mathbf{k}+\mathbf{k}')\;\langle A(\mathbf{k})B(\mathbf{k}')\rangle'$. Working at one loop in perturbation theory yields non-zero zeroth through fourth velocity moments, which we will now describe in detail.

Zeroth Moment: Power Spectrum

In LPT, the zeroth moment pairwise velocity spectrum, i.e. the real-space power spectrum $P(k)$, is given by

$$\begin{aligned} P(k) = \int d^3\mathbf{q}\; e^{i\mathbf{k}\cdot\mathbf{q}}\; e^{-\frac{1}{2}k_ik_jA^{\rm lin}_{ij}}\Big\{ & 1 - \frac{1}{2}k_ik_jA^{\rm loop}_{ij} + \frac{i}{6}k_ik_jk_kW_{ijk} \\ & + 2ib_1k_iU_i - b_1k_ik_jA^{10}_{ij} + b_1^2\xi_{\rm lin} + ib_1^2k_iU_i^{11} - b_1^2k_ik_jU_i^{\rm lin}U_j^{\rm lin} \\ & + \frac{1}{2}b_2^2\xi^2_{\rm lin} + 2ib_1b_2\xi_{\rm lin}k_iU_i^{\rm lin} - b_2k_ik_jU_i^{\rm lin}U_j^{\rm lin} + ib_2k_iU_i^{20} \\ & + b_s(-k_ik_j\Upsilon_{ij} + 2ik_iV_i^{10}) + 2ik_ib_1b_sV_i^{12} + b_2b_s\chi + b_s^2\zeta \\ & + 2ib_3k_iU_{b_3,i} + 2b_1b_3\theta + \alpha_Pk^2 + ...\Big\} + R_h^3. \end{aligned} \tag{2.22}$$

The "1" in the first line gives the (linear) Zeldovich prediction [431] for matter power spectrum $P_{\rm Zel}$. The first line gives the one-loop matter power spectrum in LPT, while the second to fifth lines give contributions successively including the linear, quadratic, shear and third-order biases. The final line also includes a counterterm, α_Pk^2 and stochastic term R_h^3. The

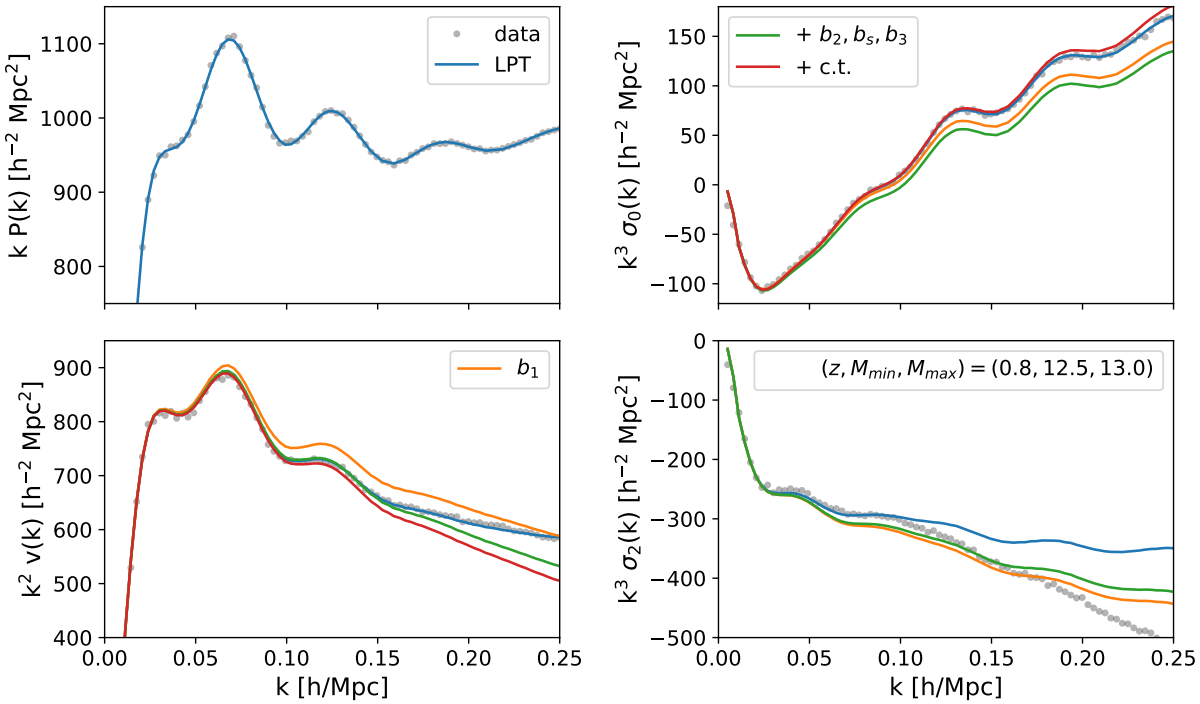

Figure 2.4: Fits to zeroth ($P(k)$, top left), first ($v(k)$, bottom left), and second (σ, right column) halo pairwise velocity moment spectra measured from simulations (gray points) in one-loop Lagrangian perturbation theory (blue) for the fiducial mass bin and redshift. The second moment is split into its monopole and quadrupole for ease of presentation. The contributions from sequentially adding linear bias (orange), nonlinear bias (green) and counterterms (red) are also shown as separate curves. The full model (blue) differs from the red curves by stochastic contributions (though they are identical for σ_2, for which we do not include any stochastic corrections in the lower right panel). We do not include the separate contributions to the power spectrum as the stochastic contribution contributes significantly at all scales. Our model fits these velocity statistics at the percent level out to $k = 0.25\,h\,\mathrm{Mpc}^{-1}$, except for σ_2 which is only fit to around $k = 0.1\,h\,\mathrm{Mpc}^{-1}$ (see text for discussion).

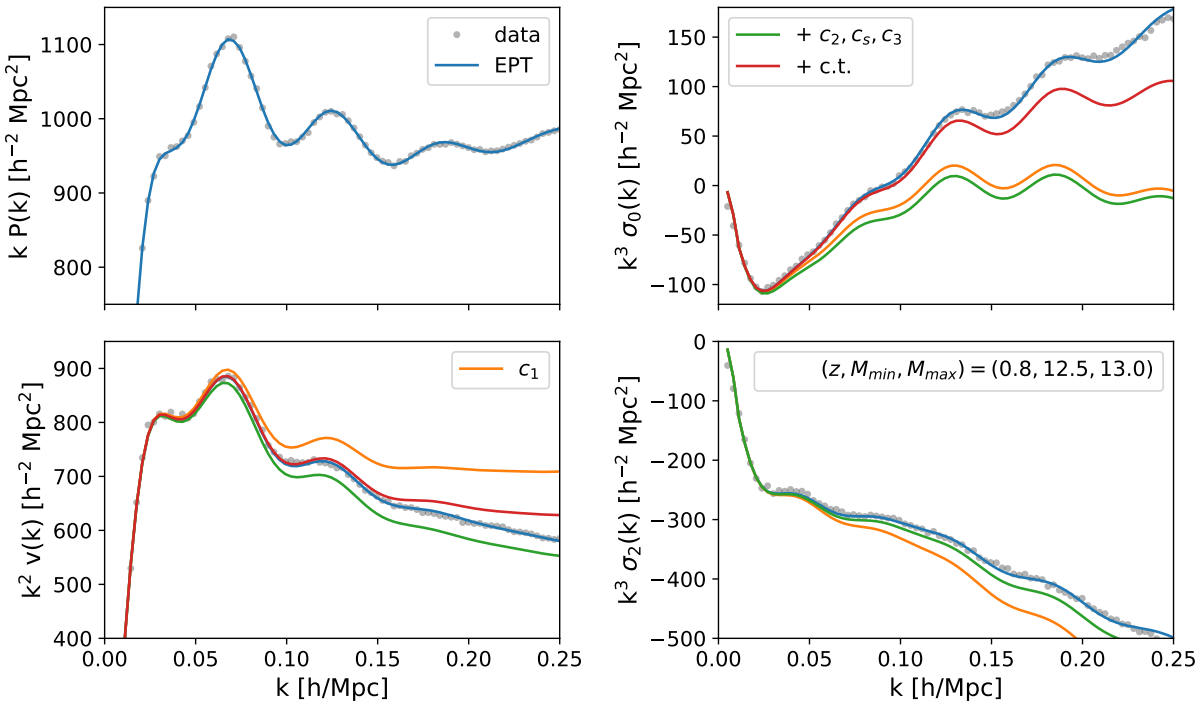

Figure 2.5: Same as Figure 2.4 but for EPT. Note that, in the lower right panel, there is almost no (numerical) difference between the green and blue lines, the former of which differs from the full prediction of EPT by a counterterm; we have not included any stochastic contributions in σ_2.

Lagrangian correlators due to third-order bias U_{b_3} and θ are defined in Appendix B.2.1; the other various Lagrangian-field correlators (e.g. U_i, A_{ij}, W_{ijk} etc.) are defined[6] in [231, 229, 58, 399, 396] and tabulated in Appendix A.3. Some quantities, such as $U_i = U_i^{\rm lin} + U_i^{\rm loop}$, contain contributions at both linear and one-loop levels, which we will use the "lin" and "loop" sub- or superscripts to denote when separated.

Lagrangian perturbation theory in principle includes a much larger set of effective contributions [290, 399] — including derivative bias b_∇ [396] — however, all of these contributions to the real-space power spectrum are proportional to $k^2 P_{\rm Zel}(k)$ at one-loop order (counting α_P as itself first order), so we will summarize their effect by one counterterm only. Finally, the autocorrelation of the stochastic modes gives a "shot-noise" contribution $R_h^3 \sim \bar{n}^{-1}$, where $\bar{n}$ is the number density of tracers [234, 280, 109].

[6]Note that there is an erroneous factor of two in the expression for V^{10} in Eq. D.17 of ref. [396] . The correct prefactor should be $-\hat{q}_i/7$ not $-2\hat{q}_i/7$.

In EPT, on the other, hand we have

$$P(k) = c_1^2 P_{\rm lin}(k) + \int_{\mathbf{p}} \Big[2c_1^2 \big[F_2(\mathbf{p}, \mathbf{k}-\mathbf{p})\big]^2 + 2c_1 c_2 F_2(\mathbf{p}, \mathbf{k}-\mathbf{p}) + 4c_1 c_s \; F_2(\mathbf{p}, \mathbf{k}-\mathbf{p}) S_2(\mathbf{p}, \mathbf{k}-\mathbf{p}) + \frac{c_2^2}{2} + 2c_2 c_s S_2(\mathbf{p}, \mathbf{k}-\mathbf{p}) + 2c_s^2 \big[S_2(\mathbf{p}, \mathbf{k}-\mathbf{p})\big]^2 \Big] P_{\rm lin}(p) P_{\rm lin}(|\mathbf{k}-\mathbf{p}|) + 6c_1 P_{\rm lin}(k) \int_{\mathbf{p}} \Big(c_1 F_3(\mathbf{p}, -\mathbf{p}, \mathbf{k}) + c_3 S_\psi(\mathbf{p}, -\mathbf{p}, \mathbf{k}) \Big) P_{\rm lin}(p) + c_0^{(0)} \frac{k^2}{k_*^2} P_{\rm lin}(k) + s_0 \quad . \tag{2.23}$$

Many of the third order bias operators listed in Equation 2.17 do not contribute explicitly to the one-loop power spectrum, and only one non-vanishing independent contribution remains. The details of the EPT derivations for this and the velocity statistics below are given in Appendix B.2.2. In addition, in EPT an explicit IR-resummation is required to tame the effects of long-wavelength modes, which is described in Appendix B.2.4 for all velocity moments and implicitly performed in all our EPT results.

In addition to the "deterministic" bias parameters there is one counter term (with coefficient $c_0^{(0)}$) that is required to regularize the one-loop, P_{13}-like terms and is degenerate with the derivative bias contribution. In general, for counterterm we will use the $c_n^{(\ell)}$ thus notation taking into account that different angular dependence can have different counterterm contributions. In addition to these terms there is a constant shot noise contribution obtained by correlating the purely stochastic component of the halo field with itself (labeled s_0 in the above).

Fits to the power spectrum extracted from N-body data, along with fits for other velocity statistics using a single, consistent set of bias parameters, are shown in Figures 2.4 and 2.5. As shown in the top-left panels of the two figures, both LPT and EPT provide good fits to the data past $k \sim 0.25\,h\,\mathrm{Mpc}^{-1}$, beyond which the shot noise accounts for an increasingly large share of the total power, reaching more than 35% of the total power by $k = 0.2\,h\,\mathrm{Mpc}^{-1}$. Setting the third-order Lagrangian parameter $b_3 = 0$, as discussed in Section 2.4.1, does not qualitatively change our results.

First Moment: Pairwise Velocity Spectrum

The pairwise velocity spectrum, the Fourier transform of $v_i(\mathbf{r}) \equiv \Xi_i(\mathbf{r})$, is given in LPT by[7]

$$\begin{aligned}\mathbf{v}_i(\mathbf{k}) = \int d^3\mathbf{q}\; e^{i\mathbf{k}\cdot\mathbf{q}}\; e^{-\frac{1}{2}k_ik_jA^{\rm lin}_{ij}}\Big\{ & ik_j\dot{A}_{ji} - \frac{1}{2}k_jk_k\dot{W}_{jki} \\ & + 2b_1\dot{U}_i + 2b_1^2ik_jU^{\rm lin}_j\dot{U}^{\rm lin}_i + \big(2ib_1k_kU^{\rm lin}_k + b_1^2\xi_{\rm lin}\big)\; ik_j\dot{A}^{\rm lin}_{ji} + 2ib_1k_j\dot{A}^{10}_{ji} + b_1^2\dot{U}^{11} \\ & + 2\big(ib_2k_jU^{\rm lin}_j + b_1b_2\xi_{\rm lin}\big)\dot{U}^{\rm lin}_i + b_2\dot{U}^{20} + 2b_s(\dot{V}^{10}_i + ik_j\dot{\Upsilon}_{ji}) + 2b_1b_s\dot{V}^{12}_i \\ & + 2b_3\dot{U}_{b_3,i} + \alpha_vk_i + ...\Big\} + R_h^4\tilde{\sigma}_vk_i. \end{aligned} \tag{2.24}$$

The dots indicate time derivatives in the displacements, which appear because we have moved on from pure density statistics to velocities; this notation has been previously used in refs. [405, 396], and we give a comprehensive list of these time derivative terms in Appendix B.1 as they will be ubiquitous in our discussion of velocity statistics in LPT. In Equation 2.24 again the first two lines give the matter and density bias contributions, while the third line contains contributions due to shear bias and an effective correction $\sim \alpha_vk_iP_{\rm Zel}$. The latter regulates, for example, UV sensitivities in $\dot{A}_{ij} = \dot{A}^{\rm LPT}_{ij} + \bar{\alpha}_v\delta_{ij} + \cdots$ and is contracted with the wavevector k_i in the velocity spectrum. By symmetry, $\mathbf{v}_i(\mathbf{k})$ must be imaginary and point in the $\mathbf{k}$ direction, so we can decompose it as $\mathbf{v}_i(\mathbf{k}) = iv(k)\hat{k}_i$. Explicit expressions for $v(k)$, written as a sum of Hankel transforms, are provided in Appendix B.6.

As in the case of the power spectrum, while there are in principle several more counterterms and derivative bias contributions in addition to the one indicated (e.g. $\sim \langle\dot{\Delta}_i\nabla^2\delta\rangle$ or $\langle\nabla_i\delta_1\delta_2\rangle$), all such contributions Fourier transform to $\sim k_iP_{\rm lin}(k)$ at lowest order and as such we account for them using only one effective correction, α_v. The final term, $R_h^4\tilde{\sigma}_vk_i$, is the leading order stochastic contribution due to the correlation between the stochastic density and velocity, $\langle\epsilon(\mathbf{q}_1)\epsilon_i(\mathbf{q}_2\rangle \sim R_h^3\tilde{\sigma}_v\nabla_i\delta_D(\mathbf{q})$ [280, 109], which can be approximated as a Dirac-δ derivative on large scales.

Similarly to the density auto power spectrum, in EPT we have contributions from all the

[7] Note that our expression for term proportional to b_s differs from that in ref. [396] by a factor of two.

bias operators introduced previously. We have

$$\begin{aligned}\mathbf{v}_i(\mathbf{k}) =& -2ic_1\frac{k_i}{k^2}P_{\rm lin}(k)\\ &-2i\int_{\mathbf{p}}\left[\frac{k_i}{k^2}\Big(2c_1F_2(\mathbf{p},\mathbf{k}-\mathbf{p})+c_2+2c_sS_2(\mathbf{p},\mathbf{k}-\mathbf{p})\Big)G_2(\mathbf{p},\mathbf{k}-\mathbf{p})\right.\\ &\qquad\left.+\frac{p_i}{p^2}\Big(2c_1^2F_2(\mathbf{p},\mathbf{k}-\mathbf{p})+c_1c_2+2c_1c_sS_2(\mathbf{p},\mathbf{k}-\mathbf{p})\Big)\right]P_{\rm lin}(p)P_{\rm lin}(|\mathbf{k}-\mathbf{p}|)\\ &-2iP_{\rm lin}(k)\int_{\mathbf{q}}\left[3\frac{k_i}{k^2}\Big(c_1F_3(\mathbf{p},-\mathbf{p},\mathbf{k})+c_1G_3(\mathbf{p},-\mathbf{p},\mathbf{k})+c_3S_\psi(\mathbf{p},-\mathbf{p},\mathbf{k})\Big)\right.\\ &\qquad\left.+2c_1^2\Big(\frac{p_i}{p^2}F_2(\mathbf{p},-\mathbf{k})+\frac{(\mathbf{k}-\mathbf{p})_i}{(\mathbf{k}-\mathbf{p})^2}G_2(\mathbf{p},-\mathbf{k})\Big)\right]P_{\rm lin}(p)\Big]\\ &-ic_1^{(0)}\frac{\hat{k}_i}{k_*^2}P_{\rm lin}(k)+s_1k_i\cdots\end{aligned}\tag{2.25}$$

where $c_1^{(0)}$ is the coefficient of the counterterm, and the s_1 is the leading stochastic velocity contribution.

A comparison to $v(k)$ from N-body data is shown in the bottom-left panels of Figure 2.4 and 2.5. Both formalisms give a good fit to the data past $k = 0.2\,h\,\mathrm{Mpc}^{-1}$, though as noted in Section 2.2, comparing the theory to the N-body data at large scales suggests that the simulations slightly under-predict velocities (by one or two percent). The stochastic contribution accounts for a significant fraction of the power in both fits at high wavenumber ($k > 0.1\,h\,\mathrm{Mpc}^{-1}$) that cannot be accounted for by the other bias parameters or counterterms. Not fiting for it leads to oscillatory residuals due to a mismatch between the BAO and overall broadband amplitude.

Second Moment: Pairwise Velocity Dispersion Spectrum

The pairwise velocity dispersion spectrum, $\Xi_{ij} \equiv \sigma^2_{12,ij}$, is given in LPT by

$$\begin{aligned}\sigma^2_{12,ij}(\mathbf{k}) =& \int d^3\mathbf{q}\; e^{i\mathbf{k}\cdot\mathbf{q}}e^{-\frac{1}{2}k_ik_jA^{\rm lin}_{ij}}\Big\{\ddot{A}_{ij}+ik_n\ddot{W}_{nij}+\big(2ib_1k_nU_n^{\rm lin}+b_1^2\xi_{\rm lin}\big)\ddot{A}^{\rm lin}_{ij}\\ &-k_nk_m\dot{A}^{\rm lin}_{ni}\dot{A}^{\rm lin}_{mj}+2(b_1^2+b_2)\dot{U}^{\rm lin}_i\dot{U}^{\rm lin}_j+2ik_nb_1\big(\dot{A}^{\rm lin}_{ni}\dot{U}^{\rm lin}_j+\dot{A}^{\rm lin}_{nj}\dot{U}^{\rm lin}_i\big)\\ &+2b_1\ddot{A}^{10}_{ij}+2b_s\ddot{\Upsilon}_{ij}+\alpha_\sigma\delta_{ij}+\beta_\sigma\xi^2_{0,L}\left(\hat{q}_i\hat{q}_j-\frac{1}{3}\delta_{ij}\right)+\cdots\Big\}+R_h^3s_v^2\delta_{ij}.\end{aligned}\tag{2.26}$$

The velocity dispersion spectrum can be decomposed into a number of possible bases such as the parallel-perpendicular basis, $\sigma^2_{ij} = \sigma_{||}(k)\hat{k}_i\hat{k}_j + \frac{1}{2}\sigma_\perp(k)(\delta_{ij}-\hat{k}_i\hat{k}_j)$, or the Legendre basis, $\sigma_{ij} = \sigma_0(k)\delta_{ij} + \frac{3}{2}\sigma_2(k)(\hat{k}_i\hat{k}_j - \frac{1}{3}\delta_{ij})$. These scalar components, expressed as Hankel transforms, are detailed in Appendix B.6.

Unlike the zeroth and first moments, the second moment (σ^2_{ij}) requires two counterterms: α_σ and β_σ. The latter contribution is proportional to the j_2 Hankel transform of the linear power spectrum, $\xi^2_{0,\rm lin}$ (Appendix B.5), and cancels UV sensitivities in the non-isotropic component of $A^{\text{1-loop}}_{ij}$. These contributions can alternatively be parametrized as counterterms $\sim \alpha_0 P_{\rm lin}(k)$ and $\alpha_2 P_{\rm lin}(k)$ to the velocity-dispersion monopole (σ_0) and quadrupole (σ_2), respectively. Finally, we include an isotropic stochastic contribution $R_h^3 s_v^2 \delta_{ij}$. Such a term can, for example, arise from the disconnected part of the second moment

$$\sigma^2_{12}(\mathbf{k}) \ni \int d^3\mathbf{r}\; e^{i\mathbf{k}\cdot\mathbf{r}}\; \sigma_v^2 \delta_{ij} \langle (1+\delta_1)(1+\delta_2)\rangle = \sigma_v^2 P_{\rm NL}(k)\; \delta_{ij} \ni \sigma_v^2 R_h^3 \delta_{ij} \tag{2.27}$$

where σ_v^2 is a contact term coming from evaluating the average velocity squared at a point and $P_{\rm NL}$ is the full nonlinear real-space power spectrum including a constant stochastic contribution R_h^3 (selectively resumming only these terms yields the exponential damping formula for FoG). Our treatment of this stochastic contribution differs from much of the literature [280, 109]; this is of no consequence when fitting the redshift-space power spectrum, since its contribution there is degenerate with that of the stochastic component to $v(k)$, but makes a signficant difference when studying pairwise velocities on their own.

It is useful to note the relations between the parameters for σ_{12} in Fourier and configuration space, the latter as presented in ref. [396]. While the bias contributions are identical, up to Fourier transforms, there are important differences in the counterterms and bias parameters. Firstly, the corresponding expression for the pairwise velocity dispersion in configuration space contains two isotropic counterterms in the curly brackets $\{\cdots\}$ in Equation 3.10 of ref. [396], corresponding to our Equation 2.26. These are $A_\sigma \delta_{ij} + B_\sigma \xi_{\rm lin} \delta_{ij}$, which both result at lowest order in contributions to $\sigma^2_{12}(\mathbf{r})$ proportional to the linear correlation function $\xi_{\rm lin}$, and thus in Fourier space to a counterterm $\propto P_{\rm lin}(k)$. For this reason, in Fourier space we have chosen to summarize them using one counterterm α_σ. However, we note that the constant counterterm proportional to δ_{ij} stems in part from the contribution of small-scale velocities to the $q \to \infty$ limit of σ_{12}, which shows up as a point-contraction of the stochastic velocities

$$\langle (1+\delta_1)(1+\delta_2) \Delta\mathbf{u}_i \Delta\mathbf{u}_j \rangle \ni \sigma_\epsilon^2 \delta_{ij}\; (1+\xi(\mathbf{r})). \tag{2.28}$$

Roughly speaking, this σ_ϵ^2 is the asymptotic value for the stochastic component of the halo velocity $\sigma_{\epsilon,ij} = \langle \Delta\epsilon_i \Delta\epsilon_j \rangle$ at scales $q > R_h$ above the halo scale. This contribution to the configuration-space velocity dispersion is closely related to the Fourier-space stochastic contribution $R_h^3 s_v^2$ to $\sigma^2_{12}(\mathbf{k})$, which is just the large scale ($k \lesssim R_h^{-1}$) limit of the Fourier-transform of σ_ϵ^2. There are therefore two free parameters in σ^2_{12} characterizing isotropic effective and stochastic contributions in both real and Fourier space; if in addition the fit is performed in both spaces, it is important to note that the counterterms in configuration space sum to that in Fourier space, i.e. $\alpha_\sigma = A_\sigma + B_\sigma$, while s_v^2 remains independent, leaving us with three parameters total. This may be especially relevant in predicting statistics for upcoming kSZ surveys.

Moving on to the EPT formulation of the velocity dispersion correlators, we find only up to second order bias parameters contributing to the velocity dispersion (c.f. the density auto

power spectrum and pairwise velocity spectrum). This is consistent with our LPT analysis. In EPT we have

$$\begin{aligned}\sigma^2_{12,ij}(\mathbf{k}) = &-2\frac{k_i k_j}{k^4}P_{\rm lin}(k) \\ &- 2\int_{\mathbf{p}}\left[\Big(2c_1F_2(\mathbf{p},\mathbf{k}-\mathbf{p}) + c_2 + 2c_sS_2(\mathbf{p},\mathbf{k}-\mathbf{p})\Big)\frac{p_i(\mathbf{k}-\mathbf{p})_j}{p^2(\mathbf{k}-\mathbf{p})^2} + 2\frac{k_ik_j}{k^4}G_2(\mathbf{p},\mathbf{k}-\mathbf{p})^2\right. \\ &\qquad\left. + 4c_1\frac{k_ip_j}{k^2p^2}G_2(\mathbf{p},\mathbf{k}-\mathbf{p}) + c_1^2\frac{p_i}{p^2}\left(\frac{p_j}{p^2} + \frac{(\mathbf{k}-\mathbf{p})_j}{(\mathbf{k}-\mathbf{p})^2}\right)\right]P_{\rm lin}(p)P_{\rm lin}(|\mathbf{k}-\mathbf{p}|) \\ &- 4P_{\rm lin}(k)\int_{\mathbf{p}}\left[3\frac{k_ik_j}{k^4}G_3(\mathbf{p},-\mathbf{p},\mathbf{k})\right. \\ &\qquad\left. + 2c_1\left(\left(\frac{k_i}{k^2}+\frac{p_i}{p^2}\right)\frac{(\mathbf{k}-\mathbf{p})_j}{(\mathbf{k}-\mathbf{p})^2}G_2(-\mathbf{p},\mathbf{k}) + \frac{k_ip_j}{k^2p^2}F_2(-\mathbf{p},\mathbf{k})\right)\right]P_{\rm lin}(p) \\ &+ 2c_1^2P_{\rm lin}(k)\delta^K_{ij}\sigma^2_{\rm lin} - 2\left(c_2^{(0)}\delta^K_{ij} + c_2^{(2)}\frac{k_ik_j}{k^2}\right)\frac{1}{k_*^2}P_{\rm lin}(k) + s_2\delta_{ij},\end{aligned} \tag{2.29}$$

where $c_2^{(0)}$ and $c_2^{(2)}$ are two counterterm coefficients corresponding to different angular dependency, $\sigma_{\rm lin}$ is the linear velocity dispersion, and we have one isotropic stochastic contribution, s_2.

Fits of LPT and EPT to $\sigma_{0,2}$ are shown in the right column of Figures 2.4 and 2.5. While both theories give an excellent fit to σ_0 to similar scales as the real-space power spectrum, the fit to σ_2 is only good up to $k \sim 0.1\,h\,\mathrm{Mpc}^{-1}$ in LPT. As we will discuss in more depth in Section 2.4.3, this is partly due to particularities of the resummation scheme in LPT, which keeps all linear displacements exponentiated. In principle, this could be somewhat mitigated by adopting an alternative IR-resummation scheme or considering higher order corrections in the current scheme. However, such a strategy would require some changes in the formalism above, and the overall effect on the redshift space power spectrum due to these differences in σ_2 is negligible. Thus we shall not pursue this strategy. We also note that the fit to σ_2 on large scales suggests that the velocities in the N-body simulations are somewhat underpredicted compared to theory[8], consistent with our expectations of their systematic error.

[8]The fit to σ_0 is less succeptible to this systematic due to a floating stochastic contribution to its amplitude.

Higher Moments

Finally, let us give expressions for the third and fourth moments despite them not figuring prominently in our redshift-space model. In one-loop LPT these are given by

$$\gamma_{ijk} = \int d^3\mathbf{q}\; e^{i\mathbf{k}\cdot\mathbf{q}-\frac{1}{2}k_ik_jA_{ij}}\left\{\dddot{W}_{ijk} + ik_l\dot{A}^{\rm lin}_{l\{i}\ddot{A}^{\rm lin}_{jk\}} + 2b_1\dot{U}^{\rm lin}_{\{i}\ddot{A}^{\rm lin}_{jk\}} + \alpha_\gamma\frac{k_{\{i}\delta_{jk\}}}{k^2} + \beta_\gamma\frac{k_ik_jk_k}{k^4}\right\}$$
$$\kappa_{ijkl} = \int d^3\mathbf{q}\; e^{i\mathbf{k}\cdot\mathbf{q}-\frac{1}{2}k_ik_jA_{ij}}\left\{\ddot{A}^{\rm lin}_{\{ij}\ddot{A}^{\rm lin}_{kl\}} + \alpha_\kappa\frac{k_{\{i}k_j\delta_{kl\}}}{k^4}\right\} + R_h^3s_\kappa^4\delta_{\{ij}\delta_{kl\}}. \tag{2.30}$$

We see that at this perturbative order only the b_1 bias parameter contributes to the third velocity moment, while the fourth moment has purely velocity contributions and does not depend on deterministic bias parameters. The expressions above also require the necessary counterterms and stochastic contributions, together with the pure FoG contributions.

In EPT, at one-loop, we equivalently have contributions to both third and fourth velocity moments. For the third moment we have

$$\begin{aligned}\tilde{\Xi}^{(3)}_{ijl} = 12i\int_{\mathbf{p}}&\left(\frac{k_{\{i}p_j(\mathbf{k}-\mathbf{p})_{l\}}}{k^2p^2(\mathbf{k}-\mathbf{p})^2}G_2(\mathbf{p},\mathbf{k}-\mathbf{p}) + c_1\frac{p_{\{i}p_j(\mathbf{k}-\mathbf{p})_{l\}}}{p^4(\mathbf{k}-\mathbf{p})^2}\right)P_{\rm lin}(p)P_{\rm lin}(\mathbf{k}-\mathbf{p}) \\ &+ 24iP_{\rm lin}(k)\int_{\mathbf{p}}\frac{k_{\{i}p_j(\mathbf{k}-\mathbf{p})_{l\}}}{k^2p^2(\mathbf{k}-\mathbf{p})^2}G_2(\mathbf{p},-\mathbf{k})P_{\rm lin}(p) \\ &- 12ic_1\frac{\delta_{\{ij}k_{l\}}}{k^2}P_{\rm lin}\sigma^2_{\rm lin} + 6i\left(c_3^{(0)}\delta_{\{ij} + c_3^{(2)}\hat{k}_{\{i}\hat{k}_j}\right)\frac{k_{l\}}}{k^2}\frac{1}{k_\star^2}P_{\rm lin} + \ldots,\end{aligned} \tag{2.31}$$

while the fourth velocity moment is given by

$$\begin{aligned}\tilde{\Xi}^{(4)}_{ijlm} = 12\int_{\mathbf{p}}&\frac{p_{\{i}p_j(\mathbf{k}-\mathbf{p})_l(\mathbf{k}-\mathbf{p})_{m\}}}{p^4(\mathbf{k}-\mathbf{p})^4}P_{\rm lin}(p)P_{\rm lin}(|\mathbf{k}-\mathbf{p}|) \\ &- 24\left(\sigma^2_{\rm lin} - c_4^{(2)}\right)\frac{\delta_{\{ij}k_lk_{m\}}}{k^4}\frac{1}{k_\star^2}P_{\rm lin}(k) + s_4\delta_{\{ij}\delta_{lm\}} + \ldots.\end{aligned} \tag{2.32}$$

We note that the structure of these velocity moments in LPT and EPT is quite similar, with equivalent counterterm and stochastic contribution structure. Further details of the one-loop EPT contributions to higher moments are discussed in Appendix B.2.2.

2.4.3 Comparing LPT and EPT

In the previous section, we described the predictions for the pairwise velocity moments within two formalisms, LPT and EPT, at one-loop in perturbation theory. A comparison of Figs. 2.4 and 2.5 shows that LPT and EPT both perform comparably well for the power spectrum, once IR resummation is taken into account. The pairwise velocity and velocity dispersion monopole likewise show a similar level of agreement for both LPT and EPT. Note however, that in the latter spectrum essentially all of the power at $k > 0.1\,h\,\mathrm{Mpc}^{-1}$ comes from the

counterterm and stochastic contributions in EPT, unlike in LPT where the contributions due to large-scale modes and deterministic bias qualitatively match the spectral shape. In both cases the power due to stochastic contributions (shot noise) becomes increasingly significant towards the highest ks plotted, with the models correctly accounting for the mild non-linearity at intermediate k. However, significant differences appear in the predictions of LPT and EPT for the second moment, σ_{12}^2, particularly in the broadband shape of the quadrupole, σ_2. Our goal in this section is to compare and contrast the LPT and EPT models described in the previous sections with these differences in mind.

As we have already noted, the two formalisms are equivalent, term-by-term, when Taylor-series expanded in powers of the linear power spectrum and differ only in the treatment of IR displacements, which are canonically included order-by-order in (non-resummed) EPT but manifestly resummed via the exponential $\exp(-k_i k_j A_{ij}^{\rm lin}/2)$ in LPT. Within LPT, we can therefore recover analagous EPT results by expanding this exponential— indeed, by splitting the linear displacements into long and short modes separated by an infrared cutoff $k_{\rm IR}$ we can recover a spectrum of theories between LPT and EPT. Specifically, writing $A_{ij}^{\rm lin} = A_{ij}^{<} + A_{ij}^{>}$, where the less-than indicates displacement two-point functions calculated by smoothing out long modes via a Gaussian filter $\exp(-(k/k_{\rm IR})^2/2)$ and the greater-than denotes all the remaining power, we have generically for velocity moments

$$\tilde{\Xi}^{(n)}(\mathbf{k}) = \int d^3\mathbf{q}\; e^{i\mathbf{k}\cdot\mathbf{q} - \frac{1}{2}k_i k_j A_{ij}^{<}(\mathbf{q})} \left(1 - \frac{1}{2}k_i k_j A_{ij}^{>} + \frac{1}{8}k_i k_j k_k k_l A_{ij}^{>} A_{kl}^{>} + \mathcal{O}(P_{\rm lin}^3)\right)\Big\{\cdots\Big\}. \quad (2.33)$$

where the $\{\cdots\}$ indicate the terms in curly brackets in Eqs. 2.24 and 2.26. Taking $k_{\rm IR} \to 0$ and keeping the product of the round and curly brackets to second order yields one-loop EPT. This implies that the differences between the LPT and EPT predictions for the velocity moments, and σ_{12}^2 in particular, in both BAO wiggles and broadband shape must be due to the selective resummation of A_{ij}, i.e. to differences at $\geq$ 2-loop order.

Let us briefly mention a technical detail in the above mapping between EPT and LPT. In addition to expanding the linear displacement two-point function A_{ij}, in order to make the low $k_{\rm IR}$ limit of LPT agree with EPT, one needs to use the bias-parameter mapping in Equation 2.19. A useful feature of this mapping is that, while LPT contains the same number of bias parameters as EPT, the contributions of these biases to various statistics are organized rather differently. For example, since $c_1^2 = 1 + 2b_1 + b_1^2$, the '1' term in LPT is equal to the c_1^2 term and the b_1 term is twice the c_1^2 term at leading order. We can take advantage of these differences to, for example, compute the third-order bias contribution in EPT using those from the biases in LPT up to second order alone. Specifically, we can write for the third-order bias contribution to the power spectrum

$$aP_{c_1 c_3} = 2P_{b_1^2} - P_{b_1} - \frac{8}{21}P_{b_1 b_2} + \frac{2}{7}P_{b_1 b_s} + \mathcal{O}(P_{\rm lin}^3) \quad (2.34)$$

and similarly for the third-order bias contribution to $v(k)$:

$$av_{c_3} = v_{b_1} - v_1 - v_{b_1^2} - \frac{8}{21}(v_{b_2} - v_{b_1 b_2}) + \frac{2}{7}(v_{b_s} - v_{b_1 b_s}) + \mathcal{O}(P_{\rm lin}^3). \quad (2.35)$$

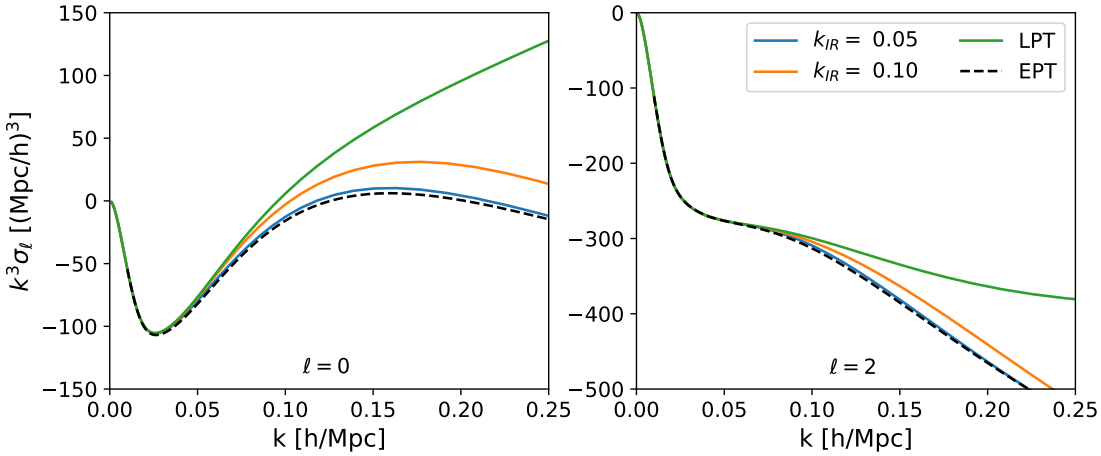

Figure 2.6: The monopole ($\ell = 0$) and quadrupole ($\ell = 2$) of $\sigma^2_{12}(k)$ predicted by 1-loop PT (Eq. 2.33) for several cutoffs, $k_{\rm IR}$, using a "no-wiggle" version of our fiducial power spectrum. The amplitude of σ_ℓ at high k is strongly affected by the choice of IR resummation in Eq. 2.33, indicating that 2-loop contributions may be important for density-weighted velocity dispersion.

We have checked these identities numerically.

To look at the effects of IR resummation, let us begin with the broadband. Figure 2.6 shows the monopole and quadrupole of the second moment σ^2_{12} for a range of cutoffs, $k_{\rm IR}$, computed using a no-wiggle version of our fiducial power spectrum, which we use in this section only to isolate broadband effects. As expected, the EPT prediction is recovered in the limit of vanishing $k_{\rm IR}$, while LPT represents the $k_{\rm IR} \to \infty$ limit. It is notable that the two limits predict dramatically different broadband shapes at even intermediate wavenumbers. For example, EPT predicts the monopole to have close-to-vanishing power at $k \sim 0.2\,h\,{\rm Mpc}^{-1}$, where LPT predicts $k^3\sigma_0$ to have significant power increasing with k; conversely, EPT predicts a more significant (more negative) quadrupole compared to LPT. These differences are particularly noteworthy because LPT shows excellent agreement with the σ_0 measured from simulations while under-predicting σ_2 at small scales (Fig. 2.4), and conversely for EPT (Fig. 2.5), where essentially all of the power at $k \simeq 0.1\,h\,{\rm Mpc}^{-1}$ and beyond in σ_0 is accounted for by the stochastic and counterterms.

In addition to the above, EPT and LPT also make different predictions for the BAO feature. In Figure 2.7 we have plotted $P(k)$, $v(k)$ and the monopole and quadruopole of σ^2_{12} with smooth broadbands—estimated using a Savitsky-Golay filter[9]—subtracted off. The blue and orange lines show the predictions of LPT and EPT modulo a quartic polynomial in k which we fit to the data. Evidently, the IR resummation inherent in one-loop LPT

[9]We use a quintic filter linear in k with width of $0.25\,h\,{\rm Mpc}^{-1}$, but note that our results are relatively robust to this choice as we are only concerned with the oscillatory components, modding out any residual broadband with a smooth polynomial fit.

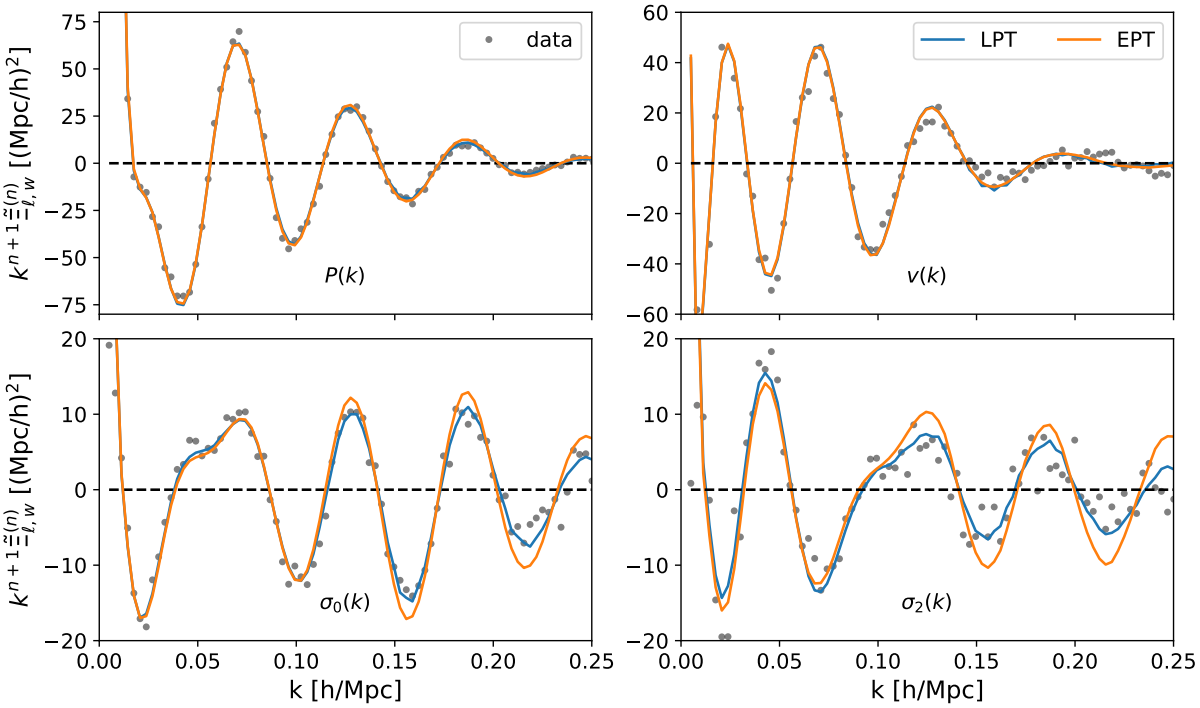

Figure 2.7: Oscillatory component of the real-space power spectrum (top left), pairwise velocity spectrum (top right) and the monopole and quadrupole (bottom left and right) of the velocity dispersion spectrum σ^2_{12} in LPT and EPT compared to N-body data (dots). The smooth component subtracted from the data is computed using a Savitsky-Golay filter, and the theory signals are supplemented with a quartic polynomial in k to improve agreement with the broadband-subtracted data. While the power spectrum and pairwise velocity show excellent agreement between LPT and EPT even when the fitted independently, the oscillatory signals in the velocity dispersion spectra differ significantly, with EPT underdamped compared to LPT. Notably, unlike in the lower velocity moments the dominant oscillations in σ^2_{12} are due to one-loop effects, whose damping seem to be more naturally captured by the IR-resummation in LPT when compared to data (black dots).

provides and excellent description for the oscillatory component in the second moment, while the resummation scheme we have employed for EPT underpredicts the requisite nonlinear damping. On the other hand, the upper two panels show that the two formalisms produce far better agreement for both the zeroth and first moments. This is likely in part due to the dominance of the one-loop b_1 contributions noted in the previous paragraph, which account for most of the oscillatory signal shown in both panels; indeed, we note that the (significantly smaller) damped linear BAO wiggles are more-or-less exactly out of phase with the nonlinear wiggles shown [22, 50, 278, 185].

The size of the one-loop terms and the divergence between one-loop LPT and EPT at even intermediate k for σ_{12}^2 can heuristically be used to gauge the magnitude of higher-order ($\geq$ 2-loop) corrections, and suggests that density-weighted pairwise velocity statistics may be significantly more nonlinear than the density-only real-space power spectrum. For example, direct inspection of bias contributions to σ_2 indicates that while the leading-order contribution is due to matter velocities only, the largest numerical contribution comes from b_1 at one loop. Indeed, at $k = 0.1\,h\,\mathrm{Mpc}^{-1}$ the one-loop σ_2 predicted by our EPT model has 50% extra power compared to linear theory and 100% by $k = 0.15\,h\,\mathrm{Mpc}^{-1}$. In this case the level of agreement between the 1-loop EPT and N-body results suggests that the two-loop contributions happen to be small for ΛCDM power spectra of the amplitude we consider, so that the additional contributions included in the IR resummation by LPT are worsening the agreement with the N-body results. We have been unable to find a symmetry that would explain why the 2-loop contribution to σ_2 should be small, so it could be that this is a numerical coincidence where 1-loop EPT is 'accidentally' performing better than expected for this particular power spectrum shape and normalization. Indeed, for σ_0 the one-loop terms in EPT — which are dominated by the stochastic and counterterms — account for a 100% difference compared to linear theory by $k = 0.1\,h\,\mathrm{Mpc}^{-1}$, suggesting that velocities at even these intermediate scales are subject to large nonlinearities. As suggested by Fig. 2.3, and we discuss further below, a detailed modeling of σ_2 is not necessary in order to obtain an accurate measure of the redshift-space power spectrum, $P(k, \mu)$, so we have not attempted to further improve the performance of either LPT or EPT for this statistic.

Before leaving the velocity statistics and turning to the redshift-space power spectrum, it is worth noting that our results have direct implications for the use of velocities (either from peculiar velocity surveys or kSZ measurements) as cosmological probes. In particular, the relative size of the perturbative contributions (green lines in Figs. 2.4 and 2.5) and the stochastic or counter terms (blue lines) can be taken as a proxy for where cosmological information dominates over small-scale information (e.g. about astrophysics). For σ_{ij}^2, in particular, it appears that the cosmological information is confined to reasonably small k, which argues that high resolution observations of this statistic will not be necessary if the goal is inference about cosmological parameters.

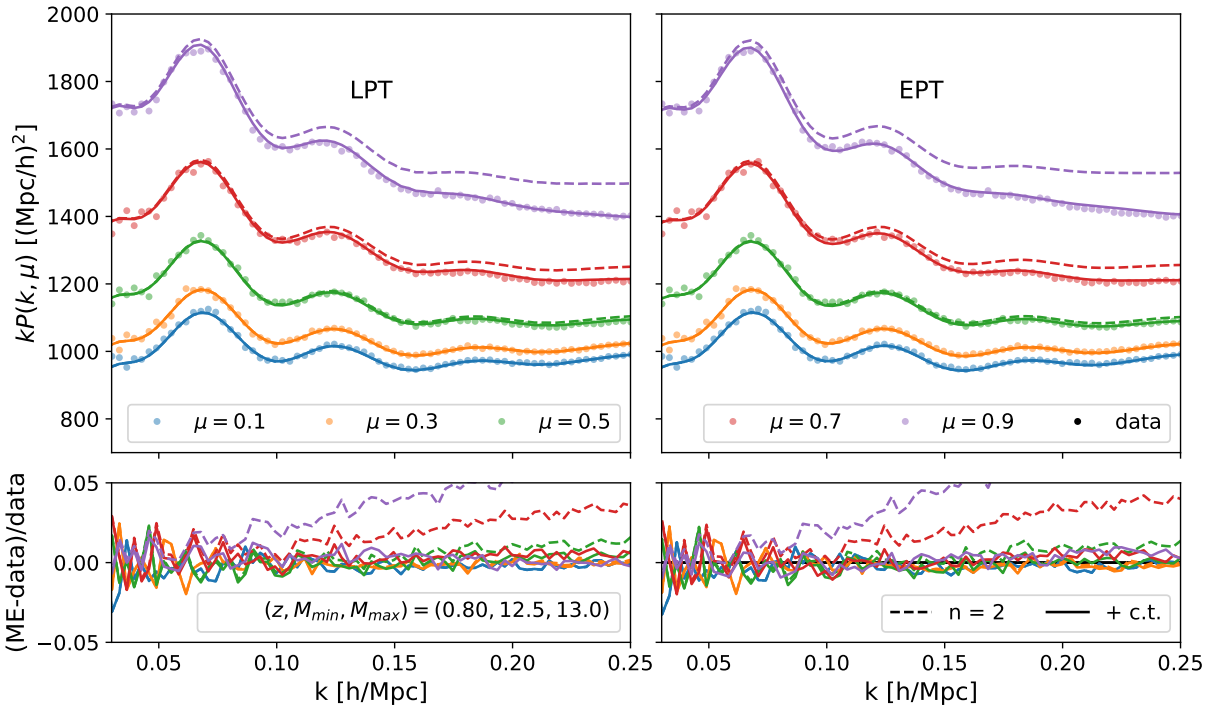

Figure 2.8: A comparison of the halo power spectrum wedges ($0.0 < \mu < 0.2, \cdots, 0.8 < \mu < 1.0$) measured in the N-body simulations (points) to the predictions from PT models where the first two velocity moments are calculated using LPT (left) and EPT (right) and the third moment is approximated using a counterterm ansatz (lines; Eq. 2.36). The upper panel shows the measurements, while the lower panel shows the fractional differences. We have chosen to show the $12.5 < \lg M < 13.0$ mass bin at $z = 0.8$ though the other masses and redshifts behave similarly. The dashed lines show the PT contributions excluding the $n = 3$ counter term, while the solid lines show the results of the full model. Note the addition of these terms significantly improves the model for high μ while the improvement is much more modest for low μ.

2.5 All Together Now: the Redshift-Space Power Spectrum in PT

Sections 2.3 and 2.4 examined the convergence of velocity expansions for the redshift-space power spectrum and how the required velocities can be computed using perturbation theory; in this section we combine these ingredients to produce a model of the redshift-space power spectrum based on 1-loop perturbation theory.

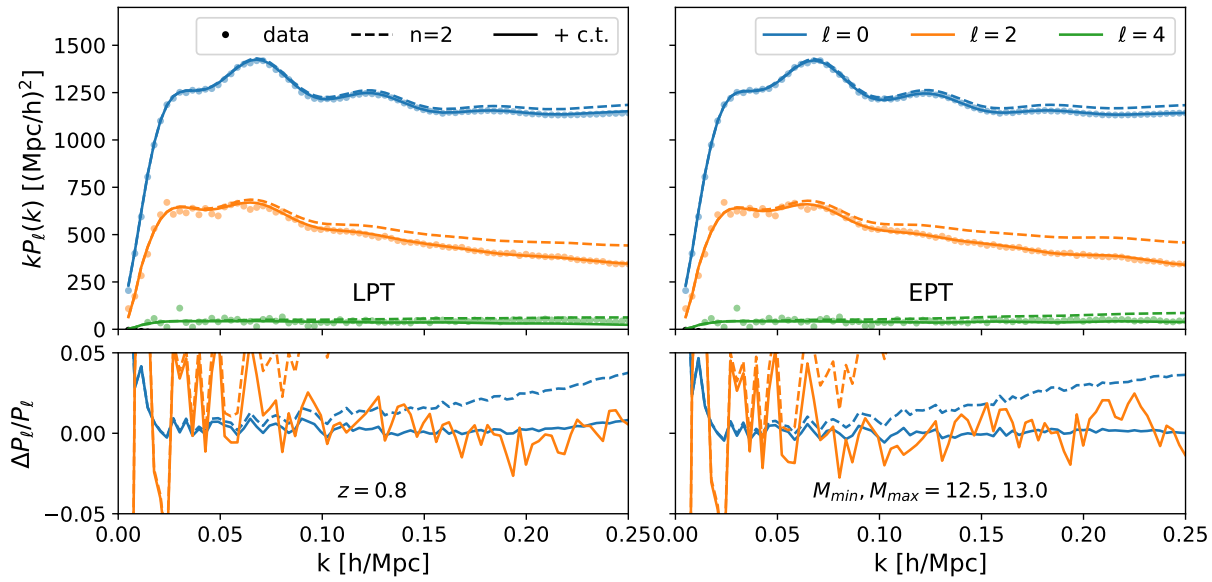

Figure 2.9: A comparison of the halo power spectrum multipoles measured in the N-body simulations (points) to the predictions from our LPT (left) and EPT (right) models (lines; Eq. 2.36). The upper panel shows the measurements, while the lower panel shows the fractional difference. The dashed lines show the PT contributions excluding the $n = 3$ counterterm, while the solid lines show the results of the full model. Note the addition of these terms significantly improves the model for $\ell > 0$, even more dramatically than in Fig. 2.8. In interpreting these differences it is important to bear in mind that the N-body data contain systematics that can bias results at the few-percent level—indeed it clearly under-predicts the quadrupole by around 2% around $k = 0.05\,h\,\mathrm{Mpc}^{-1}$ compared to both LPT and EPT— and that for any observation the error on the quadrupole and hexadecapole are dominated by the monopole contribution and are therefore fractionally much larger than for the monopole— hexadecapole errors are not plotted in the bottom panel for this reason.

2.5.1 Comparison for halos

Figures 2.8 and 2.9 show the PT predictions for the redshift-space power spectrum wedges and multipoles using the bias parameters, counterterms and stochastic contributions determined from the fits in Figs. 2.4 and 2.5, together with the moment expansion approach. Figure 2.8 demonstrates that these parameters give an excellent fit, agreeing with the data at the percent level even for the highest μ wedges. It is worth noting that the redshift-space distortions captured by the quasilinear velocities is highly nontrivial, and a naive multiplication of the real-space power spectrum by the factor $(b + f\mu^2)^2$ yields $P(k, \mu)$ that is 5% away from the data even at $k = 0.1\,h\,\mathrm{Mpc}^{-1}$ and $\mu = 0.5$.

Figure 2.9 tells a similar story to Fig. 2.8, though with some caveats. The monopole, P_0, remains well-fit by both the LPT and EPT models. The same is not true of the quadrupole, which is both noisier and possibly biased. However, recall there is some evidence that the

simulations with derated timesteps may not be converged. Indeed, the data quadrupole for $k < 0.1\,h\,\mathrm{Mpc}^{-1}$ suggests that the simulations under-predict the value of velocities by around two percent compared to perturbation theory. For such k the best fitting LPT and EPT models are in excellent agreement, being dominated by linear theory, but differ visibly with the N-body quadrupole (the contribution of the monopole to each wedge reduces the visibility of this effect substantially in Fig. 2.8). As mentioned earlier, we cannot rule out a systematic error in the N-body simulations of several per cent and so we take this difference as a rough estimate of the size of the systematic error in P_2.

The only remaining free parameter in our model once the power spectrum and first two velocity moments are fit is the coefficient of the counterterm $\propto k^2\mu^4 P(k)$, which we argued at the end of Section 2.3 was a good stand-in for the higher-order velocity statistics not explicitly included in our model. Indeed the input value, which we fit by eye, is comparable in magnitude to the contribution from the dipole of the third moment divided by the linear power spectrum. In the spirit of perturbation theory, our philosophy in adjusting this parameter was to increase agreement at low k and μ rather than minimize errors across the board, even at high μ where the convergence of the velocity expansions is poor. The model without this counterterm is shown in the dashed lines. Absent this counterterm our model still describes the power spectrum wedges with $\mu \leq 0.5$ at the percent level out to $k = 0.25\,h\,\mathrm{Mpc}^{-1}$, with errors rapidly growing towards higher μ such that $\mu = 0.7$ is 5% off at a similar wavenumber; however, the strong angular dependence of the errors means that the quadrupole is more than 10% away from the data at $k = 0.25\,h\,\mathrm{Mpc}^{-1}$. This validates our approach of modeling the redshift-space power spectrum using perturbative models of the first two velocity moments together with the counterterm ansatz for the third moment.

It is important to note, however, that many of the velocity parameters are degenerate for analyses of the redshift-space power spectrum only. In the moment expansion, all the one-loop counterterms in the velocity statistics ultimately take the form $k^2\mu^{2n}P_{\rm Zel}(k)$ [or $k^2\mu^{2n}P_{\rm lin}(k)$] at leading order when combined to form the power spectrum. For example, both the counterterm for σ_2 and the third moment take the form $k^2\mu^4 P(k)$. Similarly, the stochastic contributions will tend to contribute as $(k\mu)^{2n}$. Within the moment expansion we can thus write

$$P_s^{\rm ME}(\mathbf{k}) = \left(P(k) + i(k\mu)v_{12,\hat{n}}(\mathbf{k}) - \frac{(k\mu)^2}{2}\sigma^2_{12,\hat{n}\hat{n}}(\mathbf{k}) + ...\right)^{\rm PT} + \left(\alpha_0 + \alpha_2\mu^2 + \alpha_4\mu^4 + \cdots\right) k^2 P_{\rm lin,Zel}(k) + R_h^3\left(1 + \sigma_v^2(k\mu)^2 + \cdots\right), \quad (2.36)$$

where $(...)^{\rm PT}$ refers to contributions due only to large scale gravitational dynamics and nonlinear bias parameters computed in either EPT or LPT (with the $k^2P_{\rm lin,Zel}$ being the linear or Zeldovich power spectra in each case, respectively). This leads to a redshift-space power spectrum with 9 free parameters (4 bias, 3 counterterms, 2 stochastic) with a similar structure of effective corrections as found in the EPT analyses of refs. [96, 186][10] . If the corrections due to third-order bias (b_3, c_3) can be set by assuming the Lagrangian bias $b_3 = 0$,

[10]Indeed, Equation 2.36 is equivalent, up to details of IR resummation and choices of marginal EFT

as noted in Section 2.4.1, then this is reduced to 8 free parameters. On the other hand, if we wish to include the full one-loop expressions for the third and fourth moments, which possess their own effective and stochastic corrections, two additional non-degenerate parameters are needed, bringing the total up to 11. The aforementioned degeneracy is less manifest in the Fourier streaming model due to the nonlinear composition of the cumulants (and similarly in the configuration-space Gaussian streaming model); however, due to the high degree of quantitative agreement between the ME and FSM expansions at the data level, the various counterterms and stochastic contributions will nontheless be highly degenerate, and as such should not all be fit. Indeed, it should be sufficient to expand these effective contributions as in Equation 2.36, though doing so will break the structure of the streaming model, strictly speaking. Finally, while our model for $P(k,\mu)$ includes five free parameters for counterterms and stochastic effects a condensed set of terms can be used if fitting to more restricted summary statistics. For example, since the counterterms are of the form $k^2\mu^{2n}P_{\rm lin,Zel}(k)$ they contribute to each multipole proportional to $k^2P_{\rm lin,Zel}$. When fitting only the monopole and quadrupole (as in refs. [186, 96, 88]) one should fit only for two summary contributions $P_{\ell,ct} = \alpha_\ell k^2 P_{\rm Zel}$, though doing so necessarily obscures some of the structure in $P(k,\mu)$ which is poorly fit using only two counterterms. On the other hand, since we include only two purely stochastic terms, nondegenerate in their contribution to the monopole and quadrupole, they can be separately included even when fitting only for those two statistics.

In Section 2.4 we noted that the predictions of LPT and EPT for σ_{ij} differed, and that they appeared to depend upon higher order contributions. The fact that both the LPT and EPT models do well at describing $P(k,\mu)$ in Fig. 2.8 is thus surprising at first sight. As shown in Section 2.3 (Fig. 2.3), however, the errors in σ_2 are highly suppressed in $P(k,\mu)$ except near $\mu \approx 1$ and so this theoretical uncertainty is subdominant when predicting redshift-space clustering. Furthermore, for realistic galaxy samples we expect the role of stochastic velocities, i.e. fingers of god, to be even more significant than the halo sample studied in the figures above; these velocities further increase the role of the monopole σ_0 relative to σ_2. This also justifies our choice of modeling for σ_2, where we do not spend further effort in improving the LPT and EPT modeling, as was argued in Sec. 2.4.

2.5.2 Comparison for mock galaxies

As a further test of our power spectrum model, in Figure 2.10 we fit our RSD model in Equation 2.36 on the mock sample of galaxies embedded into the N-body data using a halo occupation distribution as described at the end of Section 2.2. Galaxy samples present a more realistic and stringent test for our model as they are affected by the virial motions of satellite galaxies and indeed, fits to the satellite velocity statistics require significantly larger

parameters, to the models in those works, with similar ranges of applicability. Specifically, compared to ref. [96] we do not including the next-order real-space stochastic correction $\propto k^2$ but include a counterterm $k^2\mu^6 P_{\rm L}$ to account for UV dependence in the fourth moment, while compared to ref. [186] we include a superset of 1-loop effective corrections but omit the 2-loop FoG correction in their Equation 3.10, which we do not require for good fits at the velocity level.

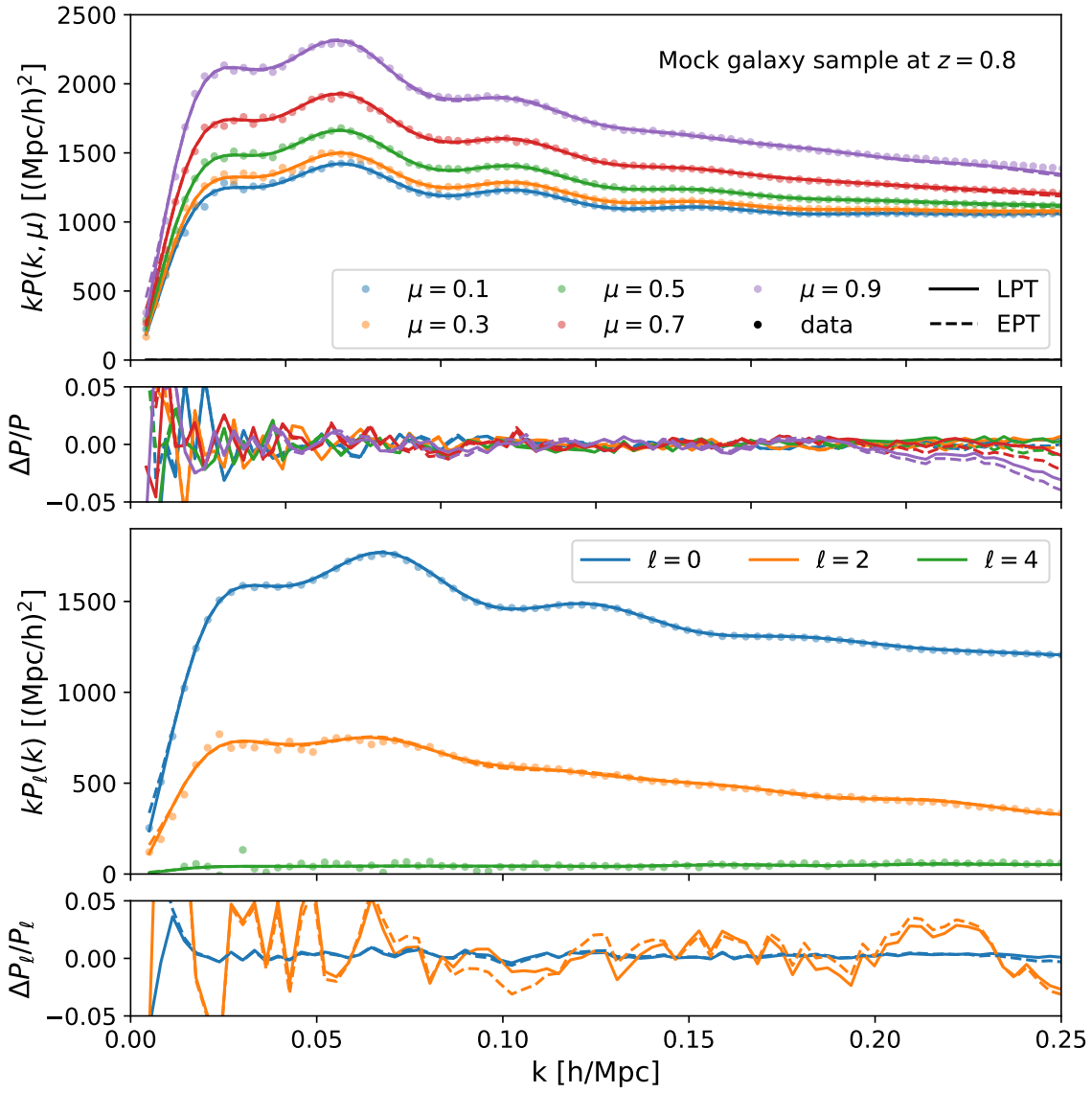

Figure 2.10: A comparison of the (top) power spectrum wedges ($0.0 < \mu < 0.2, \cdots, 0.8 < \mu < 1.0$) and (bottom) multipoles measured for our mock galaxy sample at $z \simeq 0.8$ (points) to the predictions from our PT models (lines; Eq. 2.36). The upper panel shows the measurements while the lower panel shows the fractional differences.

counterterms (see the discussion around Eq. 2.28) and stochastic contributions, particularly for the monopole σ_0 of the second moment and a slightly reduced range-of-fit ($k \sim \sigma_v^{-1}$) compared to the halo case. Nonetheless, at the power spectrum level our model fits the power spectrum wedges $P(k,\mu)$ at the percent level at least up to $k = 0.25\,h\,\mathrm{Mpc}^{-1}$ for all but the highest μ-bin ($\mu = 0.9$), where unlike in the halo case the suppression of power by random velocities towards high k is evident and which begins to deviate from our model prediction at $k = 0.15\,h\,\mathrm{Mpc}^{-1}$, reaching 3 percent off by $k = 0.2\,h\,\mathrm{Mpc}^{-1}$. Similarly, our model yields a significantly sub-percent-level fit to the galaxy power spectrum monopole on perturbative scales, while the quadrupole begins to deviate around where the highest-μ wedge does at around $k \sim 0.15\,h\,\mathrm{Mpc}^{-1}$. We also checked that, assuming Gaussian covariances and letting the growth f vary, our model (Equation 2.36) can fit the redshift-space power spectrum directly to nearly identical, sub-percent precision over a wide range of scales and recover the growth rate to 1%, consistent with the systematic error of the simulations themselves.

2.5.3 Fingers of God and stochastic terms

Despite the above, the size and structure of stochastic velocities and finger-of-god effects, particularly for the specific galaxy samples that will be observed by upcoming spectroscopic surveys, remains one of the biggest limitations of (perturbative) models of redshift-space distortions. It is thus worth discussing the pros and cons of various approaches to tame these effects, in particular the effective-theory parametrization of finger-of-god effects in EFT models such as ours (and those used in refs. [186, 88, 96]) compared to more conventional FoG models such as [272, 270, 274, 366, 418]. As discussed in ref. [138], the main difference between these approaches is that traditional[11] models assume strict forms for FoG effects (e.g. exponential or Lorentzian damping) depending on a small set of parameters, while EFT parametrizations such as ours are restricted only by symmetry arguments and thus in principle span the entire allowed space of FoG models, such that the former could be preferred if they well-describe observed FoGs. Assuming specific FoG models necessarily implies setting strong restrictions on the structure of halo or galaxy velocities at small scales. For example, in the language of the moment expansion approach, assuming Gaussian damping $\propto \exp(-k^2\mu^2\sigma_{\rm FoG}^2)$, as in the TNS model [366], is equivalent to requiring that the effects of higher-order moments of virial velocities be described by the same paramter, $\sigma_{\rm FoG}$, as the lower moments. A similar, but more EFT-minded, approach could be to input these restrictions as priors (e.g. based on fits to simulations) while enabling fitting the full set of allowed parameters to a given order. The priors would reduce the statistical impact of the additional free parameters and a comparison of the posterior to the prior would allow us to tell if the observed data were in tension with the assumptions. This is especially important since the velocities of galaxies with complex selections can have significantly more structure than usually assumed in mock catalogs.

[11] An intermediate case is represented by ref. [161], who assume a functional form with many free parameters.

Finally we note that the impact of redshift errors, which also affect the line-of-sight clustering signal, can be partly compensated by having a very flexible finger-of-god model such as we have introduced above. If there is reason to suspect that redshifts are not being accurately estimated in a survey, this could argue for broader priors on these terms than might otherwise arise just from dynamical studies of galaxy orbits in observations or simulations.

2.5.4 IR resummation

Let us comment on the role of large-scale (IR) displacements in the velocity-expansion approach to redshift-space distortions. While these large-scale modes have essentially linear dynamics, their presence results in the nonlinear damping of spatially-localized features such as baryon acoustic oscillations (BAO) that can be complicated to capture perturbatively in Eulerian treaments [335]. On the other hand, a convenient feature of Lagrangian perturbation theory is that it naturally includes a resummation of these bulk displacements, making it a natural candidate with which to understand the nonlinear damping of the BAO feature in both real and redshift space [231, 58, 402]. By extension, our LPT calculations of the real-space velocity moments naturally resums these modes.

However, the combination of these velocity moments into the redshift-space power spectrum breaks the resummation of IR *velocities* while keeping the isotropic displacements resummed. Within the framework of LPT, bulk velocities can be naturally resummed by promoting Lagrangian displacements to redshift space using matrix multiplication $\Psi_i^{(n)} \to R_{ij}^{(n)}\Psi_j^{(n)} = (\delta_{ij} + f\hat{n}_i\hat{n}_j)\Psi_j^{(n)}$ [231]. This transformation takes the exponentiated linear displacements $A_{ij} \to R_{in}R_{im}A_{nm}$, naturally endowing the resummed exponential with the angular structure of redshift-space distortions [231, 58]. For example, the isotropic part of $A_{ij} = X(q)\delta_{ij} + Y\hat{q}_i\hat{q}_j$, given by $\Sigma^2(q) = (X + Y/3)$, becomes multiplied by $(1 + f(2 + f)\mu^2)$ under this transformation. Expanding order-by-order in the velocities as we have done in this chapter, and thus in the growth rate f, necessarily breaks this structure. The procedure to capture all the IR modes, including the velocity contributions, in purely LPT framework has been outlined in [398]. We intend to return to that in future work.

In the EPT framework, an approximate but pragmatic way of handling these IR modes has been developed, relying on the wiggle/no-wiggle split. The essential feature of this IR resummation procedure is the decomposition and isolation of the wiggle part (caused by the baryon acoustic oscillations) of linear power spectra, and the damping of oscillatory components due to the wiggles by an appropriate factor dependent on the IR displacements to be resummed [22, 402, 50, 112, 185] (details in Appendix B.2.4). This procedure, however, relies on several approximation steps, from the details of the wiggle/no-wiggle splitting to ensuring that subleading corrections can be neglected at the order of interest. As highlighted earlier, and in contrast to EPT, LPT performs the resummation of long displacement modes directly and does not rely on any of these approximation steps. LPT thus constitutes a natural environment to understand the various approximation levels undertaken in the wiggle/no-wiggle splitting procedure, and thus provides the bridge from the direct and exact

treatment of IR modes to the comprehensive and intuitive picture provided by the simplicity of the wiggle/no-wiggle splitting result.

These characteristics and differences of the LPT and EPT in the treatment of the IR modes are highlighted even further once the possible additional, beyond BAO, oscillatory features of the power spectrum are considered. Such oscillatory features can be produced by, e.g., primordial physics, and are also affected by the long displacements in a similar manner to the BAO, exhibiting damping and smoothing that can again be captured by performing IR resummation [402, 44, 390]. The evident advantage of LPT in this scenario is that this resummation is performed automatically without the need for further engagement or analysis, finding saddle points etc.

Despite the incomplete resummation of IR velocities as described above, however, as shown in Figure 2.8, in Fourier space the velocity expansions are nonetheless able to capture the anisotropic BAO wiggles to high accuracy. We can attempt to estimate the effects of the missing bulk contributions to the higher velocity moments as follows. Within the context of LPT we can write, for example for the lowest-order b_1^2 contribution to the redshift-space power spectrum [402]

$$P_{b_1^2}(\mathbf{k}) = \int d^3\mathbf{q}\; e^{i\mathbf{k}\cdot\mathbf{q} - \frac{1}{2}k_i k_j R_{in} R_{jm} A_{nm}(\mathbf{q})} \xi_{\rm lin}(q) = e^{-\frac{1}{2}k^2\Sigma^2(r_s,\mu)} P_w(k) + P_{\rm smooth}. \tag{2.37}$$

Equation 2.37 can be understood as follows: since the linear correlation function $\xi_{\rm lin}$ has a prominent BAO "bump" at r_s, it picks out the exponentiated damping factor at $q = r_s$ such that the bump is smoothed by $\Sigma^2(r_s,\mu) = (1 + f(2+f)\mu^2)\ \Sigma^2(r_s)$ in Fourier space, while the correlation without the bump gets affected smoothly since it has no preferred scale. The separation into a smooth component and the BAO feature is commonly used in the literature and known as the wiggle/no-wiggle split [121, 424, 402], but LPT makes an exact prediction for the damping through the resummation of linear modes at the BAO scale. In particular, we can now understand how the BAO feature is affected if we neglect the effect of bulk velocities at $n^{\rm th}$ order in the moment expansion. Noting that the $n^{\rm th}$ velocity moment contributes to the power spectrum proportional to f^n, we can expand the exponential in Equation 2.37 as

$$P_{w,NL}(k) = e^{-\frac{1}{2}k^2\Sigma_0^2}\Big[1 - (k\mu)^2\Sigma_0^2 f + \frac{1}{2}(-(k\mu)^2\Sigma_0^2 + (k\mu)^4\Sigma_0^4)f^2 + \cdots\Big] P_w(k) \tag{2.38}$$

where the coefficients of f and f^2 correspond to contributions from the first two velocity moments in Equation 2.36. Using the moment expansion to $n = 2$ is equivalent to Taylor-expanding in f and keeping only two terms. However, a corollary of the above is that the damping beyond these terms necessarily scales strongly with μ (and k), making it negligible for all but the highest μ wedges — and indeed any residual anistropic wiggles in our fits to the redshift-space power spectrum from simulations must be well within the errors of these measurements, which are themselves tighter than state-of-the-art spectroscopic surveys like DESI.

Nonetheless, while being almost undetectable in Fourier space these errors will accumulate in configuration space to produce deviations from measurements noticeable by eye, particularly in the quadrupole, so our current strategy will need to be modified for configuration space analyses. The two most obvious options to this end are (1) to compute $P_s(\mathbf{k})$ for the broadband using P_{nw} only and add in the exponential damping factor for P_w by hand, as has been done in recent analyses in the EFT framework [186] or (2) to use the Gaussian streaming model (GSM; [396]) for configuration space analyses employing the same bias parameters and counterterms for velocity statistics in configuration space. The latter is an attractive option because the velocity expansions in Fourier space and in the GSM can be computed within the same dynamical framework employing consistent bias parameters and counterterms[12], though the GSM captures the IR displacements almost perfectly (see Appendix B.3) while the Fourier space methods can more easily capture the broadband effects of the IR displacements. A more complete but laborious approach would be to compute the power spectrum with both linear displacements and velocities resummed as in Convolution Lagrangian Perturbation Theory [58]; we intend to return to this in the near future.

2.6 Conclusions

The upcoming generation of spectroscopic surveys and CMB experiments promise to deliver unprecedented information about galaxy velocities on cosmological scales, either indirectly through the anisotropic clustering of observed galaxies due to redshift-space distortions or directly through the kinetic Sunyaev-Zeldovich effect or peculiar velocity surveys. Velocity and density statistics provide us with complementary information about structure formation, which can further be combined with probes such as weak lensing and allow us to test the predictions of ΛCDM and general relativity on the largest scales.

Our goal in this chapter is to consistently model both real-space velocity spectra and the redshift-space power spectrum of biased tracers (e.g. galaxies) within one-loop perturbation theory. The redshift-space power spectrum, $P(k,\mu)$, can be understood as an expansion in the line-of-sight wavenumber, $k_\parallel = k\mu$, multiplying $n^{\rm th}$-order pairwise velocity spectra. After describing the four $(4\,h^{-1}\,{\rm Gpc})^3$ N-body simulations we compare to in Section 2.2, we begin in Section 2.3 by using the N-body halo velocity statistics to test the convergence of two Fourier-space velocity expansions of the redshift-space power spectrum, the moment expansion approach and the Fourier streaming model. The expansions show good quantitative agreement with the $P(k,\mu)$ measured from the same set of simulations when the first three pairwise velocity moments are included, reaching percent-or-below levels of agreement on scales of interest to cosmology except when $\mu \approx 1$ (i.e. close to the line-of-sight) where the agreement is slightly worse at small scales, though still at the percent level or below for $k < 0.2\,h\,{\rm Mpc}^{-1}$ for our fiducial halo sample. Including higher moments ($n = 4$) fails to significantly improve the expansion, indicating slow convergence at scales where the nonlinear velocities of halos become dominant. We find that the redshift-space power spectrum can

[12] And keeping in mind the relation between stochastic terms in Fourier and configuration space.

be modeled at the percent level on perturbative scales by using a counterterm ansatz for moments beyond $n = 2$ valid in precisely this scenario.

In Section 2.4 we model the real-space power spectrum and the first two velocity moments within one-loop Lagrangian and Eulerian perturbation theory, comparing them to N-body simulations and highlighting their salient features and differences in the final subsection. Our model employs effective field theory (EFT) corrections to the nonlinear dynamics as well as a bias scheme including shear and cubic contributions as well as derivative bias degenerate with the counterterms. We find that, when the appropriate counterterms and stochastic corrections are included, one-loop LPT and EPT can model the zeroth and first velocity moments (the real-space power spectrum and pairwise velocity) to comparable scales for both broadband shape and oscillatory features. For the second moment (velocity dispersion) LPT shows a more limited range-of-fit while EPT relies on one-loop terms of the same order as linear theory and slightly under-predicts the damping of oscillatory features in the one-loop terms, suggesting that the velocity dispersion spectrum is subject to significant non-linearity even at intermediate scales. In general we find the higher moments to be "more non-linear" and to have larger contributions from stochastic and counter terms as we move up the hierarchy.

Finally, in Section 2.5 we combine the velocity expansions and velocity modelling to obtain a model of the redshift-space power spectrum in one-loop perturbation theory. Using the bias parameters and effective corrections derived from the data statistics in addition to the aforementioned counterterm ansatz for contributions from velocity moments beyond $n = 2$ yields a percent-level fit to the halo power spectrum for all wedges out to $k = 0.25\,h\,\mathrm{Mpc}^{-1}$ at $z = 0.8$, with similar performance for the multipoles. As a further test, we analyzed a sample of mock galaxies using the same procedure, and found qualitatively similar results despite significantly more pronounced stochastic terms (expected due to virial motions of satellites) and a slightly decreased range of fit at higher μ and in the quadruople as a result. In addition, we conducted a fit directly to the power spectrum wedges for this sample, assuming Gaussian covariances and letting both f and the bias parameters to float, and found that our model recovers the growth rate to within the systematic error of the simulations themselves with no loss of accuracy.

Our `python` code `velocileptors` to compute the aforementioned one-loop velocity statistics and redshift-space power spectrum in both EPT and LPT is publically available. For completeness, the code includes all terms up to the fourth pairwise velocity moment in both formalisms as well as modules to combine them using the moment expansion in both formalisms, full IR resummation as in Equation B.32 in EPT, and the Fourier and Gaussian streaming models in LPT. The LPT code takes slightly more than a second to compute the all relevant statistics to sub-percent precision on perturbative scales, while the EPT code takes slightly less. We make abundant use of the FFTLog algorithm throughout and compute one-loop EPT terms via manifestly Galilean invariant Hankel transforms inspired by the Lagrangian bias expansion (Appendix B.6).

The structure of the moment expansion implies that the theoretical error should be a strong function of μ, which can be taken as an argument in favor of modeling power spectrum wedges, $P(k, \mu)$, over multipoles, $P_\ell(k)$. The importance of both counterterms and stochastic

terms in the velocity statistics suggests that the cosmological information in $P(k,\mu)$ at high k and μ is less than one might naively think, since it is precisely in this regime that these non-cosmological contributions become an appreciable fraction of the total power. It is also at higher k and μ that non-trivial behavior of FoG models and observational redshift errors would be expected to impact the measurements the most.

We close by noting some possible near-term applications. Firstly, our model naturally includes precision modelling of cosmological velocities at quasilinear scales and will be directly applicable to upcoming kSZ and peculiar velocity surveys [141, 1, 182, 150]. While we have focused our predictions on velocity statistics in real-space, the conversion to redshift space can be straightforwardly obtained by the appropriate f derivatives of the redshift-space power spectrum [358], which are themselves predicted by the model as linear combinations of density-weighted pairwise velocity statistics. In this regard the increasing importance of counterterms and stochastic terms as we move higher in the moment hierarchy suggests that much of the cosmological information in velocity surveys will be contained on large scales.

In terms of redshift-space distortions, our model includes a superset of effective corrections at 1-loop level and is similar in many respects to those recently used to analyze BOSS data in ref. [186, 96, 88, 85, 94] or the "blind challenge" of ref. [255]. An obvious next step from the present analysis would be to analyze those data with the formalism described in this work. Our model should likewise be competitive in analyses of future high-redshift galaxy surveys like HETDEX [173], DESI [108], Euclid [12] and even futuristic LBG [135] or 21-cm [352] surveys, though as discussed in Section 2.3 the applicable range of scales will likely be limited more by the scale of stochastic velocities ($k_{\rm FoG} \sim \sigma_v^{-1}$), or FoGs, than by the nonlinear wavenumber k_{NL} at higher redshifts. This was demonstrated already in EFT analyses of BOSS, where $k_{\rm FoG} \sim 0.2\,h\,{\rm Mpc}^{-1}$, though specific FoG properties will depend on the galaxies sampled by each survey, and will be particularly interesting in the context of high-redshift 21-cm surveys where stochastic velocities are relatively small [392] but observations are naturally limited by foregrounds to higher μ. Finally, the aforementioned probes can be combined with upcoming lensing surveys. By letting the gravitational slip [192, 194, 12] float as a free parameter like the linear growth rate f, this will let us test the predictions of General Relativity on cosmological scales. By providing a model which can simultaneously fit all of the relevant statistics we enable a principled statistical analysis that can avoid taking ratios of noisy data points.

2.7 Acknowledgements

We would like to thank Emanuele Castorina and Marko Simonović for useful discussions during the preparation of this manuscript. We thank Yin Li for making the `mcfit` package public and similarly thank Chirag Modi for sharing his `CLEFT` code, as well as helping us check the `velocileptors` for numerics and factors of two. S.C. thanks the CERN theory group for its hospitality while part of this work was being completed. S.C. is supported by the National Science Foundation Graduate Research Fellowship (Grant No. DGE 1106400) and by the UC

Berkeley Theoretical Astrophysics Center Astronomy and Astrophysics Graduate Fellowship. M.W. is supported by the U.S. Department of Energy and the NSF. This research has made use of NASA's Astrophysics Data System and the arXiv preprint server. This research used resources of the National Energy Research Scientific Computing Center (NERSC), a U.S. Department of Energy Office of Science User Facility operated under Contract No. DE-AC02-05CH11231.

Chapter 3

Redshift-Space Galaxy Clustering II: Power Spectrum in Lagrangian Perturbation Theory

This chapter was originally published as

> Shi-Fan Chen et al. "Redshift-space distortions in Lagrangian perturbation theory". In: *JCAP* 2021.3, 100 (Mar. 2021), p. 100. DOI: 10.1088/1475-7516/2021/03/100. arXiv: 2012.04636 [astro-ph.CO]

In Chapter 2 we conducted a detailed study of the contributions of galaxy peculiar velocities to the redshift-space power spectrum to 1-loop order in perturbation theory, exhaustively enumerating the required effective-theory terms required to properly account for the effects of short modes and nonlinear velocities. In addition to these short-scale effects however, long-wavelength velocities also have a significant role, since they anisotropically contribute to the damping of the BAO feature in the same way that long-wavelength displacements do in real space and, as discussed in Chapter 1, need to be resummed. Heuristically, the large-scale linear displacements damping the BAO receive an additional contribution $\Psi_i^{(1)} \to \Psi_i^{(1)} + f\hat{n}_i\hat{n}_j\Psi_j^{(1)}$, such that the damping becomes

$$\exp\Big(-\frac{1}{2}k^2\Sigma^2_{\rm BAO}\Big) \to \exp\Big(-\frac{1}{2}k^2\big(1+f(2+f)\mu^2\big)\Sigma^2_{\rm BAO}\Big),\ \mu = \hat{n}\cdot\hat{k}. \tag{3.1}$$

Since $f \approx 1$, along the line-of-sight it is clear that these anisotropic contributions will also not be well-captured perturbatively and need to be resummed. By treating the velocity contributions order-by-order, our calculations in the previous chapter were not particularly well-suited for this resummation, though in the case of Eulerian perturbation theory we were able to approximately include this effect by performing a "wiggle no-wiggle split." Our goal in the present chapter is to amend this omission in our previous treatment of RSD in LPT.

We present the one-loop 2-point function of biased tracers in redshift space computed with Lagrangian perturbation theory, including a full resummation of both long-wavelength

(infrared) displacements and associated velocities. The resulting model accurately predicts the power spectrum and correlation function of halos and mock galaxies from two different sets of N-body simulations at the percent level for quasi-linear scales, including the damping of the baryon acoustic oscillation signal due to the bulk motions of galaxies. We compare this full resummation with other, approximate, techniques including the moment expansion and Gaussian streaming model. We discuss infrared resummation in detail and compare our Lagrangian formulation with the Eulerian theory augmented by an infrared resummation based on splitting the input power spectrum into "wiggle" and "no-wiggle" components. We show that our model is able to recover unbiased cosmological parameters in mock data encompassing a volume much larger than what will be available to future galaxy surveys. We demonstrate how to efficiently compute the resulting expressions numerically, making available a fast Python code capable of rapidly computing these statistics in both configuration and Fourier space.

3.1 Introduction

The measured redshifts of galaxies receive a contribution proportional to the relative velocity between the observer and the emitting source. This term breaks the isotropy of space, as it singles out the observer location as special, and causes a distinct anisotropic pattern in the clustering statistics of biased tracers known as Redshift Space Distortions (RSD) [196, 158, 275, 114]. Being a probe of the velocity field, RSD contain extra cosmological information compared to the density field only, and they have been shown to be a useful probe of modified gravity models [153, 410, 194, 12, 8]. Current and upcoming spectroscopic redshift surveys, like DESI [108] and Euclid [211], will provide measurements of the power spectrum of galaxies with much better precision than currently available, making the modeling of RSD of paramount importance to achieve their science goals. Within the framework of Perturbation Theory (PT) several different approaches have been put forward to compute clustering statistics in redshift space. We can divide them into two main categories: Eulerian PT (EPT) methods, where density and velocity fields are the relevant degrees of freedom (dof), and Lagrangian PT (LPT) methods, where the displacements of dark matter particles and galaxies are the fundamental dof from which observables are computed[1]. This work focuses on the latter, but more generally one of our main goals is to clarify the relation between the two approaches to RSD.

LPT has a long history, especially in the context of RSD [231, 58, 405, 415, 396, 398, 74], and LPT models of the galaxy correlation function, *i.e.* in position space, have been successfully applied to data (see e.g. refs. [303, 311, 312, 363, 439, 30] for a sampling of the literature). In Fourier space, while RSD in EPT can be straightforwardly implemented [36, 138, 110, 86, 96, 377], LPT has posed a number of technical difficulties that have only recently been overcome [398]. Using an expansion in the moments of the density-weighted

[1]In both cases we will only consider the effective field theory (EFT) approach to PT, see [28, 60, 290, 399, 332, 14] and references therein.

pairwise velocities, ref. [74] presented a derivation of the 1-loop redshift space galaxy power spectrum in LPT, finding good agreement in comparison to simulated data.

The main goal of this chapter is to compute the 1-loop redshift space power spectrum in LPT via direct evaluation of the integrals, without employing the moment expansion (MOME) [328, 400, 401, 398]. This is not only a practical choice, but, for example, it will allow us to clarify the effect on the power spectrum of various resummation schemes for the long-wavelength (IR) displacement modes [335, 333, 399, 22, 402, 50, 112, 185].

In EPT, IR-resummation is performed a posteriori, after the 1-loop power spectrum is computed, and different procedures have been discussed in the literature. In redshift space in particular, a number of approximations have been employed to render the calculation more tractable [218, 280, 112, 185]. In the current implementation of MOME in LPT [74], only the long wavelength displacements are resummed, leaving the long wavelength velocity effects un-resummed. If desired, these long wavelength velocity effects can also be resummed in a posteriori way, as is done in EPT, and as we show in Appendix C.1. Alternatively, by truncating the configuration-space velocity cumulants at second order, the Gaussian streaming model can be used to approximately resum velocities from linear (Gaussian) modes at the expense of neglecting some one-loop contributions[2] [396].

The direct LPT approach allows us to efficiently resum the long displacement contributions without relying on any of the above-mentioned approximations. Some of these different choices for IR-resummation can lead to different behaviours of the power spectra at small (UV) scales. However, as we shall discuss further below, these differences can be associated to the different perturbative expansion parameters they employ. Moreover, even though these differences arise from long wavelength displacements, which are under perturbative control, these residual contributions are also approximately degenerate with, and can thus be absorbed by, the free coefficients of the effective theory.

The results presented in this chapter complement the existing literature on the one-loop LPT power spectrum in ΛCDM cosmologies referenced above. Additionally, our work provides the analytical machinery to better understand the performance of forward model or density field reconstruction algorithms in redshift space based on Lagrangian displacements [443, 248, 323].

This paper is structured as follows. Section 3.2 will introduce the notation, Section 3.3 the relevant equations for the computation of the one-loop RSD power spectrum of biased tracers, whose evaluation is discussed in Section 3.4. Numerical fits to N-body simulations and mock catalogs are presented in Section 3.5, as well as comparisons between the different PT methods. This section also demonstrates that the model is able to recover unbiased estimates of cosmological parameters in a "blind" challenge. Our conclusions are presented in Section 3.6. A number of technical points are relegated to Appendices C.1, C.2 and C.3.

[2]See, e.g. Appendix B of ref. [74].

3.2 Overview of Lagrangian Perturbation Theory

Our goal in this section is to give a quick overview of Lagrangian perturbation theory (LPT) as pertains to this chapter, both as a review and to establish our notation and conventions. The reader is referred to the references in the introduction for further details, and especially to refs. [231, 229, 58, 415, 399, 396, 74] whose notations we adopt.

Within the Lagrangian picture the gravitational evolution of large-scale structure is described via the of motion fluid elements starting at initial (Lagrangian) positions $\mathbf{q}$ with trajectories given by $\mathbf{x}(\mathbf{q},t) = \mathbf{q} + \mathbf{\Psi}(\mathbf{q},t)$. The Lagrangian displacements, $\mathbf{\Psi}$, obey the equation of motion $\ddot{\mathbf{\Psi}}(\mathbf{q}) + \mathcal{H}\dot{\mathbf{\Psi}}(\mathbf{q}) = -\nabla_{\mathbf{x}}\Phi(\mathbf{x})$, where dots indicate derivatives with respect to the conformal time, and the gravitational potential Φ is in turn sourced by the matter overdensity δ_m given by

$$1 + \delta_m(\mathbf{x}) = \int d^3\mathbf{q}\ \delta_D(\mathbf{x} - \mathbf{q} - \mathbf{\Psi}(\mathbf{q})) \quad , \quad (2\pi)^3\delta_D(\mathbf{k}) + \tilde{\delta}_m(\mathbf{k}) = \int d^3\mathbf{q}\ e^{i\mathbf{k}\cdot(\mathbf{q}+\mathbf{\Psi})} \tag{3.2}$$

via Poisson's equation. In LPT these quantities are solved for order-by-order in the linear initial conditions $\delta_0(\mathbf{q})$, such that the displacements are given by $\mathbf{\Psi} = \mathbf{\Psi}^{(1)} + \mathbf{\Psi}^{(2)} + \mathbf{\Psi}^{(3)} + ...$ Of particular interest is the linear solution $\mathbf{\Psi}^{(1)} = -D(z)\nabla_{\mathbf{q}}^{-1}\delta_0(\mathbf{q})$, also known as the Zeldovich approximation. The specific forms of the higher-order solutions are given for example in refs. [230, 440, 296]. These solutions contain parametrizeable dependences on small-scale physics which are captured by including additional effective-theory counterterms [290, 399].

In this chapter we will be primarily interested in the clustering of biased tracers of matter like galaxies which are the target of galaxy redshift surveys. Within the Lagrangian framework biased tracers are modeled as functionals of the linear initial conditions $F[\delta_{\rm lin}](\mathbf{q})$ at their Lagrangian positions $\mathbf{q}$ and advected along with the matter fluid, such that their observed overdensities are given by number conservation to be

$$1 + \delta_g(\mathbf{x}) = \int d^3\mathbf{q}\ F(\mathbf{q})\ \delta_D(\mathbf{x} - \mathbf{q} - \mathbf{\Psi}). \tag{3.3}$$

The bias functional $F(\mathbf{q})$ is a local function of the initial conditions with effective corrections, and at one-loop order in the power spectrum includes linear and quadratic density bias, shear and third-order contributions as well as effective corrections like derivative bias ($\propto \nabla^2\delta^2$) similar to the dynamical ones described at the end of the previous paragraph. We will furthermore assume that cold dark matter and baryons can be treated as a single fluid and therefore discard bias operators and dynamics proportional to relative density and velocity of the different fluids [14, 43, 316, 70, 25, 199, 298]. These extra terms are thought to be small and therefore need only be implemented at leading order in the (relative) displacements, as discussed in ref. [70]. Our conventions follow Equation 5.1 in ref. [74].

Finally, galaxy surveys determine the line-of-sight (LOS) position of observed galaxies via redshifts z whose cosmological and peculiar-velocity contributions are degenerate. These redshift-space distortions (RSD) can be accounted for within LPT by boosting displacements along the LOS direction $\hat{n}$ by their corresponding velocities $\mathbf{\Psi}^s = \mathbf{\Psi} + (\hat{n}\cdot\mathbf{v})\hat{n}/\mathcal{H}$, where $\mathcal{H}$

is the conformal Hubble parameter. We will use the superscript s to refer to vectors boosted into redshift space throughout this work. Within the Einstein-de Sitter approximation (EdS) we have the further simplification that

$$\mathbf{\Psi}^{s,(n)} = \mathbf{\Psi}^{(n)} + nf\ (\hat{n}\cdot\mathbf{\Psi}^{(n)})\ \hat{n} \equiv R^{(n)}\mathbf{\Psi}^{(n)}, \tag{3.4}$$

where the matrix $R_{ij}^{(n)} = \delta_{ij} + nf\ \hat{n}_i\hat{n}_j$ and f is the linear growth rate. We will operate within the EdS approximation for the remainder of the paper, and further make the distant observer approximation such that $\hat{n}$ is the same for each galaxy. These approximations are known to be quite good in the limit of high redshifts and on scales where higher order perturbation theory is most applicable. A discussion of violations of these approximations within the LPT context can be found in refs. [299, 128, 139, 63, 64, 367].

3.3 Redshift-Space Power Spectrum

We now proceed to write down the power spectrum at one loop in Lagrangian perturbation theory [229, 58, 405, 415, 396, 398, 74]. From Equation 3.2 and its counterpart for biased tracers we have that the galaxy autospectrum is given by

$$P(\mathbf{k}) = \int d^3\mathbf{q}\ e^{i\mathbf{k}\cdot\mathbf{q}} \left\langle e^{i\mathbf{k}\cdot\Delta} F(\mathbf{q}_1)F(\mathbf{q}_2)\right\rangle_{\mathbf{q}=\mathbf{q}_1-\mathbf{q}_2}$$

where we have defined the pairwise Lagrangian displacement $\Delta_i = \mathbf{\Psi}_i(\mathbf{q}_1) - \mathbf{\Psi}_i(\mathbf{q}_2)$. Setting $F = 1$, for matter, the bracketed average can expressed using the cumulant theorem as [58]

$$\ln\left\langle e^{i\mathbf{k}\cdot\Delta}\right\rangle = -\frac{1}{2}k_ik_jA_{ij} - \frac{i}{6}k_ik_jk_kW_{ijk} + ...,$$

where we have defined the cumulants of the pairwise displacements as $A_{ij} = \langle\Delta_i\Delta_j\rangle_c$ and $W_{ijk} = \langle\Delta_i\Delta_j\Delta_k\rangle_c$. For biased tracers one simply needs to compute cumulants with sources like $J(\mathbf{q})\delta(\mathbf{q})$ added to the exponent and take functional derivatives; this produces terms like $U_i = \langle\delta_{\rm lin}(\mathbf{q}_1)\Delta_i\rangle$. The above calculations can be promoted to redshift space by promoting the displacements to redshift space (Δ^s) order-by-order as in Equation 3.4.

From the above, the one-loop galaxy autospectrum in redshift space is given in LPT by

[229, 58, 405, 415, 396, 398, 74]

$$
\begin{aligned}
P_s(\mathbf{k}) = \int d^3\mathbf{q}\; e^{i\mathbf{k}\cdot\mathbf{q}}\; e^{-\frac{1}{2}k_ik_jA^{s,<}_{ij}} \Big\{ & 1 - \frac{1}{2}k_ik_jA^{s,>}_{ij} + \frac{1}{8}k_ik_jk_kk_lA^{s,>}_{ij}A^{s,>}_{kl} \\
& - \frac{1}{2}k_ik_jA^{s,\mathrm{loop}}_{ij} + \frac{i}{6}k_ik_jk_kW^s_{ijk} \\
& + 2ib_1k_i(1 - \frac{1}{2}k_ik_jA^{s,>}_{ij})U^s_i - b_1k_ik_jA^{s,10}_{ij} \\
& + b_1^2(1 - \frac{1}{2}k_ik_jA^{s,>}_{ij})\xi_{\mathrm{lin}} + ib_1^2k_iU^{s,11}_i - b_1^2k_ik_jU^{s,\mathrm{lin}}_iU^{s,\mathrm{lin}}_j \\
& + \frac{1}{2}b_2^2\xi^2_{\mathrm{lin}} + 2ib_1b_2\xi_{\mathrm{lin}}k_iU^{s,\mathrm{lin}}_i - b_2k_ik_jU^{s,\mathrm{lin}}_iU^{s,\mathrm{lin}}_j + ib_2k_iU^{s,20}_i \\
& + b_s(-k_ik_j\Upsilon^s_{ij} + 2ik_iV^{s,10}_i) + 2ik_ib_1b_sV^{s,12}_i + b_2b_s\chi + b_s^2\zeta + 2ib_3k_iU^s_{b_3,i} + 2b_1b_3\theta + ... \Big\} \\
& + k^2(\alpha_0 + \alpha_2\mu^2 + \alpha_4\mu^4 + \alpha_6\mu^6)P_{s,\mathrm{ZelZel}}(\mathbf{k}) + R_h^3(1 + \sigma_2k^2\mu^2 + \sigma_4k^4\mu^4). \qquad (3.5)
\end{aligned}
$$

Here we have split the second cumulant A_{ij} into long and short linear components and a loop component, keeping only the long-wavelength piece $A^{s,<}_{ij}$ exponentiated; we will comment on this further below. In addition to A_{ij}, W_{ijk} and U_i defined above, Equation 3.5 contains additional correlators of pairwise Lagrangian displacements and higher-order bias operators like shear that are defined explicitly in refs. [58, 415, 396, 74]. The last line of Equation 3.5 includes counterterms (α_n) and stochastic contributions (σ_n) proportional to the typical scale of halo/galaxy formation R_h. These include what are traditionally referred to as the "shot noise" and "finger of god" (FoG) terms. The small-scale sensitivities that give rise to these terms are described in detail[3] in ref. [74].

While the correlators in Equation 3.5 have been extensively described elsewhere, it is instructive to elucidate their general perturbative and angular structure with an example. Let us consider the displacement two-point function up to one-loop

$$
A_{ij} \equiv \langle \Delta_i\Delta_j \rangle = A^{\mathrm{lin}}_{ij} + A^{\mathrm{loop}}_{ij} \quad , \quad A^{\mathrm{loop}}_{ij} = A^{(22)}_{ij} + 2A^{(13)}_{ij}, \qquad (3.6)
$$

which is given by a linear piece (lin) from contracting two first-order displacements and a one-loop piece from contracting two second-order displacements (22) or one first and one third-order displacement each (13). To go into redshift space, each of these pieces must be transformed separately — this is because at each order in perturbation theory the translation to redshift space depends on n, such that for example

$$
A^{s,(13)}_{ij} = R^{(1)}_{in}R^{(3)}_{im}A^{(13)}_{nm} \quad \text{but} \quad A^{s,(22)}_{ij} = R^{(2)}_{in}R^{(2)}_{im}A^{(22)}_{nm} \quad .
$$

The n-dependence of these transformations encodes information about beyond-linear velocities within the RSD spectrum and is the primary complication in extending the treatment of RSD

[3] In particular, the advantages of this form for treating fingers of god (and redshift errors) are discussed in detail in §§4.1.3, 4.2.3, 5.3 and Appendix C of ref. [74].

beyond the Zeldovich approximation, where all vectors transform via $\mathbf{R} = \mathbf{R}^{(1)}$ (see refs. [415, 398, 78]). A similar observation applies to all correlators with vector indices in Equation 3.5.

Finally, let us comment on our resummation of the linear piece of A_{ij}. A salient feature of cosmologies like ΛCDM is that large-scale displacements produce nonlinear damping of spatially localized features in the power spectrum such as baryon acoustic oscillations (BAO) that cannot be captured simply with an order-by-order expansion in the linear initial conditions [46, 121, 231, 229, 92, 266, 257, 58, 368, 232, 415, 335, 321, 22, 402, 235, 50, 338]. This is because, while the dynamics on these large scales are essentially linear, the size of these displacements on BAO scales can be large compared to wavenumbers where the BAO wiggles have support. As such, the effects of these displacements must be manually resummed in order-by-order expansions such as Eulerian perturbation theory (EPT). On the other hand, within LPT the exponential in Equation 3.2 and the cumulant theorem for a Gaussian variable

$$\left\langle e^{i\mathbf{k}\cdot\Delta^{(1)}} \right\rangle = e^{-\frac{1}{2}k_i k_j A_{ij}^{(11)}} \tag{3.7}$$

suggests a natural resummation scheme wherein the linear displacements are kept exponentiated. These exponentiated displacements should be resummed only up to an IR scale $k_{\rm IR}$; we will follow the convention in ref. [74] and perform this split by an exponential cutoff $\exp[-\frac{1}{2}(k/k_{\rm IR})^2]$ in the A_{ij} integral for the "less than" displacements kept resummed, $A_{ij}^{s,<}$ in Equation 3.5, and the "greater than" displacements (defined with $1 - \exp[-\frac{1}{2}(k/k_{\rm IR})^2]$ in the integral), $A_{ij}^{s,>}$, which are expanded to second order in the curly brackets in Equation 3.5. Within ΛCDM-like cosmologies, A_{ij} is close to saturated on BAO scales and it might be expected that an IR cutoff should make only small differences in the final theory prediction. This is true for the density statistics [415, 235, 396, 22, 185]. However, ref. [74] showed that the higher-order velocity statistics that enter into RSD are especially sensitive to IR resummation in both broadband and BAO wiggles. This is discussed in further detail in Appendix C.1. We conclude this section by noting that, contrary to EPT where the a posteriori IR-resummation has been implemented only for equal time correlators, the direct evaluation of the LPT integrals presented in this work automatically evaluates the power spectrum at unequal times. In this case, the bulk displacement contributions do not cancel exactly in the exponent in Eq.(3.7) leading to rapid suppression and decorrelation of unequal time correlators. This has recently been considered [83] in the context of weak lensing analyses, that all involve unequal time correlators. On the same topic, this should also clarify some recent concerns raised in ref. [35] about the use of perturbation theory for unequal time correlators.

3.4 Numerical Implementations

The primary challenge in evaluating the integral in Equation 3.5 lies in the angular dependence due to the three vectors, $\mathbf{q}$, $\mathbf{k}$ and $\hat{n}$, that enter the calculation (Fig. 3.1a). By symmetry, each of the tensor-indexed Lagrangian-space correlators in Equation 3.5 can be decomposed into components multiplying products of $\hat{q}$ and the Kronecker delta symbol; for example, we

can write $A_{ij}(\mathbf{q}) = X(q)\delta_{ij} + Y(q)\hat{q}_i\hat{q}_j$ [58]. In real space, where the angular dependence is due only to $\mathbf{k}$ and $\mathbf{q}$, it is customary to proceed by defining a coordinate system wherein $\mathbf{k}$ points towards the zenith such that the integrand has azimuthal symmetry. The resulting dependence on $\mu_\mathbf{q} = \hat{k}\cdot\hat{q}$, where the subscript is meant to distinguish it from the familiar LOS angle $\mu = \hat{k}\cdot\hat{n}$, can then be recast into infinite sums of spherical Bessel functions using, for example, the identity

$$\frac{1}{2}\int d\mu_\mathbf{q}\; e^{iA\mu_\mathbf{q} - \frac{1}{2}B\mu_\mathbf{q}^2} = e^{-B/2}\sum_{n=0}\left(\frac{B}{A}\right)^n j_n(A) \tag{3.8}$$

and its derivatives, with the resulting integrals in q efficiently computed using the FFTLog algorithm [159, 397]. In the particular case of LPT, we have $A = kq$ and $B = k^2Y^<(q)$, such that in the Zeldovich power spectrum (second line of Equation 3.5 in the $k_{\rm IR} = \infty$ limit) is

$$P_{\rm Zel}(k) = 4\pi\sum_{n=0}^{\infty}\int dq\, q^2\; e^{-\frac{1}{2}k^2(X+Y)}\left(\frac{kY}{q}\right)^n j_n(kq) \tag{3.9}$$

in real space. This form of the integral, suitable for using fast Hankel transforms, generalizes for higher loop terms, as well as when we go to redshift space, as we show in the rest of this section. Note that the computation calls for one transform for each k value. The expansion converges quickly for the k values of our interest and it is typically sufficient to keep only the $n < 10$ terms in the sum above. Moreover, for higher n terms the Limber approximation [221, 223] can be used

$$j_\ell(kq) \approx \sqrt{\frac{\pi}{2\ell+1}}\;\delta^D\left(kq - \ell - \frac{1}{2}\right), \quad \text{when} \quad \ell \to \infty, \tag{3.10}$$

which provides an accurate approximation for the integral above when used for $n > 3$.

In redshift space, the azimuthal symmetry is broken by the line-of-sight dependence, as shown in Figure 3.1a, which selects a preferred plane containing $\hat{k}$ and $\hat{n}$ (blue). Below, we outline one method to efficiently perform the integral in redshift space. Following previous work [398] we will call it Method II. Our development extends the Zeldovich calculations for matter and biased tracers in refs. [369, 398, 78] to one-loop order. Method II relies on an active transformation of the wavevector $\mathbf{k}$ into a frame more conducive to evaluating the integral in Equation 3.5. Of course, it is also possible to directly evaluate the integral within the original frame — this is the strategy of Method I. This alternative method is described for the interested reader in Appendix C.2.

We now outline the rough strategy for Method II. In our expressions $\mathbf{\Psi}$ enters only in the combination $\mathbf{k}\cdot\mathbf{\Psi}$. Thus instead of transforming all displacements into redshift space via $\mathbf{\Psi}^{(n)} \to \mathbf{R}^{(n)}\mathbf{\Psi}^{(n)}$ we can instead passively transform the wave vectors, multiplying them by $\mathbf{R}^T = \mathbf{R}$. In particular we shall apply the linear theory transformation $\mathbf{R}^{(1)}$ to $\mathbf{k}$ to yield the vector $K_i = R^{(1)}_{ij}k_j$. We will deal with the non-linear contributions to $\mathbf{\Psi}$ below. In this new "Zeldovich" frame, shown in Figure 3.1b, the zenith direction is set to be $\hat{K}$, and we redefine

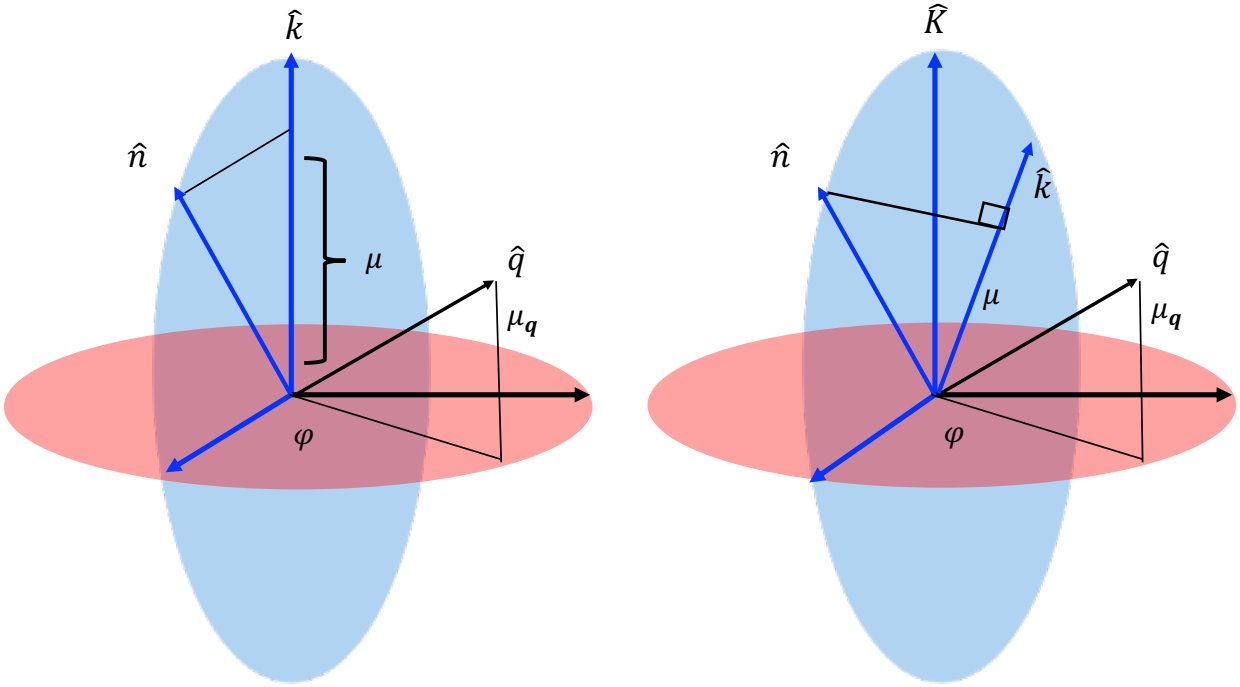

(a) Normal Frame: Method I (b) Zeldovich Frame: Method II

Figure 3.1: (a) Geometry of the vector and tensor quantities in the integral Eq. 3.5. In the absence of redshift-space distortions ($\hat{n}$ dependence) the integral over $\mathbf{q}$ is azimuthally symmetric; with RSD, a ϕ dependence occurs since $\hat{k}$ and $\hat{n}$ lie on a preferred plane. (b) In Method II, vectors are boosted into the "Zeldovich" frame where projections along the line of sight are amplified by the linear growth rate f and the zenith is redefined to be the thus-boosted $K_i = R_{ij}k_j$. In both frames, $\hat{n}$, $\hat{k}$ and $\hat{K}$ are coplanar as shown in blue.

$\mu_\mathbf{q} = \hat{K}\cdot\hat{q}$. Thus $\mathbf{K}\cdot\hat{n} = k\mu(1+f)$ and $K^2 = k^2[1+f(2+f)\mu^2]$. Note that $\hat{k}$, $\hat{K}$ and $\hat{n}$ are coplanar.

Let us begin by reviewing the angular structure of this coordinate choice. We have

$$\begin{aligned}\hat{n}\cdot\hat{q} &= A(\mu)\mu_\mathbf{q} + B(\mu)\sqrt{1-\mu_\mathbf{q}^2}\,\cos\phi,\\ \mathbf{k}\cdot\mathbf{q} &= kq\Big(c(\mu)\mu_\mathbf{q} - s(\mu)\sqrt{1-\mu_\mathbf{q}^2}\cos\phi\Big),\end{aligned} \tag{3.11}$$

with the definitions

$$\begin{aligned}A(\mu) &= \frac{\mu(1+f)}{\sqrt{1+f(2+f)\mu^2}} \quad , \quad B(\mu) = \sqrt{\frac{1-\mu^2}{1+f(2+f)\mu^2}}\\ c(\mu) &= \frac{1+f\mu^2}{\sqrt{1+f(2+f)\mu^2}} \quad , \quad s(\mu) = \frac{f\mu\sqrt{1-\mu^2}}{\sqrt{1+f(2+f)\mu^2}} \quad .\end{aligned} \tag{3.12}$$

Note the square root in the denominators is simply K/k. That the azimuthal dependence always multiplies the sine, $\sqrt{1-\mu_{\mathbf{q}}^2}$, will prove a particular convenience in this frame.

In terms of the above, the Zeldovich matter power spectrum can be succintly expressed as

$$P_s(\mathbf{k}) = \int dq\ d\mu_{\mathbf{q}}\ q^2\ e^{ikqc\mu_{\mathbf{q}} - \frac{1}{2}K^2(X+Y\mu_{\mathbf{q}}^2)} \left(\int d\phi\ e^{-ikqs\sqrt{1-\mu_{\mathbf{q}}^2}\cos\phi} \right)$$

In ref. [398] this integral was shown to be expressable in terms of Bessel functions via the identity

$$I(A,B,C) = \int d\mu_{\mathbf{q}}\ d\phi\ e^{-iC\sqrt{1-\mu_{\mathbf{q}}^2}\cos\phi + iA\mu_{\mathbf{q}} + B\mu_{\mathbf{q}}^2} = 4\pi e^B \sum_{\ell=0}^{\infty} \left(\frac{-2}{\rho}\right)^{\ell} \tilde{G}_{0,\ell}^{(0)}(A,B,\rho) j_\ell(\rho) \tag{3.13}$$

by substituting $A = kqc$, $B = -\frac{1}{2}K^2Y$ and $C = kqs$. The exact form of the kernel $\tilde{G}_{0,\ell}^{(0)}$ is given in Appendix C.3.4. Building on top of this, any bias contribution involving only the linear (Zeldovich) displacement (e.g. the linear bias term $ik_iU_i^{\rm lin}$), simply acquires powers of $\mu_{\mathbf{q}}$ and K (e.g. $iK\mu_{\mathbf{q}}$) that can be evaluated as derivatives of the above with respect to A, since correlators in Lagrangian space are always decomposable into δ_{ij} and tensor products of $\hat{q}_i$ [78].

The simple Zeldovich angular structure above is, however, broken by the inclusion of higher-order displacements. This is because these displacements get boosted along the line of sight by more than linear theory when going to redshift space. With $\mathbf{R} = \mathbf{R}^{(1)}$

$$\dot{\mathbf{\Psi}}^{(n)} = \mathbf{R}^{(n)}\mathbf{\Psi}^{(n)} = (\mathbf{R} + (n-1)f\ \hat{n}\otimes\hat{n})\mathbf{\Psi}^{(n)}. \tag{3.14}$$

In the spirit of the above calculations we can dot the matrix into the wavevectors and take

$$k_i \to K_i + f(n-1)k_{\parallel,i} \quad , \quad k_\parallel = (k\mu)\hat{n}. \tag{3.15}$$

Dotting the transformed wavevector with Lagrangian correlators thus simply requires additional powers of $\hat{n}\cdot\hat{q}$, which conveniently translates into powers of $\mu_{\mathbf{q}}$ and $\sqrt{1-\mu_{\mathbf{q}}^2}\cos\phi$, i.e. the coefficients multiplying A and C in Equation 3.13. We thus see that any contribution to the power spectrum can be evaluated via mixed (A,C) derivatives of Equation 3.13. We refer the reader to Appendix C.3 for further details and an example application to the one-loop matter power spectrum.

3.5 Results

Having laid out how the one-loop power spectrum can be efficiently computed within fully-resummed one-loop LPT, our goal in this section is to validate our model against N-body data. In addition, we compare the performance of our model with previous models such as the Gaussian streaming model (GSM; [276, 137, 301, 303, 405, 396]) and moment expansion (MOME; [398, 74]) in LPT and resummed Eulerian perturbation theory (REPT) in both Fourier and configuration space.

3.5.1 Comparison to N-body

For our main comparisons to N-body data we use halo catalogs from the simulations in ref. [359] and employ NBODYKIT [163] to compute redshift-space power spectrum wedges, multipoles and correlation function multipoles at $z = 0.8$. These simulations assume a ΛCDM cosmology with $\Omega_m = 0.2648$, $\Omega_b h^2 = 0.02258$, $h = 0.71$, $n_s = 0.963$ and $\sigma_8 = 0.8$. We adopt the mass bin $12.5 < \log(M/h^{-1}M_\odot) < 13.0$ as our fiducial sample but have checked that we get similar results for a higher mass bin as well as the mock galaxy sample described in ref. [74]. Our fiducial sample has a number density of $\bar{n} = 0.53 \times 10^{-3}\, h^3\,\mathrm{Mpc}^{-3}$ and linear (Eulerian) bias of $b \approx 1.7$, making it slightly sparser but about 40% more biased than the DESI ELG sample at $z = 0.85$ [108]. We have chosen these simulations due to their relatively large total volume (4 boxes with volume $[4h^{-1}\mathrm{Gpc}]^3$). With such a large volume the statistical errors on the two-point functions will necessarily be significantly smaller than galaxy surveys at comparable redshifts; however, we caution that the use of "derated" time steps in the running of these simulations may cause systematic errors on the few percent level, as discussed in further detail in refs. [396, 74]. We have attempted to mitigate this effect by using only the high redshift catalog at $z = 0.8$.

Figure 3.2 compares our LPT model to the power spectrum wedges and multipoles of our fiducial halo sample. We fit for the wedges, $P(k, \mu)$, up to $k_{\rm max} = 0.2\,h\,\mathrm{Mpc}^{-1}$ assuming Gaussian covariances. We use the same parameters for the multipoles. We find bias parameters of order unity and the isotropic stochastic contribution R_h^3 comparable to the shot noise, noting that extending to higher (unperturbative) $k_{\rm max}$ tends to recover apparently good fits with anomalously large bias and effective parameters. Our model is in excellent agreement with the power spectrum wedges at the scales shown, differing from the data at levels comparable to their statistical uncertainty, with qualitatively similar behavior in the multipoles, though the anisotropic contributions ($\ell > 0$) diverge faster than the monopoles as expected due to the enhanced nonlinearity of halo velocities.

In Figure 3.2, as well as throughout the main body of this work, we have adopted the fiducial choice of infrared cutoff $k_{\rm IR} = 0.2\,h\,\mathrm{Mpc}^{-1}$. As discussed in Section 3.3, compared to density statistics the velocity statistics' underlying redshift-space distortions have broadband shapes that are especially sensitive to the choice of infared cutoff. For example, as shown in ref. [74] the monopole and quadrupole of the second moment of the pairwise velocity, responsible for contributions to the power spectrum proportional to the growth rate (f) squared, respectively have broadband shapes better captured by large and small $k_{\rm IR}$. One might thus hope to find an intermediate regime wherein both statistics are reasonably captured, and indeed we find that the choice $k_{\rm IR} = 0.2\,h\,\mathrm{Mpc}^{-1}$ reproduces the hexadecapole better than either the fully-exponentiated limit ($k_{\rm IR} = \infty$) or $k_{\rm IR} = 0$. In principle, the spirit of perturbation theory should demand that the expanded displacements $k^2\Sigma^2_>$ be small[4] while the exponentiated ones kept manageable; for $k < 0.2\,h\,\mathrm{Mpc}^{-1}$ this is satisfied by our choice,

[4]Here we define

$$\Sigma^2_< = \frac{2}{3}\int \frac{dk}{2\pi^2} P_{\rm lin}(k)\; e^{-(k/k_{\rm IR})^2}, \quad \Sigma^2_> = \frac{2}{3}\int \frac{dk}{2\pi^2} P_{\rm lin}(k)\; (1 - e^{-(k/k_{\rm IR})^2}), \tag{3.16}$$

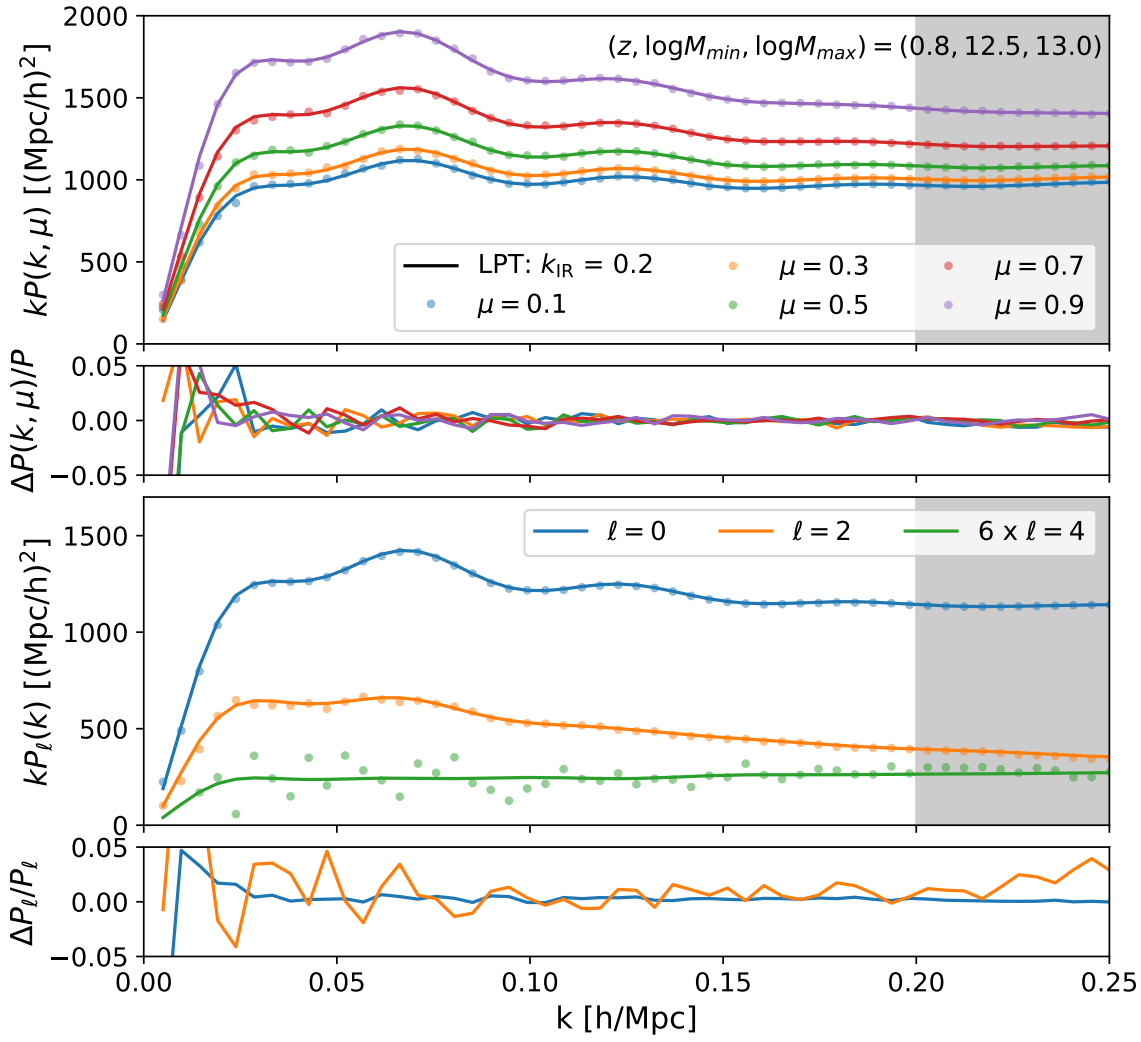

Figure 3.2: Fits to the redshift-space power spectrum wedges (top) and multipoles (bottom) of the fiducial halo sample with $10^{12.5} M_\odot < M < 10^{13.0} M_\odot$ at $z = 0.8$. Both statistics were fit assuming Gaussian covariances using a consistent set of bias parameters and with linear displacements resummed up to $k_{\rm IR} = 0.2\,h\,{\rm Mpc}^{-1}$. The fiducial LPT model gives an excellent fit to the anisotropic power spectrum inside the range of fit ($k < 0.2\,h\,{\rm Mpc}^{-1}$) well within the few-percent systematics expected from the N-body data. Shaded regions indicate wavenumbers beyond the range of fit, with higher multipoles diverging faster from the data past this point.

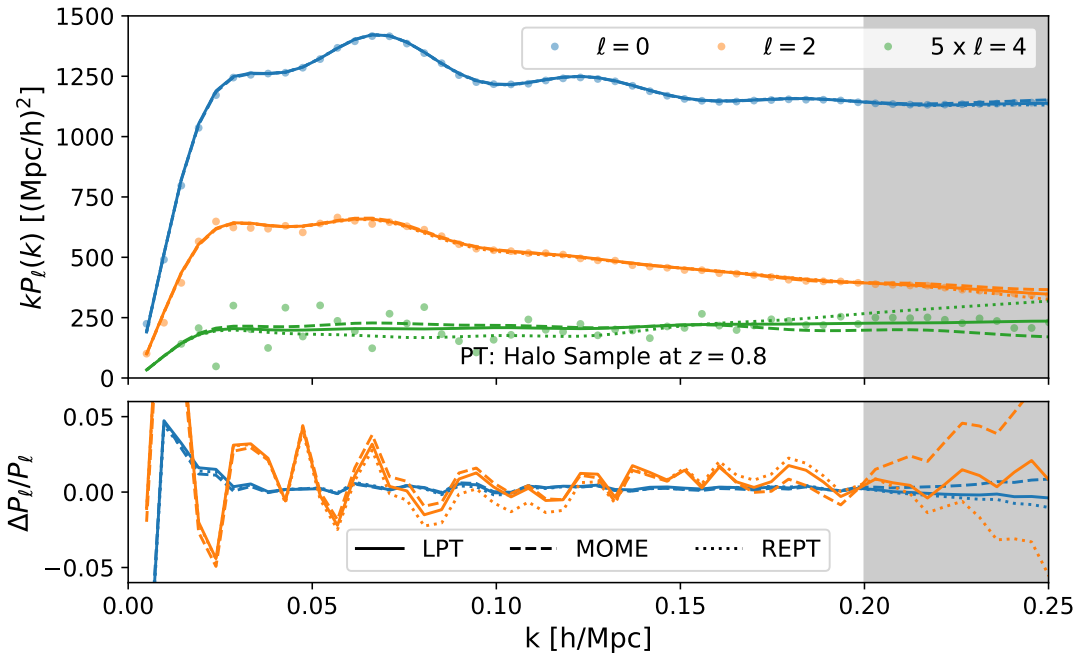

Figure 3.3: Redshift-space power spectrum multipoles of the fiducial halo sample fit using three effective theory models: the fiducial LPT model, the Lagrangian moment expansion and resummed Eulerian perturbation theory. All three models are fit as in Figure 3.2 and are in excellent quantitative agreement with the N-body data. The three models differ slightly in their prediction for the hexadecapole broadband; we have explicitly tuned our LPT IR resummation scheme to provide a good match to the data, though we note the relatively large statistical uncertainty in the hexadecapole.

though given that the *total* Zeldovich displacement for the fiducial cosmology at $z = 0.8$ is $\Sigma^{-1} \approx 0.2\,h\,\mathrm{Mpc}^{-1}$ this is relatively insensitive to the choice of IR cutoff. Moreover, while differences exist towards high k and μ, we find that in general the small-scale differences between the theory's predictions for reasonable values of k_{IR} can largely be absorbed by the effective parameters of the theory; further discussion of the interplay between k_{IR} choice and our model's predictions can be found in Appendix C.1; we intend to return to this topic in greater depth in future work.

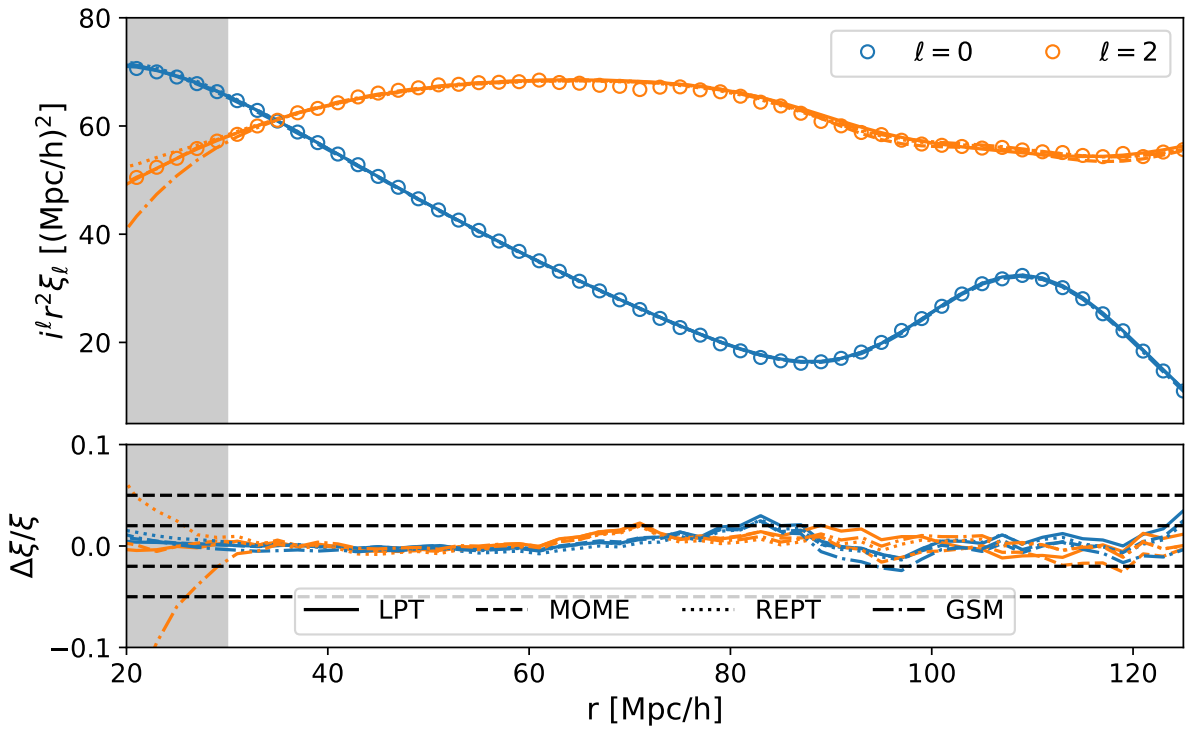

Figure 3.4: Configuration space correlation function multipoles predicted by our LPT model, the Lagrangian moment expansion, Eulerian perturbation theory and the Gaussian streaming model compared to N-body data. Each of the models are in good agreement with the data within the few-percent systematic uncertainties expected of the simulations, though we note that they all slightly overshoot the dip around 80 h^{-1} Mpc by around two percent. Note that due to the high degree of similarity between the theory predictions many of the lines lie on top of each other even in the fractional residuals in the bottom panel, particularly when comparing LPT (solid) and MOME (dashed). Black dashed lines in the lower panels indicate 2 and 5 percent errors.

3.5.2 Comparison to Other Models in Fourier and Configuration Space

The main difference between the model presented in this work and previous effective-theory models of the redshift-space galaxy two-point function lies in the IR-resummation procedure. Existing LPT formulations typically incorporate bulk velocities either via streaming model resummations [396, 398, 74] or direct expansions of velocity statistics [398, 74]. While these approaches have been shown to be sufficiently accurate to model redshift-space distortions in a variety of contexts, they have nonetheless exhibited a number of shortcomings. The

such that the sum $\Sigma^2 = \Sigma^2_< + \Sigma^2_>$ is the mean square pairwise displacement of two distant points in the Zeldovich approximation.

Gaussian streaming model allows for a partial resummation. However, the resummation procedure calls for nonlinear mapping of all the loop contributions, even those that require counterterms in order to regularize the UV dependence. Even though such mapping could in principle be restricted to only long wavelength contributions, the model also exhibits a somewhat cumbersome structure in Fourier space. The moment-expansion approach, on the other hand, relies on an explicit expansion in the velocity moments. However, in a similar way to the long wavelength displacement contributions, long wavelength velocity contributions also affect the BAO feature in a manner that then prompts the additional resummation of these contributions. In the Eulerian approach this can be done a posteriori using an ad hoc, wiggle-no-wiggle splitting of the power spectrum and resumming only the contributions related to the BAO feature (REPT). Such a procedure could also be performed for long wavelength velocity contributions in MOME, but this was not done in ref. [74] where only long wavelength displacements were resummed in the LPT manner. We outline this resummation of long wavelength velocities in Appendix C.1. While the MOME approach has been shown to give excellent predictions for the Fourier-space power spectrum, configuration space statistics (where the BAO focus is not merely few-per cent oscillations on top of the broadband) are expected to be more sensitive to the details of IR resummation and BAO damping.

More generally, IR resummation has also been extensively studied in the Eulerian context [22, 402, 50, 185, 76]. Most often, these rely on the wiggle-no-wiggle splitting procedure, separating the smooth and BAO components of the linear power spectrum (see, e.g. [121, 402, 76]). This procedure allows for a simplified treatment of the nonlinear effects of the BAO where typically only leading effects are captured, neglecting the more intricate structure captured by LPT. Nonetheless, the controlled approximations that enter into this form of IR resummation are generally subdominant to higher-order (two-loop) corrections that have been studied in e.g. refs. [402, 50, 86]. In addition to these EPT approaches, refs. [218, 280] take an intermediate approach. These rely on an LPT-like resummation procedure that tries to preserve the unresummed EPT broadband behaviour, thus effectively retaining an EPT-like perturbative structure. In this approach, the anisotropic part of the exponent in Eq. (3.7) is expanded while only the isotropic part is left resummed (see also Appendix B of ref. [399] for a more detailed connection between the two approaches).

Our goal in this subsection is to investigate how one-loop LPT with long wavelength velocity contributions fully resummed compares to the approaches mentioned above, focusing on the anisotropic redshift-space broadband and the BAO feature in configuration space. Figure 3.3 compares the Fourier-space multipoles predicted by our fiducial LPT framework to the LPT moment expansion (MOME) and one-loop resummed EPT (REPT). All three frameworks are fitted assuming Gaussian covariances up to $k_{\rm max} = 0.2\,h\,{\rm Mpc}^{-1}$ in $P(k,\mu)$ as in the previous subsection. All three frameworks show excellent agreement with the data, with any disagreements, including inter-framework disagreements, well within the few percent systematic errors we expect from these simulations. The frameworks differ most in the hexadecapole, with the pure LPT framework apparently a better fit to the broadband shape over the scales shown; this should be taken with a grain of salt, however, as the

statistical errors are large and we specifically checked our IR resummation procedure for the LPT framework using these data. Similarly, in Figure 3.4 we fit the correlation function multipoles of the fiducial halo sample using the three frameworks above as well as the Gaussian streaming model (GSM). All four are in excellent agreement with regards to both the BAO feature and broadband shape at quasi-linear scales. Since the correlation function multipoles probe a slightly different combination of modes than their Fourier-space counterparts with a hard k cut, we have adjusted the best-fit bias parameters "by eye" to yield a better fit at $r > 30\ h^{-1}$Mpc, though we note that directly transforming the previous Fourier-space results still yield theoretical predictions within the few-percent systematic errors expected from these simulations. Together, Figures 3.3 and 3.4 suggest that, despite differences in IR resummations schemes, existing effective-theory frameworks of the redshift-space two-point function offer similar levels of performance on pertubative scales. Finally, we note that, while in the above comparisons we have independently fit the bias parameters and EFT corrections of each model to most favorably evaluate the performance of each, their bias bases can in principle be mapped onto each other order-by-order; when the bias parameters are thus fixed, these models will tend to make slightly different predictions due to differences in resummed IR modes at higher order. We discuss these differences in Appendix C.1.

3.5.3 Cosmological Constraints using Blind Challenge Data

As a final test of our LPT model, we use it to model the "blind challenge" data described in ref. [255][5]. These are redshift-space power spectra for a BOSS-like HOD sample at $z \simeq 0.6$ constructed from ten N-body boxes each with sidelength $L = 3.84\,h^{-1}$Gpc sampled with 3072^3 equal mass particles. Since the total volume amounts to about 100 times the volume of the BOSS DR12 sample [7], the statistical error associated with these data are expected to be far below any realizable galaxy survey at this redshift. These data were designed for a blind challenge wherein three cosmological parameters $(\Omega_M, h, \ln[10^{10}A_s])$ need to be fit assuming these tiny statistical errors while the baryon fraction, f_b, and spectral tilt, n_s, are fixed to the values used in the simulations. The challenge was designed to evaluate the performance of different PT approaches. Any group wishing to enter the challenge submits their best fit cosmological parameters, without knowing the true ones, to Takahiro Nishimichi and collaborators. After submission one discovers if the model provides an unbiased estimate of the parameters.

We had previously submitted best fit parameters for MOME and REPT models that included scales up to $k_{\rm max} = 0.12\ h\,{\rm Mpc}^{-1}$, and in both cases the models "passed": our REPT submission yielded means for the cosmological parameters well within $1\,\sigma$ of the truth, while MOME yielded $1.1\,\sigma$ and $1.8\,\sigma$ deviations for Ω_m and h, both well within errors expected for realistic galaxy surveys[6] and possibly consistent with fluctuations in the challenge data

[5]The data and more information about the blind challenge can be found at https://www2.yukawa.kyoto-u.ac.jp/~takahiro.nishimichi/data/PTchallenge/.

[6]Indeed, MOME also yields errors below $1\,\sigma$ for $k_{\rm max} = 0.14\,h\,{\rm Mpc}^{-1}$, though we did not know this prior to submission and unblinding.

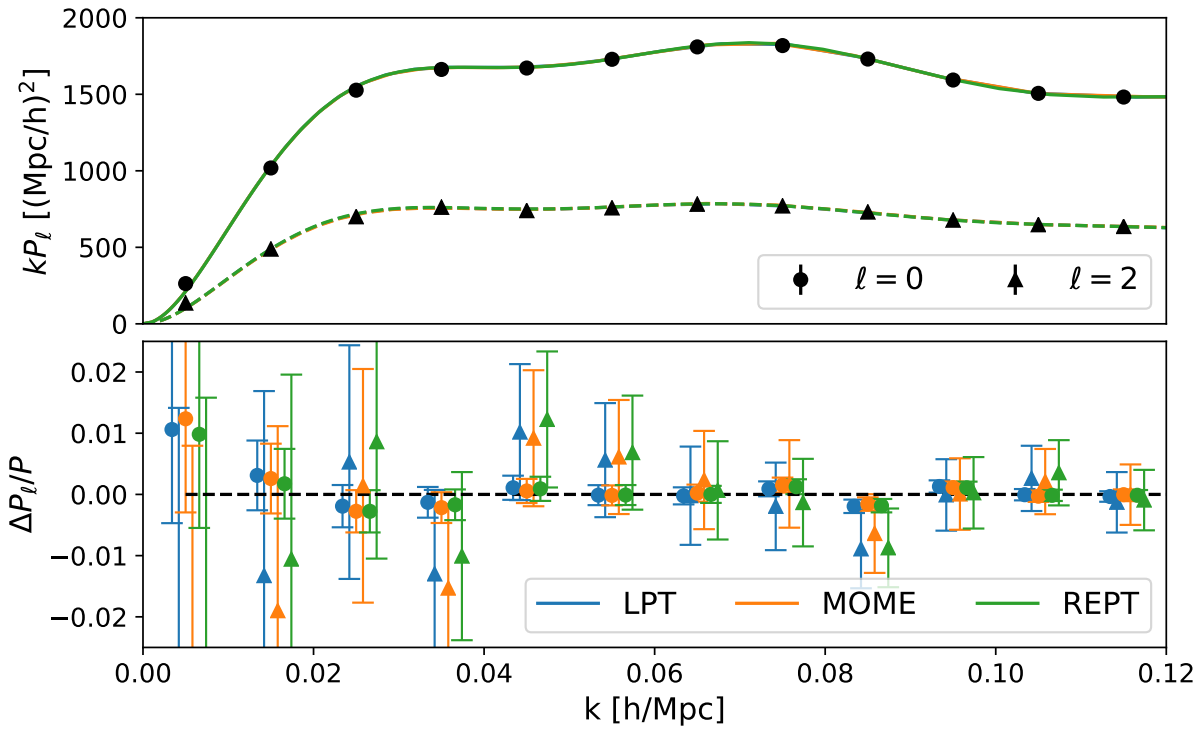

Figure 3.5: Multipoles of the blind challenge power spectrum along with the best fit one-loop LPT, MOME and REPT models. The top panels shows the (unbinned) theory curves along with the data. Both the error bars and theory differences are too small to see except in a few places. The lower panels show the fractional residuals of each (binned) theory curve, with each k and ℓ bin separated by $0.0008\,h\,\mathrm{Mpc}^{-1}$ for clarity of presentation.

themselves. We have repeated the same exercise with the direct LPT model discussed in this work, using the same set of parameters[7]. As we have already participated in the challenge, we now know the true cosmological parameters. However this should not affect the evaluation of our new LPT approach, since the analysis pipeline is the same one we adopted for MOME and REPT and we did not change the model in any way from that described in previous sections in order to participate in the challenge except to use the unblinded values as a seed in the MCMC to more quickly reach the maximum likelihood region. As in our previous submissions, uninformative priors were placed on all of the model parameters.

Figure 3.5 shows the measurements of the multipoles of the power spectrum along with the best fit one-loop LPT, MOME and EPT models. It's worth noticing that since we are also

[7]These are $b_1, b_2, b_s, \alpha_0, \alpha_2, R_h^3, \sigma_2$ in the Lagrangian basis and the equivalent set mapped onto the Eulerian basis. We have dropped the Lagrangian third-order bias because it is expected to be small and somewhat degenerate with other terms, $\alpha_{4,6}$ because we fit only up to the quadrupole and σ_4 because it was not necessary to fit the data at the scales we fit.

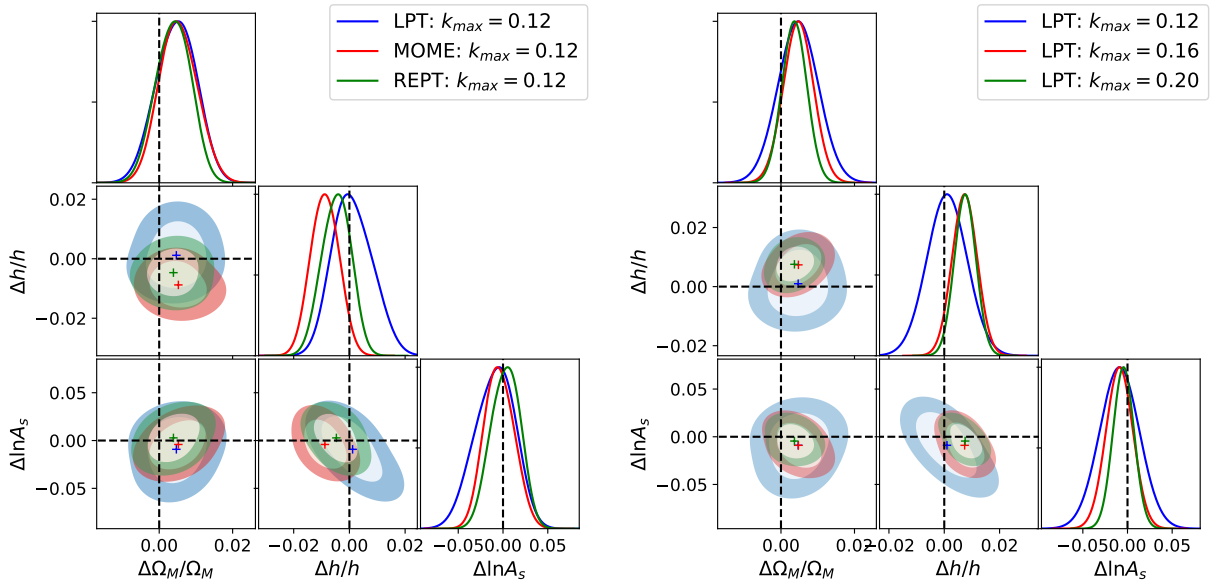

Figure 3.6: Histograms and two-dimensional contours for the three cosmological parameters in the blind challenge. (Left): Comparison of the LPT model in this chapter to our previous submissions using the moment expansion (MOME) and resummed Eulerian perturbation theory (REPT), all at $k_{\rm max} = 0.12\,h\,{\rm Mpc}^{-1}$. The LPT model performs competitively to existing models and indeed slightly improves upon the LPT-based MOME model's constraints on h. (Right): The LPT model constraints using three different scale cuts. All three scale cuts recover the truth on these parameters to within $2\,\sigma$.

fitting for cosmological parameters, compared to the previous section where the linear power spectrum was held fixed and we varied only the bias parameters, the model has to include the Alcock-Paczynski (AP) effect[8] [9, 45]. Since this plot is just for visual comparison, we only show the best fit model with $k_{\rm max} = 0.12\,h\,{\rm Mpc}^{-1}$. These data, produced using a different N-body code, halo finder and HOD prescription at a different redshift than the simulations in §3.5.1, act as an additional test of the three PT models, and indeed the agreement between the models and with the data is remarkable up to the smallest scales included in the fit. All three models have $\chi^2/{\rm dof} \approx 13/(24-10)$, demonstrating good fits compared to their degrees of freedom.

Turning to the cosmological parameters, the left panel of Figure 3.6 shows the $1\,\sigma$ and $2\,\sigma$ constraints obtained by fitting the monopole and quadrupole of $P(k)$ up to $k_{\rm max} = 0.12\,h\,{\rm Mpc}^{-1}$ using our LPT, MOME and REPT models. This was the scale cut we chose in submitting results using MOME and REPT to the blind challenge, conservatively selected given the unusually low statistical uncertainty of the sample, as well as the main case analyzed in ref. [255]. The LPT model performs slightly better than the other two, providing unbiased

[8]Specifically, we use Equations 42-46 of ref. [45], though without the factors of r_s.

constraints on the three cosmological parameters. In particular the bias in the Hubble constant, h, is reduced in LPT compared to both MOME and REPT. While the difference is less than $2\,\sigma$ and therefore well within the realm of possible statistical fluctuations in the N-body data, the improvement in our Ω_M and h constraints, particularly relative to MOME in which bulk velocities are not fully resummed, suggests that our IR resummation scheme is correctly capturing the effects of large scale modes on both the BAO feature and broadband shape.

The right panel in Figure 3.6 shows the two-dimensional confidence intervals for different choices of $k_{\rm max} = 0.12, 0.16, 0.20\,h\,{\rm Mpc}^{-1}$ for LPT. The constraints are within $2\,\sigma$ of the truth for each scale cut, but at $k_{\rm max} = 0.20\,h\,{\rm Mpc}^{-1}$ the Hubble parameter h has a mean very close to $2\,\sigma$ away from the truth while all parameters are well within $1\,\sigma$ at $0.12\,h\,{\rm Mpc}^{-1}$, suggesting growing systematic bias at higher scale cuts where higher-order corrections are expected to play a more significant role. However, it should be noted that since these error bars are derived from the covariance of the sample itself — within the Gaussian approximation no less — the exhibited errors are well within the realm of statistical possibility and we cannot conclusively determine that any model is biased. These results are summarized in Figure 3.7, which shows the shift between the inferred and true bias parameters as a function of $k_{\rm max}$. The shaded regions indicate $10\times$ the derived standard deviations, i.e. approximately the expected errors for a survey like BOSS, or a redshift slice of $\Delta z = 0.25$ at $z = 0.6$ for DESI. The LPT model presented in this work correctly recovers the underlying cosmology for all the scale cuts shown to well within the expected errors of surveys like BOSS and DESI. We anticipate that the model would perform even better at higher redshift where the degree of non-linearity is smaller. We therefore conclude that, at least for the cosmological parameters probed in the challenge, our LPT model should provide an accurate tool for modeling RSD in upcoming surveys.

3.6 Conclusions

The anisotropic galaxy clustering observed by spectroscopic surveys probes density and velocity fields on large scales, enabling us to test the growth of structure in the quasilinear regime as predicted by General Relativity. In addition, the baryon acoustic oscillations in the galaxy clustering signal provide geometric information that constrain the cosmological expansion history. Perturbation theory is an ab initio approach with clear physical assumptions, and it is therefore the preferred tool for a precise and rigorous mapping between cosmological parameters and the observed clustering signal, in the quest for a better understanding of the cosmological model and in the search for new physics.

The main purpose of this work was to further develop the modeling of the redshift-space two-point function within Lagrangian perturbation theory. Two critical aspects of any perturbation-theory model of the power spectrum or correlation function are the treatment of the nonlinear damping of the BAO signal due to large scale motions of galaxies and the inclusion of redshift-space distortions due to a degeneracy between the observed line-of-

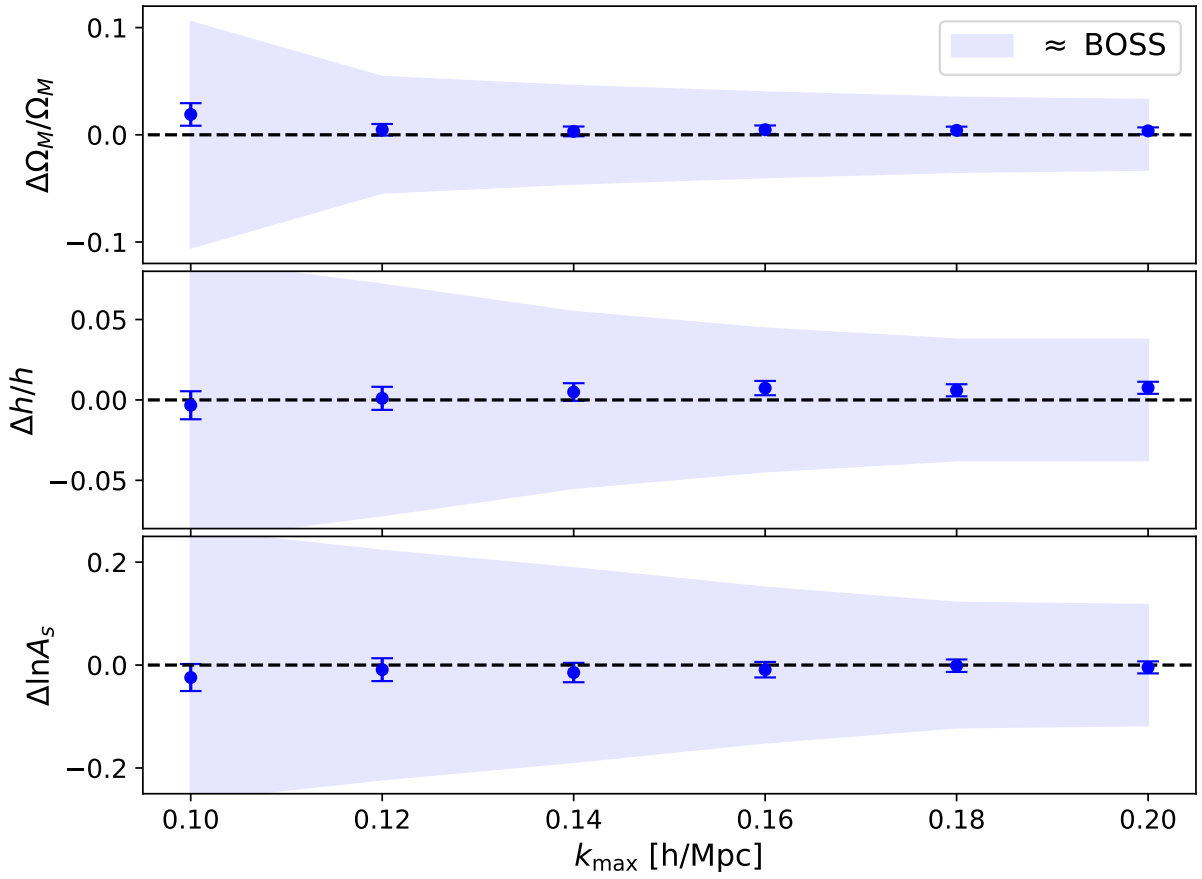

Figure 3.7: Parameter constraints using the LPT model for the blind challenge as a function of scale cut $k_{\rm max}$. The shaded blue region show errors scaled to a survey of $10\times$ less volume, i.e. BOSS or a $\Delta z = 0.1$ slice of DESI at $z = 1.2$. All constraints shown are within $2\,\sigma$ of the truth, and within $1\,\sigma$ when $k_{\rm max} \leq 0.14\,h\,{\rm Mpc}^{-1}$, well within error bars expected for future surveys as well as the realm of possible statistical fluctuations for this simulated sample.

sight positions and peculiar velocities of galaxies. By expanding directly in displacements, Lagrangian perturbation theory naturally treats both phenomena within the same framework without relying on the wiggle-no-wiggle splitting procedure to damp the BAO oscillations. In particular, LPT exponentiates linear, or Zeldovich, displacements via the cumulant theorem, thereby resumming the long-wavelength (IR) modes primarily responsible for nonlinear BAO damping.

In this work, we extend the numerical techniques developed in refs. [398, 74] for the Zeldovich approximation to calculate the one-loop LPT power spectrum of biased tracers with both bulk displacements and velocities resummed. This is in contrast to previous efforts to model redshift-space distortions within effective LPT that focused on predicting velocity statistics for which only the displacements were exponentiated[9]. In Sections 3.2 and 3.3, we outlined the effective formalism developed in those works and used them to write down the redshift-space power spectrum including third-order biasing, counterterms and stochastic contributions, of which the latter two in part play the role of "finger-of-god" terms in traditional RSD models. Then, in Section 3.4, we developed the required numerical framework for the implementation of the model. We have publically released our implementation of Method II as part of the `velocileptors` code.[10] Additional details of these calculations can be found in Appendices C.2 and C.3.

Finally, we compare the LPT model developed in this work to N-body data and previous models in Section 3.5. First, we fit the power spectrum of a halo sample drawn from a set of N-body simulations at $z = 0.8$ with masses $12.5 < \log(M/M_\odot) < 13.0$ assuming Gaussian covariances using our model in Figure 3.2, finding excellent agreement in both the wedges and first three multipoles for a consistent set of bias and effective parameters. Our model has an extra degree of freedom in the IR cutoff $k_{\rm IR}$, which dictates the wavelength beyond which displacement modes are resummed. In ref. [74] it was shown that the higher-order velocity statistics that enter into redshift-space distortions have broadband shapes that are especially sensitive to this choice, and indeed we find that a choice of $k_{\rm IR} = 0.2\,h\,{\rm Mpc}^{-1}$, which lies between the broadband predictions of full-expanded LPT and EPT, gives the best match to the hexadecapole; this choice is explored further in Appendix C.1, where we also show (Fig. C.3) that the configuration-space anisotropic BAO feature is remarkably robust to this hyperparameter.

We then compare the performance of our LPT model with other existing effective-theory models. In Figure 3.3, we compare the aforementioned power spectrum predictions to the Lagrangian moment expansion (MOME) and resummed Eulerian perturbation theory, finding that all three can fit the data to within the expected systematic error of the simulations. Similar results for the configuration-space multipoles are shown in Figure 3.4, where we also compare to the Lagrangian Gaussian streaming model. As a last numerical test we checked whether the full one-loop LPT model presented in this work can recover unbiased

[9]Earlier work, e.g. ref. [58], performed a similar calculation as the one here for the correlation function only, but exponentiated the modes coming from the one-loop contributions as well.

[10]https://github.com/sfschen/velocileptors

cosmological parameters in a data analysis challenge using a different N-body code, halo finder, halo occupation distribution and redshift. We find that LPT performs better than MOME and REPT at the reference scale cut chosen in ref. [255], and is able to recover the true cosmology with negligible biases up to $k_{\rm max} = 0.2\,h\,{\rm Mpc}^{-1}$ in a volume approximately one hundred times that of DESI or Euclid at the same redshift. Results of this test are given in Figure 3.6.

Let us conclude by noting some possible extensions of our model and numerical implementation. There has been considerable recent interest in extending the bias expansion of galaxies to include anisotropic selection effects and, indeed, the redshift-space galaxy density can be decomposed into a generalized expansion of operators with LOS symmetry [176, 110, 146, 259]. Since the angular dependencies of these operators will in general involve only tensor products of $\hat{k}$, $\hat{n}$ and $\hat{q}$ their 2-point functions (with IR displacements resummed) should follow straightforwardly from our calculations. Our calculations should also be straightforwardly extendable to modeling the reconstructed galaxy power spectrum at one-loop order, especially the "Rec-Sym" scheme [78] which features an identical structure, with the only difference being a larger set of terms involved. Concerning extensions of the ΛCDM model, perhaps the simplest one to implement is massive neutrino cosmologies. It is well known that halos and galaxies are biased tracers of the dark matter and baryon fluids only [391, 65, 66, 393, 222, 252, 136], which implies the bias expansion presented in Section 3.2 will still be valid with the trivial replacement of the total matter field with the dark matter plus baryon one. Extra care should be taken with RSD since the growth rate is now scale dependent and Equation 3.4 is no longer valid [18] (and similarly in modified gravity theories [19, 383]). However given the smallness of neutrino masses, this complication is usually neglected when evaluating loop integrals. We intend to return to these, admittedly more involved, calculations in future work.

3.7 Acknowledgements

We thank Jahmour Givans, Marko Simonović and the anonymous referee for helping us clarify various points in the draft. S.C. is supported by the National Science Foundation Graduate Research Fellowship (Grant No. DGE 1106400) and by the UC Berkeley Theoretical Astrophysics Center Astronomy and Astrophysics Graduate Fellowship. M.W. is supported by the U.S. Department of Energy and the NSF. Z.V. is supported by the Kavli Foundation. This research has made use of NASA's Astrophysics Data System and the arXiv preprint server. This research used resources of the National Energy Research Scientific Computing Center (NERSC), a U.S. Department of Energy Office of Science User Facility operated under Contract No. DE-AC02-05CH11231.

Chapter 4

Reconstruction in the Zeldovich Approximation

This chapter was originally published as

> Shi-Fan Chen, Zvonimir Vlah, and Martin White. "The reconstructed power spectrum in the Zeldovich approximation". In: *JCAP* 2019.9, 017 (Sept. 2019), p. 017. DOI: 10.1088/1475-7516/2019/09/017. arXiv: 1907.00043 [astro-ph.CO]

In the previous two chapters we developed perturbation theory models of redshift-space distortions and showed that they were up to the task to analyze data at the precision required by upcoming spectroscopic surveys. In this chapter we turn our attention to another major goal of these surveys: the measurement of the baryon acoustic oscillations. In particular, we will develop a model for the 2-point function in redshift space after reconstruction. As we have already discussed, nonlinear structure formation dampens the BAO peak due to long displacements; density reconstruction sharpens the baryon acoustic oscillations signal by undoing some of the smoothing incurred by nonlinear structure formation (Fig. 4.1)).

We present an analytical model for reconstruction based on the Zeldovich approximation, which for the first time includes a complete set of counterterms and bias terms up to quadratic order and can fit real and redshift-space data pre- and post-reconstruction data in both Fourier and configuration space over a wide range of scales. We compare our model to n-body data at $z = 0$ from the `DarkSky` simulation [350], finding sub-percent agreement in both real space and in the redshift-space power spectrum monopole out to $k = 0.4\,h\,\mathrm{Mpc}^{-1}$, and out to $k = 0.2\,h\,\mathrm{Mpc}^{-1}$ in the quadrupole, with comparable agreement in configuration space. We compare our model with several popular existing alternatives, updating existing theoretical results for exponential damping in wiggle/no-wiggle splits of the BAO signal and discuss the usually-ignored effect of higher bias contributions on the reconstructed signal. In the appendices, we re-derive the former within our formalism, present exploratory results on higher-order corrections due to nonlinearities inherent to reconstruction, and present numerical techniques with which to calculate the redshift-space power spectrum of biased tracers within the Zeldovich approximation.

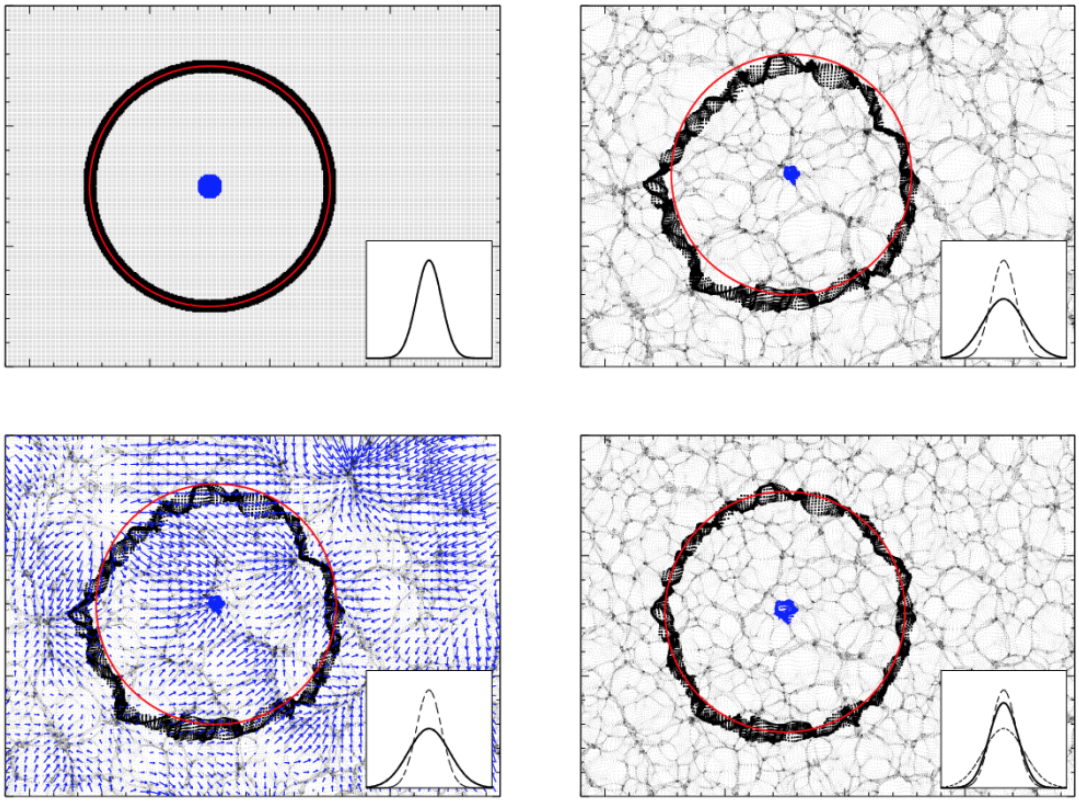

Figure 4.1: Schematic for reconstruction from ref. [267]. The top two panels show how displacments on scales smaller than $r_{\rm BAO}$ smear out the BAO feature (black ring). In the bottom two panels, the galaxy density field is used to reconstruct the large-scale Zeldovich displacement (blue arrows) which is then removed from the observed galaxy positions by shifting them in the negative direction. Insets show the width of the particle distribution at each step.

4.1 Introduction

Density field reconstruction [122] is a means of improving the determination of the distance-redshift relation using baryon acoustic oscillations (BAO) [410]. The BAO method is a "standard ruler" test which seeks to measure the scale of a feature in the 2-point function whose physical size is known. Comparison with the observed size of this feature gives the angular diameter distance and Hubble parameter as a function of redshift. While the large size of the BAO feature (100 Mpc) makes it relatively immune to systematic effects, nonlinear evolution erases the oscillations on small scales, or broadens the peak in the correlation function, and reduces the accuracy with which the scale can be measured [238, 336, 413, 337, 121]. However much of the peak broadening comes from motions sourced by very long wavelength fluctuations [121] which are well measured by surveys aiming to measure BAO.

This insight led ref. [122] to propose that density-field reconstruction could be applied to regain much of the information lost to non-linearities. It has been used in all recent BAO surveys to improve their constraints (e.g. see ref. [7] and references therein).

BAO reconstruction has been studied both numerically [424, 389, 388] and analytically [122, 266, 257, 368, 414, 321, 338, 87, 318, 171, 429, 132, 245, 155, 112, 339]. Our work builds upon these analytic calculations. Where earlier work made simplifications aimed at highlighting important physical effects, neglected complications such as redshift-space distortions, applied heuristics or otherwise simplified the calculations for explanatory effect, we aim to produce a consistent dynamical theory which can be compared directly to upcoming observational data. Hence we generalize these calculations to also consider the power spectrum and extend the model to include the complete set of quadratic bias terms. To our knowledge this is the first dynamical model with a full bias scheme that can produce consistent real and redshift-space results in both Fourier and configuration space, allowing it to be used for consistent fitting of upcoming data.

There has been significant theoretical work on reconstruction since the first algorithm [122] was suggested. Most recently, a variety of iterative or alternative reconstruction approaches have been developed [368, 429, 318, 132, 245, 155]. Though our calculations give some insights into these methods, for near-future experiments and for BAO scales these iterative methods do not lead to significant improvements and so we defer consideration of these more complex algorithms to future work.

The outline of this chapter is as follows. Section 4.2 reviews the formalism of Lagrangian perturbation theory within which we work. Section 4.3 describes the reconstruction algorithm we seek to model, while Section 4.4 gives our results in Fourier space, comparing to the configuration-space results where appropriate (Section 4.5). We discuss alternative statistics in Section 4.6. To assess the range of validity of our models we compare to N-body simulations in Section 4.7. A comparison with earlier work is given in Section 4.8 before we conclude in Section 4.9. Some technical details are elaborated in the appendices.

4.2 Lagrangian Perturbation theory

The Lagrangian framework [431, 54, 250, 177, 39, 231, 229, 58] describes cosmological structure formation by tracking the displacements $\mathbf{\Psi}(\mathbf{q})$ of infinitesimal parcels of the matter fluid from their initial (Lagrangian) positions $\mathbf{q}$. In this picture the present day matter over- and underdensities are a result of the clustering of the displaced Eulerian positions $\mathbf{x}(\mathbf{q},\tau) = \mathbf{q} + \mathbf{\Psi}(\mathbf{q},\tau)$. The displacements follow the equation of motion $\mathbf{\Psi}''(\mathbf{q}) + \mathcal{H}\mathbf{\Psi}'(\mathbf{q}) = -\nabla_x \Phi(\mathbf{x})$, where $\Phi(\mathbf{x})$ is the gravitational potential which is in turn sourced by the clustered matter fluid via Poisson's equation $\nabla^2\Phi(\mathbf{x},\tau) = \frac{3}{2}\Omega_m(\tau)\mathcal{H}^2(\tau)\delta(\mathbf{x},\tau)$ with τ the conformal time. This set of equations can be solved perturbatively in terms of the linear overdensity, δ_0, and the first order solution is given by $\mathbf{\Psi} = -D(\tau)\nabla\nabla^{-2}\delta_0$, where $D(\tau)$ is the linear growth factor [431].

The Lagrangian picture treats tracer bias and advection separately. Given a biased tracer, a, with initial overdensity $F^a(\mathbf{q}) = F^a\left[\partial^2\Phi(\mathbf{q}), ...\right]$, the time-evolved tracer overdensity at conformal time τ is given by number conservation as [229]

$$1 + \delta^a(\mathbf{x}, \tau) = \int d^3\mathbf{q}\ F^a(\mathbf{q})\ \delta_D\left(\mathbf{x} - \mathbf{q} - \mathbf{\Psi}(\mathbf{q}, \tau)\right) \quad . \tag{4.1}$$

The cross power spectrum between two biased tracer populations a and b is then

$$P^{ab}(k) = \int d^3\mathbf{q}\ e^{i\mathbf{k}\cdot\mathbf{q}}\ \langle F^a(\mathbf{q}_2)F^b(\mathbf{q}_1)\ e^{i\mathbf{k}\cdot\Delta^{ab}}\rangle_{q=|q_2-q_1|} \quad , \quad \Delta^{ab} = \mathbf{\Psi}^a(\mathbf{q}_2) - \mathbf{\Psi}^b(\mathbf{q}_1), \tag{4.2}$$

where we have used that the integrated expectation value can only depend on $\mathbf{q} = \mathbf{q}_2 - \mathbf{q}_1$, due to the translation invariance of the underlying theory. The bias functionals, $F^{a,b}$, can be Taylor expanded in terms of bias coefficients

$$F^a(\mathbf{q}) = 1 + b_1^a\delta_{\rm lin}(\mathbf{q}) + \frac{1}{2}b_2^a\left(\delta_{\rm lin}(\mathbf{q})^2 - \langle\delta_{\rm lin}^2\rangle\right) + b_s^a\left(s^2(\mathbf{q}) - \langle s^2\rangle\right) + b_{\nabla^2}^a\nabla_q^2\delta_{\rm lin}(\mathbf{q}) + \cdots, \tag{4.3}$$

where $s^2 = s_{{\rm lin},ij}s_{{\rm lin},ij}$ is the square of the shear field, i.e. the traceless part of $\partial\partial\Phi$. Following ref. [396], we also consider contributions from a "derivative bias" b_{∇^2}, i.e. corrections to the bias expansion at scales close to the halo radius R_h proportional to $\nabla^2\delta_0$; such contributions will, however, be essentially degenerate with counterterms renormalizing nonlinearities in the Zeldovich power spectrum and we will therefore not enumerate them separately in the rest of this work unless otherwise stated.

In this work our focus will be on modelling reconstruction within the Zeldovich approximation [431, 415], which keeps only the linear order term in the dynamics of $\mathbf{\Psi}$ but re-sums the effects of the displacement to all orders in a Galilean-invariant manner (this is true for reconstruction also if we take it to mean that all displacements transform the same way). This is specifically accomplished by evaluating the exponential in Equation 4.2 via the cumulant expansion, and evaluating the bias expansion using functional derivatives (see e.g. refs. [229, 58, 396]). Following standard techniques, as outlined in the references above, the resulting expression for the cross spectrum is

$$\begin{aligned} P^{ab}(k) = \int d^3\mathbf{q}\ e^{i\mathbf{k}\cdot\mathbf{q}}\ e^{-\frac{1}{2}k_ik_jA_{ij}^{ab}}\ \Big[&1 + \alpha_0k^2 + ib_1^b\mathbf{k}\cdot U^a + ib_1^a\mathbf{k}\cdot U^a + b_1^ab_1^b\xi_L + \frac{1}{2}b_2^ab_2^b\xi_L^2 \\ &- \frac{1}{2}k_ik_j\ (b_2^bU_i^aU_j^a + b_2^aU_i^bU_j^b + 2b_1^ab_1^bU_i^aU_j^b) + ik_i(b_2^bb_1^aU_i^a + b_1^bb_2^aU_i^b)\ \xi_L \\ &- \frac{1}{2}k_ik_j(b_s^a\Upsilon_{ij}^b + b_s^a\Upsilon_{ij}^b) + ik_i(b_1^ab_s^bV_i^{ab} + b_1^bb_s^aV_i^{ba}) \\ &+ \frac{1}{2}(b_2^ab_s^b + b_2^bb_s^a)\chi^{12} + b_s^ab_s^b\zeta + \cdots\Big] \end{aligned} \tag{4.4}$$

where we have defined[1] the quadratic two point functions

$$A_{ij}^{ab} = \langle\Delta_i^{ab}\Delta_j^{ab}\rangle,\ U_i^b = \langle\Delta_i^{ab}\delta_{\rm lin}(\mathbf{q}_2)\rangle,\ \xi_L = \langle\delta_{\rm lin}(\mathbf{q}_2)\delta_{\rm lin}(\mathbf{q}_1)\rangle \tag{4.5}$$

[1] These are generalizations of the similar auto-spectrum quantities defined in refs. [58, 415, 396].

and shear correlators

$$\zeta = \langle s^2(\mathbf{q}_2)s^2(\mathbf{q}_1)\rangle,\ \Upsilon^b_{ij} = \langle \Delta^{ab}_i \Delta^{ab}_j s^2(\mathbf{q}_2)\rangle,\ V^{ab}_i = \langle \Delta^{ab}_i \delta_0(\mathbf{q}_2) s^2(\mathbf{q}_1)\rangle,\ \chi^{12} = \langle \delta_0^2(\mathbf{q}_1) s^2(\mathbf{q}_2)\rangle. \tag{4.6}$$

Unless otherwise specified we will drop the superscripts and subscripts lin in this paper since we will deal only in the Zeldovich approximation. Note that in the above calculations we have, without loss of generality, associated tracers a and b with Lagrangian positions $\mathbf{q}_2$ and $\mathbf{q}_1$, respectively. The quantities in Equation 4.4 with a and b swapped can also be calculated by swapping the positions $\mathbf{q}_1 \leftrightarrow \mathbf{q}_2$. As an example, $U^b = -\langle \mathbf{\Psi}^b(\mathbf{q}_1)\delta_0(\mathbf{q}_2)\rangle$ is the two-point function between the displacement of tracer b and the matter overdensity. The vector and tensor two point functions defined above can be decomposed via rotational symmetry into scalar components, e.g. $A_{ij} = X(q)\delta_{ij} + Y(q)\hat{q}_i\hat{q}_j$ and $U_i = U(q)\hat{q}_i$. Formulae for these functions, expressed as Hankel transforms of power spectra, are given in Appendix D.1. Finally, we include the contribution $\alpha_0 k^2$ in the square brackets of Equation 4.4 as the lowest-order counterterm renormalizing sensitivities to small-scale power in A_{ij} — in practice this simply modifies the matter contribution $P_{\rm Zel}(k)$ ($\propto 1$ in the square brackets) to $(1+\alpha_0 k^2)P_{\rm Zel}(k)$ (see e.g. refs. [399, 290]). Each term in Equation 4.4 can be evaluated as Hankel transforms (see e.g. ref. [396]) using the identities given at the end of [399], which we carry out using the `mcfit` package[2].

The Lagrangian formalism allows a straightforward translation between real and redshift space via a mapping of the Lagrangian displacements. In particular, assuming the plane-parallel approximation[3] and working in the Zeldovich approximation, quantities in redshift space are given simply by substituting $\mathbf{\Psi}_i \to \mathbf{\Psi}^R_i = R_{ij}\mathbf{\Psi}_j$ [229]. Here $R_{ij} = \delta_{ij} + f\hat{n}_i\hat{n}_j$, where $\hat{n}$ denotes the line-of-sight direction and $f = d\ln D/d\ln a$ is the linear-theory growth rate. To lowest order, transforming into redshift space requires the inclusion of a second counterterm dependent on the line-of-sight angle $\mu = \hat{k}\cdot\hat{n}$. We can see this explicitly, for example, in the UV-sensitive zero-lag term in A_{ij}, which gains an angular dependence

$$k_i k_j \langle (\mathbf{\Psi}_i + \hat{n}_i\hat{n}_l\dot{\mathbf{\Psi}}_l)(\mathbf{\Psi}_j + \hat{n}_j\hat{n}_m\dot{\mathbf{\Psi}}_m)\rangle \equiv k^2(X(0) + (2\dot{X}(0) + \ddot{X}(0))\mu^2), \tag{4.7}$$

where $\dot{\mathbf{\Psi}}$ is the velocity in Hubble units equal to $f\mathbf{\Psi}$ in the Zeldovich approximation[4]; roughly speaking, we need one angle-independent counterterm $\alpha_0 k^2$ to absorb the UV dependence of $X(0)$ and another $\alpha_2 k^2\mu^2$ to absorb the UV dependence of the velocities. The complete set of counterterms in redshift space thus makes a contribution of the form $(\alpha_0 + \alpha_2\mu^2)k^2 P_{ZA}(\mathbf{k})$; since $P_{ZA}(\mathbf{k})$ is equal to $(1+f\mu^2)^2 P_L(k)$ to linear order, an equivalent viewpoint—which we will adopt in this work— is to have constant counterterms $\bar{\alpha}_0 k^2$ and $\bar{\alpha}_2 k^2$ for the monopole and quadrupole, respectively, where the barred counterterms are linear combinations of the unbarred quantities.

[2] https://github.com/eelregit/mcfit

[3] This should be an excellent approximation on BAO scales [63], but if necessary the formalism can be modified to include "wide-angle" effects [64].

[4] See refs. [405, 396] for a more detailed exposition of the "dot notation."

4.3 Reconstruction algorithm

In this section we describe two possible methods for reconstruction in redshift space, both built around the Zeldovich approximation. The standard procedure for reconstruction was developed in ref. [122] and involves displacing both observed galaxies and a spatially uniform distribution by a calculated shift field, χ, then taking the relative density contrast between the two sets of particles as the reconstructed density field. For a suitably chosen χ, this can reduce the effect of large scale (IR) bulk flows that "blur" the BAO feature. However there is no consensus in the community on the correct procedure for handling redshift-space distortions: the implementation in ref. [267] chose to multiply χ by $1 + f$ in the line-of-sight direction for δ_d but not for δ_s. This 'undoes' the supercluster infall effect [196] and reduces the $\ell > 0$ moments of the 2-point function on large scales. Ref. [414] suggested a symmetric treatment of δ_d and δ_s, which recovers linear theory on large scales. This is more natural from the point of view of perturbation theory and better behaved near the boundaries, but is less often implemented on data. A number of other choices were explored in ref. [338] but in this work we will restrict our attention to the two methods described above.

The reconstruction procedure consists of the following steps [122]:

1. Smooth the observed galaxy density field δ_g with a kernel $\mathcal{S}$ to filter out small scale (high k) modes, which are difficult to model. We use a Gaussian smoothing of scale R_s, specifically $\mathcal{S}(k) = \exp[-(kR_s)^2/2]$, though none of our analytic results will depend specifically on this choice. For galaxy surveys Gaussian smoothing has been universally adopted (though with different conventions for R_s) but in other contexts it may be advantageous to implement a Wiener filter instead (e.g. ref. [87]).

2. Compute the shift, χ, by dividing the smoothed galaxy density field by a bias factor b and linear RSD factor [196] and then take the inverse gradient. Assuming linear theory with scale-independent bias and supercluster infall holds on large scales, the calculated shift field should approximate the negative smoothed Zeldovich displacement. In a simulation with a periodic box, these first two steps can be implemented using FFTs as

$$\chi_{\mathbf{k}} = -\frac{i\mathbf{k}}{k^2}\mathcal{S}(k)\left(\frac{\delta_g(\mathbf{k})}{b + f\mu^2}\right) \approx -\mathcal{S}(k)\mathbf{\Psi}^{(1)}(\mathbf{k}) \tag{4.8}$$

   where the bias factor is related to the Lagrangian first-order bias by $b = 1 + b_1$ and we have defined the line-of-sight angle $\mu = \hat{n} \cdot \hat{k}$. For non-periodic data the relevant differential equation can be solved by multigrid[5] or by linear algebra techniques [267] or iteratively using FFTs [55].

3. Move the galaxies by $\chi_d = \mathbf{R}\chi$ and compute the "displaced" density field, δ_d.

4. Shift an initially spatially uniform distribution of particles by

[5] https://github.com/martinjameswhite/recon_code

- **Rec-Sym**: $\chi_s = \mathbf{R}\chi$, i.e. the same amount as the observed galaxies, or,
- **Rec-Iso**: The un-redshifted $\chi_s = \chi$.

to form the "shifted" density field, δ_s. Note that we have borrowed the nomenclature of ref. [338] for the latter, which "isotropizes" the reconstructed field on large scales. For the former we use "Rec-Sym" to indicate the symmetry of the treatment of δ_d and δ_s.

5. The reconstructed density field is defined as $\delta_r \equiv \delta_d - \delta_s$ with power spectrum $P_r(k) \propto \langle|\delta_r^2|\rangle$.

Throughout we shall assume that the fiducial cosmology and halo bias are properly known during reconstruction (see e.g. refs. [339, 62] for relaxation of this assumption), and take the approximation in Eq. 4.8 to be exact. For further discussion of this point see refs. [321, 171]. The procedure in real space can be straightforwardly obtained by setting $f = 0$, in which case Rec-Sym and Rec-Iso become equivalent. Taking the limit $\mathcal{S} \to 0$ or $\chi \to 0$ returns the 'raw' spectrum, before reconstruction.

4.4 Reconstructed power spectrum

There has been significant earlier work on modeling density-field reconstruction within perturbation theory [122, 266, 257, 368, 414, 321, 338, 87, 318, 171, 429, 132, 245, 155, 112, 339]. In particular ref. [414] presented a calculation of the configuration-space two-point function (the correlation function) under the assumption of Zeldovich dynamics and that $\chi = -\mathcal{S}\boldsymbol{\Psi}$. In this chapter we generalize that calculation to a more complete bias model (see §4.5), including all terms allowed by symmetries up to quadratic order as well as a proper set of counterterms, and we show how to implement the model in Fourier space. We have explicitly checked that the Hankel transform of our Fourier-space expressions matches the direct configuration-space calculation to 1% in all terms, and we release code which makes consistent predictions for both statistics with a common set of parameters. To our knowledge this is the first calculation which provides self-consistent predictions in both spaces, uses a dynamical rather than a heuristic model, works in redshift space and has a full set of bias and counterterms.

Our focus in this section will be to model the reconstructed power spectrum using Lagrangian perturbation theory in both real and redshift space (the expression for the 'propagator' is given in Appendix D.2 for completeness). Following the algorithm outlined above, the reconstructed power spectrum in real space is given by $P_{\rm recon} = P^{dd} + P^{ss} - 2P^{ds}$.

Within the Lagrangian framework we can write the displaced density field as

$$\begin{aligned} 1+\delta_d(\mathbf{r}) &= \int d^3\mathbf{x}\ (1+\delta(\mathbf{x}))\ \delta_D\left[\mathbf{r}-\mathbf{x}-\chi_d(\mathbf{x})\right] \\ &= \int d^3\mathbf{x} \int d^3\mathbf{q}\ F(\mathbf{q})\ \delta_D\left[\mathbf{x}-\mathbf{q}-\mathbf{\Psi}(\mathbf{q})\right]\ \delta_D\left[\mathbf{r}-\mathbf{x}-\chi_d(\mathbf{x})\right] \\ &= \int d^3\mathbf{q}\ F(\mathbf{q})\ \delta_D\left[\mathbf{r}-\mathbf{q}-\mathbf{\Psi}(\mathbf{q})-\chi_d(\mathbf{q}+\mathbf{\Psi}(\mathbf{q}))\right], \end{aligned} \tag{4.9}$$

where we performed the $\mathbf{x}$ integral using the first δ-function to go from the second to third lines. Importantly while the fluid displacement, $\mathbf{\Psi}$, is evaluated at the Lagrangian position, $\mathbf{q}$, the shift field is evaluated at the shifted Eulerian position, $\mathbf{q}+\mathbf{\Psi}$. The above equalities hold both when the pre-reconstruction coordinate, $\mathbf{x}$, is in real or redshift space, with the implicit substitution of $\mathbf{\Psi} \to \mathbf{R\Psi}$ in the latter case, as long as the appropriate shift field χ_d is chosen. The expression for the shifted density can be similarly derived or found by setting $\mathbf{\Psi}(\mathbf{q}) = 0$ and $\chi_d \to \chi_s$ in the above expression. In Fourier space this translates to

$$\begin{aligned} (2\pi)^3\delta_D(\mathbf{k}) + \delta_d(\mathbf{k}) &= \int d^3\mathbf{q}\ e^{-i\mathbf{k}\cdot\mathbf{q}}\ F(\mathbf{q})\ e^{-i\mathbf{k}\cdot\left[\mathbf{\Psi}(\mathbf{q})+\chi_d(\mathbf{q}+\mathbf{\Psi}(\mathbf{q}))\right]} \\ (2\pi)^3\delta_D(\mathbf{k}) + \delta_s(\mathbf{k}) &= \int d^3\mathbf{q}\ e^{-i\mathbf{k}\cdot\mathbf{q}}\ e^{-i\mathbf{k}\cdot\chi_s(\mathbf{q})}. \end{aligned} \tag{4.10}$$

Below we will make the approximation $\chi(\mathbf{q}+\mathbf{\Psi}) \approx \chi(\mathbf{q})$. The nonlinearities from the Lagrangian-to-Eulerian mapping can be understood as a perturbation series in $\mathbf{\Psi}/R$, where R is the smoothing scale, and we explore their consequences in Appendix D.5 (see also refs. [321, 171] and the discussion in ref. [414]). Within this approximation we can treat the displaced and shifted field as tracers with displacements

$$\mathbf{\Psi}^d = \mathbf{\Psi} + \chi_d, \quad \mathbf{\Psi}^s = \chi_s, \tag{4.11}$$

where the Zeldovich displacements should be understood as being in redshift space for the displaced field and in either redshift or real space for the shifted field depending on the method used. In this picture the "displaced" tracer has the same bias functional as the original galaxies ($F^d \equiv F^g$) while the "shifted" tracer is unbiased ($F^s \equiv 1$). A straightforward consequence of the reconstruction procedure is that, like that of any discrete tracer, the shift field autospectrum will contain an independent shot noise term $P^{ss}_{\rm SN} = 1/n_s$, where n_s is the number density of the uniform random particles. The full shot noise contribution to the reconstructed spectrum is the sum of the galaxy and random particle shot noises.

4.4.1 Real space

In real space both the displaced and shifted fields are moved by the same, smoothed negative Zeldovich displacement, $\chi_d = \chi_s = -S \star \mathbf{\Psi}$, such that in Fourier space

$$\mathbf{\Psi}^d(\mathbf{k}) = [1-\mathcal{S}(k)]\,\mathbf{\Psi}(\mathbf{k}), \quad \mathbf{\Psi}^s(\mathbf{k}) = -\mathcal{S}(k)\mathbf{\Psi}(\mathbf{k}). \tag{4.12}$$

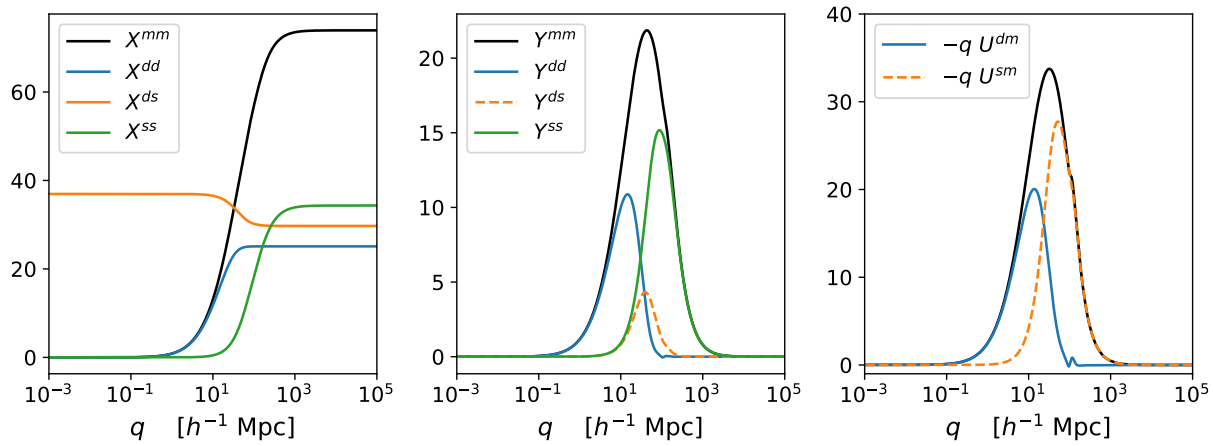

Figure 4.2: Lagrangian space two point functions used to compute reconstructed power spectra. Dashed quantities have been multiplied by an overall negative sign, and reflect that the shifted field is defined to be negatively correlated with the underlying matter field. Roughly speaking, the shifted and displaced correlators reproduce the general trend for the total matter correlators, shown in black, on large and small scales, respectively. An exception is X^{ds}, whose non-vanishing value on small scales reflect that the point values of $\mathbf{\Psi}^d$ and $\mathbf{\Psi}^s$ differ exactly by the Zeldovich displacement. Note also the small but visible features around $q = 100\,h^{-1}\,\mathrm{Mpc}$, i.e. the BAO scale.

and the auto- and cross-spectra can be calculated using Equation 4.4 and the correlators in Appendix D.1, using linear theory spectra

$$P_L^{dd}(k) = [1 - \mathcal{S}(k)]^2\, P_L(k), \quad P_L^{ds}(k) = -\mathcal{S}(k)\,[1 - \mathcal{S}(k)]\, P_L(k), \quad P_L^{ss}(k) = \mathcal{S}(k)^2 P_L(k) \tag{4.13}$$

as well as tracer-matter power spectra

$$P_L^{dm}(k) = [1 - \mathcal{S}(k)]\, P_L(k) \quad , \quad P_L^{sm}(k) = -\mathcal{S}(k) P_L(k). \tag{4.14}$$

Note that the shifted field is negatively correlated with both the matter and displaced fields by-construction, since the random particles are displaced in the opposite direction of the (smoothed) Zeldovich displacement.

The Lagrangian space two-point correlation functions required to calculate the pre- and post-reconstruction power spectra, normalized to their present-day values, are shown in Figure 4.2. For simplicity we have excluded the shear correlators and refer readers to Appendix D.1 for further details. The components X and Y describe correlation functions of two displacements, while the U's involve those with only one displacement, such that the former are Hankel transforms of the linear tracer-tracer spectra, while the latter involve the linear tracer-matter spectra. As expected, the Y's and U's for the displaced and shifted fields contain the behavior of the full matter contribution and small and large scales, respectively, and cross correlations between the shifted field and the displaced or matter fields is negative.

The $X(q)$ components however, especially the cross-correlation X^{ds}, display more subtle behavior. In particular, we have

$$A_{ij}^{ds}(\mathbf{q}) \stackrel{q\to 0}{=} \langle \mathbf{\Psi}_i^d \mathbf{\Psi}_j^d \rangle + \langle \mathbf{\Psi}_i^s \mathbf{\Psi}_j^s \rangle - 2\langle \mathbf{\Psi}_i^d \mathbf{\Psi}_j^s \rangle \equiv \Sigma^2 \delta_{ij}, \tag{4.15}$$

such that $X^{ds}(q) \to \Sigma^2$ as $q \to 0$. This is because, when evaluated at the same point, $\mathbf{\Psi}^d - \mathbf{\Psi}^s = \mathbf{\Psi}$, i.e. the difference between the displaced the shifted displacements is none other than the original Zeldovich displacement. This in turn implies that the cross spectrum is damped at small scales $\propto \exp[-k^2\Sigma^2/2]$ due to the nonzero displacement between the displaced and shifted fields. Similar behavior is seen in the evaluation of unequal-time correlation functions [83] and the baryon-cold dark matter cross-correlation [217, 70], though the physical mechanisms are of course different. At large scales, we similarly have

$$A_{ij}^{ds}(\mathbf{q}) \stackrel{q\to\infty}{=} \langle \mathbf{\Psi}_i^d \mathbf{\Psi}_j^d \rangle + \langle \mathbf{\Psi}_i^s \mathbf{\Psi}_j^s \rangle \equiv \Big(\Sigma_{dd}^2 + \Sigma_{ss}^2\Big)\delta_{ij}, \tag{4.16}$$

such that X^{ds} asymptotes to the average of X^{dd} and X^{ss} at large separations. For completeness, we give explicit expressions for the displaced and shifted X^{ab} here:

$$\begin{aligned}
X^{dd}(q) &= \frac{2}{3}\int \frac{dk}{2\pi^2}\Big[\,1 - \Big(j_0(kq) + j_2(kq)\Big)\Big]\,\Big(1-\mathcal{S}(k)\Big)^2 P_L(k) \\
X^{ds}(q) &= \frac{2}{3}\int \frac{dk}{2\pi^2}\Big[\,\frac{1}{2}\Big((1-\mathcal{S}(k))^2 + \mathcal{S}(k)^2\Big) + \mathcal{S}(k)\Big(1-\mathcal{S}(k)\Big)\Big(j_0(kq) + j_2(kq)\Big)\Big]\,P_L(k) \\
X^{ss}(q) &= \frac{2}{3}\int \frac{dk}{2\pi^2}\Big[\,1 - \Big(j_0(kq) + j_2(kq)\Big)\Big]\,\mathcal{S}^2(k) P_L(k).
\end{aligned} \tag{4.17}$$

The corresponding expressions for Y^{ab} can be directly obtained by calculating -3 times the j_2 components. As we shall discuss further in Section 4.8, the signs for the Bessel function coefficients in our expression for X^{ds} differ from those in ref. [112]. We note also, as has been emphasized before [266], each of the three contributions to $P_{\rm recon}$ has a different damping factor which can only be roughly approximated by a single Gaussian term.

The lowest-order bias terms in the reconstructed real-space power spectrum at $z = 0$ are shown Figure 4.3. The pure-matter piece (i.e. the "1" in Equation 4.4) is the only term that includes contributions from all three combinations of d and s, while the b_1^2 piece consists of only the dd contribution. While each piece individually differs from the linear power spectrum, compared to the pre-reconstruction power spectrum, the Zeldovich approximation predicts that the post-reconstruction power spectrum largely recovers the oscillatory features in the linear spectrum, as seen in the lower panels of Figure 4.3. We note that the structure of the breakdown into P^{dd}, P^{ds} and P^{ss} shown in Figure 4.3 proceeds similarly in the higher-order bias contributions: bias terms like b_1^2, that are products of two bias parameters (e.g. $b_1 b_2, b_2 b_s$, ...), do not involve any displacements ($\mathbf{\Psi}$) and can thus only enter in the autospectrum of the biased "d" tracer P^{dd}, while those like b_1 that involve only one bias parameter (e.g. b_2, b_s) involve two-point functions with one displacement contracted and thus contribute to the cross

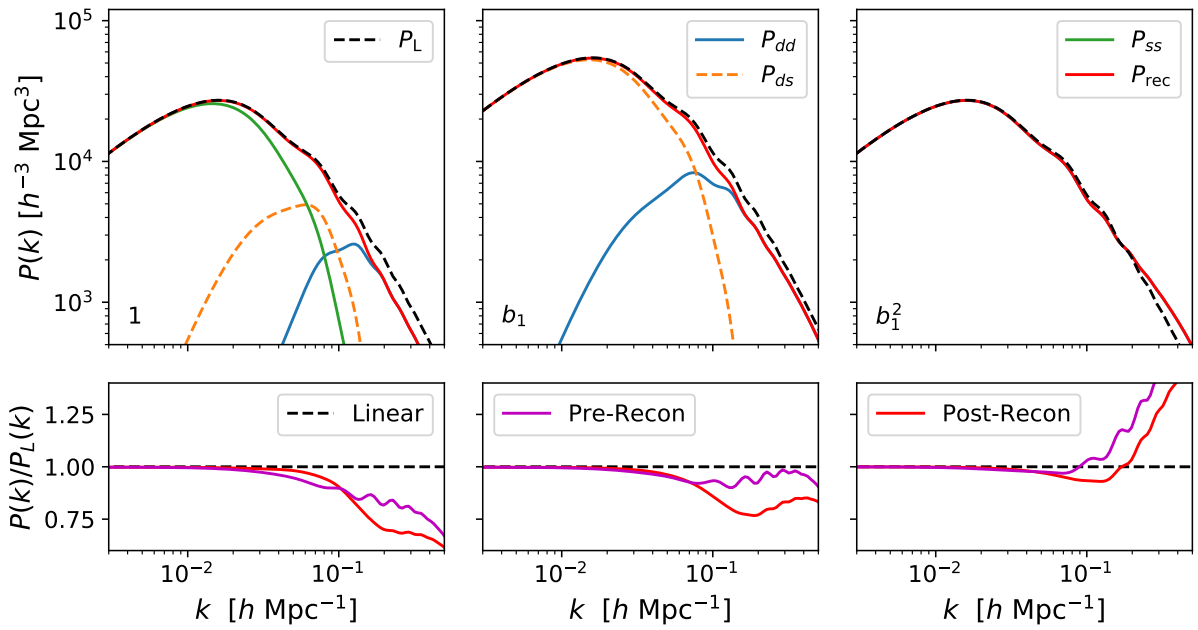

Figure 4.3: (Top) Real-space power spectra contributions, displaced-displaced, displaced-shifted and shifted-shifted, for the lowest order bias terms 1, b_1, b_1^2, and their sum, compared to linear theory at $z = 0$. The pure matter piece is the only term that receives contributions from all three combinations of d and s, and the b_1^2 term consists only of the dd contribution. All three bias terms tend to linear theory on large scales but exhibit somewhat different broadband behavior at high k. (Bottom) The ratio of the above bias terms with the linear theory power spectrum, compared with the pre-reconstruction Zeldovich power spectrum. While both the pre- and post-reconstruction Zeldovich spectra differ with the linear spectrum in the broadband at small scales, the Zeldovich approximation predicts that the oscillatory features in the reconstructed spectrum are almost identical to those in the linear spectrum, such that the wiggles are almost completely normalized out for the reconstructed spectrum.

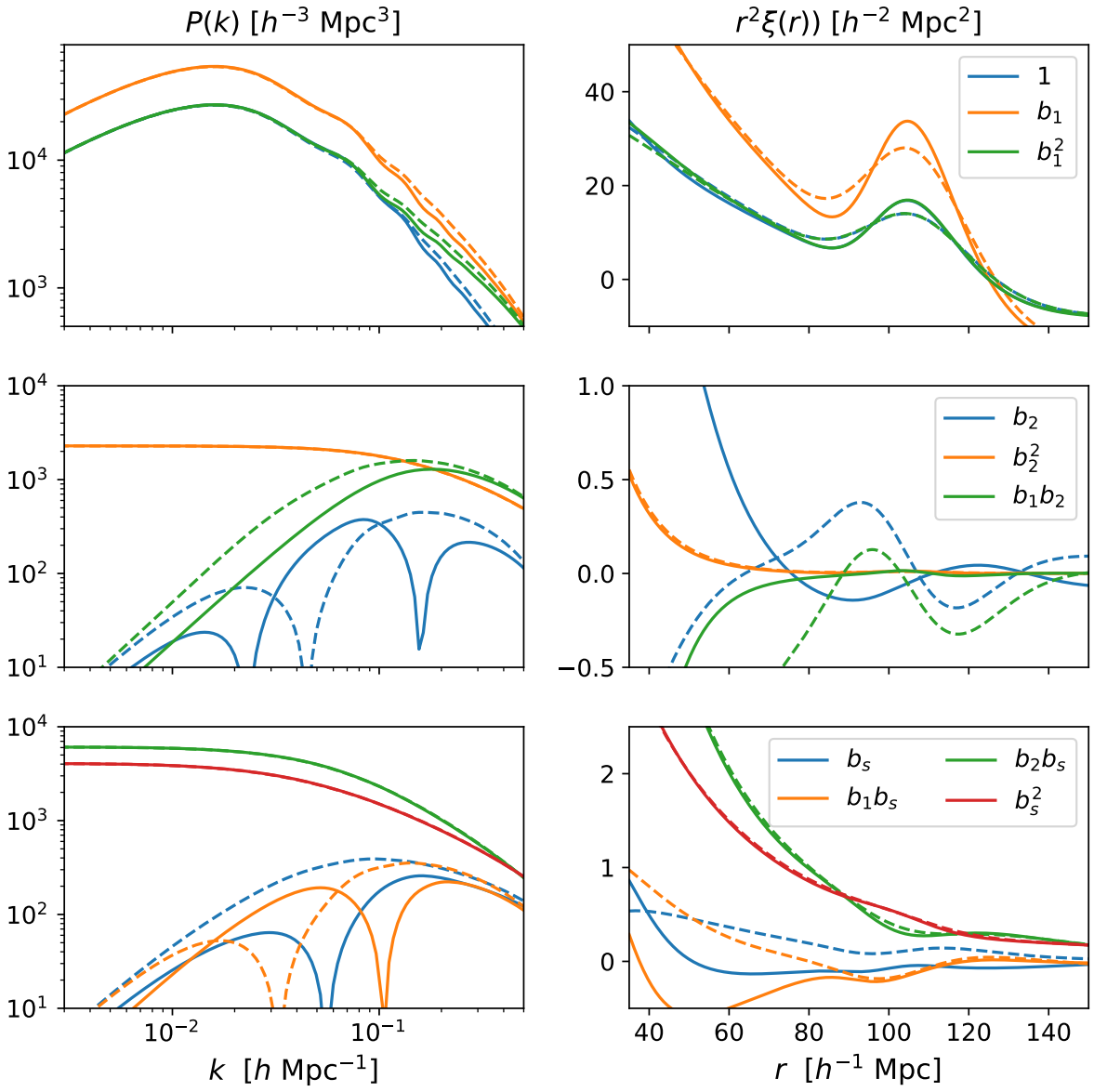

Figure 4.4: Contributions to the pre- and post-reconstruction (dashed and solid) power spectra and correlations functions (left and right columns) in real space from linear through quadratic bias terms at $z = 0$. Note that the matter (blue) and b_1^2 (green) curves in the top right panel are essentially degenerate, especially at the large scales shown.

spectrum P^{ds} as only one of the constituent tracers needs to be biased. The autospectrum P^{ss} does not contain any bias terms.

Figure 4.4 shows all the contributions to the reconstructed galaxy power spectrum and correlation function, up to the quadratic bias and shear terms. As seen in the top panel, the reduced damping in the lowest-order bias term "wiggles," barely visible in log-log plots of the reconstructed power spectrum, translate to significantly sharper and less shifted BAO features (right column). In the quadratic bias contributions (middle panels), reconstruction can be seen to dampen the amplitude of the BAO feature in the b_2 and $b_1 b_2$ contributions, which "wiggle" in Fourier space, while leaving the spectrally smooth b_2^2 contribution essentially intact. Since the BAO feature in the quadratic bias contributions will tend to smear and shift the observed BAO peak from its linear theory position, reconstruction serves to remove these confounding nonlinearities as expected. The shear terms have less pronounced (i.e. smoother) features at the BAO scale—which we will show in Section 4.8 as being essentially in-phase with the linear theory oscillations— that are less affected by reconstruction.

Finally, as noted in the discussion below Equation 4.4, the exponentiated A_{ij} in Zeldovich power spectra are assumed to be long wavelength, IR modes which can be resummed while contributions from the rest of the shorter modes are perturbatively expanded. These expanded modes thus carry also a UV (small-scale) sensitivity that should be renormalized by adding the appropriate counterterms, quadratic in wavenumber and proportional to the Zeldovich power spectrum: $\alpha_{ab} k^2 P^{ab}_{\rm Zel}$. In principle, we expect such counterterms in all three pieces of our reconstructed power spectrum, however given that the P^{ss} consists of mostly IR modes we expect its counterterm contribution to be suppressed relative to similar terms in P^{dd} and P^{ds}, though it could still be non-vanishing due to contributions we neglected in approximating Equation 4.8. While the counterterms α_{dd} and α_{ds} are highly nondegenerate due to the different supports of P^{dd} and P^{ds} (see Figure 4.3) in k-space, in this work we will also explore modelling the reconstructed power spectrum using only one counterterm, $\propto k^2 P_{\rm Zel}$, for both P^{dd} and P^{ds} contributions, since such a contribution would also be degenerate with any potential derivative biases (see e.g. ref. [396]). We will return to the difference between these options in Section 4.7.

4.4.2 Redshift space

In this section we develop analytic expressions for the redshift-space reconstructed power spectrum in both **Rec-Sym** and **Rec-Iso**. Methods recently developed in ref. [398] allow us to extend the LPT redshift-space power spectrum calculation to include bias and the specifics of reconstruction, which we summarise here and present in detail in Appendix D.3. As we will show shortly, **Rec-Sym** and **Rec-Iso** are not equivalent even to linear order. Specifically, we have

$$P_{\rm sym}(\mathbf{k}) = (b + f\mu^2)^2 P_{\rm L}(k) + \mathcal{O}(P_{\rm L}^2) \tag{4.18}$$

$$P_{\rm iso}(\mathbf{k}) = \Big[(b + f\mu^2)(1 - \mathcal{S}) + b\,\mathcal{S}\Big]^2 P_{\rm L}(k) + \mathcal{O}(P_{\rm L}^2), \tag{4.19}$$

i.e. while **Rec-Sym** restores supercluster infall at linear order, **Rec-Iso** removes redshift-space distortions at large scales while keeping them at small scales[6]. As we will see, this produces a smooth modulation in the broadband power nondegenerate with the BAO wiggles.

Since both the smoothed and displaced fields are uniformly multiplied by R_{ij} in **Rec-Sym**, it is straightforward to calculate the reconstructed power spectrum using Equation 4.4 with

$$\boldsymbol{\Psi}^d(\mathbf{k}) = [1 - \mathcal{S}(k)]\,\mathbf{R}\boldsymbol{\Psi}(\mathbf{k}) \quad , \quad \boldsymbol{\Psi}^s(\mathbf{k}) = -\mathcal{S}(k)\mathbf{R}\boldsymbol{\Psi}(\mathbf{k}) \quad . \tag{4.20}$$

In particular the angular structure of the $\mathbf{q}$ integral follows as in the calculation of the galaxy power spectrum without further modifications, and the set of bias terms in the dd, ds and ss spectra are identical to the real space case. The reconstructed power spectrum can then be calculated as one would the unreconstructed redshift space power spectrum. We develop the formalism to do the latter in Appendix D.3.2 and comment on the changes required to go to the reconstructed case therein.

The cross spectrum in **Rec-Iso** is slightly different since only the displaced field is multiplied by the redshift space transformation, R_{ij}. The displaced and shift fields in this case are thus instead

$$\boldsymbol{\Psi}^d(\mathbf{k}) = [1 - \mathcal{S}(k)]\,\boldsymbol{\Psi}^R(\mathbf{k}) = [1 - \mathcal{S}(k)]\,\mathbf{R}\boldsymbol{\Psi}(\mathbf{k}) \quad , \quad \boldsymbol{\Psi}^s(\mathbf{k}) = -\mathcal{S}(k)\boldsymbol{\Psi}(\mathbf{k}). \tag{4.21}$$

Since the displaced and shift moves thus lie in redshift and real space, respectively, their auto spectra can also respectively be calculated as in **Rec-Sym** and real space reconstruction; however, the cross spectrum is only "half transformed" into redshift space and thus requires special attention. The exponentiated two-points displacements are given by

$$\begin{aligned} A_{ij}^{ds,\mathrm{iso}} &= \langle \boldsymbol{\Psi}_i^d \boldsymbol{\Psi}_j^d \rangle + \langle \boldsymbol{\Psi}_i^s \boldsymbol{\Psi}_j^s \rangle - 2\langle \boldsymbol{\Psi}_i^d(\mathbf{q}_2) \boldsymbol{\Psi}_j^s(\mathbf{q}_1) \rangle \\ &= R_{in} R_{jm} \langle \boldsymbol{\Psi}_n^d \boldsymbol{\Psi}_m^d \rangle_{\text{Real Space}} + \langle \boldsymbol{\Psi}_i^s \boldsymbol{\Psi}_j^s \rangle_{\text{Real Space}} - 2R_{in} \langle \boldsymbol{\Psi}_n^d(\mathbf{q}_2) \boldsymbol{\Psi}_j^s(\mathbf{q}_1) \rangle_{\text{Real Space}}, \end{aligned} \tag{4.22}$$

such that the zero-lag piece due to the displaced-displaced correlation is fully transformed into redshift space, the zero-lag piece due to the shifted-shifted correlation is untransformed, and the coordinate dependent displaced-shifted correlation is"half transformed." In particular, defining as usual $\mathbf{q} = q\ \hat{q}$ and $\hat{k} \cdot \hat{q} = \mu_{\mathbf{q}}$, the last piece is

$$\begin{aligned} k_i k_j \langle \boldsymbol{\Psi}_i^d(\mathbf{q}_2) \boldsymbol{\Psi}_j^s(\mathbf{q}_1) \rangle &= k_i k_j (\delta_{ik} + f \hat{n}_i \hat{n}_k)(\tilde{X}^{ds} \delta_{kj} + \tilde{Y}^{ds} \hat{q}_k \hat{q}_j) \\ &= k^2 (1 + f\mu^2) \tilde{X}^{ds} + k^2 (\mu_{\mathbf{q}}^2 + f\mu_{\mathbf{q}} \mu (\hat{q} \cdot \hat{n})) \tilde{Y}^{ds}, \end{aligned} \tag{4.23}$$

where we have defined the tilded quantities without the usual zero lag piece[7]

$$\langle \boldsymbol{\Psi}^d(\mathbf{q}_2) \boldsymbol{\Psi}^s(\mathbf{q}_1) \rangle_{\text{Real Space}} = \tilde{X}^{ds}(q)\ \delta_{ij} + \tilde{Y}^{ds}(q)\ \hat{q}_i \hat{q}_j.$$

[6] We have amended Equation 4.11 to correct for a typo pointed out in ref. [283], wherein the $b\mathcal{S}$ in Equation 4.11 was missing a factor of b. No other results or conclusions are affected.

[7] For notational simplificity, the functions X and Y are always defined in real space.

Note that $2\tilde{Y} = -Y$ since Y does not posess a zero-lag piece. The azimuthal-angle dependence in $\hat{q}\cdot\hat{n}$ will require us to do the integral (Appendix D.3.1)

$$\int \frac{d\phi}{2\pi} e^{A\mu_{\mathbf{q}}\sqrt{1-\mu_{\mathbf{q}}^2}\cos\phi} = \sum_{\ell=0}^{\infty} H_\ell^{(0)}(A)\ (A\mu_{\mathbf{q}}^2)^\ell,$$

where we have defined

$$H_\ell^{(0)}(A) = \sum_{m=0}^{\ell} \frac{(-1)^{\ell-m} A^{2m-\ell}\Gamma(m+\frac{1}{2})}{\sqrt{\pi}\Gamma(2m+1)\Gamma(2m-\ell+1)\Gamma(\ell-m+1)}.$$

Note that the Γ functions in the denominator will kill any terms in the sum for which $2m-\ell$ is negative, such that the sum really only contains $\ell/2$ terms and is always convergent in A. The full cross spectrum is then given by

$$\begin{aligned} P^{(ds)}(\mathbf{k}) =& e^{-\frac{1}{2}k^2(\alpha_0{\Sigma^{(dd)}}^2+{\Sigma^{(ss)}}^2)} \int d^3\mathbf{q}\ e^{ikq\mu_{\mathbf{q}}+k^2(1+f\mu^2)(\tilde{X}^{(ds)}+\mu_{\mathbf{q}}^2\tilde{Y}^{(ds)})} \\ & \sum_{\ell=0}^{\infty} H_\ell^{(0)}(A) A^\ell \mu_{\mathbf{q}}^{2\ell}\left(1 + ib_1 k\mu_{\mathbf{q}} U^{(d)}(q) - \frac{1}{2}b_2 k^2\mu_{\mathbf{q}}^2 U^{(d)}(q)^2 + ...\right) \end{aligned} \tag{4.24}$$

where $A = k^2 f\mu\sqrt{1-\mu^2}\tilde{Y}^{(ds)}$ and we have defined $\Sigma^2 = \tilde{X}(0)$ and $\alpha_0 = 1 + f(f+2)\mu^2$. The remaining integrals can then be performed using the usual tricks for powers of $\mu_{\mathbf{q}}$ using the series in Equation B.53, and are explicitly given at the end of Appendix D.3.1.

Figures 4.5 and 4.6 show the various bias contributions to the reconstructed redshift space power spectrum monopoles and quadrupoles within **Rec-Sym** and **Rec-Iso**, respectively. A significant difference between the two methods can be seen by comparing the matter (i.e. "1") pieces in the top panels of the two figures. While all three linear bias contributions to the reconstructed power spectrum monopole ($\propto 1$, b_1, b_1^2) approach the Zeldovich monopole in the large scale limit in **Rec-Sym**, the matter contribution to the **Rec-Iso** monopole instead approaches the b_1^2 contribution, which does not receive redshift space distortions in the linear theory limit. This is because the power spectrum at the largest scales is dominated by the autospectrum of the un-redshifted shift field, P^{ss}. While the matter and b_1 contributions to the reconstructed quadrupole approach linear theory in **Rec-Sym**, they vanish on large scales in **Rec-Iso**. On the other hand, the majority of the higher bias contributions (excluding b_2 and b_s) are sourced only by P^{dd} and are thus identical between the two methods, as can be seen by comparing the lower two rows of Figures 4.5 and 4.6. This corresponds to our intuition that redshift-space distortions are less prominent for highly biased tracers, and that the differences between Rec-Iso and Rec-Sym disappear if we remove RSD. In addition, the contributions enumerated above are supplemented by counterterms ($\alpha_{dd}^\ell, \alpha_{ds}^\ell, \alpha_{ss}^\ell$), where we need a separate counterterm for each pair and multipole as discussed below Equation 4.7, though as in the real space case we also explore the possibility of only fitting one counterterm each for the net reconstructed monopole and quadrupole.

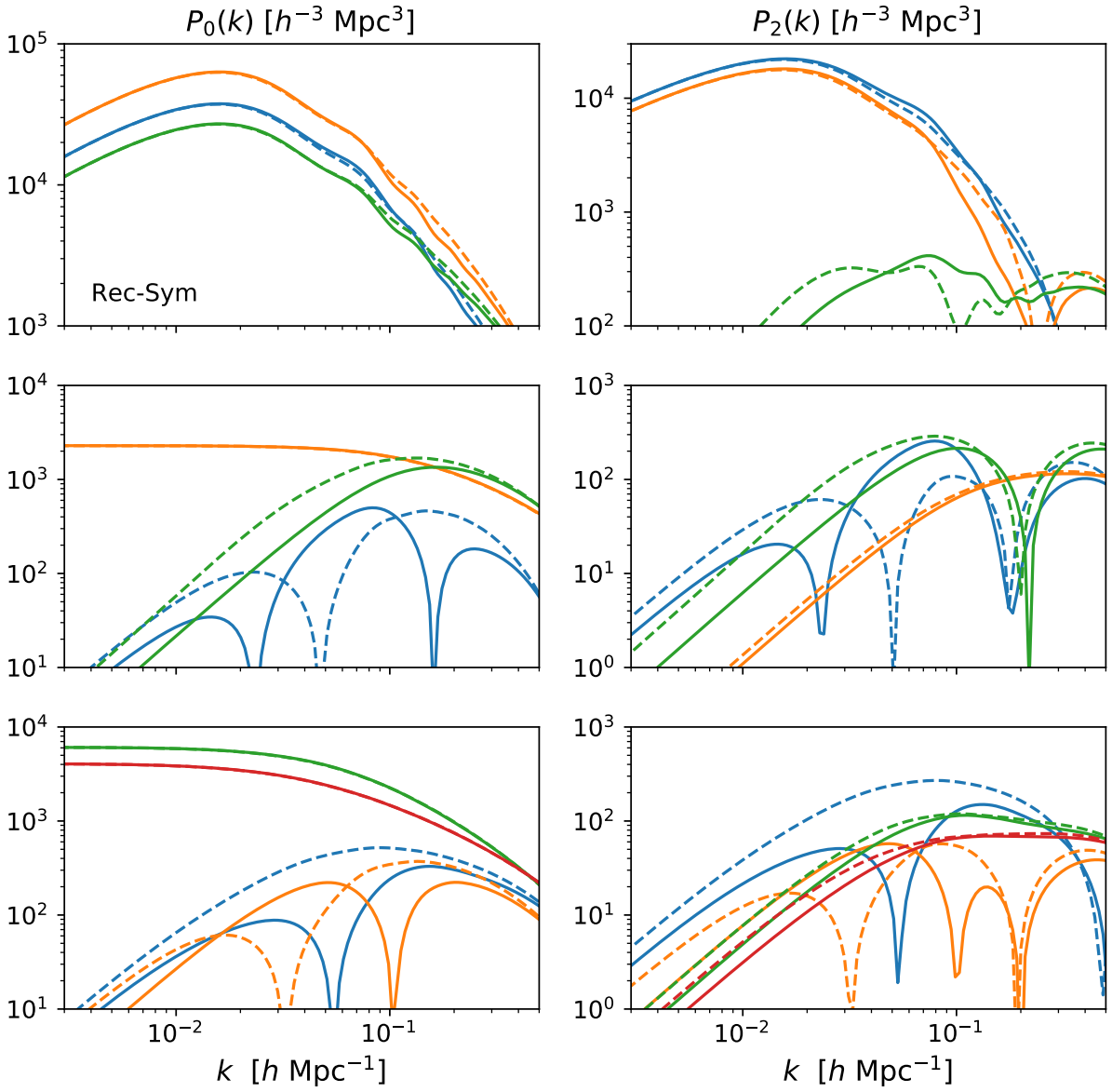

Figure 4.5: Bias contributions to the pre- and post-reconstruction (dashed and solid) $z = 0$ redshift space power spectra monopole and quadrupoles in the **Rec-Sym** scheme. The color scheme and line styles follow those in Figure 4.4. The lowest-order contributions to the reconstructed monopole and quadrupole due to the linear bias b_1 tend to the Kaiser approximation at large scales. Note the different y-axis ranges on different panels.

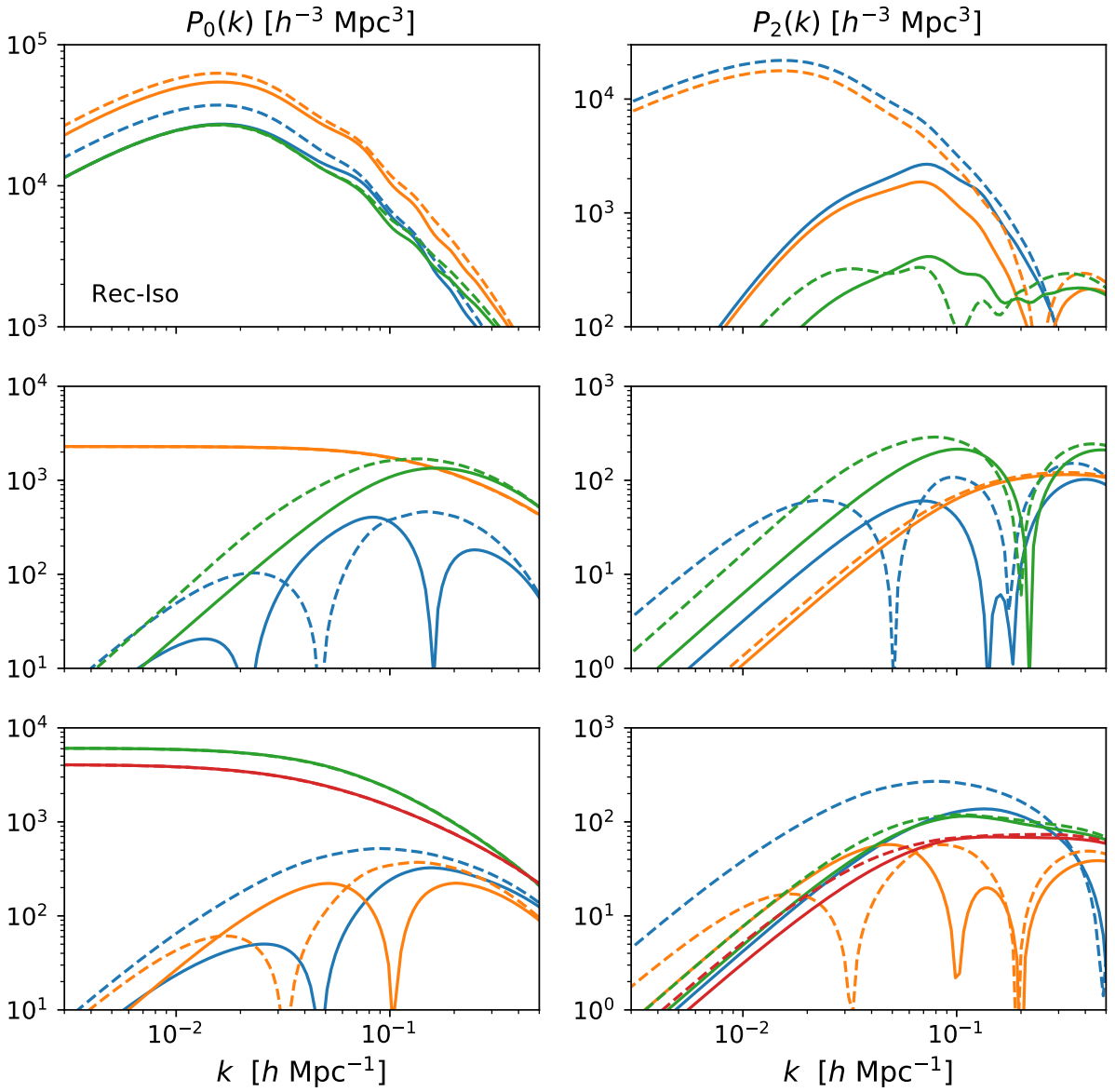

Figure 4.6: Same as Figure 4.5, but for **Rec-Iso** at $z = 0$. Unlike in **Rec-Sym**, the linear bias contributions to the monopole and quadrupole do not tend to the Kaiser limit on large scales but to the real space linear power spectrum, as evidenced by reduced power in the monopole compared to the pre-reconstruction Zeldovich power spectrum, and contributions to the quadrupole vanishing on large scales. However, many of the higher bias contributions are identical to those in **Rec-Sym** (Fig. 4.5).

4.5 Reconstructed correlation function

The configuration space two-point function (the correlation function) can be obtained from our Fourier-space results by Hankel transform. It is also possible to rewrite the q-dependent integrals to compute $\xi(r, \mu_r)$ directly, where $\mu_r = \hat{n} \cdot \hat{r}$. Here we reprise the calculation of ref. [414], extending it to include the additional bias terms and commenting explicitly on several numerical issues which arise. We have checked that our Fourier and configuration space results agree numerically to significantly sub-percent levels in both real and redshift space for both **Rec-Sym** and **Rec-Iso**.

The general formula for the cross spectrum of two tracers a and b given in Equation 4.4 can be Fourier transformed to give [415, 396, 399, 405]

$$\begin{aligned} 1 + \xi^{ab}(r) &= \int \frac{d^3q}{(2\pi)^{3/2}|A^{ab}|^{1/2}} e^{-(1/2)(q_i - r_i)(A^{-1}_{ab})_{ij}(q_j - r_j)} \\ &\times \Big\{ 1 - (b_1^b U_i^a + b_1^a U_i^b) g_i + b_1^a b_1^b \xi_L + \frac{1}{2} b_2^a b_2^b \xi_L^2 \\ &\quad - \frac{1}{2} \left[b_2^b U_i^a U_j^a + b_2^a U_i^b U_j^b + 2 b_1^a b_1^b U_i^a U_j^b \right] G_{ij} - \left[b_1^a b_2^b U_i^a + b_1^b b_2^a U_i^b \right] \xi_L g_i \\ &\quad - \frac{1}{2} \left[b_s^a \Upsilon_{ij}^b + b_s^b \Upsilon_{ij}^a \right] G_{ij} - \left[b_1^a b_s^b V_i^{ab} + b_1^b b_s^a V_i^{ba} \right] g_i \\ &\quad + \frac{1}{2} (b_2^a b_s^b + b_2^b b_s^a) \chi^{12} + b_s^a b_s^b \zeta + \alpha_{ab} \mathrm{tr} G + \ldots \Big\} , \end{aligned} \tag{4.25}$$

where we have defined

$$g_i = (A^{-1}_{ab})_{ij}(q_j - r_j), \; G_{ij} = (A^{-1}_{ab})_{ij} - g_i g_j \tag{4.26}$$

and placed the superscript ab in A^{ab} into the subscript for notational convenience. In the configuration space calculation above, the Lagrangian two-point functions (e.g. A_{ij}, U_i, Υ_{ij}) can be computed using the formulae provided in Appendix D.1. The above formula can be translated into redshift space by multiplying the Lagrangian two-point functions with vector indices by the appropriate factors of $R_{ij} = \delta_{ij} + f \hat{n}_i \hat{n}_j$. Taking the line-of-sight to be in the z direction without any loss of generality, this is equivalent to multiplying by the matrix $\mathrm{diag}(1, 1, 1 + f)$. When calculating the un-reconstructed redshift space correlation function, this multiplication is equivalent to multiplying each z component index of vector and tensor quantities (e.g. U_z^a or A_{yz}^{ab}) by $1 + f$, and dividing the corresponding components in the matrix inverse, A^{-1}_{ab}, by the same factor. The redshift-space counterterm $\alpha_2 k^2 \mu^2$ can be included in the correlation function by adding $\alpha_2 \hat{n}_i \hat{n}_j G_{ij}$, which similarly is equivalent to $\alpha_2 G_{zz}$ when picking z as the line-of-sight direction.

The reconstructed correlation function in real and redshift space can be calculated using Equation 4.25 by defining "displaced" and "shifted" tracers as in the case of the power spectrum (Sections 4.4.1 and 4.4.2) and calculating the combined quantity $\xi_{\mathrm{recon}} = \xi_{dd} + \xi_{ss} - 2\xi_{ds}$. For reconstruction using **Rec-Sym**, the same shortcuts of multiplying by

factors of $1+f$ in lieu of matrix multiplication and inversion apply, since all vector and tensor quantities undergo the same transformation by R_{ij}. The calculation for **Rec-Iso** is more complicated. As was the case in Fourier space, the displaced-displaced and shifted-shifted auto-correlation functions are equal to their counterparts in **Rec-Sym** and real-space reconstruction, while the displaced-shifted cross-correlation function contains a mix of real and redshift space factors. In particular, from Equation 4.22 we see that the two zero-lag pieces and one q-dependent piece of A_{ij}^{ds} in **Rec-Iso** are independently transformed by different numbers of R_{ij}'s. For this reason, when calculating the correlation function in **Rec-Iso**, the matrix inverse of A^{ds} in redshift space cannot be simply obtained by dividing the real space inverse by factors of $1+f$; rather, the uninverted matrix must be redshifted piece by piece as in Equation 4.22 and then inverted numerically (we use Cholesky decomposition).

4.6 Other statistics

While the correlation function and power spectrum are the most frequently considered 2-point functions, there are other variants that have some advantages. Since these can all be written in terms of the correlation function or power spectrum, our model provides a consistent prediction for them as well. Of particular interest for BAO is the ω_ℓ statistic of ref. [423], which combines the scale-localization of the Fourier-space methods with the compactness and easy treatment of masks of the configuration-space methods.

In principle ω_ℓ can be calculated from either the configuration-space or Fourier-space expressions given above, but we have found it more convenient to start from the Fourier expressions. Since these are computed using FFTlog they naturally cover a very wide range of k, making the transforms to ω_ℓ easy to implement. For example

$$\omega_0(r_s) = \int \frac{k^2\,dk}{2\pi^2} P_0(k) \widetilde{W}_0(k\,r_s) \tag{4.27}$$

with $\widetilde{W}_0$ given in ref. [423] (see their Fig. 1 and Appendix A). At large scales $\widetilde{W}_0 \propto k^2$ while at small scales $\widetilde{W}_0 \propto k^{-4}$. Our formalism naturally provides predictions for ω_ℓ using the same set of bias and nuisance parameters as for ξ_ℓ and P_ℓ.

4.7 Comparison to N-body

To look at the domain of validity of our analytic results we compare to the `DarkSky` N-body simulation suite[8], specifically simulation `ds14_a` [350]. This simulation used the `2HOT` code [406] to evolve 10240^3 particles in an $(8\,h^{-1}\mathrm{Gpc})^3$ volume to model the growth of structure in a ΛCDM cosmology with $\Omega_M = 1-\Omega_\Lambda = 0.295$, $h = 0.688$, $n_s = 0.968$ and $\sigma_8 = 0.835$. Initial conditions were generated from a glass using 2^{nd} order Lagrangian perturbation theory at

[8] http://darksky.slac.stanford.edu

lg$M$	Redshift	$\bar{n}$	b
$12.0 - 12.5$	0.0	3.45	0.87
$12.5 - 13.0$	0.0	1.18	1.05
$13.0 - 13.5$	0.0	0.38	1.30

Table 4.1: Number densities and bias values for the halo samples we use. Halo masses are $\log_{10}$ of the mass in $h^{-1}M_\odot$, number densities are times $10^{-3}\,h^3\,\mathrm{Mpc}^{-3}$.

$z = 93$. Halos were found using the `Rockstar` code [34]. We extracted the positions, velocities and masses of halos more massive than $M_{200b} = 10^{12}\,h^{-1}M_\odot$ from the publicly available data at $z = 0$ (data at higher z, which would have been a more relevant comparison, were not available). We computed the halo correlation functions and power spectra, in real and redshift space. For the redshift-space quantities we assumed the plane-parallel approximation with the line-of-sight being the z-axis. We also obtained the linear theory power spectrum used to generate the initial conditions, which we take as the input to our model.

We implemented the algorithm described in §4.3 using the periodicity of the box and FFTs to perform the smoothing and computation of the shifts. As for the power spectrum and correlation function, the plane-parallel approximation with line-of-sight the z-axis was assumed for the redshift-space quantities. The code takes as input an assumed large-scale bias, b, and growth parameter, f, in addition to a Gaussian smoothing length, R. We used the b obtained from the ratio of the linear theory and real-space halo power spectra at low k (see Table 4.1), and $f \simeq 0.508$ appropriate to the simulation cosmology at $z = 0$, and note in passing that the goodness-of-fit of our results did not seem to be greatly improved by substituting the linear bias thus obtained with the value of $1 + b_1$ obtained by fitting the pre-reconstruction data with our model up to quasi-nonlinear scales.

We computed the reconstructed field in both real and redshift space. In each case the shifted and displaced positions were computed using a 2048^3 FFT, which resolves the (Gaussian) smoothing length by $2.5 - 5$ grid cells for $R \simeq 10 - 20\,h^{-1}$Mpc. We used as many "random" positions as halos in each case, for simplicity, and computed the power spectra and correlation functions for dd, ds and ss assuming periodic boundary conditions. The reconstructed power spectrum or correlation function can then be computed as $dd - 2ds + ss$, and we can look at each of the contributions separately. Note that our choice of equal numbers of randoms and data points means the shot noise on the reconstructed power spectrum is twice that of the pre-reconstructed field.

We compare the N-body results to our model with b_1 and b_2 and include the minimal set of counterterms as described in the preceding sections (one and three pre- and post-reconstruction, respectively, in real space) as well as a constant shot noise component fit to the data. For brevity our discussion will focus on halos with masses between $12.5 < \log_{10}(M/h^{-1}M_\odot) < 13.0$., though we obtained qualitatively similar results in the lower and higher mass bin as well, and show fits of the reconstructed redshift space power spectrum in

the latter at the end of this section. We have checked that including nonzero shear bias b_s does not visibly improve the goodness-of-fit. The top-left pair of panels of Figure 4.7 compares the unreconstructed real-space power spectrum in our model with $(b_1, b_2) = (0.02, -0.8)$ with that in `DarkSky`. The quadratic bias, b_2, accounts for a non-negligible fraction of the total power at essentially all scales and significantly reduces the constant shot noise term in the fit. We find that with a counterterm $\alpha \approx 11\ h^{-2}\mathrm{Mpc}^2$ our model agrees with the data at the percent level out to $k \simeq 0.4\,h\,\mathrm{Mpc}^{-1}$. The counterterm accounts for roughly a 10% correction at $k = 0.1\,h\,\mathrm{Mpc}^{-1}$, and it is worth noting that even in its absence our model accurately captures the BAO features in the power spectrum, as evidenced by the lack of oscillatory features in the fit residuals.

The remaining panels of Figure 4.7 show the fit for the reconstructed power spectra at three smoothing scales $R = 10,\ 15,\ 20\,h^{-1}\mathrm{Mpc}$. We have tested whether the data could be reproduced using only one counterterm, α (shown in orange), or equivalently from one derivative bias b_{∇^2}, and find that such a choice dramatically reduces the range-of-validity of the model compared to three counter terms. While we adopted a rather conservative approach in fitting these data, prioritizing the accuracy of our predictions at low k rather than producing reasonable-looking fits to smaller scales, our model with three counterterms $(\alpha_{dd}, \alpha_{ds}, \alpha_{ss})$ nonetheless reproduces both the broadband power and oscillatory features of the reconstructed power spectrum out to $k = 0.2\,h\,\mathrm{Mpc}^{-1}$ at the percent level for $R = 15$ and $20h^{-1}$ Mpc. That each of the three constituent spectra in $P^{\mathrm{recon}} = P^{dd} + P^{ss} - 2P^{ds}$ has distinct short-wavelength behavior and k-space supports underlies the success of our model with three counterterms—each of which has highly nondegenerate scale dependence—versus the one-counterterm alternative. We have found that setting $\alpha_{ss} = 0$ does not qualitatively alter the degree to which our model fits the data; we have made this choice in all of our fits below, but note that as $\alpha_{ss}k^2$ vanishes quadratically towards low k, the data are also naturally rather insensitive to it. Indeed, since nonlinear corrections are typically of order $k^2\Sigma^2$, and the smoothing scale is chosen such that $(\Sigma/R)^2 \ll 1$, the insensitivity of P^{ss} to these corrections follows almost by construction. However, a bump-like feature around $k = 0.1\,h\,\mathrm{Mpc}^{-1}$ is persistent across all the fits, peaking at less than half a percent when $R = 20\,h^{-1}\mathrm{Mpc}$ and growing to a full percent at $R = 10\,h^{-1}\mathrm{Mpc}$. The appearance of such a feature, growing towards smaller smoothing scales, is consistent with our neglect of nonlinear corrections to the smoothed displacements, which should increase towards smaller smoothing scales roughly as $\boldsymbol{\Psi}/R$; we discuss one such nonlinearity in Appendix D.5. For sufficiently small smoothing scales, even the assumption that the smoothing of the BAO feature can be essentially captured with resummed *linear* displacements $\boldsymbol{\Psi}^{d,s}$ will break down, and indeed our fit residuals begin to show noticeable oscillatory behavior at the smallest smoothing scale shown ($R = 10\,h^{-1}\mathrm{Mpc}$). At $R = 15\,h^{-1}\mathrm{Mpc}$ and in the sample variance limit with Gaussian errors, the feature at $k = 0.1\,h\,\mathrm{Mpc}^{-1}$ should be detectable with $\chi^2 = V_{\mathrm{obs}}/(2h^{-3}\ \mathrm{Gpc}^3)$, where V_{obs} is the total observed volume. If we were to instead smooth using the larger $R = 20\,h^{-1}\mathrm{Mpc}$, the χ^2 is roughly halved. For such a smoothing this feature represents a χ^2-penalty of 0.2 for a sample variance limited survey of $14\,000\,\mathrm{deg}^2$ covering $0 \le z \le 0.3$, and would be slightly smaller for finite number density.

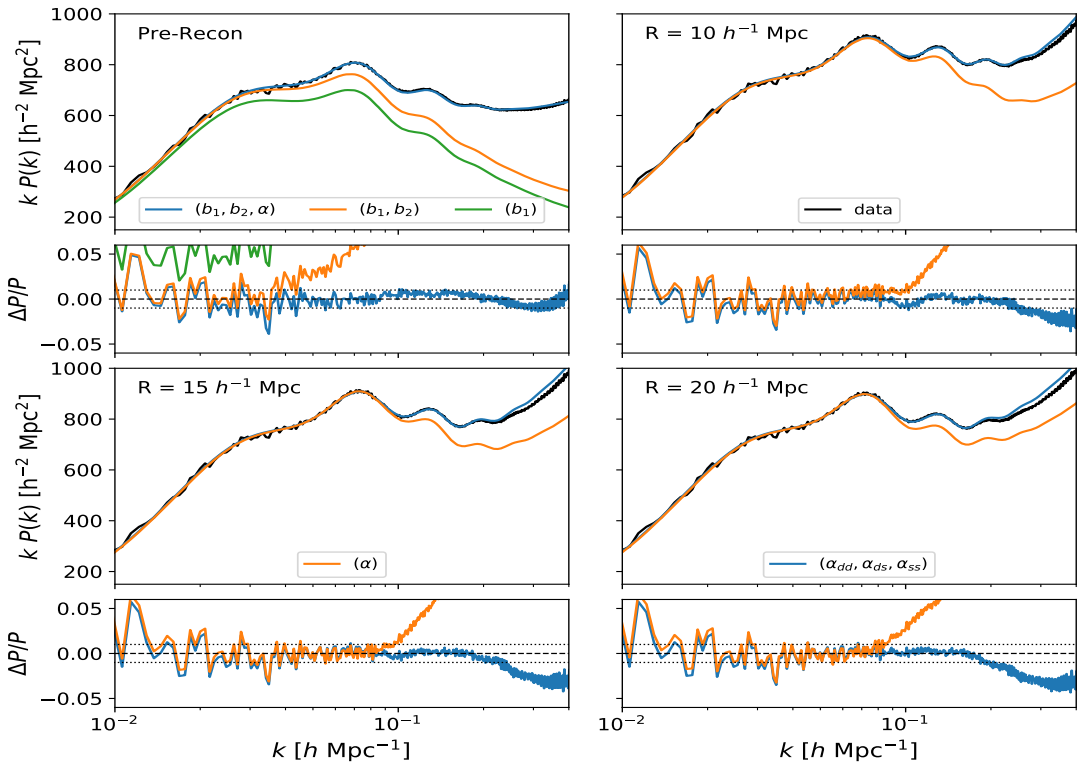

Figure 4.7: Fits to the pre- and post-reconstruction real-space halo power spectra in `DarkSky` for halos of mass between $12.5 < \log_{10}(M/h^{-1}M_\odot) < 13.0$ at three smoothing scales ($R = 10$, 15, $20\,h\,\mathrm{Mpc}^{-1}$), assuming Zeldovich power spectra with biases (b_1, b_2) and one counterterm per spectrum (three total for the reconstructed case). The upper plot of each vertical pair of panels shows the product of the wavevector magnitude and power spectrum $k\,P(k)$ while the lower plot shows the fit residuals as a fraction of measure power $\Delta P/P = (P_{\rm fit} - P_{\rm nbody})/P_{\rm nbody}$. In the top-left pair of panels we show the incremental contributions from b_2 and the counterterm α (which contributes close to 10% of the power at $k = 0.1\,h\,\mathrm{Mpc}^{-1}$) to the fit, which agrees with the simulation at the percent level (dotted line in the lower plots) at all scales shown. In the remaining panels we use the same bias parameters to fit the reconstructed power spectrum, allowing only counterterms to vary. Our model with three counterterms can fit the data at the percent level out to $k = 0.2\,h\,\mathrm{Mpc}^{-1}$, though a bump-like feature at $k = 0.1\,h\,\mathrm{Mpc}^{-1}$ becomes more prominent at smaller smoothing scales, where nonlinear corrections beyond the Zeldovich approximation presumably become more important (see text). Also shown in orange are fits using one counterterm – or equivanlently one derivative bias – which fit less well past $k = 0.1\,h\,\mathrm{Mpc}^{-1}$. We fined that setting the counterterm α_{ss} to zero does not materially affect our fits. Note that there is excess power in the data at the largest scales shown, as discussed in the text.

The pre- and post-reconstruction real-space correlation functions can be directly compared by computing the Fourier transforms of the above fits. However, in comparing our theory with `DarkSky` we found that the $z = 0$, pre-reconstruction halo power spectra all have significant excess power at low k compared to the predictions of linear theory with scale-independent bias. The origin of this excess is unclear, and is not addressed in ref. [350]. It appears to arise from a significant number of low k modes, and so is unlikely to be simply a statistical fluctuation in the initial conditions. It shows up in all of our halo samples, and is highly correlated among mass bins. This excess power is small for modes to the right of the power spectrum peak and probably has only a small impact on the dynamics on BAO scales. In Fourier space we simply confine our fitting and modeling to $k > 0.01\,h\,\mathrm{Mpc}^{-1}$. In configuration space, however, the additional long-wavelength power slightly distorts the shape of the BAO peak, and to enable a fair comparison we have added appropriate long-wavelength modes to our theoretical predictions assuming linear theory; specifically, we find that the fitting form $P_{\rm lw}(k) = A\ (k/k_0)^n$, where $A = 3.5 \times 10^4 h^{-3}\ \mathrm{Mpc}^3$, $k_0 = 10^{-3}\,h\,\mathrm{Mpc}^{-1}$ and $n = -1.7$, describes well both the long-wavelength excess seen in the power spectrum below $k < 0.01\,h\,\mathrm{Mpc}^{-1}$ and dramatically improves the agreement between the unreconstructed correlation function in theory and `DarkSky`. The contribution to the pre- and post-reconstruction power spectra and correlation function of these long wavelength modes is shown in Figure 4.8. Without the long-wavelength correction, the `DarkSky` results do not agree with theory on the large scales to the right of the BAO peak, which should be well-described within linear theory, nor in the BAO "dip," both pre- and post-reconstruction. Due to the ad-hoc nature of our correction, in the remainder of this section we will focus our comparisons on Fourier space, wherein long-wavelength modes must decouple. However, we caution that small, localized features in Fourier space can cause extended distortions in configuration space where data points are highly correlated. In Figure 4.9, we show the effect of the $k = 0.1\,h\,\mathrm{Mpc}^{-1}$ bump described in the previous section by additively "filling" it with a small, localized Gaussian profile, as shown in the left panel. The effects of this bump, Fourier-transformed, are shown in the right panel: while sub-percent in Fourier space, the $k \simeq 0.1\,h\,\mathrm{Mpc}^{-1}$ feature gives rise to visible distortions to the BAO feature in configuration space.

Finally, fits for the pre- and post-reconstruction power spectra in redshift space are shown in Figure 4.10. We have chosen to summarize the angular dependence of the redshift-space power spectrum in terms of its monopole and quadrupole, though our model predicts the full $P(k, \mu_{\mathbf{q}})$ and higher multipoles as well. As in real space, we have fitted for the bias parameters (b_1, b_2) using the unreconstructed data and applied the same set of bias parameters to predict the power spectra in both **Rec-Sym** and **Rec-Iso**. We adopt the full set of six counterterms, three each $\alpha^\ell_{dd}, \alpha^\ell_{ds}, \alpha^\ell_{ss}$ for the monopole ($\ell = 0$) and quadrupole ($\ell = 2$), but also explore the possibility of utilizing only one counterterm α^ℓ per multipole (corresponding to a derivative bias for both the halo density and velocity). In all cases, our base model with six counterterms fits the data at the percent level or below past $k = 0.2\,h\,\mathrm{Mpc}^{-1}$ in both the monopole and quadrupole moments. Notably the Zeldovich approximation produces oscillation-free residuals even in the absence of counterterms (green), with the counterterms

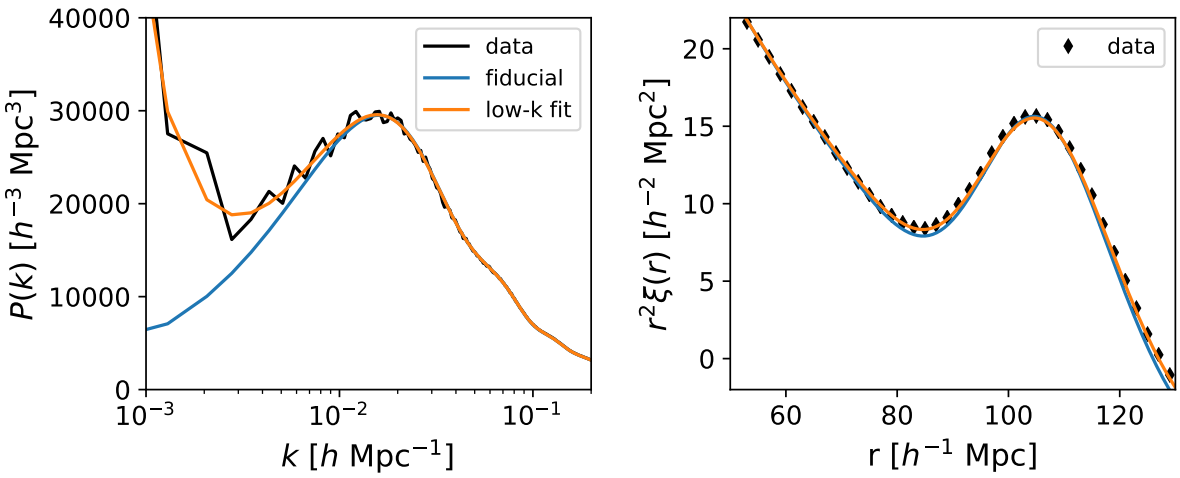

Figure 4.8: Halos in `DarkSky` exhibit significant excess power compared to theory at large scales in Fourier space which should be well-described by linear theory. (Left) Fits to the real-space power spectrum with and without our ad hoc correction $P_{\rm lw} = A\ (k/k_0)^n$, shown in blue and orange respectively. At the largest scales shown, the excess power is significantly larger than the scatter. The fits prefer slighly different, though qualitatively similar, bias values. (Right) The same fits in configuration space. The uncorrected data systematically trends below the data at separataions above the BAO peak and in the BAO "dip," while the fit with $P_{\rm lw}$ added goes through all the data points.

providing a physics-based broadband model ($\sim \alpha^\ell_{ab} k^2 P_{\ell,ab}$) that reproduces the N-body results at the percent level. Our fits do not explicitly include nonlinear redshift space distortions such as fingers-of-god, though such effects are perturbatively accounted for by velocity counterterms to lowest order. For completeness, in Figure 4.11 we show the same fits for the mass bin $13.0 < \log(M/h^{-1}M_\odot) < 13.5$, where our model fits the data at percent level over a similar range of scales using the parameters $(b_1, b_2) = (0.23, -1.0)$.

Lastly, let us comment on the comparison fits in pre- and post- reconstructed cases. Given that our shift field, χ, is constructed only from long-wavelength modes explicitly isolated from observed field, δ, by filtering out the nonlinear scales larger than $k \gtrsim 1/R$, we have no reason to suppose that the perturbative structure of our results will significantly change. In other words, by performing the mapping in Equation (4.9), we have reconstructed only the long modes, thereby reducing nonlinear smoothing due to large scale (infrared) modes, while the bulk of the small-scale nonlinear modes, as well as FoG effects, should remain unreduced. In addition, Lagrangian perturbation theory (PT) conveniently separates nonlinearities due to long and short modes, exponentially resumming the former while expanding the latter order-by-order [290, 399]. Because of this, we do not expect dramatically different PT behavior in the pre- and post-reconstructed results. These arguments are also supported by

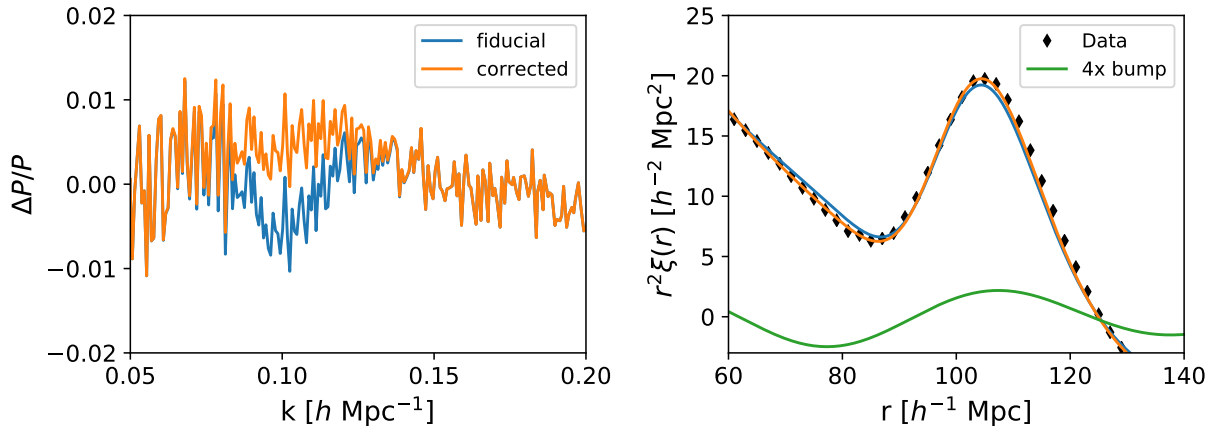

Figure 4.9: A sub-percent level feature in the power spectrum near $k = 0.1\,h\,\mathrm{Mpc}^{-1}$ can lead to visible distortions in the BAO feature in $\xi(r)$. (Left) Residuals for the fit as a fraction of total measured power in the simulations, as defined in the caption of Figure 4.7. The orange curve shows the residuals when our theory is corrected using a Gaussian profile localized at $k = 0.1\,h\,\mathrm{Mpc}^{-1}$ compared to the fiducial fit (blue), whose residuals exhibit a dip centered at $k = 0.1\,h\,\mathrm{Mpc}^{-1}$. (Right) The fiducial and corrected correlation functions. The bump in the left panel, whose Fourier transform is shown magnified in the green curve, induces distortions in the BAO feature across a range of separations $r \sim 60 - 120\,h^{-1}\mathrm{Mpc}$.

Figures 4.10 and 4.11, which show our model exhibits quantitatively similar degrees of fit pre- and post reconstruction.

4.8 Comparison to earlier work

There has been significant theoretical activity in modeling post-reconstruction clustering (see references in the introduction). Our framework encompasses most of these previous perturbation theory expressions when appropriate approximations and phenomenological choices are accounted for. To the best of our knowledge, the framework presented here captures for the first time all of the relevant post-reconstruction effects and is unique in accurately handling both Fourier and configuration space results, in real and redshift space and includes all the bias operators to quadratic order.

Not all models are based on perturbation theory calculations however, and many phenomenological models have been introduced in order to describe the post-reconstruction statistics. Restricting ourselves just to models of the 'standard' reconstruction algorithm [122], §3.1 of ref. [424] discusses early models (which were of the form $P(k) = B(k)P_{\rm lin}(k) + A(k)$ with $B(k)$ and $A(k)$ smooth functions). Starting with the first applications to data in ref. [424] the form used to fit reconstructed power spectra is based upon a split between a "smooth"

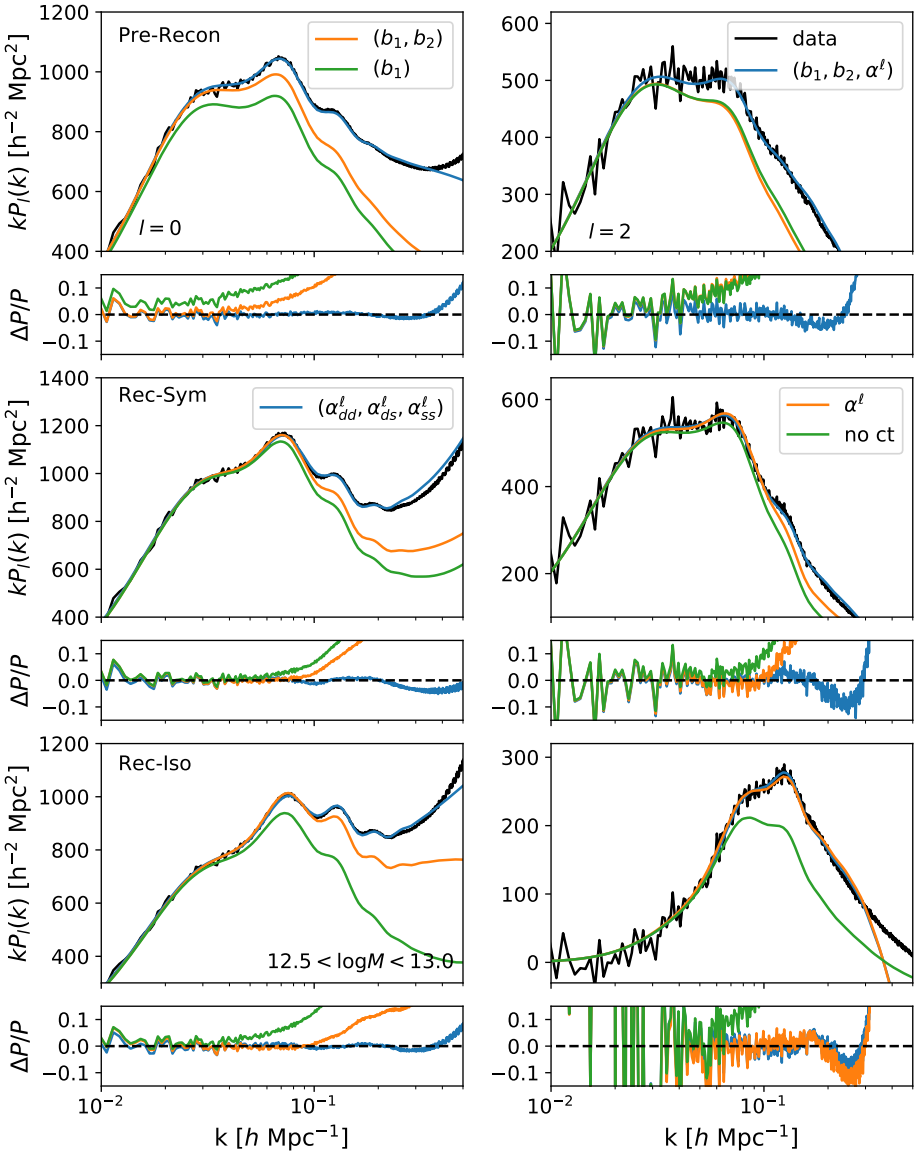

Figure 4.10: Fits for the pre- and post-reconstruction redshift-space power spectrum monopole (left) and quadrupole (right) for halos in the mass range $12.5 < \log_{10}(M/h^{-1}M_\odot) < 13.0$. The fractional residuals $\Delta P/P$ are defined in Figure 4.7. All spectra were fit using a consistent set of bias parameters $(b_1, b_2) = (0.02, -0.8)$, whose independent contributions are shown in the top row, determined by fitting the pre-reconstruction data, such that only the counterterms were fitted in constructing the curves in the bottom two rows. Our model with the full set of six counterterms—three each for the monopole and quadrupole respectively—fits both the reconstructed monopole and quadrupole in both schemes out to $k = 0.2\,h\,\mathrm{Mpc}^{-1}$ to a few percent and reproduce the phase and amplitude of the oscillatory BAO wiggles.

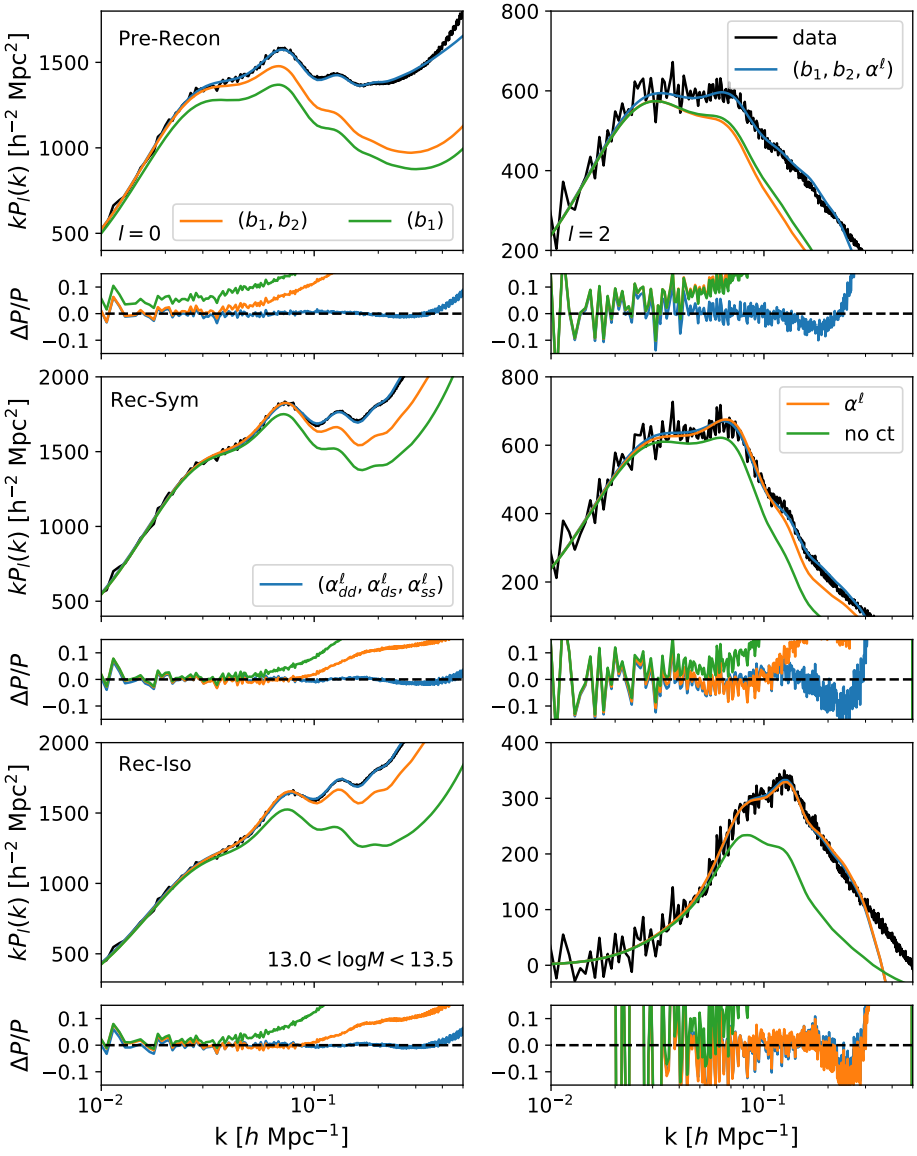

Figure 4.11: Like Figure 4.10, but for halos in the mass bin $13.0 < \log(M/h^{-1}M_\odot) < 13.5$. Here, our model prefers the bias parameters $(b_1, b_2) = (0.23, -1.0)$ and accurately fits the data over a similar range of scales.

and "wiggle" contribution to $P(k) = P_{\rm nw}(k) + \Delta P_{\rm w}(k)$, with a phenomenological damping of the wiggle component motivated by perturbation theory [121]. In ref. [424] the parameters of the model were fit to N-body simulations, and this has become common. This approach has dominated the modeling of observations to date (e.g. refs. [7, 61, 31] for recent examples)

though ref. [197] is an example of an analysis that did not take this approach. However, we note that the choice of the wiggle/no-wiggle split exhibits a certain amount of freedom in the separation of the wiggle and broadband part. This of course implies that, in order to extract accurate information from the e.g. BAO, either both wiggle and broadband part have to be modeled to the same level of accuracy, or the extracted wiggle part from the data needs to exactly correspond to the model (see also refs. [256, 254] for related discussion). The latter requirement, even though implicitly assumed in most of the current BAO treatments, is rarely subject to performance checks and scrutiny. In this context, it is also worth noting that the common choice of $P_{\rm nw}$ derived in ref. [120] does not fully capture the broadband linear power spectrum at the precision attained by modern Boltzmann codes. Figure 4.12 shows three possible linear wiggle power spectra, based on no-wiggle spectra computed using the fitting formula from ref. [120], B-splines [402] or a Savitsky-Golay filter; even the latter two, which agree asymptotically with the full linear theory power spectrum, exhibit noticeably different oscillatory behavior. This indicates that extracting the corresponding wiggle spectra from the data is a challenging and sensitive step which can, on the other hand, be avoided if the broadband is included in the theoretical framework. Models phenomenologically relying on a wide separation of scale, assuming scale-independent bias or sufficient smoothness that could be accounted for by nuisance parameters such as $A(k)$ above, might suffer from overall systematic offsets. Finally, it is also often the case that the nuisance parameters and BAO scaling parameters are not consistent between the configuration-space and Fourier-space analyses (i.e. the two do not form a Fourier transform pair) which could prove problematic if fits in both spaces are combined.

By contrast the Zeldovich calculation above gives a consistent framework for understanding the nonlinear smoothing of the BAO feature, both pre- and post-reconstruction, in both configuration and Fourier space. Roughly speaking, the Gaussian smoothing kernel in the empirical model is replaced by a Lagrangian coordinate-dependent kernel $\exp[-k_i k_j A_{ij}(\mathbf{q})/2]$. One might thus hope to formally extract the model for wiggle-only part as an approximation to the calculation presented in the main body of this chapter; indeed, such a calculation was performed in ref. [402] and extended to terms involving linear bias, redshift space distortions and reconstruction in ref. [112][9]. Figure 4.13 compares the results of our full Zeldovich calculation in the Rec-Sym scheme, with the broadband subtracted out by calculating the corresponding Zeldovich power spectrum using the no-wiggle power spectrum, versus the resummed linear wiggle power spectrum (RWiggle; using the proper exponential damping dependencies given in Appendix D.4), for the same linear bias values and with all higher bias terms set to zero. The two are in excellent agreement, especially in the case of the reconstructed power spectrum, with RWiggle slighly underdamping the BAO wiggles towards small scales compared with the full Zeldovich calculation for the unreconstructed power spectrum.

[9]We note that redshift-space reconstruction model presented in ref. [112] contains phenomenological damping factors that do not capture the exact behaviour of X_{ds} term given by in Equation (4.17). We repeat this calculation and derive the proper damping factors for the wiggle component in Appendix D.4.

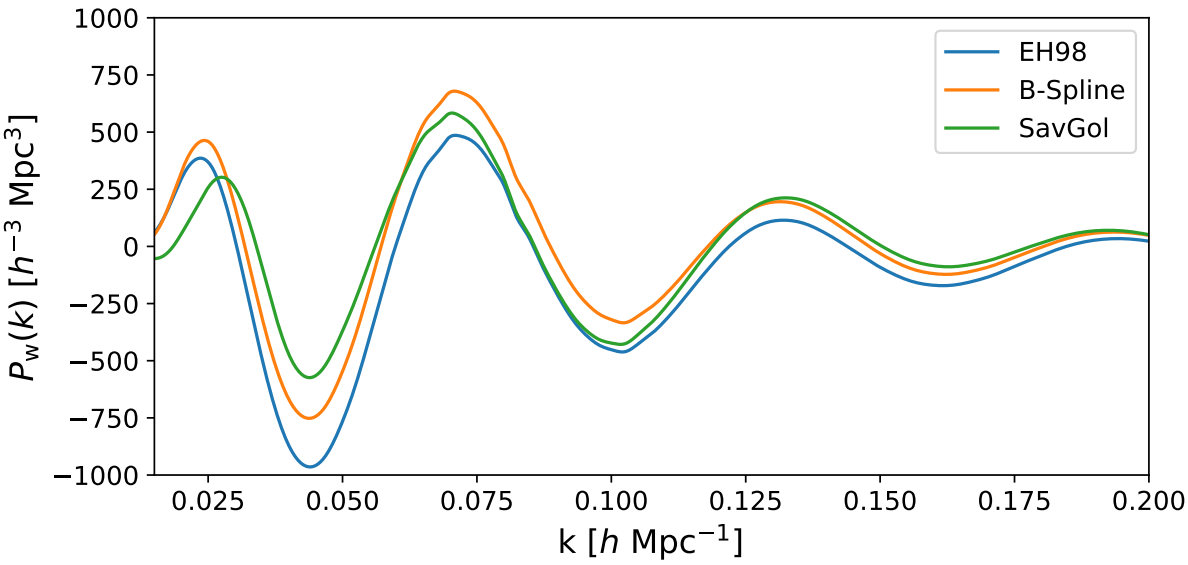

Figure 4.12: The linear wiggle power spectrum for three choices of $P_{\rm nw}$. The conventional choice (EH98 [120]) does not accurately capture the large scale power, and we have investigated two possible methods to mitigate this discrepancy: one based on B-splines, described in ref. [402] and another based on a Savitsky-Golay filter in $\ln(k)$. The wiggle power spectra isolated using these three methods exhibit visibly different oscillatory behavior.

However, even though RWiggle and the full Zeldovich calculation exhibit a high level of agreement on the shape of the wiggle component, the RWiggle method depends on the separation procedure of the wiggle and broadband components while the full Zeldovich calculation requires no such steps. Specifically, the Zeldovich calculation deals only with the combination $P_{\rm w}^{\rm Zel} + P_{\rm nw}^{\rm Zel}$, which is obviously invariant under the split, while RWiggle models only the split-dependent $P_{\rm w}^{\rm Zel}$. This implies that in order to use RWiggle in practical analyses either the broadband part needs to be modeled to equally high accuracy or a highly accurate wiggle extraction procedure is needed in order to guarantee feasible comparison of theoretical model and the data. The latter seems to be a challenging task, potentially subject to systematic offsets and bias. On the other hand, the resulting differences in the wiggle spectrum should still be broadband and could be fit away using nuisance parameters using sufficiently general broadband models.

Finally, our model differs from most in the literature in taking into account higher bias terms such as b_2 and b_s, allowing us to assess systematic effects introduced by assuming scale-independent bias. These higher biases can contribute both significant broadband power (e.g. the top-left panel of Figure 4.10) and modulate the phase and amplitude of BAO oscillations through mode-coupling effects [266]. However, explicit calculation shows that the latter effect is only noticeable at very high values of bias. Figure 4.14 shows the effects on the

wiggle component of adding nonzero quadratic density and shear biases b_2, b_s, for bias values $(b_1, b_2) \approx (5, 20)$ chosen according to the peak-background split (PBS) on a Press-Schechter mass function [292], and assuming $b_s \approx b_2$, as compared to RWiggle. The quadratic density bias, b_2, induces an apparent phase shift towards large k, and can be seen to be essentially out-of-phase with the linear BAO wiggles; however, these out-of-phase contributions are dramatically reduced by reconstruction. By contrast the shear bias, b_s, produces oscillatory features roughly in-phase with the linear theory contributions and is largely unaffected by reconstruction. For completeness, we have also plotted the potential oscillatory contribution of a derivative bias, b_{∇^2}, which modulates the overall amplitude of the power spectrum and is degenerate with the various counterterms, α_{ab}.

To investigate the extent to which the broadband and oscillatory contributions of higher bias terms can be mitigated by a suitable broadband model, we conducted an exploratory "fit" of the redshift-space monopole and quadrupole pre- and post-reconstruction in the case where the truth is given by the Zeldovich approximation including nonzero b_2 and b_s but fit by an empirical model with only b_1, an isotropic BAO scale paramter $\alpha_{\rm BAO}$ and polynomial broadband contributions of the form employed in ref. [45] before reconstruction. Specifically, we assume an empirical model of the form

$$P_{l,\rm fit}(k) = \alpha_{\rm BAO}^{-3} P_{l,b_1}\left(\frac{k}{\alpha_{\rm BAO}}\right) + \frac{a_{1,l}}{k^3} + \frac{a_{2,l}}{k^2} + \frac{a_{3,l}}{k} + a_{4,l} + a_{5,l}k, \tag{4.28}$$

both pre- and post-reconstruction, where P_{l,b_1} denotes redshift-space multipoles in the Zeldovich approximation with all higher biases set to zero. For this exercise we assumed a sample variance limited survey at $z = 0$ and $z = 1.2$ with Gaussian covariances between the monopole and quadrupole, fit up to $k_{\rm max} = 0.25\,h\,{\rm Mpc}^{-1}$ and note that the results are independent of survey volume. In Figure 4.15 we have plotted the resulting shifts in the BAO scale assuming PBS values for b_1 and b_2, taking values for b_s as a function of b_1 from ref. [4]. At $z = 0$, we find that neglecting higher biases in favor of the empirical model induces shifts of less than half a percent in the BAO scale over a wide range of halo masses both pre- and post-reconstruction, though reconstruction more than halves the forecasted shift for essentially all values of bias surveyed (Figure 4.15). At $z = 1.2$ the shifts are further reduced, amounting to less than a tenth of a percent across a wide range of bias values prior to reconstruction and essentially vanishing post reconstruction. These shifts would be well-within the margin of error of both current and next-generation surveys like DESI [108], especially post-reconstruction, suggesting that nonlinearities (e.g. higher bias) in the power spectrum should not hinder accurate recovery of the BAO signal. On the other hand, the value of the linear bias, b_1, was significantly affected by the choice of broadband model, with fits from the empirical model deviating from the true value by more than five percent in many cases.

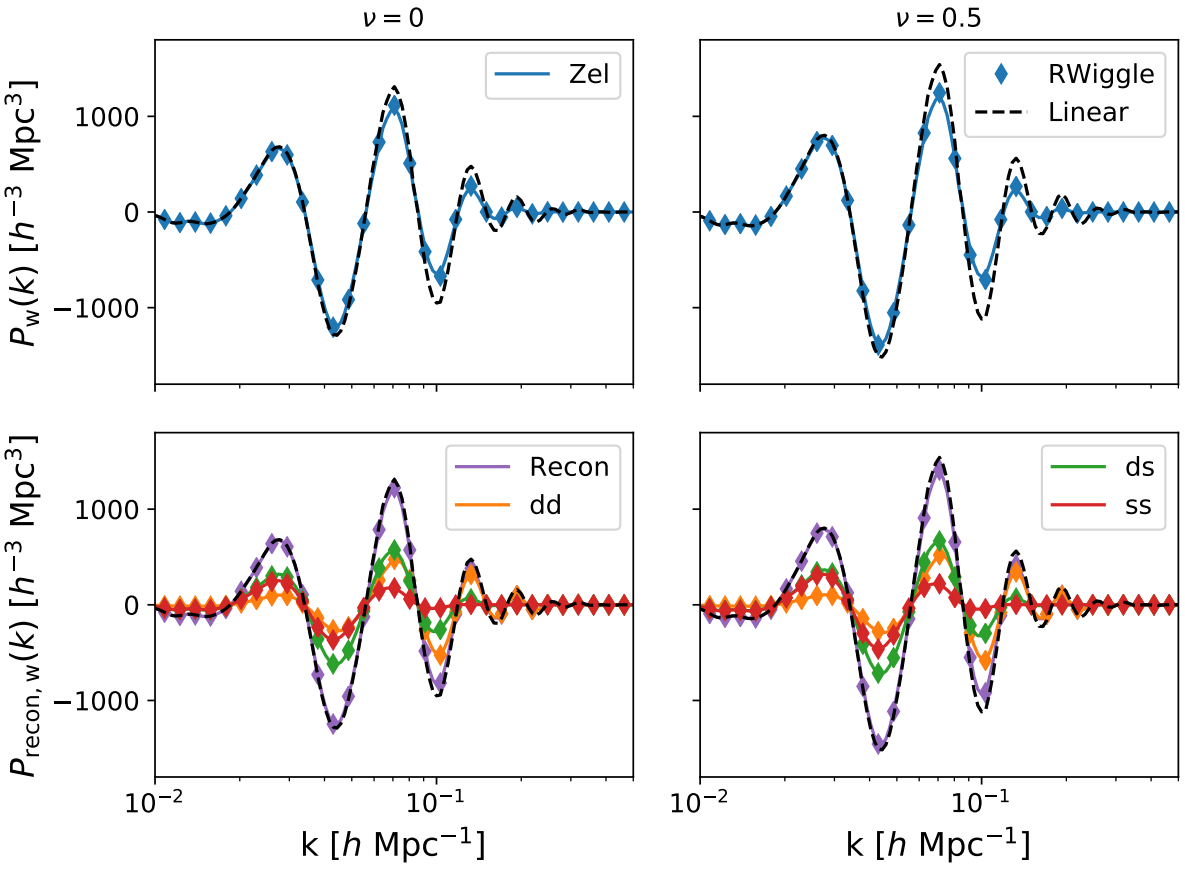

Figure 4.13: Comparison of Zeldovich with IR-resummed linear theory (RWiggle) for reconstructed and unreconstructed spectra at $z = 0$ and $\mu = 0$ and 0.5 with $b_1 = 0.5$ using Rec-Sym with higher biases set to zero. RWiggle slightly under-predicts damping at high k (but see footnote 4), especially for the unreconstructed power spectra.

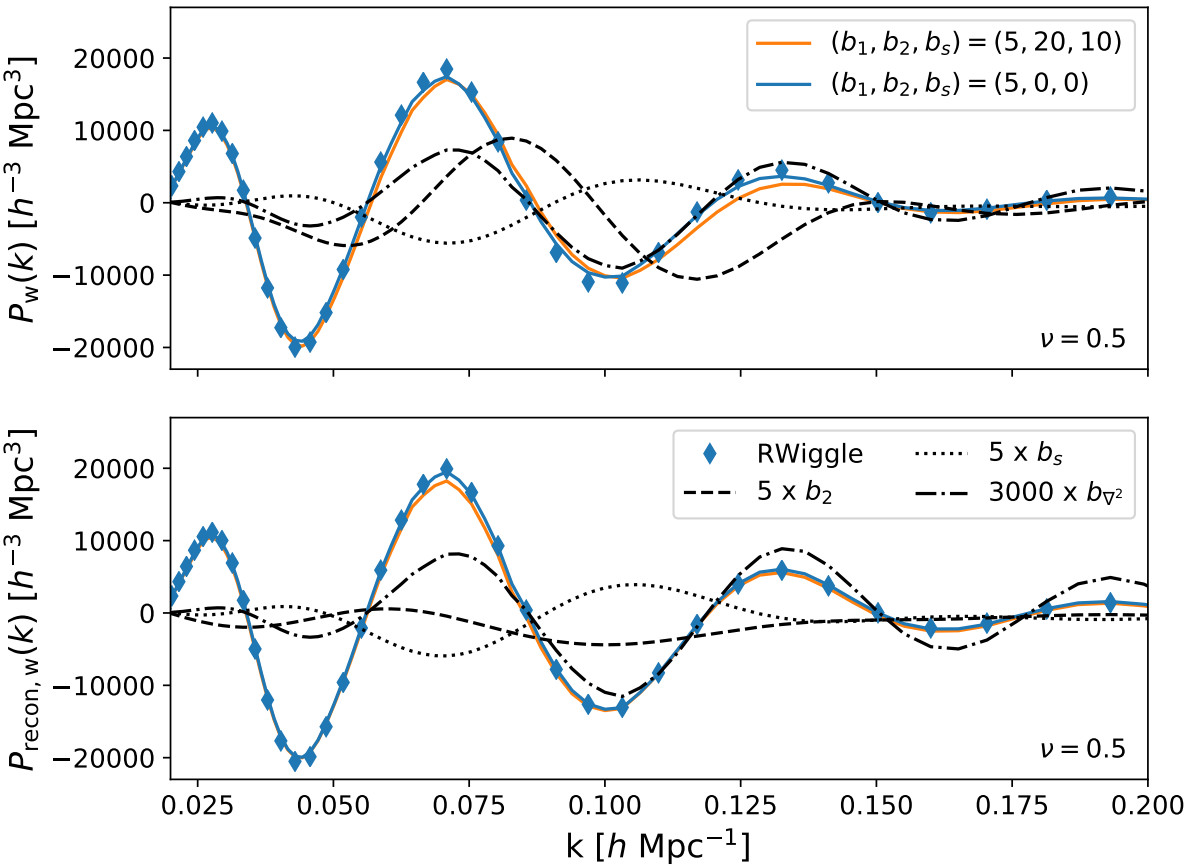

Figure 4.14: The $z = 0$ Zeldovich power spectrum at $\mu = 0.5$, before and after reconstruction using Rec-Sym, shown with and without contributions from the quadratic bias and shear biases when $(b_1, b_2, b_s) = (5, 20, 10)$. For comparison, the RWiggle prediction is shown in the diamond points, and the isolated b_2 contributions are shown as a black dot-dashed line multiplied by a factor of five. For the unreconstructed spectrum, the b_2 contributions (with shear bias set to zero) can be seen to be essentially out-of-phase with the linear theory wiggles and induce a phase shift in the power spectrum. These contributions are greatly reduced in the reconstructed spectrum. The shear contributions, on the other hand, are more-or-less in phase with linear theory and unchanged by reconstruction. For completeness, we have also plotted contributions from a possible derivative bias b_{∇^2}, which modulate the amplitude of the wiggles in a manner growing with wave number.

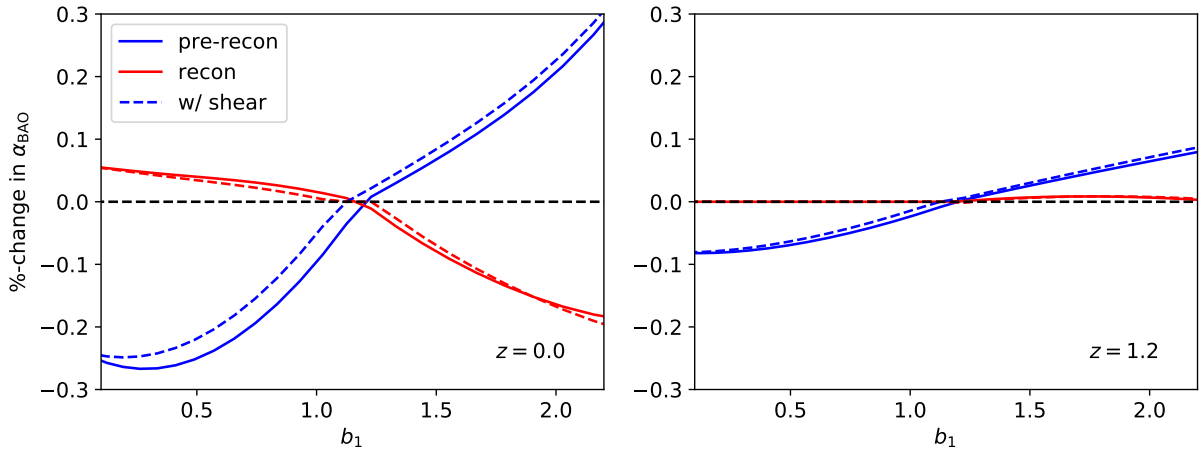

Figure 4.15: Shifts in the recovered isotropic BAO scale, $\alpha_{\rm BAO}$, in redshift space fit using a model with only b_1 nonzero and polynomial broadband contributions in both the monopole and quadrpole, when truth is given by the Zeldovich approximation with nonzero quadratic bias. Values of b_1 and b_2 were chosen according to the peak-background split, while values for b_s were taken from ref. [4]. (Left) Shifts in the BAO scale at $z = 0$. Fitting with the empirical model results in only sub-percent shifts across a wide range of halo masses, which are further more than halved after reconstruction. The solid and dashed lines show the shift with and without the quadratic shear bias b_s, whose effect is subdominant to b_2. (Right) The same shifts calculated at $z = 1.2$. Even prior to reconstruction, fitting with the empirical model results in less than a tenth of a percent shift in the BAO scale over a wide range of biases; after reconstruction the shift due to nonlinear bias becomes essentially zero.

4.9 Conclusions

Baryon acoustic oscillations (BAO) are an important probe of fundamental physics and a prime focus of upcoming surveys such as DESI [108] and EUCLID [211]. The BAO features act as a "standard ruler" whose cosmological evolution is largely immune to astrophysical effects but whose signal-to-noise ratio is lowered by nonlinear structure formation. BAO reconstruction attempts to sharpen the BAO signal by removing some of the nonlinear smearing due to large scale displacements [122]. In this chapter we develop an analytical model, within the Lagrangian perturbation theory framework, to study the algorithm for density-field reconstruction proposed in ref. [122]. Linear Lagrangian perturbation theory (the Zeldovich approximation) provides an excellent description of these nearly linear displacements and BAO smoothing pre-reconstruction [431, 415], making LPT a promising arena within which to model the effects of reconstruction.

We develop a self-consistent framework with which to calculate the two-point statistics of galaxies, employing a consistent set of parameters to fit the power spectrum and correlation functions, pre- and post-reconstruction in real and redshift space. The broad validity of

such LPT models allows for joint fits to the pre- and post-reconstruction two-point statistics enabling e.g. a fit for redshift-space distortions and the linear growth rate, $f\sigma_8$, simultaneously with Alcock-Paczynski distortions constrained by BAO analyses [414]. Based on ref. [398], we derive explicit formulae, to calculate the redshift-space power spectrum within the Zeldovich approximation, both pre- and post-reconstruction, as an infinite series of spherical Bessel transforms. Our model updates the developments for the reconstructed correlation function in ref. [414], and is – as far as we are aware – the first model of reconstruction to include a consistent set of bias terms up to quadratic order, including shear and derivative biases. We show that the oscillatory behavior induced by the quadratic density bias, b_2, are out of phase with the linear BAO feature and greatly reduced post-reconstruction, while those due to the quadratic shear bias, b_s, are in-phase and essentially unchanged. In addition, we show that each multipole moment of the reconstructed power spectrum should be, to lowest order, corrected for by a set of three counterterms each, which perturbatively correct both nonlinear smoothing and broadband power.

We compare our analytic predictions with N-body data from the `DarkSky` simulation [350] at $z = 0$, focusing on halos between $12.5 < \log_{10}(M/M_\odot) < 13.0$. Our base model, involving only b_1 and b_2 and appropriate counterterms, jointly fits the pre-reconstruction real-space power spectrum and redshift-space monopole out to $k = 0.4\,h\,\mathrm{Mpc}^{-1}$, and the quadrupole out to $k = 0.2\,h\,\mathrm{Mpc}^{-1}$, reproducing the oscillatory BAO wiggles in the data with high fidelity. Our model with the same bias parameters performs equally well in configuration space around the BAO scale, though we found it necessary to correct for a large excess in large-scale power encountered in the `DarkSky` data. Utilizing the same values for the bias parameters but allowing counterterms to vary, we find that our model performs similarly in real space post-reconstruction for smoothing scales $R = 15$ and $20\,h^{-1}$Mpc, reproducing both the oscillatory features and broadband past $k = 0.2\,h\,\mathrm{Mpc}^{-1}$, but fails to reproduce the oscillatory features when $R = 10\,h^{-1}$Mpc, likely due to the fact that we have worked to lowest order and at $z = 0$ displacements on that scale are significantly nonlinear. We point out a less severe feature in the residuals at $k = 0.1\,h\,\mathrm{Mpc}^{-1}$ that diminishes with larger smoothing scales which we believe arise from higher order terms and caution that neither our calculation nor the standard reconstruction algorithm take these into account. A more complete, iterative reconstruction scheme (e.g. ref. [318]) may reduce these features. The modeling of these nonlinearities, and possible remedies, are beyond the scope of this chapter, but as an exploratory example we calculate the effects of one possible nonlinearity due to the mapping between Eulerian and Lagrangian coordinates in Appendix D.5.

Our model also predicts the multipole moments of the redshift-space power spectrum and correlation functions in both of the redshift-space schemes (**Rec-Sym** and **Rec-Iso**) we consider. This is critical in order for it to be applied to data, since the most constraining BAO measurements are performed in redshift space. The model provides a good fit to the monopole and quadruople moments of $P(k)$ measured in `DarkSky` in both the **Rec-Sym** and **Rec-Iso** schemes for smoothing scales of $R = 15\,h^{-1}$Mpc or larger (at $z = 0$). Again, for smaller smoothing scales the Zeldovich model differs from the N-body results (as expected). These effects would be smaller at higher redshift, where the theory is more likely to be

applied.

Finally, there exists an extensive literature studying the modeling of reconstruction and the BAO signal, and we compare our model to several existing alternatives. One popular technique, based on ref. [121], is to separate the power spectrum into a smooth "no wiggle" component and an oscillatory "wiggle component," and to damp the latter by an exponential factor fit to simulations while supplementing the former with a polynomial in wavenumber to fit the broadband power. This technique can be more rigorously derived as a particular resummation of the nonlinear contribution of long-wavelength modes much like our Zeldovich calculation itself [402, 112], in which case the damping parameters can be derived theoretically. When the "wiggle" components are isolated we find that the latter is in excellent agreement with our Zeldovich calculation, particularly after reconstruction. In Appendix D.4 we re-derive the IR-resummed "wiggle" power spectrum (RWiggle) directly within our Zeldovich framework, updating the exponential damping for the cross term P^{ds}. We highlight that our Zeldovich framework naturally encompasses broadband effects, while methods depending on wiggle/no-wiggle splitting might be subject to additional systematic offsets and biases. These could originate from the fact that the wiggle/no-wiggle splitting is not unique, and thus relies on correctly predicting the broadband or extracting the corresponding wiggle part from the data to high accuracy. On the other hand, the Zeldovich framework correctly captures broadband power over a large range of scales in addition to reproducing the oscillatory features in the reconstructed power spectrum. In fits to N-body data, we show how counterterms correct the sharpness of the BAO feature and broadband power simultaneously and consistently. Moreover, our model goes beyond linear bias to include quadratic density and shear bias, which we show contribute oscillatory terms to $P(k)$ that vary independently in amplitude and phase.

We close by noting a few avenues for future work. An obvious extension of our model is to include nonlinearities arising both from gravitational clustering and the reconstruction itself (e.g. Appendix D.5). The former may be most easily included in the context streaming models [396, 398], wherein the real-space modifications due to reconstruction and those proportional to the growth rate f can be separately treated as modifications to the statistics of the galaxy density and galaxy density-weighted velocities, respectively, and which in addition have the advantage of resumming biased contributions to redshift-space distortions as well as nonlinear redshift-space phenomena like fingers-of-god. It is, however, not a-priori obvious which type of nonlinearity will present the most significant corrections. Other fruitful avenues would be to investigate the impact of wrong parameters on reconstruction (e.g. refs. [339, 62]) or to update the present treatment to newer reconstruction techniques. Finally, one could investigate the utility of our model for upcoming surveys like DESI [108] or Euclid [211]. These surveys will operate at higher redshifts where our calculations should perform even better, and our model will be a natural arena in which to understand the effects of highly biased tracers and the effects of cosmic evolution (e.g. evolving b and σ_8) on the BAO feature measured in broad redshift bins.

We have publicly released our codes for configuration[10] and Fourier[11] space reconstruction, with the hope that they will be useful to other researchers. We have checked that the Hankel transform of the Fourier space code agrees, term by term, with the configuration space code to better than 1%, except very close to zero crossings.

Acknowledgments

We thank Hee-Jong Seo and Florian Beutler for useful discussions. SC is supported by the National Science Foundation Graduate Research Fellowship (Grant No. DGE 1106400) and by the UC Berkeley Theoretical Astrophysics Center Astronomy and Astrophysics Graduate Fellowship. M.W. is supported by the U.S. Department of Energy and by NSF grant number 1713791. This research used resources of the National Energy Research Scientific Computing Center (NERSC), a U.S. Department of Energy Office of Science User Facility operated under Contract No. DE-AC02-05CH11231. This work made extensive use of the NASA Astrophysics Data System and of the `astro-ph` preprint archive at `arXiv.org`.

[10] https://github.com/martinjameswhite/ZeldovichRecon
[11] https://github.com/sfschen/ZeldovichReconPk

Chapter 5

Applications of IR Resummation I: Relative Baryon-Dark Matter Bias

The next two chapters were originally published as

> Shi-Fan Chen, Emanuele Castorina, and Martin White. "Biased tracers of two fluids in the Lagrangian picture". In: *JCAP* 2019.6, 006 (June 2019), p. 006. DOI: 10.1088/1475-7516/2019/06/006. arXiv: 1903.00437 [astro-ph.CO]
>
> Shi-Fan Chen, Zvonimir Vlah, and Martin White. "Modeling features in the redshift-space halo power spectrum with perturbation theory". In: *JCAP* 2020.11, 035 (Nov. 2020), p. 035. DOI: 10.1088/1475-7516/2020/11/035. arXiv: 2007.00704 [astro-ph.CO]

A heavy focus of the preceding chapters has been the correct treatment of the BAO feature within perturbation theory, particularly through the technique of IR resummation in LPT. As described in the Chapter 1, however, the IR resummation natural to LPT is not specific to the BAO, and unlike the wiggle-no wiggle IR resummation typically used in EPT no specific length scales have to be input to yield to yield the correct behavior. In the next two chapters, we put IR resummation to use in two non-standard cosmological scenarios. In the first chapter, we look at additional terms in the galaxy bias expansion that appear due to residual differences in baryon and dark matter clustering in the present epoch which, due to their origin in recombination era physics, have the potential to bias standard measurements of the BAO. We formulate these effects within LPT and forecast their impact on future experiments when the correct nonlinear damping is taken into account. In the second chapter, we investigate the ability to perturbation theory to model exotic features in the power spectrum due to either non-standard inflationary scenarios or modifications to the expansion history like early dark energy, showing that state-of-the-art EPT and LPT models agree to sub-percent levels in redshift space. We also show that various resummations for power spectrum features with multiple frequencies or nonlinear dispersions follow naturally as saddle-point approximations of the Lagrangian IR resummation.

5.1 Introduction

Observations of the large-scale structure (LSS) of the universe allow us to shed light on areas of physics ranging from galaxy formation and evolution to fundamental physics. A prime target of present and future LSS surveys is the measurement of baryon-acoustic oscillations (BAO) – the imprints of sound waves in the baryon-photon fluid observed in the cosmic microwave background (CMB) on the observed clustering of galaxies – which can be used as a standard ruler to constrain the expansion of the universe [410]. Upcoming surveys such as DESI [108], EUCLID [12] and WFIRST [117] will provide BAO measurements with higher-than-ever precision, and even more futuristic BAO surveys such as a Stage II 21-cm experiment [90] have been proposed. These next-generation observational campaigns will require us to model the LSS with unprecedented accuracy, at the sub-% level.

One area of recent interest in the field of LSS has been in accounting for the effects induced by the existence of multiple species (cold dark matter, baryons, neutrinos), with similar but distinct clustering properties, using analytic methods. Studies of the perturbative approach to structure formation have traditionally grouped all nonrelativistic species into a "total matter" fluid, whose gravitational collapse is the dominant source of structure on cosmological scales in the late-time universe, but many authors have recently extended these techniques to include neutrinos [309, 343, 49, 66, 334] and baryons [98, 356, 380, 40, 217, 316, 317] in the Eulerian framework of Standard Perturbation Theory (SPT). In parallel, the response of galaxy and halo formation to the existence of multiple fluid species has also been subject of extensive investigation [98, 427, 65, 222, 252, 51, 316, 317]. Of particular interest are the present-day imprint of relative perturbations between baryons and dark matter on large scales which, being seeded in the same epoch and at the same scales as the baryon acoustic oscillations, has the potential to confound future BAO measurements [98, 51, 43, 351]. While these relative perturbations do not grow significantly in time (and relative velocities in fact decay) and are thus small compared to the total-matter growing mode at late times, they amount to coherent supersonic flows post-recombination and could have significant effects on the formation of the first halos and galaxies [380, 98], which are the progenitors of the objects we observe today.

The goal of this work is to formulate perturbation theory and galaxy bias in the presence of multiple fluids within the Lagrangian framework, with a particular focus on the two-fluid baryon-dark matter scenario. Our work is a direct extension of the aforementioned SPT calculations. While Lagrangian Peturbation Theory (LPT) is order-by-order equivalent to SPT, it seamlessly allows a consistent treatment of large scales bulk flows, which are responsible for the final shape and position of the BAO features in the correlation functions or power spectrum [264, 340, 232, 415, 290, 402, 333]. The theory can also be extended to handle density field 'reconstruction' [122, 266, 257, 414, 339]. These features make LPT a natural language for investigating possible distortions to the BAO feature.

This paper is organized as follows. In Section 5.2, we introduce the linear Lagrangian equations of motion and discuss the role of non-gravitational forces such as Compton drag with the CMB. Modifications to Lagrangian galaxy bias and advection in the two-fluid limit

are then introduced in Section 5.3. In Section 5.4, we employ the results of the preceding two sections and calculate the lowest-order two-fluid corrections to the galaxy power spectrum in the Zeldovich approximation. Cross spectra and subtleties in the IR resummation are briefly discussed in Section 5.4.2. In Section 5.5 we take up whether the calculated two-fluid corrections can significantly bias BAO measurements, arguing that any such biases can be mitigated by simultaneously fitting for these easily-characterizeable effects. Our conclusions are summarized in Section 5.6.

5.2 Linear Equations of Motion in Lagrangian Space

In the Lagrangian picture, fluid dynamics is encoded in the displacements $\Psi_\sigma(q)$ of fluid elements of each species, σ, originally situated at Lagrangian positions $\mathbf{q}$, such that their Eulerian positions at conformal time τ ($d\tau = a^{-1}dt$) are given by [431, 415, 39]

$$\mathbf{x}_\sigma(\mathbf{q},\tau) = \mathbf{q} + \mathbf{\Psi}_\sigma(\mathbf{q},\tau). \tag{5.1}$$

The subscript $\sigma = \{c, b\}$ denotes the species, either cold dark matter (CDM) or baryons, respectively, whose motion we are tracking. Assuming that initial displacements are infinitesimally small compared to those at the redshifts of interest, the overdensity, δ_σ, of each species at Eulerian position x can be solved for via mass conservation

$$1 + \delta_\sigma(\mathbf{x},\tau) = \int d^3q\, \delta_D(\mathbf{x} - \mathbf{q} - \mathbf{\Psi}_\sigma(\mathbf{q},\tau)) = \int d^3q\, \frac{d^3k}{(2\pi)^3}\, e^{i\mathbf{k}\cdot(\mathbf{x}-\mathbf{q}-\mathbf{\Psi}_\sigma(\mathbf{q},\tau))}, \tag{5.2}$$

where δ_D is the Dirac delta function. Taylor expanding to first order in displacements yields the familiar result that $\delta_\sigma(x) = -\nabla\cdot\mathbf{\Psi}_\sigma(q)$, but, as seen in Equation 5.2, one feature of working in the Lagrangian picture is that the translation into Eulerian quantities, such as the density field, invariably involves nonlinear combinations of $\mathbf{\Psi}$ even when only the linear equations of motion are considered.

5.2.1 General Formalism

While CDM particles by assumption experience only the gravitational force, baryons are subject to non-gravitational effects, such as Compton drag and pressure gradients. These effects can be summarized in the equations of motion of the fluid elements

$$\begin{aligned}\ddot{\mathbf{\Psi}}_c + \mathcal{H}\dot{\mathbf{\Psi}}_c &= -\nabla_x\Phi(\mathbf{q} + \mathbf{\Psi}_c)\\ \ddot{\mathbf{\Psi}}_b + \mathcal{H}\dot{\mathbf{\Psi}}_b &= -\nabla_x\Phi(\mathbf{q} + \mathbf{\Psi}_b) + \mathbf{F}_b(\mathbf{q} + \mathbf{\Psi}_b),\end{aligned} \tag{5.3}$$

where overdots signify derivatives with respect to τ, $\mathcal{H} = d\ln a/d\tau$ is the conformal Hubble parameter, $\mathbf{F}_b$ is the non-gravitational force per unit mass felt by baryons, and Φ is the gravitational potential at Eulerian position x satisfying Poisson's equation

$$\nabla_x^2\Phi(\mathbf{x},\tau) = \frac{3}{2}\Omega_m(\tau)\mathcal{H}^2(\tau)\delta_m(\mathbf{x},\tau), \tag{5.4}$$

where Ω_m is the total matter mass density and δ_m is the total matter overdensity (see below).

At the linear level, there is no difference between the Eulerian and Lagrangian positions in the above equations of motion, and we will neglect this distinction in the rest of this section unless otherwise stated. Indeed, taking the divergence of Equation 5.3 in the linear limit ($x_\sigma \approx q$) directly yields the Euler equation when we map overdensities to displacements and velocities to their derivatives:

$$\delta_\sigma(\mathbf{x}_\sigma) \leftrightarrow -\nabla \cdot \mathbf{\Psi}_\sigma(\mathbf{q}) \quad , \quad \mathbf{v}_\sigma(x_\sigma) \leftrightarrow \dot{\mathbf{\Psi}}_\sigma(\mathbf{q}). \tag{5.5}$$

Note that the first mapping is correct only to linear order, while the second one is exact if the full $\mathbf{x}(\mathbf{q})$ is used. Assuming this translation, the solutions to the Lagrangian equations of motion as described below are essentially identical to those extracted from Boltzmann codes such as CAMB [220] or CLASS [48], provided one chooses post-recombination initial conditions for the Lagrangian displacements.

To solve Equation 5.3 in the linear limit, it is convenient to rewrite the baryonic and CDM displacements in terms of a mass-weighted matter component ($\mathbf{\Psi}_m = w_c\mathbf{\Psi}_c + w_b\mathbf{\Psi}_b$), which sources the gravitational potential, and a relative component that characterizes the differential flows between baryons and CDM ($\mathbf{\Psi}_r = \mathbf{\Psi}_b - \mathbf{\Psi}_c$), where we have defined the mass fractions of each species, $w_\sigma = \rho_\sigma/\rho_m$. These are related to the Eulerian quantities $\delta_m = w_b\delta_b + w_c\delta_c$ and $v_r = v_b - v_c$ by $\delta_a = -\nabla \cdot \mathbf{\Psi}_a$ and $v_a = \dot{\mathbf{\Psi}}_a$, where $a = \{m, r\}$, again at the linear level. The equations of motion in terms of these components are

$$\ddot{\mathbf{\Psi}}_m + \mathcal{H}\dot{\mathbf{\Psi}}_m = -\nabla\Phi + w_b\mathbf{F}_b \tag{5.6a}$$

$$\ddot{\mathbf{\Psi}}_r + \mathcal{H}\dot{\mathbf{\Psi}}_r = \mathbf{F}_b. \tag{5.6b}$$

If in addition non-gravitational forces are negligible, the matter and relative components decouple, such that Equation 5.6a can be solved as

$$\mathbf{\Psi}_m(\tau) = -\mathbf{m}_+ D_+(\tau) + \mathbf{m}_- D_-(\tau) \approx -\mathbf{m}_+ D_+(\tau) \quad , \tag{5.7}$$

where D_+ is the usual linear-theory growth factor. In the last step we have neglected the decaying mode, $\mathbf{m}_-$, since it is a tiny fraction of the total displacement at all redshifts of interest. For non-gravitational forces, like Compton drag or pressure gradients, direct integration of the linear equations of motion show that the non-gravitational terms make a negligible contribution to the matter component $\mathbf{\Psi}_m$, such that the transfer function at redshifts below $z = 6$ agree with the linear solution in Equation 5.7 to within 0.2%, with even better agreement at the lower redshifts of interest in this section. In the above we have included a minus sign for convenience such that $\delta_{m,0} = \nabla \cdot \mathbf{m}_+$.

We end this subsubsection by discussing the full solution of the relative displacement when $\mathbf{F}_b = \mathbf{F}_b(\tau)$ is independent of $\mathbf{\Psi}_r$. In this case Equation 5.6b is linear and first order in $\dot{\mathbf{\Psi}}_r$ and can be solved as:

$$\dot{\mathbf{\Psi}}_r(\tau) = \mathbf{v}_r(\tau_i)\left(\frac{a_i}{a}\right) + \frac{1}{a}\int_{\tau_i}^{\tau} d\tau' \; a(\tau')\mathbf{F}_b(\tau'), \tag{5.8}$$

where we have set the boundary conditions at initial time τ_i assuming the non-gravitational effects encoded in F_b do not turn on until $\tau > \tau_i$. Equation 5.8 turns out to be an excellent approximation for the large-scale Compton drag electrons experience in the reionization era due to their relative motion with respect to the CMB rest frame, $\mathbf{F}_b = -n_e\sigma_T(\rho_\gamma/\rho_b)a\mathbf{v}_b$, where σ_T is the Thompson scattering cross section, ρ_γ is the photon energy density and n_e the free electron number density. Eq. (5.8) also applies baryonic pressure forces on small scales $\mathbf{F}_b \propto -\nabla\delta_b$— in both cases the total-matter component may be substituted for the baryonic component (i.e. $\delta_b \approx \delta_m$) at the sub-percent level [317]. In the case of the large-scale Compton drag, assuming $\mathbf{v}_b \simeq \mathbf{v}_m$ yields

$$\dot{\mathbf{\Psi}}_r(\tau) = \dot{\mathbf{\Psi}}_r(\tau_i)\frac{a(\tau_i)}{a(\tau)} + \left[\frac{1}{a}\int_{\ln(a(\tau_i))}^{\ln(a(\tau))} d\ln(a')\left(n_e(a')\sigma_T\frac{\rho_\gamma(a')}{\rho_b(a')}\right)\frac{f(a')D_+(a')}{a'^2}\right]\frac{\mathbf{\Psi}_m(\tau_i)}{D_+(\tau_i)}\,, \quad (5.9)$$

with $f = dD_+/d\ln(a)$ the linear theory growth factor. The Compton drag thus induces a mixing between the matter and relative components through a numerical prefactor dependent only on the linear growth factor D_+ and reionization history via n_e. Finally, we can integrate 5.9 to yield

$$\mathbf{\Psi}_r(\tau) = -\mathbf{r}_+ + \mathbf{r}_- D_r(\tau,\tau_i) + \mathbf{m}_+ D_{\rm CD}(\tau,\tau_i), \qquad D_r(\tau,\tau_i) = \int_{\tau_i}^{\tau}\frac{H_0 d\tau'}{a(\tau')} \quad (5.10)$$

where we can identify $\mathbf{\Psi}_r(\tau_i) = -\mathbf{r}_+$, $a(\tau_i)\mathbf{v}_r = H_0\mathbf{r}_-$, and the Compton-drag kernel $D_{\rm CD}$ is defined as the conformal time integral of the square-bracketed function in 5.9. The linear solutions to both the total-matter and relative components are thus wholly specified by the three modes $\mathbf{m}_+$ and $\mathbf{r}_\pm$. Jeans instabilities and baryonic pressure forces affect much smaller scales and won't be further discussed in the remainder of this work.

5.2.2 Initial conditions and transfer functions

The linear evolution of the density and velocity contrasts can be easily written in terms the CDM and baryon linear transfer functions (output from, e.g. CAMB) as

$$T_{\delta_r}(k) \equiv T_{\delta_b}(k) - T_{\delta_c}(k) \quad \text{and} \quad T_{\theta_r}(k) \equiv T_{\theta_b}(k) - T_{\theta_c}(k) \quad (5.11)$$

where $\theta_{b,c}(k) \equiv -\dot{\delta}_{b,c}(k)$. It is worth noticing that while the velocity field is gauge dependent, velocity differences are not. The transfer function for $\nabla\cdot\mathbf{m}_+$ is simply the present-day matter transfer function T_m and we can furthermore define

$$\begin{aligned} T_{\nabla\cdot\mathbf{r}_+}(k) &\equiv T_b(k,z_i) - T_c(k,z_i) \\ T_{\nabla\cdot\mathbf{r}_-}(k) &\equiv [(1+z_i)H_0]^{-1}\Big(T_{\theta_b}(k,z_i) - T_{\theta_c}(k,z_i)\Big). \end{aligned} \quad (5.12)$$

These three functions specify the solution for the $\mathbf{\Psi}_m$, $\mathbf{\Psi}_r$ and $\dot{\mathbf{\Psi}}_r$ at any $z < z_i$. The choice of z_i is somewhat arbitrary but choosing redshifts before the onset of reionization has the

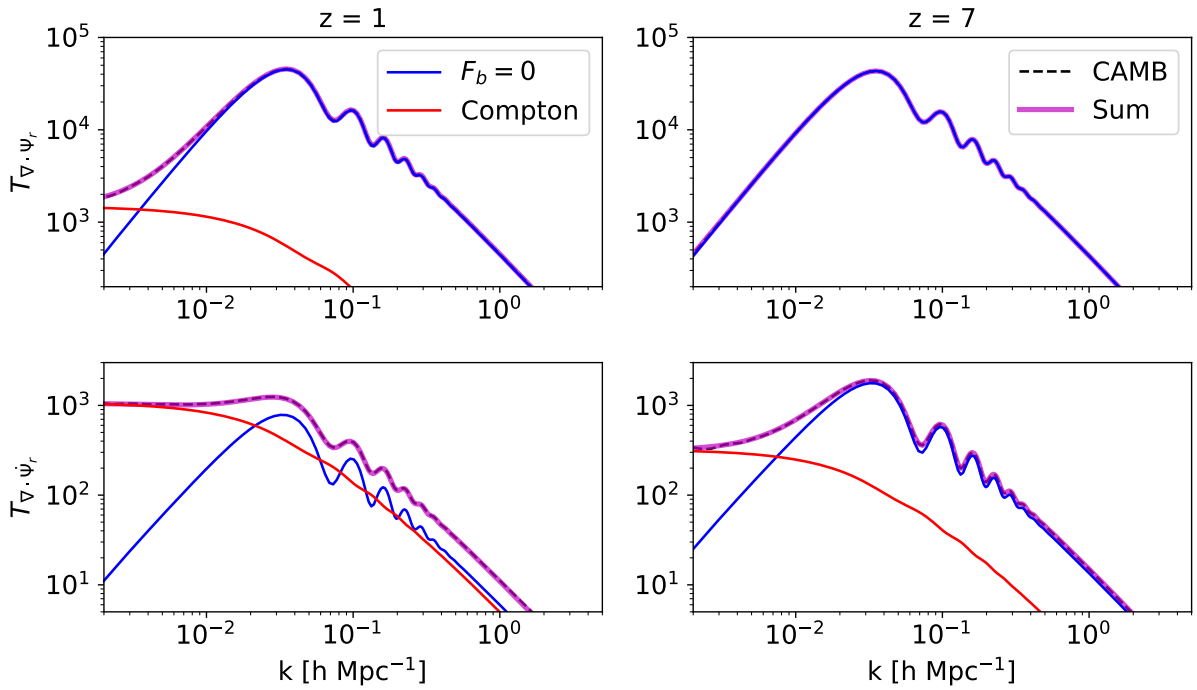

Figure 5.1: Transfer functions for the relative component from Equation 5.13 at $z = 1$ (left column) and $z = 7$ (right column). These transfer functions solve Equation 5.8. The top row shows the transfer functions for $\nabla\cdot\boldsymbol{\Psi}_r$, i.e. the relative density. The bottom row shows the transfer functions for $\nabla\cdot\dot{\boldsymbol{\Psi}}_r$, i.e. the relative velocity divergence. The free-falling ($F_b = 0$) and Compton drag contributions are shown separately, the effect of Compton drag on the relative velocity is immediately apparent even right after reionization ($z_{\rm re} = 7.90$) at $z = 7$, whereas the relative displacement is dominated by the $F_b = 0$ contribution at all but the largest scales shown. Unlike the Compton contribution, which is flat at large scales, the primordial ($F_b = 0$) contributions fall off as k^2 towards low wavenumbers, reflecting the origin of relative perturbations in pre-recombination baryonic pressure forces. At low redshifts, the solutions to the Lagrangian equations of motion, with initial conditions set at $z_i = 20$, are in excellent quantitative agreement with the results from CAMB (black dashed lines, barely visible on the plot as they lie below the purple lines).

advantage of separating the effects of gravity from Compton drag. This choice also justifies the normalization in Eq. (5.12), since $\mathbf{r}_-$ is independent of redshift. In the remainder of the paper we assume $z_i = 20$.

In addition to the above, we will show below that calculating the power spectrum at some redshift z in the Lagrangian picture requires linear-theory spectra of the relative displacement at that redshift, which will typically include corrections from Compton drag. These can be calculated via Equations 5.7 and 5.8 to give

$$T_{\nabla\cdot\boldsymbol{\Psi}_r}(k,z) = T_{\nabla\cdot\mathbf{r}_+}(k) + D_r(z,z_i)T_{\nabla\cdot\mathbf{r}_-}(k) + D_{\rm CD}(z,z_i)T_{\nabla\cdot m_+}(k). \tag{5.13}$$

Sample solutions of the equation of motion in Eq. (5.6) when F_b is given by Compton drag with the CMB are shown in Figure 5.1. After reionization most of large scale power in the relative velocity transfer function, $T_{\nabla\cdot\dot{\boldsymbol{\Psi}}_r}$, is provided by the Compton drag, which in turn affects the evolution of the relative baryon-dark matter density at large scales (see top panels in Figure 5.1). Figure 5.1 also justifies the approximations we used to compute the drag forces, as one can see by the excellent agreement with the full CAMB output. Other non-gravitational effects like pressure terms (Jeans instability) and radiative transfer effects [289, 147, 382, 56], can be written in a similar form.

Ratios of the transfer functions to the total matter one are shown in Figure 5.2. We notice that the relative density perturbation is much larger than the relative velocity one, by a factor of a hundred at least, and the two relative components have the same behavior with wave-number k at small and large scales. Nonetheless $\mathbf{r}_+$ and $\mathbf{r}_-$ have significant differences in shape around the BAO scales and therefore will have to be treated separately from the point of view of the galaxy bias expansion.

5.3 Lagrangian Bias in the Two-Fluid Dynamics

In the Lagrangian approach, galaxy bias is assumed to arise as the response of the overdensity of galaxies, or the precursors thereof, to the variation of the initial conditions encoded in the fields $\{\boldsymbol{\Psi}_\sigma(\mathbf{q})\}$ of the various species, and then transported via advection to their present-day positions $\mathbf{x}(q,t) = \mathbf{q} + \boldsymbol{\Psi}_g(\mathbf{q},t)$. Thus, when computing the density of a biased tracer the number-conservation Equation 5.2 is modified to

$$1 + \delta_g(\mathbf{x},\tau) = \int d^3q\; F_g[\mathbf{q}|\,\{\boldsymbol{\Psi}_\sigma(\mathbf{q})\}]\,\delta_D\left[\mathbf{x} - \mathbf{q} - \boldsymbol{\Psi}_g(\mathbf{q},\tau)\right]. \tag{5.14}$$

The standard picture of (local) Lagrangian bias, outlined above, has been developed in the 1-fluid case by many authors, see for example [68, 231, 229, 20, 111, 67, 242, 396, 322] and [109] for a recent review on galaxy bias. In this section our focus will be on extending these arguments to the case of multiple fluids, and in particular to the two-fluid case. In the presence of two fluids, the form of Equation 5.14 raises two questions: (1) the form of the response F_g and (2) whether biased tracers follow the dark matter, baryons, or a combination thereof. We address these in turn.

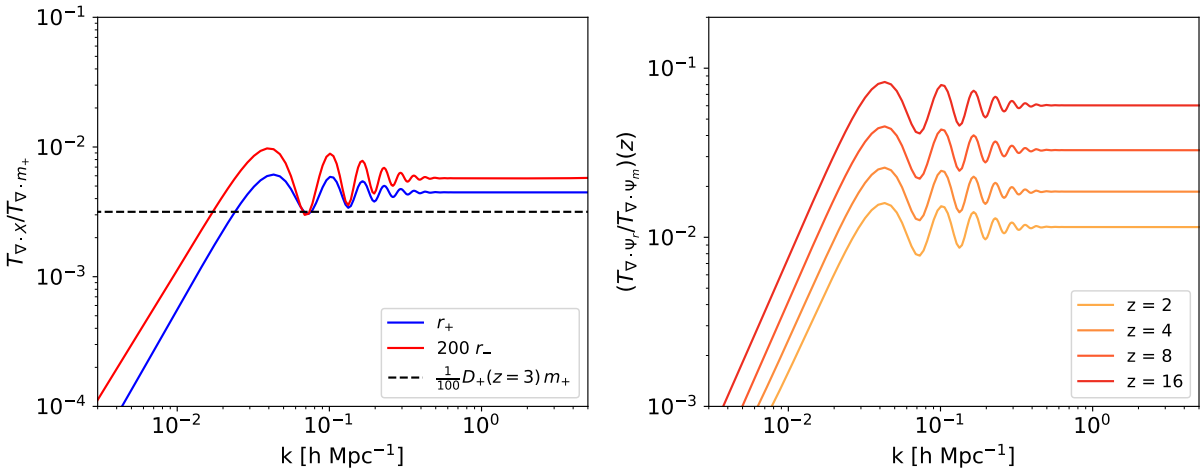

Figure 5.2: Relative to total-matter-component transfer function ratios. (Left) Transfer function ratios between the initial fields m_+ and $r_\pm$ defined at $z = 20$. The so-normalized constant r_+, which roughly corresponds to the relative overdensity mode, is a percent level contribution relative to the total-matter growing mode m_+. The decaying mode r_-, which corresponds roughly to the relative velocity, enters at significantly below the percent level. Note however that our definition somewhat exaggerates its smallness by "redshifting" it to $z = 0$. The equivalent ratio for one percent of the growing mode at $z = 3$ is plotted for comparison in black. (Right) Transfer function ratios between the evolved relative and total matter displacements at redshifts $z = 2 - 6$. While the relative displacement is a percent level effect at low redshifts ($z = 2$), it enters at close to the ten percent level at higher redshifts ($z = 16$).

5.3.1 Bias Expansion

The initial tracer overdensity, $F_g[\mathbf{q}|\,\{\mathbf{\Psi}_\sigma(\mathbf{q})\}]$, is defined to be a functional encoding the physics of gravitational collapse and galaxy formation at some Lagrangian position $\mathbf{q}$. Since the galaxy density field is a scalar quantity under rotations, F_g will also be a scalar. We will assume this functional is local, in the sense gravitational collapse depends only on the value of the fields within a characteristic patch of size R_h, which then flows coherently on large scales with $\mathbf{\Psi}_g$ [109]. In the fluid limit, these conditions imply that the system is wholly specified – albeit in some complex, nonlinear way – by the species overdensities, $\delta_\sigma(\mathbf{q})$, velocities, $\mathbf{v}_\sigma(\mathbf{q})$, and the gravitational potential[1], $\Phi(\mathbf{q})$, at some initial time τ_i. The condition that F_g is local – or rather, nonlocal with width R_h – can be equivalently (but more conveniently) expressed by requiring F_g depend only on the initial fields and their spatial derivatives, with n^{th} derivatives suppressed by n powers of R_h [109].

[1]The gravitational potential Φ, while not independent of δ_m, depends on the total matter density in a very non-local way. To make our bias expansion local, and be able to truncate the derivative expansion at a reasonable order, we thus include it as a standalone quantity here.

In addition to the assumption of locality, the form of F_g is strongly restricted by various symmetries. General relativity requires that all physical quantities be diffeomorphism invariant, which in our case reduces to rotational invariance and invariance under generalized Galilean transformations [179]:

$$\mathbf{q} \to \mathbf{q} \quad , \quad \mathbf{\Psi}_\sigma \to \mathbf{\Psi}_\sigma + \mathbf{n}(\tau) \quad , \quad \Phi \to \Phi \to \Phi - \mathbf{x} \cdot (\ddot{\mathbf{n}} + \mathcal{H}\dot{\mathbf{n}}) \quad , \tag{5.15}$$

where $\mathbf{n}$ are time-dependent but spatially constant vector fields.

Rotational invariance simply requires that only contracted scalar quantities enter the bias; the restrictions placed on the bias expansion by general Galilean invariance are more subtle, and it is here that the two-fluid case diverges from the single-fluid case. Under this symmetry, densities remain unchanged— for instance that at first order $\delta_\sigma(\mathbf{q}) = -\nabla \cdot \mathbf{\Psi}_\sigma(\mathbf{q})$— while velocities get boosted by a spatially constant amount (leaving $\partial \mathbf{v}$ invariant) and the gravitational potential changes in a spatially linear way (leaving $\partial\partial\Phi$ invariant). In the single-fluid regime, where only one set of densities and velocities exist, this directly implies that velocities can only enter with at least one spatial derivative, and the gravitational potential can only enter as second (spatial) derivatives and beyond. The single-fluid overdensity, which is unchanged under the transformation, can enter at any order.

The presence of two or multiple fluids relaxes some of the above restrictions. In particular, since all particle velocities are boosted by the same amount ($\mathbf{n}'$) under a Galilean transformation, the relative velocity $\mathbf{v}_r = \mathbf{v}_b - \mathbf{v}_c$ remains invariant and can thus enter the bias expansion at zeroth order in derivatives. The total matter velocity, $\mathbf{v}_m$, on the other hand, is boosted and can thus still only enter at the derivative level. These two quantities form an equivalent basis to the individual species velocities and there is no loss of generality in defining the bias expansion in terms of them. We may similarly write terms involving species densities, which can enter separately, in the total matter and relative density basis. In general relativity the gravitational potential is unaffected by the number of species as a consequence of the equivalence principle, *i.e.* gravitational interactions are universal. The full set of physical fields that can enter F_g in the two fluid case is then

$$F_g = F_g\left[\delta_\sigma, \mathbf{v}_\sigma, \Phi\right] \equiv F_g\left[\delta_m, \delta_r, \partial\mathbf{v}_m, \mathbf{v}_r, \partial\partial\Phi, \cdots\right], \tag{5.16}$$

where the dots stand for higher derivative operators. To first order in the fields we can therefore write[2]

$$1 + \delta_g(\mathbf{q}) = 1 + b_1\delta_m + b_r\delta_r + b_\theta\theta_r + \cdots \tag{5.17}$$

which is similar to the Eulerian linear theory expression in [316]. This is not surprising, since at first order $\mathbf{q} \simeq \mathbf{x}$, however we will see below that differential advection can introduce further terms degenerate with the initial Lagrangian bias terms above, such that the Eulerian relative-component bias will in general be a combination of these terms. Note that in this chapter "m" refers to the linear matter mode and not the nonlinear matter density.

[2] A list of bias terms up to second order is given in Appendix E.2.

Finally, since F_g is defined as a functional on the initial conditions which can be chosen to be sufficiently early that they lie deep in the linear-theory regime, its form can be further simplified and expressed purely in terms of the initial modes $\mathbf{m}_+$ and $\mathbf{r}_\pm$. In the single fluid case, this restriction leads to the simplification that all bias terms can be written in terms of spatial derivatives of the total matter displacement $\mathbf{m}_+ \sim \mathbf{\Psi}_m$; this is a direct consequence that, up to time-dependent constant factors, $\delta_m \sim \partial\mathbf{\Psi}_m$, $\mathbf{v}_m \sim \mathbf{\Psi}_m$ and $\partial\partial\Phi \sim \partial\mathbf{\Psi}$ in linear theory. In the two-fluid case these terms must be supplemented by those involving the relative modes. Specifically, including the $\mathbf{v}_r$ dependence requires the inclusion of terms proportional to $\mathbf{r}_-$ and including δ_r dependence similarly requires terms proportional to $\nabla \cdot \mathbf{r}_+$. Equation 5.17 can thus be re-expressed as:

$$F_g(\mathbf{q}) = b_1\delta_m + b_+\nabla\cdot\mathbf{r}_+ + b_-\nabla\cdot\mathbf{r}_- + \ ... \tag{5.18}$$

We therefore have a direct correspondence in the bias expansion between the initial modes expressed in Eulerian and Lagrangian space. Notice that the bias expansion defined above is complete, in the sense that it contains all possible operators compatible with the symmetries of the problem. In particular, while $\mathbf{r}_\pm$ are defined at a particular initial redshift z_i, in the linear regime this dependence amounts to a simple linear transformation and can be absorbed into the definition of the bias parameters (Appendix E.1).

Finally, an additional complication arises when halo formation is affected by Compton drag. As pointed out by [317], by picking out the local CMB rest frame such that the drag force $\propto \mathbf{v}_b$, we lose the gauge redundancy of Galilean transformations. This will in general produce heretofore forbidden terms such as those proportional to the matter-component velocity $\mathbf{v}_m$. However, the terms thus generated are required by rotational invariance to enter at second order and beyond. For the remainder of this section we will thus neglect these contributions, which are subdominant to the already sub-percent level contributions we study.

Whereas there exists quite a large literature on measuring and predicting, using approximate physical models, the value of the bias parameters in one-fluid scenarios, less attention has been devoted to the multi-fluid case. From an effective field theory perspective the dimensionless parameters should be of order unity, but in reality the actual value of the bias parameters is tracer-dependent and can be quite a bit larger or smaller. In this work we will assume, unless otherwise noted, that typical values are given by $b_+ \simeq 1$ and $b_- \simeq 6.8$ derived in [316] using a spherical collapse model. These numbers are consistent with the non-detection of relative bias effects in BOSS DR12 by ref. [43], who find e.g. $b_+ = -1.0 \pm 2.5$ to within one sigma when fitting for b_+, b_- and c_- (Section 5.4.3) across all redshift bins, with large systematic biases measured in dark-matter only simulations that had to be subtracted.

5.3.2 Modifications to Tracer Advection

Once the initial, biased tracer overdensity is set, the overdensity at later times is set by the tracer "fluid" advecting from initial (Lagrangian) q to final positions $q + \mathbf{\Psi}_g$ along trajectories described by the tracer equation of motion

$$\ddot{\mathbf{\Psi}}_g + \mathcal{H}\dot{\mathbf{\Psi}}_g = -\nabla\Phi + \mathbf{F}_{b,g}, \tag{5.19}$$

where we have included a non-gravitational term, $F_{b,g}$, to account for the possibility that tracers feel non-gravitational forces. Such non-gravitational contributions may arise, for example, from the Compton drag on the baryonic component of galaxies, or from various galaxy formation processes. Since such contributions are always local in space and time, we will assume the above equation satisfies the same symmetries of Eq. (5.15), *i.e.* the force acting on galaxies depends only on density fields and velocity gradients.

Equation 5.19 can be solved by subtracting the equation of motion of the total matter displacement (Equation 5.6a) and defining $\mathbf{\Psi}_{r,g} = \mathbf{\Psi}_g - \mathbf{\Psi}_m$. Neglecting the baryonic contributions such that the tracers' dynamics are governed only by gravity, and assuming that the initial tracer displacements are a weighted average of the baryonic and CDM displacements, i.e. $\mathbf{\Psi}_{g,i} = \mathbf{\Psi}_{m,i} + f_g \mathbf{\Psi}_{r,i}$, this immediately yields the time evolution

$$\mathbf{\Psi}_g(\tau) = \mathbf{\Psi}_m(\tau) + f_g[\mathbf{\Psi}_r(\tau)]_{\mathrm{CD}=0}, \tag{5.20}$$

where the relative displacement is evaluated assuming zero Compton drag. Note that if we assume that the tracer field is made of objects composed of the same mass fractions of baryons and CDM as the total matter content of the universe, i.e. with $f_g = 0$, Equation 5.20 reduces to the trajectory of the matter component. Similarly, objects composed purely of baryons or the CDM will (at the linear level) follow the baryon or CDM displacements, respectively.

We can alternatively think of Eq. (5.20) as a bias expansion of the galaxy displacements in terms of the underlying fields, since $\mathbf{\Psi}_m$ and $\mathbf{\Psi}_r$ are the only two linear operators allowed by symmetries at lowest order in spatial derivatives. If the tracer flow is purely gravitational, as assumed above, the equivalence principle further restricts the coefficient of the total matter displacement – which encapsulates the motion due to the gravitational potential – to be exactly 1 at all times. However, this restriction can be broken by baryonic contributions ($\propto \mathbf{F}_{b,g}$) such as the Compton drag. As seen in the second term on the right hand side of Equation 5.9, the acceleration due to Compton drag generates displacements proportional to $\mathbf{\Psi}_m$; this contribution, on top of the aforementioned gravitational displacements, can lead to an expansion $\mathbf{\Psi}_g = (1 + \alpha_{\mathrm{CD}})\mathbf{\Psi}_m + f_g \mathbf{\Psi}_r + ...$ for some nonzero coefficient α_{CD} due to Compton drag, where the total-matter coefficient deviates from unity. Consequences of this modified expansion for the power spectrum are considered at the end of Section 5.4.1 and in Figure 5.6. Other baryonic forces, such as pressure forces at small scales, can similarly be included as further terms ($\mathbf{\Psi}_g \ni c_s^2 \nabla \delta_b$) in this expansion.

5.4 Galaxy Power Spectra in the Zeldovich Approximation

5.4.1 Analytic Form

From Equation 5.14, the power spectrum at redshifts z for a biased tracer can be computed as

$$P_{gg}(k,z) = \int d^3q \; e^{i\mathbf{k}\cdot\mathbf{q}} \left\langle F_g[\mathbf{q}_1] F_g[\mathbf{q}_2] \, e^{ik\cdot(\mathbf{\Psi}_g(\mathbf{q}_1,z) - \mathbf{\Psi}_g(\mathbf{q}_2,z))} \right\rangle_{q=|\mathbf{q}_2-\mathbf{q}_1|}, \tag{5.21}$$

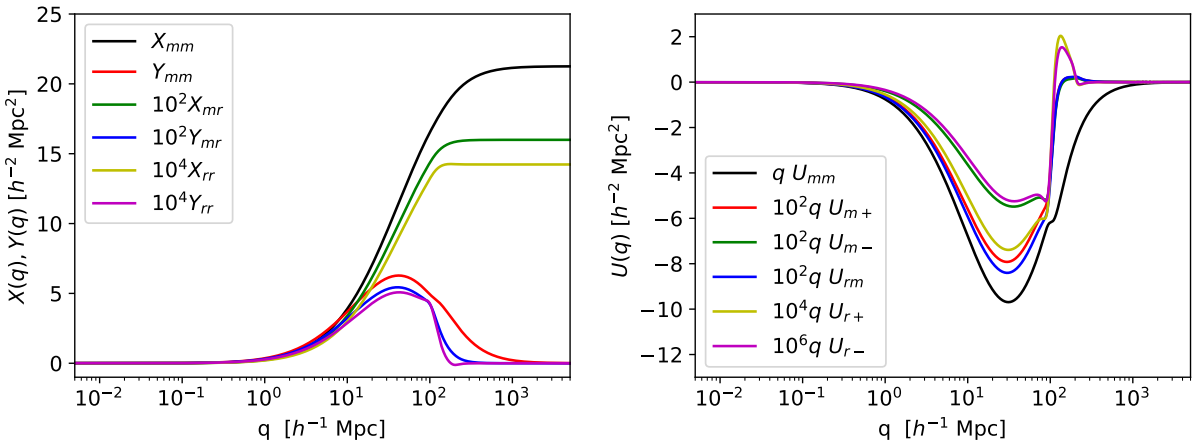

Figure 5.3: Correlation functions entering the galaxy power spectrum in Eq. (5.27) at $z = 1.2$. Left panel: the displacement auto- and cross-correlation functions between the different components. Right panel: bias-weighted, displacement correlation functions. Correlation functions involving the relative component exhibit abrupt features around $q \sim 10^2\ h^{-1}$ Mpc, reflecting the baryon acoustic oscillation scale.

where the subscripts denote quantities evaluated at two points separated by q in Lagrangian space. It is important to note that the bias functions F_g are evaluated in terms of the linear modes $m_+, r_\pm$ defined at the initial redshift z_i. In the Zeldovich approximation displacements are solved to linear order but the full mapping between initial and final times is kept. This amounts to keeping the displacement correlators exponentiated in what follows [231]. We will adopt the bias expansion in Equation 5.18. We evaluate integrals involving F_g by functional differentiation in the usual manner [231, 229, 58]: we include a term (e.g. λX) in the exponential for each argument, X, of F_g and evaluate terms like X^n via $\partial^n/\partial\lambda^n$ of $\exp[\lambda X]$.

Under the above assumptions our task reduces to evaluating

$$e^{i\mathcal{M}} \equiv \left\langle \exp\left(i\mathbf{k}\cdot\mathbf{\Delta}_g(z) + \lambda_{\delta_{m,1}}\delta_{m,1} + \lambda_{+,1}\nabla\mathbf{r}_{+,1} + \lambda_{-,1}\nabla\mathbf{r}_{-,1} + (1\leftrightarrow 2)\right)\right\rangle \tag{5.22}$$

with numerical subscripts referring to Lagrangian coordinates, q_1 and q_2, and

$$\mathbf{\Delta}_g = \mathbf{\Psi}_{g,1} - \mathbf{\Psi}_{g,2} = \mathbf{\Psi}_{m,1} - \mathbf{\Psi}_{m,2} + f_g(\mathbf{\Psi}_{r,1} - \mathbf{\Psi}_{r,2}) \equiv \mathbf{\Delta}_m + f_g\mathbf{\Delta}_r \tag{5.23}$$

The function $e^{i\mathcal{M}}$ can be evaluated using the cumulant theorem as the exponential of the connected components. The Zeldovich approximation assumes linear dynamics, such that

only quadratic terms survive

$$e^{i\mathcal{M}} = \exp\Big\{ -\frac{1}{2}k_ik_jA^{mm}_{ij} - f_gk_ik_jA^{rm}_{ij} - \frac{f_g^2}{2}k_ik_jA^{rr}_{ij} \\ + ik\cdot\big((\lambda_{\delta_{m,1}}+\lambda_{\delta_{m,2}})(U_{mm}+f_gU_{rm}) \\ + (\lambda_{+,1}+\lambda_{+,2})(U_{m+}+f_gU_{r+}) + (\lambda_{-,1}+\lambda_{-,2})(U_{m-}+f_gU_{r-})\big) \\ + \left(\,\lambda_{\delta_{m,1}}\lambda_{+,2} + (1\leftrightarrow 2)\,\right)\xi_{\delta_m\nabla\mathbf{r}_+} + (\delta_m,\nabla\mathbf{r}_-) + (\delta_m,\delta_m) \\ + (\nabla\mathbf{r}_+,\nabla\mathbf{r}_+) + (\nabla\mathbf{r}_+,\nabla\mathbf{r}_-) + (\nabla\mathbf{r}_-,\nabla\mathbf{r}_-)\Big\} \quad , \tag{5.24}$$

where we have defined

$$A^{ab}_{ij} = \left\langle \Delta^a_i(z)\Delta^b_j(z)\right\rangle , \quad U^{a\pm}_i = \left\langle \Delta^a_i(z)\nabla\cdot\mathbf{r}_\pm(\mathbf{q}_1)\right\rangle , \quad \xi_{ab} = \left\langle a(\mathbf{q}_1)b(\mathbf{q}_2)\right\rangle , \tag{5.25}$$

noting that the Δ's carry an implicit redshift dependence while the other fields do not. For the total-matter component this redshift dependence is a direct growth factor scaling and we will for convenience take the linear field's value as evaluated at the observed redshift $\delta_m = -D_m(z)\nabla\cdot\mathbf{m}_+$. The paired parentheses denote terms similar to the preceding except with the indicated pair of variables. For example, in the third line

$$(\delta_m,\nabla\mathbf{r}_-) \equiv \left(\,\lambda_{\delta_{m,1}}\lambda_{-,2} + (1\leftrightarrow 2)\,\right)\,\xi_{\delta_m\nabla\mathbf{r}_-}(q) \tag{5.26}$$

and when the elements of a pair are repeated the term should be divided by a symmetry factor of two.

Figure 5.3 shows the different correlation functions entering the above calculation. Since the correlation function of the different displacements fields, $A^{ab}_{ij}(q)$, is a tensor, we can decompose it as $A^{ab}_{ij}(q) = X^{ab}(q)\delta^K_{ij} + Y^{ab}(q)\hat{q}_i\hat{q}_j$, and the functions $X(q)$'s and $Y(q)$'s are shown in the left panel of Figure 5.3. Clearly the galaxy displacements are dominated by the total matter component, with the relative terms contributing much less than a % to the bulk flows. This fact will enable us to treat the terms proportional to f_g perturbatively, as they will be much smaller than one for wavenumbers below the nonlinear scale defined by $k^2\Sigma^2 \lesssim 1$, where the Zeldovich r.m.s. displacement is $\Sigma \propto X_{mm}(q\to\infty)$. The same conclusions apply for the bias weighted displacements $U(q)$'s, shown on the right hand panels in Figure 5.3, where $U_m(q) \gg U_\pm(q)$.

Working to linear order in the power spectrum we then have that the galaxy-galaxy power

spectrum is given by

$$P_{gg}(k) = \int d^3q\, e^{i\mathbf{k}\cdot\mathbf{q}-\frac{1}{2}k_ik_jA_{ij}^{mm}}\Big[1 - f_gk_ik_jA_{ij}^{rm} - \frac{f_g^2}{2}k_ik_jA_{ij}^{rr} + 2ik\cdot(b_1U_{mm} + b_+U_{m+} + b_-U_{m-}) + 2f_gik\cdot(b_1U_{rm} + b_+U_{r+} + b_-U_{r-}) + b_m^2\xi_{\delta_m\delta_m} + 2b_mb_+\xi_{\nabla\mathbf{r}_+\delta_m} + 2b_mb_-\xi_{\nabla\mathbf{r}_-\delta_m} + b_+^2\xi_{\nabla\mathbf{r}_+\nabla\mathbf{r}_+} + 2b_+b_-\xi_{\nabla\mathbf{r}_+\nabla\mathbf{r}_-} + b_-^2\xi_{\nabla\mathbf{r}_-\nabla\mathbf{r}_-} + \mathcal{O}(P_L^2)\Big]. \tag{5.27}$$

Figure 5.4 shows the different contributions to the galaxy power spectrum in the Zeldovich approximation at $z = 1.2$. The leading corrections to the total-matter power spectrum come at the roughly percent level from terms in Equation 5.27 linear in $\mathbf{r}_+$, i.e. in b_+ and f_g. These contributions are essentially degenerate, with differences due to the dynamical evolution of $\mathbf{\Psi}_r$ in the f_g term, as we will discuss in the next paragraph. Corrections quadratic in $\mathbf{r}_+$ or linear in $\mathbf{r}_-$ enter at roughly the same size four orders of magnitude below the total-matter contributions.

An interesting consequence of the advection of biased tracers with $|f_g| > 0$ is the appearance of relative bias terms even if none were present in the initial Lagrangian bias expansion. To see this, we can take the low-k limit of Eq. (5.27), neglecting for the moment non-gravitational contributions to $\mathbf{\Psi}_r(q)$, and obtain up to $\mathcal{O}(P(k))$

$$\begin{aligned} P_{gg}(k,z) =& (1+b_1)^2\, P_{\delta_m\delta_m}(k) \\ &+ 2(1+b_1)(b_+ + f_g)P_{m\nabla\mathbf{r}_+}(k) + 2(1+b_1)(b_- + f_gD_r(z))\, P_{m\nabla\mathbf{r}_-}(k) \\ &+ (b_+ + f_g)^2P_{\nabla\mathbf{r}_+\nabla\mathbf{r}_+}(k) + (b_- + f_gD_r(z))^2P_{\nabla\mathbf{r}_-\nabla\mathbf{r}_-}(k) \\ &+ 2(b_+ + f_g)(b_- + f_gD_r(z))P_{\nabla\mathbf{r}_+\nabla\mathbf{r}_-}(k)\,. \end{aligned} \tag{5.28}$$

We immediately recognize the familiar expression for the Eulerian linear bias, $b_1^E = 1 + b_1$, and that the relative density and velocity bias terms get renormalized by terms proportional to f_g. To make further contact with the existing literature employing the Eulerian formulation of the equations of motion [316, 317], we can identify the relative baryon dark-matter density perturbation δ_r with the divergence of $\mathbf{r}_+$, $\delta_r \equiv \nabla\cdot\mathbf{r}_+$, and the relative baryon dark-matter velocity divergence θ_r with the divergence of $\mathbf{r}_-$, $\theta_r \equiv (1+z)H_0\nabla\cdot\mathbf{r}_-$. This implies that the bias parameters in [316, 317] associated to the Eulerian fields are $b_{\delta_r}^E = b_+ + f_g$ and $b_{\theta_r}^E = (1+z)^{-1}H_0^{-1}(b_- + f_gD_r(z))$. Note that the referenced overdensities and velocities are those defined at the initial redshift z_i so should not be directly substituted for their Eulerian counterparts; for more details about the mapping of bias parameters from some initial time z_i to Eulerian coordinates see Appendix E.1.

A final caveat occurs when the non-gravitational forces on the tracer, $\mathbf{F}_{b,g}$ are nonzero. The integrated effect of such forces on $\mathbf{\Psi}_{r,g}$ must then be accounted for. For example, when dealing with baryons and dark matter, the effects of Compton drag on large scales are

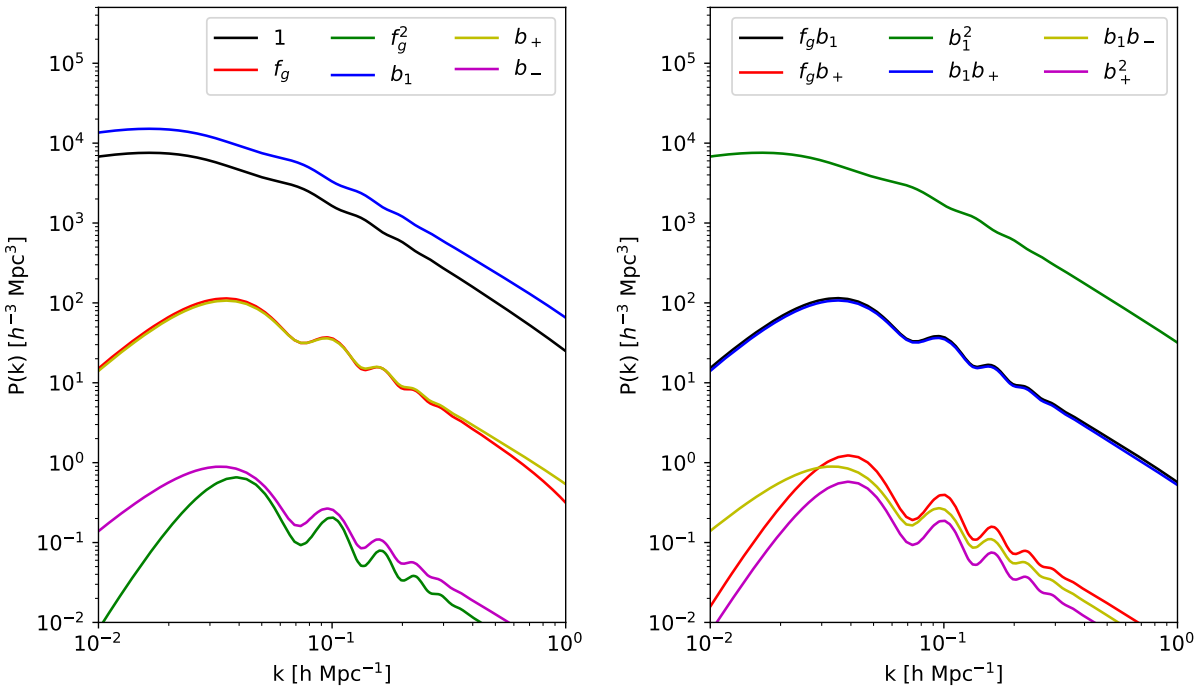

Figure 5.4: Different contributions to the galaxy power spectrum in the Zeldovich approximation, Eq. (5.27), at $z = 1.2$. Terms proportional to b_+b_-, $f_g b_-$, and b_-^2 have been omitted as they are two orders of magnitude smaller than the smallest contributions shown. Many terms, such as those involving f_g and b_+, are essentially degenerate.

non-negligible. In this case, since the Compton drag force is proportional to the total-matter displacement, the two-point functions in Eq. 5.25 involving $\mathbf{\Delta}^r$ will gain a contribution proportional to $\mathbf{\Delta}^m$ (Fig. 5.5). Such contributions can be non-negligible at large scales and can dominate in the contributions to the power spectrum proportional to f_g at low wavenumber (Fig. 5.6). Importantly, terms proportional to $b_\pm$ are unaffected since they are related only to the primordial modes $\mathbf{r}_\pm$, breaking the degeneracy between f_g and b_+. Since the difference between these terms is proportional to the total-matter component, this difference can alternatively be absorbed into the total-matter bias b_m [317]. Comparisons of these terms with and without Compton drag are shown in Figure 5.6. Comparing the f_g contribution with and without Compton drag we see, as expected, that renormalizing the linear total-matter bias b_1 to include a contribution proportional to $f_g D_{\rm CD}(z)$ (purple dotted curve) is sufficient to account for the non-gravitational Compton drag contributions.

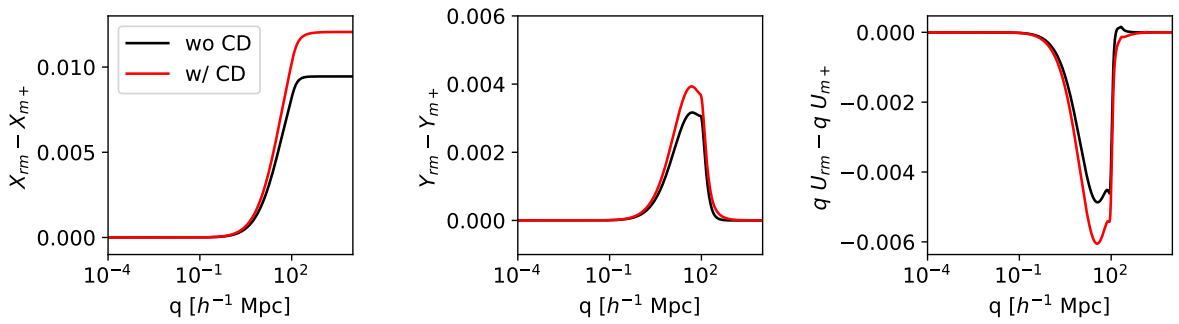

Figure 5.5: Comparison of two point functions with (red) and without (black) contributions from Compton drag. While the differences are small (c.f. Fig. 5.3), they are non-neglible at large scales. The contributions from $\mathbf{r}_+$ have been subtracted off for ease of comparison.

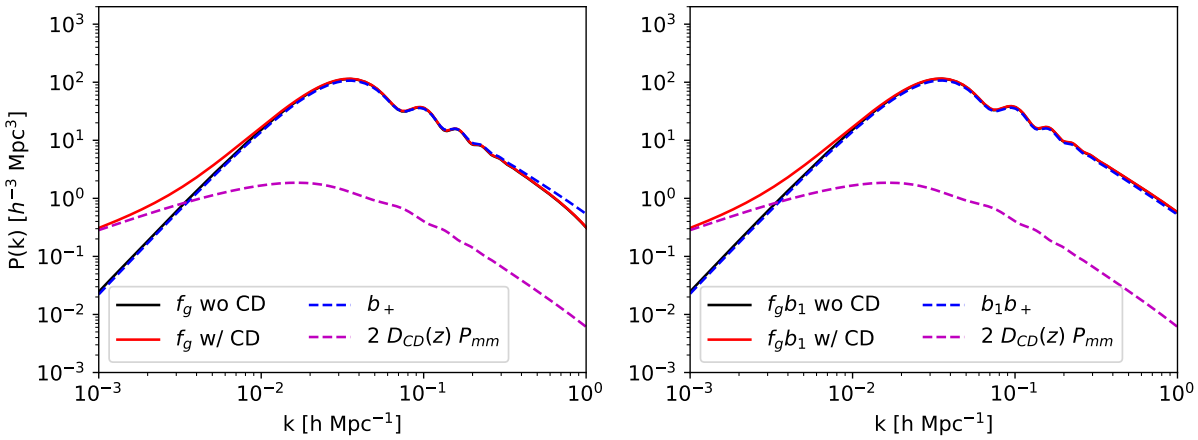

Figure 5.6: Comparison of terms involving b_+ (blue dashed) and f_g with and without Compton drag (red and black). The two are largely degenerate in the latter case, but with Compton drag the f_g terms are dominated by a contribution proportional to the total-matter power spectrum at large scales, which can alternatively be renormalized into the matter bias b_1, shown separately as a dashed magenta curve. The left panel shows contributions due to contracting the relative components ($f_g \mathbf{\Psi}_r$ or $b_+ \nabla \cdot \mathbf{m}_+$) with the total matter displacement $\mathbf{\Psi}_m$, while the right panel shows contractions with the total matter bias $b_1 \delta_m$.

5.4.2 Cross-Spectra of different tracers and IR Resummation

So far we have dealt only with tracer auto-spectra. The situation for cross-spectra is complicated by the non-cancellation of the IR-exponent at small separations, q. For two generic fluids, X and Y, such that $\mathbf{\Psi}_{X,Y} = \mathbf{\Psi}_m + f_{X,Y}\mathbf{\Psi}_r$, the cross spectrum will take the form as in Equation 5.2:

$$P_{XY}(k) = \int d^3q\, e^{i\mathbf{k}\cdot\mathbf{q}} e^{-\frac{1}{2}k_i k_j A_{ij}^{XY}} \Big[\cdots\Big], \tag{5.29}$$

where the exponentiated two-point function A^{XY} is given by

$$A_{ij}^{XY}(q) = \Big(\langle \mathbf{\Psi}_i^X \mathbf{\Psi}_j^X\rangle + \langle \mathbf{\Psi}_i^Y \mathbf{\Psi}_j^Y\rangle - 2\langle \mathbf{\Psi}_i^X \mathbf{\Psi}_j^Y\rangle\Big) + \Big(2\langle \mathbf{\Psi}_i^X \mathbf{\Psi}_j^Y\rangle - 2\langle \mathbf{\Psi}_i^X(\mathbf{q}) \mathbf{\Psi}_j^Y(0)\rangle\Big), \tag{5.30}$$

and expectation values of point operators are displayed without arguments. Both terms in parentheses on the RHS of Equation 5.30 are well-defined and invariant under generalized Galilean transformations; however the second term vanishes as $q \to 0$ while the first does not[3]. As first noted in Ref. [217], this is in contrast to the single-fluid case where A_{ij} had to vanish at small scales due to Galilean invariance.

In principle, the non-cancellation discussed above will introduce a large scale damping in the power spectrum at scales proportional to the difference $|\mathbf{\Psi}^X - \mathbf{\Psi}^Y|^2$. However, since $\mathbf{\Psi}^{X,Y}$ are both expected to have the same coefficient in the total-matter component (i.e. unity) this difference squared will generically be proportional to $(f_X - f_Y)^2\mathcal{O}(\mathbf{\Psi}_r^2)$, and thus is suppressed by about four orders of magnitude relative to the Zeldovich displacement, Σ^2, at the redshifts with which we are concerned ($z < 10$). On the other hand, while differential streaming is expected to damp cross spectra negligibly even if f_X is of order unity, as discussed in the previous section it will still generate an observable effect degenerate with the relative bias b_+.

5.4.3 Higher Order Bias

Thus far we have not discussed the fact that any perturbative model should be considered an effective field theory, working up to some scale Λ [28, 60, 332]. This forces us to introduce a set of counterterms that remove the small scale sensitivities of the perturbative calculations. For instance all the $A_{ij}(q)$ terms contain a zero-lag piece computed at zero separation, *i.e.* $q = 0$, where perturbation theory breaks down. In the single fluid case, this UV-sensitivity is renormalized to lowest order in the power spectrum by a counterterm $c_s k^2 P_{ZA}(k)$ [290, 399], where the free parameter c_s has to be matched to simulations or data. The same structure of the counterterms appears in the two fluid scenario: for instance, the $A_{ij}^{ab}(q)$ required to calculate auto and cross spectra feature the same UV-sensitive contributions as $q \to 0$, requiring one value of c_s^a for each species. In principle, terms in the equations of motion due to the relative component will add additional UV sensitivities to our predictions; in practice,

[3] A similar non-cancellation occurs in the modeling of BAO reconstruction, where the cross-term between the 'displaced' and 'shifted' fields exhibits the same behavior [266, 414].

however, such contributions are subdominant in the dynamics of the relative component and negligible for the total-matter component. To the extent that these contributions can be ignored, then, the two-fluid equations of motion can be renormalized identically to the single fluid case with one set of counterterms for each species or tracer. As counterterms have minor impact on BAO scales, and are anyway fitted to the data in both the single and multiple fluid cases, we do not include them in the Fisher calculation in the next section.

We have equally refrained from discussing bias beyond linear order. As in the equations of motion, contributions beyond first order in the linear power spectrum proportional only to the total-matter component can be added consistently as in the single-fluid case, and we will ignore small nonlinear contributions proportional to one or more powers of the relative component[4]. However, one exception must be made: operators involving the relative-velocity between the baryon and dark matter squared, which, despite being at second order in the relative component, can be non-negligible due to their distinct dimensional scaling [98, 427, 51, 316]. Such contributions were the focus of the first studies of bias [98, 427, 51] in the two-fluid picture, and we will show how their calculation fits naturally into the Lagrangian framework. For a discussion of other second order bias operators see Appendix E.2.

At second order in the bias expansion we can write

$$F_g[\mathbf{\Psi}_m,\, \mathbf{\Psi}_r|\, \mathbf{q}] \supset b_v \sigma_{v_r}^2\, \frac{[\mathbf{v}_b(\mathbf{q}) - \mathbf{v}_c(\mathbf{q})]^2}{\sigma_{v_r}^2} = b_v \sigma_{v_r}^2 \frac{\mathbf{r}_-(\mathbf{q})^2}{\sigma_{r_-}^2} \equiv c_-[\mathbf{r}_-(\mathbf{q})]^2 \tag{5.31}$$

where $\sigma_{v_r}^2$ is the 1-point variance of the relative velocities and $\sigma_{r_-}^2 = (1+z)^{-2} H_0^{-2} \sigma_{v_r}^2$. As several authors [98, 316] have pointed out, baryon-dark matter relative velocities can be quite large at the time when the first halos and galaxies form, which could result in a large value of b_v for their late time descendants. The value of $b_v \sigma_{v_r}^2$ can be as large as 0.01, which will make this contribution at second order in the power spectrum larger than the b_- terms, even on linear scales. It is however worth remembering that a value of $b_v \sigma_{v_r}^2 \simeq 10^{-5}$ is also plausible, which would substantially reduce the importance of this contribution.

To consistently compute the power spectrum contributions due to $c_- \sim b_{v^2}$ we must go beyond the Zeldovich approximation. Up to 1-loop in Lagrangian perturbation theory we have to compute 4 new terms to properly include the new bias parameter c_-. Beyond these, terms proportional to c_-^2 can be safely neglected as they are $\mathcal{O}(P^2_{\nabla \mathbf{r}_-^2})$. For the same reason we drop all the terms proportional to $b_\pm c_-$, as well as contributions of the relative component to the equations of motion. This leaves us with contributions proportional to c_-, $b_1 c_-$, $b_2 c_-$, and $b_{s^2} c_-$.

The first of these, proportional to c_-, contains a 1-loop contribution and is given by

$$P_{gg}(k) \supset c_- \int \mathrm{d}^3 q\, e^{i\mathbf{k}\cdot\mathbf{q}}\, e^{-\frac{1}{2}k_i k_j A_{ij}} \left(2ik_i \mathcal{U}_i(q) - \frac{1}{2} k_i k_j A_{ik}^{m-} A_{jk}^{m-} \right), \tag{5.32}$$

[4] A proper accounting of such terms would in addition require solving the relative-component equations of motion to beyond linear order, which is beyond our present scope.

where we have defined $A_{ij}^{m-} = \langle \Delta_{m,i} \, (\mathbf{r}_{-,2} - \mathbf{r}_{-,1})_j \rangle$ and the 1-loop contribution from the second-order Lagrangian displacement $\mathbf{\Psi}^{(2)}$ enters as

$$\mathcal{U}_i(q) \equiv \left\langle \Delta^{(2)} \mathbf{r}_{-,1}^2 \right\rangle = \hat{q}_i \int \frac{\mathrm{d}k}{2\pi^2} \, k^2 Q_{v^2}(k) j_1(kq) \tag{5.33}$$

The kernel Q_{v^2} is derived in Appendix E.3.

The remaining terms do not contain loop contributions and follow straightforwardly from evaluating the second and third cumulants in Eq. (5.21) within the Zeldovich approximation. These are those proportional to the first order bias:

$$P_{gg}(k) \supset 2ik_i \; b_1 c_- \int \mathrm{d}^3 q \, e^{i\mathbf{k}\cdot\mathbf{q}} \, e^{-\frac{1}{2}k_i k_j A_{ij}} \, A_{ij}^{m-}(q) \; U_j^{-m}(q) \, , \tag{5.34}$$

second order bias:

$$P_{gg}(k) \supset 2b_2 c_- \int \mathrm{d}^3 q \, e^{i\mathbf{k}\cdot\mathbf{q}} \, e^{-\frac{1}{2}k_i k_j A_{ij}} U_i^{m-}(q) \; U_i^{m-}(q), \tag{5.35}$$

and shear

$$P_{gg}(k) \supset 4b_{s^2} c_- \int \mathrm{d}^3 q \, e^{i\mathbf{k}\cdot\mathbf{q}} \, e^{-\frac{1}{2}k_i k_j A_{ij}} W_{ijk}^{s-}(q) \; W_{ijk}^{s-}(q), \tag{5.36}$$

where we have defined the 2-point functions $U^{-m} \equiv \langle \mathbf{r}_-(q) \delta_m(0) \rangle = U^{m-}$ and $W_{ijk}^{s-}(q) = \langle s_{ij}(q) \mathbf{r}_{-,k}(0) \rangle$. Details of the above calculation can be found in Appendix E.3.

The contributions proportional to c_- and their comparison with the 1-piece in Eq. (5.27) and with the $b_\pm$ ones computed in the previous section is shown in Fig 5.7 for $z = 1.2$, assuming $b_v \sigma^2_{v_r^2} = 0.01$. The c_- terms are indeed larger than the b_- terms on most scales, but still subdominant compared to the b_+ terms. Notably, the c_- terms feature significantly larger oscillatory features than contributions from $b_\pm$, with minima that differ from maxima by more than an order of magnitude.

5.5 Degeneracies and bias to BAO

Baryon acoustic oscillations (BAO) in the photon-baryon fluid before combination imprint a characteristic clustering scale in the distribution of galaxies that can be used as a standard ruler to constrain the cosmic expansion history [364]. In general this method is regarded as highly robust as it probes very large scales which are largely unaffected by astrophysical processes. However, relative component contributions to the two-point function also occur on very large scales and their oscillatory features, although arising from the same physical process of the standard BAO features in the matter density power spectrum, could bias our estimates of the distance scale if not properly taken into account [51, 43, 351]. Indeed, as shown in the left panel of Fig. 5.8, all the relative component contributions we have considered show distinct features around the BAO peak.

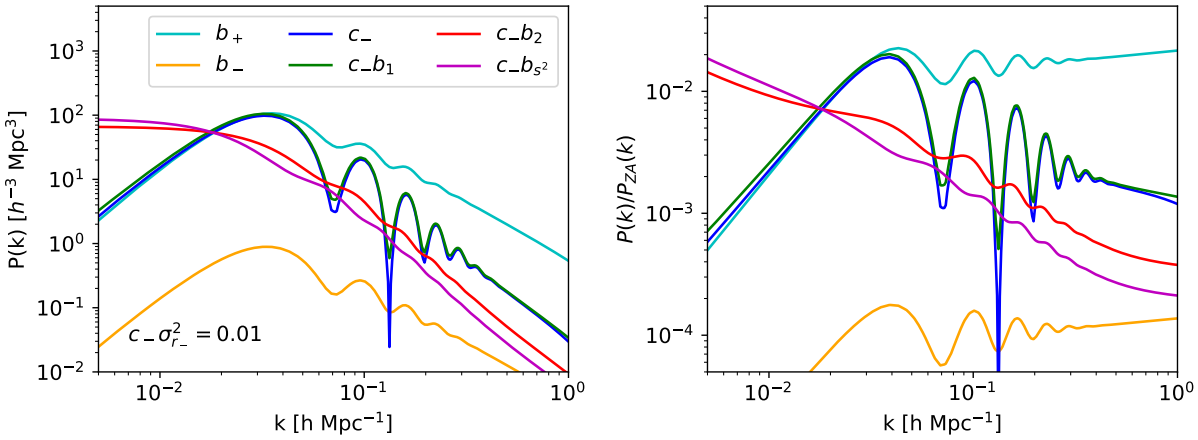

Figure 5.7: Contributions to the Zeldovich galaxy power spectrum from relative velocity bias at second order. All biases are set to unity except for c_-, which is set such that $b_v\sigma^2_{v_r} = 0.01$—in this case, the contributions from b_{v^2} are seen to be quite comparable to those from b_+, and moreover exhibit BAO "wiggles" far more prominently than does the regular ZA contribution.

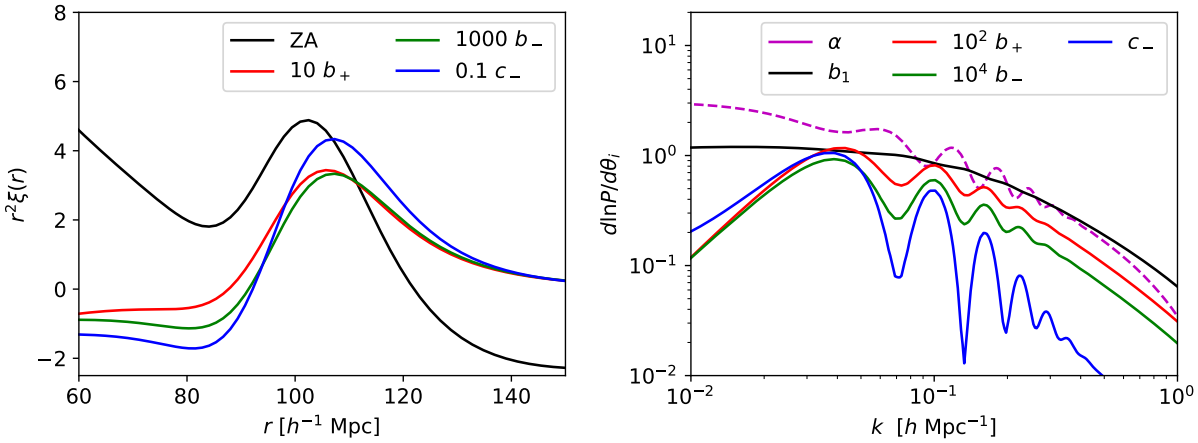

Figure 5.8: (Left) Contributions to the $z = 1.2$ correlation frunction from the various relative component biases, multiplied by constant factors for ease of comparison. All contributions have prominent features at the BAO scale, reflecting their origin in early-universe acoustic oscillations. (Right) Derivatives of the power spectrum with respect to these parameters and the BAO scale parameter α at $z = 1.2$, with $b_m = 0.5$, $b_2 = 0.2$, $b_+ = 1$, $b_- = 7$ and $c_-\sigma^2_{r_-} = 0.01$. Despite the fact that all these templates feature prominent oscillations, they nonetheless possess distinct scale dependence. Note that some of the derivatives have been multiplied by powers of ten for ease of comparison.

The extent to which contributions from the relative component can contaminate measurements of the BAO scale can be estimated using the Fisher matrix formalism [372]. The galaxy overdensity has a covariance that is diagonal in Fourier space and given by the power spectrum plus shot noise, $\hat{P}_{gg} = P_{gg}(k) + \bar{n}^{-1}$; for the parameters $\{\theta_i\}$, the Fisher matrix is given by

$$F_{ij} = V_{obs} \int \frac{d^3k}{(2\pi)^3} \frac{1}{2} \frac{\partial \ln \hat{P}_{gg}(k)}{\partial \theta_i} \frac{\partial \ln \hat{P}_{gg}(k)}{\partial \theta_j}, \tag{5.37}$$

where V_{obs} is the observed volume. For simplicity we neglect redshift space distortions and focus only on the isotropic BAO signal, though we will comment on how our Lagrangian analysis can be naturally extended to redshift space in the final paragraph. We model the power spectrum using the two-fluid Zeldovich terms derived above and include matter contributions up to one loop (see e.g. [396]), including contributions from the quadratic Lagrangian bias b_2. We consider only scales between $k_{\rm min} = 10^{-2}\ h\,{\rm Mpc}^{-1}$ and $k_{\rm max} = 0.25\ h\,{\rm Mpc}^{-1}$, and fiducial value of $b_1 = 0.53$ and $b_2 = 0.2$. The number density of galaxies is $\bar{n} = 4.2 \times 10^{-4}\ \ h^3\,{\rm Mpc}^{-3}$ and we assume $V = 5\,h^{-3}\,{\rm Gpc}^3$. These numbers are chosen to be similar to what galaxy surveys like DESI [108] or Euclid [12] are expected to measure, and in particular are based off the expected DESI ELG population at $z = 1.25$ in a bin of width $\Delta z = 0.1$ and 14,000 square degrees of observation.

To quantify the potential impact of the relative component on standard BAO analyses, we will compare two models of the power spectrum within the Fisher formalism: the "correct" model $\mathbf{M}_1$, which is a function of all total-matter and relative component biases, and the nested "standard" model $\mathbf{M}_0$, wherein the relative component biases are set to zero (i.e. $b_\pm,\ c_- = 0$). The observed power spectrum is in addition a function of the BAO scaling parameter α such that

$$P_{gg}(k, z, \alpha, \mathbf{M}) = \alpha^{-3} P_{gg}\left(\frac{k}{\alpha}, z, \mathbf{M}\right). \tag{5.38}$$

The derivative of the baseline galaxy power spectrum with respect to the parameters is shown in Figure 5.8. These templates all show oscillatory features of roughly the same frequency as the BAO scale but exhibit distinguishable scale dependence. For reference, applying Eq. (5.37) returns sub-% error on the BAO scale, with $\sigma_\alpha = 0.9\%$, for the standard analysis using $\mathbf{M}_0$.

We can now compute the systematic shifts in α that would be incurred by neglecting the relative component, i.e. by fitting to $\mathbf{M}_0$. For convenience, we will split the parameters in $\mathbf{M}_1$ into $\theta = (\phi_a, \psi_\sigma)$, where ϕ_a with Latin indices are the BAO scale and total-matter parameters and ψ_σ with Greek indices are the relative component biases, such that $\mathbf{M}_0$ is given by $\theta = (\phi_a, \psi_\sigma = 0)$. In this language the shift in α and b_1 due to using the standard model can be calculated to first order as [370]

$$\delta\theta_a = -(F_0)^{-1}_{ab} G_{b\sigma} \delta\psi_\sigma, \qquad a, b = \alpha, b_1,\ \sigma = b_\pm, c_-. \tag{5.39}$$

Here F_0 and G are respectively diagonal and off-diagonal blocks of the full Fisher matrix $F = F(\theta_0)$ calculated at the best fit parameters θ_0 for the full model $\mathbf{M}_1$, such that $F_{0,ab} = F_{ab}$

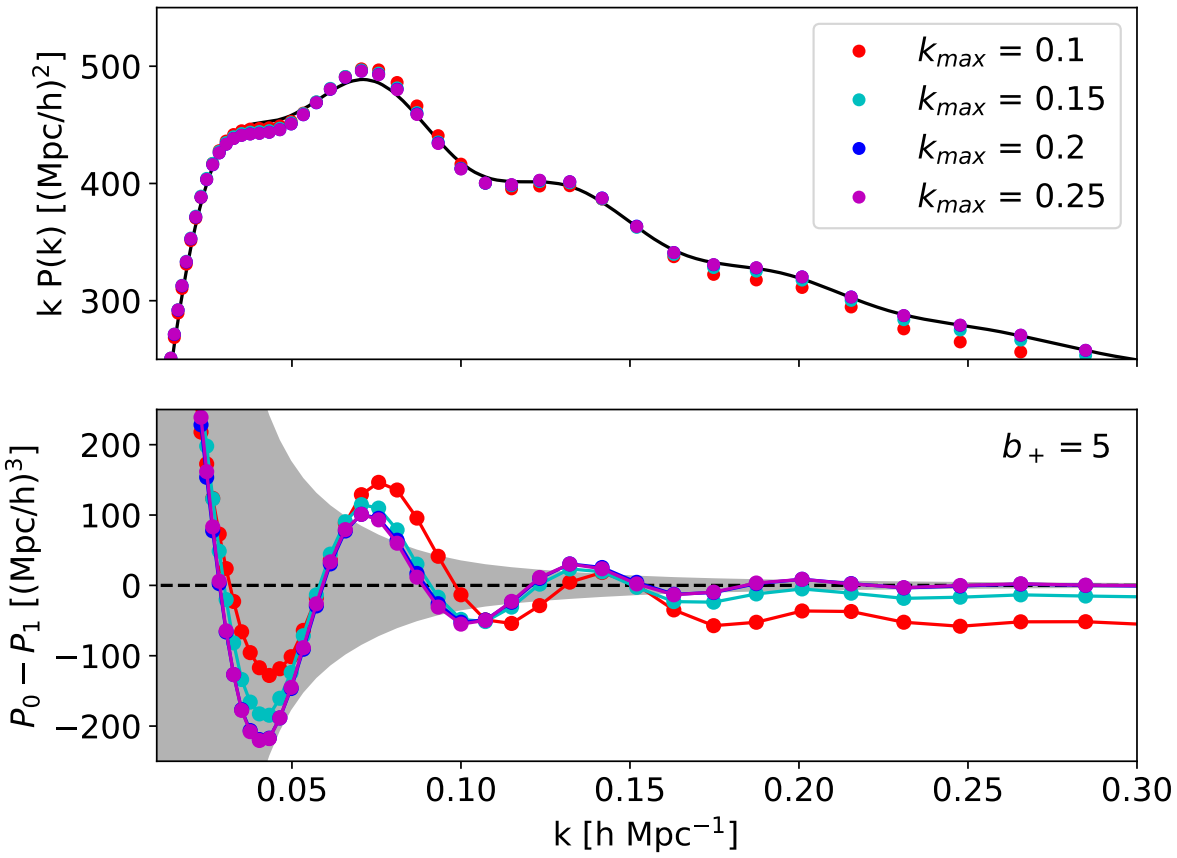

Figure 5.9: (Top) Best fit power spectra using the total-matter-component-only model, $\mathbf{M}_0$, for a universe where $b_+ = 5$ with varying maximum fitted wave numbers $k_{\rm max}$. (Bottom) Residuals of the above fits, compared to expected errors ($\Delta \ln k = 0.06$), shaded in gray. Fitting over too narrow a range ($k_{\rm max} = 0.1\,h\,{\rm Mpc}^{-1}$) results in a highly biased phase, while fits using larger wave number ranges covering more than one BAO wiggle are essentially in phase. The remaining oscillating residuals significantly exceed the expected error and are due to lack-of-fit for the oscillations in the relative component.

and $G_{b\sigma} = F_{b\sigma}$, and $\delta\psi$ is the deviation of ψ in the standard cold dark matter only model $\mathbf{M}_0$ from $\mathbf{M}_1$, i.e. $\delta\psi = -\psi_0$.

As a simple first example, we consider a toy-model Universe in which the only relative contribution is b_+. Figure 5.9 compares the "true" power spectrum, $P_1(k)$, assuming $b_+ = 5$, with best fits to the power spectrum in a dark matter only universe $P_0(k)$, described by the model parameters $\mathbf{M}_0$, where the values of α, b_1, b_2 are shifted from their true values according to Equation 5.39. Different values of the maximum wave number $k_{\rm max}$ included in the Fisher calculation are shown with different lines. For $k_{\rm max} = 0.1\,h\,{\rm Mpc}^{-1}$, we find a significant departure in phase between the two models, compared to higher limiting wavenumbers, as evident from the phase of the residual in the bottom panel. Beyond $k_{\rm max} = 0.15\,h\,{\rm Mpc}^{-1}$ there are sufficient BAO wiggles that the phase of the residuals are essentially locked. We caution that the same exercise repeated with both matter and relative terms in the Zeldovich approximation can lead to wide swings in the BAO scale $\delta\alpha$ as a function of $k_{\rm max}$. This can be understood as follows: at $k \gtrsim 0.1\,h\,{\rm Mpc}^{-1}$, b_+ contributes both oscillatory behavior and a broadband shape identical to the total matter component. The latter is essentially an amplitude change and can be roughly cancelled by a shift δb_m, which it is thus fixed independently of $k_{\rm max}$. This then requires $\delta\alpha$ to shift with $k_{\rm max}$ as more oscillations are included until the oscillations in $\mathbf{r}_+$ relative to $\mathbf{m}_+$ are damped at large k (Figure 5.2). This broadband effect is ameliorated by including nonlinear terms for BAO measurements, but the partial degeneracy of b_+ with the power spectrum amplitude likely implies that ignoring two-fluid effects may affect measurement of the amplitude of the power spectrum (though this effect will also be partially mitigated by redshift-space distortions).

The same formalism can be applied to more realistic bias models. In the upper left panel of Figure 5.10 we consider the case when the observed power spectrum contains nonzero values $b_\pm$ and $c_- = 0$, and forecast the shifts in α due to the wrong assumption of $b_\pm = 0$. Due to the small size of the b_- contributions (see Figure 5.4), we expect shifts in BAO inferred distances to be dominated by b_+, and this is indeed what we find, contours of constant $\delta\alpha$ are almost independent of b_- even when $|b_-| = 10$. On the other hand, we see that values of $b_+ \sim 5$ shift the measured α by up to 0.4%, close to half of the error on α expected when using $\mathbf{M}_0$.

However, the physics behind the relative components is quite well understood and can be easily included in Fisher forecasts or power spectrum analyses. Indeed, as seen in Figure 5.8, the templates for the various relative biases and α have distinct shape and could be distinguishable depending on the noise level of the measurements. The upper right plot in Figure 5.10 shows the increase in σ_α induced by marginalizing over $b_\pm$ in universes where $b_\pm$ and b_v are not necessarily nonzero [5]. The total loss of constraining power is modest, with less than 10% worse error bars even after marginalizing over two extra parameters. In both the computations of the shifts in α and the increase of $\sigma(\alpha)$, the volume of the survey does not enter, and the final results depend only on the shot noise levels.

[5]The nonzero $b_{\pm,v}$ produce shifts in the measured α, b_m when using $\mathbf{M}_0$, which must be taken account when computing σ_α. To first order, the shifted Fisher matrix is given by F_0.

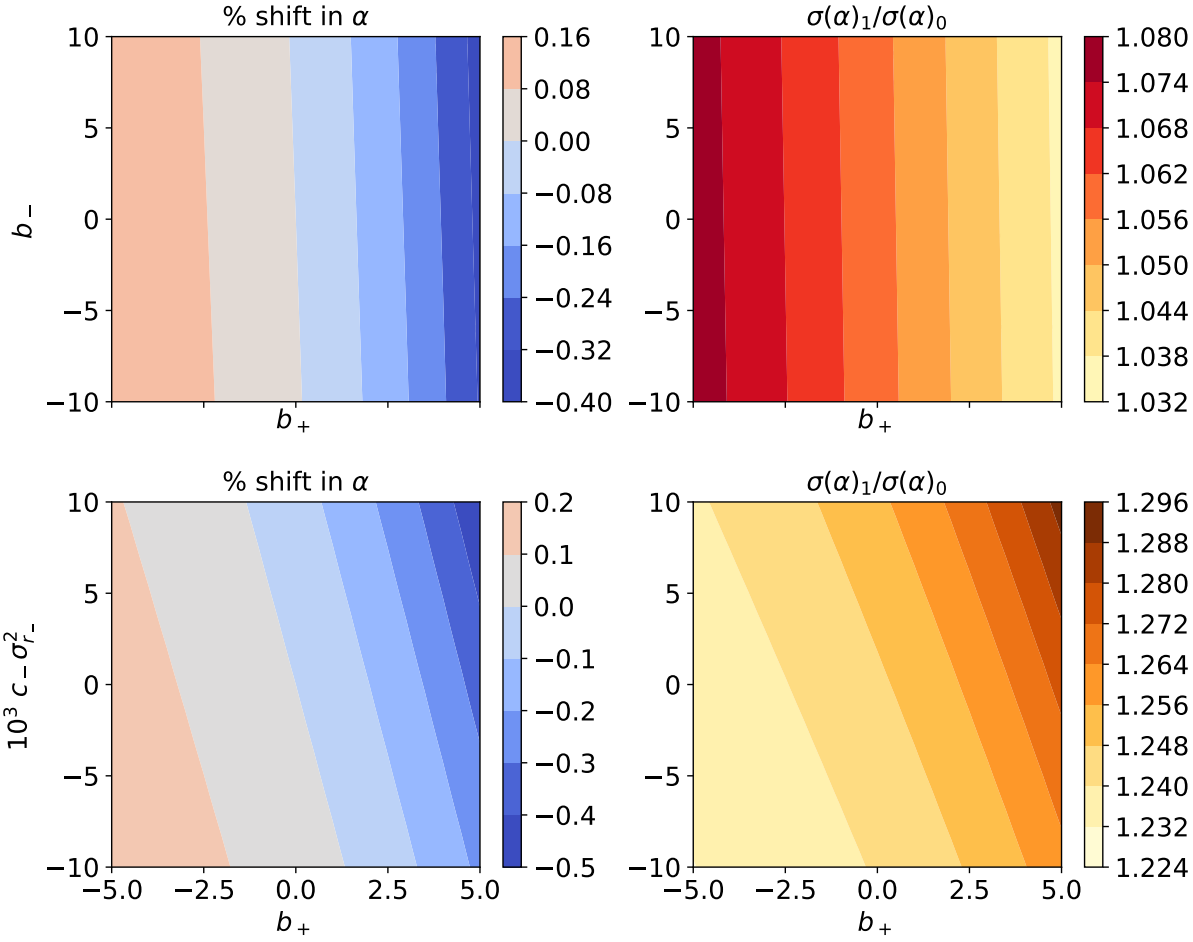

Figure 5.10: (Top Left) Shift in measured α when neglecting relative component biases as a function $b_\pm$ in the absence of c_-. While b_- contributes negligibly, $b_+ = 5$ produces a shift up to a 0.4%. (Top Right) Ratio of error bars in α when marginalizing over $b_\pm$ vs. when they are kept fixed at zero, such that the best-fit value of α is biased in the latter case. In the latter case the forecast takes into account the shift away from the true value due to incorrect model assumptions. (Bottom Row) Same as the above, but with c_- added as a nonzero parameter in $\mathbf{M}_1$. We have set the true $b_- = 0$ for convenience but marginalize over it to calculate uncertainties. While even $c_-\sigma^2_{r_-} = 0.01$ contributes only a tenth of a percent to the shift in α, the error bars are inflated relative to the top row by up to twenty percent. We assume $k_{\rm max} = 0.25\,h\,{\rm Mpc}^{-1}$ throughout.

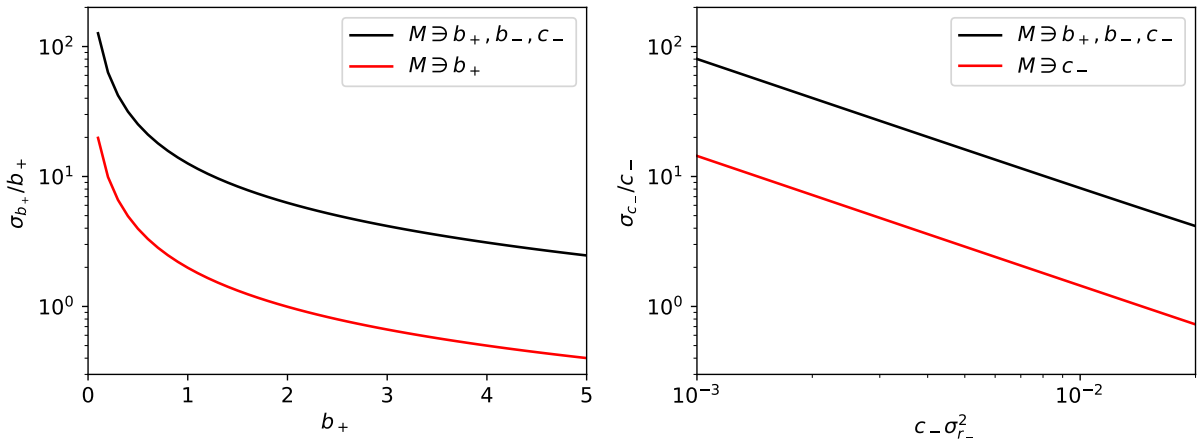

Figure 5.11: Constraints on b_+ and c_- in our fiducial setup if only each respective parameter can be varied (black), and if all relative parameters are simultaneously marginalized over (red). Notably, when the full model is taken into account detecting the relative velocity effect (c_-) will require up to ten times more signal to noise.

In the lower set of plots in Figure 5.8, we repeat the same exercise described above including c_- as an extra free parameter. Since b_- is irrelevant for the final results we set it to zero (but still marginalized over it). We find that b_+ and c_- are anti-correlated, with larger shifts compared to the $b_\pm$ case, but $\delta\alpha/\alpha \leq 0.5\%$ in all cases. Marginalizing over the extra parameter c_- results in a 20-30% increase in $\sigma(\alpha)$, which is still benign for BAO constraints. Our results therefore advocate for the implementation of relative component biases, at least of b_+ and c_-, in standard BAO data analysis of the galaxy power spectrum or correlation function.

Finally, in Figure 5.11 we investigate the detectability of the two-fluid effects in the same setup. On their own, both b_+ and c_- become 1σ detectable at the upper end of our explored parameter ranges, shown as the red lines in Figure 5.11. However, once all three relative bias parameters are marginalized over, the black set of curves in Figure 5.11, neither will be detectable within our fiducial volumes, with c_- in particular at 0.1σ, well out of reach even if all the DESI redshift bins are combined.

5.6 Conclusions

The large scale structure of the universe, whose formation is dominated by the dynamics of gravitational collapse, is one of the premier probes into fundamental physics. At subleading order, the presence of multiple particle species, broadly categorized into cold dark matter, baryons and neutrinos, with distinct properties beyond their shared gravitational attraction,

can present additional features in this structure, which will become increasingly important as future surveys push to higher precision. In particular, relative perturbations between baryons and cold dark matter are prominent at the same scale as baryon acoustic oscillations and have the potential to cause systematic biases in future BAO measurements.

In this section, we develop the Lagrangian formalism to calculate the clustering of biased tracers in the presence of multiple fluids, focusing specifically on the two-fluid scenario with dark matter and baryons. The Eulerian description of two-fluid dynamics has been studied extensively in the past and we make contact with previous work as appropriate throughout the text. LPT includes an automatic resummation over long-wavelength bulk flows and is thus able to accurately capture the shape of BAO features for biased tracers. In addition, LPT naturally maps bias terms from their initial Lagrangian positions to advected Eulerian positions, in contrast to Eulerian theory in which advective terms must be put in by hand, thereby simplifying the treatment of bias as responses to linear initial perturbations.

The presence of two fluids introduces terms beyond those encountered in traditional single fluid cosmological perturbation theory, with modifications in both the bias expansion and tracer advection. In the former, the generalized Galilean invariance that restricted the bias to contain only second derivatives of the gravitational potential in the single fluid case, allows terms including relative overdensities and velocities between different species. In the latter, initial relative displacements between various species are preserved under free fall and present an additional source of bias. Large scale non-gravitational forces such as Compton drag induced by the CMB can introduce additional corrections. We formulate modifications to tracer bias and advection in terms of three initial modes, constants of motion in the linear equations of motion, which roughly correspond to the initial total-matter displacement field and the relative displacement and velocity fields between dark matter and baryons.

We explicitly calculate the galaxy auto-power spectrum in the Zeldovich approximation within this formalism. Cross correlations between the relative modes introduce eight terms linear in the power spectrum—however, those quadratic in the relative component are suppressed by four orders of magnitude relative to the single fluid terms at low redshifts relevant for the next generation of galaxy surveys. Comparing to the Eulerian result explicitly to first order in the power spectrum, we find that the Eulerian relative component bias corresponds to linear mixtures of the Lagrangian bias, with modifications to the tracer advection entering both the Eulerian relative overdensity bias and the Eulerian relative velocity divergence bias. We then take up the calculation of cross spectra, finding a large scale damping due to an IR noncancellation in the relative component that is nonetheless negligibly small on perturbative scales. We also briefly discuss higher order corrections to the equations of motion in the presence of two fluids from an effective theory point of view, and perform an example one loop calculation for the relative velocity effect ($\propto \mathbf{v}_r^2$).

We conduct an exploratory analysis into whether two-fluid effects can cause systematic biases in measurements of the BAO scale. Taking the example of DESI ELGs at $z = 1.25$, we show that while ignoring two-fluid effects can lead to systematic shifts in the measured BAO scale as large as half a sigma, properly marginalizing over these effects induces less than ten percent loss in precision for a wide range of bias values. Since the scale dependence

of the underlying physics is well understood, these results advocate for including two-fluid terms at linear order in future analyses. The dominant relative bias term ($\propto b_+$) does not fall quadratically with the growth factor like the total-matter contributions, and we therefore expect the relative bias signal as a fraction of total power to scale with redshift as $D_+^{-1}(z)$ and become proportionally more significant for surveys (such as the proposed Stage II 21-cm survey [90]) at higher redshifts. Studies of more highly biased tracers such as DESI quasars [108], for which the total-matter contributions are correspondingly larger, will on the other hand be less influenced by the relative bias for similar reasons.

While the Lagrangian picture is a natural playground for their study, in this section we have opted not to study redshift space distortions (RSD). We note, however, that of the two relative components, $\mathbf{r}_+$ is dominant but stationary while $\mathbf{r}_-$ is so small as to be essentially negligible— two-fluid impacts should thus have a relatively small impact on RSD. However, as noted in the previous section, since the dominant relative component contribution b_+ is somewhat degenerate with the overall power spectrum amplitude, it is possible that two-fluid effects could hinder the accuracy of $f\sigma_8$ measurements beyond the percent level. We will return to this issue in future work.

Acknowledgments

We thank Jonathan Blazek and Jahmour Givans for helpful comments. SC is supported by the National Science Foundation Graduate Research Fellowship (Grant No. DGE 1106400) and by the UC Berkeley Theoretical Astrophysics Center Astronomy and Astrophysics Graduate Fellowship. M.W. is supported by the U.S. Department of Energy and by NSF grant number 1713791. This work made extensive use of the NASA Astrophysics Data System and of the `astro-ph` preprint archive at `arXiv.org`.

Chapter 6

Applications of IR Resummation II: Primordial Features

6.1 Introduction

Current observations of large-scale structure are consistent with a primordial power spectrum that is featureless, upon which 14 Gyr of evolution imprints two characteristic scales: the horizon at the epoch of matter-radiation equality and the sound horizon of photon-baryon acoustic oscillations prior to recombination [275, 114, 285]. However many modifications of the standard model would lead to deviations from this simple picture. Many inflationary models imprint features in the otherwise smooth spectrum of curvature fluctuations at early times (see e.g. refs. [84, 353] for recent reviews and references to the extensive early literature). While these features are in some sense generic, different models predict very different properties for these features, their bandwidth, amplitude and shape. Detection of such features would open new windows into the primordial Universe. In addition, the evolution of these primordial perturbations across 14 Gyr of cosmic history can 'induce' features in the observed spectrum. One class of features which has been the focus of intense observational activity are baryon acoustic oscillations [410]. However more generally new types of particle interactions, new energy components or changes in the expansion history can all alter the observed, late-time spectrum in observable ways.

The strongest constraints on primordial features to date come from a combination of cosmic microwave background anisotropies [285, 288] and large-scale structure [44]. This has placed upper limits on the amplitude of features at the several percent level for frequencies in the range $10^2 < \omega < 10^3\, h^{-1}$Mpc (see previous references for more details). Future large-scale structure surveys, especially those performed at high redshift over large cosmic volumes, should be able to tighten these constraints significantly [353].

In this section we investigate the degree to which modern perturbative calculations can quantitatively predict the clustering of biased tracers in redshift space, including the "washing out" of primordial features by mode-coupling associated with non-linear evolution, changes

to the broad-band shape of the spectrum by non-linear biasing and the mixing of the velocity and density perturbations through redshift-space distortions. We are not the first authors to address these topics, indeed there is an extensive literature on this topic within the context of baryon acoustic oscillation (BAO) studies (see §6.4 for references). An important finding of these studies is the existence of $\mathcal{O}(1)$ corrections to features for a wide range of parameters and wavenumbers of interest. This leads one to consider resumming these $\mathcal{O}(1)$ contributions, which arise from the large displacements, a process referred to as IR resummation. One method of deriving the IR resummation process is as a saddle-point approximation to a particular integral (§6.4). In this section we pay particular attention to the manner in which IR resummation, mode coupling and the mixing of density and velocity perturbations implied by redshift-space distortions appear in models with features at different scales than BAO, and how IR resummation can deal with features with k-dependent frequency where the choice of saddle is not immediately obvious.

The outline of the paper is as follows. In Section 6.2 we introduce the particle-mesh simulations that we use to validate our perturbative models. Section 6.3 describes the specific feature models that we test, which have been chosen to be representative of different classes that appear in the literature, while Section 6.4 describes the perturbative calculations we investigate. Section 6.5 presents the comparison between the theory and N-body power spectra and we conclude in Section 6.6. Throughout we will assume a ΛCDM cosmological model consistent with the latest *Planck* results [285, 286] and quote distances in comoving h^{-1}Mpc.

6.2 N-body simulations

To validate our model and further investigate the impact of non-linearity, bias and redshift-space distortions on primordial features we have run a number of N-body simulations. For each of several models we generated 6 realizations of Gaussian initial conditions at $z = 9$ using 2nd order Lagrangian perturbation theory and employed the FastPM code [134] to evolve 4096^3 particles in a $2.5\,h^{-1}$Gpc box with a $(3 \times 4096)^3$ force grid over 40 time steps linearly spaced in the scale factor, a, down to $z = 0.5$. With 40 steps, which improves the convergence at higher k, the code behaves very much as a traditional particle mesh code.

Each model employed the same background cosmology, of the ΛCDM family and consistent with the latest constraints from Planck [286]. Halo catalogs and 5 per cent of the dark matter particles were output at $z = 2$, 1 and 0.5. The density power spectra in real and redshift space and the real-space velocity spectra were computed using the Nbodykit software [163]. Fourier transforms were done on a 4096^3 mesh. We bin the spectra in linear k bins of width $\Delta k = 0.005\,h\,\mathrm{Mpc}^{-1}$ starting at $k_{\rm min} = 0.005\,h\,\mathrm{Mpc}^{-1}$. We compute power spectrum "wedges", $P(k, \mu)$, in 5 equal width μ bins centered at $\mu = 0.1$, 0.3, 0.5, 0.7 and 0.9, as well as power spectrum multipoles, $P_\ell(k)$ for $\ell = 0$, 2 and 4. We use the plane-parallel approximation throughout this work, for a periodic box within which estimating $P(k, \mu)$ amounts to simply Fourier-transforming a gridded field, squaring, and binning by k and μ

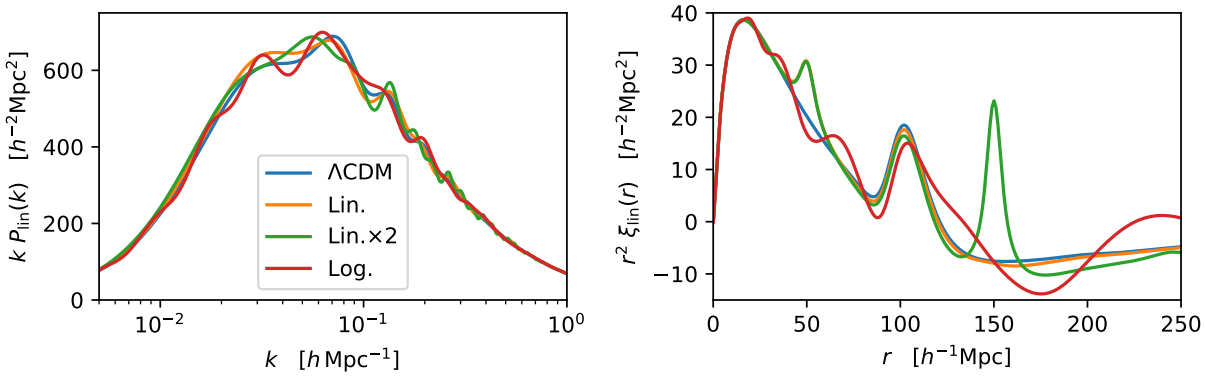

Figure 6.1: The linear theory power spectra (left) and correlation functions (right) for our fiducial ΛCDM model and models with primordial features superposed. The "Lin." model has sinusoidal oscillations linear in k (Eq. 6.1), the "Lin.×2" model has sinusoidal oscillations linear in k with two frequencies ($\omega_1 = 50\,h^{-1}$Mpc and $\omega_2 = 150\,h^{-1}$Mpc) and the "Log." model has sinusoidal oscillations in $\ln k$ (Eq. 6.2). See text for further details.

without the usual observational complications involving window functions or line-of-sight effects which would need to be accounted for in real surveys like BOSS [151]. We do not remove shot noise from any of our spectra, but rather include such contributions in our models. We present the average of the $P(k,\mu)$ with the line of sight taken along each of the cardinal directions of the box.

We have chosen to focus on two, mass limited halo samples, with densities of $10^{-3}\,h^3\,{\rm Mpc}^{-3}$ and $10^{-4}\,h^3\,{\rm Mpc}^{-3}$. These are characteristic of densities achieved by surveys such as DESI [108], MegaMapper [314] or MSE [373], though significantly sparser than one might expect from future 21 cm experiments [352]. We will highlight the results from the denser sample — which we will call the fiducial sample throughout — since it is less noisy, but the results are qualitatively similar for the lower density sample.

6.3 Feature models

We will consider two broad classes of "features" in the linear theory power spectrum. The first will arise in the very early Universe (primordial features), for example when the perturbations were originally generated by inflation. The second will be imprinted after inflation but at much earlier times than the epoch of the observations. Let us take each in turn.

6.3.1 Primordial features

We investigate several phenomenological models of primordial features, chosen to illustrate various issues and highlight results, rather than models based on fundamental physics calculations. Specifically we follow the recent literature in considering two types of oscillations that are superposed upon the linear theory power spectrum computed for ΛCDM,

$$P_{\rm lin}(k) = P_{\Lambda{\rm CDM}}(k)\left\{1 + A\sin(\omega k)\exp\left[-\frac{(kr_d)^2}{2}\right]\right\} \qquad \text{(linear)} \tag{6.1}$$

and

$$P_{\log}(k) = P_{\Lambda{\rm CDM}}(k)\left\{1 + A\sin\left(\omega\ln\frac{k}{k_\star}\right)\exp\left[-\frac{(kr_d)^2}{2}\right]\right\} \qquad \text{(logarithmic)} \tag{6.2}$$

with $A = 0.05$, $k_\star = 0.05\,h\,{\rm Mpc}^{-1}$ and $r_d = 2.5\,h^{-1}$Mpc. The first class of models have oscillations linear in k, often termed "sharp features", and tend to arise if the inflaton temporarily departs from its slow roll (attractor) evolution. The second class, with oscillations in $\ln k$, are also termed "resonant features" [353]. Compared to earlier work we have chosen a particular phase for the linear oscillations so that the modification tends to zero at low k and damped the models at high k with a Gaussian. The high k damping more closely reproduces the models based on features in the inflationary potential which tend to produce band-limited oscillations (e.g. refs. [6]), and also ensures that our simulations are properly, numerically resolving the features. While models with 5 per cent oscillations such as these are observationally disfavored [288, 44], using larger amplitude oscillations provides higher signal to noise in our simulations and a more stringent test of the modeling formalism. For the linear model we choose $\omega = 50\,h^{-1}$Mpc, to emphasize non-linear evolution of the feature compared to the BAO, while for the logarithmic model we take $\omega = 10$, which ensures we resolve the oscillations well with our $2.5\,h^{-1}$Gpc box. The linear theory power spectra and correlation functions, extrapolated to $z = 0$, are shown in Fig. 6.1.

One of the advantages of the linear model is that it can be thought of as a single mode in a Fourier decomposition of a more general class of features. Since all of our models are built upon a ΛCDM template, a second feature (due to baryon acoustic oscillations in the recombination-era Universe [114]) is always present. However, in order to gauge how well we can model non-linear evolution, bias and redshift-space distortions in the presence of multiple frequencies we also generate a linear model with two sine modes of frequencies $\omega_1 = 50\,h^{-1}$Mpc and $\omega_2 = 150\,h^{-1}$Mpc (Fig. 6.1). Each mode has the same damping and amplitude as for the "linear" model above.

6.3.2 Induced features

As a second class of features we consider changes to the matter power spectrum that arise due to non-standard expansion histories. Since the growth of structure is damped by Hubble

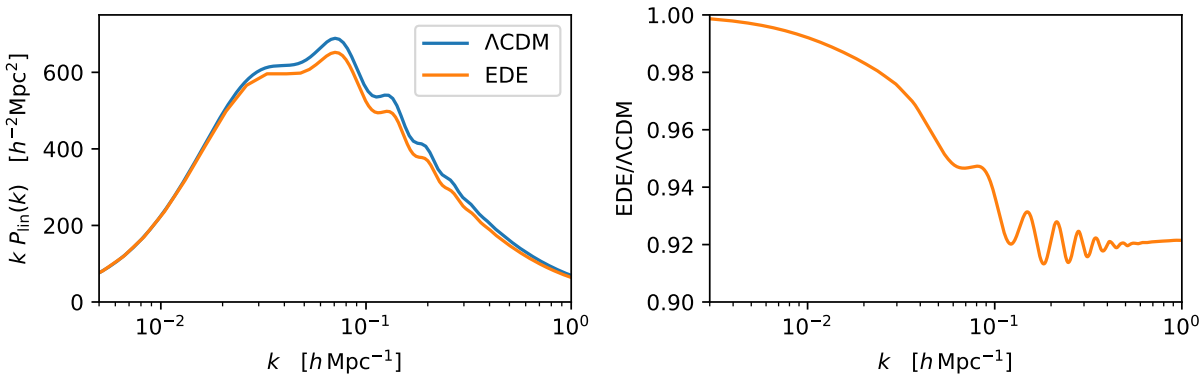

Figure 6.2: The linear theory power spectra (left) and their ratio (right) for our fiducial ΛCDM model and models with features induced by a period of early dark energy (EDE) at $z \simeq 10^4$. See text for further details.

expansion, long periods where unclustered species dominate the expansion lead to suppression of large-scale structure that can be detected by comparing early- and late-time measures of the fluctuation amplitude. A precise measurement of the power spectrum shape can also be used to place constraints on (or detect) short-term deviations from matter or radiation domination, since such periods will change the shape of the power spectrum due to differential growth of modes. Recently this reasoning was used to place constraints on early dark energy (EDE) models which contribute to the expansion near recombination [174, 86, 95, 203]. The point is more general however, and an accurate measurement of the power spectrum constrains deviations in the expansion history over a broad range of redshifts[1].

As an exploration of this class of effects we consider scalar-field based models of Early Dark Energy (EDE) wherein the impact of EDE is localized to time significantly before those probed observationally. EDE models are a timely example as they have been the subject of much recent interest as a potential way to resolve discordances between ΛCDM analyses of various data sets [291, 355, 174]. In fact we use the modification of CLASS [48] by the authors of ref. [174] and consider a model where the contribution from EDE peaks at $z \simeq 10^4$ with peak fractional contribution (to ρ) of 10 per cent.

The linear theory power spectrum for this model is compared to our fiducial ΛCDM model in Fig. 6.2, with the right panel showing the ratio to better highlight the change in shape induced by the non-standard expansion history. The position and amplitude of the feature in the right panel of Fig. 6.2 are set primarily by the redshift at which the EDE becomes non-negligible and the fraction of the energy density in dark energy (respectively).

[1]While we do not consider it here, features can also be introduced by interactions between or among particle species

6.4 Peturbative model

6.4.1 Overview of Previous Work

The effect of non-linearities and long-wavelength modes (IR-resummation) on oscillatory features in the power spectrum has long been studied in the context of BAO. A large body of work shows that these features can be accurately modeled in Lagrangian [46, 231, 229, 121, 266, 257, 58, 368, 232, 415, 402, 235] and Eulerian [92, 335, 321, 22, 50, 338, 112, 171, 278, 185] perturbation theory.

A perturbative analysis of features based on the Eulerian framework has been done recently [44, 390] (see also ref. [24]), in which the authors studied the effects of long wavelength modes on the primordial features of types given by Eqs (6.1) and (6.2). An important finding of these studies is that higher-loop corrections give rise to $\mathcal{O}(1)$ modifications to the features for a wide range of parameters and wavenumbers of interest. This leads one to consider resumming these $\mathcal{O}(1)$ contributions, arising from the large displacements, as is done in the case of BAO (see above).

For a general, oscillatory power spectrum component, refs. [44, 390] show that the long modes' effect on the one-loop contribution can be computed as

$$P^{\rm w}_{\text{1-loop}}(k) = \frac{1}{2}\int^{\Lambda} \frac{d^3p}{(2\pi)^3}\,\frac{(\mathbf{p}\cdot\mathbf{k})^2}{p^4} P^{\rm nw}(k)\Big[P^{\rm w}(|\mathbf{k}+\mathbf{p}|) + P^{\rm w}(|\mathbf{k}-\mathbf{p}|) - 2P^{\rm w}(k)\Big], \tag{6.3}$$

where Λ is a cut-off scale such that $p < \Lambda \sim k$. Taylor expanding the first two components in the brackets of integrand in q and formally integrating gives a one-loop contributions of the form

$$P^{\rm w}_{\text{1-loop, X}}(k) = -\frac{1}{2}k^2\Sigma_X^2 P^{\rm w}(k), \tag{6.4}$$

where Σ_X is the effective displacement dispersion at a point and X labels either the linear, or logarithmic shapes given in Eqs (6.1) and (6.2). The dispersion can be well approximated by

$$\Sigma_X^2 = \frac{1}{3\pi^2}\int_0^{\Lambda} dp\ \left[1 - j_0\left(\omega_X p\right) + 2j_2\left(\omega_X p\right)\right] P^{\rm nw}(p), \tag{6.5}$$

where for linear[2] shapes (Eq. (6.1)) we have $\omega_X = \omega_{\rm lin}$, while for logarithmic shapes we have $\omega_X = \omega_{\rm log}/k$. The latter makes a further approximation that, due to the shape of $P^{\rm nw}$, the $\Sigma_{\rm log}$ integral has most of its contributions from the $p \ll k$ part of the integral. In the case of linear oscillations the above expression corresponds to the results obtained in BAO studies and their IR-resummations.

Following the results of ref. [390], the total non-linear matter power spectrum at one-loop can be obtained as

$$P_{\text{1-loop},X}(k) = P^{\rm nw}(k)_L + \left(1 + \frac{1}{2}k^2\Sigma_X^2\right) e^{-\frac{1}{2}k^2\Sigma_X^2} P^{\rm w}(k)_L + P^{\rm nw}_{\text{1-loop}}\left[P_L^{\rm nw} + e^{-\frac{1}{2}k^2\Sigma_X^2} P_L^{\rm w}\right](k). \tag{6.6}$$

[2]These derivations always assume the $r_d \to 0$ limit.

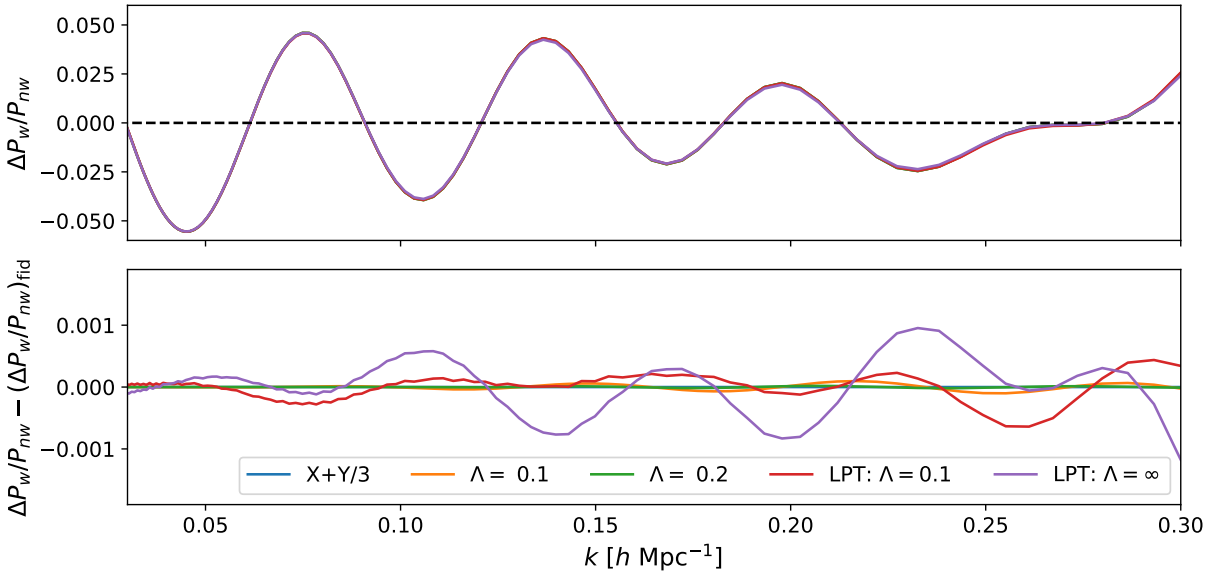

Figure 6.3: Comparison of the oscillatory components of the real-space power spectrum for our fiducial halo sample at $z = 1$ as predicted by 1-loop EPT and LPT for a range of IR-resummation choices in the ΛCDM cosmology. All choices are in excellent numerical agreement – the EPT schemes are all within 10^{-4} of the total broadband power of each other and differ at the 10^{-3} level with the LPT prediction. The latter number lets us place a minimum theoretical error on predictions for feature amplitude.

This expression can readily be extended to the power spectrum for biased tracers, since the above IR-resummation procedure remains unchanged. Moreover we see that if more than a single distinct feature is present in the power spectrum (as is the case if one studies e.g. BAO and some other feature), the above expression simply obtains additive $P^{\rm w}$ contributions, given that, to a very good approximation, we can neglect the cross-correlation contributions of different wiggle components (e.g. $P^{\rm w}_{\rm lin} \times P^{\rm w}_{\rm BAO}$). For further details on these results we refer a reader to refs [44, 390]. In what follows we shall show how the IR resummation is naturally handled in LPT, and how this leads to a different way of obtaining an Eulerian resummation procedure.

6.4.2 Lagrangian IR Resummation and Connection to Earlier Approaches

In contrast to the above, within the Lagrangian framework (LPT) IR resummation can be naturally incorporated by exponentiating long-wavelength displacements [231, 58, 402]. Within ΛCDM this is nearly equivalent to simply exponentiating the linear displacements, since in such cosmologies the variance of displacements in linear theory due to modes at high

k is relatively small while those at low k are approximately linear. In this regime the matter power spectrum is given by

$$P_m = \int d^3\mathbf{q}\; e^{i\mathbf{k}\cdot\mathbf{q} - \frac{1}{2}k_i k_j A_{ij}^{\rm lin}} \left\{1 - \frac{1}{2}k_i k_j A_{ij}^{\rm loop} + \frac{i}{6}k_i k_j k_k W_{ijk} + ...\right\}, \tag{6.7}$$

where A_{ij} and W_{ijk} are n-point statistics of pairwise displacements $\Delta = \mathbf{\Psi}_1 - \mathbf{\Psi}_2$ with separation $\mathbf{q} = \mathbf{q}_1 - \mathbf{q}_2$. In the expression above, in principle only the long modes of the linear displacement field should be resummed. This can be accomplished by splitting the exponentiated A_{ij} in the above equation with the same kind of cutoff Λ as in Equation 6.5 and Taylor-expanding the short-wavelength component[3]. However, the cumulative effect of introducing such an explicit IR scale, Λ, on any wiggle shapes (including BAO) is quite small, constituting less then the 0.1% difference, as shown in Figure 6.3. This approximation is of course true as long as the resummed displacement dispersion does not receive large contributions from small scales, which is the case for ΛCDM-like spectra.

Within LPT, the Eulerian resummation can be recovered as a saddle-point approximation; briefly, for an input linear power spectrum with smooth and wiggly components $P_{\rm lin} = P_{nw} + \Delta P_X$, the latter can be expanded out of the exponent, where its configuration-space feature at some characteristic separation q_X will pick out a nonlinear smoothing

$$e^{-\frac{1}{2}k^2\Sigma_X^2} = \left\langle \exp\left\{ -\frac{1}{2}k_i k_j A_{ij}^{nw,\rm lin}(\mathbf{q})\right\}_{|\mathbf{q}|=q_X}\right\rangle. \tag{6.8}$$

This recovers the $\Lambda \to \infty$ limit of Eq. 6.5. The brackets in the above equation refer to the angular average of the exponent in the space of $\mathbf{q}$'s. Decomposing $A_{ij} = X(q)\delta_{ij} + Y(q)\hat{q}_i\hat{q}_j$ into scalar components X and Y, the most straightforward approach is to take the average to correspond to $X + Y/3$, though we note for example that Eq. 6.5 corresponds to taking $X + Y$. If there are multiple oscillatory components, i.e. a superposition of sinusoidal components as in "Lin.x2" (Fig. 6.1), then as long as each component is perturbatively small the above argument can be applied independently to determine the saddle-point q_X and damping factor Σ_X^2 of each feature as argued for EPT in the discussion below Eq. 6.6. If the wiggly component does not have a linear dispersion $\phi = \omega k$ or is not a sum of several linear components the Eulerian treatment is equivalent to making the approximation $\phi(k) \approx \phi'(k)(k - k_0) + \phi_0$ at each k and performing the saddle-point integral there. For logarithmic scales this is

$$\sin\left(\omega \ln\frac{k}{k_*}\right) \approx \sin\left(\frac{\omega}{k_0}(k - k_0) + \phi_0\right), \tag{6.9}$$

so that $q_x(k) = \omega/k$. This approximation works increasingly well the larger ω is, and we give a formal derivation in Appendix F.1.

Based on the Eulerian and Lagrangian discussions above it may seem like there exists an over-abundance of possible IR resummation schemes. This is not, however, a matter of

[3] In practice we use a Gaussian cutoff. See also Section 4.3 in [74].

great concern since it turns out all of these schemes behave quantitatively similarly, at least within roughly ΛCDM cosmologies. For example, as noted above the difference between setting Λ to be some fraction of k and letting $\Lambda \to \infty$ as in LPT will be small in such cosmologies due to the relative smallness of linear displacements at high k. Figure 6.3 shows a comparison of these schemes for our fiducial ΛCDM cosmology at $z = 1$, with bias parameters taken from our fiducial halo sample. For clarity of presentation we have isolated the oscillatory signal by subtracting a rough broadband computed using a Savitsky-Golay filter, then supplementing each theory curve with a quartic polynomial in k such that curves identical modulo such a quartic contribution will be coincident[4]. Taking $\Sigma^2_X = X + Y/3$ derived from Eq. 6.8 as our baseline (blue curve), we see that the differences between this choice and the conventional EPT dampings with $\Lambda = 0.1,\, 0.2\,h\mathrm{Mpc}^{-1}$ are extremely small and at the level of 10^{-4} when compared to the (linear theory) broadband power. This is because much of the numerical difference between the "linear" $e^{-\frac{1}{2}k^2\Sigma^2_X}\Delta P_w$ is ameliorated by correctly accounting for damping effects at one-loop level in Eq. 6.6. On the other hand, the differences between these schemes and a direct LPT calculation in which the linear displacements are fully resummed is larger, though still in excellent numerical agreement, at about the 10^{-3} level, while an LPT calculation with $\Lambda = 0.1h$ Mpc^{-1} lies in between. Finally, let us note that while the (Gaussian) statistical error on power spectrum measurements scale as amplitude of the total power, the theory error discussed above scales as the amplitude of the wiggles only; for example, while it is at 10^{-3} of the total power for a 5% feature (BAO), non-BAO primordial features bounded at the 1% level using BOSS and Planck data by ref. [44], it will be at the 2×10^{-4} level at the same redshift.

From the above comparison, we can conclude that (1) the disagreement between LPT and EPT lets us set a minimum theoretical error on theoretical predictions for feature ampltidue at about 0.1% and (2) that the difference between the various Eulerian IR resummation schemes and their predictions for Σ^2_X are small compared to this theoretical error, such that we can be reasonably cavalier when choosing between them. Indeed, as k approaches the nonlinear scale we should expect that oscillatory signals from beyond-one-loop contributions will become increasingly prominent compared to the amplitude of the linear oscillations, dwarfing the theoretical differences highlighted above in the same way that the scale of the bottom panel of Figure 6.3 is much smaller than that of the top panel. Given that the one-loop EPT-LPT difference is only a few percent of the wiggle amplitude in ΛCDM—5 percent compare to 0.1 percent—even at the edge of our perturbative reach at $k = 0.2h$ Mpc^{-1}, the above comparison suggests that searches for primordial features should focus on exploring higher redshifts and volumes.

[4]In this and other plots of the nonlinear oscillation signal below, we remove broadband differences by fitting a quartic polynomial in k to the differences between plotted curves.

6.4.3 Redshift-Space Distortions

Since next-generation galaxy redshift surveys will be the natural hunting ground for primordial features, the focus of this section is to extend the modeling of primordial features in previous works to redshift space. We use 1-loop Lagrangian and Eulerian perturbation theory (LPT and EPT) described in the previous subsections to model both the real- and redshift-space power spectra of biased tracers (i.e. halos in our context) within the plane parallel approximation as described in detail in ref. [74]. The redshift-space power spectrum, $P_s(k,\mu)$, is evaluated as an expansion in the line-of-sight wavenumber, $k_\parallel = k\mu$, multiplying n^{th}-order pairwise velocity spectra, such that

$$P_s(k,\mu) = \sum_{n=0}^{\infty} \frac{(ik\mu)^n}{n!} \tilde{\Xi}_\parallel^{(n)}(k,\mu). \tag{6.10}$$

The model includes Lagrangian and Eulerian third-order bias expansions along with counter terms and stochastic terms to account for small-scale physics that we do not explicitly model. Our fiducial model includes terms up to second order in the velocity expansion, but employ an ansatz for the third moment which is shown to be highly accurate for ΛCDM-like models [74]. As discussed in ref. [74], while a finite-order expansion in the velocity moments $\tilde{\Xi}$ necessarily omits feature damping due to bulk velocities that would be included in a "complete" IR resummation scheme, particularly at high μ, we will show that it is nonetheless sufficiently accurate for upcoming galaxy surveys like DESI; however, for completeness we also include comparisons to (1) the Gaussian streaming model and (2) one-loop EPT wherein both bulk displacements and velocities are resummed where appropriate. We set the third order Lagrangian bias to zero since its effects are subdominant for the halos and scales of interest [214, 4].

6.5 Results

To see how well our perturbative models predict the non-linear evolution and redshift-space distortions in models with primordial or induced features we compare to our N-body results. For each model we fit to the average of the 6 simulations. The fits are done using the model "out of the box", i.e. without tweaking or adjusting any settings, letting only bias parameters and effective corrections float, and assuming the correct cosmology and linear theory power spectrum.

Figure 6.4 shows an example of our fits to the real-space halo spectra for the primordial feature models. The real-space spectra are not directly observable (except in projection, which will tend to wash out the features) but serve to show that the model is able to predict the underlying clustering well. We focus on the middle redshift ($z = 1$) and highest number density ($\bar{n} = 10^{-3}\,h^3\,\text{Mpc}^{-3}$) sample since this has the smallest error bars. The agreement between both models and N-body data is excellent over the entire range of quasi-linear scales and into the regime where shot-noise begins to dominate the spectra. While not shown, we

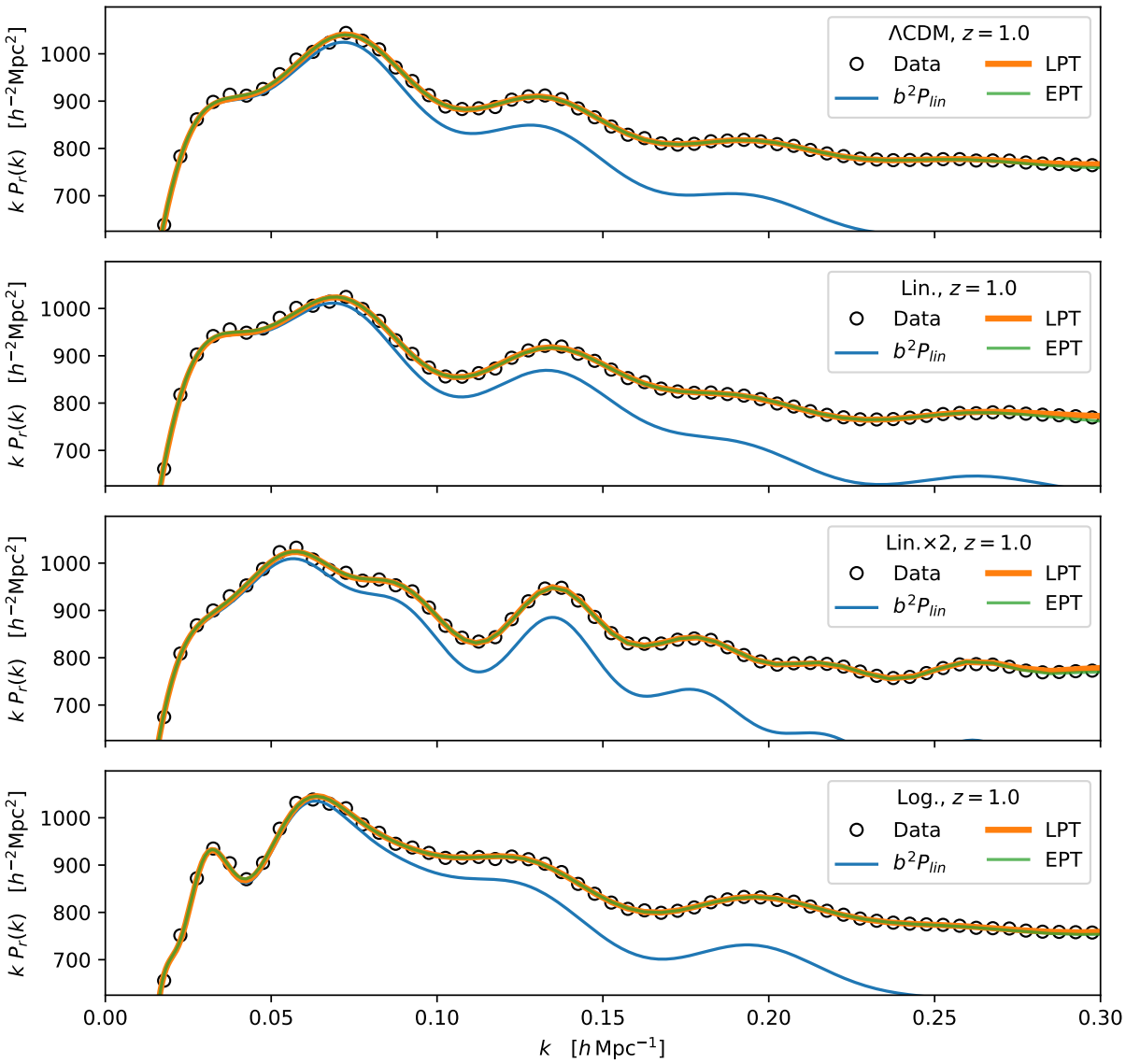

Figure 6.4: The real-space, halo power spectra from our simulations at $z = 1$ and model fits. We show results for the $\bar{n} = 10^{-3}\,h^3\,\mathrm{Mpc}^{-3}$ sample, since it has lower shot noise, but results for the sparser sample are qualitatively similar. The open, black circles show the average of $P(k)$ over the 4 boxes. The orange and green lines (which are almost on top of each other) show the best-fit LPT and EPT models while the blue line shows linear theory with the same large-scale bias as the EPT models.

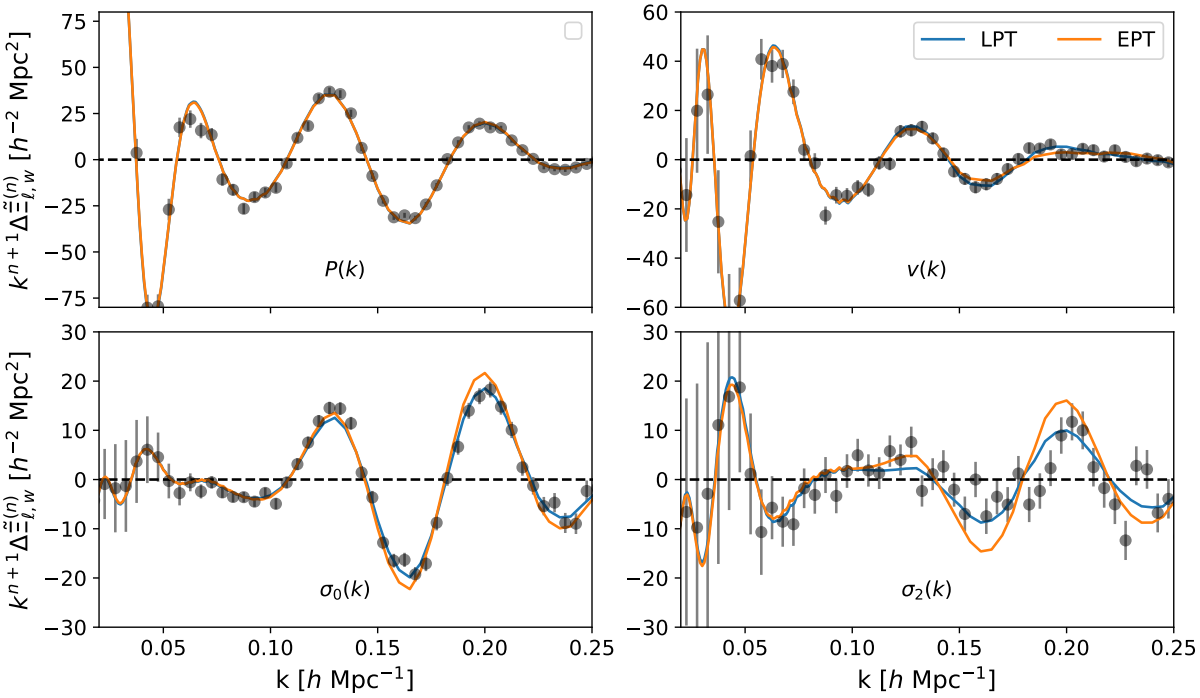

Figure 6.5: Broadband-subtracted pairwise-velocity moments in real space for our fiducial halo sample with the "Lin.×2" linear power spectrum compared to predictions from LPT and EPT. As in basic ΛCDM models, there is excellent quantitative agreement between LPT and EPT in the zeroth and first moments, while in the second moment EPT slightly underpredicts the damping of 1-loop wiggles prominent at higher k.

have checked that the more biased sample and other redshift slices show similar levels of agreement.

In addition to the real-space power spectrum we have also measured the first two, real-space pairwise velocity moments of our halo samples and compared them to perturbation theory. These velocity statistics inform the angular structure of the redshift-space power spectrum (which we expect will eventually provide our tightest observational constraints on features) in addition to being well-defined observables in their own right, and extracting them individually gives us a closer look at oscillatory features that only become prominent at high μ. Figure 6.5 shows our best-fit LPT and EPT models for the model with two linear oscillations (Lin.×2), again with broadband shapes subtracted to isolate the oscillatory components. Much as in ΛCDM models [74] there is excellent agreement between LPT and EPT for the real-space power spectrum (P), and the pairwise velocity (v), while EPT tends to slightly underpredict the damping for the second moment (σ_ℓ), especially as the one-loop oscillations become prominent at $k > 0.1\,h\mathrm{Mpc}^{-1}$. These differences are, however, small and the models predict almost identical power spectrum wedges. Nonetheless, they are helpful in informing

our theoretical error budget when searchiing for oscillations close to the line-of-sight.

As Figs. 6.4 and 6.5 make clear the Eulerian and Lagrangian descriptions provide almost identical performance over the range of scales where we expect perturbation theory to be valid. We find this persists even for the redshift-space spectra, and so to avoid clutter we shall show only the Lagrangian model in the following figures.

Figure 6.6 compares the theory prediction (LPT moment expansion) and N-body data for the anisotropic power spectrum wedges $P(k,\mu)$ in redshift space. The theory and data are in excellent agreement over a large range of scales and LOS angles μ, though we note that the shot noise $\sim \bar{n}^{-1}$ plays an increasingly dominant role at the highest k's shown. We focus on the redshift-space wedges, which are independent in linear theory, but have checked that the theory returns an equivalently good fit to the smooth and oscillatory components of the multipoles.

As an additional check on possible theory differences, Fig. 6.7 shows the predictions for the oscillatory components of $P_\ell(k)$ (i.e. with the broadband subtracted) for our fiducial halo sample using our LPT moment expansion model, Gaussian streaming model and resummed Eulerian perturbation theory. Despite the Lagrangian and Eulerian models being fit separately to the wedges, i.e. $P(k,\mu)$ data, all three models are in excellent agreement with each other and the N-body data for the multipoles, $P_\ell(k)$. The agreement is particularly impressive in comparison to the scatter in the N-body data, which are themselves tighter than expected for upcoming surveys with a total simulated volume of $> 90\,h^{-3}\mathrm{Gpc}^3$. In order to demonstrate their equivalence at low k, we have matched the countererms between the moment expansion and Gaussian streaming model predictions (Appendix F.2), but note that at the highest k's shown the GSM predictions for the quadrupole are in fact in slightly better agreement with the EPT prediction, suggesting that differences there are driven by the incomplete IR resummation of bulk velocities in the moment expansion (see ref. [74] for further discussion).

Finally, Fig. 6.8 shows similar fits to the model with 10 per cent early dark energy at $z \simeq 10^4$. Again the fiducial LPT model provides an excellent fit to the N-body data in both real and redshift space on quasi-linear scales, indicating that these scales can be used to constrain the amount of unclustered dark energy contributing to the expansion when such modes entered the horizon. A similar level of fit is obtained using other schemes such as resummed EPT, though we have not shown them for sake of brevity. Future surveys, probing large volumes at high redshift, should be able to constrain the expansion history via its effect on growth over a broad range of cosmic history.

6.6 Conclusions

We have investigated how well 1-loop perturbation theory, both Eulerian and Lagrangian, can model the redshift-space power spectra of biased tracers such as dark matter halos in models with either primordial or induced features. By comparing the models of ref. [74] to clustering statistics measured from a series of large N-body simulations, we have shown that bias, non-linear evolution and redshift-space distortions can all be accurately accounted for

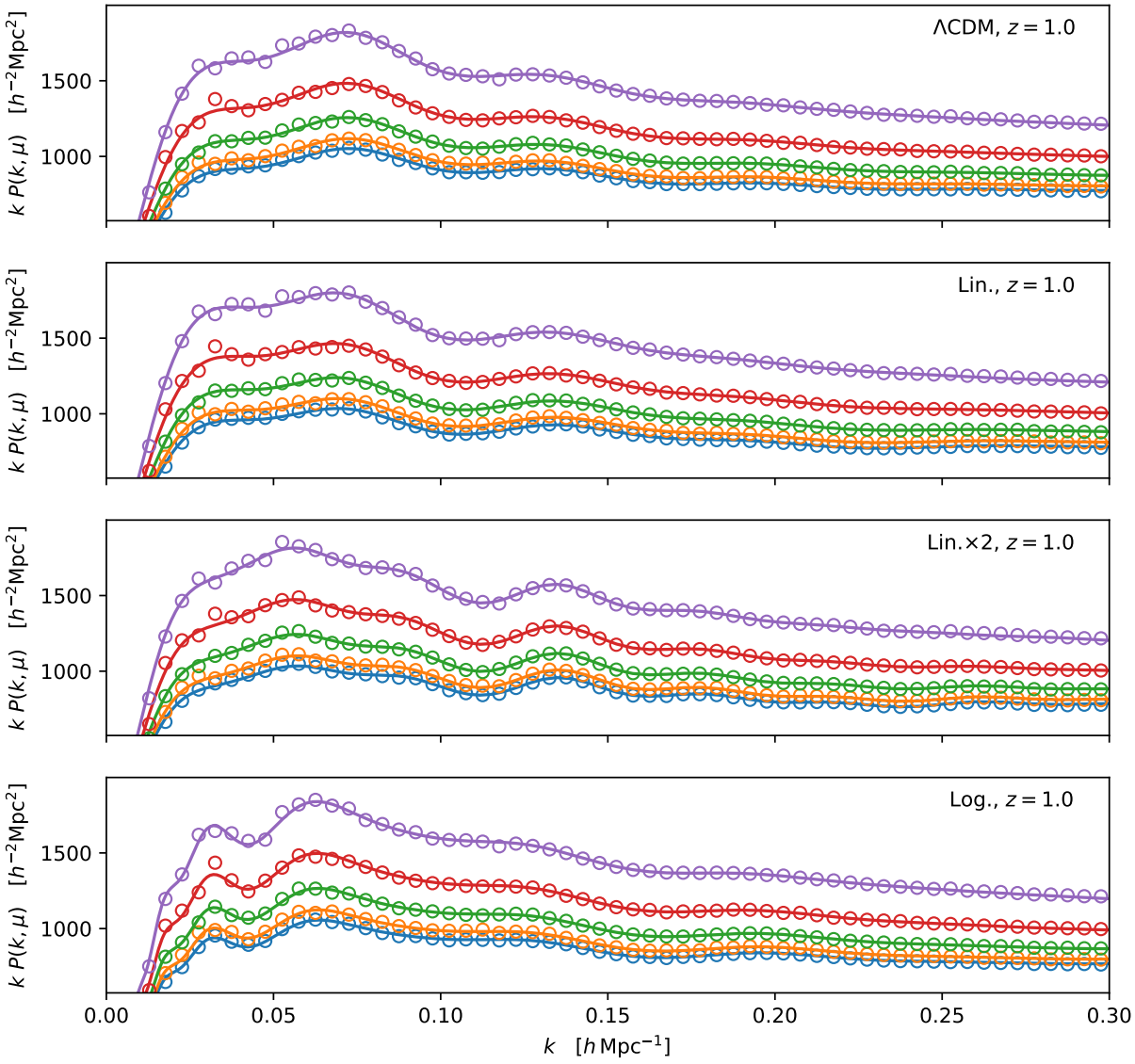

Figure 6.6: The redshift-space, halo power spectrum wedges from our simulations at $z = 1$ and model fits. We show results for the $\bar{n} = 10^{-3}\,h^3\,\mathrm{Mpc}^{-3}$ sample, since it has lower shot noise, but results for the sparser sample are qualitatively similar. The open circles show the average of $P(k, \mu)$ for $\mu = 0.1$, 0.3, ..., 0.9 (colors, bottom to top), the solid lines show the best-fit LPT model.

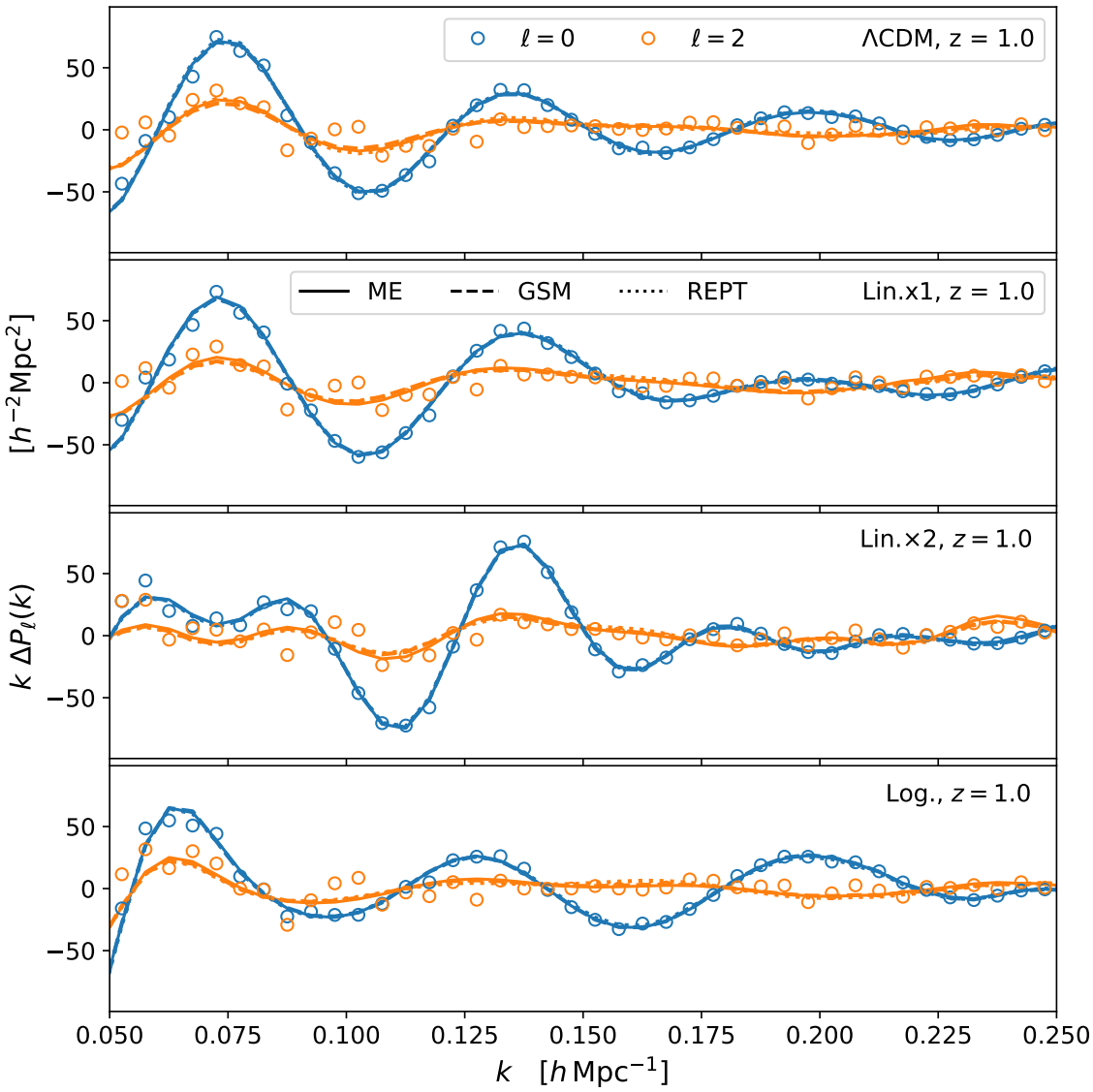

Figure 6.7: Predictions using the LPT moment expansion, Gaussian streaming model and IR-resummed EPT (REPT) for the oscillatory components of the redshift-space power spectrum monopole and quadrupole at $z = 1$ for the $\bar{n} = 10^{-3}\,h^3\,\mathrm{Mpc}^{-3}$ sample. The LPT and REPT models are in excellent agreement, especially compared to the scatter of the N-body data to which they were independently fit.

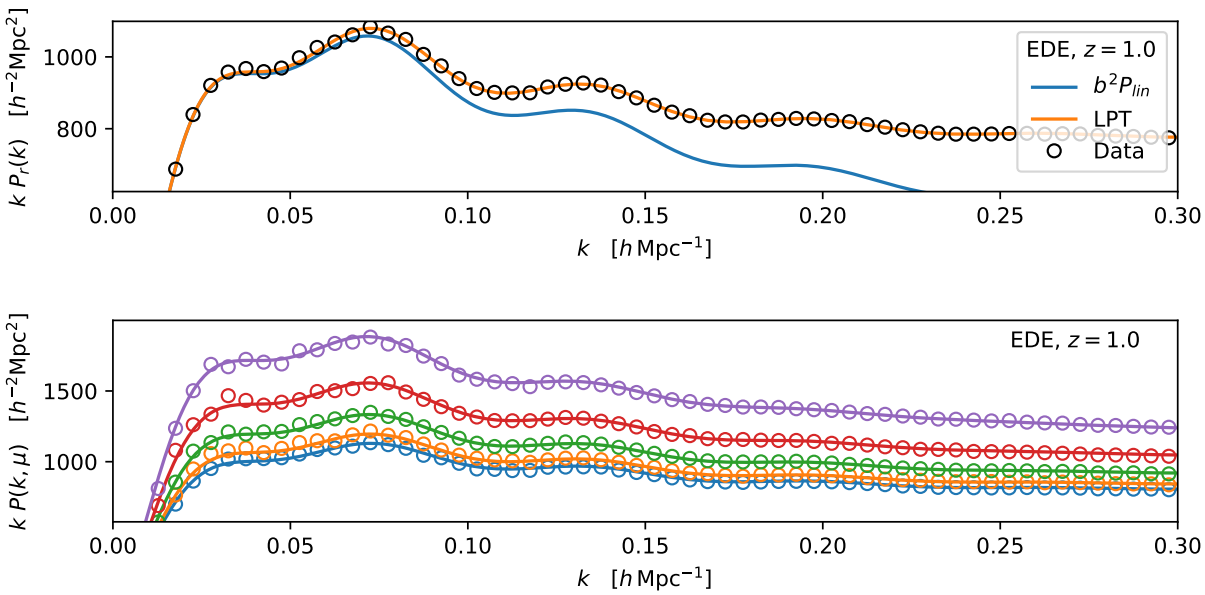

Figure 6.8: As for Figs. 6.4 and 6.6 but for the model with an "induced feature" (see text and Fig. 6.2).

by existing perturbative models with no need for any tuning or modification. This is the first demonstration that such perturbative models can fit the redshift-space clustering of biased tracers in such theories to per cent level precision on quasi-linear scales.

We compare three primordial feature models (Fig. 6.1) and one model with an "induced" feature imprinted by an epoch of early dark energy (Fig. 6.2). We investigated two different schemes for modeling the dynamics (Eulerian and Lagrangian), several different IR resummation schemes, and different methods for including redshift-space distortions (a moment expansion and a cumulant expansion: the Gaussian Streaming Model). In all cases we find excellent agreement between the different theories and the N-body simulations. Figure 6.3 shows that different methods of performing IR resummation give extremely similar predictions for the power spectrum. Figures 6.4 and 6.5 show that both LPT and EPT predict the real-space density and velocity statistics measured in our N-body simulations well to $k \simeq 0.25\,h\,\mathrm{Mpc}^{-1}$. With these ingredients, Fig. 6.6 shows that the moment expansion accurately describes the redshift-space, power spectrum wedges, $P(k,\mu)$ with Fig. 6.7 highlighting the agreement on the oscillatory features in the multipole moments for both the moment expansion and a cumulant expansion. Figure 6.8 shows the same excellent agreement for features induced by changes in the expansion history at high redshift, rather than imprinted upon the primordial power spectrum.

This extensive set of comparisons and tests imply that current perturbative models are up to the task of constraining models with features given suitably accurate redshift-space

clustering data. Future surveys, capable of operating over large volumes at high redshift — shifting the non-linear scale to higher k and the fundamental mode to lower k — would be ideal in providing such constraints. We intend to return to the detectability of these features by different surveys [24], and the impact of degeneracies, in a future paper. However, it is clear that future surveys that probe large volumes at high redshift should be able to constrain both primordial features and the expansion history over a broad range of cosmic history (via its effect on growth).

6.7 Acknowledgements

We would like to thank Emanuele Castorina, Sergey Sibiryakov, and Marko Simonović for many useful discussions. We also thank the authors of ref. [174] for making public their modification of the CLASS Boltzmann code including early dark energy. S.C. is supported by the National Science Foundation Graduate Research Fellowship (Grant No. DGE 1106400) and by the UC Berkeley Theoretical Astrophysics Center Astronomy and Astrophysics Graduate Fellowship. M.W. is supported by the U.S. Department of Energy and the NSF. This research has made use of NASA's Astrophysics Data System and the arXiv preprint server. This research used resources of the National Energy Research Scientific Computing Center (NERSC), a U.S. Department of Energy Office of Science User Facility operated under Contract No. DE-AC02-05CH11231.

Chapter 7

Simulations and Symmetries: Combining N-body Dynamics and Lagrangian Bias Expansions

This chapter was originally published as

> Chirag Modi, Shi-Fan Chen, and Martin White. "Simulations and symmetries". In: *MNRAS* 492.4 (Mar. 2020), pp. 5754–5763. DOI: 10.1093/mnras/staa251. arXiv: 1910.07097 [astro-ph.CO]

In Chapters 4, 5 and 6 we used the natural IR resummation due to the nonlinear mapping between displacements and densities in the Lagrangian formalism to study how structure formation affects the BAO peak and other features in the linear 2-point function. However, as we discussed in the Introduction, this nonlinear mapping is valid beyond the perturbative single-stream regime, as long as all solutions to the relation $\mathbf{x} = \mathbf{q} + \Psi(\mathbf{q})$ are kept. In this chapter we will construct a model for real-space correlations between galaxies and matter beyond the traditional reach of perturbation by exploiting this mapping and using displacements from N-body simulations. Since N-body simulations represent a (near) exact solution to the Lagrangian system, plugging in N-body displacements into the delta function in Equation 1.70 represents a resummation of dynamical nonlinearities to all order and, in the event that the dynamical nonlinear scale $k_{\rm nl}^{-1}$ is larger than the halo radius R_h, can extend the reach of Lagrangian bias past the reach of conventional LPT. This method represents a way to model galaxy-matter correlations past the nonlinear scale without needing to run high-resolution simulations that can resolve halos and subhalos and, indeed, since its original publication has been adopted by multiple groups to do just that [207, 156, 432].

7.1 Introduction

The study of the form and evolution of the large-scale structure in the Universe is one of the most promising probes of cosmology and fundamental physics [410, 12]. One of the major difficulties in interpreting data from large-scale structure surveys is that we measure a biased tracer of the non-linear density perturbations (and, for some surveys, in redshift space). The combination of non-linear evolution and the non-linear dependence of galaxy bias makes robust inferences difficult.

The non-linearity of the dark matter field does not itself pose insurmountable difficulties. On quasi-linear scales perturbation theory provides an accurate solution [see 396, 186, 96, for recent examples]. Further, the evolution of dark matter particles under gravity from known initial conditions is a well posed numerical problem which can be solved with high accuracy and efficiency with modern N-body codes [357, 154, 144]. With care, percent level accuracy on the low order statistics of the density field can be obtained [165, 324], and interpolation formulae ('emulators') can be devised to provide predictions as a function of cosmological model [167, 166, 212, 435, 126, 420].

By contrast the behavior of the baryonic component, including hydrodynamics, star and black hole formation and feedback, remains a challenge. Despite decades of progress in models, numerical algorithms, codes and computers a quantitative understanding of the translation from mass to light continues to elude us. However, on sufficiently large scales all of these complexities can be parameterized by a series of numbers, the bias expansion, in a way that is informed by the symmetries of the underlying laws rather than the details of the specific processes that act [see e.g. 110, for a recent review]. In detail, while the process that form and shape galaxies and other astrophysical objects are complex, all such objects arise from simple initial conditions acted upon by physical laws which obey well-known symmetries: for non-relativistic tracers these are the equivalence principle and translational, rotational and Galilean invariance. This symmetries-based approach serves as a counterpoint to the "halo model" approach [e.g. 408], which seeks to parameterize the manner in which galaxies inhabit halos of a given mass (and other properties). While the latter offers us a fuller picture, which is more closely tied to the underlying physics, the former provides a fully flexible parameterization that captures the relevant effects on the large scales that dominate most cosmological inference (i.e. on scales where the observed density field is still highly correlated with the early-Universe density field and the present day matter field).

A symmetries-based bias expansion is now quite common in theories which treat the dynamics perturbatively [396, 186, 96, 88], however the halo model approach is still more common in simulation-based approaches [see e.g. 129, 420, 433, 435, for recent examples]. The purpose of this chapter is to investigate the combination of the robust, symmetries-based bias expansion with the (well behaved) N-body solution to the dynamics. Both the bias expansion and the N-body solution represent controlled approximations which can be made increasingly accurate given sufficient parameters and computational resources. Further, the number of parameters and computational cost for a fixed accuracy can be lower than for many other schemes on the scales of relevance to next-generation large-scale structure surveys.

In this first chapter we shall investigate how well a quadratic Lagrangian bias model, coupled with a "full" N-body dynamical model, can predict the real-space power spectrum of halos and mock galaxies. Though the method can be straightforwardly extended to higher order in the bias (albeit with a large increase in the number of parameters that need to be included) and to configuration space, redshift space and higher order statistics, we focus first on the real-space power spectrum both because it is the simplest statistic and because it is of interest in interpreting projected statistics such as angular clustering and lensing (either of the CMB or of galaxies). Recent related work on the accuracy of the Lagrangian bias expansion at the field level has appeared in [322, 248] and for Eulerian fields in [411].

The outline of this chapter is as follows: in the next section (§7.2) we introduce our (Lagrangian) bias expansion. In §7.3 we describe the N-body simulations which we use to compute our basis spectra and to test the performance of the model. Our results are presented in §7.4. We present our conclusions and comment upon future directions in §7.5.

7.2 The bias expansion

In this chapter we shall work within the context of Lagrangian bias, as formulated by [229]. In such a prescription the (smoothed) initial distribution of tracers (e.g. halos or galaxies) is obtained by "weighting" fluid elements by a functional, F, of the local initial conditions in the neighborhoods of their initial (or Lagrangian) positions, $\mathbf{q}$. As long as we choose a sufficiently early time the fluctuations should be small and we can Taylor expand F. We shall work to second order in the bias expansion and thus each particle in our N-body simulation will carry a weight

$$\begin{aligned} w(\mathbf{q}) &= F\left[\delta_{\rm lin}(\mathbf{q}), \delta^2_{\rm lin}(\mathbf{q}), \nabla^2\delta_{\rm lin}(\mathbf{q}), s^2_{\rm lin}(\mathbf{q})\right] \\ &= 1 + b_1\delta_{\rm lin}(\mathbf{q}) + b_2\left(\delta^2_{\rm lin}(\mathbf{q}) - \left\langle\delta^2_{\rm lin}(\mathbf{q})\right\rangle\right) \\ &\quad + b_s\left(s^2_{\rm lin}(\mathbf{q}) - \left\langle s^2_{\rm lin}(\mathbf{q})\right\rangle\right) + b_\nabla\nabla^2\delta_{\rm lin}(\mathbf{q}). \end{aligned} \tag{7.1}$$

where $s^2_{\rm lin}(\mathbf{q})$ is the (squared) shear field. As is conventional, we define the linear overdensity, $\delta_{\rm lin}$, by its linearly-evolved value at the observed redshift, i.e. $\delta_{\rm lin} = D(z)\delta_0$, where $D(z)$ is the growth factor (normalized to unity at $z = 0$). Other conventions amount to a rescaling of the bias parameters, b_i. The arguments of F are all of the terms, to second order, allowed by symmetry and are to be interpreted as smoothed fields[1].

In general, the bias expansion quantifies the local response of the galaxy overdensity to long-wavelength density perturbations and will not hold to arbitrarily small scales. To lowest order, the effects of smoothing, as well as any "non-local" behaviors, are captured by the derivative bias b_∇. We shall use the 'natural' smoothing of our simulation grids ($0.75\,h^{-1}$Mpc), and comment upon this later [see also 17]. Going to higher order in the bias

[1] Alternative bases for this expansion are possible, and sometimes used in the literature. A change of basis would simply lead to a linear mixing of the bias parameters and would not fundamentally change our conclusions.

expansion requires the addition of many more terms, with cubic order already doubling the number of coefficients [215, 4]. Unlike the quadratic biases (b_2 and b_s), many of the cubic bias parameters have been detected in simulations with only a marginal significance even in more massive halo samples than the ones we investigate in this chapter.

The biased density field, $\delta^B(\mathbf{x})$, is then obtained by advecting the particles to their present day position, i.e.

$$1 + \delta^B(\mathbf{x}) = \int d^3\mathbf{q}\ F(\mathbf{q})\ \delta_D(\mathbf{x} - \mathbf{q} - \mathbf{\Psi}(\mathbf{q})), \tag{7.2}$$

where $\mathbf{\Psi}(\mathbf{q})$ denotes the displacement of fluid elements from their original (Lagrangian) positions to their final (Eulerian) positions. We denote $\mathbf{\Psi}$ as a function of $\mathbf{q}$ since this is common in the literature on Lagrangian perturbation theory and since in N-body simulations particles are often assigned ID numbers based on their initial positions. We take the displacement, $\mathbf{\Psi}$, for each particle directly from the simulations. Operationally δ^B can be easily computed by placing each particle onto a grid at its position at the time of interest (using the N-body position and possibly velocity) with a weight calculated from its initial position and the initial conditions according to Eq. (7.1). We note that our scheme corresponds to selectively resumming only dynamical nonlinearities in the galaxy density field or, in the language of Eulerian bias, assuming values of Eulerian bias consistent with those generated by advection given nonzero b_1, b_2 and b_s.

Within this formalism we can write halo power spectra as linear combinations of component cross spectra. Specifically, defining the component fields $\delta_i(\mathbf{x})$ as the initial fields $i = \{1, \delta_L, \delta_L^2, s_L^2, \nabla^2\delta_L\}$ advected from $\mathbf{q}$ to $\mathbf{x}$ as in Eq. (7.2), we have that the cross power spectrum between two biased tracers (a and b) is given by

$$P^{ab}(k) = \sum_{i,j} F_i^a F_j^b P_{ij}(k) + P_{\rm SN}, \tag{7.3}$$

where $F^{a,b}$ are the coefficients in $w^a(\mathbf{q}) = \sum_i F_i^a \delta_i(\mathbf{q})$ and, for example, P_{δ,δ^2} is the cross spectrum between the advected linear density field and its square while P_{11} is the (non-linear) matter power spectrum[2]. We also include a shot-noise term, $P_{\rm SN}$, to account for stochastic contributions to the halo field not accounted for by the bias expansion. The extension of Eq. (7.3) to multispectra is straightforward. We emphasize that the 15 independent spectra, P_{ij}, can be individually computed from N-body simulations as described in the previous paragraph by weighting and advecting simulation particles, independently of the tracers in question. Each of these spectra is a function only of the cosmology (and redshift), with all of the bias dependence for any tracer contained within the coefficients, F. Avoiding the need to identify halos reduces the computational burden, both of finding the halos but also of sufficiently resolving them and possibly their histories, orientation, profiles and substructure. The fact that $P(k)$ for all tracers (that can be described by quadratic bias) can be predicted

[2]We caution that our notation has e.g. $P_{\delta,\delta^2} = P_{\delta^2,\delta}$ both contributing to P^{ab}. The convention in perturbation theory calculations is often to absorb the factor of 2 into the definition of P_{δ,δ^2} and omit the second term. We keep the symmetric form as it more naturally describes cross-spectra.

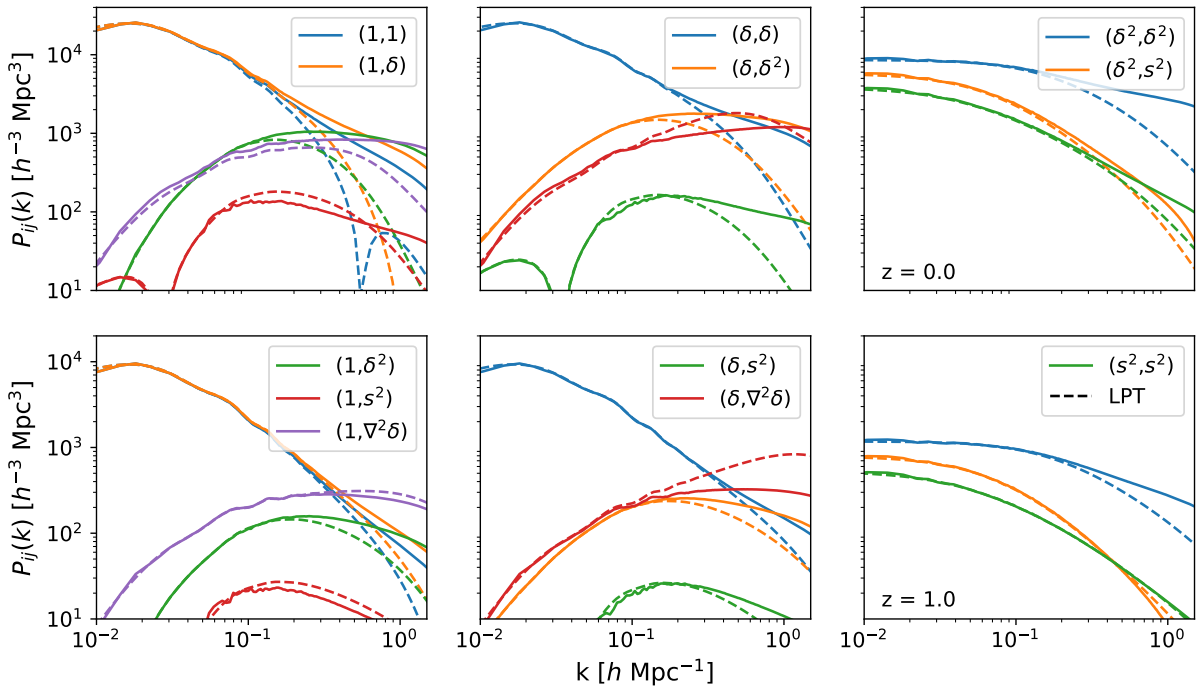

Figure 7.1: The 15 'basis' cross-spectra, P_{ij}, at $z = 0$ (upper panels) and $z = 1$ (lower panels). The halo and galaxy power spectra are formed from linear combinations of these spectra, as in Eq. (7.3). The matter and linear bias contributions (P_{11}, $P_{1,\delta}$ and $P_{\delta,\delta}$) dominate and are essentially degenerate on large scales, while differing at large k where the other components also contribute. The field $\nabla^2\delta$ has been multiplied by 10 h^{-2} Mpc^2 for ease of presentation.

from these P_{ij} using Eq. (7.3) means an emulator does not need to include any HOD-related parameters.

In the discussion above we have purposefully left out the effects of small-scale baryonic physics. This is because the bias expansion is only expected to be valid on scales where these baryonic effects – for example due to AGN feedback or ionizing radiation – are expected to be small [83, 53, 384] and manifest as perturbative corrections $\propto k^2 P_L(k)$ to the power spectrum [217, 317]. Such corrections are nearly degenerate with contributions from derivative bias, b_∇ (e.g. the fitting function of [384] is fit by k^2P to one per cent on the scales where our bias model holds). Indeed, the bias expansion itself would not be perturbative on scales where such baryonic effects are large. On larger scales, baryons can also affect galaxy power spectra through primordial relative density and velocity perturbations [427, 51, 316, 70, 25]. These effects are small and, while they are nondegenerate with contributions from our model, can be easily included at lowest order in perturbation theory. The inclusion of massive neutrinos is analogous, for light neutrinos.

7.3 N-body simulations

To investigate the performance of our quadratic bias model we make use of N-body simulations run for this purpose with the FastPM code [133]. The FastPM code uses a relatively low resolution particle mesh algorithm with large, global timesteps to evolve particles and thus does not provide accurate predictions for the profiles or substructure in halos. However, it does produce halo catalogs which are close to those produced by a more traditional N-body code [133, 112, 247, 97]. Since our purpose here is not to provide a percent level accurate prediction for a wide range of cosmologies but rather to test the performance of the bias model, any residual inaccuracy in the evolution should not be a concern: we aim to predict the clustering of halos and mock galaxies in the FastPM simulations using the particle dynamics generated by FastPM.

We ran 10 simulations, each of the same cosmology but differing in the random number seed used to generate the (Gaussian) initial conditions. Each simulation employed 2048^3 particles within a cubic, periodic box of side $1.536\,h^{-1}$Gpc, with forty time steps between redshifts z = 9 and 0 and snapshots output between $z = 3 - 0$. The forces were computed on a 4096^3 grid (i.e. $B = 2$). The simulations all assume a flat ΛCDM cosmology consistent with [285] ($\Omega_m = 0.309167, \Omega_b h^2 = 0.02247, \sigma_8 = 0.822, h = 0.677$).

We extract the particle data, and the friends-of-friends halo catalogs, from the outputs at $z = 2$, 1, 0.5 and 0. We also use the initial conditions (at $z = 9$), from which we generate the weights for each particle (Eq. 7.1). Each particle is assigned a unique ID number to allow it to be tracked across outputs, and we compute the displacements simply by matching the initial and final positions for each particle. We compute the weights from the initial conditions on a 2048^3 grid corresponding to a $0.75\,h^{-1}$Mpc cell size. We use cloud-in-cell interpolation of the particles onto the grid and of the weights onto the particles so this cell size forms a natural smoothing scale for our Lagrangian quantities. That the cells are not $\ll 1\,h^{-1}$Mpc will affect the range over which we can expect to obtain good results, but we felt $0.75\,h^{-1}$Mpc was a good compromise between efficiency and convergence. We caution, however, that all Lagrangian weights are not created equal: while the linear weights are smoothed much like the matter and halo fields, quadratic weights like δ^2 and s^2 are squares of smoothed fields which contain two factors of the window function, making them more susceptible to grid-size numerics. We compute the component spectra using the NbodyKit software [163] using FFTs on 2048^3 grids at the desired output time, with particles assigned to the grid using cloud-in-cell interpolation. We do not subtract a (Poisson) shot-noise component from the spectra, as this is included in our model (Eq. 7.3; in all cases we find a best-fit $P_{\rm SN}$ that is within twenty per cent—and typically just a few per cent— of the Poisson prediction).

We are interested in how well we can predict the real-space power spectra of (massive) halos and mock galaxies using our Lagrangian bias model. Our focus will be $M > 10^{12}\,h^{-1}M_\odot$ halos for two reasons. First, these halos are better resolved allowing more accurate comparison with our theoretical model. Second, these halos have higher and more scale-dependent bias, particularly at higher z, and so provide a stronger test of our model. We consider three mass bins (see Table 7.1) chosen to span a range of bias values while being well resolved and still

	$z = 0$		$z = 1$	
$\log_{10} M$	$\bar{n}$	b	$\bar{n}$	b
(12.0,12.5)	24.3	0.80	23.7	1.30
(12.5,13.0)	9.5	0.89	7.9	1.69
(13.0,13.5)	3.6	1.10	2.2	2.36

Table 7.1: Properties of the halo samples used in this work. Halo masses are in $h^{-1}M_\odot$ and number densities in $10^{-4}\,h^3\,\mathrm{Mpc}^{-3}$. The large-scale bias, b, is quoted as an Eulerian bias and is related to our Lagrangian bias, b_1, via $b = 1 + b_1$.

having a high enough number density to permit good measurements of the power spectra: $12.0 < \log_{10} M < 12.5$, $12.5 < \log_{10} M < 13.0$ and $13.0 < \log_{10} M < 13.5$, with M the halo mass measured in $h^{-1}M_\odot$. We describe our model for mock galaxies, which occupy a range of halo masses and include both satellites and centrals, in §7.4.3.

7.4 Results

The Lagrangian prescription enables separate treatment of tracer bias and nonlinear dynamics. Section 7.2 describes a power spectrum model in which the latter are treated exactly (to simulation accuracy) while the former is treated perturbatively. By comparison, traditional approaches to perturbation theory (PT) treat both as effective expansions. As such, our approach can be expected to improve upon these calculations in the regime where the dynamics are no longer sufficiently captured by PT but the bias expansion remains valid, for example at low redshifts where dynamics become highly nonlinear but halos have relatively low biases. At high redshifts, where biases are large but dynamics essentially linear on most the scales of interest, our model should be valid over the same range of scales as traditional PT approaches.

The goal of this section is to investigate the range of scales over which our quadratic bias expansion is valid and useful. We proceed in two steps: in §7.4.1, we extract component spectra from the simulations and compare them to their predicitions in one-loop Lagrangian perturbation theory (LPT). Then, in §7.4.2, we use the extracted component spectra to fit mass-limited halo power spectra and establish the scales over which the bias expansion is valid for various halo masses. Our model gains over traditional techniques in the regime where the dynamics are insufficiently captured by perturbation theory but the bias expansion remains valid. We extend the comparison to mock galaxies, generated from a halo occupation distribution, in §7.4.3.

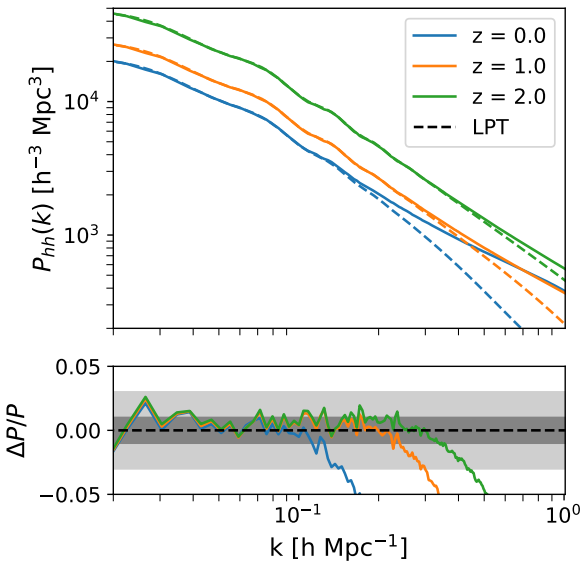

Figure 7.2: Comparison of halo autospectrum spectra predicted by our model and one-loop perturbation theory (LPT) for the same bias parameters. The latter matches our model on large scales but deviates towards large k as perturbative dynamics breaks down, particularly at towards lower redshift.

7.4.1 Component Spectra and Comparison to Perturbation Theory

Figure 7.1 shows the cross-spectra between the advected bias components, extracted from the simulations as described in §7.2 and averaged over all ten simulation boxes, at redshifts $z = 0$ and 1[3]. We note that the cross spectra between linear and quadratic initial fields (e.g. P_{δ,δ^2}) are particularly noisy since their variance includes contributions cubic in the linear spectrum (e.g. $\sigma^2_{\delta,\delta^2} \ni P_{\delta,\delta}P_{\delta^2,\delta^2} \sim \mathcal{O}(P_L^3)$) while their means are $\mathcal{O}(P_L^2)$ at lowest order, leading to a signal-to-noise ratio below unity. We substitute the predictions of 1-loop LPT for these spectra at $k < 0.08\,h\,\mathrm{Mpc}^{-1}$, where the theory is accurate but the N-body results very noisy[4].

Figure 7.1 demonstrates that the matter and linear bias contributions ($P_{11}, P_{1,\delta}, P_{\delta,\delta}$) dominate and are essentially degenerate on large scales, as expected. The dashed lines show the one-loop LPT predictions for these component spectra, which agree with the simulated component spectra on large scales but deviate on small scales where contributions due to

[3]A similar plot appeared in Fig. 7 of [4], who compared cross-spectra of cubic fields to two-loop standard perturbation theory.

[4]Since this component noise will also be present in any fitted data, given simulated volumes comparable to a given survey the summed model components will be no more noisy than the data even if some individual components have SNR less than unity.

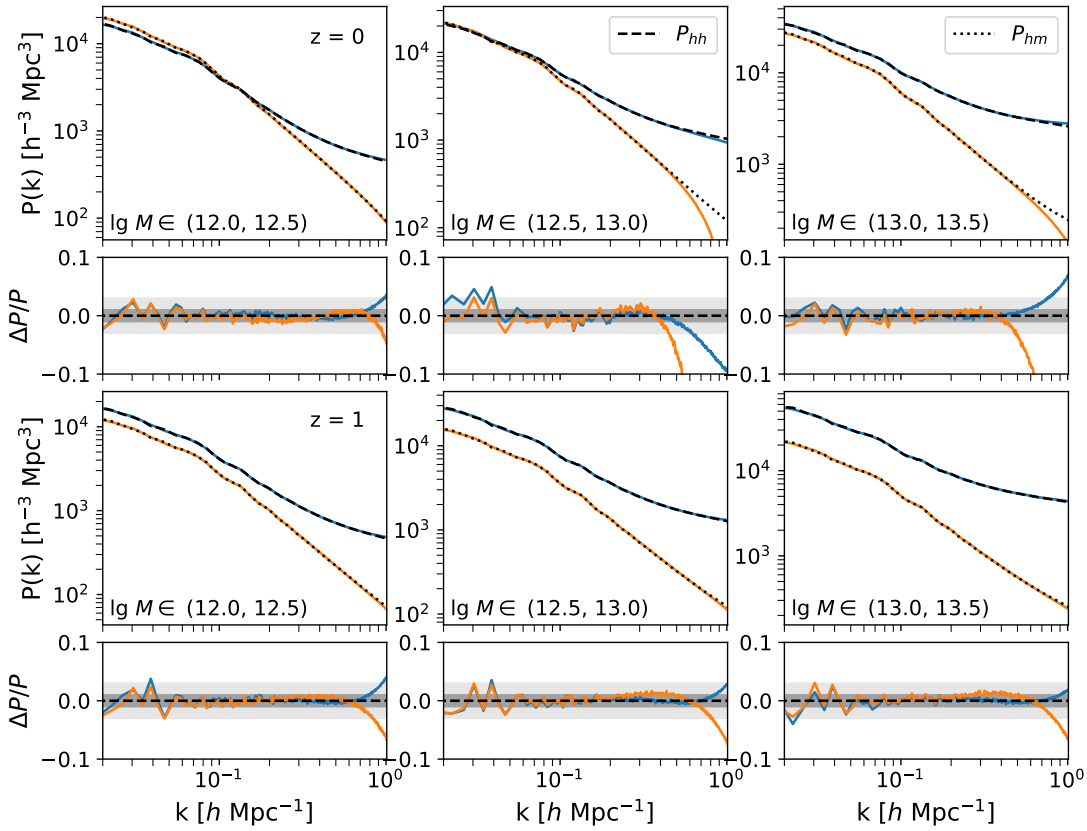

Figure 7.3: Halo auto-spectra (dashed) and halo-matter cross-spectra (dotted) for our three halo samples (Left: $12.0 < \log_{10} M < 12.5$, Middle: $12.5 < \log_{10} M < 13.0$ and Right: $13.0 < \log_{10} M < 13.5$) at $z = 0$ (top) and $z = 1$ (bottom). Black lines show the N-body spectra while the colored line shows the best-fit model of Eq. (7.3). For each combination we show both the full spectra and the fractional error as a function of k. The gray lighter and darker shaded regions show 3 and 1 percent errors, respectively.

quadratic and derivative bias also become significant, especially towards low redshifts[5].

The dashed comparisons shown in Fig. 7.1 were computed using "traditional" perturbation techniques; however, there has been much recent progress towards properly treating small-scale physics within the LPT framework using effective field theory techniques [290, 399], which must be included for a fair comparison with N-body simulations. Figure 7.2 shows the predicted halo spectra within our model of quadratic bias plus N-body displacements (solid) compared to one-loop Lagrangian perturbation theory for values of bias (b_1, b_2, b_s) that best fit the $12.5 < \log_{10} M < 13.0$ halos at $z = 0, 1$ and 2. For simplicity we have not included nonzero derivative bias b_∇, but adjust a one-loop counterterm $\propto k^2 P_L(k)$ for the LPT spectra to improve the agreement with simulation. In performing these fits we have adjusted the counterterm by eye to ensure good asymptotic behavior at large scales instead of maximizing the degree-of-fit over a wider range of k in order to best show the domain of validity of LPT. At $z = 2$, one-loop perturbation theory shows good quantitative agreement with the the modeled N-body spectrum out to $k \simeq 0.5\,h\,\mathrm{Mpc}^{-1}$, while even with a relatively large counterterm it agrees with simulation only to $k \simeq 0.2\,h\,\mathrm{Mpc}^{-1}$ at $z = 0$. These ranges-of-fit are consistent with the studies of the matter power spectrum within Lagrangian perturbation theory cited above and, roughly speaking, tell us when the nonlinear dynamics are no longer sufficiently described by perturbation theory (though some of the disagreement could also come from limited resolution in the simulations). They suggest $P(k)$ cannot be fit beyond $k\Sigma \lesssim \mathcal{O}(1)$, where Σ is the rms displacement of particles computed in linear theory, as would be expected on theoretical grounds. We note that this comparison with LPT shares only one free parameter – the counterterm – with usual fits to N-body halo spectra, as the bias parameters are fixed.

Our conclusions are in good agreement with those of [251], who showed that even if protohalo particles were properly identified in the initial conditions of a simulation using only perturbative displacements leads to poor prediction of $P(k)$ at non-linear scales. Comparing[6] to their Fig. 3, it seems that the Lagrangian bias expansion does roughly as well as properly identifying protohalo particles in the initial conditions.

7.4.2 Fitting halo spectra

Next we consider how well our model with N-body displacements predicts the (real space) halo auto-spectra and halo-matter cross-spectra for our three halo samples ($12.0 < \log_{10} M < 13.0$, $12.5 < \log_{10} M < 13.0$ and $13.0 < \log_{10} M < 13.5$). In each case we adjust both the 4 bias parameters plus the shot noise component to jointly fit the N-body halo autospectrum and halo-matter cross-spectrum. We use a Gaussian approximation to the covariance of $P(k)$ to avoid noise in the error estimate from having only 10 independent realizations and consider the fits as a function of k_{max}. Once the k-modes become non-linear they also become increasingly correlated, and our error estimate thus gives too much weight to the high k

[5] We have rescaled the b_∇ components to match $k^2 P_L(k)$ in physical units at large scales.

[6] We thank E. Castorina for emphasizing this point to us.

modes. However, in this regime the noise is also very small and simply requiring our model to fit within 1 per cent is an effective strategy.

Figure 7.3 compares the halo auto-spectra and halo-matter cross-spectra for our two halo samples at $z = 0$ and $z = 1$ to the best-fit model of Eq. (7.3). The agreement for both statistics, with a common set of bias parameters, is excellent out to $k \simeq 0.6\,h\,\mathrm{Mpc}^{-1}$ for all three halo samples and both redshifts. This substantially increases the range of fit at $z = 0$, compared to the LPT described earlier, and corresponds to $kR_{\rm grid} \simeq 0.45$. We have found that we could get even better agreement with only $P_{hh}(k)$, but at the cost of worsening the fit to P_{hm}. This suggests that such good agreement with P_{hh} is partially artificial, so we deal only with the joint fits in this chapter.

There are several important features to note in Fig. 7.3. First we see that the model is performing at the percent-level or better, and usually well within the errors of the simulation (visible as 'noise' in the lines in the lower panels) at low and intermediate k, before a sudden shortfall of model power near $k \simeq 0.6\,h\,\mathrm{Mpc}^{-1}$ in the cross spectrum (P_{hm}). This rapid decline indicates that our component spectra are not well resolved at large k, which is to be expected given the finite size of the smoothing ($0.75\,h\,\mathrm{Mpc}^{-1}$) we applied to estimate δ_L, δ_L^2 and s^2. This is especially true for the latter two which, as noted in §7.3, are particularly sensitive to smoothing. The auto spectrum (P_{hh}) is typically saturated by shot noise at $k \simeq 0.6\,h\,\mathrm{Mpc}^{-1}$ and therefore less sensitive to these effects.

Secondly, the model does better at $z = 1$ than $z = 0$, even though the values of the bias are higher. This is because the linear growth factor drops by 40 per cent between $z = 0$ and $z = 1$, and for these samples the contributions from quadratic bias are relatively smaller at $z = 1$ than $z = 0$. The improvement in the model performance is thus expected.

Finally, we note that in Fig. 7.3 we haven't imposed any priors on the values of our bias parameters. While values of the derivative bias b_∇ will be sensitive to small-scale details such as smoothing and are therefore not expected to be universal, an extensive literature exists studying physical models for b_1, b_2, b_s (see §7.1 for references). To this end, we have checked that enforcing, to within a few per cent, the peak-background split relations between (b_1, b_2) from [342] (keeping ν as a free parameter) and values of b_s from [4] only degrades our fits at the few (~ 3) per cent level in P_{hh} and P_{hm} and doesn't significantly alter the range of fit.

It is important to note that the quadratic bias model fits the auto- and cross-power spectra of the halo samples shown well into the quasi- or non-linear regime. As modes become increasingly non-linear they also become increasingly correlated with each other and the halo field is much less correlated with the matter field or the initial density field. Figure 7.4 shows the scale-dependent halo-matter cross-correlation coefficients

$$r_{cc}(k) = \frac{P_{hm}(k)}{\sqrt{P_{hh}(k)P_{mm}(k)}} \tag{7.4}$$

of two of our mass bins at $z = 0$.[7] We have computed r_{cc} with and without the shot noise subtracted to better showcase the decorrelation due to nonlinear dynamics and bias,

[7] We have avoided the highest mass bin with $\log_{10} M \in (13.0, 13.5)$ as the halo power includes a significant contribution from shot noise at all scales.

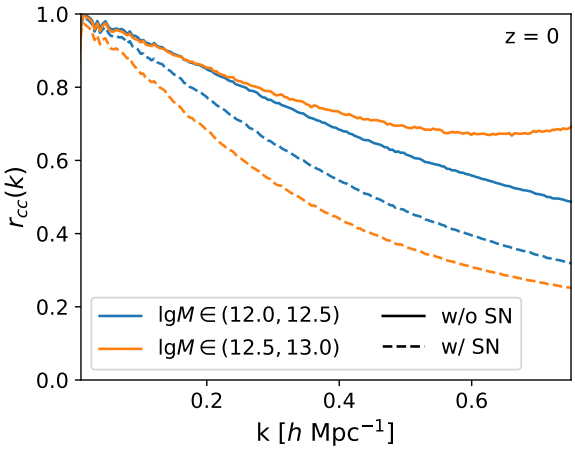

Figure 7.4: The scale-dependent matter-halo cross correlation coefficient, $r_{cc}(k)$, at $z = 0$ for mass bins $\log_{10} M \in (12.0, 12.5)$ (blue) and $(12.5, 13.0)$ (orange). The dashed lines show the "true" r_{cc} while the solid lines show r_{cc} computed without shot noise in the halo autospectrum, which gives a qualitative measure of the halo-matter decorrelation due to nonlinear dynamics and bias. In all cases the cross-correlation drops below one as the field goes non-linear and is less than 90 percent for most of the scales fit by our model.

though we caution that strictly speaking the latter is the "true" cross-correlation coefficient. Nonetheless, in both cases r_{cc} is at least ten per cent below unity across most of our fit range. For these reason the information content is substantially less than a simple mode-counting argument would suggest [see e.g. 394, 404, for discussion]. It is also at these smaller scales that scale-dependent bias and complex physics involving the baryonic components becomes relevant, potentially requiring many more parameters to model faithfully. Furthermore, most large-scale structure surveys are designed so that shot noise becomes comparable to the clustering signal near the non-linear scale, which further limits the information available from high k modes. Bearing all of this in mind, the performance of the quadratic bias model demonstrated above is likely to be sufficient for many science goals and we have not attempted to further improve it.

Figures 7.2 and 7.3 demonstrate that, at low redshift, the perturbative dynamics breaks down before the quadratic bias model. As we move to higher redshifts, and more biased tracers, the limitations imposed by perturbative dynamics become less severe and eventually we expect the bias model to become more limiting than the inaccuracies in the perturbative dynamics. We have not investigated this limit.

7.4.3 Fitting galaxy spectra

As a final test we fit to a mock galaxy sample, generated from our simulations by populating halos using a simple halo occupation distribution. Specifically we assume the now-standard form [441]

$$\langle N_{\rm cen}\rangle\,(M_h) = \frac{1}{2}\left\{1 + {\rm erf}\left[\frac{\lg M/M_{\rm min}}{\sigma}\right]\right\} \tag{7.5}$$

and

$$\langle N_{\rm sat}\rangle\,(M_h) = \Theta(M_h - M_{\rm min})\left(\frac{M_h - M_{\rm min}}{M_1}\right)^{\alpha} \tag{7.6}$$

For each halo in the simulation we draw a Poisson number of satellites and either 0 or 1 centrals. The centrals are placed at the halo centers while the satellites are placed assuming an NFW profile [253] dependent only on radius.

Figure 7.5 shows P_{gg} and P_{gm} for a 'galaxy' sample with $M_{\rm min} = 10^{12.5}\,h^{-1}M_\odot$, $M_1 = 20\,M_{\rm min}$, $\sigma = 0.2\,$dex and $\alpha = 0.9$. These are chosen to be similar to HODs found for magnitude limited samples of galaxies, though none of our conclusions depend upon the exact values of these parameters. For reference, our HOD parameters correspond to satellite fractions of $f_{\rm sat} = 0.18$ and 0.1 at $z = 0$ and 1, respectively.

The results are very similar to those shown in Fig. 7.3. The Lagrangian bias model fits the auto- and cross-spectra of our mock galaxies, simultaneously, within 3 per cent out to $k \simeq 0.6\,h\,{\rm Mpc}^{-1}$ for $0 \le z \le 1$ (Fig. 7.5). This would be sufficient to model the angular clustering of galaxies in photometric surveys, galaxy-galaxy lensing or the cross-correlation of galaxies with CMB lensing out to angular multipole $\ell \approx k_{\rm max}\chi$ where χ is the characteristic distance to the objects in question. Assuming $k_{\rm max} = 0.6\,h\,{\rm Mpc}^{-1}$ and $\chi \approx 1.3\,h^{-1}$Gpc ($z = 0.5$) gives $\ell_{\rm max} \simeq 800$ or $\ell_{\rm max} > 10^3$ for $z > 0.7$. Beyond this $\ell_{\rm max}$ the errors grow, but smoothly rather than dramatically. It is on these smaller scales that we expect contributions from baryonic physics to become increasingly important.

7.4.4 Common bias model

It is also instructive to compare our approach to the commonly assumed approximation of a constant or scale-dependent bias times the non-linear matter power spectrum. Specifically we test the model

$$P_{hm} = \left[b'_0 + b'_1 k + b'_2 k^2\right]\;\; P_m(k) \tag{7.7}$$

$$P_{hh} = \left[b'_0 + b'_1 k + b'_2 k^2\right]^2 P_m(k) + P_{SN} \tag{7.8}$$

with three bias and one constant shot noise parameter. The parameter b'_0 denotes a scale-independent bias, and is the most widely used model for galaxy or halo bias. The b'_2 term describes a correction due to peaks theory [110] and has been used in modeling data [e.g. 145]. The term $b'_1\,k$ has no theoretical justification and is included merely because we noted that it improved the fit. We use the N-body determined $P_m(k)$ in Eqs. (7.7, 7.8) as we found the

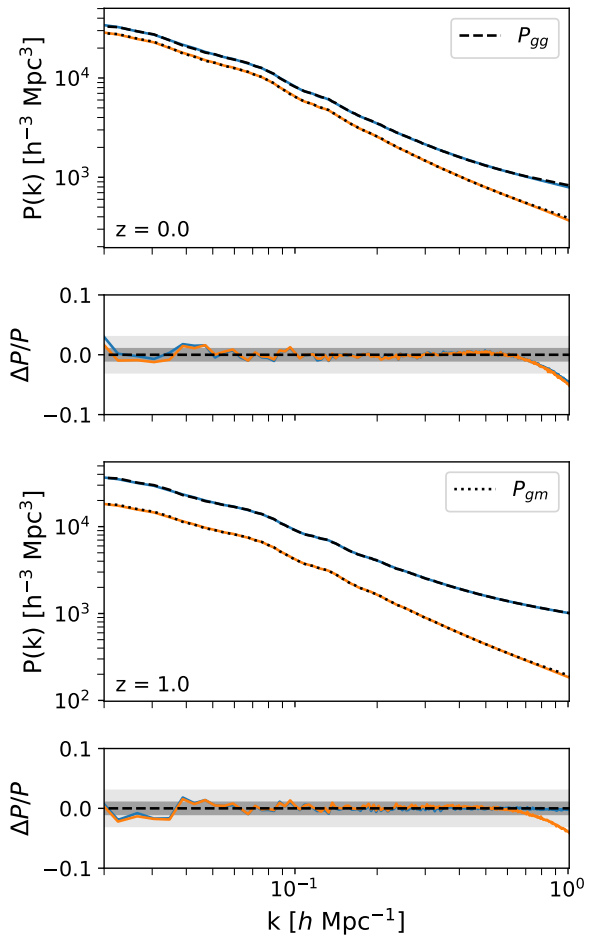

Figure 7.5: Comparison of the auto- and cross-spectra for samples of mock galaxies, generated from the simulations using a halo occupation distribution at $z = 0$ (top) and $z = 1$(bottom). The blue and orange curves show the fits from our model for the galaxy autospectrum (dashed) and galaxy-matter cross spectrum (dotted), respectively. The model performance is qualitatively similar for our mock galaxies and halo samples.

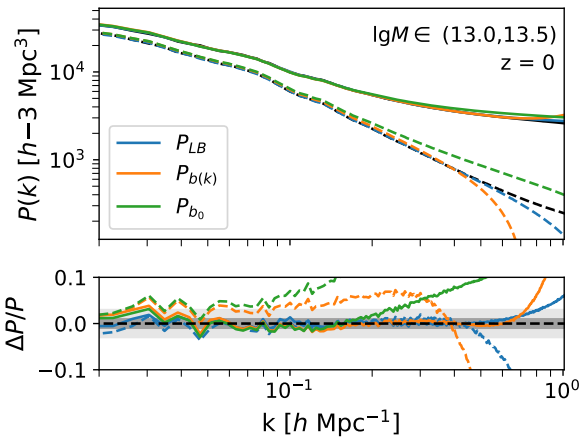

Figure 7.6: A comparison of our Lagrangian bias model with the model of Eqs. (7.7, 7.8) and the benchmark linear bias model. Solid lines show the fits of each model to the halo-halo autospectrum, while dashed lines show fits to the halo-matter cross spectrum. The linear bias model only fits the data on the largest scales. While the scale-dependent bias model can be made to fit the autospectrum, only our model fits both auto- and cross-spectra with a consistent set of parameters.

HaloFit model [160, 273, 354, 362, 237, 236] was not as accurate and we wished to provide the most fair comparison.

Note the assumption above that the prefactor of the halo-halo auto-correlation is the square of the prefactor in the halo-mass cross-spectrum. This is equivalent to the assumption that the halo and matter field have cross-correlation coefficient $r_{cc} \approx 1$. However, this assumption increasingly breaks down as dynamics and bias become nonlinear at low redshift and high mass (Fig. 7.4; see also [246, 421]). The model of Eq. (7.3) allows us to relax the assumption that $r_{cc} = 1$.

Figure 7.6 shows the results at $z = 0$ for the 4-parameter model (Eqs. 7.7, 7.8) on the halo sample with $13.0 < \log_{10} M < 13.5$. We have chosen this redshift and mass bin as it illustrates dynamics and biasing at their most nonlinear, though other choices yield qualitatively similar results. As a reference, we also consider the case of constant bias (only $b_0 \neq 0$ above). While the Lagrangian bias model provides a good fit to both spectra simultaneously, as we have seen previously, this is not true of Eqs. (7.7, 7.8). We have chosen to adjust the parameters in $b(k)$ to predict P_{hh} on quasi-linear scales as in observations P_{hh} would most likely have the highest signal to noise ratio. The freedom inherent in the quadratic function, $b'_0 + b'_1 k + b'_2 k^2$, allows us to fit P_{hh} well up to $k \approx 0.8\,h\,\mathrm{Mpc}^{-1}$, comparable to our Lagrangian bias model. However the form preferred by P_{hh} provides a very bad fit to P_{hm} at intermediate to high k, as can most easily be seen in the lower panel of Fig. 7.6. This leads to a significant misestimate of P_{hm}, which would translate into errors in the inferred large-scale bias and underlying matter clustering amplitude (σ_8).

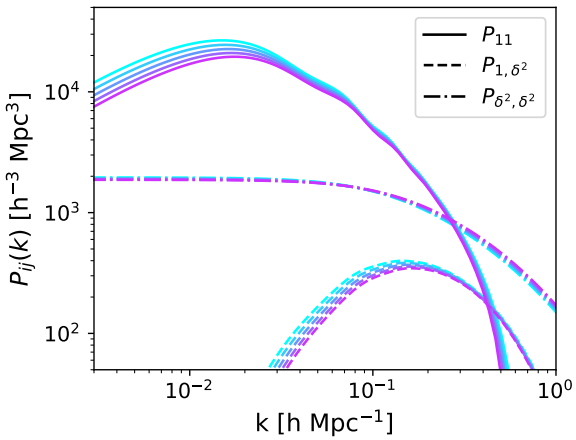

Figure 7.7: The cosmology dependence of the component spectra. Here we show three representative components: $P_{11}, P_{1,\delta^2}, P_{\delta^2,\delta^2}$ at $z = 0$ for values of Ω_m within ten percent of our fidicucial cosmology, with all other parameters kept fixed. For simplicity we have used 1-loop LPT as a proxy for the N-body spectra. The components vary smoothly with cosmology, with P_{δ^2,δ^2} showing very little variation. Critically, the component spectra change with cosmology at about the same rate as (or less than) the matter power spectrum, $P_{1,1}$.

Despite its ubiquity in analyses, the constant bias model does even more poorly. The significant scale-dependent bias inherent in the clustering of this mock galaxy sample makes it impossible to fit both the auto- and cross-spectra except at the very largest scales, $k < 0.1\,h\,\mathrm{Mpc}^{-1}$. Inferences about cosmological parameters from using this model would be highly biased unless drastic scale cuts were employed.

7.5 Conclusions

We have tested the performance of a power spectrum model for biased tracers based on a quadratic, Lagrangian bias expansion. The model uses N-body simulations to compute the gravitational evolution of dark matter particles, which are resummed to all order using the Lagrangian $\mathbf{q} \to \mathbf{x}$ mapping, but substitutes a 4-parameter bias model for the halo-based galaxy modeling more traditionally employed in simulations. Both the dynamical model and bias expansion are theoretically well motivated, and the method places only modest requirements on the input simulations since it does not explicitly use properties of halos or subhalos. This is an advantage given that properly resolving halos and subhalos is quite computationally demanding [385, 106, 97] and complex halo occupations – potentially including halo assembly information – can be required in order to properly model samples selected by emission lines, color cuts or other complex selections [302, 130, 436, 57, 408, 129,

226, 420, 433, 435]. The approach combines methods from the 'analytic' and 'numerical' communities in a manner which plays to their relative strengths.

The Lagrangian bias model is quite accurate on large and intermediate scales. We have showed that going to quadratic order in the bias expansion enables us to fit the (real space) auto- and cross-power spectra of halos and mock galaxies to a few per cent out to $k \simeq 0.6\,h\,\mathrm{Mpc}^{-1}$ for $0 \leq z \leq 1$ (Figs. 7.3, 7.5). To fit beyond this scale would require increasing the number of parameters (and component spectra) and calculating the P_{ij} with higher resolution simulations. However, this performance is already highly encouraging, as these scales provide the bulk of the information in many cosmological analyses. Smaller scales tend to be non-linear and significantly affected by scale-dependent bias and baryonic effects. The mode-coupling associated with non-linearity implies that there is less information about primordial physics in these modes than a simple mode-counting exercise would imply [e.g. 394, 404] and the combination of non-linearity and baryonic effects means that such modes do not faithfully trace the primordial perturbations. The many parameters needed to describe complex, scale-dependent effects can lead to degeneracies with cosmological parameters. Furthermore, most large-scale structure surveys are designed so that shot noise becomes comparable to the clustering signal near the non-linear scale, which further limits the information available from high k modes. For these reasons, the performance of the quadratic bias model is likely to be sufficient for many science goals.

In this chapter we have worked at fixed cosmology in order to focus on the range of applicability of the quadratic bias expansion. While we intend to return to the problem of emulating the power spectrum for different cosmologies in future work, we comment here on the basic strategy. The component spectra in Eq. (7.3) vary with cosmology smoothly, with variations similar to the linear power spectrum. As an example, in Figure 7.7 we have plotted variations in the component spectra when Ω_m is varied within ± 10 per cent from our fiducial cosmology; leading order terms like the matter power spectrum P_{11} vary like the linear power spectrum, while the component spectra vary smoothly by similar factors or, in the case of P_{δ^2,δ^2}, significantly less. The variations with other cosmological parameters are qualitatively similar. Thus the same techniques that have been used to emulate matter power spectra will apply almost unchanged for emulating P_{ij}. As shown in Fig. 7.2 we can use perturbative methods for the low k part of the component spectra, which tends to be relatively noisy when estimated from simulations of computationally tractable volumes, and switch to N-body determined spectra at higher k. Given a grid of N-body simulations spanning the cosmologies of interest standard Gaussian process regression, which has been successfully used for matter power spectrum interpolation [167, 166, 213, 126, 384], can easily be used to predict each of the component spectra as a function of cosmology. In a similar vein, the ratio of the N-body to perturbation theory spectra can be emulated rather than the spectra themselves, removing some of the cosmology dependence. Since the perturbation theory spectra can be efficiently and accurately computed for any cosmology, this shouldn't significantly change the efficiency of the emulator.

An alternate emulation which also does not explicitly use properties of halos and subhalos was adopted by [330, 162]. Those authors used Pade approximants to fit correction factors to

perturbation theory or halo model inspired terms and then fit the coefficients as power laws in the relevant cosmological parameters. Such an approach could also be attempted with our component spectra, which are in large part relatively featureless and vary smoothly with parameters.

While we have chosen a Lagrangian bias expansion, a similar procedure could be followed using a complete set of Eulerian bias operators. However, we note that [322, 248] find that the Lagrangian scheme outperforms the Eulerian bias expansion for a wide range of halo masses, redshifts and weightings. Thus we do not expect it to improve over the prescription we have developed here.

In this chapter our focus has been on the real-space power spectrum, of direct relevance to modeling photometric and lensing surveys, though one can extend the method to higher order functions, covariances and to redshift space. For the latter, one can either model the contributions to $P(k, \mu)$ directly in simulations, or one can choose to model the real-space power spectrum and velocity moments and construct the redshift-space power spectrum from those components (see e.g. [162] for a recent example and [398] for a recent discussion of such methods for modeling redshift-space distortions). We intend to return to this topic, and to the construction of an emulator, in future publications.

7.6 Acknowledgements

The authors thank E. Castorina, J. Cohn, M. Schmittfull and U. Seljak for helpful comments on an earlier draft. S.C. also thanks M. Simonovic and Z. Vlah for helpful discussions while this chapter was being revised. S.C. is supported by the National Science Foundation Graduate Research Fellowship (Grant No. DGE 1106400) and by the UC Berkeley Theoretical Astrophysics Center Astronomy and Astrophysics Graduate Fellowship. M.W. is supported by the U.S. Department of Energy and by NSF grant number 1713791. This research used resources of the National Energy Research Scientific Computing Center (NERSC), a U.S. Department of Energy Office of Science User Facility operated under Contract No. DE-AC02-05CH11231. This work made extensive use of the NASA Astrophysics Data System and of the `astro-ph` preprint archive at `arXiv.org`.

Chapter 8

Cosmological Analysis of the Power Spectrum and Post-Reconstruction BAO in the BOSS Survey

This chapter was originally published as

> Shi-Fan Chen, Zvonimir Vlah, and Martin White. "A new analysis of galaxy 2-point functions in the BOSS survey, including full-shape information and post-reconstruction BAO". in: *JCAP* 2022.2, 008 (Feb. 2022), p. 008. DOI: 10.1088/1475-7516/2022/02/008. arXiv: 2110.05530 [astro-ph.CO]

We have spent the first six chapters of this dissertation developing theoretical models of galaxy clustering in perturbation theory, with a particular focus on Lagrangian perturbation theory methods. In this chapter and the next, we will make a change of pace and apply these models to data. In this chapter, our focus will be on the two main prongs of modern spectroscopic surveys, BAO and RSD.

We present a new method for consistent, joint analysis of the pre- and post-reconstruction galaxy two-point functions of the BOSS survey. The post-reconstruction correlation function is used to accurately measure the distance-redshift relation and expansion history, while the pre-reconstruction power spectrum multipoles constrain the broad-band shape and the rate-of-growth of large-scale structure. Our technique uses Lagrangian perturbation theory to self-consistently work at the level of two-point functions, i.e. directly with the measured data, without approximating the constraints with summary statistics normalized by the drag scale. Combining galaxies across the full redshift range and both hemispheres we constrain $\Omega_m = 0.303 \pm 0.0082$, $H_0 = 69.23 \pm 0.77$ and $\sigma_8 = 0.733 \pm 0.047$ within the context of ΛCDM. These constraints are consistent both with the Planck primary CMB anisotropy data and recent cosmic shear surveys.

8.1 Introduction

The large-scale structure of the Universe, as traced by galaxies, provides fundamental physics information through its connection to both initial conditions in the primordial universe and general relativity through the gravitational formation of structures on the largest observable scales [275, 114]. A well-established measure of this structure is the redshift-space two-point function as measured by galaxy redshift surveys [196, 158], which encodes both the power spectrum shape of fluctuations in the early universe and, through the quirk that line-of-sight distances in such surveys are inferred from their redshifts, cosmological velocities in the form of redshift-space distortions (RSD).

A particularly interesting and relevant interplay of the initial conditions and gravitational dynamics occurs in the galaxy baryon acoustic oscillations (BAO) signal. The BAO signal is the imprint of early-universe acoustic waves on the observed clustering of galaxies, manifesting as a localized peak in the galaxy correlation function at separations around the characteristic size of these waves [410]. The linear physics underlying the size and shape of the BAO feature is well-understood [120, 238], making it a robust cosmological signal of both the early universe and the redshift-distance relation. However, the process of nonlinear structure formation leads to a slight wrinkle in this picture: nonlinearities, particular due to bulk displacements of galaxies on large scales, tend to dampen and shift the BAO signal [121, 92]. To better extract the BAO signal, ref. [122] proposed a now-standard method known as "reconstruction" to cancel a large portion of these effects by estimating large-scale displacements and subtracting them from the observed positions of galaxies.

In recent years there have been significant advances in the modeling and theoretical understanding of both redshift-space distortions and the nonlinear damping of BAO. For the former, the recasting of cosmological perturbation theory in the language of effective field theories has provided a systematic way in which to write down the possible contributions to galaxy clustering on quasilinear scales based on fundamental symmetries while clarifying and taming dependences on small-scale physics (see e.g. refs [234, 28, 60, 399, 280, 398, 74, 82]). For the latter, improved understanding of the effects of large-scale displacements through so-called infrared (IR) resummations allows us to quantitatively describe nonlinear damping of the BAO peak, both for the raw and reconstructed power spectrum, in perturbation theory [231, 58, 402, 112, 78]. These developments allow us to model diverse sets of cosmological observables— in real and redshift space, power spectrum and correlation function, pre- and post-reconstruction— within the consistent theoretical framework of perturbation theory.

Our aim in this chapter is to present a consistent analysis of the pre- and post-reconstruction 2-point correlation function in Fourier and configuration space using the BOSS survey [101] as an example. We will work within the framework of Lagrangian perturbation theory [39], which the present authors have used to develop models for redshift-space distortions and reconstruction [78, 82]. We will operate directly at the level of two-point correlation functions, i.e. given a set of cosmological and galaxy bias parameters Θ, we will use the redshift-space power spectra and correlation function multipoles, pre- or post-reconstruction, to construct a

likelihood:

$$\mathcal{L} \propto \exp\Big\{ -\frac{1}{2}\big(m(\Theta) - \hat{d}\big)^T C^{-1} \big(m(\Theta) - \hat{d}\big)\Big\} \quad , \quad \hat{d} = (P_\ell, \xi_\ell^{\rm recon}, \cdots), \tag{8.1}$$

where $m(\Theta)$ is the model, $\hat{d}$ is a data vector composed of two-point correlation functions measured from data and C is the covariance matrix.

This work is not the first to analyze galaxy clustering with an effective theory framework, and follows a number of papers analyzing the BOSS redshift space power spectrum using effective Eulerian perturbation theory [86, 96] as well as work by refs. [283, 94] combining these analyses with additional BAO information through reconstruction. Our goal, rather, is to perform a joint analysis of pre- and post-reconstruction data without resorting to additional assumptions or machinery (Fig. 8.1). In particular, previous work combining pre- and post-reconstruction measurements (e.g. refs [45, 283, 94]) have typically sought to distill the content of the latter by fitting a set of BAO parameters $\tilde{\alpha}_{\parallel,\perp}$ (§ 8.3.2) which scale the BAO signal in a template, or fiducial, linear power spectrum to match that of the observed signal. Then, since the BAO oscillations in the template differ from the observed by the cosmological dependence of the sound horizon (r_d) in addition to simple distance scalings by redshift, these best-fit $\tilde{\alpha}$'s are fit to the ratio of cosmological distances to r_d in conjunction to the pre-reconstruction power spectra, such that the data vector is instead $\hat{d} = (P_\ell, \tilde{\alpha}_\parallel, \tilde{\alpha}_\perp)$. The covariance of the power spectra and $\tilde{\alpha}$'s is then inferred from measurements of $\tilde{\alpha}$ from the power spectra in mock catalogs. A schematic comparing our approach in this work to the standard one is shown in Fig. 8.1. For a given set of cosmological parameters the information about r_d and cosmological distances is inherent in the perturbation-theory prediction $\xi_\ell^{\rm recon}(\Theta)$, allowing us to bypass the need to approximate the BAO signal as a scaled version of a fixed power spectrum template and directly compare cosmology with data. In particular, since the BAO information in the correlation function is effectively isolated in configuration space as a sharp peak at large scales, our fiducial setup will combine the post-reconstruction correlation function around the peak with a full-shape analysis of the pre-reconstruction power spectrum. Note that while we have focused our discussion on the post-reconstruction BAO measurement, the BOSS collaboration (but not refs. [283, 94]) similarly also distilled the RSD signal pre-reconstruction into a best-fit $f\sigma_8$, such that the final data vector fit to cosmological parameters was $\hat{d} = (f\sigma_8, \tilde{\alpha}_\parallel, \tilde{\alpha}_\perp)$.

The simplified approach advocated for in this work has a number of advantages for obtaining cosmological constraints from surveys like BOSS. For a given set of theory parameters (including cosmology and galaxy bias) there is a unique 'forward' mapping — shown in the top row of Fig. 8.1 — from these parameters to the (model-independent) observational data. This implies that constraining information in the data that is implied by the theory model is captured without loss. By comparison, in the standard approach one assumes e.g. that any BAO information post-reconstruction can be distilled into two BAO scaling parameters which, by themselves, do not uniquely map into the space of post-reconstruction observables, potentially leading to information loss (§8.3). Furthermore, while the standard approach requires measuring the covariance of these summary statistics from approximate

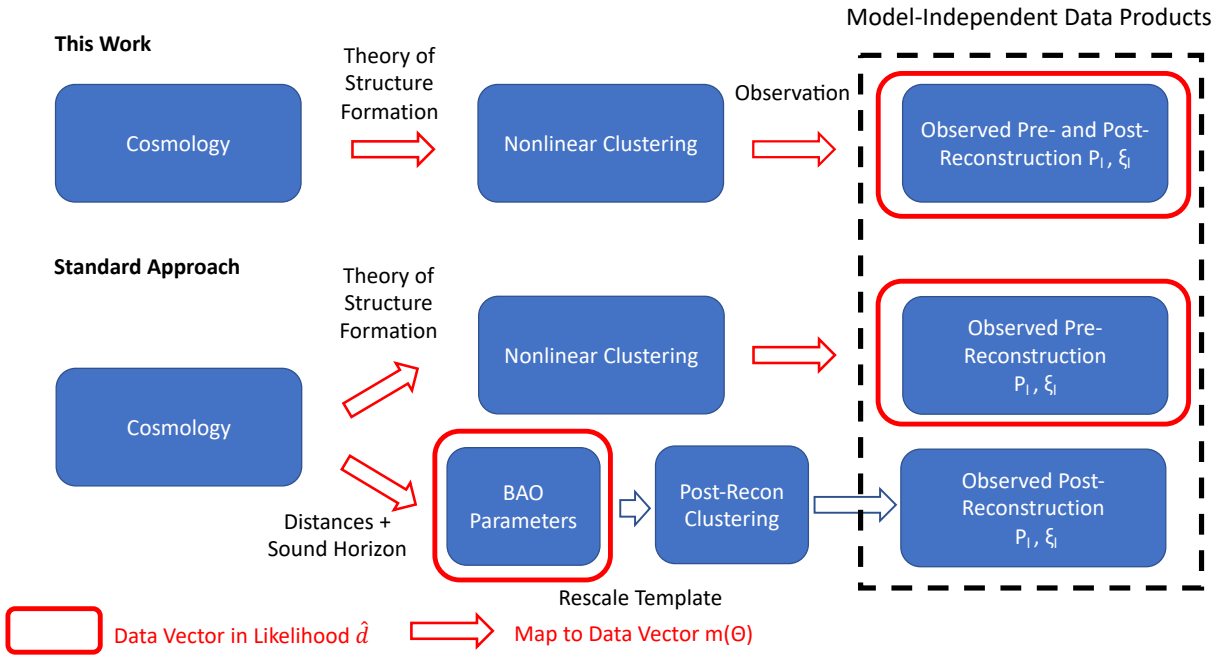

Figure 8.1: Flowchart comparing our method with the standard approach to combining full-shape RSD and BAO analyses. Arrows denote the unique mapping from theory parameters to observed data. Our approach allows for a direct translation from cosmological parameters into measured 2-point correlation functions (black dashed box) via a theory of structure formation (LPT) and does not rely on power spectrum templates or model-dependent BAO parameters derived therefrom. Squares highlighted in red indicate the actual data vector fit in the likelihoods of each approach, related to cosmological parameters through a model $m(\Theta)$ (red arrows), and each row to the right of "cosmology" indicates separate fits which must be combined using simulated mocks. Our approach features a single fit to the observed data while the standard approach separately fits theory-dependent BAO parameters that depend highly non-linearly on the data and the pre-reconstruction clustering.

mock catalogs, computing the likelihood at the level of model-independent data in principle allows us to straightforwardly use the statistical uncertainties implied by the theory model itself, e.g. by computing covariance matrices analytically within perturbation theory [404][1]. Future theory calculations of noise-free data covariances have the potential to ease numerical difficulties from estimating covariances of statistics beyond the pre-reconstruction power spectrum with only a finite number of mocks.

The outline of the chapter is as follows. In §8.2 we present the galaxy samples that we analyze, which are all drawn from the BOSS survey [101]. The models we fit to these data, all based on cosmological perturbation theory, are described in §8.3. Our fiducial analysis setup, including scale cuts, parameter choices and priors are presented in §8.4. Our final

[1]See, however, ref. [283] for an idealized calculation using Fisher matrices.

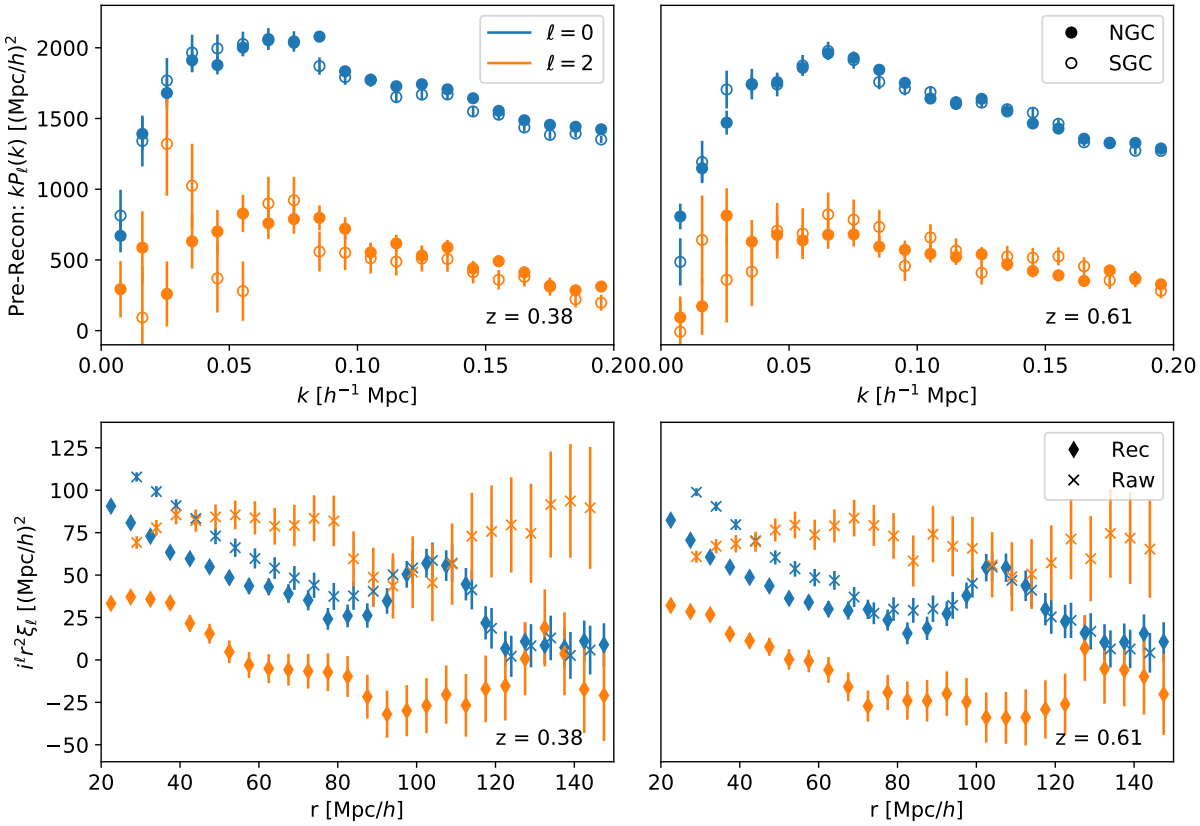

Figure 8.2: The pre-reconstruction power spectrum (top) and pre- and post-reconstruction correlation functions (bottom) of the BOSS DR12 galaxies. The monopole and quadrupole of each are both shown in blue and orange, respectively. For the power spectrum, the separate measurements for the NGC and SGC samples are shown as filled and open circles. Pre- and post-reconstruction ("Raw" and "Rec") correlation function measurements are shown with round and crossed markers. The correlation function is measured jointly across both galactic caps. Error bars represent the diagonals of the covariance matrix computed using 1000 Patchy mocks.

cosmoloical constraints are given in §8.5, where we also discuss constraints from different subsamples of the BOSS data and compare to constraints from other groups and experiments. We conclude in §8.6. Some technical details are relegated to a series of Appendices.

8.2 Data

We analyze the clustering of galaxies drawn from the BOSS galaxy redshift survey [101], part of the Sloan Digital Sky Survey III [123]. Galaxies in BOSS were targeted with two independent selection criteria: one (LOWZ) targeted luminous red galaxies up to $z = 0.4$

while another (CMASS) targeted massive galaxies with $0.4 < z < 0.7$; however, due to an incorrect application of the LOWZ criteria in the first nine months of the survey, two additional samples (LOWZE2, LOWZE3) had to be separated out. All of these samples are described in more detail in ref. [300]. Ref. [7] combined these samples into three redshift bins with $0.2 < z < 0.5$, $0.4 < z < 0.6$ and $0.5 < z < 0.75$ (named **z1**, **z2** and **z3**, respectively). Since **z2** overlaps both **z1** or **z3** in redshift and thus gives correlated constraints we choose to analyze **z1** and **z3** only in this work. Each redshift bin can be further split into galaxies observed in the Northern (NGC) and Southern (SGC) galactic caps. Because the imaging in the north and the south differ slightly, the samples have slightly different properties and should be analyzed separately. The final BOSS sample covers 1,198,006 galaxies in total over 10,252 square degrees of sky.

The power spectra and correlation function multipoles of these samples were measured in refs. [45, 388] and the data are shown in Fig. 8.2. The BOSS two-point function measurements were computed assuming a flat ΛCDM cosmology with present-day matter density $\Omega_{M,\mathrm{fid}} = 0.31$. This implies that the reported redshift-space power spectrum is related to its value in the coordinates of the true cosmology by

$$P_s^{\mathrm{obs}}(\mathbf{k}_{\mathrm{obs}}) = \alpha_\perp^{-2}\alpha_\parallel^{-1} P_s(\mathbf{k}) \quad , \quad k_{\parallel,\perp}^{\mathrm{obs}} = \alpha_{\parallel,\perp} k_{\parallel,\perp} \quad ,$$

where the Alcock-Paczynski parameters are defined as [9, 265]

$$\alpha_\parallel = \frac{H^{\mathrm{fid}}(z)}{H(z)} \quad , \quad \alpha_\perp = \frac{D_A(z)}{D_A^{\mathrm{fid}}(z)} \quad . \tag{8.2}$$

Since all distances are reported in h^{-1}Mpc units the above ratios should be computed assuming a fixed h. The equivalent relations for the correlation function are simply the Fourier transforms of the above equations. The mismatch between true and fiducial coordinates imprints additional anisotropy in the galaxy two-point function and serves as a further source of cosmological information known as the Alcock-Paczynski (AP) effect [9] (Appendix G.3).

For the power spectrum we use the updated pre-reconstruction measurements of both data and mock catalogs presented in ref. [42]. On top of the AP effect the geometry of the survey itself leaves an imprint in the clustering of the galaxies, so that the measured power spectra are the convolution of the true clustering signal with a window function and taking into account wide-angle effects [131, 422, 63, 41]; to this end ref. [42] provide for each sample a wide angle matrix $\mathbf{M}$ and window function matrix $\mathbf{W}$ such that for an input vector of appropriately-binned theoretical (including AP) power spectrum multipoles $\mathbf{P}$ the observed (binned) power spectra are given by[2]

$$\mathbf{P}^{\mathrm{conv}} = \mathbf{WMP}, \quad \mathbf{P} = (P_0, P_2, P_4).$$

[2]We use the updated values of the power spectrum multipoles and window functions from a revised version of ref. [42]. These measurements fix a mismatch in the normalizations of the window function and power spectra at the roughly 10% level that afflicted earlier results and which improves the agreement with correlation function fits which do not require multiplying by a window function. This normalization issue is discussed in detail in the published version of ref. [42], with resulting amplitude corrections to each BOSS sample tabulated in Table

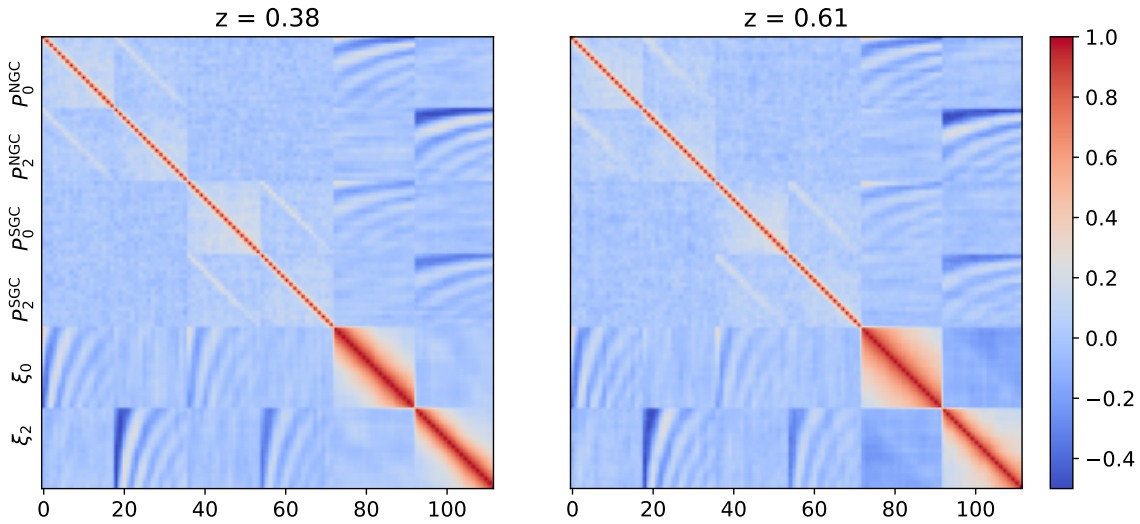

Figure 8.3: The joint correlation matrix of the **z1** and **z3** pre- and post-reconstruction two-point function samples, computed using 1000 Patchy mocks. For clarity of presentation we have restricted the power spectrum to wavenumbers $0.02\,h\,\mathrm{Mpc}^{-1} < k < 0.20\,h\,\mathrm{Mpc}^{-1}$ (18 bins) and the correlation function to $80\,h^{-1}\mathrm{Mpc} < r < 130\,h^{-1}\mathrm{Mpc}$ (20 bins). The numbers on the x axis denote bin number.

While the output $\mathbf{P}^{\mathrm{conv}}$ contains both the hexadecapole as well as odd multipoles $P_{1,3}$ we will restrict our analysis in this chapter to the monopole and quadrupole only.

For our post-reconstruction BAO analysis we use the post-reconstruction correlation function multipoles obtained in ref. [388]. Both pre- and post-reconstruction correlation function multipoles were measured for the combined NGC and SGC samples at the redshift bins **z1** and **z3**. The reconstruction in the public BOSS data was performed using the so-called **RecIso** convention, with reconstructed displacements solved-for using a finite-difference approach on the observed galaxy density field smoothed by a Gaussian filter with width $R = 15h^{-1}$ Mpc. We will discuss further details of the procedure in Section 8.3.2.

Finally, to obtain the joint covariances of the power spectrum[3] and correlation function[4] measurements used in our analysis we used the V6C BigMultiDark Patchy mocks [202] released with DR12 of the SDSS-III Survey. These mocks were prepared using approximate gravity solvers with galaxy biasing calibrated to the BigMultiDark simulation in a redshift-dependent way to capture the time-depedence of the BOSS galaxy sample [202]. The thus-derived

1 of that work; roughly, there is an overall degeneracy between the power spectrum and window function amplitudes, such that no results are affected when both are adjusted simultaneously by a single multiplicative factor–however, this is premised upon the two being normalized consistently when computed. We thank Pat McDonald and Florian Beutler for helpful discussions of this issue. Upated versions of the BOSS power spectra and window functions can be found in https://fbeutler.github.io/hub/deconv_paper.html.

[3]For the power spectrum mocks, see: https://fbeutler.github.io/hub/deconv_paper.html.

[4]We thank Mariana Vargas for providing the correlation function mock measurements.

correlation matrix for the power spectrum and post-reconstruction correlation function is shown in Fig. 8.3. Since the correlation-function mock measurements were only obtained for 1000 of these mocks that is also the number of power spectrum measurments we use to obtain the joint pre- and post-reconstruction covariance. The thousand mocks are sufficient for our purposes; concretely, our most extensive analysis setup will include (for each independent redshift bin) 18 k-bins per power spectrum multipole per galactic cap and 10 radial bins per correlation function multipole, yielding a 92-element data vector. Applying a multiplicative correction to unbias the precision matrix [164] would lead to rescalings of the parameter errors of less than 5%, with no change in the matrix structure. As a further test, reducing to $N_{\rm mocks} = 500$ changed the χ^2 of the best-fit model found for the **z3** sample by $\Delta\chi^2 = 3.5$, i.e. far less than one per d.o.f. for our fiducial setup (§ 8.4.1), suggesting that one thousand mocks measurements is sufficient for our purposes. Finally, while we have not found it necessary in our analysis, we note that if we were to rebin the power spectrum data into broader k bins we would reduce the number of degrees of freedom and more cleanly separate the BAO and broadband shape information between the correlation function and power spectrum. This may be beneficial in future analyses.

8.3 Model

Our aim in this work is to jointly model the redshift-space galaxy two-point function both pre- and post-reconstruction within a consistent theoretical framework. Specifically, we will operate within Lagrangian perturbation theory (LPT; [39, 231]), which models nonlinear structure formation through the evolution of galaxy displacements $\Psi(\mathbf{q}, \tau)$, relating observed (Eulerian) positions $\mathbf{x}$ at a given time τ to initial (Lagrangian) positions $\mathbf{q}$ through $\mathbf{x} = \mathbf{q} + \Psi$. The displacements are expanded order-by-order in the initial conditions $\Psi = \Psi^{(1)} + \Psi^{(2)} + \Psi^{(3)} + ...$ In this work we will operate within the EdS approximation wherein the $\mathrm{n}^{\rm th}$ order displacement scales as the $\mathrm{n}^{\rm th}$ power of the linear growth factor $D(z)$; this has been shown to be an excellent approximation for current and upcoming galaxy surveys in [361, 128, 36, 139, 115], with a slight caveat due to scale dependence from massless neutrinos which we will address in Section 8.4. The nature of the mapping between Lagrangian and Eulerian coordinates makes LPT a natural arena in which to understand both redshift-space distortions and nonlinear BAO damping, which we discuss in term below. In addition, in order to speed up our calculations and avoid repeatedly calling Boltzmann codes at each new point in our Markov chains, in this chapter we have chosen to approximate our theory components as a Taylor series in the cosmological parameters. The grid of PT predictions used to compute the Taylor-series coefficients was computed using `CLASS` [48] and `velocileptors` [74, 82]. The details of our approximation scheme are discussed in Appendix G.1.

8.3.1 One-Loop Redshift Space Power Spectrum

In spectroscopic galaxy surveys like BOSS a galaxy's position along the line of sight (LOS) is inferred from its measured redshift. Since a galaxy's cosmological redshift and peculiar velocities both contribute to this redshift, its redshift-space position \ is boosted along the LOS by its peculiar LOS velocity in the appropriate units, that is $\backslash = \mathbf{x} + \mathbf{u}$, where $\mathbf{u} = (\hat{n}\cdot\mathbf{v})\hat{n}/\mathcal{H}$ and $\mathcal{H}$ is the conformal Hubble parameter [196]. Within LPT this is equivalent to boosting the displacement Ψ by the LOS component of its (appropriately normalized) time derivative, i.e. $\Psi_s = \Psi + \dot{\Psi}$ [231, 82]; conveniently, this boost can be recast as a coordinate transformation

$$\Psi^{(n)}_{s,i} = \Psi^{(n)}_i + nf\hat{n}_i\hat{n}_j\Psi^{(n)}_j \equiv R^{(n)}_{ij}\Psi^{(n)}_j \quad . \tag{8.3}$$

For the remainder of this chapter we will in addition make the plane-parallel approximation that the LOS vector $\hat{n}$ is a constant independent of position.

The translation between densities and displacements follows from number conservation. Assuming galaxies are sampled from the initial conditions δ_0 according to some functional $\rho_g(\mathbf{q}) = F[\delta_0(\mathbf{q})]$ this implies that the present day density satisfies $\rho_g(\mathbf{x})d^3\mathbf{x} = \rho_g(\mathbf{q})d^3\mathbf{q}$ or, in Fourier space, [229, 402, 110, 82]

$$1 + \delta_g(\mathbf{k}) = \int d^3\mathbf{q}\; e^{i\mathbf{k}\cdot(\mathbf{q}+\Psi)}F(\mathbf{q}) \quad . \tag{8.4}$$

The equivalent equation in redshift space follows by substituting Ψ for Ψ_s. The bias functional $F(\mathbf{q})$ can be perturbatively expanded as

$$F(\mathbf{q}) = b_1\delta_{\rm lin}(\mathbf{q}) + \frac{1}{2}b_2(\delta_{\rm lin}(\mathbf{q})^2 - \langle\delta^2_{\rm lin}\rangle) + b_s(s^2_{\rm lin}(\mathbf{q}) - \langle s^2_{\rm lin}\rangle) \tag{8.5}$$

where $s^2_{\rm lin} = (\partial_i\partial_j/\partial^2 - \delta_{ij}/3)\delta_{\rm lin}$ is the shear tensor. For a complete accounting of terms relevant to the one-loop power spectrum we in principle have to also account for third order bias operators; however, since we expect them to be small for all but the most massive halos [140, 86, 74], and highly degenerate with the effective-theory corrections discussed below, we will set them to zero for the rest of this work.

The power spectrum in redshift space is then given by [231, 82]

$$P_s(\mathbf{k}) = \int d^3\mathbf{q}\;\left\langle e^{i\mathbf{k}\cdot(\mathbf{q}+\Delta_s)}F(\mathbf{q}_1)F(\mathbf{q}_2)\right\rangle_{\mathbf{q}=\mathbf{q}_1-\mathbf{q}_2}, \tag{8.6}$$

where we have defined the pairwise displacement in redshift space $\Delta_s = \Psi_s(\mathbf{q}_1) - \Psi_s(\mathbf{q}_2)$. In the case of matter ($F = 1$) within first-order LPT (Zeldovich approximatin) Equation 8.6 can be evaluated exactly to give $P_{\rm Zel} = \int d^3\mathbf{q}\exp[ik_iq_i - k_ik_jA_{ij}/2]$ where we have defined the second cumulant of pairwise displacements $A_{ij} = \langle\Delta_i\Delta_j\rangle$. The exponentiation of the pairwise displacement in Equation 8.6 is highly significant and allows LPT to capture the nonlinear damping of BAO due to the large-scale (bulk) displacements [335, 399, 22, 402, 50]. In practice we keep only these long-wavelength displacements exponentiated and perturbatively

expand those above a certain wavenumber ($k_{\rm IR} = 0.2\,h\,{\rm Mpc}^{-1}$) perturbatively; for further details we refer interested readers to ref. [82], which also provides a detailed exposition of the various terms implied in Equation 8.6 as well as relevant numerical methods. Finally, as an effective perturbation theory LPT requires a number of counterterms to properly tame its sensitivity to small-scale (UV) physics; in this work we adopt the parametrization of ref. [74] and write

$$P_s(\mathbf{k}) = P_s^{\rm PT}(\mathbf{k}) + (\alpha_0 + \alpha_2\mu^2)k^2 P_{\rm Zel}(\mathbf{k}) + R_h^3(1 + \sigma^2 k^2\mu^2) \tag{8.7}$$

where $P_{\rm Zel}$ is the Zeldovich matter power spectrum. Note that while the above parametrization is not exhaustive (i.e. we should in principle include terms like $\alpha_4\mu^4$), this parameter set has been tested extensively against simulations (e.g. refs. [78, 74, 76, 82]) and the neglected terms are extremeley degenerate with those listed when fitting the monopole and quadrupole only. The above parameter set can also be used to fit the pre-reconstruction correlation function, which can be obtained directly by Fourier transforming the theory prediction for the power spectrum.

8.3.2 Nonlinear BAO Damping Post Reconstruction

It is well known that nonlinear structure formation smooths out the BAO peak in the galaxy two-point function [46, 121, 231, 92, 266, 257], reducing its prominence and as a result also the signal-to-noise of BAO measurements. Within LPT this phenomenon can be understood by looking at contributions to Equation 8.6 such as [76]

$$P_{\rm BAO}(\mathbf{k}) \sim \int d^3\mathbf{q}\; e^{i\mathbf{k}\cdot\mathbf{q} - \frac{1}{2}k_i k_j A_{ij}(\mathbf{q})}\; \xi_{\rm BAO}(\mathbf{q}) \approx e^{-\frac{1}{2}k^2\Sigma^2} \int d^3\mathbf{q}\; e^{i\mathbf{k}\cdot\mathbf{q}}\; \xi_{\rm BAO}(\mathbf{q}).$$

Since the BAO peak is well-localized at the sound horizon at the drag epoch r_d, it acts to pick out a particular scale at which to evaluate A_{ij}, from which a specific damping scale $\Sigma^2 = \langle A_{ij}\rangle_{|\mathbf{q}|=r_d}$, leading to Gaussian damping of the BAO. Within ΛCDM most of the displacement power comes from relatively low wavenumbers [121].

The purpose of standard reconstruction [122] is to sharpen the BAO feature by undoing some of this damping. To do so, one smooths the observed galaxy density field using a Gaussian filter $S(k)$ on a sufficiently large scale that the Kaiser formula $\delta_g(\mathbf{k}) = (b + f\mu^2)\delta_m$ is a good approximation, uses the smoothed field to solve for the (smoothed) linear Zeldovich displacement $S(k)\Psi_{\rm Zel}(\mathbf{k}) = i\mathbf{k}/k^2 S(k)\delta_m$, and subtracts these displacements from the observed galaxy positions. To preserve power on large scales a random catalog is shifted using the same displacements, with the difference between the displaced galaxies (d) and shifted randoms (s) constituting the full reconstructed density field $\delta_{\rm rec} = \delta_d - \delta_s$. The presence of redshift space distortions presents a slight complication and there is no general settled-upon convention in the literature: the BOSS data analyzed in this work followed the so-called **RecIso** convention wherein the galaxies were displaced with RSD (that is, the reconstructed displacement multiplied by $R_{ij}^{(1)}$) while the randoms were shifted without RSD [267].

The residual damping left in the BAO signal after reconstruction can be modeled in the same way as was the damping pre-reconstruction. Specifically, we can think of the displaced galaxies (d) and shifted randoms (s) as two additional tracers with displacements [266, 257, 414, 78]

$$\Psi_i^d = R_{ij}^{(1)}(1-\mathcal{S}) * \Psi_j^{\rm Zel} \quad , \quad \Psi_i^s = -\mathcal{S} * \Psi_i^{\rm Zel}. \tag{8.8}$$

The two-point statistics of these displacements can then be computed at the sound horizon r_d as in the pre-reconstruction case and used to damp the BAO feature. Specifically, for a given linear power spectrum $P_{\rm lin}$ we can decompose it into a "wiggle" component with the BAO feaure and a smooth component without, i.e. $P_{\rm lin} = P_w + P_{nw}$. The prediction for each (cross) spectrum between d, s is then

$$P^{ab}(\mathbf{k}) = K^{ab}(k,\mu)\left[P_w(k)e^{-k^2\Sigma^{ab}(\mu)/2} + P_{nw}(k)\right] \tag{8.9}$$

where $K^{ab}(k,\mu)$ is a linear-theory function of the growth rate $f(z)$ and linear bias b_1 taking into account Kaiser infall and the smoothing filter.

Equation 8.9 captures (resums) the nonperturbative effect of bulk displacements on linear-theory BAO wiggles; in principle, nonlinear effects such as mode coupling can induce further modifications to the BAO feature. A full treatment of these additional effects for galaxies at one-loop order is complex and beyond the scope of this work (see however ref. [172] for the calculation in the case of matter only). Calculations taking into account nonlinear bias within the Zeldovich approximation show that phase shifts due to mode coupling are substantially reduced post-reconstruction, suggesting that the in-phase damping of the BAO feature due to IR displacements is the dominant nonlinear effect [78]. However, in order to further insulate our full-shape fits from potential systematics of the reconstruction procedure, including due to residual nonlinear contributions, we set the linear bias and growth rate in the BAO model to be free parameters called F and B_1, and in addition allow for broadband deviations between the theory predictions for ξ_ℓ and the data by fitting adding a linear template to the theory predictions, that is

$$\xi_\ell(r) = \xi_\ell^{\rm th}(r) + a_{\ell,0} + \frac{a_{\ell,1}}{r} \tag{8.10}$$

where $\xi_\ell^{\rm th}$ are the multipoles of the Fourier transformed (with AP) theory predictions of Equation 8.9. Detailed functional forms and integrals are given in Appendix G.2.

Let us conclude this section by comparing our approach in BAO fitting with that in previous work. Traditionally, the BAO have been fit using a template power spectrum whose BAO component is scaled by

$$\tilde{\alpha}_{\parallel,\perp} = \left(\frac{r_d^{\rm fid}}{r_d}\right)\alpha_{\parallel,\perp}. \tag{8.11}$$

This takes into account stretching of the BAO signal due both to changing distance scales ($\alpha_{\parallel,\perp}$) and sound horizon (r_d). Typically this template model is used to fit directly for the $\tilde{\alpha}$'s,

whose output likelihoods can then be used in broader cosmological analyses. Note that this prescription mixes two in-principle distinct physical effects: the cosmological dependence of the sound horizon r_d and the anisotropy due to the Alcock-Paczynski effect ($\alpha_{\parallel,\perp}$), While the latter would exist even in the absence of the BAO peak, the conventional method assumes the BAO carries the bulk of the signal, with other effects from the broadband shape of the power spectrum discarded, or marginalized away, via polynomial parameters.

In this work we eschew the use of templates for both pre- and post-reconstruction fitting, choosing instead to extract the BAO wiggles for each cosmology directly from the transfer-function outputs of Boltzmann codes, with the perspective that Equation 8.6 and 8.9 are definite predictions of the pre- and post-reconstruction galaxy two-point function for any given cosmology. This obviates the need for the r_d scaling in $\tilde{\alpha}$, since the frequency of the BAO wiggles is automatically encoded in the linear power spectrum, and automatically includes any distance and anisotropy information present in the data. Modeling the reconstructed BAO at the data instead of the summary statistic level also has advantages for constraining non-standard physical effects like beyond ΛCDM physics. While measurements of the BAO scale are robust to many such physical effects [38], there are notable and theoretically well-understood exceptions, for example features around the BAO scale due to relative perturbations between baryons and dark matter [317, 70]. Beyond robustness, measurements of BAO scaling parameters alone cannot capture many effects related to oscillatory features in the power spectrum that can be sharpened by reconstruction, including neutrino or light-relic induced phase shifts in the BAO [27] or inflationary signatures [390, 44, 76]. Indeed, ref. [29] detected the neutrino-induced phase shift in reconstructed BOSS data by expanding the standard template fit with an additional phase-shift parameter. On the other hand, for a given cosmological model, any such effects are automatically included when fitting at the data level without modification and, once included in a theory model, cannot act as a theoretical systematic by default. For completeness, and to correct some typos in the literature, we include a detailed description of the standard method in Appendix G.3.

8.4 Analysis Setup

In this chapter we aim to perform a joint analysis combining full-shape information in pre-reconstruction power spectrum and additional information in the post-reconstruction correlation function. To this end, our fiducial setup will combine the former with the latter in a narrow band around the peak where most of the BAO information is isolated. Our goal in this section is to outline and explain this setup, and lay out the accompanying cosmological and effective-theory parameter choices and priors.

8.4.1 Scale Cuts

We begin by setting up the Fourier-space side of our analysis. Throughout this chapter we will adopt the Fourier-space scale cuts $k_{\rm min} = 0.02\,h\,{\rm Mpc}^{-1}$ and $k_{\rm max} = 0.20\,h\,{\rm Mpc}^{-1}$. The

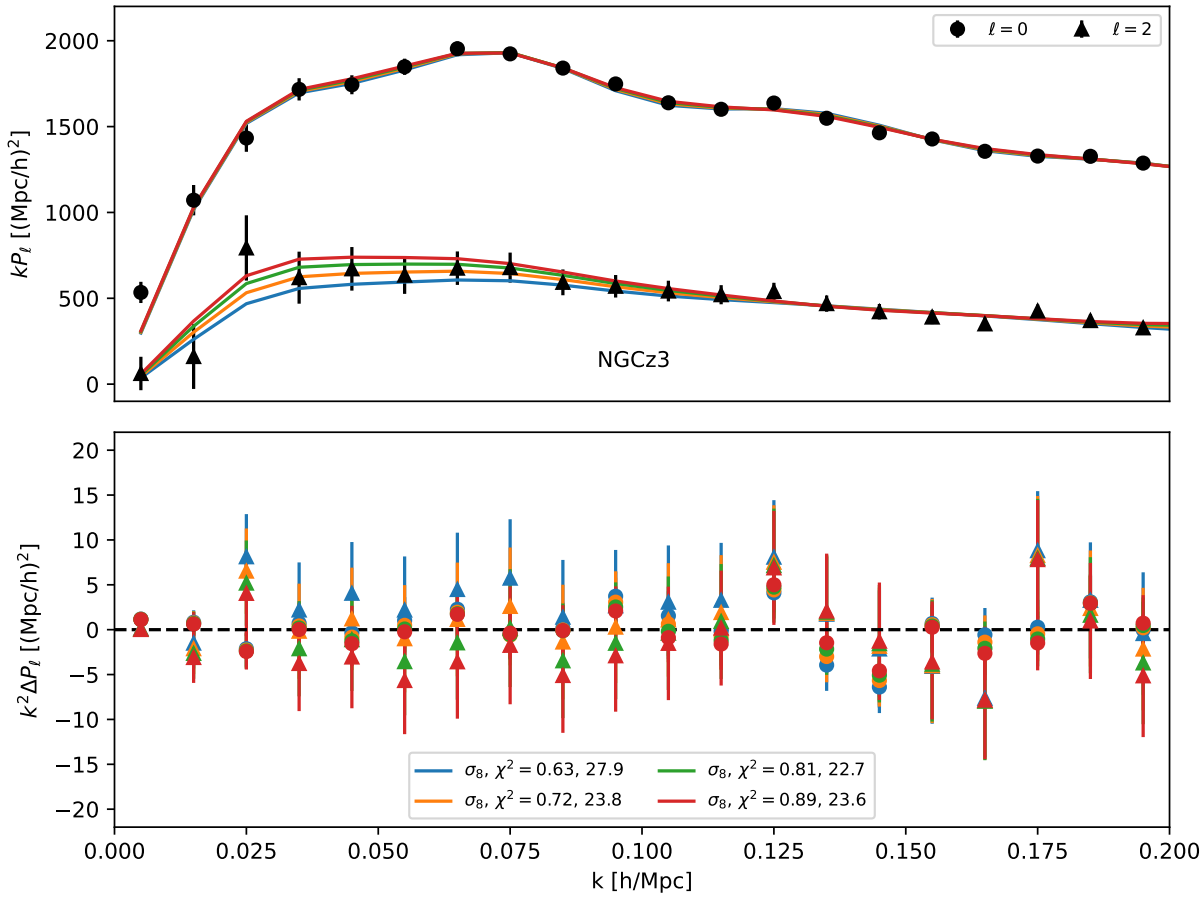

Figure 8.4: Best fit models to the **NGCz3** pre-reconstruction power spectrum multipoles (top) and their residuals (bottom), fixing Ω_m and h to their Planck best-fit values and a scan in σ_8 (different curves; see legend). The biases and counterterms are varied to find the best fit for each σ_8 and so differ between curves. The models primarily vary in their predictions for the low k quadrupole amplitude while making essentially identical predictions to the high k amplitude across different σ_8's. This suggests the constraining power on σ_8 comes primarily from large scales.

LPT model we use in this work was shown to yield unbiased cosmological constraints on this range of scales for BOSS-like samples even at significantly larger volumes [82]. We drop the lowest two k bins below $0.02\,h\,\mathrm{Mpc}^{-1}$; including them increased the best-fit χ^2 for the **NGCz3** sample when limiting to a Planck cosmology by $\Delta\chi^2 = 20$, suggesting systematic errors in the data beyond our theoretical modeling.

It is worth noting that we have chosen to adopt a more conservative scale cut than some other works in the literature, like Ref. [86] who adopt $k_{\mathrm{max}} = 0.25\,h\,\mathrm{Mpc}^{-1}$, even though we expect our theoretical model to perform as well as other effective-theory models on the pre-reconstruction power spectrum. We have made this choice on the reasoning that the information on the primordial (linear) power spectrum rests primarily on large scales, such that fitting smaller scales mainly serves to fit the shape of nonlinearities in the redshift-space power spectrum like fingers of god (FoGs). In fact, ref. [74] found that P_ℓ became dominated by nonlinear, higher-order velocity statistics at around our chosen scale cut for $\ell > 0$. As an illustrative example of these effects, in Figure 8.4 we show the best-fit models to the **NGCz3** power spectrum multipoles for a series of cosmologies with Ω_m and h fixed to their Planck best-fit values and σ_8 scanned from 0.63 to 0.89. For each σ_8 we then vary the bias parameters and counter terms to fit the **NGCz3** multipoles. Notably, the only change from varying σ_8 is in the quadrupole at $k \lesssim 0.1\,h\,\mathrm{Mpc}^{-1}$, with the higher k points having essentially the same residuals compared to the data across a broad range of power spectrum amplitudes. The best-fitting values of the biases and counter terms that we find appear reasonable for each of the σ_8 values we tried. We can understand this effect as follows: since the linear bias is well-constrained by the monopole, varying σ_8 effectively tunes the linear quadrupole amplitude, but as effective-theory corrections like nonlinear bias turn on at higher wavenumbers this variation is erased by all the nonlinear parameters conspiring to fit a relatively smooth and featureless P_2. This suggests that, absent a detailed understanding of the small-scale physics underlying the bias parameters, there is not signficant information to be gained at smaller scales. Conversely, the fact that the variations in the quadrupole amplitude on large scales cannot be fit away by (reasonable) bias parameters is a demonstration that in effective theories the large scale clustering signal cannot be polluted by small-scale physics in unphysical ways. This also suggests that future surveys capable of reducing the errors at low k would significantly improve the constraints on the amplitude.

For the configuration-space side of our analysis, since we are primarily interested in fitting the BAO feature, we restrict our fitting of the post-reconstruction correlation function to $80 < s < 130\,h^{-1}$ Mpc for our fiducial setup. This range of scales effectively isolates the BAO peak and most of the additional distance information coming from reconstruction. It is worth noting that a fit using the same model in Fourier space would have required fitting over a wide range of wavenumbers to cover all the BAO wiggles in the power spectrum and risked numerical issues in the covariance matrix due to significant correlation with the pre-reconstruction power spectrum; the fact that the BAO feature is localized at a large scale in the correlation function, which happens to also be significantly sharpened by reconstruction at those radii, is thus a useful fact in combining pre- and post-reconstruction data. We also note that using broader bins in $P_\ell(k)$ could further separate the BAO and broad-band

information, making the constraints even less correlated, but we have not needed to take that step for BOSS. Finally, as a consistency check we will also want to compare fits to the pre-reconstruction correlation functions for **z1** and **z3** samples to our fiducial setup fitting the pre-reconstruction power spectrum; for these fits we will fit the correlation function over the entire range shown in the bottom panel of Figure 8.2, i.e. $r > 25\,h^{-1}\,\mathrm{Mpc}$.

8.4.2 Parameters and Priors

We choose to sample the cosmological parameter space uniformly in Ω_m, h and $\ln(10^{10}A_s)$. For the purposes of our analysis we will fix the values of the baryon density $\Omega_b h^2 = 0.02242$ and spectral index $n_s = 0.9665$ to the best-fit values from Planck [286], since the BOSS data are not very sensitive to these parameters which are very well-determined in the CMB and, in the case of the baryon density, also big-bang nucleosynthesis (BBN) [86]. We also fix the sum of the neutrino masses to be the minimal allowed $M_\nu = 0.06$ eV. While a number of recent works (e.g. ref. [18]) have sought to more exactly integrate the scale-dependent effects of massive neutrinos into LPT, in this work we will approximate the effect of neutrinos on galaxy clustering by using the "cb" prescription [66]. This prescription is motivated by the intuition that galaxies trace the cold dark-matter and baryon fluid with linear power spectrum P_{cb} and small-scale growth rate $f_c = (1 - 3f_\nu/5)f_{\Lambda\mathrm{CDM}}$, where f_ν is the neutrino mass fraction. This was recently shown to be an excellent approximation using phase-matched simulations in ref [33].

For our pre-reconstruction power spectrum model we choose to fit each of the four samples with independent sets of bias parameters. As can be seen in Figure 8.2 the NGC and SGC samples at **z1** have signficantly different power spectrum multipoles on all scales shown; indeed, using the best-fit bias parameters for a Planck cosmology for the NGC sample and convolving it with the **SGCz1** window function yields a noticeably worse fit ($\Delta\chi^2 = 19$ with our fiducial scale cuts). The multipoles at **z3** show greater agreement, and performing the same exercise of convolving the best fit model from one galactic cap with the window function of the other yields a much better fit. Nonetheless, we have opted for the more conservative approach and fit all four (statistically independent) samples pre-reconstruction using separate sets of bias parameters. Since the correlation function data were computed jointly for the NGC and SGC samples we are forced to use a unified set of bias parameters when fitting in configuration space; however, since our primary interest in fitting the post-reconstruction ξ_ℓ's are to extract large-scale BAO information, and since we find that the linear biases between the two galactic caps are in good agreement in our power-spectrum only fits, we do not expect this to significantly affect our results.

Our priors on the effective-theory and bias parameters are listed in Table 8.1. We adopt broad, uninformative priors for the BAO broadband parameters B_1, F, with similarly broad priors on the polynomial broadband terms with widths such that they do not dominate the clustering signal on BAO scales. For the pre-reconstruction power spectrum we use generally broad priors for the quadratic biases b_2, b_s on the assumption that they are free effective-theory coefficients of order unity. Our counterterms α_0, α_2 are set to Gaussian

Parameter	Prior	Parameter	Prior
$\ln(10^{10}A_s)$	$\mathcal{U}(1.61, 3.91)$	$(1+b_1)\sigma_8$	$\mathcal{U}(0.5, 3.0)$
Ω_m	$\mathcal{U}(0.20, 0.40)$	b_2	$\mathcal{N}(0, 10)$
H_0 [km/s/Mpc]	$\mathcal{U}(60.0, 80.0)$	b_s	$\mathcal{N}(0, 5)$
B_1	$\mathcal{U}(0, 5.0)$	α_0 [h^{-2} Mpc^2]	$\mathcal{N}(0, 100)$
F	$\mathcal{U}(0, 5.0)$	α_2 [h^{-2} Mpc^2]	$\mathcal{N}(0, 100)$
$a_{\ell,0}$	$\mathcal{N}(0, 0.05)$	R_h^3 [h^{-3} Mpc^3]	$\mathcal{N}(0, 1000)$
$a_{\ell,1}$ [h^{-1} Mpc]	$\mathcal{N}(0, 5)$	$R_h^3\sigma^2$ [h^{-5} Mpc^5]	$\mathcal{N}(0, 5\times10^4)$

Table 8.1: Parameter priors for our analysis. Uniform and normal distributions are indicated by $U(x_{min}, x_{max})$ and $N(\mu, \sigma)$, respectively.

priors with the expectation that the galaxy power spectrum deviate from linear theory by a factor less than unity on perturbative scales. Finally, while one might expect the isotropic stochastic term R_h^3 to be a free parameter in the ball-park of the inverse galaxy number density $\bar{n}^{-1} \approx 3000\, h^{-3}\,\mathrm{Mpc}^3$, we put a relatively tight Gaussian prior with width $1/(3\bar{n})$ on it given that we find an almost exact degeneracy between it and α_0 in our fits that did not correlate significantly with any cosmological parameters for reasonable values of R_h^3 and α_0. We put a physically motivated prior on $R_h^3\sigma^2$ based on the expectation that characteristic halo velocities for BOSS LRGs are around 500 km/s, or about $5\, h^{-1}\,\mathrm{Mpc}$. Our pre-reconstruction fits to the pre-reconstruction correlation function follow the same set of priors as the power spectrum fits.

8.4.3 Test on Mocks

As we have discussed, the model described in Section 8.3, i.e. LPT, has been tested extensively against simulated galaxy samples both pre- and post-reconstruction, e.g. in refs. [82, 78]. These tests were performed using periodic boxes without observational effects like window functions and realistic survey geometries; while these effects are well understood and not expected to significantly affect the accuracy of our models over the relevant scales, it is worth checking that our fiducial setup in this chapter (jointly fitting the redshift-space power spectrum and post-reconstruction correlation function near the BAO peak) does not yield unexpected biases in cosmological constraints. To this end, in this subsection we apply the same analysis pipeline we will use to analyze the BOSS data to obtain mock constraints from the mean of the 1000 Patchy mocks released by the BOSS collaboration described in Section 8.2. In particular, we perform our test on mocks of the **z3** sample, including the NGC and SGC power spectra and combined correlation function multipoles. While these mocks employ approximate dynamics that may not exactly match the *ab initio* predictions of perturbation theory, they are designed to match the survey geometry and observational systematics of the BOSS survey, and are thus a reasonable way to test whether these effects or our joint Fourier and configuration space setup meaningfully affect our results.

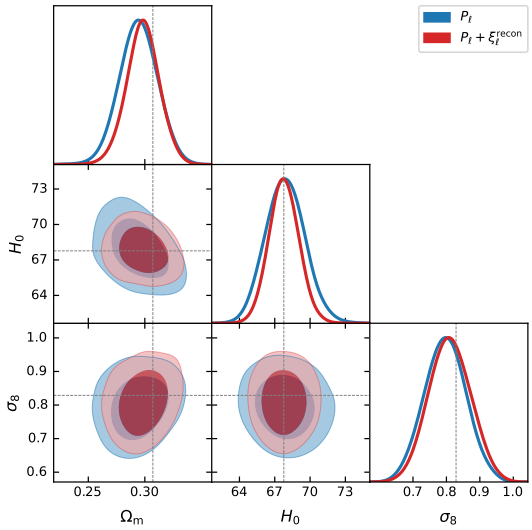

	P_ℓ	P_ℓ + BAO
$\ln(10^{10}A_s)$	3.09 ± 0.18	3.10 ± 0.17
Ω_m	0.294 ± 0.017	0.298 ± 0.014
H_0 [km/s/Mpc]	67.9 ± 1.7	67.8 ± 1.3
σ_8	0.797 ± 0.062	0.810 ± 0.063

Figure 8.5: (Left) Contours of mock constraints from the mean of 1000 Patchy mocks for the **z3** sample fitting redshift-space power spectrum monopole and quadrupole between $0.02\,h\,\mathrm{Mpc}^{-1} < k < 0.20\,h\,\mathrm{Mpc}^{-1}$ with (red) and without (blue) additional BAO information from the post-reconstruction correlation function near the BAO peak. Gray lines show the true cosmology of the Patchy mocks. (Right) A table of the mock constraints (mean$\pm 1\sigma$). The true cosmology is given by $\Omega_m = 0.307115, H_0 = 67.77, \sigma_8 = 0.8288$, well within the 1σ bounds shown.

The results of this test are shown in Figure 8.5. The constraints both with and without BAO information recover the true cosmology ($\Omega_m = 0.307115, H_0 = 67.77, \sigma_8 = 0.8288$) of the Patchy mocks to within 1σ, and adding in the post-reconstruction correlation function tightens but does not lead to significant ($< 0.3\sigma$) shifts in the resulting constraints. We note that our results both with and without reconstruction show up to 0.5σ deviations from "truth" in both Ω_m and σ_8 despite the low statistical scatter from averaging over 1000 mocks, which could be due to either the approximate nature of the mocks themselves or parameter projection effects; nonetheless, these results are satisfactory for our purposes since (1) they demonstrate the main goal of this subsection, which was to show that adding in the post-reconstruction correlation function does not bias our results and (2) the parameter shifts occur both with and without reconstruction, despite our having tested the latter case in simulation volumes significantly ($100\times$; [255]) larger than the BOSS survey and with correspondingly tighter constraints and recovered unbiased constraints. Indeed, adding in post-reconstruction BAO shifts both Ω_m and σ_8 closer to "truth" while leaving H_0 firmly centered at the true value, potentially due to reduced parameter-projection effects coming from tighter constraints.

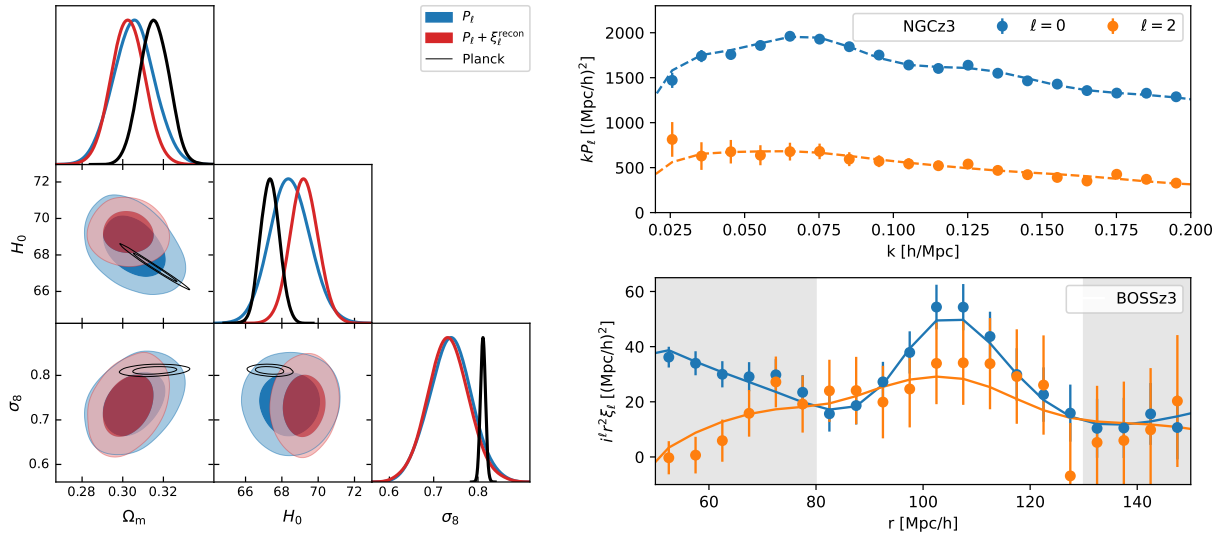

Figure 8.6: (Left) Constraint contours for fits to the BOSS galaxy power spectra alone (blue) and with post-reconstruction correlation function multipoles (BAO) added (red) compared to posteriors from Planck (blue), with which our constraints are broadly consistent. (Right) Binned best-fit models for the power spectrum and post-reconstruction correlation function multipoles from our chains. Here we show only the results for **NGCz3** power spectra and **z3** correlation functions for brevity; the other samples are similarly well fit, with total $\chi^2/\text{d.o.f} = 1.06$. Gray bands in the correlation function plot show separations excluded by our fit.

8.5 Results

8.5.1 ΛCDM Constraints from BOSS with and without BAO

The main results of this chapter – constraints on ΛCDM parameters from pre-reconstruction power spectra and post-reconstruction correlation function multipoles for the full BOSS sample, including both galactic caps and redshift slices – are shown in Figure 8.6 and listed in

	P_ℓ	P_ℓ + BAO	Planck
$\ln(10^{10}A_s)$	2.84 ± 0.13	2.81 ± 0.12	3.044 ± 0.014
Ω_m	0.305 ± 0.01	0.303 ± 0.0082	0.3153 ± 0.0073
H_0 [km/s/Mpc]	68.5 ± 1.1	69.23 ± 0.77	67.36 ± 0.54
σ_8	0.738 ± 0.048	0.733 ± 0.047	0.8111 ± 0.0060

Table 8.2: Constraints from the full BOSS sample, i.e. **NGCz1 SGCz1**, **NGCz3** and **SGCz3**, with and without additional BAO information from the reconstructed correlation function, summarized as mean $\pm 1\sigma$. The equivalent constraints from Planck are also tabulated for comparison.

Table 8.2. Fitting to pre-reconstruction power spectra alone we constrain $\Omega_m = 0.305 \pm 0.01$, $H_0 = 68.5 \pm 1.1$ and $\sigma_8 = 0.738 \pm 0.048$; adding in the post-reconstruction correlation function gives $\Omega_m = 0.303 \pm 0.0082$, $H_0 = 69.23 \pm 0.77$ and $\sigma_8 = 0.733 \pm 0.047$. When fit with a shared set of cosmological parameters, our model provides good fits to all of the individual statistics included in the likelihood (pre-recon P_ℓ and post-recon ξ_ℓ with $\ell = 0$ and 2), with a combined $\chi^2/\text{d.o.f} = 1.05$. As an example, the right panel of Figure 8.6 shows the best-fit P_ℓ and ξ_ℓ for the **NGCz3** and **z3** samples, respectively. The other samples look similar.

Comparing the red and blue contours in Figure 8.6, we see that the primary effect of including post-reconstruction correlation functions is to tighten constraints on the Hubble parameter H_0 (by around 40%) while also slightly tightening constraints on Ω_m and keeping the σ_8 constraint largely untouched. This is to be expected since (1) the main purpose of standard reconstruction is to sharpen the BAO peak and (2) we have fit the post-reconstruction correlation function only near the peak at $80\,h^{-1}\,\text{Mpc} < r < 130\,h^{-1}\,\text{Mpc}$. Our motivation to include the post-reconstruction correlation function in this chapter was to include the information in the linear power spectrum isolated at the BAO peak in configuration space and not to use it as a further probe of nonlinearities in structure formation; indeed, the purpose of freeing the Kaiser factors B_1, F and linear broadband polynomials in our correlation-function model was precisely to prevent systematics in reconstruction from biasing our constraints on the broadband amplitude of the linear power spectrum.

Let us conclude this subsection by comparing our results to those of other groups and experiments. As can be seen in the left panel of Figure 8.6, our constraints from BOSS, both with and without additional information in the form of the reconstructed correlation function, are also broadly consistent with cosmic microwave background (CMB) constraints, lensing included, from Planck [286]. Indeed, our pre-reconstruction fit has the Planck best-fit Ω_m and H_0 within its 1σ contours, and σ_8 at about 1.5σ lower. This is in contrast with earlier chapters using effective theory approaches to fitting the BOSS data, e.g. ref.'s [86, 188, 96], which found σ_8's significantly ($> 2\sigma$) lower than Planck. These discrepancies are potentially attributable to the data normalization issue described in Section 8.2 as our pre-reconstruction Ω_m and H_0 constraints are in much better agreement with those earlier works; specifically, this normalization issue resulted in power spectra that were roughly 10% too low in amplitude for a fixed window function normalization, translating to a roughly 5% lower best-fit σ_8. We recover essentially identical σ_8 constraints to previous works if this correction is neglected. Indeed, after our paper was first posted to the arXiv, updated results free of window-function systematics from the authors of the aforementioned works appeared: specifically, ref. [438] used correlation functions to obtain $\sigma_8 = 0.7537^{+0.055}_{-0.06}$ and $0.7559^{+0.052}_{-0.062}$ with and without BAO, in good agreement with results from their independently measured power spectra, and ref. [282] obtained $\sigma_8 = 0.729^{+0.040}_{-0.045}$ using a window-function free power spectrum estimator and $\sigma_8 = 0.737^{+0.040}_{-0.044}$ when using the same updated BOSS power spectra as the present work, virtually identical to our pre-reconstruction constraints[5]. Our results are also in excellent

[5]For a clean comparison, we have quoted their constraints fixing the spectral tilt n_s and without including the bispectrum monopole or finger-of-god reduced two-point statistics.

agreement with constraints from the BOSS data using an emulator approach [204] and the configuration-space analysis in ref. [331].

Adding the post-reconstruction correlation function, which sharpens the BAO peak and tightens the H_0 constraint, puts the Hubble parameter best-fit from Planck at about 2σ. This is in contrast to the BOSS fits in Ref. [283], who find $H_0 = 67.81^{+0.686}_{-0.69}$ after adding in fits to $\tilde{\alpha}$'s from post-reconstruction power spectra despite a similar tightening of constraints, though we note that we use different post-reconstruction data (P_ℓ vs. ξ_ℓ) and covariance matrices and that the mock tests in §8.4.3 suggest that adding in the post-reconstruction correlation function does not bias our results. Nonetheless, our constraints with and without BAO both lie on the surface of constant $\Omega_m h^3$ given by the Planck best-fit parameters; this combination is close to a principle component of the Planck posterior and is much better constrained than either H_0 or Ω_m alone.

Finally, our redshift-space constraints offer an independent check to the measurements of power spectrum amplitude from weak lensing surveys like DES and KiDS, which primarily measure the hybrid quantity $S_8 = \sigma_8(\Omega_m/0.5)^{0.5}$ and have found it to be significantly lower than the value implied by Planck (0.832 ± 0.013 [286]). Figure 8.7 summarizes these constraints in the $\Omega_m - \sigma_8$ plane. Since σ_8 and Ω_m are positively correlated in our posteriors, our constraints are not optimized to measure S_8; nonetheless, we obtain $S_8 = 0.736 \pm 0.051$, slightly less than 2σ lower than the Planck result and measurements of $0.775^{+0.026}_{-0.024}$ (3×2pt only) or 0.812 ± 0.008 (+BAO, RSD and SNIA) from DES Y3 [2][7] and of $0.766^{+0.020}_{-0.014}$ from a joint KiDS, BOSS and 2dFLenS analysis [169]. At lower redshifts, once BAO and weak priors are included, the constraint from CMB lensing measured by Planck is $\Sigma_8 \equiv \sigma_8(\Omega_m/0.3)^{0.25} = 0.815 \pm 0.016$ [287]. Our joint analysis finds $\Sigma_8 = 0.735 \pm 0.0495$, about 1.5σ lower.

8.5.2 Consistency Checks

As discussed in Section 8.3, (Lagrangian) perturbation theory provides a framework within which we can model large-scale structure observables like the power spectrum and correlation function with a consistent theoretical model. This allows us to, for example, jointly model the pre-reconstruction power spectrum and post-reconstruction BAO feature without resorting to intermediate statistics like $\alpha_{\rm BAO}$'s measured from fixed-shape templates. In addition, the fact that we can model all these observables within the same framework allows us check the consistency of our model assumptions about the background cosmology and nonlinear structure formation or, alternatively, to check for systematics in each statistic. In this subsection we will describe two such consistency tests: between the high and low redshift samples and between Fourier and configuration space.

The left panel of Figure 8.8 shows constraints obtained by fitting the two redshift slices, **z1** and **z3**, independently while including post-reconstruction BAO information in each. The

[6] We compare to their results keeping n_s fixed rather than free for a more apples-to-apples comparison.

[7] We caution that these analyses, unlike ours, freed the total neutrino mass M_ν.

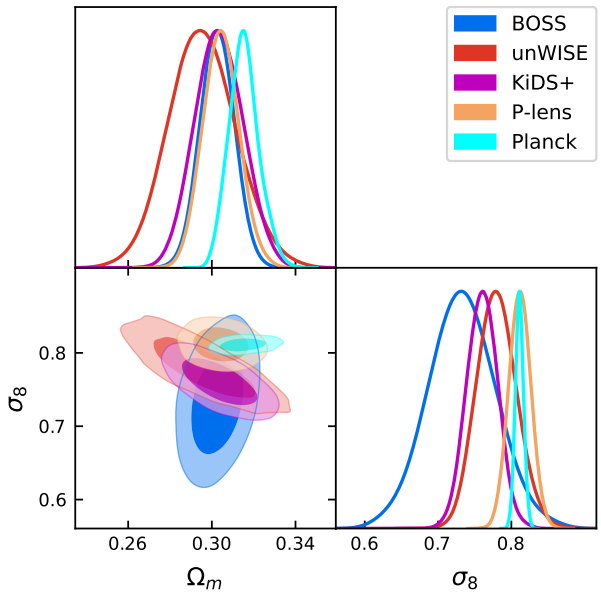

Figure 8.7: A comparison of our σ_8-Ω_m constraints with a selection of other experiments, including Planck (including lensing) [286], Planck lensing (P-lens) with BAO prior [287], KiDS+BOSS+2dFlens analysis [169], and unWISE galaxy-CMB lensing cross correlations [208]. Our BOSS constraint probes different degeneracy directions than these (primarily lensing) surveys, but is nonetheless consistent with each.

cosmological posteriors derived from the two samples are broadly consistent with each other, with significant overlap between the 1σ regions: the Ω_m and σ_8 distributions both have means consistent to within 1σ. On the other hand, while the **z1** sample prefers a value of H_0 very similar to the Planck (black contours) best fit, **z3** prefers values around 2σ above Planck; we emphasize however that the combined constraints are themselves consistent with Planck.

The right panel of Figure 8.8 compares fits to the pre-reconstruction power spectra (solid) and correlation functions (dashed) in each redshift slice. Again, the constraints from each P_ℓ, ξ_ℓ pair are broadly consistent, with overlapping 1σ regions for all three cosmological parameters. However, while both σ_8 and H_0 constraints vary consistently across samples, slightly decreasing and increasing respectively with sample redshift, the Ω_m constraints are slightly lower in configuration space than Fourier space. Given the different ranges over which we fit these statistics and the different data subsamples we do not expect perfect agreement. Nonetheless, all three parameters are broadly consistent, especially taking into account that (1) the configuration space constraints on Ω_m and H_0 are substantially less tight than their Fourier space counterparts and (2) unlike the power spectra, the correlation functions were computed assuming that the NGC and SGC subsamples could be meaningfully combined into one. While we find the large scale (linear) bias to be compatible between the two galactic caps at both redshifts, this does not appear to be true for the full set of bias

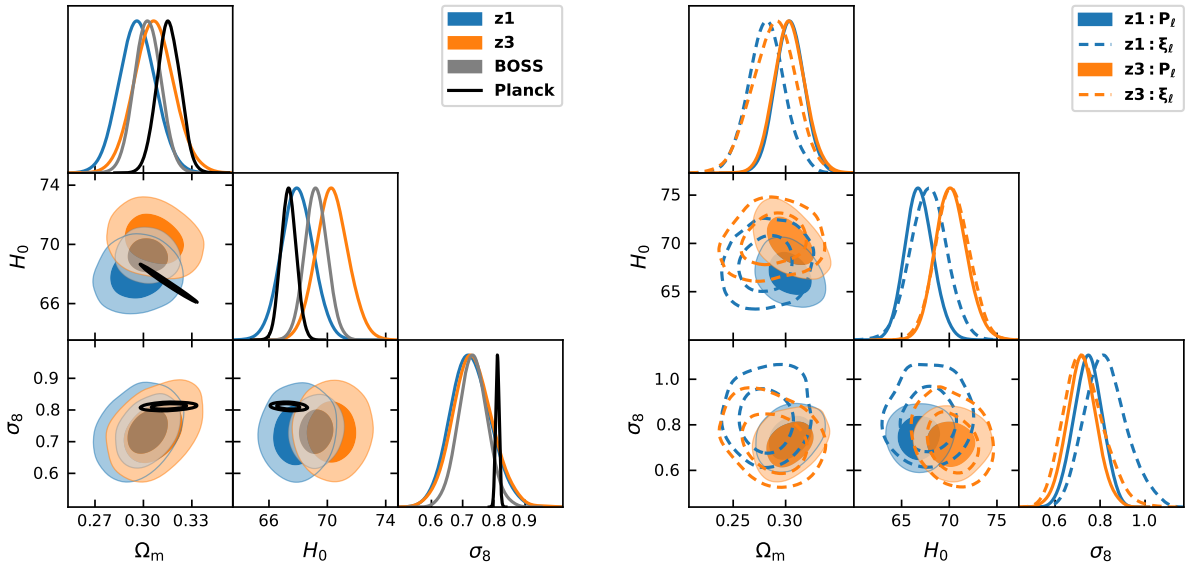

Figure 8.8: (Left) Constraints from the two independent redshift slices **z1** (blue) and **z3** (orange) compared to the joint constraint (BOSS) from both samples (gray). The two redshift bins are broadly consistent with each other, as well as with constraints from Planck (black). (Right) Constraints using pre-reconstruction power spectra and correlation functions in each of the redshift slices, fit using the same theory model.

parameters, i.e. taking the unconvolved best fit power spectrum from fitting the NGC and convolving it with the SGC window function does not yield a comparably good fit to the SGC power spectrum, particularly for the **z1** samples, leading to potential systematic differences between the configuration and Fourier space fits. The differences are not important for our post-reconstruction BAO constraints, and a full re-measurement of the BOSS correlation function, and its covariance, in each galactic cap is beyond the scope of this chapter.

We can also compare our results to the growth-rate ($f\sigma_8$) measurements made by the BOSS survey: our indepenent chains for each redshift bin imply $f\sigma_8(z_{\rm eff} = 0.38) = 0.419^{+0.035}_{-0.041}$ and $f\sigma_8(z_{\rm eff} = 0.61) = 0.422^{+0.035}_{-0.040}$, in mild tension with the official BOSS survey results. Their consensus results (including full-shape and BAO, both using template fits) were 0.497 ± 0.046 and 0.436 ± 0.035[8], respectively [7]. It is worth noting that the BOSS consensus results are a weighted combination of various analyses, including both Fourier-space and configuration-space results. The configuration space results are not affected by issues like that of window-function normalization discussed in Section 8.2. Comparison of results in each of these categories within the BOSS full-shape analysis shows differences between mean $f\sigma_8$'s greater than one standard deviation, whereas our analysis using the new window function

[8]Here we have combined the statistical and systematic uncertainties via quadrature. A complete table of the official BOSS results can be found in Table 7 of ref. [7].

normalizations yield Fourier and configuration space means within 1σ; for **z1** we get $f\sigma_8$ constraints of 0.434 ± 0.038 and 0.470 ± 0.054 and for **z3** we get 0.413 ± 0.039 and 0.414 ± 0.050 in Fourier and configuration space, respectively, pre-reconstruction.

8.6 Conclusions

Galaxy redshift surveys are an important source of cosmological information, allowing us to constrain properties of the early universe and general relativity through measurements of redshift-space distortions and baryon acoustic oscillations in galaxy clustering. Recent developments in cosmological perturbation theory, particularly in the arena of effective theories and IR resummation, have further put these data on rigorous and precise footing, making it possible to consistently fit a range of measurements from these surveys within a consistent framework. In the next few years, surveys like DESI [108] and Euclid [211] will probe larger volumes at higher redshifts, greatly increasing our constraining power on cosmological parameters while making accurate modeling on quasilinear scales ever more important.

In this chapter we have presented an analysis of the pre- and post-reconstruction power spectra and correlation functions from the BOSS survey [101] within the framework of Lagrangian perturbation theory. Unlike previous works, we do not combine pre- and post-reconstruction data through additional fitting parameters for the BAO (e.g. $\tilde{\alpha}_{\parallel,\perp}$) whose covariances are determined from mocks. Rather, for a given set of cosmological parameters (Ω_m, h, σ_8) and galaxy bias coefficients we compute directly the power spectrum and correlation function as predicted by perturbation theory and compare them with observations to compute the likelihood.

For our main result, we jointly fit pre-reconstruction power spectrum and post-reconstruction correlation function multipoles for the full BOSS sample. In order to avoid undue correlation with the power spectrum measurements, we take advantage of the fact that the BAO signal is well-isolated in the correlation function, particularly after reconstruction, and only fit the correlation function in a narrow band containing the peak ($80\,h^{-1}\,\mathrm{Mpc} < r < 130\,h^{-1}\,\mathrm{Mpc}$). Our results are consistent with constraints from Planck, as well as with S_8 measurements from weak lensing surveys. We have further checked our analyses by considering constraints from each of the redshift slices ($z_{\mathrm{eff}} = 0.38$, 0.61) with and without post-recon BAO, and in the former case by fitting both the power spectrum and correlation function, finding that constraints from each subsample or observable are broadly consistent.

Let us conclude by pointing out some possible future directions. A natural extension of this work is to include further observables in our analysis: LPT in the context of galaxy-lensing cross correlations has been studied in ref. [246, 421, 201] and formed the basis of the model applied to the unWISE data in ref. [208], as well as luminous red galaxies (LRGs) from DESI in ref. [417]. Recent work [244, 206, 156, 432] combining the Lagrangian bias scheme used in this chapter with nonlinear dynamics from N-body simulations should further extend the

reach and applicability of LPT for analyzing lensing cross correlations within a Lagrangian framework. This would allow for a consistent analysis of lensing surveys along with RSD and BAO (as shown in this chapter) which will become very powerful in the era of DESI [108], Euclid [211], Rubin [224] and CMB-S4 [1]. In parallel, our analysis can be extended to include other physical effects such as relative baryon-dark matter perturbations or more exotic early-universe physics such as early dark energy light relics or primordial features in the power spectrum; the modeling of these effects have been studied within LPT [70, 76, 298] and applied to data within Eulerian perturbation theory without reconstruction [43, 317, 187, 95]. Many of these signatures are sharpened by reconstruction. Another potential effect is that of anisotropic secondary bias due to line-of-sight selection biases, which have the potential to skew measurements of σ_8 from RSD [176]. These effects have so far not been modeled with LPT, though the equivalent Eulerian framework have been explored in e.g. Ref. [110]. We discuss the current status of evidence for these effects in Appendix G.4. Of course, many of these additional effects will likely be better constrained by combining data: for example, relative baryon-dark matter perturbations have a potential to bias BAO measurements but conversely, by including its effects in a theory model, it may be easier to constrain the size of their effect on galaxy clustering when post-reconstruction data is included in the analysis. We leave these developments for future work.

8.7 Acknowledgements

We thank Pat McDonald for useful discussions about, and help with, the window functions used in this work. We thank Mariana Vargas Magaña for providing data and mock measurements of the BOSS correlation functions. S.C. is supported by the National Science Foundation Graduate Research Fellowship (Grant No. DGE 1106400) and by the UC Berkeley Theoretical Astrophysics Center Astronomy and Astrophysics Graduate Fellowship. M.W. is supported by the U.S. Department of Energy and by NSF grant number 1713791. Z.V. acknowledges the support by the Kavli Foundation. We acknowledge the use of `Cobaya` [378, 379], `Class` [48], `GetDist` [219] and `velocileptors` [74] and thank their authors for making these products public. This research used resources of the National Energy Research Scientific Computing Center (NERSC), a U.S. Department of Energy Office of Science User Facility operated under Contract No. DE-AC02-05CH11231. This work made extensive use of the NASA Astrophysics Data System and of the `astro-ph` preprint archive at `arXiv.org`.

Chapter 9

Joint Cosmological Analysis of Redshift-Space Clustering and CMB Lensing from the BOSS and Planck Surveys

This chapter was originally published as

> Shi-Fan Chen et al. "Cosmological Analysis of Three-Dimensional BOSS Galaxy Clustering and Planck CMB Lensing Cross Correlations via Lagrangian Perturbation Theory". In: *arXiv e-prints*, arXiv:2204.10392 (Apr. 2022), arXiv:2204.10392. arXiv: 2204.10392 [astro-ph.CO]

In this final chapter we augment our analysis of the three-dimensional clustering of galaxies in the BOSS survey in Chapter 8 by adding in cross correlations of the galaxy and matter densities, with the latter represented by the weak lensing of the CMB. We present a formalism for jointly fitting pre- and post-reconstruction redshift-space clustering (RSD) and baryon acoustic oscillations (BAO) plus gravitational lensing (of the CMB) that works directly with the observed 2-point statistics. The formalism is based upon (effective) Lagrangian perturbation theory and a Lagrangian bias expansion, which models RSD, BAO and galaxy-lensing cross correlations within a consistent dynamical framework. As an example we present an analysis of clustering measured by the Baryon Oscillation Spectroscopic Survey in combination with CMB lensing measured by Planck. The post-reconstruction BAO strongly constrains the distance-redshift relation, the full-shape redshift-space clustering constrains the matter density and growth rate, and CMB lensing constrains the clustering amplitude. Using only the redshift space data we obtain $\Omega_{\rm m} = 0.303 \pm 0.008$, $H_0 = 69.21 \pm 0.78$ and $\sigma_8 = 0.743 \pm 0.043$. The addition of lensing information, even when restricted to the Northern Galactic Cap, improves constraints to $\Omega_m = 0.300 \pm 0.008$, $H_0 = 69.21 \pm 0.77$ and $\sigma_8 = 0.707 \pm 0.035$, in tension with CMB and cosmic shear constraints. The combination of Ω_m and H_0 are consistent with Planck, though their constraints derive mostly from redshift-space

clustering. The low σ_8 value are driven by cross correlations with CMB lensing in the low redshift bin ($z \simeq 0.38$) and at large angular scales, which show a 20% deficit compared to expectations from galaxy clustering alone. We conduct several systematics tests on the data and find none that could fully explain these tensions.

9.1 Introduction

The large-scale structure of the Universe provides information on galaxy formation, cosmology and fundamental physics [275, 114]. Perhaps the most powerful measure to date has been the redshift-space two-point function measured by galaxy redshift surveys, which measures both the shape of the primordial power spectrum including distance information in baryon acoustic oscillations (BAO; [410, 120, 238]) and cosmological velocities in the form of redshift-space distortions (RSD; [196, 158]). A complementary view of large-scale structure comes from gravitational lensing, which probes the projected (Weyl) potential sourced by fluctuations in the matter density. Of particular interest to us here is the lensing of the cosmic microwave background (CMB) anisotropies, which provide a well-characterized source screen at a well-known redshift [285] far behind the lensing potentials. Either of these probes, or their combination, can be used to measure the amplitude and growth rate of large-scale structure over cosmic time with high precision, providing valuable constraints on our cosmological model and its constituents.

The theoretical study of large scale structure is by now quite mature thanks to continued developments in perturbation theory (PT). Within PT the growth of structure is treated systematically, order-by-order in the initial conditions with nonlinearities at small scales marginalized away using effective-theory techniques [28, 60, 399]. Biased tracers of large-scale structure like galaxies can similarly be treated by identifying contributions to their clustering at each order allowed by fundamental symmetries [234, 332, 109, 396, 74, 139]. Much of this modeling effort has focused on the clustering of galaxies in redshift-space, as measured in spectroscopic surveys, leading to models with accuracy well beyond the expected statistical uncertainty in any realistic surveys [255, 82, 189], and which have been tested extensively on existing surveys like BOSS and eBOSS [186, 96, 184, 73, 438, 282]. The same models can also be used to predict weak-lensing measurements, particularly their cross-correlations with galaxy surveys (which allow for cleaner separation of scales by virtue of being more localized in redshift). These measurements probe matter clustering and its cross-correlation with galaxy densities, both without redshift-space distortions, and are in fact easier to model within PT since they do not involve large contributions from small-scale velocities. Such predictions have received less attention to date, though there is a long history of PT-inspired models of galaxy lensing cross correlations applied to both simulations and data (e.g. refs. [21, 208, 269]), and full PT models have recently been successfully applied to cross-correlations between Planck CMB lensing and galaxies from the DESI Legacy Imaging Survey [201, 417].

A particular advantage of perturbative models of large-scale structure is that they rely on only a minimal set of theoretical assumptions to consistently model a wide range of clustering

data. For example, the same bias parameters used to model the redshift-space clustering of BOSS galaxies in ref. [73] also make robust predictions for their cross-correlation in weak lensing. Figure 9.1 shows the posterior predictive distribution for these cross correlations, summarized as the angular multipoles of their 2-point function ($C_\ell^{\kappa g}$), with clustering and cosmological parameters conditioned on the redshift-space clustering data; those data tightly predict $C_\ell^{\kappa g}$ on large scales, while nonlinear bias and an additional effective-theory contribution to the matter-galaxy cross spectrum not probed by redshift-space clustering broaden the range of clustering amplitudes at smaller scales. Indeed, we can already see an intriguing feature of the joint BOSS and Planck data: the CMB lensing cross correlations at large scales (low ℓ) are lower than what might be expected from the redshift-space clustering of BOSS galaxies, even after we marginalize over cosmology and nonlinear bias. This is interesting, as the theoretical assumptions underlying the predictions are quite minimal: weak field gravity, at-most-weakly interacting and cold particle dark matter and a FLRW metric (by now well constrained by distance-redshift measurements). Figure 9.1 also illustrates a more general feature of perturbative analyses of large-scale structure, which tend to extract cosmological information from large scales while[1] marginalizing over the transition to nonlinearity with bias and effective-theory parameters. Conversely, since additional information about these parameters cannot straightforwardly be gained by extending beyond the nonlinear scale, combining competing probes of the same structure (e.g. redshift-space clustering and weak lensing) can help better constrain these nuisance parameters by probing different combinations on perturbative scales.

The purpose of this chapter is to demonstrate the viability of combined redshift-space and lensing analyses within perturbation theory using publically available data. In particular, we will use galaxies from the BOSS survey [101] and CMB lensing maps from Planck [287], along with a theoretical model based on one loop (Lagrangian) perturbation theory [82]. We are not the first to look at this combination of data (see e.g. refs. [294, 346, 119, 347]), but are, to our knowledge, the first to apply the full machinery of perturbation theory in this context, applying a consistent dynamical model without empirical prescriptions for galaxy clustering to model both the two and three-dimensional data, a technique which we expect will be critical given the significantly enhanced accuracy needs and scientific promise of the currently operating cosmological surveys like the Dark Energy Spectroscopic Instrument [108], the Atacama Cosmology Telescope [374], the South Pole Telescope [37] and their even more powerful successors. Since our main purpose is to perform a proof-of-principle study on public data, throughout this work we follow the BOSS collaboration's choices for systematics weights, masks and redshift binning in order to leverage the considerable effort that has gone into measuring the statistics, performing systematics checks and creating mock catalogs for covariance matrices for these samples, with only a few small, theoretically-motivated tweaks which we believe will be useful in future analyses.

The outline of the chapter is as follows. In the next section we discuss the data sets that we use. Section 9.3 describes the mock catalogs used to validate our analysis pipeline, while

[1] See e.g. Fig. 4 of ref. [73] for a demonstration in the case of redshift-space clustering.

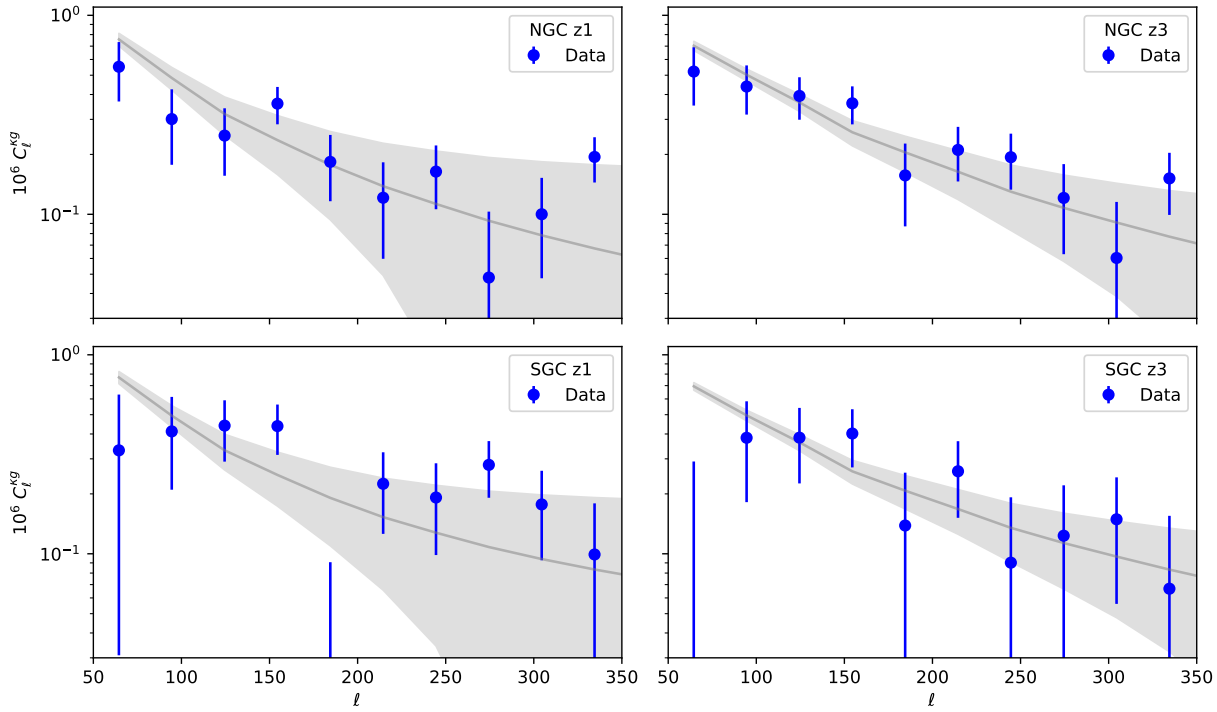

Figure 9.1: The posterior-predictive distribution (grey bands) for the cross-correlation between BOSS galaxies and CMB lensing convergence, conditioned on the redshift-space galaxy clustering (including redshift-space distortions and baryon acoustic oscillations). The measured cross-correlation (blue points) at high ℓ don't give much constraint within the context of perturbative models due to the combination of their large errors and the marginalization over counterterms (an effect which is more significant at lower redshifts i.e. **z1**). The effect of the lensing data is thus largely a downward pull due to the low ℓ points.

section 9.4 describes our theoretical models and assumptions. Our results are presented in section 9.5, along with a comparison to previous results. We conclude in section 9.6, while some technical details of how we handle massive neutrinos are relegated to an appendix.

9.2 Data

9.2.1 BOSS Galaxies

The BOSS survey [101] is a spectroscopic galaxy survey part of the Sloan Digital Sky Survey III [123], covering 1,198,006 galaxies over 10,252 square degrees of sky. Our analysis of the three-dimensional clustering of these galaxies follows that of [73], which is described in detail in Section 2 of that work. Briefly, we follow the convention in ref. [7] and split the

BOSS galaxies into four independent samples, defining two redshift bins $0.2 < z < 0.5$ (**z1**) and $0.5 < z < 0.75$ (**z3**) split between the Northern (**NGC**) and Southern (**SGC**) galactic caps. In particular, we make use of the publicly available power spectrum, window function and mock measurements of each of these samples presented in ref. [42]. In order to better utilize the cosmological distance information in galaxy clustering, particularly through baryon acoustic oscillations (BAO), we will also use the post-reconstruction correlation functions measured in ref. [388]. Unlike the power spectra, these correlation functions were measured assuming that the **NGC** and **SGC** samples could be combined into one homogeneous sample. In order to take into account the cross-correlations between the power spectra and correlation function measurements, we construct our covariance matrix using measurements of these quantities in the V6C BigMultiDark Patchy mocks described in [202]; these measurements are also publicly provided by refs. [42, 388]. Both power spectra and and correlation functions were computed assuming a fiducial cosmology with $\Omega_{m,\mathrm{fid}} = 0.31$.

In order to cross-correlate the BOSS galaxy density with CMB lensing, as described below, we also generate projected two-dimensional sky maps of the galaxy density. These maps are generated in the standard manner. We first cut the galaxies to the desired hemisphere and redshift range (using the spectroscopic redshift). Each galaxy is assigned a weight, $w_{\text{sys-tot}}(w_{\text{cp}} + w_{\text{no-z}} - 1)$, as described in detail in the BOSS papers [300, 307]. The weighted counts of galaxies are computed in Healpix [149] pixels at $N_{\text{side}} = 2048$ to form a "galaxy map" in galactic coordinates. The random points supplied by the BOSS team are also binned into Healpix pixels to form the "random map". The overdensity field is defined as the "galaxy map" divided by the "random map", normalized to mean density and mean subtracted. We obtain a (binary) mask for the galaxies by keeping only those pixels where the random counts exceed 20% of the mean random count (computed over the non-empty pixels) and overdensities outside of the mask are set to zero. We use the magnification bias slopes measured in [403], viz. $s_{z1} = 0.77 \pm 0.02$ and $s_{z3} = 1.05 \pm 0.11$.

Since the 2D (auto) clustering information within the galaxy map is a subset of that included in the 3D clustering measurements described above, we do not use the 2D galaxy angular power spectrum C_ℓ^{gg} derived from these maps except when estimating covariances, as described below. Not including C_ℓ^{gg} somewhat immunizes our analysis against purely angular systematics in the galaxy maps since, unlike C_ℓ^{gg} which only depends on line-of-sight angles $\mu \approx 0$, the clustering information in redshift-space multipoles are weighted across all μ, though we note that our model fits either measurement in the data consistently.

9.2.2 Planck CMB Lensing

Our treatment of the Planck CMB lensing maps is quite standard, and in detail follows that in refs. [201, 417]. Specifically we use the 2018 Planck release [287] available from the Planck Legacy Archive.[2] These data are provided as spherical harmonic coefficients of the convergence, $\kappa_{\ell m}$, in HEALPix format [149] and with $\ell_{\text{max}} = 4096$. We use the

[2]PLA: https://pla.esac.esa.int/

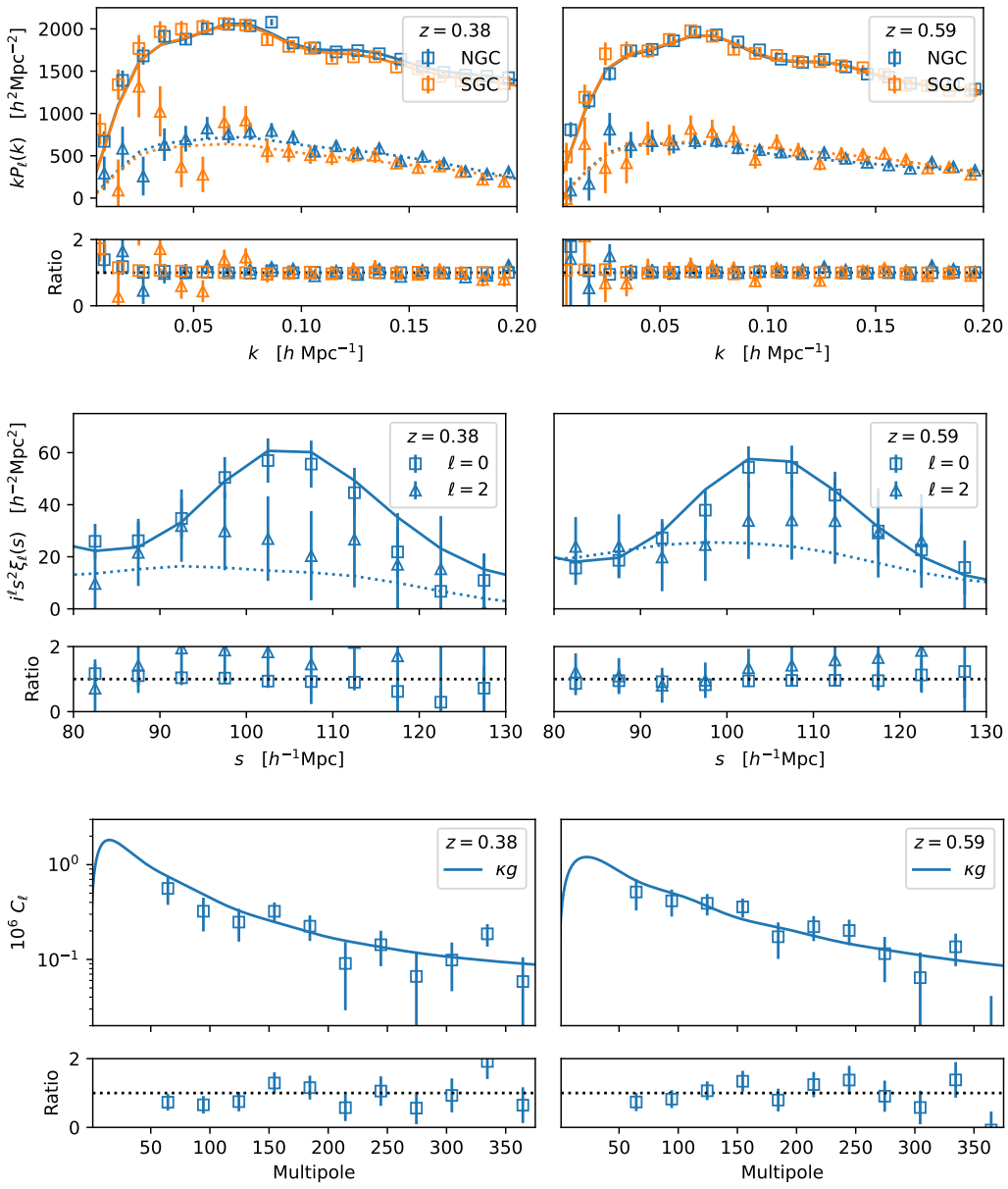

Figure 9.2: The data to which we fit, in the form of 2-point functions vs. linear or angular scale. The top row shows the pre-reconstruction redshift-space galaxy power spectrum multipoles for the two galactic hemispheres (NGC and SGC) and two redshift slices. The middle row shows the post-reconstruction galaxy correlation function multipoles. The bottom row shows the angular cross-spectrum between the galaxy overdensity and CMB convergence. In each row the upper panels show the data while the lower panels show the ratio of the data to the best-fitting theoretical model (shown as the lines in the upper panels in each case).

minimum-variance (MV) estimate obtained from both temperature and polarization, based on the `SMICA` foreground-reduced CMB map. The maps are low-pass filtered and apodized as in ref. [417] to produce a κ map in HEALPix format at $N_{\rm side} = 2048$.

Since the MV reconstruction in Planck is dominated by temperature, residual galactic and extragalactic foregrounds may contaminate the signal. Extensive testing has been performed by the Planck team, indicating no significant problems at the current statistical level [287]. However, as a test, we repeated the analysis with a lensing reconstruction provided by the Planck team that is based upon `SMICA` foreground-reduced maps where the thermal tSZ effect [360] has been explicitly deprojected [287]. While they mitigate the effect of tSZ, these maps also tend to enhance the effect of other foregrounds like the cosmic infrared background (CIB) [308]. Swapping in these maps for the fiducial ones can therefore serve as a sanity check to test our sensitivity to residual foregrounds. We found that our results are very consistent between analyses, with the deprojected map leading to larger uncertainties, as expected. This is in line with the expectation that extragalactic foregrounds lead to very small biases compared to our error bars [387, 262, 32, 308, 100], though those biases would typically be to lower κ if the foregrounds have significant small-scale power (since they "appear" like a demagnified region). We shall return to this in §9.5. Additionally, the Planck lensing maps mask regions with SZ clusters, removing high-density regions; biases due to this effect are known to be very subdominant, however [287].

In order to estimate the cross-correlation of the CMB κ map with BOSS galaxies, we use the pseudo-C_ℓ method [178] as implemented within the `NaMaster` package [11] to estimate our angular power spectra. This technique is now very standard and has been described in detail elsewhere (e.g. refs. [143, 417] and the many references therein). Briefly, this approach first computes the (pseudo) angular power spectrum as an average over m-modes of the spherical harmonic transform of the masked field. The pseudo-spectra are binned into a discrete set of bandpower bins, L, and the mode coupling is deconvolved [178]. We use the `compute_full_master` method in `NaMaster` [11] to calculate the binned power spectra and the bandpower window functions relating them to the underlying theory: $\langle C_L \rangle = \sum_\ell W_{L\ell} C_\ell$. We choose a conservative binning scheme with linearly spaced bins of size $\Delta\ell = 30$ starting from $\ell_{\rm min} = 50$. The bin width is larger than expected correlations between modes induced by the survey masks, while being narrow enough to preserve the structure in our angular spectra. To avoid power leakage near the edge of the measured range we perform the computation to $\ell = 6000$, and simply discard the bins beyond some $\ell_{\rm max}$ [209].

9.2.3 Covariance

Throughout we shall make use of a Gaussian likelihood function with fixed covariance. The covariance matrix for the three dimensional clustering (both pre- and post-reconstruction) is computed from mock catalogs supplied by the BOSS collaboration. The covariance matrix for the lensing-galaxy cross-correlation is computed using `NaMaster` taking into account the disconnected contributions which dominate in the regimes of interest.

We neglect the covariance between the three dimensional clustering measures and the lensing-galaxy cross-correlation. Since the lensing kernel is so broad, the lensing-galaxy cross-correlation probes modes with very low wavenumber $k_\parallel$ along the line of sight, while the three dimensional clustering measurements are dominated by $k_\parallel \sim k$, leading to little overlap in Fourier space [371]. In addition, the lensing signal is predominantly from matter clustering at higher redshifts than the range we probe in this work, and moreover are dominated by noise in the temperature maps used for the lensing reconstruction over most of the ℓ range that we fit to.

9.3 Mock catalogs

In this section we describe the N-body-based mock catalogs that we used to validate our analysis pipeline and compare their clustering to the BOSS data. Since the mock catalogs used for pipeline validation were not used as inputs to the analysis (e.g. as part of the theory model or covariance calculation) but rather simply as validation tools the requirements on those mocks can be quite relaxed.

Our analysis was not conducted blindly, because the catalogs and clustering measurements have long been public and we had previously done cosmology fits to the BOSS data alone [73]. However, we did validate a number of the analysis choices on mock catalogs prior to performing the cosmology fits and we did not modify those choices when we fit to the data itself.

9.3.1 Mock BOSS Catalogs

Our mock catalogs are constructed from the `Buzzard v2.0` simulations [107, 103] in order to approximately reproduce the **z3** bin from the data. We do not use the **z1** bin from the simulations as the redshift range of this bin overlaps the transition between two distinct N-body simulations that the `Buzzard` catalogs are constructed from. Galaxies are included in these simulations using the `Addgals` algorithm [409, 104], which assigns galaxies with mock SEDs, shapes and sizes to particles in the N-body lightcones. The spectra are integrated over the desired bandpasses to obtain broadband apparent magnitudes. The simulations are ray-traced in order to compute weak-lensing deflections, shears and magnifications for each galaxy. In order to select a CMASS-like sample from our simulations, we apply the CMASS color selection to our simulated catalogs, with minor adjustments to the color cuts that are tuned in order to better reproduce the redshift distribution of the **z3** sample. The effective redshift of our mock sample is $z_{\rm eff} = 0.575$ and a magnification coefficient of $\alpha_{\rm mag} = 1.3$. All mock measurements used in this work are the mean of 7 quarter-sky simulations.

9.3.2 Power spectrum multipoles

We compute mock spectra in our simulations using an independent pipeline from that used in the data. We compute $P_\ell(k)$ using the algorithm described in [161], making use of FKP weights and assuming the same k binning as used in the BOSS data. In order to account for the effect of the window function, integral constraint, and wide-angle effects on our redshift-space clustering measurements, we follow the formalism described in [42], implemented in an independent pipeline from that used on the data, and validated against the BOSS DR12 NGC **z3** window and wide-angle matrices used in this work.

9.3.3 Lensing cross-correlations

We compute $C_\ell^{\kappa g}$ and mode coupling matrices from our simulations using `NaMaster`, using the same ℓ binning and mask apodization as that used in the data. The CMB lensing convergence field is computed using the Born approximation. We also use the same weighting scheme as applied to the BOSS data, including both FKP and inverse lensing kernel weights as described in section 9.4.3.

9.3.4 Post-reconstruction correlation functions

Non-linear evolution broadens the BAO peak in the correlation function, weakening the inferred distance constraints [121, 92]. However much of the broadening comes from large scales that can be well modeled and measured by a galaxy redshift survey. The displacements induced by these large-scale modes can be inferred from the data and their impacts 'undone', in a process known as reconstruction [122]. This has become a standard feature of BAO analyses, and was used throughout the BOSS survey [388]. We apply the same procedure to the mock catalogs. We use `recon_code`[3], adopting the isotropic BAO (or 'Rec-Iso') [414, 266, 338] convention as in ref. [388]. To form the overdensity field, the galaxy and random catalogs are converted to Cartesian coordinates using the correct distance-redshift relation for the cosmology of our mocks and deposited to grids using cloud-in-cell interpolation to a grid with $N_g = 512$ points in each dimension. The over-density field is $\delta_g(\mathbf{x}) = \rho_{\rm gal}(\mathbf{x})/\rho_{\rm rand}(\mathbf{x}) - 1$, where regions with $\rho_{\rm rand} = 0$ are set to zero by default. This field is then smoothed by a Gaussian kernel given by $\exp\left[-(x/R_f)^2/2\right]$, with $R_f = 15\,h^{-1}\,$Mpc, giving a smoothed field $\tilde{\delta}(\mathbf{x})$. The displacement field, $\hat{\mathbf{\Psi}}^{\rm rec}$, is the solution of

$$\partial_i \hat{\Psi}_i^{\rm rec} + \beta \partial_i \left(\hat{r}_i \hat{r}_j \hat{\Psi}_j^{\rm rec} \right) = \frac{\tilde{\delta}}{b}. \tag{9.1}$$

where we have used $b = 1.8$ and $f = 0.872$ since the values used by BOSS were not given in ref. [388]. This equation is solved using a multigrid relaxation technique with a V-cycle based on damped Jacobi iteration. Both randoms and galaxies are then shifted by $\hat{\mathbf{\Psi}}^{\rm rec}$, with

[3] https://github.com/martinjameswhite/recon_code

Parameter	Prior
$\ln(10^{10}A_s)$	$\mathcal{U}(1.61, 3.91)$
Ω_m	$\mathcal{U}(0.20, 0.40)$
H_0 [km/s/Mpc]	$\mathcal{U}(60.0, 80.0)$

Parameter	Value
$\Omega_b h^2$	0.02242
n_s	0.9665
M_ν	0.06 eV

Table 9.1: Cosmological parameter priors and values for our analysis. Uniform distributions are denoted $U(x_{\min}, x_{\max})$.

their appropriate factors in the "Rec-Iso" scheme, and their locations are converted back to angular coordinates and redshifts.

The multipoles of the correlation function $\xi_\ell(\backslash)$ are measured from the above catalogs using `corrfunc` [349]. Denoting by D, S and R the shifted data and randoms and the fiducial random catalogs, respectively, the Landy-Szalay estimator

$$\xi^{\rm rec}(s,\mu) = \frac{DD(s,\mu) - 2DS(s,\mu) + SS(s,\mu)}{RR(s,\mu)}, \tag{9.2}$$

is used to estimate $\xi^{\rm rec}(s,\mu)$. We adopt linearly spaced bins of width $\Delta s = 5\,h^{-1}\,$Mpc and 100 bins in $\mu \in [0,1)$ following ref. [307]. Multipoles of the correlation function are constructed by integrating in the μ direction.

9.4 Theory Model

In this work we aim to obtain cosmological constraints combining the three-dimensional distribution of galaxies in redshift space and the distribution of dark matter that they trace, reflected in its contribution to CMB lensing. To this end we will use Lagrangian perturbation theory (LPT), which models the gravitational clustering underlying RSD, BAO and CMB lensing within a unified dynamical framework. In the following subsections we describe how to connect this clustering with observables, provide a brief summary of LPT and describe how we efficiently emulate its predictions using Taylor series for the purposes of MCMC.

9.4.1 Cosmological Parameters, Neutrinos and Linear Theory

Throughout this chapter, we will assume a ΛCDM cosmology with uniform priors on Ω_m, H_0 and $\ln(10^{10}A_s)$ as described in Table 9.1, with all other parameters fixed to their Planck best-fit values and assuming a minimal neutrino mass scenario $M_\nu = 0.06$ eV, mirroring the setup in ref. [73]. Given such a set of cosmological parameters, we use CLASS [48] to compute the linear-theory power spectrum as the input to our one-loop perturbation theory. We operate within the EdS approximation wherein higher-order corrections scale linearly with powers of the linear power spectrum amplitude [361, 128, 36, 139, 115].

In order to account for the effect of massive neutrinos we use the now-standard approximation that galaxies trace the cold dark matter and baryon *cb* field [66], i.e. $\delta_g = \delta_g[\delta_{cb}]$, which was recently shown to be an excellent approximation well into the quasilinear regime [33]. Within this approximation the redshift-space galaxy power spectrum can be computed simply by plugging $P_{\rm cb,lin}$ as the linear power spectrum into the perturbation theory formulae.

Weak lensing-galaxy cross correlations, on the other hand, require a bit more care. In particular, as lensing is sourced by all matter, we must take the contribution from neutrinos into account explicitly. Indeed, this explicit neutrino mass dependence is precisely what allows galaxy-lensing cross correlations to be a potentially powerful probe of the neutrino mass [428, 33]. At linear order this implies that $P_{gm} = bP_{cb,m}$, where b is the Eulerian galaxy bias. Since neutrinos contribute negligible clustering power below the free-streaming scale, one approximation [209] is to use the fact that $\Omega_m\delta_m \approx \Omega_{cb}\delta_{cb}$ on these scales to make the substitution $\Omega_m P_{cb,m} \approx \Omega_{cb}P_{cb}$. However, as shown in Fig. 9.3, the quasilinear scales on which our analysis is based covers much of the transition region between the high k modes with 'unclustered' neutrinos and the low k regime where neutrinos cluster with cold dark matter. In order to better capture this transition, we will instead compute perturbation predictions for the matter-galaxy cross power spectrum using $P_{cb,m}$ as the input linear power spectrum assuming the same bias coefficients as those in $\delta_g = \delta_g[\delta_{cb}]$. As we show in Appendix H.1, such a scheme is accurate to order $f_\nu\mathcal{O}(P_{\rm L}^2)$, that is of order the neutrino mass fraction times the typical (subleading) one-loop correction, and thus more than adequate for any upcoming analyses.

9.4.2 Lagrangian Perturbation Theory

Lagrangian perturbation theory models gravitational structure formation by following the displacements $\Psi(\mathbf{q},\tau)$ of fluid elements starting at Lagrangian positions $\mathbf{q}$ at the initial time. These displacements follow Newtonian gravity in expanding spacetimes $\ddot{\Psi} + \mathcal{H}\dot{\Psi} = -\nabla_{\mathbf{x}}\Phi$, where dots are with respect to conformal time, and map the initial positions of fluid elements to their observed ones via $\mathbf{x} = \mathbf{q} + \Psi(\mathbf{q},\tau)$. The Newtonian potential Φ is in turn sourced by the overdensity δ_m of fluid elements under this evolution, given via mass conservation to be [231]

$$1 + \delta_m(\mathbf{x},\tau) = \int d^3\mathbf{q}\ \delta_D(\mathbf{x} - \mathbf{q} - \Psi(\mathbf{q},\tau)). \tag{9.3}$$

Within this framework the displacements are then solved order-by-order, that is perturbatively, in the initial conditions, i.e. $\Psi = \Psi^{(1)} + \Psi^{(2)} + \Psi^{(3)} + ...$, with the first-order solution commonly referred to as the Zeldovich approximation [431, 39]. Finally, within the effective-theory approach of LPT the effect of short-wavelength densities and velocities are integrated out, resulting in free counterterms and stochastic contributions whose form are restricted by symmetries but whose values must be fit to data and cannot be determined a priori [290, 399].

To model the distribution of galaxies we need to account for the fact that galaxies are imperfect and nonlinear tracers of matter. In the Lagrangian picture this is accomplished by

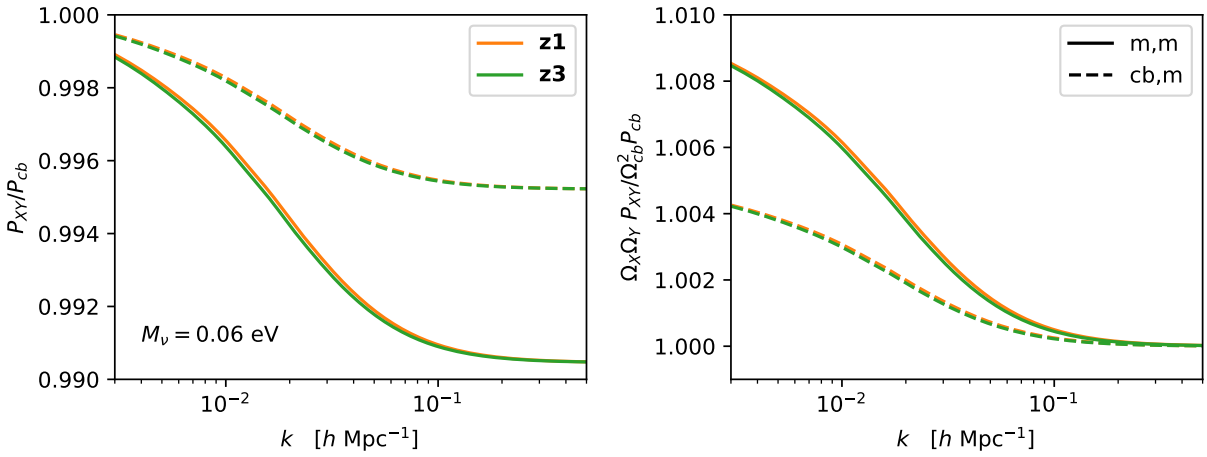

Figure 9.3: Ratios of linear theory total-matter power spectrum and matter and dark matter-baryon cross spectrum to the dark matter-baryon power spectrum (left), as well as the corresponding ratios for mass-weighted power spectra (right) in the Planck cosmology with minimal neutrino mass $M_\nu = 0.06$ eV. Green and orange shaded regions show the corresponding wave numbers probed by the lensing-galaxy cross correlations and grey regions show the wavenumbers probed in our RSD analysis.

writing the initial number density of proto-galaxies $F(\mathbf{q})$ as a local functional of the initial conditions. These proto-galaxies are then advected to their observed positions to give

$$1 + \delta_g(\mathbf{x}, \tau) = \int d^3\mathbf{q}\ F(\mathbf{q})\ \delta_D(\mathbf{x} - \mathbf{q} - \Psi(\mathbf{q}, \tau)). \tag{9.4}$$

In this chapter we follow [73] and use the form [229, 58, 396, 74]

$$F(\mathbf{q}) = 1 + b_1\delta_{\rm lin}(\mathbf{q}) + \frac{1}{2}b_2(\delta^2_{\rm lin}(\mathbf{q}) - \langle\delta^2_{\rm lin}\rangle) + b_s(s^2_{\rm lin}(\mathbf{q}) - \langle s^2_{\rm lin}\rangle). \tag{9.5}$$

In particular we will operate under the assumption that third-order Lagrangian bias is small for small-to-intermediate mass halos [4, 215] and, along with the lowest-order derivative bias $\propto \nabla^2\delta_{m,0}$, highly degenerate with counterterms. The matter density is equivalent to a tracer with all the Lagrangian bias parameters equal to zero, i.e. $F(\mathbf{q}) = 1$.

Our analysis in this chapter specifically requires LPT predictions for the matter and galaxy two-point functions, in real and redshift space, pre- and post-reconstruction. Briefly, from Equation 9.4 the power spectrum can be written as

$$(2\pi)^3\delta_D(\mathbf{k}) + P(\mathbf{k}) = \int d^3\mathbf{q}\ \left\langle e^{i\mathbf{k}\cdot(\mathbf{q}+\Delta)}F(\mathbf{q}_1)F(\mathbf{q}_2)\right\rangle_{\mathbf{q}=\mathbf{q}_1-\mathbf{q}_2}, \tag{9.6}$$

where the pairwise displacement is given by $\Delta = \Psi(\mathbf{q}_1) - \Psi(\mathbf{q}_2)$. To compute the power spectrum in redshift space, wherein line-of-sight distances are inferred from redshifts and hence

include a contribution from peculiar velocities $\dot{\Psi}$, simply requires swapping in redshift-space displacements Ψ_s boosted by line-of-sight velocities.

A notable feature of Equation 9.6 is that the exponentiation of the pairwise displacement allows for resummation of long-wavelength (IR) displacements which captures important physical effects such as the nonlinear damping of the BAO peak; to maintain consistency between the pre-reconstruction galaxy-galaxy and matter-galaxy power spectrum predictions we use the scheme proposed in ref. [82] wherein linear displacements and velocities below $k_{\rm IR} = 0.2\,h\,{\rm Mpc}^{-1}$ are resummed while shorter-wavelength modes are perturbatively expanded. This scheme is different than the one used in refs. [201, 417], where all the linear displacements were resummed, but has been tested extensively in simulations and mocks [82, 73][4]. In a similar vein, since reconstruction subtracts part of the large-scale displacements responsible for the nonlinear damping of the BAO, computing the two-point function after reconstruction requires the displacements in Equation 9.6 have these subtracted as well; following [73] we will in addition make use of a saddle point approximation at the BAO scale to model the BAO damping form in the post-reconstruction correlation function, using a broadband model linear in $1/r$ to capture any residual smooth contributions. Our calculations throughout this work make use of the publically available code [74] `velocileptors`[5]; we refer the interested reader to refs. [82] and [78] for further discussions on modeling redshift-space distortions and reconstruction within LPT, respectively.

9.4.3 Galaxy Clustering in 2D and 3D

The observables we analyze in this work — 3D clustering in redshift surveys and 2D angular cross-correlations with weak lensing from CMB experiments — jointly probe matter and galaxy clustering within the cosmological volume surveyed by BOSS. While they reflect the same underlying clustering, however, the particularities of each measurement are sufficiently different that it is worth describing in some detail the connection between this clustering and each observable.

Redshift-Space Clustering

The 3D galaxy correlation function and power spectrum multipoles are measured in dimensionful coordinates ($\mathbf{r}$ and $\mathbf{k}$ respectively)— a cosmological model must thus be assumed to convert angles and redshifts into comoving distances. For BOSS the Cartesian coordinates of the galaxies were computed assuming a fiducial ΛCDM cosmology with $\Omega_{M,\rm fid} = 0.31$. This implies that when we test a model with a different redshift-distance relation to the fiducial model we must apply a rescaling of distances relative to the "true" cosmology in directions parallel and perpendicular to the line of sight. This is often referred to as the Alcock-Paczynski effect [9, 265] and is included in our model for the power spectrum and

[4]In particular, we use the $\mu = 0$ output of the redshift-space power spectrum in `velocileptors` for the real-space power spectrum.

[5]https://github.com/sfschen/velocileptors

post-reconstruction correlation function. Finally, the observed Fourier-space clustering power of galaxies in redshift surveys is the convolution of the true power with the survey window function; to take into account this and wide angle effects we adopt the formalism and data outputs of ref. [42]. Our treatment of these steps is identical to that in ref. [73], to which we refer readers seeking further details.

Angular Power Spectra

The 2D galaxy-lensing cross correlation, on the other hand, is reported in dimensionless angular coordinates. Within the Limber approximation [221] the angular multipoles are related to the matter-galaxy cross power spectrum P_{mg} by

$$C_\ell^{\kappa g} = \int d\chi \left(\frac{W^\kappa(\chi) W^g(\chi)}{\chi^2} \right) P_{mg}\Big(k = \frac{\ell + 1/2}{\chi}, z\Big); \tag{9.7}$$

All the dependence on cosmological distances is implicit in this integral such that the end result is independent of any fiducial cosmology. The galaxy and lensing kernels are given by

$$W^g(\chi) = H(z)\frac{dN}{dz}, \quad W^\kappa(\chi) = \frac{3}{2}\Omega_m^2 H_0^2 (1+z)\frac{\chi(\chi_* - \chi)}{\chi_*}, \tag{9.8}$$

where dN/dz is the weighted galaxy distribution and χ_* is the distance to last scattering. In addition to the above term the projected galaxy density also receives a contribution from the so-called magnification bias. The magnification term is only a small contribution to the total signal, but because it probes the line of sight all the way to small radial distances it is sensitive to smaller scales than the other contributions. We make use of the `HaloFit` fitting function for P_{mm} ([354, 362] as implemented in `CLASS`) for the magnification contributions.

Effective Redshift

Both the two- and three-dimensional measurements above average galaxy and matter clustering over large spans of redshift (**z1** and **z3**) over which the universe expands by up to 20%, with comparable changes in other cosmological quantities like the linear growth factor, $D(z)$. In order to account for the evolution of both the background and galaxy sample we will make use of the effective-redshift approximation which we will now describe in some detail.

Defining the auto- and cross-spectra of each sample to evolve with redshift as $P_{gg,g\kappa}(\mathbf{k}, z)$, both the two- and three-dimensional power spectra in this work can be written in the form

$$\hat{\Theta} = \sum_i w_i P(\mathbf{k}(z_i), z_i) \tag{9.9}$$

$$= \sum_i w_i \Big(P(\mathbf{k}_i, z_{\rm eff}) + (z_i - z_{\rm eff})\partial_z P(\mathbf{k}_i, z_{eff}) + \frac{1}{2}(z_i - z_{\rm eff})^2 \partial_z^2 P(\mathbf{k}_i, z_{\rm eff}) + ... \Big) \tag{9.10}$$

The effective redshift[6] $z_{\rm eff}$ is then defined such that the linear term cancels, i.e. $z_{\rm eff} = \sum_i w_i z_i$. For example, cross-correlation of galaxies and CMB κ has [246]

$$z_{\rm eff}^{\rm xcorr} = \int \frac{d\chi}{\chi^2}\, W^g(\chi) W^\kappa(\chi) z(\chi). \tag{9.11}$$

Similarly the galaxy auto-spectrum has an effective redshift given by [228, 416, 419, 442, 102]

$$z_{\rm eff}^{\rm 3D} = \frac{\int d^3\mathbf{r}\ \bar{n}(\mathbf{r})^2 z(\mathbf{r})}{\int d^3\mathbf{r}\ \bar{n}(\mathbf{r})^2} = \frac{\sum_i w_i \bar{n}_i z_i}{\sum_i w_i \bar{n}_i} \tag{9.12}$$

where the sum is over the galaxies, $\bar{n}$ is the galaxy number density accounting for systematic and FKP weights, and w_i are the product of the weights on each galaxy. The second equality above uses that $\int d^3\mathbf{r}\ \bar{n} = \sum_i w_i$. The above definition is distinct from, and more accurate when used on two-point clustering statistics [293], than the one defined in the official BOSS analysis [45]. The BOSS analyses used the mean redshift, written as

$$z_{\rm mean} = \frac{\sum_{ij} w_i w_j (z_i + z_j)/2}{\sum_{ij} w_i w_j} = \frac{1}{2}\frac{\sum_i w_i z_i \sum_j w_j}{\sum_i w_i \sum_j w_j} + \frac{1}{2}\frac{\sum_j w_j z_j \sum_i w_i}{\sum_j w_j \sum_i w_i} = \frac{\sum_i w_i z_i}{\sum_i w_i} \tag{9.13}$$

Since the product fD is quite slowly varying, the difference in $z_{\rm eff}$ and $z_{\rm mean}$ is of little import for analyses of redshift-space distortions or baryon acoustic oscillations. However it is potentially more important for measurements depending upon $D(z)$ itself, such as our lensing-galaxy cross-correlation. Comparing these definitions, the linear growth factor $D(z)$ is 1% higher at $z_{\rm eff} = 0.59$ compared to $z_{\rm mean} = 0.61$ for the **z3** bin, though they agree to within a fifth of a percent for **z1** ($z_{\rm eff} \simeq z_{\rm mean} \simeq 0.38$).

The above discussion makes clear that the two and three-dimensional clustering analyzed in this work primarily reflect galaxy clustering at $z_{\rm eff}^{\rm xcorr}$ and $z_{\rm eff}^{\rm 3D}$, respectively. These can in principle be quite different; for the fiducial BOSS samples they are 0.367 and 0.380 for **z1** and 0.589 and 0.602 for **z3**, respectively. Since we are interested in using the shared galaxy clustering from the two statistics, we take the additional step to weight the galaxies in the lensing cross correlation such that $z_{\rm eff}^{\rm xcorr} \approx z_{\rm eff}^{\rm 3D}$. In particular, we weight each galaxy by an additional factor $w(z) = W^g/W^\kappa$ (calculated assuming $\Omega_m^{\rm fid} = 0.31$) such that $W^g W^\kappa \to (W^g)^2$ and the cross-correlation has the same effective redshift as the (un-weighted) auto-correlation. To maintain consistency between the 2D and 3D clustering statistics it is

[6] We will follow convention and use the redshift, z, as the 'time' coordinate. This is not a unique choice and it is in principle possible to adopt other time coordinates, for example the scale factor a — the varying accuracy of the "effective time" approximation, i.e. dropping all but the leading term in Equation 9.10, then depends on the size of the quadratic correction. As an example, in linear theory where we have that the matter power spectrum scales approximately as $D^2(z) \sim a^2 \sim (1+z)^{-2}$, the error incurred by adopting $z_{\rm eff}$ would be three times larger than if we had instead chosen $a_{\rm eff}$. Since $b(z)D(z)$ and $f(z)D(z)$ are both extremely flat functions of redshift, we expect our analysis to be insensitive to this choice, though we do note that in the same limit $C^{\kappa g} \propto b(z)D^2(z) \sim a$ is linear in the scale factor, suggesting that using $a_{\rm eff}$ might be somewhat better for future analyses with greater accuracy needs.

important to employ the same set of weights in each; in particular, each galaxy receives the same set of systematic and FKP weights when computing the power spectrum, correlation function and angular multipoles. The two- and three-dimensional autocorrelation effective redshifts, as defined above, are equivalent. For example, for the 2D autocorrelation we have

$$z_{\rm eff}^{\rm 2D} = \frac{1}{\mathcal{N}} \int \frac{d\chi}{\chi^2} \, [W^g(\chi)]^2 \, z(\chi) = \frac{1}{\mathcal{N}} \int \frac{d\chi}{\chi^2} \left[H(z) \frac{dN}{dz} \right]^2 z(\chi) \quad \text{with} \quad \mathcal{N} = \int \frac{d\chi}{\chi^2} \, [W^g]^2 \, .$$

Since $H\, dN/dz \propto \chi^2\, \bar{n}$ and $d^3\mathbf{r} \propto \chi^2 d\chi$ the integral in the numerator reduces to $\int d^3\mathbf{r}\ \bar{n}^2\, z$, i.e. given the same galaxy weights and distributions, $z_{\rm eff}^{\rm 2D} = z_{\rm eff}^{\rm 3D}$. We have checked that our weighting leads to effective redshifts agreeing to within a tenth of a percent for the cosmologies of interest in this work.

9.4.4 Gravitational slip

Within general relativity, weak lensing and redshift-space distortions jointly probe the amplitude of matter clustering through gravity's effect on the trajectories of massless (photons) and massive (galaxies) particles. In principle, photon and galaxy trajectories are influenced by different components of the metric, the latter by the Newtonian potential Ψ and the former by the Weyl potential $(\Phi + \Psi)/2$ — these are equal at late times within General Relativity but could be different in modified theories of gravity. To test for such differences we include a free factor multiplying the amplitude of the lensing-galaxy cross correlation,

$$c_\kappa = \frac{1+\gamma}{2} \quad , \tag{9.14}$$

where $\gamma = \Phi/\Psi$ is the gravitational slip (see ref. [193] and references therein), and similarly the magnification bias-CMB lensing cross correlation by c_κ^2. Since our analysis is sensitive to the relative amplitude difference between redshift-space clustering and lensing cross-correlations, any deviation of the fit γ from unity could indicate departures from general relativity in either velocities or gravitational lensing. Were we to free the neutrino mass within our analysis, this effect would be somewhat degenerate with the additional suppression of matter clustering due to free-streaming neutrinos — our constraint on γ therefore will also serve as some indication of our ability to constrain the neutrino mass through combining galaxy clustering with CMB lensing.[7] Alternatively, within a fixed physical model comparing the relative amplitudes of the lensing and RSD signals through c_κ allows us to perform a consistency check between the two datasets and check for systematics, akin to the scaling parameter $X_{\rm lens}$ multiplying cross spectra in the DES Y3 3×2pt analysis [2].

[7] In particular, if we think of the lensing amplitude as probing $\delta_m \approx (1 - f_\nu)\delta_{cb}$ and the RSD as probing $f(z)\ \sigma_{8,cb}(z) \sim f_{M_\nu=0}(z)\ (1 - \frac{3}{5} f_\nu)\ \sigma_{8,cb}(z)$ then the relative amplitude of the lensing to RSD compared to the case where $M_\nu = 0$ is $c_\kappa \sim 1 - \frac{2}{5} f_\nu$.

9.4.5 Emulators

We use the now-standard method of Markov Chain Monte Carlo to explore the posterior distribution of our parameters. In a high dimensional parameter space such as ours this involves many likelihood evaluations. In order to minimize the computing resources we require, we replace the model calculations involved in the likelihood computation with an emulator based on Taylor series expansions [96, 88, 240, 73, 105]. This reduces the time-per-likelihood-evaluation to tens of milliseconds. Evaluation of the Taylor series coefficients is very fast (a few minutes per spectrum on one node of the `Cori` machine at NERSC[8]). Using a $4^{\rm th}$ order Taylor series, with coefficients computed by finite difference from a 9^3 element grid centered around $\Omega_m = 0.31$, $h = 0.68$ and $\log(10^{10}A_s) = 2.84$ we achieve an accuracy of better than 10^{-3} for real-space power spectra and the redshift-space monopole, and 10^{-2} for the redshift-space quadrupole, or better than 10^{-3} at $k < 0.1\,h\,{\rm Mpc}^{-1}$, in terms of $68^{\rm th}$ percentile fractional residuals, corresponding to less than one-tenth of the statistical error in any entry in our data vector. To further speed up model evaluations we emulate the (un-windowed) two and three-dimensional clustering directly — given a set of cosmological parameters we predict the bias contributions to P_ℓ, ξ_ℓ and $C^{\kappa g}$ taking into account the effective redshifts, fiducial distances and redshift kernels assumed for each sample.

9.5 Results

Having laid out both the theory models and data measurements in the previous sections we are now in a position to extract cosmological constraints from the combined BOSS and Planck data. Since, unlike in the case of pure spectroscopic data, our methodology has not been previously tested, and in the view of preparing for the next-generation of cross-correlations analyses, we will proceed cautiously, starting by validating our theory model against the mock data described in §9.3 and performing sanity checks on the data before describing the cosmological constraints themselves.

9.5.1 Priors and Scale Cuts

We begin by defining the scales over which we will fit the data. For the BAO and RSD data we largely follow ref. [73], fitting the pre-reconstruction monopole and quadrupole moments of the power spectrum for $0.02 < k < 0.20\,h\,{\rm Mpc}^{-1}$ and the post-reconstruction monopole and quadrupole moments of the correlation function for $80 < s < 130\,h^{-1}{\rm Mpc}$. These scale cuts have been extensively validated against simulations to show that our perturbative model works to the desired accuracy within them. For the angular cross-clustering, $C_\ell^{\kappa g}$, we choose $\ell_{\rm max} = 250$ for the **z1** slice and 350 for the **z3** slice. We have chosen these conservatively to correspond to $k_{\rm max} \approx 0.20\,h\,{\rm Mpc}^{-1}$, the same scale cut we use for the redshift-space analysis,

[8] www.nersc.gov

Parameter	Prior
$(1+b_1)\sigma_8$	$\mathcal{U}(0.5, 3.0)$
b_2	$\mathcal{N}(0, 10)$
b_s	$\mathcal{N}(0, 5)$
α_0 [h^{-2} Mpc^2]	$\mathcal{N}(0, 30)$
α_2 [h^{-2} Mpc^2]	$\mathcal{N}(0, 50)$
α_x [h^{-2} Mpc^2]	$\mathcal{N}(0, 30)$
R_h^3 [h^{-3} Mpc^3]	$\mathcal{N}(0, \frac{1}{3\bar{n}})$
$R_h^3\sigma^2$ [h^{-5} Mpc^5]	$\mathcal{N}(0, 5\times 10^4)$

Parameter	Prior
B_1	$\mathcal{U}(0, 5.0)$
F	$\mathcal{U}(0, 5.0)$
$a_{\ell,0}$	$\mathcal{N}(0, 0.05)$
$a_{\ell,1}$ [h^{-1} Mpc]	$\mathcal{N}(0, 5)$

Table 9.2: Perturbation theory (left) and nuisance broadband parameter (right) priors and values for our analysis. Uniform distributions are denoted $\mathcal{U}(\min, \max)$ while normal distributions are denoted by $\mathcal{N}(\mu, \sigma)$. The prior isotropic stochastic term R_h^3 has its width set to one-third of Poisson value after shot-noise subtraction — this is roughly $\bar{n}^{-1} \approx 3000\,h^{-3}\mathrm{Mpc}^3$ for **z1** and $6000\,h^{-3}\mathrm{Mpc}^3$ for **z3**.

at the distance implied by the mean redshift of each sample. Our results are not very sensitive to either choice because the Planck κ maps are very noisy at these scales.

In addition to the cosmological parameters (Table 9.1), our model contains numerous bias parameters, counter terms and stochastic terms for each redshift slice and galactic cap. The priors we adopt for these are given in Table 9.2, and are based on those adopted in ref. [73] with two exceptions: we have narrowed the counterterm α_n priors in the view that they are in any case sufficiently well constrained by the data that the priors are uninformative, and that they should represent only modest corrections to linear theory on scales where perturbation theory is valid. We have also updated the prior on the isotropic stochastic term R_h^3 for the higher-redshift sample to better reflect the effective number density of the **z3**, where $\bar{n}^{-1} \approx 6000\,h^{-3}\,\mathrm{Mpc}^3$, such that the priors on R_h^3 in both **z1** and **z3** reflect the latest studies on stochasticity in BOSS-like galaxies [206]. Adopting these new priors shift our constraints on σ_8 by roughly $0.2\,\sigma$, with all other parameters essentially unaffected, compared to ref. [73].

9.5.2 Tests on Mock Data

While the models we use in this chapter have been tested extensively on mocks and data in the context of both spectroscopic surveys [82, 73] and angular cross correlations of galaxy clustering and lensing [246, 417], they have not been tested on the combination of these data as required for this work. In this subsection we use the mock data described in §9.3 to test whether LPT can indeed jointly and consistently model the matter and galaxy clustering encoded in our data to the required accuracy. To this end we apply the same pipeline, swapping only the input data vectors, that we will apply to the observed data, with the same scale cuts and priors. By necessity, this test only covers one redshift bin (**z3**), and the fixed

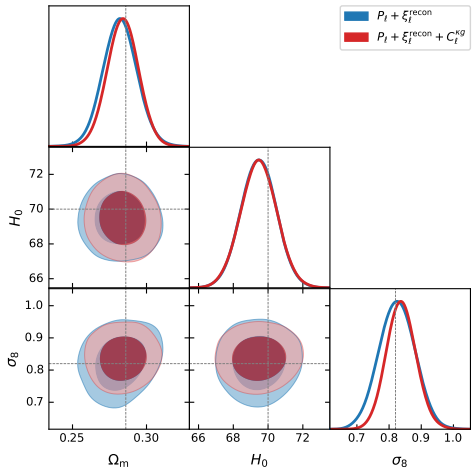

	P_ℓ, $\xi_\ell^{\rm rec}$	P_ℓ, $\xi_\ell^{\rm rec}$, $C_\ell^{\kappa g}$
$\ln(10^{10}A_s)$	3.12 ± 0.15	3.15 ± 0.13
Ω_m	0.282 ± 0.012	0.284 ± 0.011
H_0 [km/s/Mpc]	69.5 ± 1.0	69.5 ± 1.0
σ_8	0.825 ± 0.056	0.838 ± 0.046

Figure 9.4: (Left) Mock constraints from the mean of the Buzzard mocks for the **z3** sample fitting redshift-space power spectrum and post-reconstruction correlation function, with and without (red and blue) galaxy-CMB lensing cross-correlations multipoles. Gray lines indicate the true cosmology of mocks given by $\Omega_m = 0.286$, $h = 0.7$ and $\sigma_8 = 0.82$. (Right) Summary of the mock constraints (mean$\pm 1\,\sigma$). Adding angular cross-correlations to the data vector improves σ_8 constraints by close to 20%.

cosmological parameters (ω_b, n_s, M_ν) have been adjusted to those of the mocks.

Our results are shown in Figure 9.4. Fits using LPT recover the true cosmology of the Buzzard mocks to well within $1\,\sigma$ both before (blue, left) and after (red, right) the addition of angular galaxy-lensing cross correlations. Indeed, the implied means of both Ω_m and σ_8 fall within $0.38\,\sigma$ of the truth, roughly the expected statistical deviation for these mocks given that the Buzzard mocks cover 7 times the sky area of BOSS[9]. The Hubble parameter H_0 falls $0.5\,\sigma$ from truth, also not inconsistent with statistical scatter, especially since the H_0 constraint derives almost entirely from redshift space and previous tests on simulations [82, 73] with far lower statistical scatter have shown that our model can recover unbiased H_0 in these cases. These results therefore validate our perturbation theory modeling of the underlying gravitational nonlinearities studied in this work. In addition, including angular CMB-lensing and galaxy cross correlations improves the σ_8 constraint from these mocks by close to 20%, and the Ω_m constraint by 10% — even given the relatively noisy Planck lensing data — demonstrating the potential gains from cross-correlations analyses like ours.

[9]We note that this scaling is not exact for a number of reasons, including that the redshift-space quadrupole is roughly 25% larger than that in the BOSS data, and therefore noisier than the covariance matrix we use might imply, and that the lensing maps in the simulations are in principle "noiseless" and therefore cosmic-variance dominated at all scales, unlike the Planck maps for which this is true only at large scales ($\ell \lesssim 150$) — which are however the scales from which most of the σ_8 constraint is derived.

9.5.3 Systematics Checks and Analysis Setup

To check for non-cosmological contributions to the projected clustering in the BOSS galaxy maps, we cross-correlate the **z1** and **z3** samples in both the NGC and SGC. Since these maps are separated in redshift, with galaxy redshifts determined spectroscopically, in the absence of systematics the cross-correlation signal should be dominated by the effects of magnification. A similar test was conducted in ref. [119], who cross correlate the LOWZ and CMASS samples (which were combined to form jointly form the **z1** and **z3** samples used in this work) and find no significant evidence of correlations due to either systematics or magnification bias. This is not true for the **z1** and **z3** samples, as we show in Fig. 9.5. This apparent discrepancy could potentially be due to the fact that the BOSS systematic weights were computed to normalize the angular distributions of LOWZ and CMASS individually and account for effects like stellar density and seeing — however this re-weighting may not be optimal for the combined sample, split by redshift, if the weights are not readjusted for this purpose, as we show in Appendix H.2, particularly if the effects of the systematics are redshift-dependent. Any such angular systematics can in turn correlate with the CMB κ map and bias our results.

Concentrating first on the inset panels of Fig. 9.5 we see a very large cross-correlation at $\ell < 50$, that is inconsistent with the expected size of any magnification signal. In order to match the amplitude seen at $\ell < 50$ the slope of the number counts in the **z3** slice would need to be $s_\mu \approx 8$, which would then result in a signal grossly inconsistent with the points at $\ell > 50$. Given the rapid drop in cross-power with ℓ we suspect this contamination may be galactic in origin. To isolate ourselves from this effect, we have chosen $\ell_{\rm min} = 50$ when computing $C_\ell^{\kappa g}$ (§9.2).

The second thing to note in Fig. 9.5 is the negative cross-correlation for $50 < \ell < 200$ in the SGC, with no such signal in the NGC. Such an anti-correlation is unlikely to arise from magnification given reasonable slopes for the number counts, s_μ. The signal is well detected, statistically, and covers the whole range of scales where we expect significant S/N in our cross-correlation signal. We do not know the cause of this anti-correlation, and we are not certain that this systematic would correlate with the CMB lensing signal. Out of an abundance of caution, and because the SGC contains relatively little statistical weight overall, we choose to drop the lensing cross-correlation in the SGC from our data vector, retaining only the NGC data.

It is worth noting[10] that the LOWZ sample comprising most of the galaxies in **z1** contains early "chunks" in the NGC selected using a slightly different algorithm than later ones [300, 307]. These data could potentially have different systematics than the later chunks, and indeed one of them was found to require corrections based on seeing. Simply masking these data in the cross-correlation is not possible however, as they may represent a different subset of galaxies than the full sample and our assumption that a single set of biases describes both the redshift-space and projected clustering would be invalidated. In order to make use of the publicly available clustering data released by the BOSS collaboration, including window

[10] We thank Ashley Ross for pointing out this potential source of systematics.

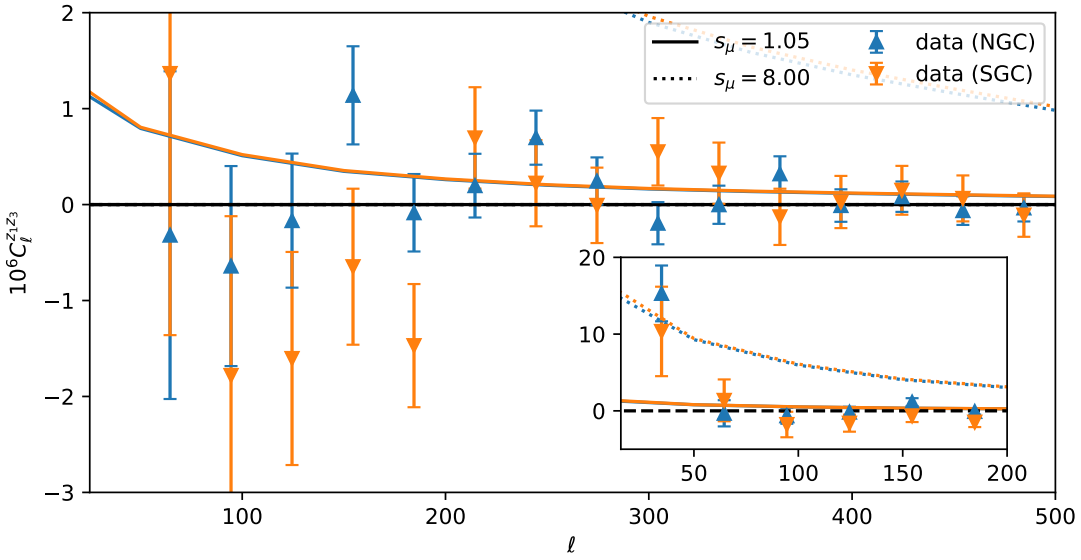

Figure 9.5: The (angular) cross-power-spectra for the low (**z1**) and high (**z3**) redshift galaxy samples. Since the two maps are disjoint in redshift, any signal should be dominated by magnification of the higher redshift sample (solid lines). The main panel shows the cross-correlation in the NGC (blue) and SGC (orange) respectively, while the inset shows a zoom-out on the y-axis to capture the large signal seen at $\ell < 50$. The dotted lines show the size of the magnification bias predicted for $s_\mu \approx 8$.

functions and mocks, thus depends critically on the collaboration's determination that the combined sample is sufficiently uniform after the corrections they performed [300, 307].

As an additional check[11] we cross-correlated a map constructed from the systematics weights applied to the galaxies with the Planck κ map. In principle there should be no correlation, but we find something small but non-zero for both **z1** and **z3**. This must arise due to correlations between signal, foregrounds or noise patterns in the κ map that correlate with the inputs from which the systematics weights are derived (for the BOSS CMASS sample these were stellar density and seeing, no such weights were applied for LOWZ [300]). The measured correlation is about an order of magnitude lower than the cross-correlation signal between galaxy density and κ, so any error in the weights would have to be very significant to make a large impact on our results.

As a last test we cross-correlated a map of extinction [315] against each of our galaxy overdensities in the NGC and the Planck κ map. Since the extinction map used to perform magnitude corrections is tracing both galactic and extragalactic structure [216, 425], it is possible that incorrect extinction corrections may cause artificial correlation between galaxy overdensity and κ. Assuming the projected galaxy over-density receives an additive

[11] We thank Anton Baleato Lizancos for suggesting this test.

	P_ℓ, $\xi_\ell^{\rm rec}$	P_ℓ, $\xi_\ell^{\rm rec}$, $C_\ell^{\kappa g}$	Planck
$\ln(10^{10}A_s)$	2.83 ± 0.11	2.75 ± 0.11	3.044 ± 0.014
Ω_m	0.3032 ± 0.0084	0.3001 ± 0.0078	0.3153 ± 0.0073
H_0 [km/s/Mpc]	69.21 ± 0.78	69.21 ± 0.77	67.36 ± 0.54
σ_8	0.743 ± 0.043	0.707 ± 0.035	0.8111 ± 0.0060

Table 9.3: Cosmological constraints from fitting the full BOSS RSD+BAO data, with and without cross correlations with CMB lensing from Planck in the Northern Galactic Cap. The corresponding constraints from Planck are shown as comparison.

contribution proportional to the extinction, we find that the galaxy autospectrum receives a bias due to extinction that should be well-below the percent level, in agreement with the finding of the regression analysis by the BOSS team that established no correlation of pixelized galaxy density with extinction value (and hence no need to include extinction as a contributor to the angular systematics weights [307, 300]), though those tests were done on the LOWZ and CMASS samples individually not the shuffled **z1** and **z3** samples. On the other hand, while our measurements are noisy, we find that the galaxy-κ cross spectrum could be biased by up to a few percent from the extinction component in the observed galaxy field alone, even before taking into account the effect it has on the lensing estimator. If present, such a correction would constitute a significant fraction of our error budget, since our mock tests show that the **z3** bin alone should give us close to 5% constraints on σ_8. However, we also find that our results are largely insensitive to changing the MV κ map for the SZ-deprojected map, which should have larger contributions from galactic emission and CIB and thus suggests that any such bias is small. In any case, while such a bias would still be subdominant to our statistical uncertainty in this work, this test demonstrates that cross-correlation analyses can require more stringent foreground mitigation than each experiment individually.

9.5.4 ΛCDM Constraints from Full Sample

Table 9.3 and Figure 9.6 shows the cosmological constraints obtained using the fiducial setup described in the previous sections, which includes RSD and BAO from the full BOSS sample, with and without additional information from cross-correlations with CMB lensing in the Northern galactic cap, as compared to constraints from Planck. The redshift-space only results are essentially identical to those recovered in ref. [73] and while lower in amplitude are consistent with Planck constraints; we refer the reader to that work for further discussion of the information contained within RSD-only fits. As was seen in our mock analysis, adding in $C_\ell^{\kappa g}$ mainly serves to to tighten constraints on the amplitude σ_8, with slight improvement in the Ω_m constraint as well due to degeneracy breaking. Including lensing cross correlations in our analysis also decreases the mean σ_8 to 0.707 ± 0.035, in roughly $3\,\sigma$ tension with Planck and close to $1\,\sigma$ below the constraints from redshift-space alone. In terms of the $S_8 = \sigma_8(\Omega_m/0.3)^{0.5}$

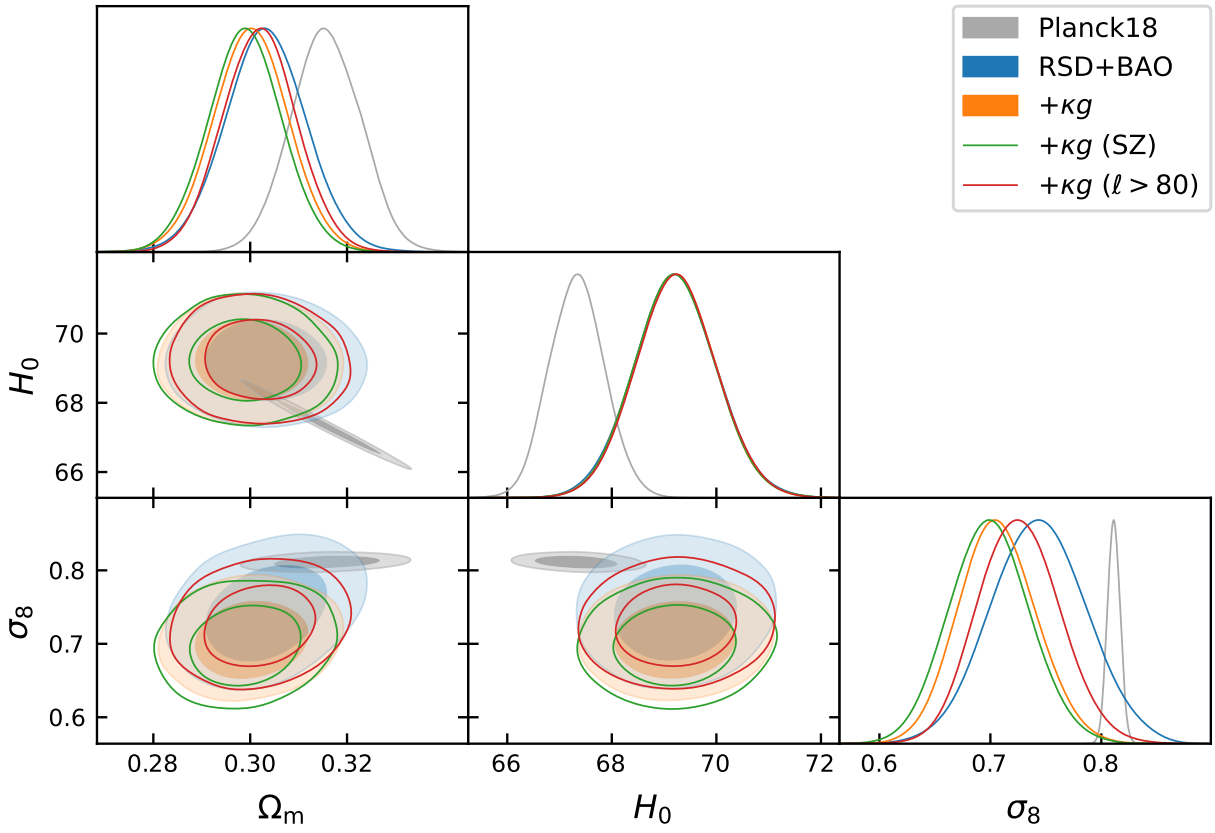

Figure 9.6: The marginalized posteriors for the cosmological parameters from our analyses, compared to Planck (grey contours). The blue shaded contours show constraints including only the RSD and BAO data, the other contours include the CMB lensing cross-correlation. The orange contours include the full range of $C_\ell^{\kappa g}$, the green contours show the effect using the SZ-deprojected Planck lensing map and the red contours illustrate the effect of dropping the lowest ℓ point $C_\ell^{\kappa g}$.

parameter best-probed by weak lensing, our analysis finds $S_8 = 0.707 \pm 0.037$, compared to $S_8 = 0.747 \pm 0.047$ from redshift-space data alone. Adding in lensing data leads to fractional improvements in the S_8 constraint greater than improvements in the σ_8 constraint due to degeneracy breaking; however, it is worth noting that even after including $C_\ell^{\kappa g}$ our σ_8 and Ω_m constraints remain slightly positively correlated due to the relative dominance of the redshift-space data. Future surveys where the lensing-galaxy cross correlation can be better measured should lead to further degeneracy breaking and further narrow constraints on the shape (Ω_m, H_0) of the power spectrum by better measuring its amplitude (σ_8).

We can perform a few simple tests within the fiducial setup to ensure the robustness of our analysis and data. Our results are almost unchanged if we swap out the fiducial lensing map for the tSZ-deprojected one, also provided by the Planck collaboration: σ_8 changes to 0.699 ± 0.036, a $0.2\,\sigma$ shift. This is a valuable cross check because the amount of cosmic

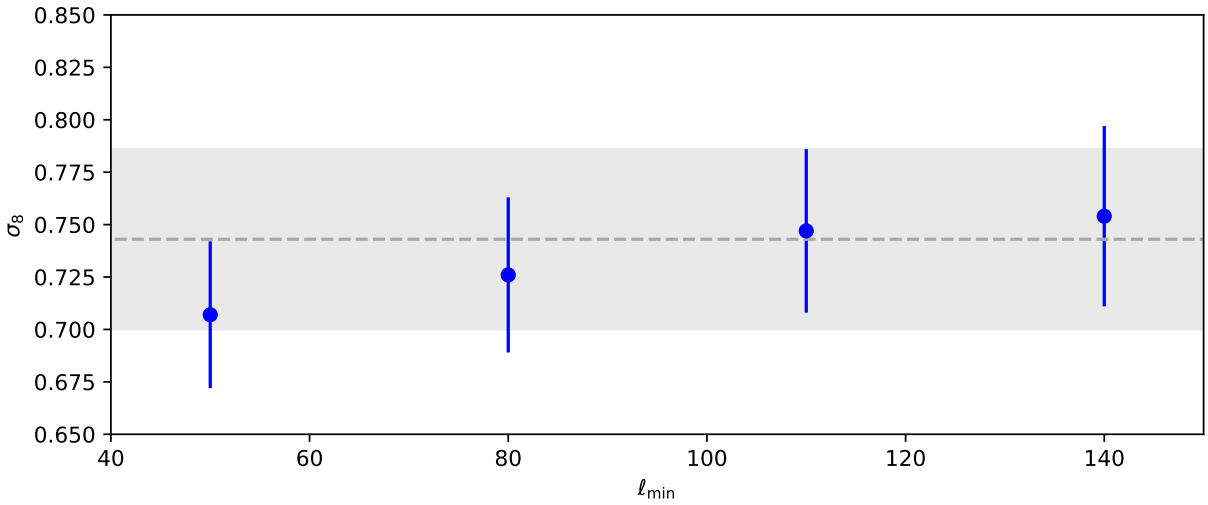

Figure 9.7: Our marginalized constraints on σ_8 as a function of the minimum ℓ included in the lensing-galaxy cross-correlations, $\ell_{\rm min}$. Note that we quote the minimum ℓ, which starts at $\ell = 50$, rather than the band center which would be larger by $\Delta\ell/2 = 15$. The shaded grey band with dashed line shows the result from just the BAO+RSD data.

infrared background and galactic foregrounds in the tSZ-deprojected maps is expected to be larger than in the (default) minimum variance map. We can also restrict our constraints to smaller scales, or larger ℓ, since our systematics checks showed nontrivial large-scale angular systematics in the galaxy maps. As shown in the red contour in Figure 9.6, dropping the lowest ℓ bin shifts the σ_8 constraint upwards to 0.726 ± 0.037, representing a more than $0.5\,\sigma$ shift. Shifts of this magnitude are not unexpected when dropping data points, simply due to statistical fluctuations, though we note that the change in constraining power from dropping this one point is relatively meager. Figure 9.7 shows the effect of removing lensing data up to some scale $\ell_{\rm min}$. Removing the lowest ℓ's reduces the statistical tension with the redshift-space, with mean σ_8 steadily rising with $\ell_{\rm min}$. Much of this shift is because the most statistically constraining κg data are the low ℓ values (due to a combination of observational and theoretical errors), and thus the joint fit becomes increasingly dominated by the RSD+BAO, with increased error bars to match. However a part of the shift to larger σ_8 is due to the κg pulling upwards.

Our analysis in this work is relatively constrained to work primarily at large angular scales. We have been very conservative in our scale cuts when modeling $C_\ell^{\kappa g}$, fitting to the same implied $k_{\rm max}$ as the redshift-space data which exhibit far more onerous nonlinearities due to small-scale velocities like fingers-of-god. More importantly, the Planck κ map is signal dominated only at the lowest ℓ that we fit, significantly limiting our ability to better constrain the onset of nonlinearities in the data. Better data from current and planned CMB surveys will significantly expand the available information towards high ℓ, allowing us

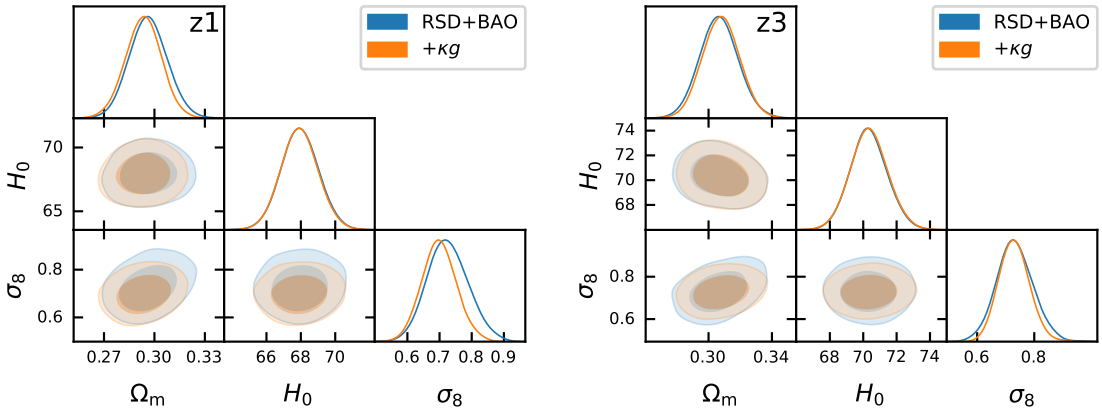

Figure 9.8: The marginalized posteriors for the cosmological parameters from our analyses of the **z1** (left) and **z3** (right) samples. The blue contours show the results using just the redshift-space data (i.e. BAO+RSD) while the orange contours include the galaxy-lensing cross-correlation.

to break bias degeneracies and check for systematics by comparing constraints from large and small scales. In order to maximally leverage this new information we will need to either validate PT models to beyond the conservative scales we use in this work or, more ambitiously, extend our modeling to smaller scales using simulations-based techniques. A particular class of these techniques, the so-called "hybrid EFT" (HEFT) approaches [244, 207, 432, 156], show particular promise because they share an identical set of clustering parameters with LPT, to which they reduce on large scales, while employing N-body dynamics to accurately predict clustering to the halo scale through a resummation scheme based on LPT. By extending perturbative bias modeling into the regime where dynamical nonlinearities are non-negligible, HEFT has the potential to break bias degeneracies and significantly tighten cosmological constraints from lensing-galaxy cross correlations, as we discuss in more detail in Appendix H.3.

9.5.5 Consistency Tests

Our main result — ΛCDM constraints from the combination of two- and three-dimensional data — is not only in strong tension with Planck, but also in some tension with constraints from redshift-space data only. Our goal in this subsection is to investigate the source of this tension through considering subsamples of the BOSS data and by testing the consistency of amplitudes between RSD and lensing.

Fig. 9.8 shows the marginal posteriors for the cosmological parameters, with and without lensing, for the two BOSS redshift slices **z1** and **z3**. Within each subsample, the redshift-space data (including BAO) tightly constrain Ω_m and h while the lensing data mainly sharpen constraints on σ_8. Comparing results with and without lensing, we see that σ_8 is more-or-less consistent with and without lensing in **z3**, but that the lensing data in **z1** prefer lower σ_8

than RSD and BAO alone, producing visible shifts in both Ω_m and, more significantly, in σ_8. It is worth noting that redshift-space only constraints on σ_8 are highly consistent across redshift bins (see ref. [73]) — these results therefore suggest that the downward shift in σ_8 with the addition of lensing data are being driven chiefly by the **z1** sample.

As a further test, we can free the lensing amplitude $c_\kappa = (1+\gamma)/2$ from its prediction within general relativity and constrain it directly from the data. Measuring c_κ acts both as a test of general relativity through measuring the gravitational slip γ and as a consistency test between the redshift-space and lensing data. Figure 9.9 shows the marginal posterior on c_κ. The blue line shows the combined constraint from the high and low redshift samples while orange and green lines show **z1** and **z3**, respectively. The combined-sample constraint is $\gamma = 0.74^{+0.17}_{-0.21}$, with the **z1** sample giving $\gamma = 0.66^{+0.17}_{-0.37}$ and **z3** giving $\gamma = 0.94^{+0.28}_{-0.36}$. In line with our σ_8 results from the redshift subsamples, c_κ constraints from **z3** are consistent with the prediction from general relativity, while those from **z1** show a mild preference for lower values, with a peak approximately 25% below unity. This implies that the lensing-galaxy cross correlation in the latter sample is roughly 25% lower than might be expected from the redshift-space data within ΛCDM, consistent with expectations based on Figs. 9.8 and 9.1. Nonetheless, our findings for both redshift slices and the combined sample are broadly consistent with the general-relativistic prediction of $\gamma = 1$, though they are again suggestive that lensing in the lower-redshift slice is driving our low σ_8 constraint. It is worth noting that, while it is possible to suppress the weak lensing amplitude relative to RSD via massive neutrinos, the mean suppression for our combined sample would translate (§9.4.4) to a neutrino mass fraction f_ν of roughly 30%, corresponding to $M_\nu \approx 4$ eV, well above limits set by ground-based experiments.

9.5.6 Comparison to Previous Results: When they go low, we go...

Our results add to the growing number of measurements at "low z" that have less clustering than inferred by Planck within the context of ΛCDM. This is typically summarized in terms of $S_8 = \sigma_8(\Omega_m/0.3)^{0.5}$. In terms of this statistic we find $S_8 = 0.707 \pm 0.037$ for the combined sample, lower than Planck's $S_8 = 0.832 \pm 0.012$. To further illustrate the tension, Figure 9.10 compares predictions for the CMB temperature and lensing anisotropies conditioned on our fiducial cosmological constraints and our redshift-space-only constraints compared to data from WMAP and Planck. Even when only redshift-space data are included the models with high likelihood underpredict both CMB statistics, and adding in cross correlations with lensing puts the best-fit models in strong tension with the CMB both by lowering the mean amplitude and tightening constraints.

We are not the first to study the combination of CMB lensing from Planck and galaxy clustering from BOSS. A number of authors have investigated cross correlations between the 2D (projected) galaxy clustering with lensing. Among the earliest was ref. [294], who found within the best-fit Planck 2013 cosmology that the CMASS-lensing cross correlation

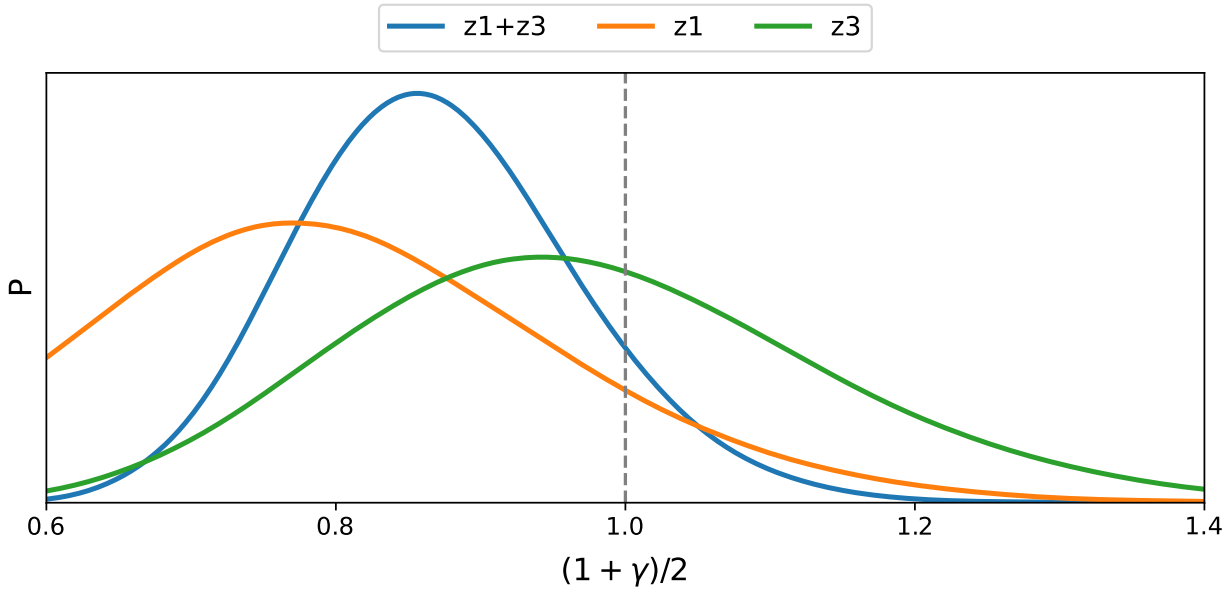

Figure 9.9: Marginal posterior on the parameter, $c_\kappa = (1+\gamma)/2$, by which the galaxy-lensing cross-spectra are scaled in models with gravitational slip (§9.4.4). The blue line shows the combined constraint from the high and low redshift samples while orange and green lines show **z1** and **z3**, respectively. All of the constraints are consistent with the GR prediction of $\gamma = 1$, though the lower redshift sample has lower $C_\ell^{\kappa g}$ than expected at modest significance. We put a prior that $0.2 < \gamma < 1.8$, so values of c_κ below 0.6 are not allowed. The **z1** sample hits this prior at the low end.

amplitude was 0.754 ± 0.097 times the expected value. Ref. [346] studied the galaxy-galaxy and galaxy-CMB lensing cross correlations using the BOSS LOWZ and CMASS samples assuming the Planck 2015 [284] cosmology, finding correlation coefficients of $r_{cc} = 1.0 \pm 0.2$ and 0.78 ± 0.13, respectively, on scales with projected radii larger than $20\,h^{-1}\,\mathrm{Mpc}$; in addition, cross-correlating with galaxy shears from the Sloan Digital Sky Survey they found that the amplitude of CMB lensing is reduced by a factor $A = 0.63 \pm 0.18$ below angular separations roughly corresponding to radial distances of $100\,h^{-1}\,\mathrm{Mpc}$.

Varying cosmological parameters, ref. [119] investigated the cross correlations of both BOSS galaxies and quasars, again finding that analyzing only the relatively low redshift galaxy-galaxy and galaxy-lensing cross correlations yields lower power spectrum amplitudes $\ln(10^{10}A_s)$, with a mean of roughly 2.9, than when the CMB-lensing autospectra, which predominantly probe matter clustering at $z \gtrsim 2$, are included, in which case the derived amplitudes are consistent with Planck[12]. It should be noted that the low-redshift constraint includes the (relatively) higher redshift BOSS quasars, whose cross-correlation amplitude

[12]We have inferred these numbers from the Figure 14 of ref. [119] since no tables with constraints for each of these data combinations was provided.

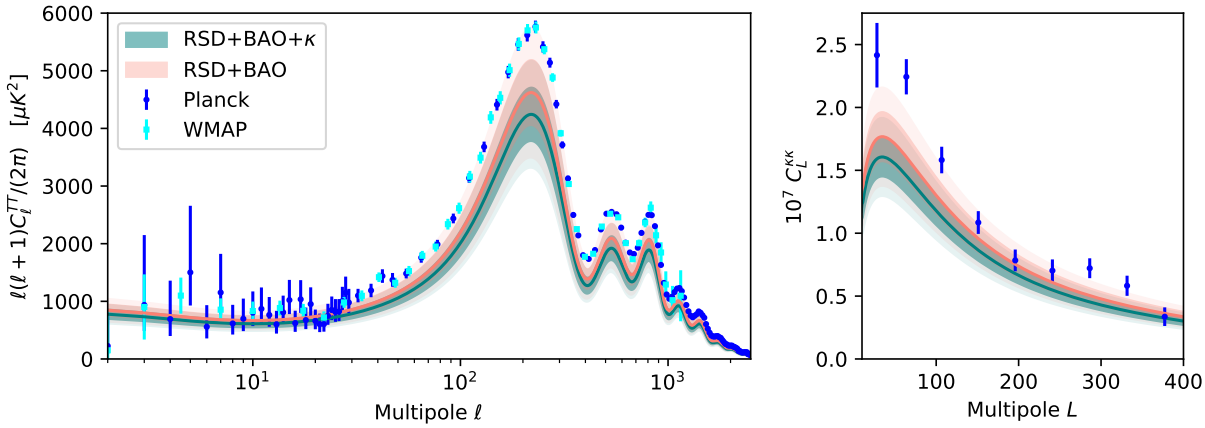

Figure 9.10: The predictions for the ΛCDM model conditioned on our full data set (green; RSD+BAO+κ) or without the lensing (red; RSD+BAO) compared to the CMB angular power spectra measured by Planck [286] and WMAP [175] (left) or the convergence auto-spectrum ($C_L^{\kappa\kappa}$; right). The shaded bands show the mean and ±1- and ±2-standard-deviation range for the model predictions while the points with errors show the best-estimate, foreground cleaned temperature or convergence power spectra from the CMB satellite missions.

with CMB lensing more closely matches the Planck prediction than either LOWZ and CMASS; should the quasar data be dropped the galaxy-galaxy and galaxy-lensing data would presumably prefer even lower σ_8. Similarly, ref. [347] analyzed the cross-correlation with LOWZ and CMASS and constrained the combination $\sigma_8^{0.8}\Omega_m^{0.6}$ to be 0.9 ± 0.12 times that predicted by Planck for both samples. None of the BOSS and Planck κ analyses above adopt the full set of bias and dynamical contributions to galaxy clustering required by fundamental symmetries as we do in this work and therefore do not exhaustively account for the possible contributions to clustering in the quasilinear regime — they thus extract their amplitude information from a different set of scales, with greater theoretical uncertainty; however they are nonetheless suggestive (with relatively low significance) of a deficit in cross-clustering power between lensing and galaxy clustering at low redshifts when compared to Planck due to either unknown physics or systematics, as our more complete analysis finds at roughly $3\,\sigma$ significance.

Previous authors have also studied the combination of three-dimensional BOSS galaxy clustering and lensing analyzed in this work. These works have typically employed the so-called E_G statistic, a test of general relativity proposed in ref. [437]. In that work, the linear theory of matter and galaxy clustering are combined with general-relativistic considerations to relate the ratio of galaxy-lensing cross correlations and redshift-space clustering anisotropies

to fundamental quantities; schematically,

$$\hat{E}_G \sim \frac{C_\ell^{\kappa g}}{P_2}, \quad \left\langle \hat{E}_G \right\rangle = \frac{(1+\gamma)\Omega_m}{2f(z)}. \tag{9.15}$$

Assuming Ω_m is known, measuring this ratio in galaxy-lensing cross correlations constrains the gravitational slip, as we have done above. Previous works leveraging BOSS redshift-space clustering and CMB lensing arrived at mixed results; ref. [294] found lensing to be $2.6\,\sigma$ lower than that predicted for CMASS while ref. [348] found both CMASS and LOWZ to be in excellent agreement with general relativity. It should be noted however that, unlike in our approach, using E_G to constrain gravity requires working within linear theory with scale-independent bias — the state-of-the-art in analyses such as ref. [348], who compare compute this ratio using a combination of BOSS galaxies, CMB lensing and cosmic shear surveys, account for the neglected gravitational nonlinearities by calibrating to simulations. In addition, the E_G statistic is defined to be a single number computed by combining summary statistics of galaxy clustering and lensing evaluated at different scales and redshifts, reliant on the acceptability of the linear-theory prediction at a single redshift across these scales and redshifts in order to be compared to Equation 9.15. By comparison, our approach is able to constrain the (scale-independent) gravitational slip leveraging both linear and quasilinear scales while simultaneously marginalizing over cosmological parameters directly, confirming the result of ref. [294] that the lensing-galaxy cross correlations measured from BOSS and Planck are lower than their observed redshift-space distortions imply, particularly for **z1**, though with only modest significance.

Beyond those combining BOSS and Planck there have been a wealth of recent results obtaining cosmological constraints from weak lensing and its cross correlation with galaxy clustering, most of which find S_8 to be lower than Planck but higher than that implied by our analysis, as shown in Figure 9.11. In the case of weak lensing only, the DES Y3 shear-only correlation function [13, 327] and harmonic space analyses [118] find $S_8 = 0.772 \pm 0.017$ and $S_8 = 0.784 \pm 0.026$ respectively, $2\,\sigma$ lower than Planck but also in tension with our fiducial constraints at the $2\,\sigma$ level, though the tension is slightly reduced if we instead compare to the fiducial scale cut results instead of the ΛCDM optimized setup. A recent analysis of the KiDS-1000 data [386] similarly found $S_8 = 0.748^{+0.021}_{-0.025}$, in slightly more tension with Planck but slightly closer to our result. Earlier analyses of cosmic shear in HSC [170] and CFHTLenS [168] paint a similar picture. Adding in galaxy clustering from non-BOSS surveys, the DES Y3 "3 × 2" analysis finds $S_8 = 0.776 \pm 0.017$ [2] and, dropping the weak lensing autocorrelation, a cross-correlation of unWISE-selected galaxies with Planck lensing [208] found $S_8 = 0.784 \pm 0.015$, while using luminous red galaxies selected from DECALS ref. [417] found $S_8 = 0.73 \pm 0.03$. Our constraints are in modest ($\lesssim 2\,\sigma$) tension with most of these cross-correlations analyses except for this last work, for which S_8 is just shy of $1\,\sigma$ higher than our result. A combined analysis of cosmic shear, CMB lensing and galaxy clustering data, mostly sensitive to growth between $0.2 < z < 0.7$, by ref. [143] found $S_8 = 0.7781 \pm 0.0094$. The combination of these previous results (many of which probe similar redshift ranges to this work) could be an indication that the BOSS galaxy and Planck CMB

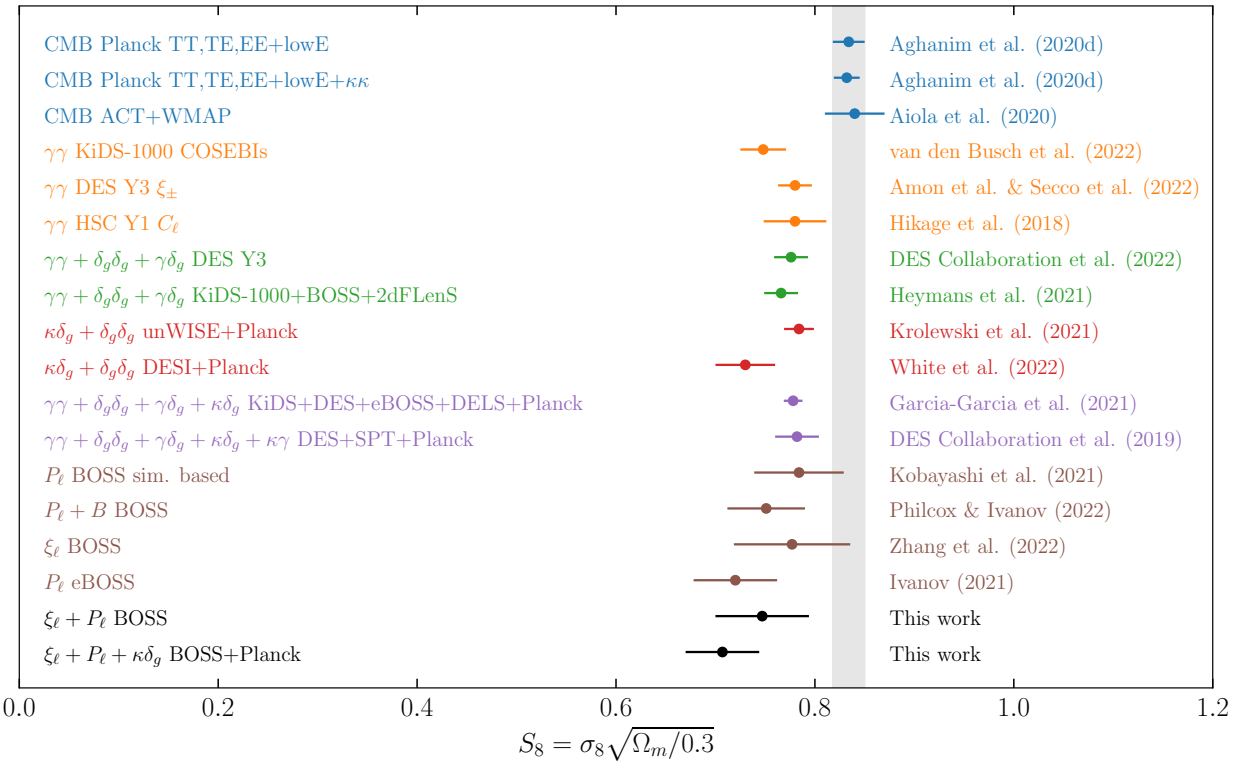

Figure 9.11: A summary of recent S_8 constraints. The different colored points indicate different combinations of data that have been used in the constraints. In particular, we include constraints from the CMB (blue), cosmic shear (orange, $\gamma\gamma$), projected galaxy clustering and galaxy-galaxy lensing (green; $\delta_g\delta_g + \gamma\delta_g$), projected galaxy clustering and CMB lensing (red; $\delta_g\delta_g + \kappa\delta_g$), a combination of all of these (purple), redshift space clustering in various forms (brown), and the combination of data used in this work (black). As in Figure 9.12, we have limited ourselves to analyses using large scales. Despite the different models and statistics being used in these analyses, they all yield constraints below those from the CMB.

κ cross correlation measurement may be contaminated by some yet-unidentified foreground or systematic, since in the absence of such an effect we would be probing similar epochs of structure formation, though more concrete conclusions regarding these tensions will likely have to wait for upcoming CMB lensing measurements from e.g. ACT, whose instrument noise on the scales we study will be significantly reduced.

The fact that $C_\ell^{\kappa g}$ has an amplitude close to 20% lower than implied by redshift-space clustering hints that there may be an unknown systematic leading to internal inconsistency within the data. The latter measurement is by now under excellent theoretical control and, in addition to our results, recent analyses of BOSS by refs [438, 282] using the redshift-space galaxy 2-point function in configuration and Fourier space give $\sigma_8 = 0.766 \pm 0.055$ and

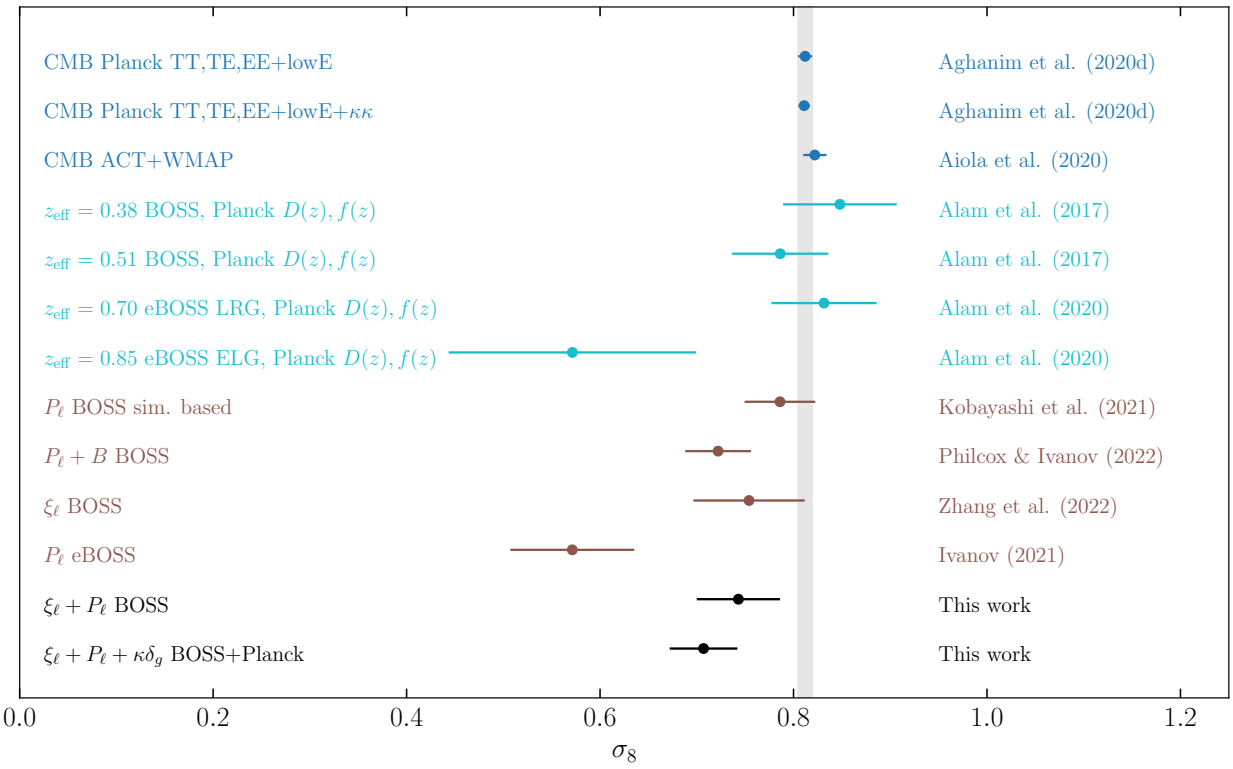

Figure 9.12: A summary of σ_8 constraints from recent CMB measurements (blue) compared to those made using template based (cyan) and full-shape (brown) fits to anisotropic redshift space correlation functions (ξ_ℓ), power spectra (P_ℓ), and bispectra (B), as well as including $C^{\kappa g}$ in this work (black). For the purposes of this figure, we have limited ourselves to analyses that focus on large scales, although we provide a more complete overview in Section 9.5.6. For the template based fits, we quote "consensus" constraints, which are weighted averages of multiple analyses. These template based fits constrain $f\sigma_8(z_{\rm eff})$ directly, so we have assumed the best fit cosmology from [286] to compute $D(z_{\rm eff})$ and $f(z_{\rm eff})$ in order to convert to $\sigma_8(z = 0)$. The template based fits are largely more consistent with the CMB constraints, other than the eBOSS ELG point. The full-shape analyses yield lower σ_8 values than the template based fits and the CMB, and are relatively consistent despite using significantly different models and statistics. The inclusion of the CMB lensing data in our analysis tightens our σ_8 constraint by partially breaking the degeneracy between $\Omega_{\rm m}$ and σ_8, but also drives it significantly lower than our RSD-only fits.

$0.737^{+0.040}_{-0.044}$[13] both in excellent agreement with our results, as shown in Figure 9.12. These recent analyses employ improved models of galaxy clustering compared to the earlier (official) results of the BOSS collaboration, marginalize over cosmological parameters like Ω_m and H_0 beyond the growth rate $f(z)$, and also correct for errors in the window-function normalization. Together, this new generation of BOSS constraints confirms that there is a deficit of power in $C^{\kappa g}$ compared to that inferred from the velocity-induced anisotropy in galaxy clustering[14], though at lower significance given that redshift-space constraints on σ_8 are considerably weaker due to bias degeneracies. Unlike in the case of weak lensing, however, redshift-space analyses like the above are able to independently constrain parameters like Ω_m and σ_8 instead of highly degenerate combinations like S_8. It is worth noting that analyses of BOSS galaxy clustering using N-body based emulators [204, 434, 430], or similar simulation based techniques [210], also return constraints very close to our redshift-space result, with smaller error bars, though we caution that these constraints rely on far more restrictive assumptions about the small-scale behavior of galaxy clustering and thus have a larger systematic error. A more theoretically robust alternative for improving cosmological constraints from galaxy clustering is to also perturbatively model higher n-point functions; when the bispectrum is taken into account, ref. [282] find that their σ_8 constraint tightens to $\sigma_8 = 0.722^{+0.032}_{-0.036}$, a similar gain in constraining power to the addition of lensing information seen in this work. The bispectrum in principle breaks the $f\sigma_8$ degeneracy in galaxy clustering and can provide σ_8 information beyond that in the velocities; curiously, this nonlinear information also prefers (slightly) lower σ_8 than the linear RSD alone. In discussing ref. [282] here and above we have used their results with the spectral index n_s fixed to better match the analysis setup employed in this work—freeing n_s in our analysis yields verys similar redshift-space only constraints to that work, while adding in lensing data lowers σ_8 by about 1σ as in the fixed n_s case, as we show in Appendix H.4. Higher-order statistics and cross correlations with nonlinear matter through lensing yield competitively tight constraints on cosmological parameters, and will provide complimentary clustering information in upcoming surveys useful both as internal consistency checks and probes of new physics beyond the standard, linear redshift-space distortions traditionally probed by spectroscopic surveys.

9.6 Conclusions

The two and three dimensional clustering of galaxies measured by spectroscopic surveys offer complementary cosmological information: the latter encodes the shape of the primordial power spectrum, distance information through baryon acoustic oscillations, and cosmic velocities through redshift-space distortions, while the former, when in combination with probes of

[13] We have adopted their constraints using the public power spectra modeled with fixed n_s, for better comparison with our analysis.

[14] The σ_8 constraints from eBOSS ELG's in refs. [184, 8] are notably lower than the others shown in Figure 9.12, but the strong tension with other measurements at similar redshifts, including eBOSS LRG's, suggest that this may be due to systematics (e.g. the large redshift range fit).

weak lensing like the CMB, probes the amplitude of matter fluctuations through their induced Weyl potential. In this chapter we lay out a formalism to jointly analyze these two distinct probes in the language of effective perturbation theories, presenting a proof-of-principle analysis using Lagrangian perturbation theory to model publicly available data from galaxies in the BOSS survey [101, 7] and CMB lensing data from the Planck satellite [287]. To our knowledge this is the first such joint analysis to use a consistent theoretical model valid into the quasilinear regime taken all the way to the data (2-point functions), rather than utilizing linear theory and compressed statistics derived from it. This is significant because perturbation theory allows for rigorous and systematic modeling of structure formation on large scales scales with minimal theoretical assumptions and will be invaluable to distinguish true cosmological signals from either theory or data systematics for current and upcoming surveys.

A particular goal of this work has been to set up this analysis in a theoretically well-motivated way (§9.4). To this end we have, for example, been careful in our perturbative treatment of neutrinos, which affect galaxy-galaxy and galaxy-matter spectra in meaningfully different ways, and we introduced redshift-dependent weights to the galaxy-lensing cross-correlations measurements to ensure they probe clustering at the same effective redshift as the three-dimensional power spectrum. As a test of our formalism, we validate our various theoretical choices and approximations using lightcone mocks of BOSS galaxies (§9.3) based on the Buzzard simulations [107], showing that our model is able to recover the "truth" to within the statistical scatter expected from the volume of these simulations (§9.5.2).

The data consist of 1,198,006 galaxies covering 25% of the sky (10,252 sq.deg.) [300], and the Planck lensing map covering approximately 60% of the sky, though for cross-correlation with the Planck lensing maps we utilize only the 7,143 sq.deg. in the NGC. The Planck lensing map is signal dominated near $\ell \approx 40$ [287]. We use the low- (**z1**; $0.2 < z < 0.5$) and high-redshift (**z3**; $0.5 < z < 0.75$) samples based on spectroscopic redshifts as defined by the BOSS collaboration [7]. As also discussed in ref. [73], while making new galaxy samples and measurements more tailored to our analysis is in principle possible, doing this work — including re-making enough mock measurements to estimate the covariance matrix — would require resources beyond the scope of this project. We therefore leave data-side optimization of this analysis to future work.

The main results of our analysis, constraints on Ω_m, H_0 and σ_8 based on the combination of BOSS galaxy clustering and Planck CMB lensing, are described in §9.5. We perform systematics tests of the galaxy and lensing maps in §9.5.3, finding that the systematics weights for the BOSS galaxies would have to have left significant traces of the mitigated systematics in the maps to have even few-percent effects on the cross-correlation amplitude, $C_\ell^{\kappa g}$. Cross correlating the galaxy and lensing maps with maps of extinction, an effect not included in the systematics weights for BOSS galaxies due to its relatively small effect, indicates that extinction errors also have a small impact at the at-most few-percent level in cross correlations. We also cross-correlate the non-overlapping low and high redshift (**z1**, **z3**) samples, finding spurious large scale correlations in the lowest ℓ bins and in the SGC — out of an abundance of caution we therefore drop these data points from our main analysis.

Our main result, using the full three-dimensional galaxy clustering data from BOSS and CMB lensing in the NGC, is summarized in Table 9.3 and Figure 9.6. While the three-dimensional clustering data including power spectra and reconstructed correlation functions strongly constrain Ω_m, H_0 through the shape of the linear power spectrum, including lensing information through $C_\ell^{\kappa g}$ sharpens the amplitude (σ_8) constraint by roughly 20% and, since lensing probes this amplitude multiplied by the matter density, also somewhat sharpens the constraint on Ω_m. Adding the lensing data, which are substantially lower on large scales than the redshift-space data might predict (Fig. 9.1), has the effect of lowering both, though Ω_m decreases by less than half a sigma and our model still predicts an acoustic scale ($\sim \Omega_m h^3$) highly consistent with the narrow range allowed for by Planck. On the other hand, including lensing we constrain $\sigma_8 = 0.707 \pm 0.035$, in roughly $3\,\sigma$ tension with Planck constraints, and an implied lensing amplitude, S_8, roughly $2\,\sigma$ lower than cosmic shear analyses, though in good agreement with another effective-theory based analysis of BOSS galaxy clustering including the bispectrum.

Looking at subsamples of our data separately we find that the drop in σ_8 is driven primarily by the low redshift sample **z1** (§9.5.5). By freeing the gravitational slip γ, we find for that sample that the implied ratio of the Weyl to Newtonian potentials $c_\kappa = (1+\gamma)/2$ is roughly 20% lower than predicted by general relativity, but at less than $2\,\sigma$ significance (Fig 9.9), and indeed we do not detect any deviation from unity for this ratio at more than $2\,\sigma$ significance in either the redshift slices separately or in combination. It is worth noting that our ability to leverage the relative amplitudes of galaxy clustering and galaxy-lensing cross correlations has implications beyond gravitational slip. For example, massive neutrinos will tend to suppress the latter relative to the former, though at a level far below the current level of constraints. Conversely, much recent attention has been paid to whether selection-induced anisotropic bias can be a significant contaminant of the RSD signal [176, 259]. Such an effect would add a term $b_{zz}s_{zz}$, where s_{zz} is the component of the shear tensor along the line-of-sight, to the bias expansion (at leading order) such that the linear galaxy overdensity in redshift-space becomes

$$\delta_{g,s}(\mathbf{k},z) = \left[1 + b_1 - \frac{b_{zz}}{3} + (f(z) + b_{zz})\,\mu^2\right]\,\delta_m(\mathbf{k}) + \cdots\,, \tag{9.16}$$

leading to an exact degeneracy between b_{zz} and the amplitude of the RSD anisotropy, and to biases in values of σ_8 inferred from redshift surveys. However, this degeneracy can be broken by the inclusion of lensing cross correlations, which measure σ_8 through the $\mu \approx 0$ component; together with spectroscopic clustering measurements, which also determine Ω_m and thus $f(z)$, this combination allows for a clean measurement of b_{zz} and σ_8. Indeed, since Figure 9.9 implies that lensing and redshift-space clustering amplitudes are roughly in agreement, b_{zz} at least cannot be of order unity for either redshift slice. Future surveys will significantly improve our ability to exploit this synergy between lensing and RSD.

While our results are sufficiently constraining to considerably sharpen the tension in σ_8 between the CMB and LSS in ΛCDM, we still remain limited by the data that we use and by our modeling. Luckily, we anticipate rapid progress in both directions in the very near

future. The galaxy maps are already sample variance dominated on the large scales from which we derive most of our cosmological information, so the next major improvement in errors at intermediate ℓ will come from CMB lensing maps with lower noise than Planck. Redshift-space clustering measured from DESI will also dramatically improve over those we used here. Using maps optimized for cross-correlations, with careful attention to foreground cleaning or hardening, derived from more sensitive and higher angular resolution ground-based experiments will dramatically lower the uncertainties of $C_\ell^{\kappa g}$. These lower-noise measurements should allow us to better distinguish between the shapes of various nonlinear contributions to $C_\ell^{\kappa g}$ even on the scales we have analyzed in this work. More ambitiously, as discussed in Appendix H.3, recent work extending the LPT modeling in real space to more nonlinear scales using hybrid N-body models [244] can allow us to self-consistently double the ℓ reach of our formalism by switching the perturbative calculations of $C_\ell^{\kappa g}$ for an emulator (e.g. [207]). Combined with improved modeling future experiments will improve the constraints on the power spectrum amplitude, σ_8, and allow us to check the consistency between constraints derived from large and small scales, even from within the same and related theoretical models. The well-motivated and tested theoretical framework outlined herein should be ideal for such future work.

In terms of improvements in the input maps, we note that reducing systematics at low ℓ is particularly important for improving constraints. Scale-dependent bias and astrophysical effects become increasingly important at small scales (larger k) and having sufficiently constraining data over a range of scales is crucial for constraining departures from linearity and breaking degeneracies between bias and effective-theory parameters. While upcoming CMB experiments will straightforwardly reduce the noise in CMB lensing measurements on quasilinear scales (intermediate ℓ), there is also much to be gained by ensuring that both the galaxy and CMB lensing data are uncontaminated on large scales.

9.7 Acknowledgements

We thank Simone Ferraro, Anton Baleato Linzancos and Noah Sailer for helpful conversations about CMB lensing and foregrounds, and suggestions for limiting systematic errors. We similarly thank Noah Weaverdyck for useful discussions of foregrounds in galaxy surveys, and Ashley Ross for enlightening discussions of potential systematics in the BOSS catalogs. We thank Zvonimir Vlah for continued discussions on perturbation theory. M.W. thanks Uros Seljak for numerous conversations on cosmological modeling and inference and for comments on an early draft. S.C. is supported by the DOE. M.W. is supported by the DOE and the NSF. J.D. is supported by the Lawrence Berkeley National Laboratory Chamberlain Fellowship. N.K. is supported by the Gerald J. Lieberman Fellowship. We acknowledge the use of `NaMaster` [11], `Cobaya` [378, 379], `GetDist` [219], `CAMB` [220] and `velocileptors` [74] and thank their authors for making these products public. This research has made use of NASA's Astrophysics Data System and the arXiv preprint server. This research is supported by the Director, Office of Science, Office of High Energy Physics of the U.S. Department of

Energy under Contract No. DE-AC02-05CH11231, and by the National Energy Research Scientific Computing Center, a DOE Office of Science User Facility under the same contract.

Appendix A

Introduction

A.1 Eulerian and Lagrangian Kernels to Third Order

For the Eulerian kernels we have [40] for the density

$$\begin{aligned} F_1(\mathbf{p}_1) &= 1 \\ F_2(\mathbf{p}_1,\mathbf{p}_2) &= \frac{5}{7} + \frac{1}{2}\Big(\frac{\mathbf{p}_1\cdot\mathbf{p}_2}{p_1^2} + \frac{\mathbf{p}_1\cdot\mathbf{p}_2}{p_1^2}\Big) + \frac{2}{7}\frac{(\mathbf{p}_1\cdot\mathbf{p}_2)^2}{p_1^2p_2^2}. \end{aligned} \tag{A.1}$$

and velocity

$$\begin{aligned} G_1 &= 1 \\ G_2(\mathbf{p}_1,\mathbf{p}_2) &= \frac{3}{7} + \frac{1}{2}\Big(\frac{\mathbf{p}_1\cdot\mathbf{p}_2}{p_1^2} + \frac{\mathbf{p}_1\cdot\mathbf{p}_2}{p_1^2}\Big) + \frac{4}{7}\frac{(\mathbf{p}_1\cdot\mathbf{p}_2)^2}{p_1^2p_2^2}. \end{aligned} \tag{A.2}$$

The Lagrangian kernels are given by ($\mathbf{k} = \sum_i \mathbf{p}_i$) [231]

$$\begin{aligned} L_1(\mathbf{p}_1) &= \frac{\mathbf{k}}{k^2} \\ L_2(\mathbf{p}_1,\mathbf{p}_2) &= \frac{3}{7}\frac{\mathbf{k}}{k^2}\Big(1 - \frac{(\mathbf{p}_1\cdot\mathbf{p}_2)^2}{p_1^2p_2^2}\Big) \\ L_3^a(\mathbf{p}_1,\mathbf{p}_2,\mathbf{p}_3) &= \frac{5}{7}\frac{\mathbf{k}}{k^2}\Big(1 - \frac{(\mathbf{p}_1\cdot\mathbf{p}_2)^2}{p_1^2p_2^2}\Big)\left(1 - \Big(\frac{(\mathbf{p}_1+\mathbf{p}_2)\cdot\mathbf{p}_3}{|\mathbf{p}_1+\mathbf{p}_2|p_3}\Big)^2\right) \\ &+ \frac{1}{3}\frac{\mathbf{k}}{k^2}\Big(1 - 3\frac{(\mathbf{p}_1\cdot\mathbf{p}_2)^2}{p_1^2p_2^2} + 2\frac{(\mathbf{p}_1\cdot\mathbf{p}_2)(\mathbf{p}_2\cdot\mathbf{p}_3)(\mathbf{p}_3\cdot\mathbf{p}_1)}{p_1^2p_2^2p_3^2}\Big) + \mathbf{k}\times T(\mathbf{p}_1,\mathbf{p}_2,\mathbf{p}_3). \end{aligned} \tag{A.3}$$

Here T is the transverse piece of the third-order displacement, which we will not need explicitly in the following. It is convenient to define the symmetrized kernel $L_3 = \frac{1}{3}(L_3(123) + L_3(231) + L_3(312))$. The third-order EPT kernels can be computed by combining the Lagrangian ones so we will not independently list them here (see e.g. [148] for an explicit expression).

A.2 Equivalence of Green's Function and Power Series Solution in EdS

In this section we will derive the second-order kernel F_2 using the Green's function approach and show that it recovers the same solution as the power series ansatz described in the text. See refs. [268] and [290] for similar discussions in the context of EPT and LPT.

To begin we can use the nonlinear continuity equation to eliminate θ, since[1]

$$\theta = -\frac{\partial\delta}{\partial\tau} - \int_{\mathbf{p}} \alpha(\mathbf{p}, \mathbf{k}-\mathbf{p})\ \theta(\mathbf{p})\delta(\mathbf{k}-\mathbf{p}).$$

From this we can rewrite the Euler equation as

$$\frac{\partial^2\delta}{\partial\tau^2} + \mathcal{H}\frac{\partial\delta}{\partial\tau} - \frac{3}{2}\mathcal{H}^2\Omega_m\delta = -\int_{\mathbf{p}} \alpha(\mathbf{p}, \mathbf{k}-\mathbf{p})\Big(\dot\theta(\mathbf{p})\delta(\mathbf{k}-\mathbf{p}) + \theta(\mathbf{p})\dot\delta(\mathbf{k}-\mathbf{p}) + \mathcal{H}\theta(\mathbf{p})\delta(\mathbf{k}-\mathbf{p})\Big) + \int_{\mathbf{p}} \beta(\mathbf{p}, \mathbf{k}-\mathbf{p})\theta(\mathbf{p})\theta(\mathbf{k}-\mathbf{p}).$$

For simplicity in the following we will work to second order only and neglect any higher-order terms. In order to proceed we will make use of the linear theory expressions

$$\begin{aligned}
&\delta^{(1)} = D(\tau)\delta_0, \quad \dot\delta^{(1)} = -\theta^{(1)} = f(\tau)\mathcal{H}(\tau)D(\tau)\delta_0 \\
&\dot\theta^{(1)} = -\mathcal{H}(\tau)\theta^{(1)} - \frac{3}{2}\mathcal{H}^2(\tau)\Omega_m(\tau)\delta^{(1)} = f(\tau)\mathcal{H}^2(\tau)\delta^{(1)} - \frac{3}{2}\mathcal{H}^2(\tau)\Omega_m(\tau)\delta^{(1)};
\end{aligned} \tag{A.4}$$

Using this a bit of algebra gives

$$\frac{\partial^2\delta}{\partial\tau^2} + \mathcal{H}\frac{\partial\delta}{\partial\tau} - \frac{3}{2}\mathcal{H}^2\Omega_m\delta = \Big(\frac{3}{2}\mathcal{H}^2\Omega_m + f^2\mathcal{H}^2\Big)D^2\int_{\mathbf{p}} \alpha(\mathbf{p}, \mathbf{k}-\mathbf{p})\ \delta_0(\mathbf{p})\delta_0(\mathbf{k}-\mathbf{p}) + f^2\mathcal{H}^2D^2\int_{\mathbf{p}} \beta(\mathbf{p}, \mathbf{k}-\mathbf{p})\ \delta_0(\mathbf{p})\delta_0(\mathbf{k}-\mathbf{p}).$$

Notice that the time- and scale-dependence are decoupled, as expected.

In an EdS universe we have $f, \Omega_m = 1$, $D = a$ and $\mathcal{H} = aH = a^{-1/2}$, and the time evolution simplies dramatically. Defining the retarded Green's function

$$G(\tau, \tau') = \frac{D(\tau)D_-(\tau') - D_-(\tau)D(\tau')}{\dot D(\tau')D_-(\tau') - \dot D_-(\tau')D(\tau')},$$

where dots denote conformal time derivatives, we have that in this case

$$G(\tau, \tau') = \frac{2}{5}\Big(a^{-1/2}(\tau')a(\tau) - a^2(\tau')a^{-3/2}\Big) \tag{A.5}$$

[1] In what follows we will ignore time and wavenumber labels for δ and θ and write $\int_{\mathbf{p}} = \int d^3\mathbf{p}/(2\pi)^3$ for brevity.

and, integrating, we get

$$\begin{aligned}\delta^{(2)}(\mathbf{k},\tau) &= \int d\tau'\ G(\tau,\tau')F[\delta^{(1)},\theta^{(1)}] \\ &= \frac{2}{7}D^2\int_{\mathbf{p}}\left(\frac{5}{2}\alpha(\mathbf{p},\mathbf{p}-\mathbf{k})+\beta(\mathbf{p},\mathbf{k}-\mathbf{p})\right)\delta_0(\mathbf{p})\delta_0(\mathbf{k}-\mathbf{p}) \\ &\equiv D^2\int_{\mathbf{p}}F_2(\mathbf{p},\mathbf{k}-\mathbf{p})\delta_0(\mathbf{p})\delta_0(\mathbf{k}-\mathbf{p}) \end{aligned} \tag{A.6}$$

where F_2 is as defined in the previous appendix.

The derivation of the Lagrangian equivalent L_2 involves the exact same integral $\int d\tau' G(\tau,\tau')D^2(\tau)$ but is even more straightforward since it doesn't involve any time derivative conversions. Following the discussion above Equation 1.26 we have for the second-order equations of motion

$$\begin{aligned}&\frac{\partial^2\Psi^{(2)}_{i,i}}{\partial\tau^2}+\mathcal{H}\frac{\partial\Psi^{(2)}_{i,i}}{\partial\tau}-\frac{3}{2}\mathcal{H}^2\Omega_m\Psi^{(2)}_{i,i}=-\frac{3}{2}\Omega_m\mathcal{H}^2\left(\frac{1}{2}\left(\Psi^{(1)}_{i,i}\right)^2-\frac{1}{2}\Psi^{(1)}_{i,j}\Psi^{(1)}_{j,i}\right)\\ &\frac{\partial^2(\nabla\times\Psi^{(2)})}{\partial\tau^2}+\mathcal{H}\frac{\partial(\nabla\times\Psi^{(2)})}{\partial\tau}=0.\end{aligned}$$

The right-hand side of the top equation has the same time dependence within EdS as the second-order overdensity, $\mathcal{H}^2D^2$, so we can write integrate it to give

$$\Psi^{(2)}_{i,i}=-\frac{1}{2!}\frac{3}{7}\left(\left(\Psi^{(1)}_{i,i}\right)^2-\Psi^{(1)}_{i,j}\Psi^{(1)}_{j,i}\right)$$

and, since no vorticity is generated at second order, we have

$$\Psi^{(2)}_i(\mathbf{k},\tau)=\frac{i}{2}\int\frac{d^3\mathbf{p}}{(2\pi)^3}L^{(2)}_i(\mathbf{p},\mathbf{k}-\mathbf{p}) \tag{A.7}$$

where $L^{(2)}_i$ is as defined in the previous appendix. For a related discussion see ref. [290].

A.3 Lagrangian Correlators

The goal of this section is to provide a *definitive* list of all the correlators in Lagrangian space required to compute various two-point functions within LPT, as discussed in both the Introduction and the body of the dissertation, correcting for various typos that have accumulated in the literature over time. Following [58] we use the notation

$$C^{n_1n_2(m_1m_2\ldots)}_{i_1i_2\ldots}=\langle\delta_1^{n_1}\delta_2^{n_2}\Delta^{(m_1)}_{i_1}\Delta^{(m_2)}_{i_2}\ldots\rangle \tag{A.8}$$

where the numbers in parentheses denote the order of the Lagrangian solution and the ellipsis denotes further powers of Δ. The same quantities with parentheses omitted imply the sums to all orders, e.g. $C^{00}_{ij}=C^{00(11)}_{ij}+C^{00(22)}_{ij}+C^{00(13)}_{ij}+C^{00(31)}_{ij}+\ldots$ to quadratic order.

In the below we will sometimes make use of the notation

$$\xi_n^\ell(r) = \int \frac{dk}{2\pi^2}\, k^{2+n} j_\ell(kr) P_{\rm lin}(r) \tag{A.9}$$

for generalized linear correlation functions as defined in ref. [320]. In addition, in the below we will express many integrals in the form of PT kernels $R_n(k)$ and $Q_n(k)$. These were originally defined in ref. [229] to describe correlators between Lagrangian bias operators $O_i(\mathbf{q})$ and displacements $\Psi^{(m)}$) and can be inferred from the definitions below; readers interested in further details should consult that authoritative work. Expressions for these kernels in terms of the above generalized correlation functions can be found in Appendix B.5.

A.3.1 Linear Correlators

At linear order we have the correlators

$$\begin{aligned} A_{ij}^{\rm lin}(\mathbf{q}) &= \langle \Delta_i^{(1)} \Delta_j^{(1)} \rangle = X^{\rm lin}(q)\delta_{ij} + Y^{\rm lin}\hat{q}_i\hat{q}_j \\ U_i^{\rm lin}(\mathbf{q}) &= \langle \delta_1 \Delta_i^{(1)} \rangle = U^{\rm lin}(q)\hat{q}_i \\ \xi_{\rm lin}(q) &= \langle \delta_1 \delta_2 \rangle . \end{aligned} \tag{A.10}$$

The scalar components are given by

$$\begin{aligned} X^{\rm lin}(q) &= \frac{2}{3}\int \frac{dk}{2\pi^2}\Big[\, 1 - \Big(j_0(kq) + j_2(kq)\Big) P_{\rm lin}(k)\Big] \\ Y^{\rm lin}(q) &= 2\int \frac{dk}{2\pi^2}\, j_2(kq) P_{\rm lin}(k) \\ U^{\rm lin}(q) &= -\int \frac{dk\; k}{2\pi^2}\, j_1(kq) P_{\rm lin}(k) \\ \xi_{\rm lin}(q) &= \int \frac{dk\; k\; k^2}{2\pi^2}\, j_0(kq) P_{\rm lin}(k). \end{aligned} \tag{A.11}$$

A.3.2 1-loop Terms

At next to leading order there are many terms, which we now list:

1. **Matter Terms:**
   - $A_{ij}^{\text{1-loop}} = A_{ij}^{(22)} + A_{ij}^{(13)} + A_{ij}^{(31)}$

Defining as usual $A_{ij} = X\delta_{ij} + Y\hat{q}_i\hat{q}_j$:

$$X^{(22)} = \int \frac{dk}{2\pi^2}\ \frac{9}{98}Q_1(k)\Big(\frac{2}{3} - \frac{2}{3}(j_0(kq) + j_2(kq))\Big)$$
$$Y^{(22)} = \int \frac{dk}{2\pi^2}\ \frac{9}{98}Q_1(k)\ 2j_2(kq)$$
$$X^{(13)} = \int \frac{dk}{2\pi^2}\ \frac{5}{21}R_1(k)\Big(\frac{2}{3} - \frac{2}{3}(j_0(kq) + j_2(kq))\Big)$$
$$Y^{(13)} = \int \frac{dk}{2\pi^2}\ \frac{5}{21}Q_1(k)\ 2j_2(kq)$$

- $W_{ijk} = W^{(112)}_{ijk} + (211) + (121)$
  Defining $W^{(112)}_{ijk} = V_1(\hat{q}_i\delta_{jk} + \hat{q}_j\delta_{ik}) + V_3\hat{q}_k\delta_{ij} + T\hat{q}_i\hat{q}_j\hat{q}_k$, we have[2]

$$V_1 = \int \frac{dk}{2\pi^2}\ k^{-1}\ \Big(-\frac{3}{7}R_1(k)\Big)j_1(kq) + S(q)$$
$$V_3 = \int \frac{dk}{2\pi^2}\ k^{-1}\ \Big(-\frac{3}{7}Q_1(k)\Big)j_1(kq) + S(q)$$
$$S = \int \frac{dk}{2\pi^2}\ k^{-1}\ \frac{3}{7}\Big(2R_1 + 4R_2 + Q_1 + 2Q_2\Big)\frac{j_2(kq)}{kq}$$
$$T = \int \frac{dk}{2\pi^2}\ k^{-1}\ -\frac{3}{7}\Big(2R_1 + 4R_2 + Q_1 + 2Q_2\Big)j_3(kq).$$

  The above form can be rewritten using the identity $j_1(x) + j_3(x) = 5j_2(x)/x$ to get

$$V_1 = \int \frac{dk}{2\pi^2}\ k^{-1}\ \frac{3}{35}\Big(-3R_1 + 4R_2 + Q_1 + 2Q_2\Big)j_1(kq) - \frac{T}{5}$$
$$V_3 = \int \frac{dk}{2\pi^2}\ k^{-1}\ \frac{3}{35}\Big(2R_1 + 4R_2 - 4Q_1 + 2Q_2\Big)j_1(kq) - \frac{T}{5}$$

  This is empirically more numerically stable and avoids large cancellations at low k. Summing up the components we have

$$W_{ijk} = \frac{1}{3}\tilde{V}(q)(\hat{q}_i\delta_{jk} + \hat{q}_j\delta_{ik} + \hat{q}_k\delta_{ij}) + \tilde{T}(q)\hat{q}_i\hat{q}_j\hat{q}_k \tag{A.12}$$

  where we have defined $\tilde{V}(q) = 3(2V_1 + V_3)$ and $\tilde{T}(q) = 3T$.

2. **Density Bias Terms**

- $U^{(3)}_i = \langle\delta_1\Delta^{(3)}_i\rangle$:
  Defining as usual $U_i = U\hat{q}_i$, we have

$$U^{(3)} = \int \frac{dk}{2\pi^2}\ k\Big(-\frac{5}{21}R_1 j_1(kq)\Big)$$

[2]Note that the corresponding expression in [58] has a typo and omits the $S(q)$ terms in the first two lines.

- $A^{10}_{ij} = A^{10(12)}_{ij} + A^{10(21)}_{ij}$

$$X^{10(12)} = \int \frac{dk}{2\pi^2}\ \frac{1}{14}\Big(2(R_1 - R_2) - (4R_2 + 2Q_5)j_0(kq) - (3R_1 + 4R_2 + 2Q_5)j_2(kq)\Big)$$
$$Y^{10(12)} = \int \frac{dk}{2\pi^2}\ \frac{3}{14}\Big((3R_1 + 4R_2 + 2Q_5)j_2(kq)\Big)$$

- $U^{11}_i = U^{11(2)}_i$ and $U^{20}_i = U^{20(2)}_i$
  Note that the parentheses (2) here is redundant.

$$U^{11} = \int \frac{dk}{2\pi^2}\ k\Big(-\frac{6}{7}(R_1 + R_2)\ j_1(kq)\Big)$$
$$U^{20} = \int \frac{dk}{2\pi^2}\ k\Big(-\frac{3}{7}Q_8(k)\ j_1(kq)\Big)$$

3. **Shear Terms**
   In fact there is only one (connected) one loop shear term which is given by[3]

$$V^{10}_i(\mathbf{q}) = \langle s_1^2 \Delta_i \rangle = -\frac{1}{7}\hat{q}_i \int \frac{dk}{2\pi^2}\ k\ Q_{s^2}(k) j_1(kq). \tag{A.13}$$

However for convenience we also include the following "disconnected" two point functions at second order in the power spectrum

$$\Upsilon_{ij} = \left\langle s_1^2 \Delta_i \Delta_j \right\rangle = X_{s^2}(q)\delta_{ij} + Y_{s^2}(q)\hat{q}_i\hat{q}_j$$
$$V^{12}_i = \left\langle \delta_1 s_2^2 \Delta_i \right\rangle = V^{12}(q)\hat{q}_i$$
$$\chi(q) = \left\langle \delta_1^2 s_2^2 \right\rangle, \quad \zeta(q) = \left\langle s_1^2 s_2^2 \right\rangle$$

where the scalar components are given by [396]

$$X_{s^2} = 4\mathcal{J}_3^2, \quad Y_{s^2} = 6\mathcal{J}_2^2 + 8\mathcal{J}_2\mathcal{J}_3 + 4\mathcal{J}_2\mathcal{J}_4 + 4\mathcal{J}_3^2 + 8\mathcal{J}_3\mathcal{J}_4 + 2\mathcal{J}_4^2$$
$$V^{12} = 4\mathcal{J}_2\xi^2_0, \quad \chi = \frac{4}{3}(\xi^2_0)^2, \quad \zeta = \frac{8}{45}(\xi^0_0)^2 + \frac{16}{63}(\xi^2_0)^2 + \frac{16}{35}(\xi^4_0)^2$$

with

$$\mathcal{J}_2 = \frac{2}{15}\xi^1_{-1} - \frac{1}{5}\xi^3_{-1} \quad \mathcal{J}_3 = -\frac{1}{5}\xi^1_{-1} - \frac{1}{5}\xi^3_{-1}, \quad \mathcal{J}_4 = \xi^3_{-1}. \tag{A.14}$$

Whew! Hopefully this is all correct!

[3]Note that this is different by a factor of two from [396].

Appendix B

Redshift-Space Galaxy Clustering I

B.1 Lagrangian Time Derivative Correlators

In this section we offer a hopefully comprehensive list of Lagrangian correlators involving displacement time derivatives that appear in the first five pairwise velocity moments and are therefore necessary to compute the 1-loop redshift-space power spectrum. These correlators are denoted with dots ($\dot{}$), where the number of dots is equal to the number of velocities $\dot{\Psi}$. Many of these expressions have previously appeared in refs. [405, 396], but we include this appendix here for completeness and to correct for typos, hopefully without introducing new ones.

B.1.1 Terms Linear in the Pairwise Velocity

1. **Matter Terms**

   - Defining, $\dot{A}_{ij} = \left\langle \Delta_i \dot{\Delta}_j \right\rangle = (11) + 2(22) + 3(13) + (31)$, we have:
     $\dot{A}_{ij} = \dot{X}\delta_{ij} + \dot{Y}\hat{q}_i\hat{q}_j$, i.e. $f^{-1}\dot{X} = X^{\rm lin} + 2X^{22} + 4X^{31}$ and similarly for $\dot{Y}$.
   - $\dot{W}_{ijk} = \left\langle \Delta_i\Delta_j\dot{\Delta}_k \right\rangle = 2(112) + (121) + (211)$:
     Here instead of writing result explicitly we will only comment on the relevant contraction(s), which is in this case given by $\hat{k}_i\hat{k}_j\hat{k}_k\dot{W}_{ijk} = \frac{4f}{3}\hat{k}_i\hat{k}_j\hat{k}_kW_{ijk}$ by symmetry.

2. **Density Bias Terms**

   - $\dot{A}^{10}_{ij} = \left\langle \delta_1\Delta_i\dot{\Delta}_j \right\rangle = 2(12) + (21) = \frac{3}{2}fA^{10}_{ij}$
   - $\dot{U}_i = \left\langle \delta_1\dot{\Delta}_i \right\rangle = (1) + 3(13) = f\ U^{\rm lin}_i + 3f\ U^{(3)}_i$
   - $\dot{U}^{(11)} = \left\langle \delta_1\delta_2\dot{\Delta} \right\rangle = 2(2) = 2f\ U^{11}$
   - $\dot{U}^{(20)} = \left\langle \delta^2_1\dot{\Delta} \right\rangle = 2(2) = 2f\ U^{20}$

3. **Shear Bias Terms**
   - $\dot{V}_i^{10} = \left\langle s_1^2 \dot{\Delta}_i \right\rangle = 2(2) = 2fV_i^{10}$
   - The other contributions are all linear-theory at one loop order, e.g. $\left\langle s_1^2 \delta_2 \dot{\Delta}_i \right\rangle = f \left\langle s_1^2 \delta_2 \dot{\Delta}_i \right\rangle$ and $\left\langle s_1^2 \Delta_i \dot{\Delta}_j \right\rangle = f \langle s_1^2 \Delta_i \Delta_j \rangle$.

B.1.2 Terms Quadratic in the Pairwise Velocity

There are way fewer terms at quadratic order.

1. **Matter Terms**
   - $\ddot{A}_{ij} = \left\langle \dot{\Delta}_i \dot{\Delta}_j \right\rangle = (11) + 4(22) + 3(13) + 3(31)$, i.e. $f^{-2}\ddot{X} = X^{\rm lin} + 4X^{22} + 6X^{13}$.
   - $\ddot{W}_{ijk} = \left\langle \Delta_i \dot{\Delta}_j \dot{\Delta}_k \right\rangle = 2(112) + 2(121) + (211)$.[1]
     As in the previous subsection we will focus on the various contractions, of which there are two:
     a) $f^{-2}\hat{k}_i\hat{k}_j\hat{k}_k\ddot{W}_{ijk} = \frac{5}{3}\hat{k}_i\hat{k}_j\hat{k}_k W_{ijk}$ by symmetry.
     b) $f^{-2}\hat{k}_i\delta_{jk}\ddot{W}_{ijk} = (18V_1 + 7V_3 + 5T)\mu$

     Note that there is in principle a third contraction $\hat{k}_k\delta_{ij}$ but it does not appear in any quantities of interest.

2. **Density Bias Terms**
   The only nontrivial one is $\ddot{A}_{ij}^{10} = \left\langle \delta_1 \dot{\Delta}_i \dot{\Delta}_j \right\rangle = 2(12) + 2(21) = 2f^2 A_{ij}^{10}$.

3. **Shear Bias Terms** The only contribution here is the trivial $\ddot{\Upsilon}_{ij} = f^2\Upsilon_{ij}$, where the velocities can only enter at lowest order at one loop.

B.1.3 Terms Cubic in the Pairwise Velocity

Here we will only look at one term

$$\dddot{W}_{ijk} = 2(112) + 2(121) + 2(211) = 2f^3 W_{ijk}. \tag{B.1}$$

The relevant contractions are

$$\hat{k}_i\hat{k}_j\hat{k}_k\dddot{W}_{ijk} = 2f^3\big(\tilde{V}\mu + \tilde{T}\mu^3\big), \quad \hat{k}_i\delta_{jk}\dddot{W}_{ijk} = 2f^3\Big(\frac{5}{3}\tilde{V} + \tilde{T}\Big)\mu. \tag{B.2}$$

Equivalently we can define $\dddot{V} = 2f^3\tilde{V}$ and identically for $\dddot{T}$.

[1] Note that the expression in [396] is wrong–the indices should not be permuted along with the orders.

B.2 Velocity moments and RSD power spectrum in Eulerian PT

B.2.1 Third-Order Bias Expansion in EPT and LPT

In this chapter we extend the expressions for the real-space power and pairwise-velocity spectra found in [396] to include contributions from third-order bias operators. In principle, going to third order in bias requires an additional four bias parameters (see e.g. [109]), however as shown in [234] for EPT at one-loop order many of these contributions are either zero or amount to re-definitions of the linear bias parameter b_1. The remaining contributions are all degenerate and can be combined into a single (EPT or LPT) third-order bias parameter c_3 or b_3. In this subsection we will review the bias expansion in EPT and provide details for including the effects of third-order bias in LPT predictions of the velocity moments.

In order to evaluate these velocity moment correlators in Eulerian PT we adopt the biasing scheme of ref. [234] in Equation 2.17 up to third order, which we repeat here for convenience:

$$\delta_h = c_1\delta + \frac{c_2}{2}\delta^2 + c_s s^2 + \frac{c_3}{6}\delta^3 + c_{1s}\delta s^2 + c_{st} st + c_{s3} s^3 + c_\psi \psi, \tag{B.3}$$

where $s^2 = s_{ij}s_{ij}$, $s^3 = s_{ij}s_{jl}s_{li}$ and $st = s_{ij}t_{ij}$, and the shear operators are defined as

$$\psi = \eta - \frac{2}{7}s^2 + \frac{4}{21}\delta^2, \quad s_{ij} = \left(\frac{\partial_i\partial_j}{\partial^2} - \frac{1}{3}\delta_{ij}\right)\delta, \quad t_{ij} = \left(\frac{\partial_i\partial_j}{\partial^2} - \frac{1}{3}\delta_{ij}\right)\eta, \quad \eta = \theta - \delta. \tag{B.4}$$

As usual we assume subtraction of mean field values like $\langle\delta^2\rangle$. In Fourier space, the second and third order shear operators are given by the kernels in momentum space

$$\begin{aligned}
S_2^{(2)}(\mathbf{k}_1,\mathbf{k}_2) &= \frac{(\mathbf{k}_1\cdot\mathbf{k}_2)^2}{k_1^2k_2^2} - \frac{1}{3}, \qquad\qquad (B.5)\\
S_2^{(3)}(\mathbf{k}_1,\mathbf{k}_2,\mathbf{k}_3) &= 2S_2\left(\mathbf{k}_1,\mathbf{k}_2+\mathbf{k}_3\right)F_2\left(\mathbf{k}_2,\mathbf{k}_3\right),\\
S_3^{(3)}(\mathbf{k}_1,\mathbf{k}_2,\mathbf{k}_3) &= \frac{(\mathbf{k}_1\cdot\mathbf{k}_2)(\mathbf{k}_2\cdot\mathbf{k}_3)(\mathbf{k}_3\cdot\mathbf{k}_1)}{k_1^2k_2^2k_3^2} - \frac{(\mathbf{k}_1\cdot\mathbf{k}_2)^2}{3k_1^2k_2^2} - \frac{(\mathbf{k}_1\cdot\mathbf{k}_3)^2}{3k_1^2k_3^2} - \frac{(\mathbf{k}_3\cdot\mathbf{k}_2)^2}{3k_3^2k_2^2} + \frac{2}{9},\\
S_{st}^{(3)}(\mathbf{k}_1,\mathbf{k}_2,\mathbf{k}_3) &= \frac{2}{7}S_2\left(\mathbf{k}_1,\mathbf{k}_2+\mathbf{k}_3\right)\left[S_2\left(\mathbf{k}_2,\mathbf{k}_3\right) - \frac{2}{3}\right],\\
S_\psi^{(3)}(\mathbf{k}_1,\mathbf{k}_2,\mathbf{k}_3) &= G_3\left(\mathbf{k}_1,\mathbf{k}_2,\mathbf{k}_3\right) - F_3\left(\mathbf{k}_1,\mathbf{k}_2,\mathbf{k}_3\right) - \frac{4}{7}\left(S_2\left(\mathbf{k}_1,\mathbf{k}_2+\mathbf{k}_3\right) - \frac{2}{3}\right)F_2\left(\mathbf{k}_2,\mathbf{k}_3\right).
\end{aligned}$$

Given that in this chapter we are interested only in two-point statistics, many of the third order bias operators listed above do contribute to the one-loop power spectrum in degenerate manner. After shot-noise renormalization only one non-vanishing independent contribution

remains. The relevant correlators in one-loop EPT for the real-space power spectrum are:

$$\begin{aligned}
\left\langle \delta_{\rm lin}|\left[\delta s^2\right]^{(3)}\right\rangle' &= \left\langle \delta_{\rm lin}|[s^3]^{(3)}\right\rangle' = 0, \\
\left\langle \delta_{\rm lin}|[\delta^2]^{(3)}\right\rangle' &= \frac{68}{21}\left\langle \delta^2_{\rm lin}\right\rangle P_{\rm L}(k), \\
\left\langle \delta_{\rm lin}|\psi^{(3)}\right\rangle' &= 3P_{\rm lin}(k)\int_{\mathbf{p}} S_\psi(\mathbf{p},-\mathbf{p},\mathbf{k})P_{\rm lin}(p), \\
&= \frac{16}{21}\left(\left\langle \delta_{\rm lin}|[st]^{(3)}\right\rangle' + \frac{16}{63}\left\langle \delta^2_{\rm lin}\right\rangle' P_{\rm L}\right) \\
&= -\frac{16}{105}\left(\left\langle \delta_{\rm lin}|(s^2)^{(3)}\right\rangle' - \frac{136}{63}\left\langle \delta^2_{\rm lin}\right\rangle' P_{\rm L}\right),
\end{aligned} \tag{B.6}$$

The corresponding contributions to the pairwise velocity, due to the correlator $\langle\delta_h|v_i\rangle$ can be obtained by simply multiplying these terms by $\frac{ik_i}{k^2}$.

The above degeneracies also exist in one-loop LPT. In particular, for two third-order EPT operators $O_3(\mathbf{x})$ and $O_3'(\mathbf{x})$ such that $\langle\delta_{\rm lin}|O_3\rangle = \langle\delta_{\rm lin}|O_3' + A\left\langle\delta^2_{\rm lin}\right\rangle\delta_{\rm lin}\rangle$ at one-loop, we also have the degeneracies

$$\begin{aligned}
\langle O_3(\mathbf{q}_1)\Delta_i\rangle &= \langle O_3'(\mathbf{q}_1)\Delta_i\rangle + A\left\langle\delta^2_{\rm lin}\right\rangle U_i^{\rm lin}(\mathbf{q}), \\
\langle O_3(\mathbf{q}_1)\delta_{\rm lin}(\mathbf{q}_2)\rangle &= \langle O_3'(\mathbf{q}_1)\delta_{\rm lin}(\mathbf{q}_2)\rangle + A\left\langle\delta^2_{\rm lin}\right\rangle\xi_{\rm lin}(q)
\end{aligned} \tag{B.7}$$

in one-loop LPT. In the main body of the chapter we will thus summarize these contributions with the third-order parameter $O_3(\mathbf{q}) = s_{ij}(\mathbf{q})t_{ij}(\mathbf{q}) + \frac{16}{63}\left\langle\delta^2_{\rm lin}\right\rangle$. This introduces the additional correlators

$$\begin{aligned}
U_{b_3,i}(\mathbf{q}) = U_{b_3}(q)\ \hat{q}_i &= \langle O_3(\mathbf{q}_1)\Delta_i\rangle = -\int\frac{dk\ k}{2\pi^2}R_{b_3}(k)j_1(kq) \\
\theta(\mathbf{q}) &= \langle O_3(\mathbf{q}_1)\delta_{\rm lin}(\mathbf{q}_2)\rangle = \int\frac{dk\ k^2}{2\pi^2}R_{b_3}(k)j_0(kq).
\end{aligned} \tag{B.8}$$

An explicit formula for R_{b_3} expressed as a Hankel transform is given in Appendix B.6. Finally, the expression for the pairwise velocity spectrum requires the time derivative of U_{b_3}, which is given by $\dot{U}_{b_3} = \left\langle O_3\dot{\Delta}\right\rangle = fU_{b_3}$.

B.2.2 Eulerian moment expansion

In this section we give a short overview of the Eulerian moment expansion framework for RSD based on the distribution function model [328, 400, 401], using one-loop, Eulerian effective PT to compute the components. These results, after including IR-resummation, are equvivalent to those recently used in refs. [96, 186].

The velocity moments are combined to give the RSD power spectrum as in Eq. (2.5). Up to one-loop we need to consider the contributions of several velocity moments

$$\begin{aligned}
\tilde{\Xi}^{(0)}_{\hat{n}}(\mathbf{k}) &= P_{00}(k), \\
\tilde{\Xi}^{(1)}_{\hat{n}}(\mathbf{k}) &= P_{01}(k,\mu) - P^*_{01}(k,\mu) \\
&= 2i\mathrm{Im}[P_{01}(k,\mu)], \\
\tilde{\Xi}^{(2)}_{\hat{n}}(\mathbf{k}) &= P_{02}(k,\mu) - 2P_{11}(k,\mu) + P^*_{02}(k,\mu) \\
&= 2\mathrm{Re}[P_{02}(k,\mu) - P_{11}(k,\mu)], \\
\tilde{\Xi}^{(3)}_{\hat{n}}(\mathbf{k}) &= P_{03}(k,\mu) - 3P_{12}(k,\mu) + 3P^*_{12}(k,\mu) - P^*_{03}(k,\mu) \\
&= 2i\mathrm{Im}[P_{03}(k,\mu) - 3P_{12}(k,\mu)], \\
\tilde{\Xi}^{(4)}_{\hat{n}}(\mathbf{k}) &= P_{04}(k,\mu) - 4P_{13}(k,\mu) + 6P_{22}(k,\mu) - 4P^*_{13}(k,\mu) + P^*_{04}(k,\mu) \\
&= 2\mathrm{Re}[P_{04}(k,\mu) - 4P_{13}(k,\mu) + 3P_{22}(k,\mu)].
\end{aligned} \tag{B.9}$$

where the component spectra $P_{LL'}$ are the cross-correlations of different velocity moments

$$P_{LL'}(k,\mu) \equiv \left\langle \big(1+\delta\big) * u^L_{\hat{n}} \middle| \big(1+\delta\big) * u^{L'}_{\hat{n}} \right\rangle' \equiv \left\langle \big(1+\delta(\mathbf{k})\big) * u^L_{\hat{n}}(\mathbf{k}) \ \big(1+\delta(\mathbf{k}')\big) * u^{L'}_{\hat{n}}(\mathbf{k}') \right\rangle', \tag{B.10}$$

where, for brevity, we introduce the primed expectation values to denote expectation values with Dirac delta function dropped, i.e. $\langle A|B\rangle \equiv \langle A(\mathbf{k})B(\mathbf{k}')\rangle = (2\pi)^3\delta_D(\mathbf{k}+\mathbf{k}')\ \langle A(\mathbf{k})B(\mathbf{k}')\rangle'$.

Note that $P_{LL'} = P^*_{L'L}$, so, without loss of generality, we can assume $L \le L'$. See ref. [398] for a more detailed connection between the moment expansion and streaming models.

Contributions to $\Xi^{(0)}$ arise from only P_{00}. This is the usual real space halo-halo power spectrum. We have

$$\begin{aligned}
\langle \delta_h|\delta_h\rangle' = {} & c_1^2 P_{\rm lin}(k) + 2c_1^2 \int_{\mathbf{p}} \left(\big[F_2(\mathbf{p},\mathbf{k}-\mathbf{p})\big]^2 P_{\rm lin}(|\mathbf{k}-\mathbf{p}|) + 3F_3(\mathbf{p},-\mathbf{p},\mathbf{k}) P_{\rm lin}(k) \right) P_{\rm lin}(p) \\
& + 2c_1c_2 \int_{\mathbf{p}} F_2(\mathbf{p},\mathbf{k}-\mathbf{p}) P_{\rm lin}(p) P_{\rm lin}(|\mathbf{k}-\mathbf{p}|) \\
& + 4c_1c_s \int_{\mathbf{p}} F_2(\mathbf{p},\mathbf{k}-\mathbf{p}) S_2(\mathbf{p},\mathbf{k}-\mathbf{p}) P_{\rm lin}(p) P_{\rm lin}(|\mathbf{k}-\mathbf{p}|) \\
& + \frac{c_2^2}{2} \int_{\mathbf{p}} P_{\rm lin}(p) P_{\rm lin}(|\mathbf{k}-\mathbf{p}|) \\
& + 2c_2c_s \int_{\mathbf{p}} S_2(\mathbf{p},\mathbf{k}-\mathbf{p}) P_{\rm lin}(p) P_{\rm lin}(|\mathbf{k}-\mathbf{p}|) \\
& + 2c_s^2 \int_{\mathbf{p}} \big[S_2(\mathbf{p},\mathbf{k}-\mathbf{p})\big]^2 P_{\rm lin}(p) P_{\rm lin}(|\mathbf{k}-\mathbf{p}|) \\
& + 6c_1c_3 P_{\rm lin}(k) \int_{\mathbf{p}} S_\psi(\mathbf{p},-\mathbf{p},\mathbf{k}) P_{\rm lin}(p) \qquad \text{(in EPT)}
\end{aligned} \tag{B.11}$$

where the third-order bias operators can be combined into a single term with the coefficient c_3. Counter terms that are required to regularise the one loop $\Xi^{(0)}$ terms are of form $(k^2/k_\star^2)P_{\rm lin}(k)$ ($k_\star$ is a characteristic proto-halo size scale) and thus degenerate with the derivative bias contribution. Besides these there is a constant shot noise contributions obtained by correlating the stochastic component of the halo density field $\epsilon_h(\mathbf{k})$, and we neglect the higher derivative stochastic terms. Thus the total $\Xi^{(0)}$ expression reads

$$\tilde{\Xi}^{(0)}_{\text{1-loop}}(k) = (\text{B.11}) + c_0^{(0)}\frac{k^2}{k_*^2}P_{\rm lin}(k) + s_0 + \ldots, \tag{B.12}$$

where $s_0 = \langle\epsilon_h|\epsilon_h\rangle'$, and $c_0^{(0)}$ is the leading derivative counterterm. In general, for counterterms we will use the notation $c_m^{(\ell)}$ taking into account that different angular dependences can have different counterterm contributions.

Contributions to $\Xi^{(1)}$ arise from only the P_{01} term. This gives us

$$\big\langle\delta_h|(1+\delta_h)*v_\parallel\big\rangle' \approx \big\langle\delta_h|v_\parallel\big\rangle' + \big\langle\delta_h|\delta_h*v_\parallel\big\rangle', \tag{B.13}$$

where in one-loop EPT we have

$$\begin{aligned}\big\langle\delta_h|v_\parallel\big\rangle' \approx -i\frac{\mu}{k}\Bigg(& c_1P_{\rm lin}(k) + 2c_1\int_{\mathbf{p}} F_2(\mathbf{p},\mathbf{k}-\mathbf{p})G_2(\mathbf{p},\mathbf{k}-\mathbf{p})P_{\rm lin}(p)P_{\rm lin}(|\mathbf{k}-\mathbf{p}|) \\ &+ 3c_1P_{\rm lin}(k)\int_{\mathbf{p}}\Big[F_3(\mathbf{p},-\mathbf{p},\mathbf{k}) + G_3(\mathbf{p},-\mathbf{p},\mathbf{k})\Big]P_{\rm lin}(p) \\ &+ c_2\int_{\mathbf{p}} G_2(\mathbf{p},\mathbf{k}-\mathbf{p})P_{\rm lin}(p)P_{\rm lin}(|\mathbf{k}-\mathbf{p}|) \\ &+ 2c_s\int_{\mathbf{p}} S_2(\mathbf{p},\mathbf{k}-\mathbf{p})G_2(\mathbf{p},\mathbf{k}-\mathbf{p})P_{\rm lin}(p)P_{\rm lin}(|\mathbf{k}-\mathbf{p}|) \\ &+ 3c_3P_{\rm lin}(k)\int_{\mathbf{p}} S_\psi(\mathbf{p},-\mathbf{p},\mathbf{k})P_{\rm lin}(p)\Bigg), \qquad \text{(in EPT)}\end{aligned} \tag{B.14}$$

and

$$\begin{aligned}\big\langle\delta_h|\delta_h*v_\parallel\big\rangle' \approx -2i\Bigg(& c_1^2\int_{\mathbf{p}}\frac{p_\parallel}{p^2}F_2(\mathbf{p},\mathbf{k}-\mathbf{p})P_{\rm lin}(p)P_{\rm lin}(|\mathbf{k}-\mathbf{p}|) \\ &+ c_1^2P_{\rm lin}(k)\int_{\mathbf{p}}\left[\frac{p_\parallel}{p^2}F_2(\mathbf{p},-\mathbf{k}) + \frac{(\mathbf{k}-\mathbf{p})_\parallel}{(\mathbf{k}-\mathbf{p})^2}G_2(\mathbf{p},-\mathbf{k})\right]P_{\rm lin}(p) \\ &+ c_1c_2\frac{1}{2}\int_{\mathbf{p}}\frac{p_\parallel}{p^2}P_{\rm lin}(p)P_{\rm lin}(|\mathbf{k}-\mathbf{p}|) \\ &+ c_1c_s\int_{\mathbf{p}}\frac{p_\parallel}{p^2}S_2(\mathbf{p},\mathbf{k}-\mathbf{p})P_{\rm lin}(p)P_{\rm lin}(|\mathbf{k}-\mathbf{p}|),\Bigg). \qquad \text{(in EPT)}\end{aligned} \tag{B.15}$$

Note that, due to the angular symmetry, c_2 and c_s do not contribute to the tadpole diagrams, i.e. to the P_{13}-like terms.

Counter terms that are needed to regularise the one-loop $\Xi^{(1)}$ terms scale as $\mu(k^2/k_\star^2)P_{\rm lin}(k)$ and are again degenerate with the derivative bias contribution. Collecting all the contributions to $\Xi^{(1)}$ we have

$$\tilde{\Xi}^{(1)}_{\text{1-loop}}(k) = 2\left[(\text{B.14}) + (\text{B.15})\right] - ic_1^{(0)}\frac{\mu k}{k_\star^2}P_{\rm lin}(k) + \dots . \tag{B.16}$$

Contributions to $\Xi^{(2)}$ arise from two correlators P_{02} and P_{11}. P_{02} starts to contribute at one-loop order, while P_{11} also has a linear contribution. We can write for the former

$$\begin{aligned}
\left\langle \delta_h|(1+\delta_h)*v_\parallel^2\right\rangle' &\approx \left\langle \delta_h|v_\parallel^2\right\rangle' + \left\langle \delta_h|\delta_h\right\rangle'\left\langle v_\parallel^2\right\rangle, \qquad \text{(B.17)}\\
&= -2c_1\int_{\mathbf{p}}\frac{p_\parallel(\mathbf{k}-\mathbf{p})_\parallel}{p^2(\mathbf{k}-\mathbf{p})^2}F_2(\mathbf{p},\mathbf{k}-\mathbf{p})P_{\rm lin}(p)P_{\rm lin}(|\mathbf{k}-\mathbf{p}|)\\
&\quad - 4c_1P_{\rm lin}(k)\int_{\mathbf{p}}\frac{p_\parallel(\mathbf{k}-\mathbf{p})_\parallel}{p^2(\mathbf{k}-\mathbf{p})^2}G_2(\mathbf{p},-\mathbf{k})P_{\rm lin}(p)\\
&\quad - c_2\int_{\mathbf{p}}\frac{p_\parallel(\mathbf{k}-\mathbf{p})_\parallel}{p^2(\mathbf{k}-\mathbf{p})^2}P_{\rm lin}(p)P_{\rm lin}(|\mathbf{k}-\mathbf{p}|)\\
&\quad - 2c_s\int_{\mathbf{p}}\frac{p_\parallel(\mathbf{k}-\mathbf{p})_\parallel}{p^2(\mathbf{k}-\mathbf{p})^2}S_2(\mathbf{p},\mathbf{k}-\mathbf{p})P_{\rm lin}(p)P_{\rm lin}(|\mathbf{k}-\mathbf{p}|)\\
&\quad + c_1^2P_{\rm lin}(k)\sigma^2_{\rm lin}, \qquad \text{(in EPT)}
\end{aligned}$$

and for the latter

$$\begin{aligned}
\left\langle (1+\delta_h)*v_\parallel|(1+\delta_h)*v_\parallel\right\rangle' &\approx \left\langle v_\parallel|v_\parallel\right\rangle' + 2\left\langle v_\parallel|\delta_h v_\parallel\right\rangle' + \left\langle \delta_h v_\parallel|\delta_h v_\parallel\right\rangle' \qquad \text{(B.18)}\\
&= \frac{\mu^2}{k^2}\Bigg(P_{\rm lin} + 2\int_{\mathbf{p}}\left[G_2(\mathbf{p},\mathbf{k}-\mathbf{p})\right]^2P_{\rm lin}(p)P_{\rm lin}(|\mathbf{k}-\mathbf{p}|)\\
&\qquad\qquad + 6P_{\rm lin}(k)\int_{\mathbf{p}}G_3(\mathbf{p},-\mathbf{p},\mathbf{k})P_{\rm lin}(p)\Bigg)\\
&\quad + 4c_1\frac{\mu}{k}\Bigg(\int_{\mathbf{p}}\frac{p_\parallel}{p^2}G_2(\mathbf{p},\mathbf{k}-\mathbf{p})P_{\rm lin}(p)P_{\rm lin}(|\mathbf{k}-\mathbf{p}|)\\
&\quad + P_{\rm lin}(k)\int_{\mathbf{p}}\left[\frac{(\mathbf{k}-\mathbf{p})_\parallel}{(\mathbf{k}-\mathbf{p})^2}G_2(-\mathbf{p},\mathbf{k}) + \frac{p_\parallel}{p^2}F_2(-\mathbf{p},\mathbf{k})\right]P_{\rm lin}(p)\Bigg)\\
&\quad + c_1^2\int_{\mathbf{p}}\frac{p_\parallel}{p^2}\left(\frac{p_\parallel}{p^2} + \frac{(\mathbf{k}-\mathbf{p})_\parallel}{(\mathbf{k}-\mathbf{p})^2}\right)P_{\rm lin}(p)P_{\rm lin}(|\mathbf{k}-\mathbf{p}|). \qquad \text{(in EPT)}
\end{aligned}$$

The second contribution in P_{02} (i.e. $\propto c_1^2P_{\rm lin}\sigma^2_{\rm lin}$) and the last term in P_{11} ensure IR cancelation in the soft limit.

A new feature of the $\Xi^{(2)}$ correlator is that it has terms with isotropic angular dependence, μ^0, as well as μ^2 dependence. Both of these have one-loop terms that need to be regularised and thus we have to introduce counterterms of form $(k^2/k_\star^2)P_{\rm lin}(k)$ for each of these two angular dependencies. The contribution to the isotropic angular dependence comes primarily due to the small-scale velocity dispersion contribution in the P_{02} term, i.e. $P_{00}\sigma^2 \ni c_1^2 P_{\rm lin}(k)\sigma^2_{\text{non-lin}}$. Here $\sigma_{\text{non-lin}}$ encapsulates the non-perturbative, small-scale, contribution to the halo velocity dispersion.

In addition to these derivative terms the $\Xi^{(2)}$ correlator contains both isotropic and anisotropic stochastic contribtuions. For example, the UV dependence of the c_2 contribution to P_{02} needs to be renormalized by a constant, isotropic contribution proportional to δ_{ij}. Moreover, $\Xi^{(2)}$ will generically inherit a stochastic contribution via P_{00} in (B.17). We can write

$$\left\langle \delta_h | \delta_h * v_\parallel^2 \right\rangle' \ni \left\langle \epsilon_h | \epsilon_h \right\rangle' \left\langle v_\parallel^2 \right\rangle = s_0 \left(\sigma^2_{\rm lin} + \sigma^2_{\text{non-lin}}\right), \tag{B.19}$$

where, in the last line, we split the halo velocity dispersion into the linear component and the residual non-linear component coming from small-scales. However a similar contribution can be obtained from the last term in P_{11}, where we again have

$$\left\langle \delta_h * v_\parallel | \delta_h * v_\parallel \right\rangle' \ni \text{FT}\Big[\left\langle \epsilon_h | \epsilon_h \right\rangle \left\langle v_\parallel | v_\parallel \right\rangle \Big]' = \left\langle \epsilon_h | \epsilon_h \right\rangle' \left\langle v_\parallel^2 \right\rangle = s_0 \left(\sigma^2_{\rm lin} + \sigma^2_{\text{non-lin}}\right), \tag{B.20}$$

and the two shot noise contributions exactly cancel in the sum. In the more general case, the power spectrum of stochastic field ϵ_h can have some nontrivial scale dependence, i.e. $\langle \epsilon_h | \epsilon_h \rangle' = P_\epsilon(\mathbf{k})$. In that case, the above discussed cancellation is no longer exact and we have

$$\left\langle \delta_h | \delta_h * v_\parallel^2 \right\rangle' - \left\langle \delta_h * v_\parallel | \delta_h * v_\parallel \right\rangle' \ni \int_{\mathbf{p}} \Big(P_\epsilon(\mathbf{k}) - P_\epsilon(\mathbf{k}-\mathbf{p}) \Big) P_{vv}(\mathbf{p}) \approx s_2 + \cdots, \tag{B.21}$$

where $P_{vv}(\mathbf{p}) = \left\langle v_\parallel | v_\parallel \right\rangle'$ is the halo velocity spectrum. It is also instructive to investigate a polynomial scale dependence of the stochastic power spectrum, $P_\epsilon(\mathbf{k}) = a_0 + a_2 k^2 + a_4 k^4 + \ldots$. In that case it follows that the noise contribution takes the simple form

$$\int_{\mathbf{p}} \Big(P_\epsilon(\mathbf{k}) - P_\epsilon(\mathbf{k}-\mathbf{p}) \Big) P_{vv}(\mathbf{p}) \approx s^{(0)}_{2,0}{}'' + s^{(0)}_{2,2} k^2 + s^{(2)}_{2,2} \mu^2 k^2 + \cdots, \tag{B.22}$$

from which it follows that only the isotropic part obtains a shot noise like contribution. Collecting all the contributions we get

$$\tilde{\Xi}^{(2)}_{\text{1-loop}}(k) = 2\big[\text{(B.17)} - \text{(B.18)}\big] - 2\left(c_2^{(0)} + c_2^{(2)}\mu^2\right)\frac{1}{k_\star^2} P_{\rm lin}(k) + s_2 + \ldots. \tag{B.23}$$

Contributions to $\Xi^{(3)}$ arise from two correlators, P_{03} and P_{12}, both of which contribute at one-loop

$$\left\langle \delta_h | (1+\delta_h) * v_\parallel^3 \right\rangle' \approx 3 P_{01}\sigma^2 \tag{B.24}$$

$$= -3i\frac{\mu}{k} c_1 P_{\rm lin}\sigma^2_{\rm lin}, \qquad \text{(in EPT)}$$

$$\begin{aligned}\left\langle (1+\delta_h)*v_\parallel | (1+\delta_h)*v_\parallel^2 \right\rangle' &\approx \left\langle v_\parallel | v_\parallel^2 \right\rangle' + \left\langle v_\parallel | \delta_h v_\parallel^2 \right\rangle' + \left\langle \delta_h v_\parallel | v_\parallel^2 \right\rangle' \qquad \text{(B.25)}\\ &= -\frac{i}{k}\Bigg(2\mu \int_{\mathbf{p}} \frac{p_\parallel(\mathbf{k}-\mathbf{p})_\parallel}{p^2(\mathbf{k}-\mathbf{p})^2} G_2(\mathbf{p},\mathbf{k}-\mathbf{p}) P_{\rm lin}(p) P_{\rm lin}(|\mathbf{k}-\mathbf{p}|)\\ &\quad + 4\mu P_{\rm lin}(k) \int_{\mathbf{p}} \frac{p_\parallel(\mathbf{k}-\mathbf{p})_\parallel}{p^2(\mathbf{k}-\mathbf{p})^2} G_2(\mathbf{p},-\mathbf{k}) P_{\rm lin}(p)\\ &\quad + 2kc_1 \int_{\mathbf{p}} \frac{p_\parallel^2(\mathbf{k}-\mathbf{p})_\parallel}{p^4(\mathbf{k}-\mathbf{p})^2} P_{\rm lin}(p) P_{\rm lin}(\mathbf{k}-\mathbf{p})\\ &\quad - c_1\mu P_{\rm lin}\sigma^2_{\rm lin}\Bigg), \qquad \text{(in EPT)}\end{aligned}$$

The combination of P_{03} and the last two terms of P_{12} ensure IR cancelation in the soft limit. Collecting all the one-loop contributions we get

$$\tilde{\Xi}^{(3)}_{\text{1-loop}}(k) = 2\big[\text{(B.24)} - 3\text{(B.25)}\big] + 6i\left(c_3^{(0)} + c_3^{(2)}\mu^2\right)\frac{\mu}{k}\frac{1}{k_\star^2}P_{\rm lin} + \ldots. \qquad \text{(B.26)}$$

Contributions to $\Xi^{(4)}$ can be approximated by a contribution giving zero lag (which we can consider as a non-perturbative contribution) multiplied by the lower order moments. Heuristically we can write:

$$\begin{aligned}\left\langle \delta_h | (1+\delta_h)*v_\parallel^4 \right\rangle' &\approx 3P_{02}\sigma^2 \approx 3P_{00}\sigma^4 \qquad \text{(B.27)}\\ &= 3c_1^2 P_{\rm lin}\sigma^4_{\rm lin}, \qquad \text{(in EPT)}\\ \left\langle (1+\delta_h)*v_\parallel | (1+\delta_h)*v_\parallel^3 \right\rangle' &\approx 3P_{11}\sigma^2 \qquad \text{(B.28)}\\ &= 3\frac{\mu^2}{k^2}P_{\rm lin}\sigma^2_{\rm lin}, \qquad \text{(in EPT)}\\ \left\langle (1+\delta_h)*v_\parallel^2 | (1+\delta_h)*v_\parallel^2 \right\rangle' &\approx \left\langle v_\parallel^2 | v_\parallel^2 \right\rangle' + P_{00}\sigma^4 \qquad \text{(B.29)}\\ &\approx 2\int_{\mathbf{p}} \left[\frac{p_\parallel(\mathbf{k}-\mathbf{p})_\parallel}{p^2(\mathbf{k}-\mathbf{p})^2}\right]^2 P_{\rm lin}(p) P_{\rm lin}(|\mathbf{k}-\mathbf{p}|)\\ &\quad + c_1^2 P_{\rm lin}\sigma^4_{\rm lin} \qquad \text{(in EPT)}\end{aligned}$$

The only proper one-loop contributions in the fourth moment come from $P_{13} \propto P_{\rm lin}\sigma^2_{\rm lin}$ and $P_{22} \sim \left\langle v_\parallel^2 | v_\parallel^2 \right\rangle'$, terms that also exhibit a degree of IR cancelation in the soft limit in their μ^2 angular dependence. Similar cancelation also appears at the two-loop level for the μ^0 angular dependence where all of the $c_1^2 P_{\rm lin}\sigma^4_{\rm lin}$ terms cancel in the IR limit.

Similarly to the case of $\Xi^{(2)}$, we can show that the scale dependence of the stochasticity field generates a shot-noise contribution in the $\Xi^{(4)}$ term, even though to show these explicitly a two-loop calculation is formally required. However, treatment of the shot noise terms on equal perturbative footing as the deterministic fields might not generally be justified and thus even an indication of the presence of such stochastic terms could serve as a justification

for adding a shot noise contribution. These stochastic terms would be suppressed by $(\mu k)^4$ factors in the total power spectrum.

Collecting all the one-loop contributions we get

$$\tilde{\Xi}^{(4)}_{\text{1-loop}}(k) = 2\big[(\text{B.27}) - 4(\text{B.28}) + 3(\text{B.29})\big] + 24c_4^{(2)}\frac{\mu^2}{k^2}\frac{1}{k_\star^2}P_{\text{lin}}(k) + s_4 + \dots . \tag{B.30}$$

B.2.3 Eulerian redshift-space power spectrum

Using the moment expansion of the redshift-space power spectrum given in Eq. (2.5) we obtain the one-loop result

$$\begin{aligned} P^s_{\text{1-loop}}(\mathbf{k}) &= \tilde{\Xi}^{(0)}(\mathbf{k}) + ik\mu\tilde{\Xi}^{(1)}(\mathbf{k}) - \frac{1}{2}k^2\mu^2\tilde{\Xi}^{(2)}(\mathbf{k}) - \frac{i}{6}k^3\mu^3\tilde{\Xi}^{(3)}(\mathbf{k}) + \frac{1}{24}k^4\mu^4\tilde{\Xi}^{(4)}(\mathbf{k}) \qquad \text{(B.31)} \\ &= \Big[(\text{B.11}) + 2if k\mu\left[(\text{B.14}) + (\text{B.15})\right] - f^2k^2\mu^2\big[(\text{B.17}) - (\text{B.18})\big] \\ &\quad - \frac{i}{3}f^3k^3\mu^3\big[(\text{B.24}) - 3(\text{B.25})\big] + \frac{1}{12}f^4k^4\mu^4\big[(\text{B.27}) - 4(\text{B.28}) + 3(\text{B.29})\big]\Big]_{\text{EPT}} \\ &\quad + \Big(c_0 + fc_1\mu^2 + f^2c_2\mu^4 + f^3c_3\mu^6\Big)\frac{k^2}{k_*^2}P_{\text{lin}}(k) + \left(s_0 + s_1f^2\mu^2\frac{k^2}{k_\star^2} + s_2f^4\mu^4\frac{k^4}{k_\star^4}\right). \end{aligned}$$

The first two lines above refer to the EPT expressions of the given one-loop power spectra, while in the last line counter terms and stochastic contributions are listed. The counter terms are redefined so that $c_0 = c_0^{(0)}$, $c_1 = c_1^{(0)} + fc_2^{(0)}$, $c_2 = c_2^{(2)} + fc_3^{(0)}$ and $c_3 = c_3^{(2)} + fc_4^{(2)}$. This ensures that all the UV sensitive P_{13} terms are under control. In the last line we have also defined the stochastic parameters $s_1 = -\frac{1}{2}k_\star^2\frac{s_2}{s_0}$ and $s_1 = \frac{1}{24}k_\star^4\frac{s_4}{s_0}$. In the result above we have neglected higher derivative contributions to the stochasticity. This result, up to the couple of different choices for the counter terms and stochastic contributions, agree with recent references [96, 186].

B.2.4 IR resummation of Velocity Moments and RSD power spectrum

Eulerian perturbation theory expands density and velocity fields, and correlators thereof, in powers of long wavelength modes that are assumed to be small. However, this assumption does not hold for long displacement modes that can have order one contributions and thus should be resummed, i.e. treated non-perturbatively. Given that in the equal time correlators most of the effects of such long wavelength displacements cancel out standard Eulerian PT is still an operational framework. However, the presence of the BAO feature on fairly large scales makes it more prone to these displacements and thus it is of interest to handle these non-perturbative contributions. The procedure for handling these long modes goes under the name of IR-resummation, and is most naturally done in Lagrangian perturbation theory

[121, 231, 335, 399, 402, 112]. However, in Eulerian perturbation theory results can also be resummed in order to obtain the equivalent behavior [22, 50, 278, 185].

In the Eulerian framework the most pragmatic rendering of these IR-resummation procedures relies on splitting the linear power spectrum into smooth and oscillatory parts, $P_{\rm lin}(k) = P^{\rm nw}_{\rm lin} + P^{\rm w}_{\rm lin}$. The choice of splitting is in many ways arbitrary. The displacement resummation is taken to act on $P^{\rm w}_{\rm lin}$ alone, and is usually applied to produce the real-space power spectrum. However, the procedure can be generalised to any velocity moment power spectrum giving

$$\begin{aligned}\tilde{\Xi}^{(n),IR}_{\text{1 - loop}}(\mathbf{k}) &= \tilde{\Xi}^{(n),\rm nw}_{\rm lin}(\mathbf{k}) + e^{-\frac{1}{2}\Sigma^2 k^2}\left(1+\tfrac{1}{2}\Sigma^2 k^2\right)\tilde{\Xi}^{(n),\rm w}_{\rm lin}(\mathbf{k}) \\ &\quad + \tilde{\Xi}^{(n)}_{loop}(\mathbf{k})\left[P_{\rm lin}(\mathbf{k}) \to P^{\rm nw}_{\rm lin}(\mathbf{k}) + e^{-\frac{1}{2}\Sigma^2 k^2} P^{\rm w}_{\rm lin}(\mathbf{k})\right] \\ &\approx \tilde{\Xi}^{(n),\rm nw}_{\text{1 - loop}}(\mathbf{k}) + e^{-\frac{1}{2}\Sigma^2 k^2}\left(1+\tfrac{1}{2}\Sigma^2 k^2\right)\tilde{\Xi}^{(n),\rm w}_{\rm lin}(\mathbf{k}) + e^{-\frac{1}{2}\Sigma^2 k^2}\left(\tilde{\Xi}^{(n)}_{loop}(\mathbf{k}) - \tilde{\Xi}^{(n),\rm nw}_{loop}(\mathbf{k})\right)\end{aligned} \tag{B.32}$$

where the label "*loop*" stands for the next-to-linear-order correction in PT while the label "1 - loop" stands for the total one-loop result, i.e. a sum of linear and next-to-linear orders. In the above Σ is the estimated dispersion of the long wavelength displacement contributions:

$$\Sigma^2 = \int_0^\Lambda \frac{dk}{3\pi^2}\left[1 - j_0\left(kr_{\rm bao}\right) + 2j_2\left(kr_{\rm bao}\right)\right]P_{\rm lin}(k), \tag{B.33}$$

and Λ is the scale of the IR mode split. In practice, Λ can be chosen to be arbitrarily large given that the integral is naturally saturated by the power law drop of $P_{\rm lin}$ at high k.

For redshift space power spectra, in addition to the long wavelength displacements one can also resum long wavelength velocity modes. This introduces slight change to the expression above, making the total redshift space dispersion $\Sigma_{\rm s}$ dependent on the angle to the line of sight, i.e.

$$\Sigma^2_s(\mu) = \left[1 + f(f+2)\mu^2\right]\Sigma^2, \tag{B.34}$$

where the Σ^2 is given by Eq. (B.33). The power spectrum becomes

$$\begin{aligned}P^{s,IR}_{\text{1 - loop}}(\mathbf{k}) &= P^{s,\rm nw}_{\rm lin}(\mathbf{k}) + e^{-\frac{1}{2}\Sigma^2_s(\mu)k^2}\left(1+\tfrac{1}{2}\Sigma^2_s(\mu)k^2\right)P^{s,\rm w}_{\rm lin}(\mathbf{k}) \\ &\quad + P^{s}_{loop}(\mathbf{k})\left[P_{\rm lin}(\mathbf{k}) \to P^{\rm nw}_{\rm lin}(\mathbf{k}) + e^{-\frac{1}{2}\Sigma^2_s(\mu)k^2} P^{\rm w}_{\rm lin}(\mathbf{k})\right] \\ &\approx P^{s,\rm nw}_{\text{1 - loop}}(\mathbf{k}) + e^{-\frac{1}{2}\Sigma^2_s(\mu)k^2}\left(1+\tfrac{1}{2}\Sigma^2_s(\mu)k^2\right)P^{s,\rm w}_{\rm lin}(\mathbf{k}) + e^{-\frac{1}{2}\Sigma^2_s(\mu)k^2}\left(P^{s}_{loop}(\mathbf{k}) - P^{s,\rm nw}_{loop}(\mathbf{k})\right),\end{aligned} \tag{B.35}$$

where the wiggle and no-wiggle $P^s_{\text{1 - loop}}$ (and similarly the P^s_{loop} by dropping the linear Kaiser part) are given by Equation (B.31).

B.3 Gaussian Streaming Model

The Gaussian Streaming Model (GSM), like the ME and FSM described in the main body of the text, is yet another way to expand the exponential in Equation 2.4. However, it differs

from the two aforementioned models in that it is a cumulant expansion in configuration space [396, 398]. Our goal in this section is to explain why this structure makes it particularly easy to handle the effects of bulk (IR) velocities within the GSM.

We begin by reviewing the derivation of the GSM as presented in ref. [396]. The exponential in Equation 2.4 can be expanded using configuration space statistics as

$$\left\langle (1+\delta_g(\mathbf{x}_1))(1+\delta_g(\mathbf{x}_2))e^{i\mathbf{k}\cdot\Delta\mathbf{u}}\right\rangle = (1+\xi_g(r))\exp\left\{\sum_{n=0}^{\infty}\frac{i^n}{n!}k_{i_1}...k_{i_n}C^{(n)}_{i_1...i_n}(\mathbf{r}=\mathbf{x}_1-\mathbf{x}_2)\right\}$$

where, for example, the first two configuration-space cumulants are given by

$$\begin{aligned} C^{(1)}_i(\mathbf{r}) &= (1+\xi_g)^{-1}\Xi^{(1)}_i(\mathbf{r}) \\ C^{(2)}_{ij}(\mathbf{r}) &= (1+\xi_g)^{-1}\Xi^{(2)}_{ij}(\mathbf{r}) - C^{(1)}_i C^{(1)}_j, \end{aligned} \tag{B.36}$$

and can be straightforwardly interpreted as the mean and variance of the density-weighted pairwise velocity. Truncating the cumulant expansion at second order and Fourier transforming yields the intuitive form [301]

$$1+\xi_s(\mathbf{s}) = \int \frac{dy}{\sqrt{2\pi C^{(2)}_\parallel}}\ (1+\xi_g)\exp\left\{\frac{\left(s_\parallel - y - \mu C^{(1)}_\parallel\right)^2}{2C^{(2)}_\parallel}\right\}. \tag{B.37}$$

As shown in Section 2.3, truncating the velocity expansion at second order yields rather imperfect fits to the redshift-space power spectrum, especially towards small scales and large μ, and thus does not yield a good model for the power spectrum broadband. However, the configuration space structure is particularly suited to the close-to-Gaussian statistics of the large-scale bulk motions critical to describing the BAO feature. This is because, roughly speaking, $C^{(n>2)}$ do not contribute to BAO damping, which can be attributed to

- The correlation function is much smaller than unity, such that $1+\xi_g \approx 1$.
- For the nonlinear damping of the BAO we only need to consider the Gaussian statistics of the linear Δ and $\Delta\mathbf{u}$, such that higher moments factorize via Wick's contraction.

For example, for the fourth cumulant we can write

$$C^{(4)} \sim \langle \Delta\mathbf{u}\Delta\mathbf{u}\Delta\mathbf{u}\Delta\mathbf{u}\rangle - 6C^{(2)}C^{(2)} \approx 6\langle\Delta\mathbf{u}\Delta\mathbf{u}\rangle\langle\Delta\mathbf{u}\Delta\mathbf{u}\rangle - 6C^{(2)}C^{(2)} \sim 0. \tag{B.38}$$

Thus the truncation at second order, while not a good approximation for the power spectrum broadband in general, well-describes physics around the BAO scale. Note that this is not the case for the FSM, because the Fourier-space cumulants do not factor multiplicatively via Wick contractions.

B.4 Wedges vs. Multipoles

While perturbation theory models of the power spectrum expand in $k_\parallel = k\mu$ and thus naturally predict the values of power spectrum wedges, analyses of actual spectroscopic surveys naturally produce power spectrum multipoles $P_\ell(k)$ [426, 325, 47, 161]. Since $P(k,\mu)$ is a relatively smooth function of μ, dominated in amplitude by the monopole and quadrupole, choosing to analyze the first few multipoles of the power spectrum vs. wedges should amount to little more than a change of basis. However, as we have seen in Figures 2.1 and 2.2, this choice of basis can make a dramatic and somewhat counterintuitive difference in the apparent goodness of fit or range of model validity, which we comment on briefly in this appendix.

Perhaps the most surprising aspect of multipoles vs. wedges is that the errors on $\ell > 0$ do not have to be lesser in magnitude than wedge errors. Perhaps more importantly, even the quadruople can diverge from perturbative predictions while all but the highest μ wedges are predicted at the sub-percent level. This was already seen in Figures 2.1 and 2.2; however, since in that case much of the monopole power at higher k derives from shot noise it is worth considering a simpler example which emphasizes the point.

Specifically, let us consider a shot-noise free example wherein our theory model is linear theory, $P(k,\mu) = (b + f\mu^2)^2 P_{\rm lin}(k)$, while "truth" is given by that model multiplied by $1 + k^2\sigma^2\mu^6$, with σ normalized to produce a 10% error at $k = 0.2\,h\,{\rm Mpc}^{-1}$ and $\mu = 1$. Such an error term is exactly what one might expect from the virial velocities in the fourth velocity moment which we do not model in this work. In this example, shown in Figure B.1, we see that while the $\mu = 0$ and 0.5 wedges are predicted by "theory" at sub-percent levels for all scales shown, the quadrupole already differs from theory by ten percent by $k = 0.15\,h\,{\rm Mpc}^{-1}$. The mathematical reason for this is straightforward: unlike the monopole, the quadrupole is not a positive-definite average of power spectrum wedges. Indeed, the Legendre polynomial $\mathcal{L}_2(\mu) = \frac{1}{2}(3\mu^2 - 1)$ will tend to pick up *differences* in the error between $\mu = 0$, where errors are small and $\mathcal{L}_2$ is negative, and $\mu = 1$, where errors are maximal and $\mathcal{L}_2$ is positive. The situation is particularly acute for perturbative treatments of redshift space, which as we have shown expand order-by-order in μ, making much better predictions perpendicular to the line-of-sight than parallel to it.

The error properties of multipoles vs. wedges described above carry implications for data analysis. From an aesthetic standpoint, presenting data in terms of $P(k,\mu)$ has the slight advantage that fractional errors $\Delta P(k,\mu)/P$ roughly correspond to standard deviations in the Gaussian approximation while $\Delta P_\ell/P_\ell$ are hard to interpret as the errors for $P_{\ell>0}$ are dominated by the monopole. Nonetheless, as the two statistics are connected by a basis transformation, the choice between them should in principle be irrelevant to data analysis as long as errors are properly taken into account, and theory errors[2] for higher-order FoGs that scale strongly with μ will have the desired effect of down-weighting data from higher μ. However, the magnitude and shape of the theory error can be hard to estimate for

[2]See ref. [85] for an example calculation of the theory error on multipoles. Their calculation uses a different ansatz for higher-order FoG effects than our $k^2\mu^4 P(k)$, underscoring the difficulty of modeling FoG effects not incorporated into the base model.

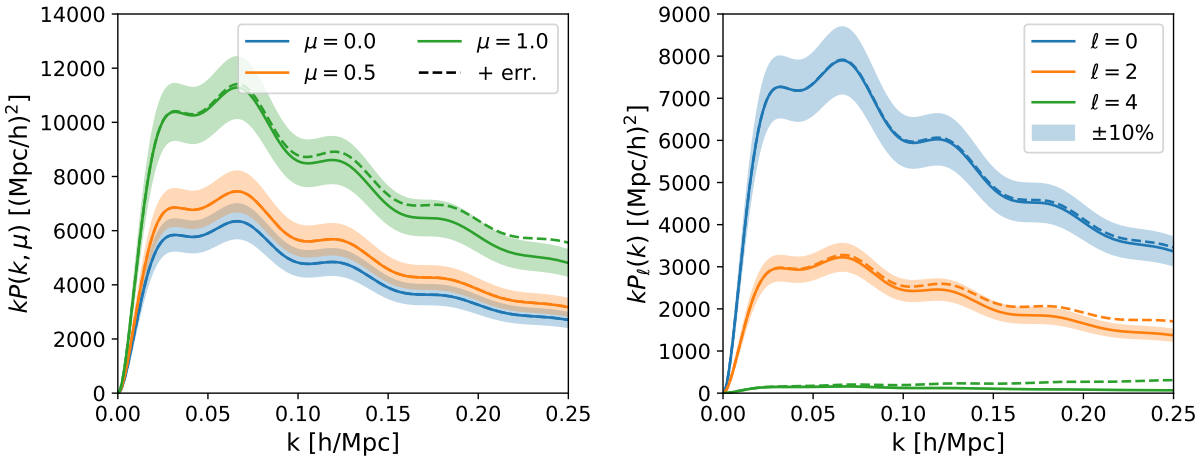

Figure B.1: Toy model illustrating the different error properties of wedges (left) vs. multipoles (right). In this example the "theory" is given by the Kaiser approximation with $b = 2$ and $f = 1$ while "truth" is given by Kaiser multiplied by $1 + k^2\sigma^2\mu^6$ normalized such that the power spectrum is 10% away from theory at $k = 0.15\,h\,\mathrm{Mpc}^{-1}$ and $\mu = 1$. While the $\mu = 0$ and 0.5 wedges agree with theory at sub-percent level over the entire range shown, the quadrupole deviates from theory by more than 10% already at $k = 0.2\,h\,\mathrm{Mpc}^{-1}$, showing that fractional errors on the quadruople do not have to be less than or equal to those on the wedges.

non-simulated samples, and a far more common choice in the literature is to adopt hard scale cuts $k_{\rm max}$ when fitting to theory (corresponding to infinite theoretical error beyond that scale). In this case, operating in wedges corresponds to defining an angular theshold $k_{\rm max}(\mu)$ where all but the highest μ wedge can be fit over most perturbative scales, while $\mu \approx 1$ has be cut off at much smaller k due to virial motions, fingers-of-god and (for real surveys) redshift errors. On the other hand, operating within the multipole formalism means setting $k_{{\rm max},\ell}$, which means much of the angular information carried by the lower-μ wedges will be lost by the scale-cut in the quadrupole due to contamination from the highest-μ bin (complementary discussions of the robustness of wedges can be found in refs. [306, 186, 85]). However, since redshift space power spectra are naturally measured as multipoles, an alternative approach beyond the strict wedges/multipoles dichotomy might be to weight multipoles in a scale-dependent fashion to minimize contamination by FoG effects at high μ. Devising such an estimator is outside the scope of this work, though we note that related strategies have been suggested to deal with systematics in configuration space [302, 249] and plane-of-the-sky effects near $\mu = 0$ [161]. The above suggests that rather than simply discarding one wedge or finding an orthogonal basis on the range $[-\mu_{\rm max}, \mu_{\rm max}]$, the practical need to go through the multipole basis promotes an apodization or tapering of the wedges in μ to restrict the support in ℓ. Making predictions for apodized wedges presents no problems over the case of sharp-edged wedges.

B.5 Fast Evaluation of LPT Kernels via FFTLog

One of the more time-consuming steps in computing LSS statistics beyond linear order in perturbation theory is the evaluation of one-loop integrals [229, 58, 396]. Recently, ref. [320] proposed a method to dramatically speed up these calculations by exploiting the underlying spherical symmetry of these integrals. To do so they note that these kernels can generally be decomposed into sums of integrals of the form

$$\int d^3\mathbf{q}\, q^{n_1}|\mathbf{k}-\mathbf{q}|^{n_2}\, P_\ell(\hat{q}\cdot\widehat{k-q})\, P_{\rm L}(q)P_{\rm L}(|\mathbf{k}-\mathbf{q}|) = (-1)^\ell 4\pi \int dr\, r^2 j_0(kr)\xi^\ell_{n_1}(r)\xi^\ell_{n_2}(r) \quad \text{(B.39)}$$

where P_ℓ are Legendre polynomials and the generalized linear correlation functions are defined by

$$\xi^\ell_n(r) = \int \frac{dk}{2\pi^2}\, k^{2+n} j_\ell(kr) P_{\rm L}(k). \quad \text{(B.40)}$$

The intuition behind Equation B.39 is that, as the scalar-valued left hand side must be independent of the orientation of $\mathbf{k}$, the angular integral in $\mathbf{q}$ can be performed analytically, for example using the plane-wave expansion, to yield the spherical Bessel integrals in right-hand-side expression. Conveniently, these spherical Bessel integrals can be readily computed as Hankel transforms, which can in turn be efficiently computed using the FFTLog algorithm.

Ref. [320] applied the above-described method to LPT kernels relevant to the matter power spectrum, which can be written as

$$\begin{aligned}
R_1(k) &= k^2 P_{\rm L}(k)\left[\frac{8}{15}\int dr\ r\ j_0(kr)\xi^0_0 - \frac{16}{21}\int dr\ r\ j_2(kr)\xi^2_0 + \frac{8}{35}\int dr\ r\ j_4(kr)\xi^4_0\right] \\
R_2(k) &= k^2 P_{\rm L}(k)\Bigg[-\frac{2}{15}\int dr\ r\ j_0(kr)\xi^0_0 - \frac{2}{21}\int dr\ r\ j_2(kr)\xi^2_0 + \frac{8}{35}\int dr\ r\ j_4(kr)\xi^4_0 \\
&\qquad + \frac{2k}{5}\int dr\ r\ j_1(kr)\xi^1_{-1} - \frac{2k}{5}\int dr\ r\ j_3(kr)\xi^3_{-1}\Bigg]
\end{aligned} \quad \text{(B.41)}$$

and

$$\begin{aligned}
Q_1(k) &= 4\pi\int dr\ r^2 j_0(kr)\left[\frac{8}{15}(\xi^0_0)^2 - \frac{16}{21}(\xi^2_0)^2 + \frac{8}{35}(\xi^4_0)^2\right] \\
Q_2(k) &= 4\pi\int dr\ r^2 j_0(kr)\left[\frac{4}{5}(\xi^0_0)^2 - \frac{4}{7}(\xi^2_0)^2 - \frac{8}{35}(\xi^4_0)^2 - \frac{4}{5}\xi^1_1\xi^1_{-1} + \frac{4}{5}\xi^3_1\xi^3_{-1}\right] \\
Q_3(k) &= 4\pi\int dr\ r^2 j_0(kr)\Bigg[\frac{38}{15}(\xi^0_0)^2 + \frac{68}{21}(\xi^2_0)^2 + \frac{8}{35}(\xi^4_0)^2 \\
&\qquad + \frac{2}{3}\xi^0_2\xi^0_{-2} - \frac{32}{5}\xi^1_1\xi^1_{-1} + \frac{4}{3}\xi^2_2\xi^2_{-2} - \frac{8}{5}\xi^3_1\xi^3_{-1}\Bigg],
\end{aligned} \quad \text{(B.42)}$$

where the r dependence of the generalized correlation functions is left implicit. In this Appendix we complete this list by deriving Hankel-transform expressions for the remaining LPT kernels relevant to biased tracers up to one-loop order; these are:

$$\begin{aligned}
Q_5(k) &= 4\pi \int dr\ r^2 j_0(kr) \Big[\frac{2}{3}(\xi_0^0)^2 - \frac{2}{3}(\xi_0^2)^2 - \frac{2}{5}\xi_1^1\xi_{-1}^1 + \frac{2}{5}\xi_1^3\xi_{-1}^3 \Big] \\
Q_8(k) &= 4\pi \int dr\ r^2 j_0(kr) \Big[\frac{2}{3}(\xi_0^0)^2 - \frac{2}{3}(\xi_0^2)^2 \Big] \\
Q_{s^2}(k) &= 4\pi \int dr\ r^2 j_0(kr) \Big[-\frac{4}{15}(\xi_0^0)^2 + \frac{20}{21}(\xi_0^2)^2 - \frac{24}{35}(\xi_0^4)^2 \Big] \\
R_{b_3}(k) &= \frac{8}{63}P(k) \int dr\ r\ \Big[\frac{24k^2}{5}\xi_0^0 j_0(kr) - \frac{16k}{5}\xi_1^1 j_1(kr) - \big(\frac{20k^2}{7}\xi_0^2 - 4\xi_2^2\big) j_2(kr) \\
&\qquad - \frac{24k}{5}\xi_1^3 j_3(kr) + \frac{72k^2}{35}\xi_0^4 j_4(kr) \Big],
\end{aligned} \tag{B.43}$$

where the final kernel is defined such that

$$\langle \delta_{\rm lin} | (st + \frac{16}{63}\sigma_\delta^2 \delta_{\rm lin}) \rangle = R_{b_3}(k). \tag{B.44}$$

The relation of these kernels to physical quantities in LPT can be found in, for example, refs. [229, 58, 396].

B.6 Hankel Transforms

In this section we give expressions for the Hankel transforms that give the k-space velocity moments in both LPT and EPT described in the main chapter. We begin with LPT, from which we show that the expressions for EPT can be extracted as an especially simple limit. Similar approaches to evaluating the integrals in EPT are discussed in e.g. [320, 319, 127, 344, 377]. We differ from these mainly in that the FFTLog expressions are derived using the Lagrangian bias basis, which naturally organizes 1-loop contributions into combinations of linear generalized correlation functions ξ_ℓ^n that are automatically Galilean invariant. We set the linear growth rate $f = 1$ throughout this section, with the n$^{\rm th}$ velocity moment carrying an implicit factor f^n.

B.6.1 LPT

The integrals for velocity moments in LPT take the form

$$\begin{aligned}
&\int d^3\mathbf{q}\ e^{i\mathbf{k}\cdot\mathbf{q} - \frac{1}{2}k_i k_j A_{ij}^{\rm lin}}\ \mu^m f(q) \\
&\qquad = \sum_{n=0}^{\infty} 4\pi \int dq\ q^2\ e^{-\frac{1}{2}k^2(X^{\rm lin}+Y^{\rm lin})} f_n^m(k^2 Y_{\rm lin}) \Big(\frac{kY_{\rm lin}}{q}\Big)^n f(q)\ j_n(kq),
\end{aligned} \tag{B.45}$$

where $\mu = \hat{k} \cdot \hat{q}$ and we have used Equation B.61; explicit expressions for f_n^m are provided in Appendix B.7. The summands are Hankel transforms and can be efficiently evaluated using the FFTLog algorithm. In practice we find that this series converges quickly; for the matter contribution in the power spectrum (i.e. $f(q) = 1$) the series converges to sub-percent precision at $z = 0.8$ and $k = 0.25\,h\,\mathrm{Mpc}^{-1}$ for typical cosmologies when $n_{\max} = 5$, with improving performance towards smaller wavenumbers and higher redshifts. Our expressions agree with those in ref. [398] up to shear and counterterms, as well as that for the power spectrum in ref. [396], and we follow the conventions in refs. [58, 396] for the Lagrangian-space two-point functions (U_i, A_{ij}, W_{ijk} etc.) though we correct for minor algebraic mistakes in a few cases. In this section only we will ignore the stochastic contributions and counterterms as they have trivial scale dependence.

Real-Space Power Spectrum

The real-space power spectrum expressed as an infinite sum of Hankel transforms was given in Appendix B of ref. [396]. As it is an important component of our model, we include it here for completeness:

$$\begin{aligned} P(k) = \int d^3\mathbf{q}\; e^{i\mathbf{k}\cdot\mathbf{q}} e^{-\frac{1}{2}k_i k_j A_{ij}^{\rm lin}} \Big\{ & 1 - \frac{1}{2}k^2\Big(X^{\rm loop} + Y^{\rm loop}\mu^2\Big) - \frac{i}{6}k^3\Big(\tilde{V}\mu + \tilde{T}\mu^3\Big) \\ & + b_1\Big(2ikU\mu - k^2(X^{10} + Y^{10}\mu^2)\Big) + b_1^2\Big(\xi_{\rm lin}^2 - k^2U_{\rm lin}^2\mu^2 + ikU^{11}\mu\Big) \\ & + b_2\Big(- k^2U_{\rm lin}^2\mu^2 + ikU^{20}\mu\Big) + 2ib_1b_2k\xi_{\rm lin}U^{\rm lin}\mu + \frac{1}{2}b_2^2\xi_{\rm lin}^2 \\ & + b_s\Big(- k^2(X_s + Y_s\mu^2) + 2ikV^{10}\mu\Big) + 2ib_1b_skV^{12}\mu + b_2b_s\chi + b_s^2\zeta \\ & + 2ib_3kU_{b_3}\mu + 2b_1b_3\theta\Big\} \end{aligned} \tag{B.46}$$

where for brevity we have defined we have defined $\tilde{V} = 3(2V_1 + V_3)$[3], $\tilde{T} = 3T$ and $\Upsilon_{ij} = X_s\delta_{ij} + Y_s\hat{q}_i\hat{q}_j$.

[3]Note that there is a typo in Equations B21, B22 of ref. [58], such that one should substitute $V_{1,3} \to V_{1,3}+S$, where $S(q)$ is defined in Equation B23, for the correct expressions.

Pairwise Velocity Spectrum

This scalar decomposition of the pairwise velocity spectrum is given by $v_i(k) = iv(k)\hat{k}_i$, with

$$\begin{aligned} v(k) = \int d^3\mathbf{q}\, e^{i\mathbf{k}\cdot\mathbf{q}}\, e^{-\frac{1}{2}k_ik_jA^{\rm lin}_{ij}} \Big\{ & k\Big(\dot{X} + \dot{Y}\mu^2\Big) + \frac{ik^2}{2}\Big(\dot{V}\mu + \dot{T}\mu^3\Big) \\ & + 2b_1\Big(i(k^2U^{\rm lin}\dot{X}^{\rm lin} - \dot{U})\mu + ik^2U^{\rm lin}\dot{Y}^{\rm lin}\mu^3 + k(\dot{X}^{10} + \dot{Y}^{10}\mu^2)\Big) \\ & + b_1^2\Big(k\xi_{\rm lin}\dot{X}^{\rm lin} + k(\xi_{\rm lin}\dot{Y}^{\rm lin} + 2U^{\rm lin}\dot{U}^{\rm lin})\mu^2 - i\dot{U}^{11}\mu\Big) \\ & + b_2\Big(2kU^{\rm lin}\dot{U}^{\rm lin}\mu^2 - i\dot{U}^{20}\mu\Big) - 2ib_1b_2\xi_{\rm lin}\dot{U}^{\rm lin}\mu \\ & + b_s\Big(- 2i\dot{V}^{10}\mu + 2k(\dot{X}_s + \dot{Y}_s\mu^2)\Big) - 2ib_1b_s\dot{V}^{12}\mu - 2ib_3\dot{U}_{b_3}\mu\Big\} \end{aligned} \tag{B.47}$$

where we have followed the dot notation of Refs. [405, 396] such that each dotted quantity is proportional to f. We have used dots on the scalar components to denote the components of the vector quantities, e.g. $\dot{U}_i = \dot{U}\hat{q}_i$. However, the three-indexed $\dot{W}_{ijk}$ has a somewhat more complicated structure than the one- or two-indexed quantities[4] and we have chosen to summarize its contributions in terms of its contractions with $\hat{k}$ alone, i.e. $\dot{V} = \frac{4f}{3}\tilde{V}$ and $\dot{V} = \frac{4f}{3}\tilde{T}$.

[4] Any one-indexed Lagrangian correlator must be proportional to $\hat{q}_i$ and any two-indexed correlator must be a linear sum of δ_{ij} or $\hat{q}_i\hat{q}_j$ and therefore symmetric, whereas $W^{(112)}_{ijk}$ for example is not symmetric in all indices.

Pairwise Velocity Dispersion Spectrum

For the pairwise velocity dispersion we have chosen to compute the two contractions $\sigma^2_{\hat{k}\hat{k}}$ and σ^2_{ii}. These are related to the multipole moments via $\sigma^2_{ii} = 3\sigma_0$ and $\sigma^2_{\hat{k}\hat{k}} = \sigma_0 + \sigma_2$.

$$\begin{aligned}\sigma^2_{\hat{k}\hat{k}} = \int d^3\mathbf{q}\; e^{i\mathbf{k}\cdot\mathbf{q}}\; e^{-\frac{1}{2}k_ik_jA^{\rm lin}_{ij}}\Big\{&\Big((\ddot{X} - k^2\dot{X}^2_{\rm lin}) + (\ddot{Y} - 2k^2\dot{X}_{\rm lin}\dot{Y}_{\rm lin})\mu^2 - k^2\dot{Y}^2_{\rm lin}\mu^4\Big)\\ &+ \frac{5f^2ik}{3}\Big(\tilde{V}\mu + \tilde{T}\mu^3\Big)\\ &+ 2b_1\Big(ik(U^{\rm lin}\ddot{X}^{\rm lin} + 2\dot{U}^{\rm lin}\dot{X}^{\rm lin})\mu + ik(U^{\rm lin}\ddot{Y}^{\rm lin} + 2\dot{U}^{\rm lin}\dot{Y}^{\rm lin})\mu^3 + \ddot{X}^{10} + \ddot{Y}^{10}\mu^2\Big)\\ &+ b_1^2\Big(\xi_{\rm lin}\ddot{X}^{\rm lin} + (\xi_{\rm lin}\ddot{Y}^{\rm lin} + \dot{U}^{\rm lin}\dot{U}^{\rm lin})\mu^2\Big) + 2b_2\dot{U}^{\rm lin}\dot{U}^{\rm lin}\mu^2 + 2b_s\Big(\ddot{X}_{s^2} + \ddot{Y}_{s^2}\mu^2\Big)\Big\}\end{aligned}$$

$$\begin{aligned}\sigma^2_{ii} = \int d^3\mathbf{q}\; e^{i\mathbf{k}\cdot\mathbf{q}}\; e^{-\frac{1}{2}k_ik_jA^{\rm lin}_{ij}}\Big\{&\Big(3\ddot{X} + \ddot{Y} - k^2\dot{X}^2_{\rm lin} - k^2(\dot{Y}^2_{\rm lin} + 2\dot{X}_{\rm lin}\dot{Y}_{\rm lin})\mu^2\Big)\\ &+ if^2k(18V_1 + 7V_3 + 5T)\mu\\ &+ 2b_1\Big(ik(U^{\rm lin}(3\ddot{X}^{\rm lin} + \ddot{Y}^{\rm lin}) + (3\ddot{X}^{10} + \ddot{Y}^{10}) + 2\dot{U}^{\rm lin}(\dot{X}^{\rm lin} + \dot{Y}^{\rm lin}))\mu\Big)\\ &+ b_1^2\Big(\xi_{\rm lin}(3\ddot{X}^{\rm lin} + \ddot{Y}^{\rm lin}) + 2\dot{U}^{\rm lin}\dot{U}^{\rm lin}\Big) + 2b_2\dot{U}^{\rm lin}\dot{U}^{\rm lin} + 2b_s(3\ddot{X}_{s^2} + \ddot{Y}_{s^2})\Big\}. \quad \text{(B.48)}\end{aligned}$$

Quantities with two dots are proportional to f^2. Once again, the time derivative $\ddot{W}_{ijk}$ is more complicated than the one- or two-indexed quantities, and in this case we have chosen to simply write them out as f^2 multiplied by the relevant un-dotted quantities[5].

Higher Moments

As usual we decompose $-i\gamma_{ijk} = \frac{1}{3}\gamma_1\;\hat{k}_{\{i}\delta_{jk\}} + \gamma_3\;\hat{k}_i\hat{k}_j\hat{k}_k$ where the scalar components can be derived from the contractions:

$$\begin{aligned}-i\hat{k}_i\hat{k}_j\hat{k}_k\gamma_{ijk} = \gamma_1 + \gamma_3 = -i\int d^3\mathbf{q}\; e^{i\mathbf{k}\cdot\mathbf{q}-\frac{1}{2}k_ik_jA^{\rm lin}_{ij}}\Big\{&\dddot{V}\mu + \dddot{T}\mu^3\\ &+ 3ik\Big(\dot{X}^{\rm lin}\big(\ddot{X}^{\rm lin} + \ddot{Y}^{\rm lin}\mu^2\big) + \dot{Y}^{\rm lin}\mu^2\big(\ddot{X}^{\rm lin} + \ddot{Y}^{\rm lin}\mu^2\big)\Big)\\ &+ 6b_1\dot{U}^{\rm lin}\mu\big(\ddot{X}^{\rm lin} + \ddot{Y}^{\rm lin}\mu^2\big)\Big\}\\ -i\hat{k}_i\delta_{jk}\gamma_{ijk} = \frac{5}{3}\gamma_1 + \gamma_3 = -i\int d^3\mathbf{q}\; e^{i\mathbf{k}\cdot\mathbf{q}-\frac{1}{2}k_ik_jA^{\rm lin}_{ij}}\Big\{&\Big(\frac{5}{3}\dddot{V} + \dddot{T}\Big)\mu\\ &+ ik\Big(\dot{X}^{\rm lin}\big(5\ddot{X}^{\rm lin} + (1+2\mu^2)\ddot{Y}^{\rm lin}\big) + \dot{Y}^{\rm lin}\mu^2\big(5\ddot{X}^{\rm lin} + 3\ddot{Y}^{\rm lin}\big)\\ &+ 2b_1\dot{U}^{\rm lin}\big(5\ddot{X}^{\rm lin} + 3\ddot{Y}^{\rm lin}\big)\mu\Big)\Big\}.\end{aligned}$$

[5]Note that Equation C. 11 in ref. [396] should instead be $\ddot{W}_{ijk} = f^2(2W^{(112)}_{ijk} + 2W^{(121}_{ijk} + W^{211)}_{ijk})$, i.e. the indices on the right-hand side should not be permuted with the order of solution.

For the sake of brevity we have defined the triple-dotted quantities $\dddot{V} = 2f^3\tilde{V}$ and $\dddot{T} = 2f^3\tilde{T}$ such that $\hat{k}_i\hat{k}_j\hat{k}_k\dddot{W}_{ijk} = \dddot{V}\mu + \dddot{T}\mu^3$ and $\hat{k}_i\delta_{jk}\dddot{W}_{ijk} = \frac{5}{3}\dddot{V} + \dddot{T}$.

The fourth moment $\kappa_{ijkl} = \left\langle (1+\delta_1)(1+\delta_2)\dot{\Delta}_i\dot{\Delta}_j\dot{\Delta}_k\dot{\Delta}_l \right\rangle$ has only one contribution at one loop order; in Fourier space this is

$$\kappa_{ijkl} = \int d^3\mathbf{q}\; e^{i\mathbf{k}\cdot\mathbf{q} - \frac{1}{2}k_ik_jA_{ij}} \left\langle \dot{\Delta}_i\dot{\Delta}_j\dot{\Delta}_k\dot{\Delta}_l \right\rangle = \int d^3\mathbf{q}\; e^{i\mathbf{k}\cdot\mathbf{q} - \frac{1}{2}k_ik_jA_{ij}}\, \ddot{A}_{\{ij}\ddot{A}_{kl\}} \tag{B.49}$$

where the distinct unordered indices are now $\{ijkl\} = (ij)(kl) + (ik)(jl) + (il)(jk)$. This can be similarly decomposed as $\kappa_{ijkl} = \frac{1}{3}\kappa_0\delta_{\{ij}\delta_{kl\}} + \frac{1}{6}\kappa_2\hat{k}_{\{i}\hat{k}_j\delta_{kl\}} + \kappa_4\hat{k}_i\hat{k}_j\hat{k}_k\hat{k}_l$, for which the following linear equations hold

$$\begin{aligned}
5\kappa_0 + \frac{5}{3}\kappa_2 + \kappa_4 &= \int d^3\mathbf{q}\; e^{i\mathbf{k}\cdot\mathbf{q} - \frac{1}{2}k_ik_jA^{\rm lin}_{ij}} \left\{ 15\ddot{X}^2_{\rm lin} + 10\ddot{X}_{\rm lin}\ddot{Y}_{\rm lin} + 3\ddot{Y}^2_{\rm lin} \right\} \\
\frac{5}{3}\kappa_0 + \frac{4}{3}\kappa_2 + \kappa_4 &= \int d^3\mathbf{q}\; e^{i\mathbf{k}\cdot\mathbf{q} - \frac{1}{2}k_ik_jA^{\rm lin}_{ij}} \left\{ 5\ddot{X}^2_{\rm lin} + (1+7\mu^2)\ddot{X}_{\rm lin}\ddot{Y}_{\rm lin} + 3\mu^2\ddot{Y}^2_{\rm lin} \right\} \\
\kappa_0 + \kappa_2 + \kappa_4 &= \int d^3\mathbf{q}\; e^{i\mathbf{k}\cdot\mathbf{q} - \frac{1}{2}k_ik_jA^{\rm lin}_{ij}} \left\{ 3\ddot{X}^2_{\rm lin} + 6\mu^2\ddot{X}_{\rm lin}\ddot{Y}_{\rm lin} + 3\mu^4\ddot{Y}^2_{\rm lin} \right\}.
\end{aligned} \tag{B.50}$$

B.6.2 EPT

As described in Section 2.4.3, EPT is equivalent to LPT when the exponential of

$$-\frac{1}{2}k_ik_jA^{\rm lin}_{ij} = -\frac{1}{2}k^2(X^{\rm lin} + Y^{\rm lin}\mu^2)$$

is expanded as its Taylor series. Doing so reduces Equation B.45 to the simpler form

$$\int d^3\mathbf{q}\;\; e^{i\mathbf{k}\cdot\mathbf{q}}\; \mu^n\; f(q) = \sum_{\ell=0}^{n} 4\pi \int dq\; q^2\; f(q)\; \alpha^{(n)}_\ell\; j_\ell(kq), \tag{B.51}$$

where Hankel transform no longer has k-dependence beyond the spherical bessel function $j_\ell(kq)$ and the coefficients $\alpha^{(n)}_\ell$ are defined such that $\mu^n = \sum_\ell \alpha^{(n)}_\ell \mathcal{L}_\ell(\mu)$. The fact that the k dependence is isolated to the Bessel function in EPT means that bias contributions at each k can be calculated all at once, instead of requiring one set of FFTLogs per k point as in LPT. Transforming these expanded LPT integrands into the EPT bias basis using Equation 2.19 yields Hankel transform expressions for all one-loop contributions to the EPT redshift-space power spectrum at one loop. An especially convenient feature of computing EPT integrals in the LPT basis is that the IR cancellations in the small k limit are explicitly satisfied in each expression.

Since the expressions required in the calculation outlined above are essentially identical to those in the previous section for LPT, we have chosen not to explicitly enumerate them. However, let us briefly comment on two particular numerical choices that both simplify the calculation and improve stability. Firstly, a subset of the terms involved, due to "connected"

$\tilde{\Xi}^{(0)}$	$F(q)$	$\tilde{F}(k)$
1	$-\frac{1}{2}k_ik_j\left(A_{ij}^{\rm lin}+A_{ij}^{\rm loop}\right)-\frac{i}{6}k_ik_jk_kW_{ijk}$	$P_{\rm L}+\frac{9}{98}Q_1+\frac{10}{21}R_1+\frac{6}{7}R_2+\frac{3}{7}Q_2$
b_1	$2ik_iU_i-k_ik_jA_{ij}^{10}$	$2P_{\rm L}+\frac{10}{21}R_1+\frac{1}{7}(6R_1+12R_2+6Q_5)$
b_1^2	$\xi_{\rm lin}+ik_iU_i^{11}$	$P_{\rm L}+\frac{6}{7}(R_1+R_2)$
b_2	$ik_iU_i^{20}$	$\frac{3}{7}Q_8$
b_s	$2ik_i\dot{V}_i^{10}$	$\frac{2}{7}Q_{s^2}$
b_3	$2ik_iU_{b_3}$	$2R_{b_3}$
b_1b_3	2θ	$2R_{b_3}$

Table B.1: Contributions to the real-space power spectrum from "connected" cumulants in LPT.

$\tilde{\Xi}_i^{(1)}$	$F(q)$	$k^2\tilde{F}(k)$
1	$ik_j\left(\dot{A}_{ij}^{\rm lin}+\dot{A}_{ij}^{\rm loop}\right)-\frac{1}{2}k_jk_k\dot{W}_{ijk}$	$-ik_i(2P_{\rm L}+\frac{18}{49}Q_1+\frac{40}{21}R_1+\frac{12}{7}Q_2+\frac{24}{7}R_2)$
b_1	$2\dot{U}_i+2ik_j\dot{A}_{ij}^{10}$	$-ik_i(2P_{\rm L}+4R_1+\frac{36}{7}R_2+\frac{18}{7}Q_5)$
b_1^2	$\dot{U}_i^{11}$	$-ik_i(12/7)(R_1+R_2)$
b_2	$\dot{U}_i^{20}$	$-ik_i(6/7)Q_8$
b_s	$2\dot{V}_i^{10}$	$-ik_i(4/7)Q_{s^2}$
b_3	$2\dot{U}_{b_3,i}$	$-ik_i2R_{b_3}$

Table B.2: Contributions to the pairwise velocity spectrum from "connected" cumulants in LPT.

correlators in Fourier space, can be Fourier-transformed explicitly as the kernels (R_n, Q_n) involved were themselves already computed using FFTLogs of products of generalized linear correlation functions (App. B.5). For example the matter power spectrum contains both the connected terms

$$P_1(k) \ni \int d^3\mathbf{q}\; e^{i\mathbf{k}\cdot\mathbf{q}}\Big\{1-\frac{1}{2}k_ik_j\left(A_{ij}^{\rm lin}+A_{ij}^{\rm loop}\right)-\frac{i}{6}k_ik_jk_kW_{ijk}\Big\}$$
$$= P_{\rm lin}(k)+\frac{9}{98}Q_1(k)+\frac{10}{21}R_1(k)+\frac{6}{7}R_2(k)+\frac{3}{7}Q_2(k)$$

and a disconnected contribution equal to the Fourier transform of $k_ik_jk_kk_lA_{ij}^{\rm lin}A_{kl}^{\rm lin}/8$ — the former need not be Fourier transformed a second time. Note that since all displacement correlators appear as pairwise displacements Δ, this split does not break Galilean invariance. The connected components for each of the velocity moments are given in Tables B.1, B.2, B.3 and B.4.

Secondly, the coefficients $\alpha_\ell^{(n)}$ are not unique and can be expressed in a number of ways by utilizing the recurrence relations of spherical Bessel functions. Perhaps the most obvious in the context of LPT corresponds taking the $B\to 0$ limit of Equation B.53, in which case

$\tilde{\Xi}^{(2)}_{\hat{k}\hat{k}}$	$F(q)$	$k^2\tilde{F}(k)$
1	$\ddot{A}_{\hat{k}\hat{k}} + ik_n\ddot{W}_{\hat{k}\hat{k}n}$	$-(2P_{\rm L} + \frac{36}{49}Q_1 + \frac{20}{7}R_1 + \frac{30}{7}Q_2 + \frac{60}{7}R_2)$
b_1	$2\ddot{A}^{10}_{\hat{k}\hat{k}}$	$-(24/7)(R_1 + 2R_2 + Q_5)$
$\tilde{\Xi}^{(2)}_{ii}$		
1	$\ddot{A}_{ii} + ik_n\ddot{W}_{iin}$	$-(2P_{\rm L} - \frac{4}{7}R_1 - \frac{6}{49}Q_1 + \frac{60}{7}R_2 + \frac{30}{7}Q_2\ )$
b_1	$2\ddot{A}^{10}_{ii}$	$-(24/7)(2R_2 + Q_5)$

Table B.3: Contributions to the pairwise velocity dispersion from "connected" cumulants in LPT, decomposed into its trace $\sigma^2_{12,ii}$ and $\hat{k}$ component $\sigma^2_{12,\hat{k}\hat{k}}$.

$\tilde{\Xi}^{(3)}_{ijk}$	$k^3\tilde{F}(k)$
$-i\hat{k}_i\hat{k}_j\hat{k}_k\gamma_{ijk}$	$(36/7)(2R_2 + Q_2)$
$-i\hat{k}_i\delta_{jk}\gamma_{ijk}$	$-(12/7)(2R_1 - 6R_2 + Q_1 - 3Q_2)$

Table B.4: Contributions to the third pairwise velocity moment from "connected" cumulants in LPT, decomposed into its contractions with the unit vector $\hat{k}$ and δ_{ij}. At one-loop order, all such contributions are due to matter velocities in the form of $\dddot{W}_{ijk}$ and therefore aren't multiplied by any bias paremeters.

for example

$$\int d^3\mathbf{q}\ e^{i\mathbf{k}\cdot\mathbf{q}}\ \mu^2 f(q) = 4\pi\int dq\ q^2\ f(q)\ \Big(j_0(kq) - \frac{2j_1(kq)}{kq}\Big).$$

This choice, however, leads to extra factors of kq multiplying j_ℓ that make the separation of k-dependences messier. Thus, we have chosen in our calculations to use, e.g.

$$\int d^3\mathbf{q}\ e^{i\mathbf{k}\cdot\mathbf{q}}\ \mu^2 f(q) = 4\pi\int dq\ q^2\ f(q)\ \left(\frac{1}{3}j_0(kq) - \frac{2}{3}j_2(kq)\right). \tag{B.52}$$

B.7 Useful Mathematical Identies

To evaluate the power spectrum we make use of the angular integrals of the form

$$I_{2m(+1)}(A,B) = \frac{1}{2}\int d\mu\ \mu^{2m(+1)}e^{iA\mu - \frac{B\mu^2}{2}} = i^{0(+1)}e^{-B/2}\sum_{n=0}^{\infty} f_n^{2m}(B)\Big(\frac{B}{A}\Big)^n j_{n(+1)}(A) \tag{B.53}$$

where the series coefficients $f_n^{2m}(B)$ can be explicitly written using confluent hypergeometric functions of the second kind

$$f_n^{2m}(B) = \Big(\frac{2}{B}\Big)^m\ U(-m, n-m+1, \frac{B}{2}) \tag{B.54}$$

. For convenience we list the first few such integrals (see also Refs. [396, 398]):

$$\frac{1}{2}\int d\mu\, \mu^0 e^{iA\mu-\frac{B\mu^2}{2}} = e^{-B/2}\sum_{n=0}^{\infty}\left(\frac{B}{A}\right)^n j_n(A) \tag{B.55}$$

$$\frac{1}{2}\int d\mu\, \mu^1 e^{iA\mu-\frac{B\mu^2}{2}} = ie^{-B/2}\sum_{n=0}^{\infty}\left(\frac{B}{A}\right)^n j_{n+1}(A) \tag{B.56}$$

$$\frac{1}{2}\int d\mu\, \mu^2 e^{iA\mu-\frac{B\mu^2}{2}} = e^{-B/2}\sum_{n=0}^{\infty}\left(1-\frac{2n}{B}\right)\left(\frac{B}{A}\right)^n j_n(A) \tag{B.57}$$

$$\frac{1}{2}\int d\mu\, \mu^3 e^{iA\mu-\frac{B\mu^2}{2}} = ie^{-B/2}\sum_{n=0}^{\infty}\left(1-\frac{2n}{B}\right)\left(\frac{B}{A}\right)^n j_{n+1}(A) \tag{B.58}$$

$$\frac{1}{2}\int d\mu\, \mu^4 e^{iA\mu-\frac{B\mu^2}{2}} = e^{-B/2}\sum_{n=0}^{\infty}\left(1-\frac{4n}{B}+\frac{4n(n-1)}{B^2}\right)\left(\frac{B}{A}\right)^n j_n(A) \tag{B.59}$$

The integrals that begin with j_{n+1} can be merged with those that do not by shifting indices, e.g.

$$\frac{1}{2}\int d\mu\, \mu^3 e^{iA\mu-\frac{B\mu^2}{2}} = ie^{-B/2}\sum_{n=0}^{\infty}\left(\frac{A\Theta_n}{B}\right)\left(1-\frac{2(n-1)}{B}\right)\left(\frac{B}{A}\right)^n j_n(A), \tag{B.60}$$

where $\Theta_n = 1$ for integers n greater than zero and is zero for $n = 0$, such that we can write

$$I_m(A,B) = \frac{1}{2}\int d\mu\, \mu^m e^{iA\mu-\frac{B\mu^2}{2}} = e^{-B/2}\sum_{n=0}^{\infty} c_n^m(B)\left(\frac{B}{A}\right)^n j_n(A). \tag{B.61}$$

B.8 Implementation in Python

Our PYTHON code to calculate the velocity components and combine them into redshift-space power spectra, `velocileptors`, is publicly available[6] and includes example Jupyter notebooks and scripts introducing the main modules.

The library is split into two main subdirectories, `LPT` and `EPT` which house the calculations performed in LPT and EPT, respectively. The main workhorse module in each is called **moment_expansion_fftw.py**, which produces the IR-resummed velocity moments and contains functions to combine them into redshift-space power spectra. This is supplemented by **fourier_streaming_model_fftw.py** and **gaussian_streaming_model_fftw.py** in `LPT` and **ept_fullresum_fftw.py** in `EPT`, the latter of which calculates the one-loop EPT redshift-space power spectrum directly.

[6] https://github.com/sfschen/velocileptors

In addtion to these the folder `Utils` contains various useful functions necessary for the above calculations, the most important of which is **qfuncfft.py**, which comptues various one-loop PT kernels and correlators using the FFTLog formalism described in ref. [320] and expressions derived in Appendix B.5.

The structure of the basic LPT, and by extension EPT, class **cleft_fftw.py** is based on earlier code[7], with a few modifications. Most importantly, the FFTLogs are evaluated using **spherical_bessel_transform_fftw.py**, a custom FFTLog module based on `mcfit`[8] that saves time on the Hankel transforms used to compute the various LPT spectra by storing the FFTLog kernels[9], whose evaluations were the slowest steps of previous LPT codes, rather than computing them on the fly. To further speed up these Hankel transforms we use a multi-threadable python wrapper for FFTW[10], pyFFTW[11], which can be installed via **pip**. Our LPT code takes less than one and a half seconds to generate power spectra at 50 wavenumbers running on one thread on a Macbook Pro purchased in 2013 and summing over spherical Bessel functions up to $\ell = 5$, generating all the bias contributions independently such that power spectra within the same cosmology (but potentially different f) can be re-computed essentially instantly, as can power spectra at different LOS angles μ. We found that this setting was sufficient to produce $< 0.5\%$ errors out to $k = 0.25\,h\,\mathrm{Mpc}^{-1}$ on all relevant spectra. Results at an arbitrary number of ks can then be provided via cubic spline interpolation with no loss of accuracy. The EPT code is slightly faster still and takes less than a second to run (independent of the number of k points). For completeness, we include the capability to set 1-loop terms to zero (for Zeldovich calculations) as well as a module to compute correlation functions in redshift-space via the Gaussian streaming model.

[7] C. Modi. https://github.com/modichirag/CLEFT
[8] Y. Li. https://github.com/eelregit/mcfit
[9] https://jila.colorado.edu/ ajsh/FFTLog/index.html
[10] http://www.fftw.org/
[11] https://hgomersall.github.io/pyFFTW

Appendix C

Redshift-Space Galaxy Clustering II

C.1 Infrared Resummation and the Broadband

Our goal in the main body of this paper was to develop the fully-resummed LPT model and compare its performance to existing models such MOME and REPT. To be as fair as possible to each of these models, we have independently fit for the bias parameters in counterterms in each. However, it should be noted that in principle the bias bases for LPT and MOME are identical, and equivalent up to a mapping to the Eulerian basis employed in REPT[1]. However, while all three models should be equivalent order-by-order under these mappings, they tend to make somewhat different predictions, especially towards small scales, due to the different IR resummation schemes involved. Namely, each of the three schemes organizes the perturbative expansion in slightly different expansion parameters. While LPT resums all the two-point long wavelength displacement and velocity contributions, in EPT these are considered perturbative and are accordingly expanded. Nevertheless, in EPT what is resummed are the contributions to the BAO feature from the relative motions of the long modes. In the MOME expansion, RSD contributions are organized following the moment expansion [328, 400, 401, 398], while each of the contributions is then evaluated in LPT [74]. This seemingly leaves the long velocity contributions expanded, contrary to the full LPT approach. In ref. [74] these were left un-resummed, although a straight forward approach to add these would follow the EPT procedure, just excluding the displacement contributions which have already been resummed. For MOME we can thus write

$$P^{s,IR}_{\text{1-loop}}(\mathbf{k}) \approx P^{s,\text{nw}}_{\text{1-loop}}(\mathbf{k}) + e^{-\frac{1}{2}\Sigma_s^2(\mu)k^2}\left(1+\tfrac{1}{2}\Sigma_s^2(\mu)k^2\right)P^{s,\text{w}}_{\text{lin}}(\mathbf{k}) + e^{-\frac{1}{2}\Sigma_s^2(\mu)k^2}\left(P^{s}_{\text{loop}}(\mathbf{k}) - P^{s,\text{nw}}_{\text{loop}}(\mathbf{k})\right),$$

where the wiggle and no-wiggle $P^s_{\text{1 - loop}}$ (and similarly the P^s_{loop} by dropping the linear Kaiser part) are given by MOME predictions computed in ref. [74]. The difference with the EPT resummation scheme is in the definition of Σ_s which now contains only the velocity

[1] See, for example, Equation 4.8 in ref. [74]

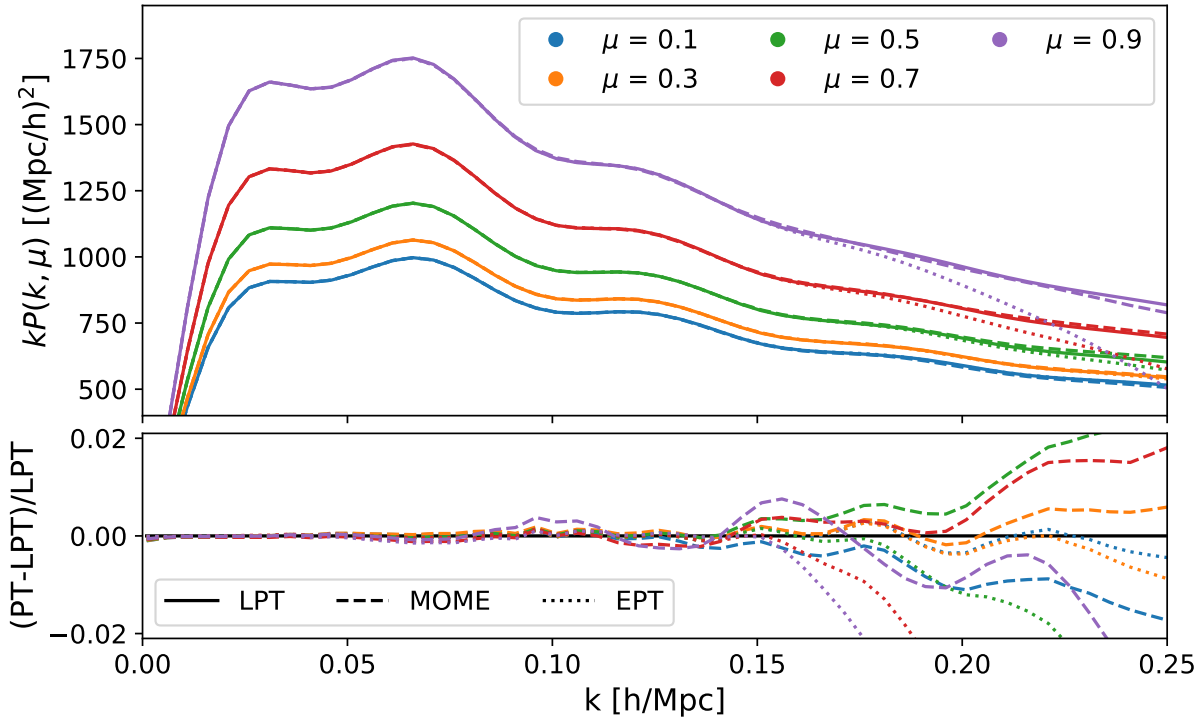

Figure C.1: Power spectrum predictions of the three models (LPT, MOME, REPT) given the same set of bias parameters, but with all counterterms and stochastic parameters adjusted in the MOME and REPT curves to match the LPT prediction with no counterterms or stochastic terms . While much of the differences between the three formalisms can be soaked up by the counterterms, the fractional residuals (lower panel) at high k and μ begin to show less trivial behavior, suggesting non-negligible theory error.

contributions

$$\Sigma_s^2(\mu) = f(f+2)\mu^2\Sigma^2, \tag{C.1}$$

where Σ^2 is the velocity dispersion due to the long wavelength modes.

Figure C.1 shows the predictions for $P(k,\mu)$ of LPT, MOME and REPT when the bias parameters (b_1, b_2, b_s, b_3) are fixed to the best-fit values for the fiducial halo sample in LPT, with counterterms and stochastic contributions in the MOME and REPT cases adjusted to fit the LPT result. The three schemes differ systematically towards higher k and μ. Compared to its Eulerian counterpart, LPT shows significant supression of power towards high k, particularly along the line of sight; this suppression is absorbed by adjusting counterterms and stochastic contributions in Figure C.1, though the theories nonetheless begin to diverge at the percent level around $k = 0.15\,h\,\mathrm{Mpc}^{-1}$, especially towards higher μ. The LPT and MOME schemes are quite similar at low μ since they differ only in the inclusion of higher-order

velocities along the line of sight in the former[2]—and both are damped relative to REPT—but closer to the line of sight their oscillatory components begin to differ significantly more than between LPT and REPT since long velocity modes are not resummed in MOME.

The above differences in the three schemes have their origin in the fact that the expansion parameters in these schemes do not match exactly. As we mentioned before, in LPT the long wavelength displacement and velocity two-point contributions are directly resummed, while in REPT only the relative effects of these are resummed and thus affect only the BAO. The MOME scheme, on the other hand, takes a hybrid approach between the previous two. Since the predictions of the three schemes, as plotted in Figure C.1, are equal up to second (one-loop) order in the linear power spectrum when expanded order-by-order; the apparent differences therefore reflect differences at two-loop order or beyond, even though these residuals are due to the long mode contributions and are nominally under the perturbative control. At low k they manifest as contributions proportional to the wavenumber squared and can be largely absorbed by existing counterterms $\propto k^2\mu^{2n}P(k)$ and stochastic contributions. The residual deviations at higher k and μ, can also provide rough estimates of the theory error of these common perturbative schemes, indicating the range of validity of current perturbative models. We intend to return to a more in-depth comparison of these schemes in a future work.

In addition, as noted in the main body of the text, the choice of infrared cutoff $k_{\rm IR}$ has a significant effect on the broadband power of the anisotropic power spectrum within the LPT model itself. Figure C.2 shows this effect on the power spectrum multipoles, with bias parameters fixed to those obtained by fitting the fiducial sample to LPT with $k_{\rm IR} = 0.2\,h\,{\rm Mpc}^{-1}$. In all three multipoles shown, decreasing the IR cutoff results in increasing power at high k, with higher ℓ increasingly sensitive to these nonlinearities. Indeed, by $k = 0.1\,h\,{\rm Mpc}^{-1}$ the hexadecapoles with $k_{\rm IR}$ equal to zero is close to twice as large as that with no IR cutoff, i.e. $k_{\rm IR} = \infty$. In the $k_{\rm IR} \to 0$ limit the LPT prediction is equal to that in EPT without any additional IR resummation and with the bias parameters appropriately mapped. Of course, we caution that while the differences shown in Figure C.2 are intended to demonstrate the full spectrum of resummations possible in our scheme, in reality much of these differences can be absorbed by effective corrections as in Figure C.1.

The increasing effect of the IR cutoff on redshift space distortions at high μ can be understood intuitively within the language of the moment expansion. In general, higher-order velocities will tend to be more sensitive to the IR cutoff. This can be seen as follows: the velocity statistics of interest for RSD can be schematically written as $M_n = \langle X^n e^{iX}\rangle$ where $X = \mathbf{k}\cdot\Delta$. Approximating X to be Gaussian with variance σ^2 we can write the even moments as

$$M_{2n} = \langle X^{2n}\rangle(1 + a_2\sigma^2 + a_4\sigma^4 + \dots)\ \exp\left[-\sigma^2/2\right]. \tag{C.2}$$

For $n > 0$ we always have $a_2 < 0$, i.e. M_{2n} damps faster than the exponential damping in M_0. This is easily understood: higher M_n receive more contributions from larger values of X, where the complex exponential oscillates rapidly, and are suppressed by X^n at small

[2]In fact, MOME also shows slightly *more* suppression at low μ since we have followed the main text of ref. [74] and the `velocileptors` code in not including any IR cutoffs in the expanded velocity moments.

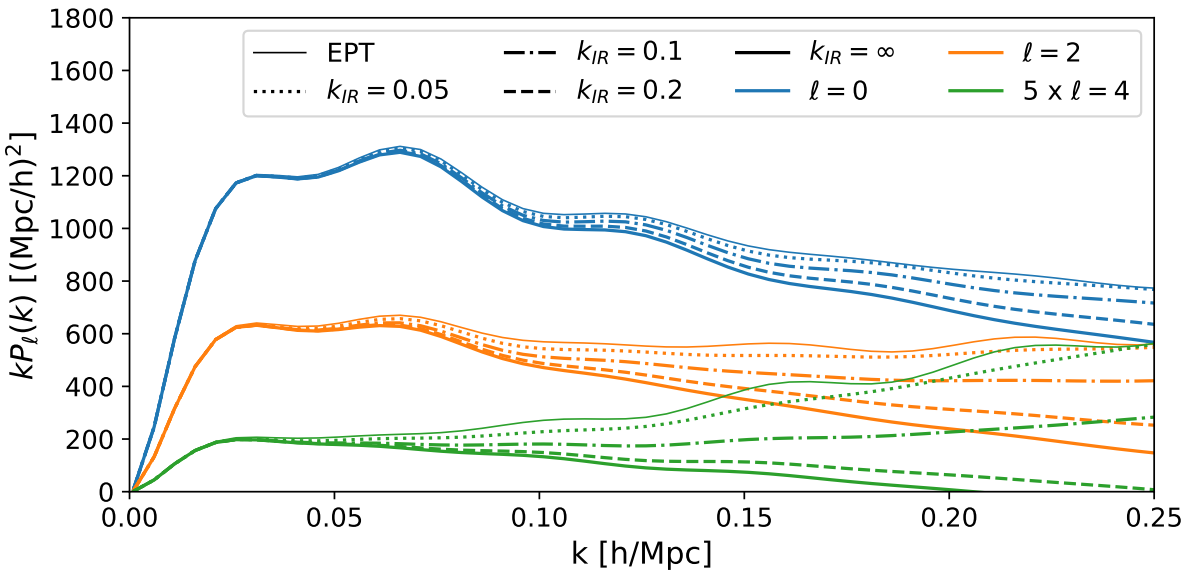

Figure C.2: Power spectrum multipole predictions for a range of IR cutoffs $k_{\rm IR}$. Including more IR modes by upping $k_{\rm IR}$ damps the total power at high k, especially in the higher multipoles. The limit of $k_{\rm IR} \to 0$ corresponds to unresummed EPT (thin solid lines), with noticeably larger BAO oscillations at both linear and one-loop order, though even $k_{\rm IR} = 0.05\,h\,{\rm Mpc}^{-1}$ dramatically reduces these.

X where the exponential varies slowly. Indeed, this effect was observed in ref. [74], where it was noted that the broadband of the second moment of the pairwise velocity, $\sigma_{12,\,\rm ij} = \left\langle (1+\delta_1)(1+\delta+2)\dot{\Delta}_i\dot{\Delta}_j \right\rangle$ is very sensitive to cutoff choice, with its monopole and quadrupole respectively being better predicted by higher and lower values of $k_{\rm IR}$. Since the second moment's quadrupole is the leading μ^4 contribution to the anisotropic power spectrum, one might expect that P_4 should in turn be very sensitive to this choice. In light of the effects of $k_{\rm IR}$ on the second moment, in this paper we have chosen the "intermediate" value of $0.2\,h\,{\rm Mpc}^{-1}$ as our fiducial IR cutoff (at $z \approx 0.8$), though we caution that further investigation is warranted when operating at significantly higher or lower redshifts or with highly biased tracers.

Finally, let us note that, in contrast to the anisotropic broadband, the corresponding BAO features in the correlation function monopole and quadrupole, shown in Figure C.3, are rather insensitive to the specific choice of $k_{\rm IR}$. Indeed, even $k_{\rm IR} = 0.05\,h\,{\rm Mpc}^{-1}$, which is almost identical to EPT in its broadband, demonstrates significant damping of the BAO feature. This figure also shows the unresummed EPT ($k_{\rm IR} = 0$) prediction, which clearly illustrates the non-convergence of the configuration-space BAO feature in one-loop EPT that necessitates the a posteriori IR resummation implemented in these models.

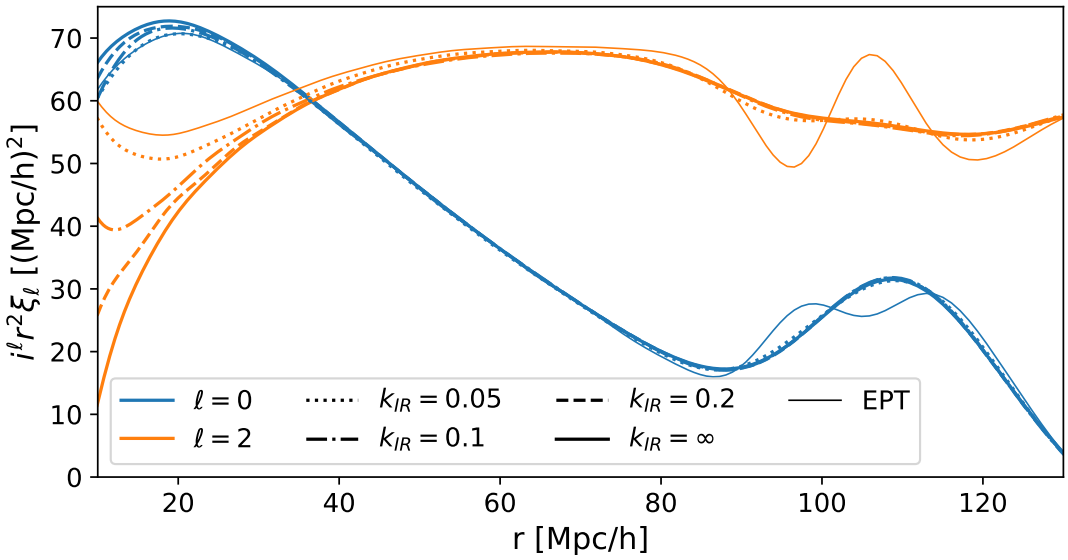

Figure C.3: Correlation function multipole predictions with a range of IR cutoffs $k_{\rm IR}$ for bias parameters fixed to those obtained from the fiducial halo sample. The BAO features in both the monopole and quadrupole are rather robust, showing little change for $k_{\rm IR} > 0.05\,h\,{\rm Mpc}^{-1}$, despite significant differences in the corresponding power spectrum broadbands. For reference, the unresummed EPT ($k_{\rm IR} = 0$) prediction, which clearly illustrates the non-convergence of the nonlinear configuration-space BAO feature absent IR resummation, is also shown (thin solid lines).

C.2 Method I

In this section we extend Method I, first presented in [398], to include terms up to one-loop order. In contrast to Method II, described in the main body of the text, this method does not rely on boosting the wavevector $\mathbf{k}$ into a more convenient frame but rather evaluates the integral in Equation 3.5 directly in the observed frame.

From the form of the RSD operator $R_{ij}^{(n)} = \delta_{ij} + nf\hat{n}_i\hat{n}_j$, where n index counts a given order in PT, we can see that all integrals in Eq.(3.5) can be written in terms of scalar functions and dot products between three unit vectors ($\hat{q}$, $\hat{k}$ and $\hat{n}$). The angular structure is given in terms of products

$$\hat{n}\cdot\hat{k} = \mu, \quad \hat{q}\cdot\hat{k} = \mu_{\mathbf{q}}, \quad \hat{q}\cdot\hat{n} = \mu_{\mathbf{q}}\mu + \sqrt{1-\mu_{\mathbf{q}}^2}\sqrt{1-\mu^2}\,\cos\phi, \tag{C.3}$$

where ϕ is the azimuthal angle in a polar coordinate system where the zenith is given by $\hat{k}$ and the plane $\phi = 0$ is spanned by $\hat{k}$ and $\hat{q}$. The effect of RSD operators $\mathbf{R}^{(n)}$ can then be

captured by looking how it acts on the tensor basis comprised of $\hat{q}_i, \delta_{ij},$. We have

$$k_i k_j \delta_{ij} \to k_i k_j R_{in}^{(m_1)} R_{jn}^{(m_2)} = k^2 \left[1 + f(m_1 + m_2 + m_1 m_2 f)\mu^2\right], \tag{C.4}$$

$$k_i \hat{q}_i \to k_i R_{ij}^{(m)} \hat{q}_j = k\mu_{\mathbf{q}} \left[1 + mf\mu^2 + mf\mu^2\gamma(\mu_{\mathbf{q}}, \mu)\cos\phi\right], \tag{C.5}$$

where $\gamma(\mu_{\mathbf{q}}, \mu) = \sqrt{1-\mu_{\mathbf{q}}^2}\sqrt{1-\mu^2}/\mu_{\mathbf{q}}\mu$. The azimuthal dependence of the exponentiated linear displacements A_{ij}^s requires us to calculate polar-coordinate integrals of the form [398]

$$I_n(f, \mu_{\mathbf{q}}, \mu) = \int_0^{2\pi} \frac{d\phi}{2\pi}\, e^{-\frac{1}{2}k^2 Y(\alpha_2\gamma\cos\phi + \alpha_3\gamma^2\cos^2\phi)\mu_{\mathbf{q}}^2}, \tag{C.6}$$

where $\alpha_2 = f\mu^2(m_1 + m_2 + fm_1m_2\mu^2)$ and $\alpha_3 = m_1m_2f^2\mu^4$. This expression can be used to compute all the other loop contributions (except the W_{ijk} term). These can be calculated by taking derivatives in either α or β of the identity

$$I_\phi(\alpha, \beta, \mu_{\mathbf{q}}) = \int_0^{2\pi} \frac{d\phi}{2\pi}\, e^{\alpha\mu_{\mathbf{q}}\sqrt{1-\mu_{\mathbf{q}}^2}\cos\phi + \beta(1-\mu_{\mathbf{q}}^2)\cos^2\phi} = \sum_{\ell=0}^{\infty} F_\ell(\alpha, \beta)\left(\alpha^2\mu_{\mathbf{q}}^2/\beta\right)^\ell, \tag{C.7}$$

where

$$F_\ell(\alpha, \beta) = \sum_{m=0}^{\ell} \frac{\Gamma(m+\frac{1}{2})}{\pi^{1/2}\Gamma(m+1)\Gamma(1+2m-\ell)\Gamma(2\ell-2m+1)} \left(-\frac{\beta^2}{\alpha^2}\right)^m \times M\left(\ell-2m; \ell-m+\tfrac{1}{2}; \frac{\alpha^2}{4\beta}\right) M\left(m+\frac{1}{2}; m+1; \beta\right) \tag{C.8}$$

and $M(a, b, z)$ are hypergeometric functions of the first kind.

In order to capture the contribution of W_{ijk} a slight generalisation of the integrals above is required. The integral we need is of the form

$$\int_0^{2\pi} \frac{d\phi}{2\pi}\left(\sqrt{1-\mu_{\mathbf{q}}^2}\cos\phi\right) e^{\alpha\mu_{\mathbf{q}}\sqrt{1-\mu_{\mathbf{q}}^2}\cos\phi + \beta(1-\mu_{\mathbf{q}}^2)\cos^2\phi} = \frac{1}{\mu_{\mathbf{q}}}\frac{d}{d\alpha} I_\phi(\alpha, \beta, \mu_{\mathbf{q}}). \tag{C.9}$$

However, since $F_0(\alpha, \beta)$ does not depend on α we have

$$\frac{1}{\mu_{\mathbf{q}}}\frac{d}{d\alpha} I_\phi(\alpha, \beta, \mu_{\mathbf{q}}) = \mu_{\mathbf{q}}\frac{1}{\beta}\frac{d}{d\alpha}\sum_{\ell=0}^{\infty}\alpha^2 F_{\ell+1}(\alpha, \beta)\left(\alpha^2\mu_{\mathbf{q}}^2/\beta\right)^\ell. \tag{C.10}$$

C.3 Method II

C.3.1 General Mathematical Structure

The workhorse integral of Method II is [398]

$$I(A, B, C) = \int d\mu_{\mathbf{q}}\, d\phi\, e^{-iC\sqrt{1-\mu_{\mathbf{q}}^2}\cos\phi + iA\mu_{\mathbf{q}} + B\mu_{\mathbf{q}}^2} = 4\pi e^B \sum_{\ell=0}^{\infty}\left(\frac{-2}{\rho}\right)^\ell \tilde{G}_{0,\ell}^{(0)}(A, B, \rho) j_\ell(\rho),$$

where $\rho^2 = A^2 + C^2$. The exact form of the kernel $\tilde{G}^{(0)}_{0,\ell}$ is given in Section C.3.4.

To compute the redshift-space power spectrum for biased tracers we will need the integrals derived from A, C derivatives of I, i.e.

$$I_{n,m}(A,B,C) = i^{m-n}\int d\mu_{\mathbf{q}}\, d\phi\; e^{-iC\sqrt{1-\mu^2_{\mathbf{q}}}\cos\phi + iA\mu_{\mathbf{q}} + B\mu^2_{\mathbf{q}}}\left(\sqrt{1-\mu^2_{\mathbf{q}}}\cos\phi\right)^n \mu^m_{\mathbf{q}} \tag{C.11}$$

$$= 4\pi e^B \sum_{\ell=0}^{\infty}\left(\frac{-2}{\rho}\right)^\ell \tilde{G}^{(m)}_{n,\ell}(A,B,\rho) j_\ell(\rho). \tag{C.12}$$

These satisfy the recursion relations

$$\tilde{G}^{(m)}_{n,\ell} = \frac{d\tilde{G}^{(m)}_{n,\ell}}{dA} + \frac{A}{2}\,\tilde{G}^{(m-1)}_{n,\ell-1}, \quad \tilde{G}^{(m)}_{n,l} = \frac{\partial\tilde{G}^{(m)}_{n,\ell}}{\partial C} + \frac{C}{2}\tilde{G}^{(m-1)}_{n,\ell-1}. \tag{C.13}$$

For convenience we list the first few $\tilde{G}^{(m)}_{0,\ell}$:

$$\begin{aligned}
\tilde{G}^{(1)}_{0,\ell} &= \frac{\partial\tilde{G}^{(0)}_{0,\ell}}{\partial A} + \frac{A}{2}\tilde{G}^{(0)}_{0,\ell-1} \\
\tilde{G}^{(2)}_{0,\ell} &= \frac{\partial^2\tilde{G}^{(0)}_{0,\ell}}{\partial A^2} + A\frac{\partial\tilde{G}^{(0)}_{0,\ell-1}}{\partial A} + \frac{1}{2}\tilde{G}^{(0)}_{0,\ell-1} + \frac{A^2}{4}\tilde{G}^{(0)}_{0,\ell-2} \\
\tilde{G}^{(3)}_{0,\ell} &= \frac{\partial^3\tilde{G}^{(0)}_{0,\ell}}{\partial A^3} + \frac{3A}{2}\frac{\partial^2\tilde{G}^{(0)}_{0,\ell-1}}{\partial A^2} + \frac{3}{2}\frac{\partial\tilde{G}^{(0)}_{0,\ell-1}}{\partial A} + \frac{3A^2}{4}\frac{\partial\tilde{G}^{(0)}_{0,\ell-2}}{\partial A} + \frac{3A}{4}\tilde{G}^{(0)}_{0,\ell-2} + \frac{A^3}{8}\tilde{G}^{(0)}_{0,\ell-3}.
\end{aligned} \tag{C.14}$$

The derivatives with respect to C are entirely analogous, swapping C for A and m for n. In addition, we will need

$$\tilde{G}^{(1)}_{1,\ell} = \frac{\partial^2\tilde{G}^{(0)}_{0,\ell}}{\partial A\partial C} + \frac{C}{2}\frac{\partial\tilde{G}^{(0)}_{0,\ell-1}}{\partial A} + \frac{A}{2}\frac{\partial\tilde{G}^{(0)}_{0,\ell-1}}{\partial C} + \frac{AC}{4}\tilde{G}^{(0)}_{0,\ell-2}$$

$$\begin{aligned}
\tilde{G}^{(2)}_{1,\ell} = &\frac{\partial^3\tilde{G}^{(0)}_{0,\ell}}{\partial A^2\partial C} + \frac{C}{2}\frac{\partial^2\tilde{G}^{(0)}_{0,\ell-1}}{\partial A^2} + A\frac{\partial^2\tilde{G}^{(0)}_{0,\ell-1}}{\partial A\partial C} + \frac{1}{2}\frac{\partial\tilde{G}^{(0)}_{0,\ell-1}}{\partial C} \\
&+ \frac{AC}{2}\frac{\partial\tilde{G}^{(0)}_{0,\ell-2}}{\partial A} + \frac{A^2}{4}\frac{\partial\tilde{G}^{(0)}_{0,\ell-2}}{\partial C} + \frac{C}{4}\tilde{G}^{(0)}_{0,\ell-2} + \frac{A^2C}{8}\tilde{G}^{(0)}_{0,\ell-3}
\end{aligned}$$

C.3.2 Example: One-Loop Matter Power Spectrum in Redshift Space

Let us consider the one-loop matter power spectrum as an example for the kinds of angular terms that can arise. For simplicity, we focus on what happens to the un-exponentiated

one-loop contribution $A_{ij}^{(22)}$. In this case we have that the relevant quantity in redshift space is

$$k_i k_j (\mathbf{R}^{(1)} + f\ \hat{n}\otimes\hat{n})_{in}(\mathbf{R}^{(1)} + f\ \hat{n}\otimes\hat{n})_{jm} A_{nm}^{(22)} = \left(K_i K_j + 2f k_{\parallel,i} K_j + f^2 k_{\parallel,i} k_{\parallel,j}\right) A_{ij}^{(22)}. \tag{C.15}$$

The first piece $(K_i K_j)$ is identical in angular structure to those in the Zeldovich case, so we restrict our attention to the other two.

Let's begin with the term proportional to f in Equation C.15. We have (dropping the (22) for brevity)

$$\begin{aligned} K_i k_{\parallel,j} A_{ij} &= (K\cdot k_\parallel) X + (\hat{q}\cdot K)(\hat{q}\cdot k_\parallel) Y \\ &= k^2\mu^2(1+f)\ X + (K\mu_{\mathbf{q}})\ k\mu(A(\mu)\mu_{\mathbf{q}} + B(\mu)\sqrt{1-\mu_{\mathbf{q}}^2}\cos\phi)\ Y. \end{aligned}$$

The piece proportional to X poses no problem since it has no angular dependence. The term proportional to Y has a piece proportional to $\mu_{\mathbf{q}}^2$, which can be computed via two derivatives of Equation 3.13 w.r.t. A, and another with ϕ dependence calculable via a C derivative; both are of the form C.12. The term proportional to f^2 is similar and involves

$$k_{\parallel,i} k_{\parallel,j} A_{ij} = k^2\mu^2\left[X + (\hat{q}\cdot\hat{n})^2 Y\right].$$

This piece proportional to Y then involves up to two C derivatives.

C.3.3 General Angular Structure of Bias Contributions

Let us now list all the possible angular dependencies at one-loop order, organized in powers $\mu_{\mathbf{q}}^a(\hat{n}\cdot\hat{q})^b$. This format is convenient because each such power can be readily integrated in ϕ and $\mu_{\mathbf{q}}$ to give

$$\begin{aligned} \mu_{\mathbf{q}}^a(\hat{n}\cdot\hat{q})^b = \sum_{n=0}^{b}\binom{b}{n} A^n(\mu)B^{b-n}(\mu)\mu_{\mathbf{q}}^{a+n}\left(\sqrt{1-\mu_{\mathbf{q}}^2}\cos\phi\right)^{b-n} \to \\ 4\pi\sum_{n=0}^{b}\binom{b}{n} A^n(\mu)B^{b-n}(\mu)\left(\frac{-2}{kq}\right)^{\ell}\tilde{G}_{b-n,\ell}^{a+n}\ j_\ell(kq) \end{aligned}$$

The simplest case involves correlators with one order n displacement, of the form $U_i^{(n)} = U(q)\hat{q}_i$:

$$k_i U_i^{s,(n)} = \left[K\mu_{\mathbf{q}} + f(n-1)k\mu(\hat{q}\cdot\hat{n})\right] U(q) \tag{C.16}$$

Then we have terms involving two displacements with order n, m, which we can write as $A_{ij}^{(n,m)} = X\delta_{ij} + Y\hat{q}_i\hat{q}_j$:

$$\begin{aligned} k_i k_j A_{ij}^{s,(n,m)} =& K^2[X(q) + Y(q)\mu_{\mathbf{q}}^2] + (n+m-2)fk\mu[X(q)(\hat{K}\cdot\hat{n}) + Y(q)\mu_{\mathbf{q}}(\hat{q}\cdot\hat{n})] \\ &+ (n-1)(m-1)f^2k^2\mu^2[X(q) + Y(q)(\hat{q}\cdot\hat{n})^2]. \end{aligned} \tag{C.17}$$

bias	(n,m,l): correlator
1	$(1,3)$: $A_{ij}^{(13)}$, $(2,2)$: $A_{ij}^{(22)}$, $(1,1,2)$: $W_{ijk}^{(112)}$
b_1	(3): $U_i^{(3)}$, $(1,2)$: A_{ij}^{10}
b_1^2	(2): U_i^{11}
b_2	(2): U_i^{20}
b_s	(2): V_i^{10}

Table C.1: Contributions to the one-loop power spectrum and the perturbative order of the displacements they contain.

Finally, at one-loop order there is one term involving three displacements involving their (112) bispectrum $W_{ijk}^{(112)} = V_1(\hat{q}_i\delta_{jk} + \hat{q}_j\delta_{ik}) + V_3\hat{q}_k\delta_{ij} + T\hat{q}_i\hat{q}_j\hat{q}_k$:

$$\begin{aligned} k_ik_jk_kW_{ijk}^{(112)} &= 2\big(K^3 + fK(k\mu)^2(1+f)\big)\mu_{\mathbf{q}}\, V_1(q) \\ &\quad + K^2\big(K\mu_{\mathbf{q}} + f(k\mu)(\hat{n}\cdot\hat{q})\big)\, V_3(q) \\ &\quad + K^2\big(K\mu_{\mathbf{q}}^3 + f(k\mu)\mu_{\mathbf{q}}^2(\hat{n}\cdot\hat{q})\big)\, T(q). \end{aligned} \tag{C.18}$$

The full list of non-Zeldovich angular dependences required for the one-loop power spectrum is given in Table C.1.

C.3.4 $\tilde{G}_{0,m}^{(0)}$ and Its Derivatives

The basic kernel for Method II is the function

$$\tilde{G}_m^{(0)}(A,B,\rho) = \sum_{n=m}^{\infty} f_{nm}\Big(\frac{BA^2}{\rho^2}\Big)^n {}_2F_1\Big(\frac{1}{2}-n,-n;\frac{1}{2}-m-n;\frac{\rho^2}{A^2}\Big), \tag{C.19}$$

where $\rho = \sqrt{A^2+C^2}$, ${}_2F_1$ is the ordinary hypergeometric function and f_{nm} is

$$f_{nm} = \frac{\Gamma(m+n+\frac{1}{2})}{\Gamma(m+1)\Gamma(n+\frac{1}{2})\Gamma(1-m+n)} \quad . \tag{C.20}$$

The angular dependences in Method II require us to take A and C derivatives of the above. The first three derivatives of $\tilde{G}_0^{(0)}$ with respect to A are given by

$$\begin{aligned} \frac{d\tilde{G}_{0,m}^{(0)}}{dA} = \sum_{n=m}^{\infty}\Big(\frac{BA^2}{\rho^2}\Big)^n f_{nm}\Bigg[&\Big(\frac{2n}{A}-\frac{2nA}{\rho^2}\Big){}_2F_1\Big(\frac{1}{2}-n,-n;\frac{1}{2}-m-n;\frac{\rho^2}{A^2}\Big) \\ &+\Big(-\frac{2\rho^2}{A^3}+\frac{2}{A}\Big)\frac{(\frac{1}{2}-n)(-n)}{(\frac{1}{2}-m-n)}{}_2F_1\Big(\frac{3}{2}-n,1-n;\frac{3}{2}-m-n;\frac{\rho^2}{A^2}\Big)\Bigg] \end{aligned} \tag{C.21}$$

$$\frac{d^2\tilde{G}^{(0)}_{0,m}}{dA^2} = \sum_{n=m}^{\infty}\Big(\frac{BA^2}{\rho^2}\Big)^n f_{nm}\Big(\frac{\rho^2-A^2}{\rho^4}\Big) \Bigg[(2m-1-4n(m+1))\ {}_2F_1\Big(\frac{1}{2}-n,-n;\frac{1}{2}-m-n;\frac{\rho^2}{A^2}\Big) + (1-4n^2+m(4n-2))\ {}_2F_1\Big(\frac{3}{2}-n,-n;\frac{1}{2}-m-n;\frac{\rho^2}{A^2}\Big)\Bigg]. \tag{C.22}$$

$$\frac{d^3\tilde{G}^{(0)}_{0,m}}{dA^3} = \frac{C^2}{A\rho^6}\sum_{n=m}^{\infty}\Big(\frac{BA^2}{\rho^2}\Big)^n f_{nm} \Bigg[\Big((2(1-m)(1-2m)+8n(2-m)(1+m)+8n^2(1+m))A^2 - (1-2m+4n(1+m))C^2\Big)\ {}_2F_1\Big(\frac{1}{2}-n,-n;\frac{1}{2}-m-n;\frac{\rho^2}{A^2}\Big) - (1-2n)\Big(2(1-2m+2n)(1-m+n)A^2 - (1-2m+4n(1+m))C^2\Big)\ {}_2F_1\Big(\frac{3}{2}-n,1-n;\frac{1}{2}-m-n;\frac{\rho^2}{A^2}\Big)\Bigg]$$

The derivatives with respect to C are

$$\frac{d\tilde{G}^{(0)}_{0,m}}{dC} = -\frac{C}{\rho^2}\sum_{n=m}^{\infty}\Big(\frac{BA^2}{\rho^2}\Big)^n f_{nm}\Big[{}_2F_1\Big(\frac{1}{2}-n,-n;\frac{1}{2}-m-n;\frac{\rho^2}{A^2}\Big) - (1-2n)\ {}_2F_1\Big(\frac{3}{2}-n,1-n;\frac{1}{2}-m-n;\frac{\rho^2}{A^2}\Big)\Big] \tag{C.23}$$

$$\frac{d^2\tilde{G}^{(0)}_{0,m}}{dC^2} = \rho^{-4}\sum_{n=m}^{\infty}\Big(\frac{BA^2}{\rho^2}\Big)^n f_{nm} \Big[\big((1+2m-4n(1+m))A^2+2C^2\big){}_2F_1\Big(\frac{1}{2}-n,-n;\frac{1}{2}-m-n;\frac{\rho^2}{A^2}\Big) - (1-2n)\big((1+2m-2n)A^2+2C^2\big){}_2F_1\Big(\frac{3}{2}-n,-n;\frac{1}{2}-m-n;\frac{\rho^2}{A^2}\Big)\Big]. \tag{C.24}$$

Note that we can use $dG/dA = -(C/A)\ dG/dC$ to recast the first derivative w.r.t. A in a convenient form as well.

In addition, we need two mixed derivatives $\partial_C \partial_A^{(1,2)} G$. These are

$$\frac{\partial^2 \tilde{G}^{(0)}_{0,m}}{\partial C \partial A} = -\frac{C}{A\rho^4} \sum_{n=m}^{\infty} \Big(\frac{BA^2}{\rho^2}\Big)^n f_{nm} \Bigg[(2(m-2n(1+m))A^2 + C^2)\, {}_2F_1(\frac{1}{2}-n, -n; \frac{1}{2}-m-n; \frac{\rho^2}{A^2}) - (1-2n)(2(m-n)A^2 + C^2)\, {}_2F_1(\frac{3}{2}-n, -n; \frac{1}{2}-m-n; \frac{\rho^2}{A^2}) \Bigg] \quad \text{(C.25)}$$

$$\frac{\partial^3 \tilde{G}^{(0)}_{0,m}}{\partial C \partial A^2} = \frac{C}{\rho^6} \sum_{n=m}^{\infty} \Big(\frac{BA^2}{\rho^2}\Big)^n f_{nm} \Big(\big(2(m-2m^2-4n(1-m^2)-4n^2(1+m))A^2 + 3(1-2m+4n(1+m))C^2\big)\, {}_2F_1(\frac{1}{2}-n, -n; \frac{1}{2}-m-n; \frac{\rho^2}{A^2}) - (1-2n)\big(2(1-2m+2n)(m-n)A^2 + (3-6m+8n+4mn)C^2\big)\, {}_2F_1(\frac{3}{2}-n, -n; \frac{1}{2}-m-n; \frac{\rho^2}{A^2}) \Big) \quad \text{(C.26)}$$

C.3.5 Implementation in Python

Our implementation of Method II, **lpt_rsd_fftw.py**, is available as part of `velocileptors`[3], a PYTHON package for the one-loop redshift-space power spectrum that also includes modules implementing the moment expansion, Gaussian streaming model, and resummed Eulerian perturbation theory. The LPT module includes auxiliary functions to compute multipoles, add Alcock-Paczynski parameters not equal to one and combine the various bias contributions. We also include a sample JUPYTER notebook containing example usage.

Our IR-resummation procedure is inherently rather numerically involved because of the angular dependence of the resummed displacements. To speed up this calculation (in Python) we can take advantage of the fact that the derivatives $\partial_C^b \partial_A^a \tilde{G}^{(0)}_{0,\ell}$ can be written as

$$\sum_{n=\ell}^{\infty} \Big[-\frac{1}{2} K^2 Y^{\rm lin}(q) \Big]^n (kq)^{-(a+b)} c^{2n} F_n(f,\mu),$$

of which the only vector operations involve multiplying by q and $Y(q)$. The remaining factors are independent of k and q and can be tabulated for each value of μ. Further, the only special functions we need are ${}_2F_1(\frac{1}{2}-n, -n; \frac{1}{2}-m-n; x)$, ${}_2F_1(\frac{3}{2}-n, -n; \frac{1}{2}-m-n; x)$, and the Γ-functions in f_{nm}, which can all be tabulated in advance and do not have to be calculated at each wavenumber. With these simplifications, it takes about two and a half seconds to

[3] https://github.com/sfschen/velocileptors

compute the mutipoles at 50 k points between 0.01 and 0.25 $h\,\mathrm{Mpc}^{-1}$; applying a cubic spline to interpolate between these points is sufficient to achieve sub-percent accuracy for any k in this range. Similarly, it takes less than a second to compute $P(k,\mu)$ over the same number of points for a fixed μ.

C.3.6 An alternative formulation of Method II

In this section we provide an alternative numerical solution to the direct evaluation of the RSD integrals in LPT. For simplicity we will present only the leading order term, *i.e.* the Zeldovich approximation, but the main result is trivially extended to one-loop, for which we will provide the necessary ingredients. We begin by writing the Zeldovich RSD power spectrum as

$$P_{s,\mathrm{Zel}}(k,\mu) = 2\pi \int dq q^2 e^{-\frac{1}{2}K^2(X(q)+Y(q))} \int_{-1}^{1} d\mu_{\mathbf{q}}\; e^{i\mu_{\mathbf{q}}A+(\mu_{\mathbf{q}}^2-1)B} J_0(C\sqrt{1-\mu_{\mathbf{q}}}) \tag{C.27}$$

with $A \equiv kqc$, $B \equiv -K^2Y(q)/2$ and $C \equiv kqs$. We then Taylor series expand in B and integrate the A piece by parts n times, when n goes to infinity eventually, to rewrite the integral over $\mu_{\mathbf{q}}$ as

$$\sum_{n=0}^{\infty}(-1)^n \int_{-1}^{1} d\mu_{\mathbf{q}}\; \frac{e^{i\mu_{\mathbf{q}}A}}{(iA/B)^n} 2^n \frac{d^n}{d\mu_{\mathbf{q}}^n}\left(\frac{(\mu_{\mathbf{q}}^2-1)^n}{2^n n!} J_0(C\sqrt{1-\mu_{\mathbf{q}}^2})\right) . \tag{C.28}$$

Then use 10.1.48 of ref. [5] to expand the J_0,

$$J_0(C\sqrt{1-\mu_{\mathbf{q}}^2}) = \sum_{\alpha=0}^{\infty}(4\alpha+1)\frac{(2\alpha)!}{2^{2\alpha}(\alpha!)^2} j_{2\alpha}(C)\mathcal{P}_{2\alpha}(\mu_{\mathbf{q}}) \tag{C.29}$$

to arrive, using the plane wave expansion of the exponential, at

$$\text{C.28} = \sum_{n,\alpha,\ell}(-1)^n \frac{2^n(2\alpha)!}{2^{2\alpha}(\alpha!)^2}(4\alpha+1)(2\ell+1)\frac{(i)^\ell j_\ell(A) j_{2\alpha}(C)}{(iA/B)^n} \tag{C.30}$$

$$\times \int_{-1}^{1} d\mu_{\mathbf{q}}\; \mathcal{P}_\ell(\mu_{\mathbf{q}}) \frac{d^n}{d\mu_{\mathbf{q}}^n}\left(\frac{(\mu_{\mathbf{q}}^2-1)^n}{2^n n!}\mathcal{P}_{2\alpha}(\mu_{\mathbf{q}})\right) . \tag{C.31}$$

Now it turns out that

$$\text{C.31} = \int_{-1}^{1} d\mu_{\mathbf{q}}\; \mathcal{P}_\ell(\mu_{\mathbf{q}}) \sum_{k=0}^{n}\binom{n}{k}\mathcal{P}_n^{-k}(\mu_{\mathbf{q}})\mathcal{P}_{2\alpha}^{k}(\mu_{\mathbf{q}}) \tag{C.32}$$

$$= 2\sum_{k=0}^{n}\binom{n}{k}\sqrt{\frac{(2\alpha+k)!(n-k)!}{(n+k)!(2\alpha-k)!}}\begin{pmatrix}\ell & n & 2\alpha\\ 0 & -k & k\end{pmatrix}\begin{pmatrix}\ell & n & 2\alpha\\ 0 & 0 & 0\end{pmatrix}$$

in terms of 3-j symbols. Putting the above equations together, the angular part of the Zeldovich RSD integral can be computed analytically

$$\text{C.28} = \sum_{n,\alpha,\ell} (-1)^n \frac{2^n (2\alpha)!}{2^{2\alpha}(\alpha!)^2} (4\alpha+1)(2\ell+1) \frac{(i)^\ell j_\ell(A) j_{2\alpha}(C)}{(iA/B)^n} \tag{C.33}$$

$$\times 2 \sum_k \binom{n}{k} \sqrt{\frac{(2\alpha+k)!(n-k)!}{(n+k)!(2\alpha-k)!}} \begin{pmatrix} \ell & n & 2\alpha \\ 0 & -k & k \end{pmatrix} \begin{pmatrix} \ell & n & 2\alpha \\ 0 & 0 & 0 \end{pmatrix} \tag{C.34}$$

$$\equiv \sum_{\ell,\alpha} c_{\ell,\alpha}(k,\mu,q) j_\ell(A) j_{2\alpha}(C)\,, \tag{C.35}$$

and we can rewrite ZA power spectrum in redshift space as

$$P_{s,\mathrm{Zel}}(k,\mu) = 2\pi \sum_{\ell,\alpha=0}^{\infty} \int \frac{dq}{q} q^3 e^{-1/2K^2(X(q)+Y(q))} c_{\ell,\alpha}(k,\mu,q) j_\ell(A) j_{2\alpha}(C)\,. \tag{C.36}$$

The two remaining sums over α and ℓ run from zero to infinity, but in practice only the first 5 terms are relevant for sub-% precision. Upon expanding the non oscillatory part of the integrand above in complex power laws (FFTlog) [159, 15],

$$q^3 e^{-1/2K^2(X(q)+Y(q))} c_{\ell,\alpha}(k,\mu,q) \equiv \sum_n d_{\ell,\alpha,n}(k,\mu) q^{\nu_n} \tag{C.37}$$

and then using the following analytic integral

$$\int \frac{dq}{q} q^{\nu_n} j_\ell(kqc) j_{2\alpha}(kqs) \tag{C.38}$$

$$= (kc)^{-\nu_n} \frac{\pi 2^{\nu_n-3} t^{2\alpha} \Gamma\left(\frac{1}{2}(2\alpha+\ell+\nu_n)\right) {}_2\tilde{F}_1\left(\frac{1}{2}(2\alpha-\ell+\nu_n-1), \frac{1}{2}(2\alpha+\ell+\nu_n); 2\alpha+\frac{3}{2}; t^2\right)}{\Gamma\left(\frac{1}{2}(-2\alpha+\ell-\nu_n+3)\right)} \tag{C.39}$$

$$\equiv (kc)^{-\nu_n} I(\ell,\alpha,\nu_n,t) \tag{C.40}$$

with $t \equiv s/c$, and ${}_2\tilde{F}_1$ a regularized Hypergeometric function, we can perform the remaining integral in Eq. C.36 [4]. The Zeldovich RSD power spectrum can then be computed as

$$P_{\mathrm{ZA}}(k,\mu) = 2\pi \sum_{\ell,\alpha,n} d_{\ell,\alpha,n}(k,\mu)(kc)^{-\nu_n} I(\ell,\alpha,\nu_n,t)\,. \tag{C.41}$$

For a given set of FFTlog parameters, the function $I(\ell,\alpha,\nu_n,t)$ can be tabulated in advance and the sum above performed quickly.

[4] See for example p. 401 (13.4) of ref. [407]. The integral exists for any $\nu_n > -2$, which is the case by an appropriate choice of the FFTlog parameters.

Loop integrals and bias terms introduce two main complications. First, new terms proportional to $\mu_{\mathbf{q}}^{\beta}$ appear in the angular integral in Equation C.27. They can be easily included by rewriting them as derivatives with respect to A or B, analogously to what is done in the real space calculation [399]. Second, the loop structure will replace the J_0 in Equation C.27 with more complicated functions. For the one-loop calculation at hand, we have to perform the angular integral in Equation C.28 with the following two terms

$$-i\sqrt{1-\mu_{\mathbf{q}}^2}\; J_1(C\sqrt{1-\mu_{\mathbf{q}}^2}) \quad \text{and} \quad \frac{1}{2}(1-\mu_{\mathbf{q}}^2)\left[J_0(C\sqrt{1-\mu_{\mathbf{q}}^2}) - J_2(C\sqrt{1-\mu_{\mathbf{q}}^2})\right] \tag{C.42}$$

instead of the J_0. Those are easy to deal with by noticing that

$$-i\sqrt{1-\mu_{\mathbf{q}}^2}\; J_1(C\sqrt{1-\mu_{\mathbf{q}}^2}) = i\partial_C J_0(C\sqrt{1-\mu_{\mathbf{q}}^2}) \longrightarrow i\partial_C j_{2\alpha}(C) \tag{C.43}$$

$$= i\frac{2a\, j_{2a}(C)}{C} - i j_{2a+1}(C) \tag{C.44}$$

and

$$\frac{1}{2}(1-\mu_{\mathbf{q}}^2)\left[J_0(C\sqrt{1-\mu_{\mathbf{q}}^2}) - J_2(C\sqrt{1-\mu_{\mathbf{q}}^2})\right] = -\partial_C^2 J_0(C\sqrt{1-\mu_{\mathbf{q}}^2}) \longrightarrow -\partial_C^2 j_{2\alpha}(C) \tag{C.45}$$

$$= -\frac{(4a^2-2a-C^2)\, j_{2a}(C) + 2C j_{2a+1}(C)}{C^2}\,, \tag{C.46}$$

which boil down to a reshuffling of the coefficients in the sums of Equation C.35.

Appendix D

Reconstruction in the Zeldovich Approximation

D.1 Cross-spectra correlators

In this appendix we give analytic expressions for the two-point functions required to calculate cross-spectra, which are slightly different from those required to calculate the auto-spectra more commonly seen in the literature.

The two-point function for the Lagrangian displacement between two species separated by Lagrangian distance $\mathbf{q}$ is given by

$$A_{ij}^{ab}(\mathbf{q}) = \langle \mathbf{\Psi}_i^a \mathbf{\Psi}_j^a \rangle + \langle \mathbf{\Psi}_i^b \mathbf{\Psi}_j^b \rangle - 2\langle \mathbf{\Psi}_i^a(\mathbf{q}_2) \mathbf{\Psi}_j^a(\mathbf{q}_1) \rangle \equiv X^{ab}(q)\ \delta_{ij} + Y^{ab}(q)\ \hat{q}_i \hat{q}_j \tag{D.1}$$

where

$$\begin{aligned} X^{ab}(q) &= \frac{2}{3} \int \frac{dk}{2\pi^2} \Big[\ \frac{1}{2} \Big(P_L^{aa}(k) + P_L^{bb}(k) \Big) - \Big(j_0(kq) + j_2(kq) \Big) P_L^{ab}(k) \Big] \\ Y^{ab}(q) &= 2 \int \frac{dk}{2\pi^2}\ j_2(kq) P_L^{ab}(k). \end{aligned} \tag{D.2}$$

Note that for cross spectra $X^{ab}(q)$ does not in general vanish as $q \to 0$. Similarly we have

$$U_i^b = \langle \Delta_i^{ab} \delta_0(\mathbf{q}_2) \rangle \equiv U^b(q) \hat{q}_i, \quad U_i^a = \langle \Delta_i^{ab} \delta_0(\mathbf{q}_1) \rangle \equiv U^a(q) \hat{q}_i \tag{D.3}$$

where

$$U^a(q) = -\int \frac{dk\ k}{2\pi^2}\ j_1(kq) P_L^{am}(k) \tag{D.4}$$

and P^{am} is the linear theory cross spectrum between tracer a and matter, and the corresponding expression for U^b follows by direct substitution.

Finally, the non-scalar shear correlators are given by

$$V_i^{ab} = V^a(q) \hat{q}_i, \quad \Upsilon_{ij}^a = X_{s^2}^a(q) \delta_{ij} + Y_{s^2}^a(q) \hat{q}_i \hat{q}_j \tag{D.5}$$

where the functions of q are given by

$$V^a(q) = 2\int \frac{dk\ k}{2\pi^2}\ P_L^{am}(k)\ \left[\frac{4}{15}j_1(kq) - \frac{2}{5}j_3(kq)\right]\ \int \frac{dk\ k^2}{2\pi^2}\ P_L^{mm}(k)\ j_2(kq) \tag{D.6}$$

and

$$X_{s^2}(q) = 4(\mathcal{J}_3^a)^2, \quad Y_{s^2}(q) = 6(\mathcal{J}_2^a)^2 + 8\mathcal{J}_2^a\mathcal{J}_3^a + 4\mathcal{J}_2^a\mathcal{J}_4^a + 4(\mathcal{J}_3^a)^2 + 8\mathcal{J}_3^a\mathcal{J}_4^a + 2(\mathcal{J}_4^a)^2 \tag{D.7}$$

where following refs. [415, 396] we have defined

$$\mathcal{J}_2^a = \int \frac{dk\ k}{2\pi^2}\ P_L^{am}(k)\ \left[\frac{2}{15}j_1(kq) - \frac{1}{5}j_3(kq)\right] \tag{D.8}$$

$$\mathcal{J}_3^a = \int \frac{dk\ k}{2\pi^2}\ P_L^{am}(k)\ \left[-\frac{1}{5}j_1(kq) - \frac{1}{5}j_3(kq)\right] \tag{D.9}$$

$$\mathcal{J}_4^a = \int \frac{dk\ k}{2\pi^2}\ P_L^{am}(k)\ j_3(kq). \tag{D.10}$$

The remaining scalar shear correlators, ζ and χ^{12}, are identical to those found in evaluating the auto-spectrum, and we refer readers to refs. [415, 396].

D.2 The pre- and post-reconstruction Zeldovich propagator

In this appendix we give expressions for the normalized cross-spectrum between the initial and final or reconstructed field. This is essentially a correlation coefficient, though it is also referred to as the propagator [92]. Specifically we define $G_a(\mathbf{k}) = \langle\delta_0(-\mathbf{k})\delta_a(\mathbf{k})\rangle/\langle\delta_0(-\mathbf{k})\delta_0(\mathbf{k})\rangle$, within the Zeldovich approximation, which quantifies the extent to which a tracer field a is (de)correlated with the initial density δ_0, and apply our results to derive the reconstructed field. Our results generalize those in ref. [257] to include halo bias.

As defined, the propagator G_a is a special case of the cross spectrum and can be evaluated using Equation 4.4 by assuming that the linear field δ_0 is a tracer b with displacement $\mathbf{\Psi}^b = 0$ and bias functional $F^b = \delta_0$, such that any Lagrangian two-point functions involving the displacement $\mathbf{\Psi}^b$ (e.g. U^b) or higher biases (e.g. b_2^b) vanish identically. Unlike in the conventional case, however, F^b does not have a zero order piece equal to unity— we can thus compute our result directly by taking the derivative of Equation 4.4 with respect to b_1^b with the above assumptions. This gives

$$P_L(k)G_a(\mathbf{k}) = \int d^3\mathbf{q}\, e^{i\mathbf{k}\cdot\mathbf{q}}\, e^{-k^2\Sigma_{aa}^2/4}\left[ik_iU_i^a + b_1^a\xi_L\right] = e^{-k^2\Sigma_{aa}^2/4}\Big(P^{am}(k) + b_1^aP^{mm}(k)\Big), \tag{D.11}$$

where we have used that

$$A_{ij}^{a0}(\mathbf{q}) = \langle\mathbf{\Psi}_i^a\mathbf{\Psi}_j^a\rangle \equiv \frac{1}{2}\Sigma_{aa}^2\delta_{ij}, \tag{D.12}$$

only receives "half" of the zero-point contribution c.f. the power spectrum (where $\langle \mathbf{\Psi}^b \mathbf{\Psi}^b \rangle \neq 0$). Note that all higher bias contributions vanish. The generalization to the redshift space field can be straightforwardly accomplished by multiplying by appropriate factors of R_{ij} in the numerator, though we will focus on real space in this appendix as RSD introduce an equally important but parallel form of decorrelation into the problem.

From the above results, the reconstructed-field ($\delta_{\rm rec} = \delta_d - \delta_s$) propagator can be written as $G_{\rm rec} = G_d - G_s$, where

$$G_d(\mathbf{k}) = \frac{e^{-k^2\Sigma_{dd}^2/4}\Big(P^{dm}(k) + b_1 P^{mm}(k)\Big)}{P_L(k)} \quad , \quad G_s(\mathbf{k}) = \frac{e^{-k^2\Sigma_{ss}^2/4}P^{sm}(k)}{P_L(k)}, \tag{D.13}$$

where the various linear spectra are defined as in Equation 4.14. The real-space post-reconstruction propagator is then

$$G_{\rm rec}(\mathbf{k}) = e^{-k^2\Sigma_{dd}^2/4}\left[(1 - \mathcal{S}(k) + b_1\right] + \mathcal{S}(k)e^{-k^2\Sigma_{ss}^2/4}. \tag{D.14}$$

The expression for $G_{\rm rec}$ helps to quantify how much of the decorrelation between the initial conditions and the final field arises due to bulk motions, and the manner in which this can be restored by the standard reconstruction algorithm. Roughly speaking, reconstruction reduces the decorrelation from the full matter Σ^2 to Σ_{dd}^2 past the smoothing scale for the matter piece, with the correlation at low k close to unity assuming that the damping due to Σ_{ss}^2 there is negligible.

D.3 Integrals for redshift space distortions via direct Lagrangian expansion

Calculating the power spectrum in redshift space within the Zeldovich approximation requires a few extra steps when compared to the calculation in real space due to the line-of-sight dependence of RSD. In Appendices C.2 and C.3 we discussed two methods to compute the requisite integrals corresponding, roughly speaking, to active and passive transformations in Fourier space via $R_{ij} = \delta_{ij} + f\hat{n}_i\hat{n}_j$, respectively. The goal of this section is not to repeat those discussions but to discuss specifics related to the reconstruction problem.

D.3.1 Direct Lagrangian Expansion: MI

In Appendix C.2 we described a general approach for computing contributions to the power spectrum in LPT with linear displacements resummed. For reconstruction in the Zeldovich approximation we only need those pieces corresponding to linear displacements, such that all of the redshift-space transformation matrices are $R_{ij} \equiv R_{ij}^{(1)}$.

An additional simplified but demonstrative example of MI can be found in the calculation of the displaced-shifted cross spectrum in redshift space reconstruction via **Rec-Iso**. The H_ℓ^0

expansion in Equation 4.24 is essentially Equation C.7 in the limit where $\beta \to 0$. To proceed from Equation 4.24, we can use the identity in Equation B.53 and refactor the resulting double sum over n and ℓ to get

$$P^{(ds)}(\mathbf{k}) = e^{-\frac{1}{2}k^2(\alpha_0\Sigma^{(dd)^2}+\Sigma^{(ss)^2})}\ 4\pi\sum_{n=0}^{\infty}\int dq\ q^2 e^{k^2(1+f\mu^2)(\tilde{X}^{ds}+\tilde{Y}^{ds})}\Big(\frac{-2k\tilde{Y}^{ds}}{q}\Big)^n\ (1+f\mu^2)^n$$
$$\Big[K_n^{(0)}(q)j_n(kq) - b_1 kU^d(q)K_n^{(0)}(q)j_{n+1}(kq) - \frac{1}{2}b_2k^2U^d(q)^2K_n^{(2)}(q)j_n(kq) + \cdots\Big] \tag{D.15}$$

where the redshift-space kernels are given by

$$K_n^{(0)}(q) = \sum_{\ell=0}^{\infty}\Big(-\frac{f\mu\sqrt{1-\mu^2}}{1+f\mu^2}\Big)^{\ell} H_\ell(A)\ U(-\ell, n-\ell+1, -B)$$
$$K_n^{(2)}(q) = \sum_{\ell=0}^{\infty}\Big(-\frac{f\mu\sqrt{1-\mu^2}}{1+f\mu^2}\Big)^{\ell} H_\ell(A)\ \Big[U(-\ell, n-\ell+1, -B) + \frac{n}{B}\ U(-\ell, n-\ell, -B)\Big]$$

and, as before, $A = k^2 f\mu\sqrt{1-\mu^2}\,\tilde{Y}^{ds}$ and $B = k^2(1+f\mu^2)\,\tilde{Y}^{ds}$. Deriving these kernels for the other terms is entirely analagous[1].

D.3.2 Direct Lagrangian Expansion: MII

In Appendix C.3, we discussed a method to compute LPT integrals in redshift space relying on active transformations from Ψ to its redshift-space counterpart. From those arguments the Zeldovich power spectrum for biased tracers can be calculated using spherical Bessel transforms of the specific form

$$P_s(\mathbf{k}) \ni 4\pi\sum_{\ell=0}^{\infty}\ \int dq\ q^2\ e^{-\frac{1}{2}K^2(X+Y)}\ \Big(\frac{-2}{kq}\Big)^{\ell}\ \tilde{G}^{(n)}_{0,\ell}(kqc, -\frac{1}{2}K^2Y, kq)\ \mathcal{A}_n(q)\ j_\ell(kq), \tag{D.16}$$

where the scalar function $\mathcal{A}_n$ are tabulated in Table D.1.

D.4 Wiggle/No-Wiggle split

Most analyses of BAO data to date have employed empirical models for the post-reconstruction power spectrum or correlation function often motivated by theoretical calculations and calibrated to N-body simulations. Refs. [402, 112] showed that the analytic form of these empirical models can be interpreted within perturbation theory as a resummation of bulk displacements at the BAO scale. In this appendix we re-derive their results within our

[1]The mater contribution was given in ref. [398].

$\mathcal{A}_n$	$n=0$	$n=1$	$n=2$	...
1	1	0	0	
b_1	0	$2KU(q)$	0	
b_1^2	$\xi_L(q)$	0	$K^2U(q)^2$	
b_2	0	0	$K^2U(q)^2$	
b_1b_2	0	$KU(q)\xi_L(q)$	0	
b_2^2	$\frac{1}{2}\xi_L(q)^2$	0	0	
b_s	$-K^2X_{s^2}(q)$	0	$K^2Y_{s^2}(q)$	
b_1b_s	0	$2KV(q)$	0	
b_2b_s	$\chi^{12}(q)$	0	0	
b_s^2	$\zeta(q)$	0	0	

Table D.1: Table of power spectrum contributions in MII.

Zeldovich calculation, updating the scale dependences and redshift-space factors where appropriate.

Let us first examine the displaced-displaced cross spectrum in redshift space. Following refs. [402, 112] we split the displacement two-point function into $A_{ij}^{dd} = A_{ij}^{dd,\mathrm{nw}} + \Delta A_{ij}^{dd,\mathrm{w}}$, where the no-wiggle and wiggle pieces are calculated by substituting P_{nw} and ΔP_{w} into Equation D.2. Making the assumption that the latter, $\Delta A_{ij}^{dd,\mathrm{w}}$, is small enough as to be perturbative[2], we can Taylor expand the exponential in the Zeldovich integrand to get

$$P^{dd}(\mathbf{k}) = \int d^3\mathbf{q}\; e^{-i\mathbf{k}\cdot\mathbf{q}-\frac{1}{2}K_iK_jA_{ij}^{dd,\mathrm{nw}}}\left(1-\frac{1}{2}K_iK_j\Delta A_{ij}^{dd,\mathrm{w}}+\mathcal{O}(k^4\Sigma^4)\right)\Big(1+2ib_1K_iU_i^d(q)+...\Big),$$

where we have used the transformed $K_i = R_{ij}k_j$ to encode redshift-space effects. Given that the no-wiggle spectrum reproduces the broadband scale dependence of the linear theory power spectrum, we can think of the no-wiggle exponential as resumming the non-BAO component of large scale bulk flows. Since the wiggle component contributes negligibly to the displacement power in the perturbative limit, keeping only one power of the wiggle power spectrum in our calculations serves to distinguish the effect of the IR bulk flows from BAO phenomena. The two-point functions entering the bias terms can likewise be split into no-wiggle and wiggle pieces, e.g. $U(q) = U^{\mathrm{nw}} + \Delta U^{\mathrm{w}}$, where again, roughly speaking, the former will contribute only to the broadband power while the latter will give rise to oscillatory behavior. Keeping the above expression to order[3] $\mathcal{O}(k^2\Sigma^2)$, and discarding terms that don't

[2]Taking the nonlinear scale to be given by $k_{\mathrm{nl}}^2\Sigma^2(z) \sim 1$, we have $k_{\mathrm{nl}} \propto D^{-1}(z)$, such that the peak magnitude of $k_ik_j\Delta A_{ij}^{\mathrm{w}}$ is roughly in the few tenths of a percent range for our reference cosmology independent of redshift.

[3]Note, however, that terms involving more powers of the wiggle displacement will be more suppressed than those involving no-wiggle displacements.

contain any no-wiggle pieces, we then have

$$P^{dd}(\mathbf{k}) \ni \int d^3\mathbf{q}\; e^{-i\mathbf{k}\cdot\mathbf{q}-\frac{1}{2}K_iK_jA_{ij}^{dd,\mathrm{nw}}}\left(-\frac{1}{2}K_iK_j\Delta A_{ij}^{dd,\mathrm{w}}+2ib_1K_i\Delta U_i^{d,\mathrm{w}}(q)+b_1^2\xi_L^{\mathrm{w}}(q)+...\right)$$
$$\approx e^{-\frac{1}{2}K_iK_j\bar{A}_{ij}^{dd,\mathrm{nw}}}\int d^3\mathbf{q}\; e^{-i\mathbf{k}\cdot\mathbf{q}}\left(-\frac{1}{2}K_iK_j\Delta A_{ij}^{dd,\mathrm{w}}+2ib_1K_i\Delta U_i^{d,\mathrm{w}}(q)+b_1^2\xi_L^{\mathrm{w}}(q)+...\right)$$

where in the final line we have used the fact that the wiggle contributions will be confined in support around the BAO scale ($q\sim 100\,\mathrm{Mpc}$) and the non-wiggle pieces vary smoothly at this Lagrangian separation, so we can pull the exponentiated no-wiggle contribution out of the integral as an average. Following ref. [402], we have defined the quantity $\bar{A}_{ij}^{dd,\mathrm{nw}}$ as the "average" of the un-barred quantity over the support of the wiggle component; to zeroth order in the approximation this is equivalent to evaluating A_{ij} at the peak $q_{\max}$ of the support of the wiggle feature. Neglecting any angular effects in $\mu=\hat{q}\cdot\hat{k}$, which will enter at higher order in the wave number, we further have that $\bar{A}_{ij}^{dd,\mathrm{nw}}\simeq(X^{dd,\mathrm{nw}}+\frac{1}{3}Y^{dd,\mathrm{nw}})\delta_{ij}$[4]. Plugging in for the expression of $\mathbf{K}=\mathbf{R}^{\mathbf{T}}\mathbf{k}$, with $K^2=(1+f(f+2)\mu^2)k^2$, the wiggle contribution to the power spectrum is then approximately

$$\begin{aligned}P^{dd}(\mathbf{k})_{\mathrm{wiggle}} &\approx e^{-\frac{1}{2}K^2\Sigma_{dd}^2}\left[\left(\hat{K}\cdot\hat{k}\right)^2P^{dd,\mathrm{w}}(k)+2b_1\left(\hat{K}\cdot\hat{k}\right)P^{dm,\mathrm{w}}(k)+b_1^2P^{mm,\mathrm{w}}(k)\right]\\ &= e^{-\frac{1}{2}K^2\Sigma_{dd}^2}\left[(1+f\mu^2)^2(1-\mathcal{S}(k))^2+2b_1(1+f\mu^2)(1-\mathcal{S}(k))+b_1^2\right]P_{\mathrm{w}}(k)\\ &= e^{-\frac{1}{2}K^2\Sigma_{dd}^2}\left[(1+f\mu^2)(1-\mathcal{S}(k))+b_1\right]^2P_{\mathrm{w}}(k)\end{aligned}\tag{D.18}$$

where in the penultimate equality we have used the definition of the displaced field and defined $\Sigma_{dd}^2=(X^{dd,\mathrm{nw}}+\frac{1}{3}Y^{dd,\mathrm{nw}})(q_{max})$ to be evaluated at the peak of the wiggle displacements. This recovers the form of the empirical model in ref. [112] when we take the Eulerian bias to be $b_1^E=1+b_1$, and stick to the damping expansion approximation introduced in ref. [402]. Explicit expressions for X and Y are given in Equation 4.17. Taking $S\to 0$ in the above expression gives the unreconstructed power spectrum within this approximation.

We can now derive the analytical form of the reconstructed power spectrum for **Rec-Sym** in this approximation. Explicitly, we have

$$P_{\mathrm{wiggle}}^{ds}(\mathbf{k})=-e^{-\frac{1}{2}K^2\Sigma_{ds}^2}\Big((1+f\mu^2)(1-\mathcal{S}(k))+b_1\Big)(1+f\mu^2)\mathcal{S}(k)P_{\mathrm{w}}(k)\tag{D.19}$$

$$P_{\mathrm{wiggle}}^{ss}(\mathbf{k})=e^{-\frac{1}{2}K^2\Sigma_{ds}^2}(1+f\mu^2)^2\mathcal{S}(k)^2P_{\mathrm{w}}(k).\tag{D.20}$$

[4]The factor of a third, included also in ref. [402] but not in ref. [112], comes from the angular average $\langle\hat{q}_i\hat{q}_j\rangle=\delta_{ij}/3$. This can be justified by noting that the integral

$$\frac{1}{2}\int d\mu_{\mathbf{q}}\; e^{ikq\mu_{\mathbf{q}}-\frac{1}{2}k^2\mu_{\mathbf{q}}^2Y/2}=e^{-k^2Y/6}j_0(kq)+\mathcal{O}(k^4\Sigma^4)\tag{D.17}$$

We note, however, that this prescription is only approximate; for example, the same integral with an additional factor of $\mu_{\mathbf{q}}$ in the integrand, relevant for the b_1 contribution, would instead yield $\exp[-3k^2Y/10]\,j_1(kq)$ at leading order. In general, bias contributions with more angular dependence will be damped more. This effect is automatically included in the full Zeldovich calculation.

The Σ^2_{ab} are defined as in the *dd* case. These are the same expressions as derived in ref. [112], though we differ on the expressions for the Σ^2_{ab} that are involved. Our expressions also agree with those in refs. [87, 339] in the limit that $q_{max} \to \infty$, though we note that this limit doesn't as accurately capture the damping of the feature since it resums the IR displacements at q beyond the BAO scale. Adding the three spectra together, we recover the Kaiser limit as $k \to 0$, with different damping factors entering at different scales via Σ^2_{ab}. Note that in **Rec-Sym** the angular dependence of the damping is identical in each piece and is encoded within the μ dependence of K^2.

The reconstructed power spectrum with **Rec-Iso** requires a few additional modifications. The displaced-displaced auto spectrum is unchanged, and the shifted-shifted auto spectrum can be calculated by setting $f = 0$ in all formulae, as noted in the main body of the text. However, the *ds* cross spectrum requires more care, since the zero lag pieces do not transform equally. In particular, direct inspection of the exact expression in Equation 4.24 shows that we should instead define

$$-\frac{1}{2}k^2\Sigma^2_{ds,\rm iso} = -\frac{1}{2}k^2\left[(1+f(f+2)\mu^2)\Sigma^{(dd)} + \Sigma^{(ss)} - 2(1+f\mu^2)\left(\tilde{X}^{ds} + \frac{1}{3}\tilde{Y}^{ds}\right)\right]_{q=q_{\rm max}} . \tag{D.21}$$

Note this expression differs in detail from that in ref. [112]. The cross spectrum is then instead

$$P^{ds,\rm iso}_{\rm wiggle}(\mathbf{k}) = -e^{-\frac{1}{2}k^2\Sigma^2_{ds,\rm iso}}\left[(1+f\mu^2)(1-\mathcal{S}(k)) + b_1\right]\mathcal{S}(k)P_{\rm w}(k), \tag{D.22}$$

where the angular dependence is subsumed into the defintion of $\Sigma_{ds,\rm iso}$. Unlike **Rec-Sym**, the damping factor in **Rec-Iso** is not captured by a single angular dependence.

We end this section with a discussion of the inclusion of higher bias terms and other corrections. As seen in the main body of the text, higher bias terms b_2 and b_s, incorporated in our Zeldovich calculation, contribute not only to the broadband but also serve to shift and smear the BAO feature itself. It might thus be of interest to extend the above approximation to include also these higher bias contributions. A potential avenue has been highlighted in ref. [112], although an approach closer to our perturbative bias expansion could also be explored.

Finally, the calculation in ref. [112] included a derivative bias, $b_{\nabla^2}\nabla^2\delta$, as a proxy to estimate the contributions of the higher bias operators. These derivative bias terms can easily be included in the above expressions by substituting $b_1 \to b_1 + k^2 b_{\nabla^2}$. However, there is another context in which such a term might arise in which it would differ across the three pieces *dd*, *ds* and *ss*: if the smoothing due to the Σ^2_{ab}'s as defined above do not accurately capture the IR bulk flows – for example if the broadband properities of $P_{\rm nw}$ are slightly off – but differ by some perturbatively small $k^2\delta\Sigma^2_{ab}$, the resulting correction could be corrected for by terms of the form $c^2_{ab}k^2P^{ab,\rm w}(k)$, where c^2_{ab} would constants fit individually to *dd*, *ds* and *ss*. Such corrections are essentially identical to the EFT corrections described in the text for the full Zeldovich calculation.

D.5 Nonlinearities from the Lagrangian to Eulerian mapping

In standard density field reconstruction, each galaxy is shifted by a smoothed displacement field χ evaluated at the galaxy's current *Eulerian* position $\mathbf{x} = \mathbf{q} + \mathbf{\Psi}(\mathbf{q})$ (Equation 4.10). In the main body of the text, we worked in the approximation that $\chi(\mathbf{x}) \approx \chi(\mathbf{q})$, with the understanding that nonlinear corrections would be suppressed by the smoothing scale $\sim \mathbf{\Psi}/R$. The goal of this appendix is to flesh out this statement by explicitly computing the leading order corrections to the reconstructed matter power spectrum due to the mapping nonlinearity in real space. For the sake of brevity we will defer the effects of other nonlinearities, such as those arising from dynamics or from translating between displacements and densities, to future work. Earlier treatments of such effects in Eulerian perturbation theory can be found in refs. [321, 171].

Assuming that the shift field $\chi(\mathbf{q})$ defined in Lagrangian space is Gaussian, the displaced field with mapping nonlinearities unsuppressed is given by

$$\tilde{\mathbf{\Psi}}^d_i(\mathbf{q}) = \mathbf{\Psi}^d_i(\mathbf{q}) + \mathbf{\Psi}_n\partial_n\chi_i(\mathbf{q}) + \frac{1}{2}\mathbf{\Psi}_n\mathbf{\Psi}_m\partial_n\partial_m\chi_i(\mathbf{q}) + ... \equiv \mathbf{\Psi}^d_i + \mathbf{\Psi}^{(d,2)}_i + \mathbf{\Psi}^{(d,3)}_i + ... \quad \text{(D.23)}$$

where we have kept the convention used in the main text to refer to the linear piece as $\mathbf{\Psi}^d = (1-\mathcal{S})*\mathbf{\Psi}$, referring to the nonlinear field as $\tilde{\mathbf{\Psi}}^d = \mathbf{\Psi}(\mathbf{q}) + \chi(\mathbf{q}+\mathbf{\Psi})$. For the remainder of this appendix we will focus on corrections due to $\mathbf{\Psi}^{(d,2)}$.[5]

From the above,we can write the nonlinear displaced-displaced autospectrum as

$$P^{dd}(k) - P^{dd}_{\rm Zel}(k) = \int d^3\mathbf{q}\; e^{i\mathbf{k}\cdot\mathbf{q} - \frac{1}{2}k_ik_jA^{dd}_{ij}}\left(\exp\left[-\frac{1}{2}k_ik_jA^{dd,\text{1-loop}}_{ij} - \frac{i}{6}k_ik_jk_kW^{dd}_{ijk}\right] - 1\right) + \mathcal{O}(P_L^3)$$

where we have defined

$$\begin{aligned} A^{dd,\text{1-loop}}_{ij} &= \left\langle \Delta^{(dd,2)}_i\Delta^{(dd,2)}_j\right\rangle_c + 2\left\langle \Delta^{(dd,1)}_i\Delta^{(dd,3)}_j\right\rangle_c \\ W^{dd}_{ijk} &= \left\langle \Delta^{(dd,1)}_i\Delta^{(dd,1)}_j\Delta^{(dd,2)}_k\right\rangle_c + (121) + (211). \end{aligned} \quad \text{(D.25)}$$

as in the case of the nonlinear matter power spectrum (e.g. [399]). To calculate these we note that

$$\begin{aligned} \langle \mathbf{\Psi}^{(d,2)}_i(\mathbf{q}_2)\mathbf{\Psi}^{(d,2)}_j(\mathbf{q}_1)\rangle_c &= \left\langle \big(\mathbf{\Psi}_n\partial_n\chi_i\big)(\mathbf{q}_2)\big(\mathbf{\Psi}_m\partial_m\chi_j\big)(\mathbf{q}_1)\right\rangle_c \\ &= \langle \mathbf{\Psi}_n(\mathbf{q}_2)\mathbf{\Psi}_m(\mathbf{q}_1)\rangle\,\langle\partial_n\chi_i(\mathbf{q}_2)\partial_m\chi_j(\mathbf{q}_1)\rangle + \langle\mathbf{\Psi}_n(\mathbf{q}_2)\partial_m\chi_j(\mathbf{q}_1)\rangle\,\langle\mathbf{\Psi}_m(\mathbf{q}_1)\partial_n\chi_i(\mathbf{q}_2)\rangle \end{aligned}$$

[5] At one loop order all corrections due to $\mathbf{\Psi}^{(d,3)}$ are degenerate with the counterterms in our model. To see this, note that such corrections contractions with linear displacements, e.g.

$$\langle \mathbf{\Psi}^a_{1,i}\mathbf{\Psi}^{(d,3)}_{2,j}\rangle = \langle\mathbf{\Psi}_m\partial_m\partial_n\chi_j\rangle\langle\mathbf{\Psi}^a_{1,i}\mathbf{\Psi}_{2,n}\rangle + \frac{1}{2}\langle\mathbf{\Psi}_n\mathbf{\Psi}_m\rangle\langle\mathbf{\Psi}^a_{1,i}\partial_n\partial_m\chi_{2,j}\rangle,\ a = d, s. \quad \text{(D.24)}$$

Multiplied by the appropriate factor of $-\frac{1}{2}k_ik_j$, the two pieces on the right hand side Fourier transform into $\sim k^2P^{am}_L(k)$ and $\sim k^2P^{as}_L(k)$, respectively, thus taking the form of our counterterms $\sim k^2P^{ab}(k)$.

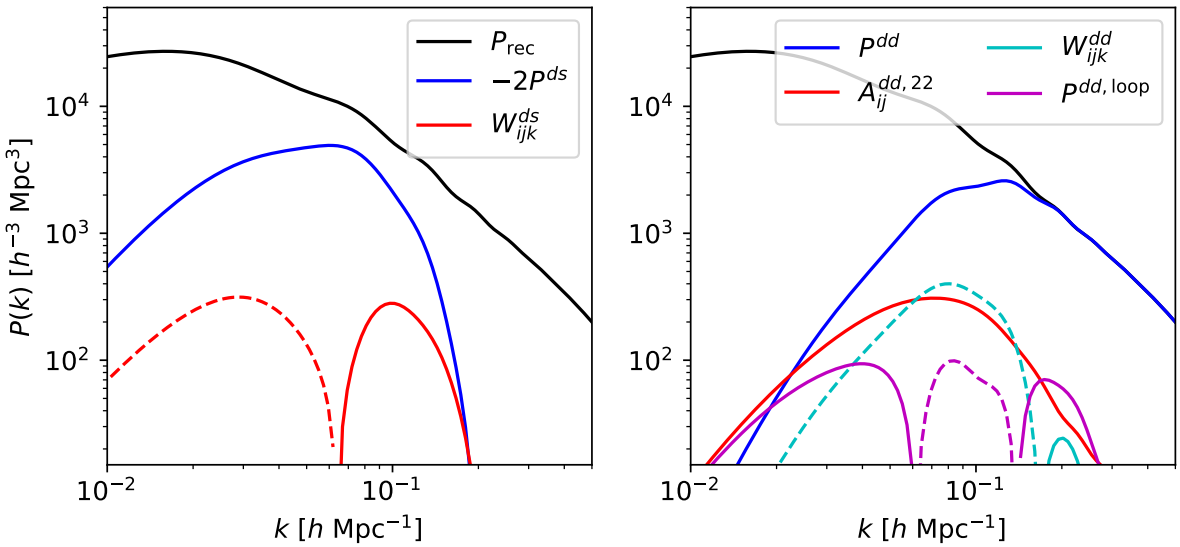

Figure D.1: Nonlinear corrections to the reconstructed matter power spectrum due to the Lagrangian-to-Eulerian mapping at one loop order, for $z = 0$ and $R = 15\ h^{-1}$ Mpc. The left and right panels show contributions to the ds and dd power spectra, respectively. Even for the worst case of $z = 0$, the corrections are never more than a few percent of the total reconstructed power spectrum, though they can become larger than the constituent dd, ds spectra at large or small scales.

and

$$W^{dd,112}_{ijk} = 2\left\langle \mathbf{\Psi}^d_{1,i}\mathbf{\Psi}_{2,n} - \mathbf{\Psi}^d_i\mathbf{\Psi}_n\right\rangle\left\langle \mathbf{\Psi}^d_{1,j}\partial_n\chi_{2,k}\right\rangle + \Big(i \leftrightarrow j\Big) \tag{D.26}$$

where numerical subscripts refer to coordinates $\mathbf{q}_{1,2}$ as usual.

The mapping corrections to the cross spectrum P^{ds} can be similarly calculated. In this case we need the displacement correlators

$$A^{ds,22}_{ij} = \left\langle \mathbf{\Psi}^{(d,2)}_i \mathbf{\Psi}^{(d,2)}_j \right\rangle = \left\langle \mathbf{\Psi}_n\mathbf{\Psi}_m\right\rangle\left\langle \partial_n\chi_i\partial_m\chi_j\right\rangle \tag{D.27}$$

where all expectation values are evaluated at a point since $\mathbf{\Psi}^s$ receives no nonlinear corrections from the Eulerian-Lagrangian mapping and similarly

$$\begin{aligned} W^{ds,112}_{ijk} &= \left\langle \mathbf{\Psi}^s_{i,1}\mathbf{\Psi}^s_{j,1}\mathbf{\Psi}^{(d,2)}_{k,2}\right\rangle - \left\langle \mathbf{\Psi}^d_{i,2}\mathbf{\Psi}^s_{j,1}\mathbf{\Psi}^{(d,2)}_{k,2}\right\rangle - \left\langle \mathbf{\Psi}^s_{i,1}\mathbf{\Psi}^d_{j,2}\mathbf{\Psi}^{(d,2)}_{k,2}\right\rangle \\ &= \Big(\left\langle \mathbf{\Psi}^s_{1,i}\mathbf{\Psi}_{2,n}\right\rangle - \left\langle \mathbf{\Psi}^d_i\mathbf{\Psi}_n\right\rangle\Big)\left\langle \mathbf{\Psi}^s_{1,j}\partial_n\chi_{2,k}\right\rangle + \Big(i \leftrightarrow j\Big) \end{aligned} \tag{D.28}$$

to one loop order.

As might have been expected, the mapping corrections above all take the form of products of displacement two point functions and their derivatives. Roughly speaking these corrections each have amplitudes given by powers of the Zeldovich displacement Σ^2 and wavenumber k capped at R^{-1} by the smoothing filter; we can thus expect the corrections to enter at order $(\Sigma/R)^4$. For a $15h$ Mpc^{-1} filter at $z = 0$ this amounts to a percent-level effect, with smaller effects at higher z. Concretely, these two point functions can be calculated using

$$\begin{aligned}
\langle \partial_n \chi_i(\mathbf{q}_2) \partial_m \chi_j(\mathbf{q}_1) \rangle &= \mathcal{A}^{ss}(q)(\delta_{ij}\delta_{nm} + \dots) + \mathcal{B}^{ss}(q)(\hat{q}_i\hat{q}_j\delta_{nm} + \dots) + \mathcal{C}^{ss}(q)\hat{q}_i\hat{q}_j\hat{q}_n\hat{q}_m \\
\langle \mathbf{\Psi}_n(\mathbf{q}_2) \partial_m \chi_i(\mathbf{q}_1) \rangle &= \mathcal{D}^{sm}(q)(\hat{q}_i\delta_{nm} + \dots) + \mathcal{E}^{sm}(q)\hat{q}_i\hat{q}_n\hat{q}_m \\
\langle \mathbf{\Psi}^a_n(\mathbf{q}_2) \partial_m \chi_i(\mathbf{q}_1) \rangle &= \mathcal{D}^{as}(q)(\hat{q}_i\delta_{nm} + \dots) + \mathcal{E}^{as}(q)\hat{q}_i\hat{q}_n\hat{q}_m
\end{aligned}$$

where the ellipses denote all distinct permutations and the scalar functions are given by

$$\begin{aligned}
\mathcal{A}^{ss}(q) &= \frac{1}{105}\int \frac{dk\ k^2}{2\pi^2}\ \big(7j_0(kq) + 10j_2(kq) + 3j_4(kq)\big)P_L^{ss}(k) \\
\mathcal{B}^{ss}(q) &= -\frac{1}{7}\int \frac{dk\ k^2}{2\pi^2}\ \big(j_2(kq) + j_4(kq)\big)P_L^{ss}(k) \\
\mathcal{C}^{ss}(q) &= \int \frac{dk\ k^2}{2\pi^2} j_4(kq)P_L^{ss}(k) \\
\mathcal{D}^{ab}(q) &= \frac{1}{5}\int \frac{dk\ k}{2\pi^2}\ \big(j_1(kq) + j_3(kq)\big)P_L^{ab}(k) \\
\mathcal{E}^{ab}(q) &= -\int \frac{dk\ k}{2\pi^2}\ j_3(kq)P_L^{ab}(k)
\end{aligned} \tag{D.29}$$

where we have used the identification $\chi = \mathbf{\Psi}^s$. The remaining correlator $\langle \mathbf{\Psi}_{2,i}\mathbf{\Psi}_{1,j}\rangle$ is simply minus the non-zero lag piece of A_{ij}. Finally, when some or all of the displacement correlators in each product are contracted at the same point, as for example in the first term in Equation D.26 and Equation D.27, the resulting contribution becomes proportional to $k^2 P_{ab,\mathrm{Zel}}$ and degenerate with the counterterms included in our model. The above corrections from the nonlinear Eulerian-Lagrangian mapping are plotted at $z = 0$ for the smoothing scale $R = 15h^{-1}$ Mpc in Figure D.1. As expected, even at $z = 0$ they are never more than a few percent of the total reconstructed power, though interestingly they can become comparable or larger than the Zeldovich P^{dd} and P^{ds} individually on scales where the Zeldovich spectra lose support. We caution that these curves do not include comparable corrections due to bias or dynamical nonlinearities.

We close with some general comments about nonlinearities in reconstruction. Firstly, the mapping corrections enumerated above are not the only ones at one-loop order; by focusing only on corrections due to $\mathbf{\Psi}^{(d,2)}$ we have explicitly avoided the (13) contributions due to third-order mapping corrections. Moreover, as this was an exploratory exercise with which to evaluate the magnitude of mapping nonlinearities, we chose not to include the effects of bias, which would require the inclusion of terms such as $\langle \delta_1^2 \mathbf{\Psi}_i^{(d,2)}\rangle$, though these will be in general decomposable into components much like those in Equation D.29. Finally, in addition to

mapping nonlinearities, by approximating the shift vector χ with the smoothed Zeldovich displacement we have ignored nonlinearities induced by translating between the density field and displacements. We expect these will be of similar importance to the mapping corrections but defer their evaluation for future work, noting that only that both nonlinearities can be trivially reduced by pushing the smoothing scale R deeper into the linear regime. That these effects are expansions in Σ/R distinguishes them from nonlinear bias or dynamics.

Appendix E

Applications of IR Resummation I

E.1 Redshift dependence and size of the of bias parameters

The bias expansion in Equation 5.18 has an implicit dependence on the initial redshift z_i that must be taken into account to reach consistent conclusions. Since the initial conditions mix at most linearly, no information can be lost by choosing one initial time τ_i over another; for example, the sensitivity of halos to the relative velocity divergence after reionization, which contains a contribution from the total matter overdensity (Eq. 5.9), can be directly accounted for by calibrating the bias parameter for δ_m at an earlier redshift.

As a simple example we consider the redshift dependence of the relative components in the sourceless ($F_b = 0$) case. If we set our initial time at τ_i' instead of τ_i we will get

$$\mathbf{\Psi}_r(\tau) = \Big(-\mathbf{r}_+ + \mathbf{r}_- D_r(\tau_i', \tau_i)\Big) + \mathbf{r}_- D_r(\tau, \tau_i') \equiv -\mathbf{r}_+' + \mathbf{r}_-' D_r(\tau, \tau_i'). \tag{E.1}$$

Re-expanding F_g at τ_i' thus yields

$$F_g(\mathbf{q}) = b_1\delta_m + b_+'\nabla\cdot\Big(r_+ - r_- D_r(\tau_i', \tau_i)\Big) + b_-'\nabla\cdot r_-' + ... \tag{E.2}$$

Since b' and b apply to the same field configurations at different times, they must yield the same initial overdensity F_g — this requirement can be satisfied by enforcing the differential equations

$$\frac{db_+}{d\tau} = 0, \qquad \frac{db_-}{d\tau} = \frac{b_+}{a(\tau)} \qquad . \tag{E.3}$$

Intriguingly, the presence of a relative overdensity bias can "generate" a relative velocity bias at later times. This can be understood as follows: the relative overdensity at late times is a linear combination of the relative overdensity and velocities at earlier times. Similar, though more complicated, versions of this relation hold when $F_b \propto \mathbf{m}_+$, in which case mixing of all three initial fields must be taken into account.

E.2 Biasing at second order

Below we list all contributions to the bias expansion up to second order in the initial fields omitting derivative corrections:

$$\begin{aligned} F_g = \; & b_1\delta_m + b_{\delta_r}\delta_r + b_{\theta_r}\theta_r \\ & + \frac{1}{2}b_2\delta_m^2 + b_{s^2}s_{ij}s_{ij} + b_{\delta_m\delta_r}\delta_m\delta_r + b_{\delta_m\theta_r}\delta_m\theta_r + b_{v_r\partial\delta_m}(\mathbf{v}_r)_i\,\partial_i\delta_m + b_{s\,\partial v}\partial_i(\mathbf{v}_r)_j s_{ij} \\ & + b_{v_r^2}\mathbf{v}_r^2 + ... \end{aligned} \tag{E.4}$$

In the main body of this paper we consider relative bias terms up to first order in the power spectrum, since even these represent only percent level effects, with the exception of the relative velocity effect $\propto \mathbf{v}_r^2$, which has a distinct scaling. As noted in the text, we note that the presence of Compton drag can introduce additional terms due to loss of gauge redundancy; we refer readers to the extensive discussion in [317].

E.3 Relative Velocity Bias Terms

In this appendix we provide details for the contributions of the relative velocity bias b_{v^2} at $\mathcal{O}(P^2)$ to the galaxy power spectrum. These contributions require the calculation of two new 2-point functions, the one-loop correlation between matter displacements and the squared relative velocity, and the correlation function between the shear field s_{ij} and the relative velocity. We describe these in turn.

The second order solution to the total-matter displacement (correct up to first order in the relative component) is given by

$$\mathbf{\Psi}_i^{(2)}(k) = \frac{1}{2}\frac{3}{7}\frac{i\,k_i}{k^2}\int\frac{d^3p}{(2\pi)^3}\Big[1-\Big(\frac{(k-p)\cdot p}{|k-p||p|}\Big)^2\Big]\,\delta_{m,0}(p)\,\delta_{m,0}(k-p), \tag{E.5}$$

and more simply the "normalized" relative velocity at first order is given by

$$\mathbf{r}_{-,i}(k) = \frac{-i\,k_i}{k^2}\big(\nabla\cdot\mathbf{r}_-\big)(k). \tag{E.6}$$

From this we can calculate the two-point function

$$\begin{aligned} \langle\mathbf{\Psi}^{(2)}(q)\;\mathbf{r}_-^2(0)\rangle = \frac{3}{7}\int\frac{d^3k}{(2\pi)^3}\,e^{ik\cdot q}\Big(\frac{-i\,k_i}{k^2}\Big)\frac{d^3p}{(2\pi)^3} \\ \Big[1-\Big(\frac{(k-p)\cdot p}{|k-p||p|}\Big)^2\Big]\frac{p\cdot(k-p)}{p^2(k-p)^2}P_{\delta_m\nabla\mathbf{r}_-}(p)P_{\delta_m\nabla\mathbf{r}_-}(k-p), \end{aligned} \tag{E.7}$$

which can be simplified to give

$$\langle\mathbf{\Psi}^{(2)}(q)v_{r,0}^2(0)\rangle = \hat{q}\int\frac{d^3k}{(2\pi)^3}\,e^{ik\cdot q}Q_{v^2}(k), \tag{E.8}$$

where the kernel is defined as

$$Q_{v^2}(k) \equiv \frac{3}{7}\int_0^\infty \mathrm{d}r\ P_{m-}(kr)\ \int_{-1}^1 \frac{\mathrm{d}x}{4\pi^2}\frac{r\ (x-r)(1-x^2)}{(1+r^2-2rx)^2}\ P_{m-}(k\sqrt{1+r^2-2rx}). \tag{E.9}$$

Next, the shear-velocity correlation function W_{ijk}^{s-} is given in Fourier space by

$$W_{ijk}^{s-}(q) = i\int \frac{d^3k}{(2\pi)^2}\ e^{ik\cdot q}\left(\frac{k_ik_jk_k}{k^4} - \frac{1}{3}\delta_{ij}\frac{k_k}{k^2}\right)P_{m-}(k) \equiv \tilde{W}_{ijk}^{s-}(q) - \frac{1}{3}\delta_{ij}U_k^{m-}(q). \tag{E.10}$$

where in the last equality we have split W_{ijk}^{s-} into a totally-symmetric piece and a familiar piece proportional to U^{m-}. The former can be decomposed into scalar components

$$\tilde{W}_{ijk}^{s-}(q) = \mathcal{A}(q)\ \hat{q}_i\hat{q}_j\hat{q}_k + \mathcal{B}(q)\ (\hat{q}_i\delta_{jk} + \hat{q}_j\delta_{ki} + \hat{q}_k\delta_{ij}), \tag{E.11}$$

with the scalar components defined as spherical Bessel transformations:

$$\mathcal{A}(q) = \int \frac{dk\ k}{2\pi^2}\ j_3(kq)\ P_{m-}(k) \tag{E.12}$$

$$\mathcal{B}(q) = -\int \frac{dk\ k}{2\pi^2}\ \frac{1}{5}\ \Big(j_1(kq) + j_3(kq)\Big)\ P_{m-}(k). \tag{E.13}$$

Appendix F

Applications of IR Resummation II

F.1 Saddle-Point Approximation for Nonlinear Dispersions

In this appendix we expand upon the argument for selecting scale $q = \omega/k$ in the logarithmic case, and show it follows as a special case of a more general expression in the large ω limit. Suppose we have

$$\Delta P_X(k) = P_{\Lambda\mathrm{CDM}}(k)\sin(\omega\phi(k)) \tag{F.1}$$

where ω is a constant tunable parameter such that $\omega\phi(k)$ is the (nonlinear) phase of the oscillating feature. We are interested in applying the saddle-point result for linear oscillations to this case.

Around some wavenumber $k = k_0$ of interest, we can Taylor-expand the phase as

$$\omega\phi(k) \simeq \omega\left(\phi_0 + \phi_0'(k-k_0) + \frac{1}{2}\phi_0''(k-k_0)^2 + ...\right) \tag{F.2}$$

where primes indicate derivatives with respect to k. Roughly, the linear approximation $\phi_L = \phi_0 + \phi_0'(k-k_0)$ will be good provided that $|k-k_0| < |\phi_0'/\phi_0''|$ independently of ω. This also defines the window within which to a good approximation $d\phi/dk \approx \phi_0'$.

However, unless $\phi(k)$ is linear, this window is not guaranteed to cover all interesting k. To restrict our calculation to the interval around k_0 where the linear approximation is valid, let us multiply by a function $W(k,k_0)$ with support in the interval and which falls to zero away from k_0 with characteristic width $\sigma_k = |\phi_0'/\phi_0''|$. Then we can approximate $W(k,k_0)\sin(\omega\phi(k))$ as $W(k,k_0)\sin(\omega\phi_L(k))$ everywhere. In addition, for the saddle-point approximation to work we also require that the Fourier-transformed feature be sharply localized at some scale, which will be equal to $q_X = |\omega\phi_0'|$ in our case. This condition is controlled by ω, since the number of cycles within our interval is $N_{\mathrm{cyc}} = (2\pi)^{-1}|\omega\phi_0'^2/\phi_0''|$; for a given $\phi(k)$ the bigger ω is the better.

Following the above we have that the "windowed" feature $W(k,k_0)\ \Delta P_X(k)$ receives a damping factor well-approximated by $\Sigma^2(q_X = |\omega\phi_0'|)$. By the same logic we can fill out

the oscillatory signal by sequence of windows $W(k, k_i)$ each with width $\sim |\phi_i'/\phi_i''|$ such that $\sum_i W(k, k_i) = 1$ at all k. Then, at any k we have that the damping is given by $\Sigma^2(q_X = |\omega\phi_i'|)$, which will to a very good approximation be equal to $\phi'(k)$ from our previous arguments.

Let us apply this argument for the logarithmic features as an example. Setting $\phi(k) = \ln(k/k_*)$, we see that the width is set by $\sigma_k \sim k$ and that the requirement $N_{\rm cyc} \gg 1$ is equivalent to $\omega \gg 2\pi$. This limit is met by our fiducial $\omega = 10$ and by the frequencies explored in the BOSS data in ref. [44], who also set a related criterion for the sharpness of primordial features. Note that the fact that the corresponding ω's are large also implies that the approximation $\phi'(k) \approx \phi_i'$ is a good one, with corrections of order ω^{-1} for fixed $N_{\rm cyc}$.

F.2 GSM vs. moment expansion

Beyond the moment expansion, the velocity statistics underlying redshift-space distortions can also be expanded via cumulant expansions to yield a variety of so-called streaming models [398]. A popular example is the Gaussian streaming model (GSM) [301, 396], which derives from the cumulant expansion in (real) configuration space at second order. A particular strength of the GSM is its ability to accurately capture the nonlinear smoothing of the BAO feature in redshift space, which can be roughly attributed to the responsible bulk displacements truncating at second order in the configuration-space cumulants [74].

Recently [74], we argued that percent-level modeling of the redshift-space power spectrum requires including the third moment, or at least approximating its effect via a counterterm ansatz. Naively, this would rule out using the GSM for full-shape RSD analyses at intermediate (but perturbative) scales; however, a proper accounting of the counterterms in the second moment shows that its quadrupole requires a counterterm degenerate with the above ansatz. Specifically, splitting the two-point function into contributions from large-scale bias and effective corrections as in Eq. 5.1 of ref. [74] and comparing with expressions for the velocity moments in LPT (Eqs. 4.11-15) one sees that the complete set of counterterms for the power spectrum can be obtained within the GSM by setting

$$\alpha_P = \alpha_0, \quad \alpha_v = \alpha_2 - \frac{1}{18}\alpha_4, \quad \alpha_\sigma^{(2)} = -\frac{2}{9}\alpha_4, \tag{F.3}$$

where $\alpha_\sigma^{(2)}$ is the counterterm to the quadrupole of $\sigma_{12}^2(\mathbf{k})$ multiplying the Zeldovich power spectrum $P_{\rm Zel}(k)$. This implies that the Fourier-transformed GSM can adequately model the redshift-space power spectrum while also accurately capturing nonlinear smoothing of power spectrum features.

Appendix G

Cosmological Analysis of BOSS

G.1 Fast Evaluation via Taylor Series

In order to speed up our model evaluations (obtaining transfer functions from `CAMB` alone takes a few seconds per cosmology) we use a Taylor series centered around a representative cosmology (Ω_m, h, $\sigma_8 = 0.31, 0.68, 0.73$[1]) to evaluate the perturbation-theory predictions of each cosmology in our chains. This technique has previously been applied to both full-shape forecasts [240] and data analyses of BOSS data [96, 88], and even at the linear level to approximate the predictions of a hybrid N-body/Lagrangian bias model of real-space clustering [156]. Specifically, both the pre-reconstruction power spectrum and post-reconstruction correlation functions (minus broadband terms) can written as inhomogeneous quadratic polynomials in the bias parameters, e.g. for a fixed cosmology Θ

$$\big(P_0(\mathbf{k}), P_2(\mathbf{k}), P_4(\mathbf{k}), \xi_0(\backslash), \xi_2(\backslash)\big)(\Theta) = \beta_i \beta_j \mathcal{M}^{ij}(\Theta)$$

where the vector $\beta = (1, b_1, b_2, b_s, \alpha_0, \alpha_2, R_h^3, R_h^3\sigma^2, B_1, F)$. Each component of the matrix $\mathcal{M}^{ij}$ is a smooth function of the cosmological parameters so can be approximated as

$$\mathcal{M}^{ij}(\Theta) = \sum_{n=0}^{N} \frac{1}{n!} (\Theta - \Theta_0)_{i_1} ... (\Theta - \Theta_0)_{i_n} \, \partial_{i_1 ... i_n} \mathcal{M}^{ij}(\Theta_0).$$

We evaluate the derivatives numerically using the publicly available `FinDiff`[2] package. In order to take advantage of central differences these derivatives are computed using a grid with $2N + 1$ points along each axis, where we find $N = 4$ to be sufficient for any cosmology relevant for constraints from any of the sets of samples considered in our analysis. In Figure G.1 we show differences between the unconvolved power spectrum multipoles as computed

[1] This central σ_8 value was chosen prior to discovering the window-function normalization issue resulting in systematically low σ_8 constraints. The resulting Taylor-series predictions are nonetheless sufficiently accurate for our final constraints, as shown below.

[2] https://findiff.readthedocs.io/en/latest/

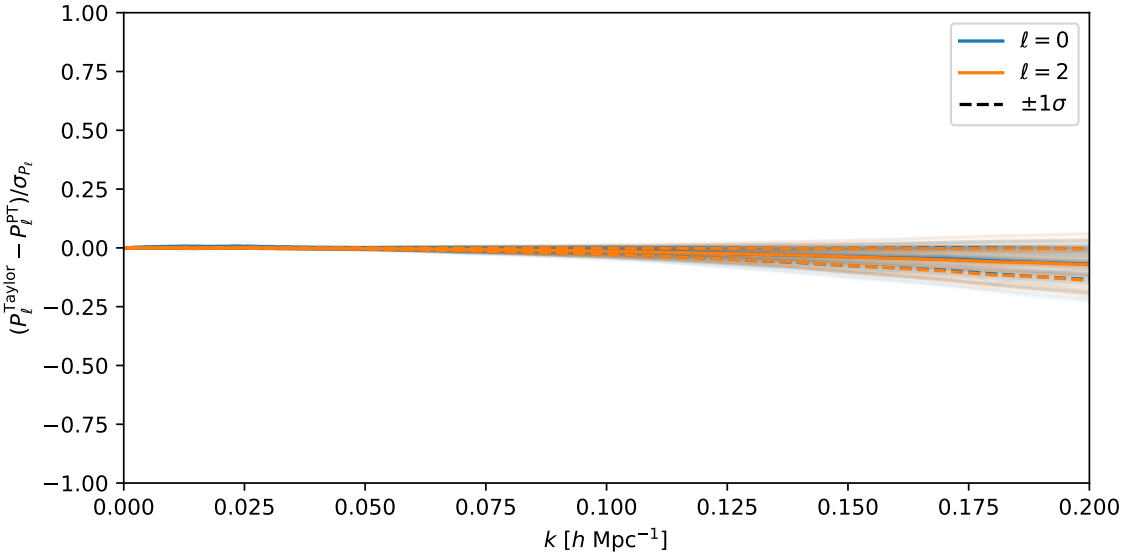

Figure G.1: Differences between unconvolved power spectra computed directly from `CLASS` and `velocileptors` vs. approximated by a 4$^{\rm th}$-order Taylor series, sampled from a chain fitting the **NGCz3** power spectrum, compared to the data error bars on that sample. Solid lines show mean deviation while $\pm 1\sigma$ deviations are shown as dashed lines. The monopole and quadrupole deviations are shown in blue and orange, respectively.

directly from `velocileptors` and the Taylor series approximation for 100 representative elements of a power-spectrum fit to **NGCz3**, compared to the much larger error bars of the data itself. Producing the grids used to compute derivatives using one core on `Cori`[3] takes about three minutes, while evaluating the Taylor series itself given the coefficients takes less than a hundredth of a second.

G.2 Nonlinear Damping of the BAO within RecIso

In this appendix we give the specific form of the BAO damping in the reconstructed power spectrum within the **RecIso** scheme. The reconstructed field is defined to be the difference between the overdensities of *displaced* galaxies d and *shifted* galaxies s, i.e. $\delta_{\rm recon} = \delta_d - \delta_s$. Theoretical modeling of the nonlinear damping of the reconstructed field involves calculating cross correlations between the Lagrangian displacements of the two fields. Thus in general we expect each piece of

$$P_s^{\rm recon}(k,\mu) = P_s^{dd} - 2P_s^{ds} + P_s^{ss}, \quad P_s^{ab} = P_{lin,nw}^{ab} + e^{-\frac{1}{2}k^2\Sigma_{ab}^2(\mu)} P_{lin,w}^{ab} + ...,$$

[3] https://docs.nersc.gov/systems/cori/

to have a different damping form, where P^{ab}_{lin} refers to the (undamped) linear-theory predictions for each spectrum and Σ^2_{ab} its damping parameter. Specifically, Σ^2_{ab} is the isotropic component of the displacement two-point function

$$A^{ab}_{ij} = \left\langle \Delta^{ab}_i \Delta^{ab}_j \right\rangle , \ \Delta^{ab} = \Psi^a(\mathbf{q}_1) - \Psi^b(\mathbf{q}_2). \tag{G.1}$$

evaluated at the BAO scale, i.e. $\Sigma^2_{ab} = \frac{1}{3}\delta_{ij}A^{ab}_{ij}$ for $q = r_d$.

Applying the above logic we then have the linear-theory forms

$$\begin{aligned}
P^{dd}_{lin}(k,\mu) &= \Big(b - \mathcal{S} + f\mu^2(1-\mathcal{S})\Big)^2 P_{\rm lin}(k) \\
P^{ds}_{lin}(k,\mu) &= -\mathcal{S}\Big(b - \mathcal{S} + f\mu^2(1-\mathcal{S})\Big) P_{\rm lin}(k) \\
P^{ss}_{lin}(k,\mu) &= \mathcal{S}^2 P_{\rm lin}(k)
\end{aligned}$$

and damping parameters

$$\begin{aligned}
\Sigma^2_{dd}(\mu) &= (1 + f(2+f)\mu^2)\left(2\tilde{\Sigma}^2_{dd}(0) - 2\tilde{\Sigma}^2_{dd}(r_d)\right) \\
\Sigma^2_{ds}(\mu) &= (1 + f(2+f)\mu^2)\tilde{\Sigma}^2_{dd}(0) + \tilde{\Sigma}^2_{ss}(0) - 2(1+f\mu^2)\tilde{\Sigma}^2_{ds}(r_d) \\
\Sigma^2_{ss}(\mu) &= 2\tilde{\Sigma}^2_{ss}(0) - 2\tilde{\Sigma}^2_{ss}(r_d)
\end{aligned}$$

where the tilded Σ's are defined as

$$\begin{aligned}
\tilde{\Sigma}^2_{dd}(r) &= \frac{1}{3}\int \frac{dk}{2\pi^2}\Big[\big(1-\mathcal{S}\big)^2 P_{\rm lin}(k)\ j_0(kr)\Big] \\
\tilde{\Sigma}^2_{ss}(r) &= \frac{1}{3}\int \frac{dk}{2\pi^2}\Big[\mathcal{S}^2 P_{\rm lin}(k)\ j_0(kr)\Big] \\
\tilde{\Sigma}^2_{ds}(r) &= \frac{1}{3}\int \frac{dk}{2\pi^2}\Big[-\mathcal{S}\big(1-\mathcal{S}\big) P_{\rm lin}(k)\ j_0(kr)\Big].
\end{aligned} \tag{G.2}$$

We refer the readers to [78] for a detailed derivation of these damping parameters.

G.3 Parameters for BAO Fit

Our goal in this appendix is to explicitly spell out the assumptions of the standard template fits to the BAO (e.g. in [45, 388, 283, 94]). We begin by writing down Alcock-Paczynski scalings needed to convert between fiducial and true cosmology before writing down the additional assumptions that result in the traditional template fit with r_d-dependent BAO parameters.

G.3.1 Alcock-Paczynski Effect

Galaxy survey data are typically presented in units wherein redshifts and angles are translated into distances via the Hubble function $E^{\rm fid}(z)$ and angular-diameter distance $D^{\rm fid}_A(z)$ of some

fiducial cosmology[4]. Given this choice of coordinates it is necessary given any cosmological model Θ to rescale theory predictions from the true physical separations in the theory into theory units. For the anisotropic power spectrum this is given by

$$P_s^{\rm obs}(k_\parallel^{\rm obs}, k_\perp^{\rm obs}) = \alpha_\parallel^{-1}\alpha_\perp^{-2}\, P^{\rm true}(k_\parallel^{\rm true}, k_\perp^{\rm true}), \quad k_{\parallel,\perp}^{\rm true} = \frac{k^{\rm obs}}{\alpha_{\parallel,\perp}} \tag{G.3}$$

where the Alcock-Paczynski (AP) parameters are defined as

$$\alpha_\parallel = \frac{E^{\rm fid}(z)}{E(z)}, \quad \alpha_\perp = \frac{D_A(z)}{D_A^{\rm fid}(z)}. \tag{G.4}$$

For covenience we will drop the superscript for the "true" quantities in the remainder of this appendix. In terms of these quantities we can write the true wavenumber magnitude and angle as [45]

$$\begin{aligned} k &= \alpha_\perp^{-1}\sqrt{1+\mu_{\rm obs}^2(F_{\rm AP}^{-2}-1)}\, k^{\rm obs} \\ \mu &= \frac{1}{F_{\rm AP}}\left(\sqrt{1+\mu_{\rm obs}^2(F_{\rm AP}^{-2}-1)}\right)^{-1}\mu^{\rm obs} \end{aligned} \tag{G.5}$$

where $F_{\rm AP} = \alpha_\parallel/\alpha_\perp$. Note that both $F_{\rm AP}$ and the μ are invariant under isotropic scaling $\alpha_{\parallel,\perp} \to c\alpha_{\parallel,\perp}$.

G.3.2 BAO in the Power Spectrum

In standard template fits to the BAO the wiggles from a fixed "template" power spectrum are rescaled to model the observed BAO signal. In this case we must allow for the possibility that the true linear power spectrum of the universe has BAO wiggles with a slightly different shape.

The trick is to assume that the linear power spectrum for a given cosmology Θ can be split into a smooth "no-wiggle" component P_{nw} and a "wiggle" component P_w whose cosmology dependence can be approximated in terms of its amplitude A and a template scaled by the BAO radius r_d:

$$P_{\rm lin}(k) = P_{nw}(k|\Theta) + A(\Theta)g(r_d(\Theta)k). \tag{G.6}$$

In particular, for a given "template" power spectrum at the fiducial cosmology we can extract the BAO template

$$G^{\rm fid}(k) = A^{\rm fid}g(r_d^{\rm fid}k). \tag{G.7}$$

The "wiggle" component should be understood to be unique only up to a smooth (polynomial) broadband that does not carry scale information.

[4]For concreteness we will assume throughout that all distances are given in h^{-1} units.

The anisotropic redshift-space power spectrum, taking into nonlinear BAO damping due to bulk displacements, is

$$P_s(k,\mu) = (b+f\mu^2)^2\big(P_{nw}(k) + e^{-\frac{1}{2}k^2\Sigma^2(\mu)}P_w(k)\big) + ...$$

where the ellipsis stands for higher order terms, which we will assume can be absorbed by smooth broadband terms, particularly post-reconstruction. Combining with the above parametrization of the linear power spectrum we get that the observed linear power spectrum is

$$P_s^{\rm obs}(k_{\rm obs},\mu_{\rm obs}) = \alpha_\parallel^{-1}\alpha_\perp^{-2}(b+f\mu^2)^2\Big(P_{nw}(k) + e^{-\frac{1}{2}k^2\Sigma^2(\mu)}A(\Theta)g(r_dk)\Big) + ..., \tag{G.8}$$

In particular, the damped "wiggle" component takes the form

$$\begin{aligned}
P_w^{\rm obs} &= \alpha_\parallel^{-1}\alpha_\perp^{-2}(b+f\mu^2)^2 e^{-\frac{1}{2}k^2\Sigma^2(\mu)}Ag(r_dk) \\
&= \alpha_\parallel^{-1}\alpha_\perp^{-2}(b+f\mu^2)^2 e^{-\frac{1}{2}k^2\Sigma^2(\mu)}A\,g\left(r_d^{\rm fid}\Big(\frac{r_d}{r_d^{\rm fid}}\Big)\alpha_\perp^{-1}\sqrt{1+\mu_{\rm obs}^2(F_{\rm AP}^{-2}-1)}k_{\rm obs}\right) \\
&= \left(\frac{r_d^{\rm fid}}{r_d}\right)^{-3}\tilde\alpha_\parallel^{-1}\tilde\alpha_\perp^{-2}(b+f\mu^2)^2 e^{-\frac{1}{2}k^2\Sigma^2(\mu)}\Big(\frac{A}{A^{\rm fid}}\Big)\,G^{\rm fid}\left(\tilde\alpha_\perp^{-1}\sqrt{1+\mu_{\rm obs}^2(\tilde F_{\rm AP}^{-2}-1)}\,k_{\rm obs}\right) \\
&\equiv \tilde A(b+f\mu^2)^2 e^{-\frac{1}{2}k^2\Sigma^2(\mu)}G^{\rm fid}\left(\tilde\alpha_\perp^{-1}\sqrt{1+\mu_{\rm obs}^2(\tilde F_{\rm AP}^{-2}-1)}\,k_{\rm obs}\right) \\
&\equiv (B+F\mu^2)^2 e^{-\frac{1}{2}k^2\Sigma^2(\mu)}G^{\rm fid}\left(\tilde\alpha_\perp^{-1}\sqrt{1+\mu_{\rm obs}^2(\tilde F_{\rm AP}^{-2}-1)}\,k_{\rm obs}\right)
\end{aligned}$$

where we have dropped the cosmology dependence in $A = A(\Theta)$ and $r_d = r_d(\Theta)$ and defined the modified AP parameters

$$\tilde\alpha_{\parallel,\perp} = \left(\frac{r_d^{\rm fid}}{r_d}\right)\alpha_{\parallel,\perp}, \quad \tilde F_{\rm AP} \equiv \frac{\tilde\alpha_\parallel}{\tilde\alpha_\perp} = F_{\rm AP} \tag{G.9}$$

casting the BAO measurement specifically as one of ratios of cosmological distances with the sound horizon. Note that the ratio $\beta = F/B = f/b$ is equal to that in the normal Kaiser formula and is invariant to the AP effect and template normalization. For the sake of brevity we will not repeat the above derivation for the case of reconstruction but note that the essential features (i.e. r_d scaling with fixed $F_{\rm AP}$) are unchanged in that case.

In practice we would like to expand the power spectrum, broadband included, about the fiducial cosmology, at which all the ratios $X/X^{\rm fid}$ are equal to unity. In this case, the "wiggle" component can be exactly rescaled as above while changes in the broadband power spectrum

are expected to be smooth and degenerate with smooth polynomials, i.e.

$$P_s^{\rm obs}(k_{\rm obs},\mu_{\rm obs}) = (B+F\mu_{\rm obs}^2)^2 P_{nw}^{\rm fid}(k_{\rm obs}) + (B+F\mu^2)^2 \\ e^{-\frac{1}{2}k^2\Sigma^2(\mu)} G^{\rm fid}\left(\tilde{\alpha}_\perp^{-1}\sqrt{1+\mu_{\rm obs}^2(\tilde{F}_{\rm AP}^{-2}-1)}\,k_{\rm obs}\right) + \sum_{n,m} a_{nm}k^n\mu^{2m}. \quad \text{(G.10)}$$

where $P_{nw}^{\rm fid}$ is the "no-wiggle" power spectrum at the fiducial cosmology. In practice we work with multipoles, in which case we can write

$$P_\ell^{\rm obs}(k_{\rm obs}) = \Big(...\Big)_\ell + \sum_n a_{\ell,n}k^n \quad \text{(G.11)}$$

where the ellipses stand for multipoles of the non-polynomial terms. Equivalently, for configuration space analyses we can simply supplement the Fourier transform of these terms with a polynomial in the (inverse) radius:

$$\xi_\ell^{\rm obs}(s_{\rm obs}) = {\rm FT}\left\{(...)\right\}_\ell + \sum_n b_{\ell,n}s_{\rm obs}^{-n} \quad \text{(G.12)}$$

where we have implicitly used that the Fourier transform of the smooth broadband is also smooth over the range of interest.

G.4 Anisotropic secondary bias

Our analysis, in common with most other analyses in the field, has assumed that the probability that a galaxy makes it into the sample is independent of the large-scale tidal field in which that galaxy sits. Specifically, we assume that the galaxy overdensity is a function of scalar quantities that can be constructed from second and higher derivatives of the gravitational potential. Since several "non-scalar" halo properties, like shapes and angular momenta, depend upon the large-scale tidal fields in which the halos are situated [258] there is the possibility that important galaxy properties also inherit this dependence and if the probability of the galaxy appearing in the catalog with a successful redshift depends upon those properties we would introduce a non-scalar component to the bias [176, 110]. This would invalidate our analysis.

The case for or against anisotropic secondary (or "assembly") bias for BOSS galaxies is currently uncertain [227, 259, 345]. The strongest claim so far is that of ref. [259], who argue they have detected such a bias at $5\,\sigma$ by splitting the galaxies using a combination of stellar mass and line-of-sight velocity dispersion. Specifically they show that for two subsamples of galaxies, selected in the $M_\star - \sigma_\star$ plane, they can obtain different power spectrum quadrupoles while matching the power spectrum monopole. Within linear theory and in the absence of anisotropic bias $P(k,\mu) = (b+f\mu^2)^2 P_{\rm lin}(k)$ [196] and so matching the monopoles should imply that the quadrupoles also match. However in the presence of anisotropic secondary

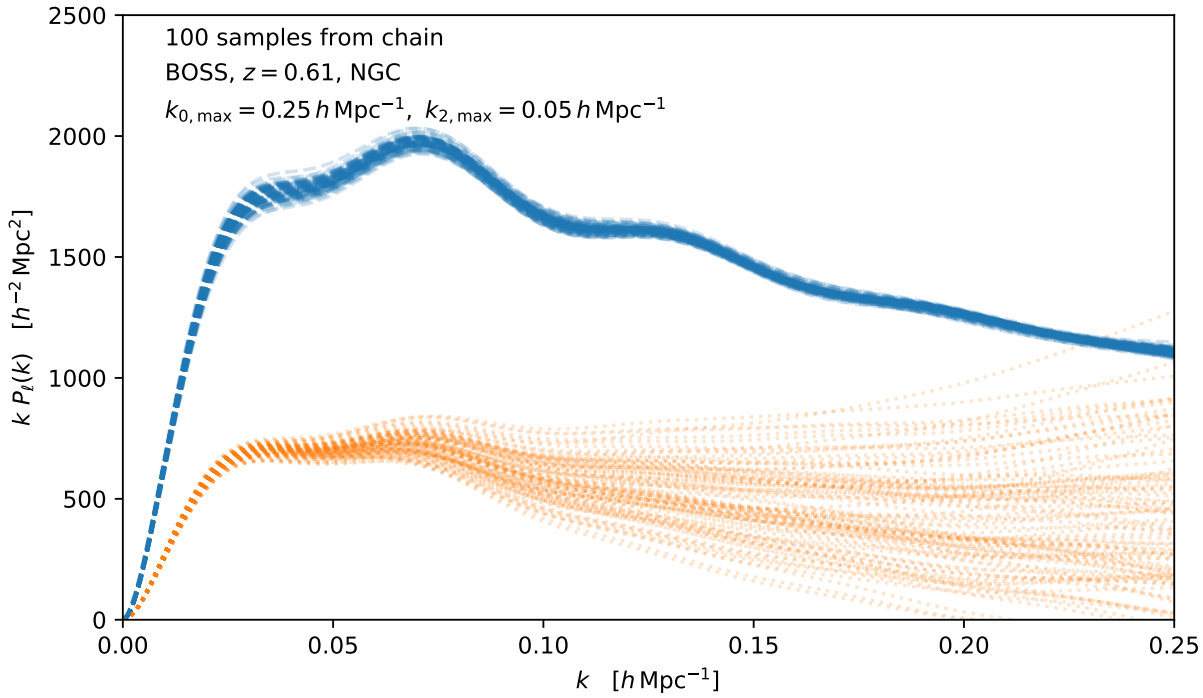

Figure G.2: Model power spectra for 100 models chosen at random from a Markov chain fit to the $z = 0.61$ NGC power spectrum with $k_{\mathrm{max}} = 0.25\,h\,\mathrm{Mpc}^{-1}$ for the monopole but $k_{\mathrm{max}} = 0.05\,h\,\mathrm{Mpc}^{-1}$ for the quadrupole. All of the models are thus consistent within statistical errors with a constant monopole while being essentially unconstrained as to the quadrupole. Note the monopoles (blue dashed lines) form a tight envelope while the quadrupoles (orange dotted lines) agree only at low k. By $k \simeq 0.1\,h\,\mathrm{Mpc}^{-1}$ the differences are about a factor of 2.

bias the prefactor becomes $(b + f\mu^2 + b_q[\mu^2 - 1/3])^2$, where b_q is the anisotropic bias [259] and it is possible to have different quadrupoles while matching the monopoles.

We should treat this claim with caution, since it is based upon a very simple model. Indeed, we have already seen that samples of galaxies in the NGC and SGC regions of the BOSS survey can have quite similar monopoles with relatively different quadrupoles. A careful look at Figs. 3-6 of ref. [259] shows that most of the evidence for anisotropic secondary bias arises from $k > 0.1\,h\,\mathrm{Mpc}^{-1}$ where the linear analysis for the quadrupole is completely inadequate. As one example, our models contain terms going as $k^2\,P_{\mathrm{lin}}(k)$ that can have different amplitudes between the monopole and quadrupole for different samples, showing that the high-k part of the quadrupole can be quite different than linear theory estimates may imply. Phrased differently, models that vary significantly in their satellite content and finger-of-god can cause variations in the quadrupole at high k that are significantly larger than the variations in the monopole that they induce.

To get a sense for how much non-linear bias and non-linear dynamics within the standard

model (without anisotropic secondary bias) can modify the quadrupole at fixed monopole we did the following experiment. We picked the $z = 0.61$ NGC sample, and fit our standard pre-reconstruction power spectrum model to $k \simeq 0.25\,h\,\mathrm{Mpc}^{-1}$ for the monopole but only $k \simeq 0.05\,h\,\mathrm{Mpc}^{-1}$ for the quadrupole[5] at fixed cosmology. We then sampled 100 models from the chain, each model having equal monopoles within statistical errors, to see how much the quadrupoles can differ as a function of k. The results are shown in Fig. G.2. Note the monopoles (blue dashed lines) form a tight envelope while the quadrupoles (orange dotted lines) agree only at low k. By $k \simeq 0.1\,h\,\mathrm{Mpc}^{-1}$ the differences are about a factor of 2.

Based upon this calculation we believe the case for anisotropic secondary bias in the BOSS galaxies remains unproven. While our calculations do not prove the absence of such an effect, existing measurements are also consistent with differences expected in currently popular models that neglect these effects. Given its importance as a source of systematic errors for future redshift surveys, further investigation is clearly warranted.

[5]Since the quadrupole is now highly unconstrained we narrowed the prior on α_2 to be $\mathcal{N}(0, 25)$, corresponding to a finger-of-god velocity dispersion of $\mathcal{O}(500\mathrm{km\,s}^{-1})$ which is comparable to the values of α_2 we obtain from the fits in the main body of the paper.

Appendix H

Joint Analysis of BOSS and CMB Lensing

H.1 Neutrinos

Throughout this paper we have worked within the approximation that galaxy clustering within massive neutrino cosmologies traces the dark matter-baryon component and that its autocorrelation can be modeled by computing perturbation-theory predictions using $P_{\rm cb,lin}$ as the input linear power spectrum. On the other hand, within the same approximation the nonlinear galaxy-matter cross correlation has to be computed via a mixture of loop integrals involving $P_{\rm cb,lin}$, $P_{\rm m,lin}$ and $P_{\rm cb,\ m,lin}$, which are shown in Figure H.1 as red, blue and purple lines, respectively. Roughly speaking, this is because contractions involving only galaxy ("cb") or matter ("m") vertices involve autospectra while contractions across vertices produce cross spectra.

While the computation of these mixed diagrams is in principle straightforward, in this paper we would like to make use of existing perturbation codes like `velocileptors` and therefore make use of the additional approximation that cross spectra can be computed using only $P_{\rm cb,\ m,lin}$ as the input power spectrum. As discussed in §9.4.1, this properly captures the shape of the transition from clustered to unclustered neutrinos at the free streaming scale. However, at the 1-loop level this prescription is not strictly correct—as shown in Figure H.1, the $(2,2)$ contributions (left) depend on the cross $P_{\rm cb,\ m,lin}$ and will be correctly captured but the $(1,3)$ contributions involve cb-m autospectra, which differ from calculations using the cross spectrum by order $\mathcal{O}(f_\nu P_{\rm L})$.

Fortunately, the differences due to the above mistake will tend to be small for two reasons: the neutrino mass fraction f_ν is small and, since they only appear at the 1-loop level, they will be further suppressed relative to leading contributions, such that the total error will be of order $\mathcal{O}(f_\nu P_{\rm L}^2)$. For example, the error incurred by evaluating the bottom-right diagram in

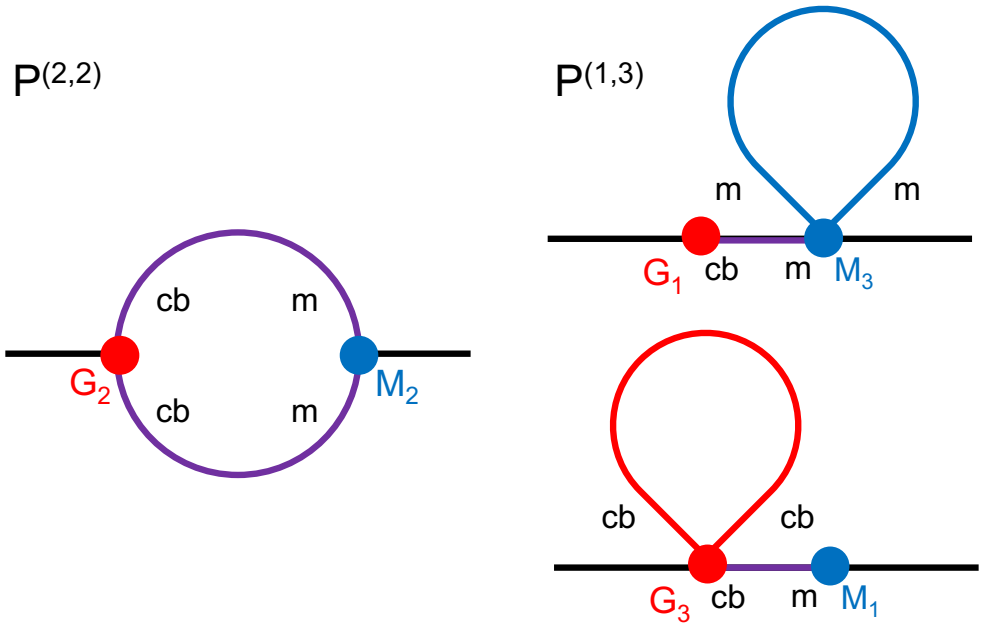

Figure H.1: Diagrams of contributions to the 1-loop matter-galaxy power spectrum. Red vertices (G_n) and lines (linear spectra) correspond to galaxies and the "cb" component while blue ones (M_n) correspond to matter including neutrinos. Purple lines indicate the cb-m cross spectrum.

Figure H.1 will be

$$3M_1(\mathbf{k})P^{\rm lin}_{\rm cb,m}(\mathbf{k})\int_{\mathbf{p}} G_3(\mathbf{k},\mathbf{p},-\mathbf{p})\big(P^{\rm lin}_{\rm cb,m}(\mathbf{p})-P^{\rm lin}_{\rm cb}(\mathbf{p})\big) \\ \sim f_\nu P^{\rm lin}_{\rm cb,m}(\mathbf{k})\int_{|\mathbf{p}|>k_{fs}} G_3(\mathbf{k},\mathbf{p},-\mathbf{p})P^{\rm lin}_{\rm cb}(\mathbf{p})$$

where we have used that, at wavenumbers larger than the free streaming scale k_{fs}, $P_{cb,m} \approx (1-f_\nu)P_{cb}$ and we have defined the galaxy third-order kernel G_3 and $\int_{\mathbf{p}} = \int \frac{d^3\mathbf{p}}{(2\pi)^3}$. A particular concern might be that the above mistake would lead to a contribution degenerate with the linear bias $\Delta b\, P^{\rm lin}_{cb,m}$, where Δb would be sourced by dark matter density fluctuations above the k_{fs}, leading to inconsistencies in the bias definitions used in our real and redshift-space analyses; however, such a contribution due to short-wavelength (UV) modes can be prevented by adopting normal-ordered bias operators [234, 109], sometimes also referred to as renormalized operators, as is done in `velocileptors` [74, 82]. Beyond this the next leading correction will be of the form $f_\nu k^2\Sigma^2 P^{\rm lin}_{cb}$, where Σ^2 is the variance of linear (cb) displacements from small-wavelength modes[1]. Since such a correction has to be subleading even without

[1]We might also expect the cross-spectrum BAO damping paramater $\Sigma^2_{\rm BAO}$ to be modified by order f_ν, but this will not concern us since the projected $C_\ell^{\kappa g}$ are insensitive to BAO.

the factor of f_ν in order for perturbation theory to be valid, it will be highly suppressed and negligble for most purposes.

H.2 Redshift-Dependent Galaxy Selection Effects and Cuts

One possibility for the non-zero cross-correlation we observe between the **z1** and **z3** slices, whereas the similar correlation between the LOWZ and CMASS samples is smaller [119], is that the systematics weights have a redshift dependence, either implicitly or induced by a redshift-dependence in some other property (size, luminosity, color, etc.). Since such a dependence has been neglected in deriving and applying the weights this would imply that deriving the weights on one set of samples but then analyzing a shuffled set leads to correlations.

The BOSS collaboration derived the weights by which they correct for observational systematics by removing linear trends in the pixelized, projected galaxy number density vs. systematic template [300]. He we provide a simple toy model for how redshift-dependence in the impact of systematics could lead to a bias in such a procedure. Let the "true" redshift distribution of a galaxy sample be dN/dz. Given a multiplicative selection bias, say due to some galactic foreground, the observed distribution is

$$\frac{dN_{\rm obs}(\theta)}{dz} = [1 + T(\theta, z)] \ \frac{dN}{dz} \tag{H.1}$$

where the angular dependence is entirely due to the foreground contamination. To correct for this we define a systematic weight, $w(\theta)$, whose θ-dependence arises from the systematics template, such that the distribution of projected densities is uniform when plotted against the value of the systematic, i.e.

$$\begin{aligned} w^{-1}(\theta) &= \frac{1}{\bar{N}} \int dz \ \frac{dN}{dz} \ \big(1 + T(\theta, z)\big) \\ &\approx 1 + T(\theta, z_0) + \frac{1}{\bar{N}} \Big(\int dz \ \frac{dN}{dz} \ (z - z_0) \Big) \ T'(\theta, z_0) \end{aligned} \tag{H.2}$$

where $\bar{N}$ is the average projected number density of the sample *sans* systematics and we have Taylor-expanded the redshift dependence to first order. The final term vanishes when $z_0 = z_{\rm mean}$. However, if the sample is now split up into further redshift bins $z \in (z_a, z_b)$ this will lead to an angular correction proportional to the offset in the mean redshift of the new

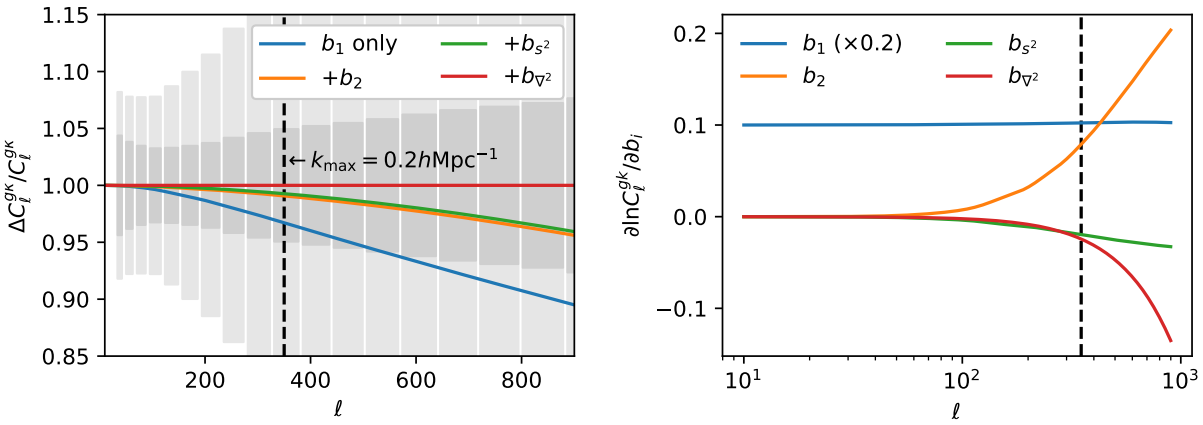

Figure H.2: *Left*: The impact of including higher order Lagrangian bias in the observable signal of $C_\ell^{g\kappa}$, compared to the uncertainty expected for a $z_{\rm eff} \approx 0.59$ DESI-like number density and lensing noise corresponding to the Planck and Simons Observatory (SO) surveys. *Right:* The logarithmic derivatives of the $C_\ell^{g\kappa}$ power spectrum with respect to bias parameters as a function of scale. The vertical dashed line indicates the highest ℓ used in this analysis, which as discussed in § 9.5.1 corresponds to scales of $k \approx 0.2h{\rm Mpc}^{-1}$. The highest ℓ shown corresponds to $k \approx 0.6h{\rm Mpc}^{-1}$ for this sample, the smallest scales where we expect second-order hybrid LPT approaches to recover unbiased results.

sample compared to the old one:

$$\begin{aligned} N_{ab}(\theta) &= w^{-1}(\theta) \int_{z_a}^{z_b} dz \, \frac{dN}{dz} \, \big(1 + T(\theta, z)\big) \\ &= \frac{\bar{N}_{ab}(1 + T_0 + T_0' \, \Delta z_{ab})}{1 + T_0} \\ &\approx \bar{N}_{ab}(1 + T_0'(\theta)\Delta z_{ab}) \quad \text{with} \quad \Delta z_{ab} \equiv \frac{1}{\bar{N}_{ab}} \int_{z_a}^{z_b} dz \, \frac{dN}{dz} \, (z - z_{\rm mean}). \end{aligned} \tag{H.3}$$

H.3 Prospects for degeneracy breaking by pushing to smaller scales

A limitation of the techniques used in this paper arises from the fact that contributions from higher order biases (as well as shot-noise in the case of the auto-spectrum) are nearly degenerate on the quasi-linear scales we have probed in this work. In Fig. 9.1, we can see the uncertainties associated with poorly constrained counterterms reduce the constraining power of scales which are well within the perturbative regime. While the combination of probes we use depends on these parameters in different ways, these degeneracies are fundamentally present in the 3D spectra, P_{gg} and P_{gm}, at these scales.

In Fig. H.2 we show the fractional change in including higher order bias operators in the model for $C_\ell^{g\kappa}$ for a DESI-like sample of galaxies cross-correlated with Planck and SO CMB lensing. The bias parameters used are derived from the field-level inference of [206] for a DESI-like HOD. The binning adopted uses bins $\Delta\ell \approx 3\sqrt{\ell}$, and each error bar should be thought of as an independent data point. At scales $\ell > 350$, relative to the SO uncertainties, the impact of including each additional operator is significant. The sole exception is the tidal bias b_{s^2}, which is known to impact the P_{gm} spectrum weakly. In the galaxy–κ cross-spectrum we can also observe that for ℓs that probe $k < 0.2h\text{Mpc}^{-1}$, many of the contributions are approximately degenerate, as shown in the right-hand panel of Fig. H.2. However, at smaller scales the responses of observables like $C_\ell^{g\kappa}$ to changes in bias parameters become distinct, implying that accessing these smaller scales can help lift these degeneracies.

Despite the challenges of pushing to smaller scales in redshift space, the prospect of extending galaxy-κ analyses to higher ℓ is tantalizing. This observable is largely insensitive to the imapact of RSDs and can be readily modelled by hybrid LPT techniques [244, 207, 432, 156] that combine the same Lagrangian bias expansion (Eqn. 9.5) with N-body dynamics to give an accurate model of P_{gm} up to $k_{\rm max} \simeq 0.6\,h\,{\rm Mpc}^{-1}$, corresponding to $\ell_{\rm max} \approx 900$. Extending our analysis to such $\ell_{\rm max}$, once the CMB lensing noise is sub-dominant at these scales, will allow for a significantly longer lever arm that will simultaneously break degeneracies between bias parameters, include more independent modes in the analysis, and reduce the impact of potentially systematics-dominated lower-ℓ modes.

H.4 Fits with Free Spectral Index n_s

As described in the body of the paper, our main analyses in this work have been performed by fixing the spectral index to the best-fit value for Planck [285]. We have made this choice because the large-scale structure data we consider in this work are unable to robustly constrain n_s and leaving it free results in the exploration of parts of the ΛCDM parameter space strongly ruled out by Planck. However, for completeness, and to more fully compare with other results in the literature, in this Appendix we consider the effect of extending our fits to include n_s with an uninformative uniform prior $\mathcal{U}(0.5, 1.5)$.

The main results of this extended analysis are shown in Table H.1 and Figure H.3. When only three-dimensional redshift-space galaxy data, including BAO, are considered, this analysis yields a mild ($\sim 1.5\sigma$) preference for values of n_s below the Planck value, leading to noticeable shifts and widening in the Ω_m, H_0, σ_8 posteriors — notably, the mean σ_8 shifts further downward relative to the CMB — though the redshift-space only posteriors are still in decent agreement with Planck, as the shifts in these parameters mostly lie along poorly constrained degeneracy directions[2] and the 2σ regions of BOSS and Planck overlap in all cases. These shifts in the RSD constraints are in excellent agreement with ref. [282]. This

[2]Indeed, we note that both the best-fit elements in the chain and found by COBAYA's in-built optimization routine have n_s and σ_8 roughly 1σ above the mean and in agreement with the posteriors with n_s fixed, suggesting a potential volume effect.

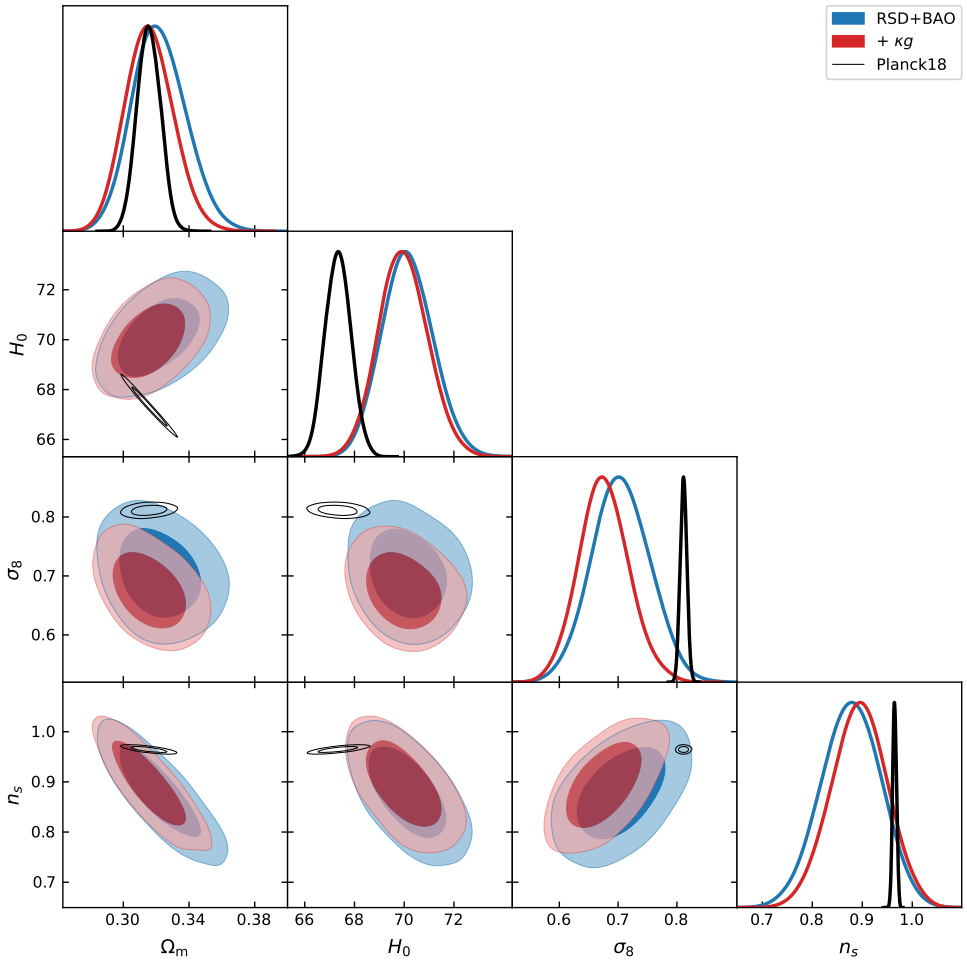

Figure H.3: Marginalized cosmological posteriors as in Figure 9.6 for the case where n_s is varied. Blue and red contours show results without and with lensing data. The corresponding posteriors from Planck are shown in black for comparison.

	P_ℓ, $\xi_\ell^{\rm rec}$	P_ℓ, $\xi_\ell^{\rm rec}$, $C_\ell^{\kappa g}$	Planck
$\ln(10^{10}A_s)$	2.66 ± 0.16	2.60 ± 0.15	3.044 ± 0.014
Ω_m	$0.322^{+0.015}_{-0.018}$	$0.316^{+0.014}_{-0.015}$	0.3153 ± 0.0073
H_0 [km/s/Mpc]	70.2 ± 1.0	70.0 ± 1.0	67.36 ± 0.54
n_s	0.878 ± 0.060	0.893 ± 0.055	0.9649 ± 0.0042
σ_8	0.705 ± 0.049	0.674 ± 0.042	0.8111 ± 0.0060

Table H.1: Cosmological constraints from BOSS with and without CMB lensing when n_s is varied.

one-parameter extension does not alleviate the low σ_8 tension in the main analysis; and as in the main analysis, adding in cross correlations with CMB lensing leads to a further drop in σ_8 of roughly the same fractional size as that in our fiducial analysis ($\approx 5\%$) while the other ΛCDM parameters remain largely unchanged.

Bibliography

[1] Kevork N. Abazajian et al. "CMB-S4 Science Book, First Edition". In: *arXiv e-prints*, arXiv:1610.02743 (Oct. 2016), arXiv:1610.02743. arXiv: 1610.02743 [astro-ph.CO].

[2] T. M. C. Abbott et al. "Dark Energy Survey Year 3 results: Cosmological constraints from galaxy clustering and weak lensing". In: *Phys. Rev. D* 105.2, 023520 (Jan. 2022), p. 023520. DOI: 10.1103/PhysRevD.105.023520. arXiv: 2105.13549 [astro-ph.CO].

[3] Abdalla et al. "Cosmology Intertwined: A Review of the Particle Physics, Astrophysics, and Cosmology Associated with the Cosmological Tensions and Anomalies". In: *Contribution to Snowmass 2021*. 2022.

[4] Muntazir Mehdi Abidi and Tobias Baldauf. "Cubic halo bias in Eulerian and Lagrangian space". In: *JCAP* 2018.7, 029 (July 2018), p. 029. DOI: 10.1088/1475-7516/2018/07/029. arXiv: 1802.07622 [astro-ph.CO].

[5] M. Abramowitz and I. A. Stegun. *Handbook of Mathematical Functions*. 1972.

[6] Jennifer Adams, Bevan Cresswell, and Richard Easther. "Inflationary perturbations from a potential with a step". In: *Phys. Rev. D* 64.12 (Dec. 2001), p. 123514. DOI: 10.1103/PhysRevD.64.123514. arXiv: astro-ph/0102236 [astro-ph].

[7] Shadab Alam et al. "The clustering of galaxies in the completed SDSS-III Baryon Oscillation Spectroscopic Survey: cosmological analysis of the DR12 galaxy sample". In: *MNRAS* 470.3 (Sept. 2017), pp. 2617–2652. DOI: 10.1093/mnras/stx721. arXiv: 1607.03155 [astro-ph.CO].

[8] Shadab Alam et al. "Towards testing the theory of gravity with DESI: summary statistics, model predictions and future simulation requirements". In: *JCAP* 2021.11, 050 (Nov. 2021), p. 050. DOI: 10.1088/1475-7516/2021/11/050. arXiv: 2011.05771 [astro-ph.CO].

[9] C. Alcock and B. Paczynski. "An evolution free test for non-zero cosmological constant". In: *Nature* 281 (Oct. 1979), p. 358. DOI: 10.1038/281358a0.

[10] Steven W. Allen, August E. Evrard, and Adam B. Mantz. "Cosmological Parameters from Observations of Galaxy Clusters". In: *Ann. Rev. Astron.& Astrophys.* 49.1 (Sept. 2011), pp. 409–470. DOI: 10.1146/annurev-astro-081710-102514. arXiv: 1103.4829 [astro-ph.CO].

[11] David Alonso et al. "A unified pseudo-C_ℓ framework". In: *MNRAS* 484.3 (Apr. 2019), pp. 4127–4151. DOI: 10.1093/mnras/stz093. arXiv: 1809.09603 [astro-ph.CO].

[12] Luca Amendola et al. "Cosmology and fundamental physics with the Euclid satellite". In: *Living Reviews in Relativity* 21.1, 2 (Apr. 2018), p. 2. DOI: 10.1007/s41114-017-0010-3. arXiv: 1606.00180 [astro-ph.CO].

[13] A. Amon et al. "Dark Energy Survey Year 3 results: Cosmology from cosmic shear and robustness to data calibration". In: *Phys. Rev. D* 105.2, 023514 (Jan. 2022), p. 023514. DOI: 10.1103/PhysRevD.105.023514. arXiv: 2105.13543 [astro-ph.CO].

[14] Raul Angulo et al. "On the statistics of biased tracers in the Effective Field Theory of Large Scale Structures". In: *JCAP* 2015.9, 029 (Sept. 2015), p. 029. DOI: 10.1088/1475-7516/2015/09/029. arXiv: 1503.08826 [astro-ph.CO].

[15] Valentin Assassi, Marko Simonović, and Matias Zaldarriaga. "Efficient evaluation of angular power spectra and bispectra". In: *JCAP* 11 (2017), p. 054. DOI: 10.1088/1475-7516/2017/11/054. arXiv: 1705.05022 [astro-ph.CO].

[16] Valentin Assassi et al. "Renormalized halo bias". In: *JCAP* 2014.8, 056 (Aug. 2014), p. 056. DOI: 10.1088/1475-7516/2014/08/056. arXiv: 1402.5916 [astro-ph.CO].

[17] Alejandro Aviles. "Renormalization of Lagrangian bias via spectral parameters". In: *Phys. Rev. D* 98.8, 083541 (Oct. 2018), p. 083541. DOI: 10.1103/PhysRevD.98.083541. arXiv: 1805.05304 [astro-ph.CO].

[18] Alejandro Aviles and Arka Banerjee. "A Lagrangian perturbation theory in the presence of massive neutrinos". In: *JCAP* 2020.10, 034 (Oct. 2020), p. 034. DOI: 10.1088/1475-7516/2020/10/034. arXiv: 2007.06508 [astro-ph.CO].

[19] Alejandro Aviles and Jorge L. Cervantes-Cota. "Lagrangian perturbation theory for modified gravity". In: *Phys. Rev. D* 96.12, 123526 (Dec. 2017), p. 123526. DOI: 10.1103/PhysRevD.96.123526. arXiv: 1705.10719 [astro-ph.CO].

[20] Tobias Baldauf, Vincent Desjacques, and Uroš Seljak. "Velocity bias in the distribution of dark matter halos". In: *Phys. Rev. D* 92.12, 123507 (Dec. 2015), p. 123507. DOI: 10.1103/PhysRevD.92.123507. arXiv: 1405.5885 [astro-ph.CO].

[21] Tobias Baldauf et al. "Algorithm for the direct reconstruction of the dark matter correlation function from weak lensing and galaxy clustering". In: *Phys. Rev. D* 81.6, 063531 (Mar. 2010), p. 063531. DOI: 10.1103/PhysRevD.81.063531. arXiv: 0911.4973 [astro-ph.CO].

[22] Tobias Baldauf et al. "Equivalence principle and the baryon acoustic peak". In: *Phys. Rev. D* 92.4, 043514 (Aug. 2015), p. 043514. DOI: 10.1103/PhysRevD.92.043514. arXiv: 1504.04366 [astro-ph.CO].

[23] Tobias Baldauf et al. "Halo stochasticity from exclusion and nonlinear clustering". In: *Phys. Rev. D* 88.8, 083507 (Oct. 2013), p. 083507. DOI: 10.1103/PhysRevD.88.083507. arXiv: 1305.2917 [astro-ph.CO].

[24] Mario Ballardini et al. "Non-linear damping of superimposed primordial oscillations on the matter power spectrum in galaxy surveys". In: *JCAP* 2020.4, 030 (Apr. 2020), p. 030. DOI: 10.1088/1475-7516/2020/04/030. arXiv: 1912.12499 [astro-ph.CO].

[25] Alexandre Barreira et al. "Baryon-CDM isocurvature galaxy bias with IllustrisTNG". In: *JCAP* 2020.2, 005 (Feb. 2020), p. 005. DOI: 10.1088/1475-7516/2020/02/005. arXiv: 1907.04317 [astro-ph.CO].

[26] Daniel Baumann. "TASI Lectures on Inflation". In: *arXiv e-prints*, arXiv:0907.5424 (July 2009), arXiv:0907.5424. arXiv: 0907.5424 [hep-th].

[27] Daniel Baumann, Daniel Green, and Benjamin Wallisch. "Searching for light relics with large-scale structure". In: *JCAP* 2018.8, 029 (Aug. 2018), p. 029. DOI: 10.1088/1475-7516/2018/08/029. arXiv: 1712.08067 [astro-ph.CO].

[28] Daniel Baumann et al. "Cosmological non-linearities as an effective fluid". In: *JCAP* 2012.7, 051 (July 2012), p. 051. DOI: 10.1088/1475-7516/2012/07/051. arXiv: 1004.2488 [astro-ph.CO].

[29] Daniel Baumann et al. "First constraint on the neutrino-induced phase shift in the spectrum of baryon acoustic oscillations". In: *Nature Physics* 15.5 (Feb. 2019), pp. 465–469. DOI: 10.1038/s41567-019-0435-6. arXiv: 1803.10741 [astro-ph.CO].

[30] Julian E. Bautista et al. "The completed SDSS-IV extended Baryon Oscillation Spectroscopic Survey: measurement of the BAO and growth rate of structure of the luminous red galaxy sample from the anisotropic correlation function between redshifts 0.6 and 1". In: *MNRAS* 500.1 (Jan. 2021), pp. 736–762. DOI: 10.1093/mnras/staa2800. arXiv: 2007.08993 [astro-ph.CO].

[31] Julian E. Bautista et al. "The SDSS-IV Extended Baryon Oscillation Spectroscopic Survey: Baryon Acoustic Oscillations at Redshift of 0.72 with the DR14 Luminous Red Galaxy Sample". In: *ApJ* 863.1, 110 (Aug. 2018), p. 110. DOI: 10.3847/1538-4357/aacea5. arXiv: 1712.08064 [astro-ph.CO].

[32] E. J. Baxter et al. "Dark Energy Survey Year 1 results: Methodology and projections for joint analysis of galaxy clustering, galaxy lensing, and CMB lensing two-point functions". In: *Phys. Rev. D* 99.2, 023508 (Jan. 2019), p. 023508. DOI: 10.1103/PhysRevD.99.023508. arXiv: 1802.05257 [astro-ph.CO].

[33] Adrian E. Bayer, Arka Banerjee, and Uroš Seljak. "Beware of Fake νs: The Effect of Massive Neutrinos on the Non-Linear Evolution of Cosmic Structure". In: *arXiv e-prints*, arXiv:2108.04215 (Aug. 2021), arXiv:2108.04215. arXiv: 2108.04215 [astro-ph.CO].

[34] Peter S. Behroozi, Risa H. Wechsler, and Hao-Yi Wu. "The ROCKSTAR Phase-space Temporal Halo Finder and the Velocity Offsets of Cluster Cores". In: *ApJ* 762.2, 109 (Jan. 2013), p. 109. DOI: 10.1088/0004-637X/762/2/109. arXiv: 1110.4372 [astro-ph.CO].

[35] Lucia F. de la Bella, Nicolas Tessore, and Sarah Bridle. "The unequal-time matter power spectrum: impact on weak lensing observables". In: (Nov. 2020). arXiv: 2011.06185 [astro-ph.CO].

[36] Lucıa Fonseca de la Bella et al. "The matter power spectrum in redshift space using effective field theory". In: *JCAP* 11 (2017), p. 039. DOI: 10.1088/1475-7516/2017/11/039. arXiv: 1704.05309 [astro-ph.CO].

[37] B. A. Benson et al. "SPT-3G: a next-generation cosmic microwave background polarization experiment on the South Pole telescope". In: *Millimeter, Submillimeter, and Far-Infrared Detectors and Instrumentation for Astronomy VII*. Ed. by Wayne S. Holland and Jonas Zmuidzinas. Vol. 9153. Society of Photo-Optical Instrumentation Engineers (SPIE) Conference Series. July 2014, 91531P, 91531P. DOI: 10.1117/12.2057305. arXiv: 1407.2973 [astro-ph.IM].

[38] José Luis Bernal et al. "Robustness of baryon acoustic oscillation constraints for early-Universe modifications of Λ CDM cosmology". In: *Phys. Rev. D* 102.12, 123515 (Dec. 2020), p. 123515. DOI: 10.1103/PhysRevD.102.123515. arXiv: 2004.07263 [astro-ph.CO].

[39] F. Bernardeau et al. "Large-scale structure of the Universe and cosmological perturbation theory". In: *Phys. Rep.* 367.1-3 (Sept. 2002), pp. 1–248. DOI: 10.1016/S0370-1573(02)00135-7. arXiv: astro-ph/0112551 [astro-ph].

[40] Francis Bernardeau, Nicolas Van de Rijt, and Filippo Vernizzi. "Power spectra in the eikonal approximation with adiabatic and nonadiabatic modes". In: *Phys. Rev. D* 87.4, 043530 (Feb. 2013), p. 043530. DOI: 10.1103/PhysRevD.87.043530. arXiv: 1209.3662 [astro-ph.CO].

[41] Florian Beutler, Emanuele Castorina, and Pierre Zhang. "Interpreting measurements of the anisotropic galaxy power spectrum". In: *JCAP* 2019.3, 040 (Mar. 2019), p. 040. DOI: 10.1088/1475-7516/2019/03/040. arXiv: 1810.05051 [astro-ph.CO].

[42] Florian Beutler and Patrick McDonald. "Unified galaxy power spectrum measurements from 6dFGS, BOSS, and eBOSS". In: *JCAP* 2021.11, 031 (Nov. 2021), p. 031. DOI: 10.1088/1475-7516/2021/11/031. arXiv: 2106.06324 [astro-ph.CO].

[43] Florian Beutler, Uroš Seljak, and Zvonimir Vlah. "Constraining the relative velocity effect using the Baryon Oscillation Spectroscopic Survey". In: *MNRAS* 470.3 (Sept. 2017), pp. 2723–2735. DOI: 10.1093/mnras/stx1196. arXiv: 1612.04720 [astro-ph.CO].

[44] Florian Beutler et al. "Primordial features from linear to nonlinear scales". In: *Physical Review Research* 1.3, 033209 (Dec. 2019), p. 033209. DOI: 10.1103/PhysRevResearch.1.033209. arXiv: 1906.08758 [astro-ph.CO].

[45] Florian Beutler et al. "The clustering of galaxies in the completed SDSS-III Baryon Oscillation Spectroscopic Survey: anisotropic galaxy clustering in Fourier space". In: *MNRAS* 466.2 (Apr. 2017), pp. 2242–2260. DOI: 10.1093/mnras/stw3298. arXiv: 1607.03150 [astro-ph.CO].

[46] Somnath Bharadwaj. "The Evolution of Correlation Functions in the Zeldovich Approximation and Its Implications for the Validity of Perturbation Theory". In: *ApJ* 472 (Nov. 1996), p. 1. DOI: 10.1086/178036. arXiv: astro-ph/9606121 [astro-ph].

[47] Davide Bianchi et al. "Measuring line-of-sight-dependent Fourier-space clustering using FFTs". In: *MNRAS* 453.1 (Oct. 2015), pp. L11–L15. DOI: 10.1093/mnrasl/slv090. arXiv: 1505.05341 [astro-ph.CO].

[48] Diego Blas, Julien Lesgourgues, and Thomas Tram. "The Cosmic Linear Anisotropy Solving System (CLASS). Part II: Approximation schemes". In: *JCAP* 2011.7, 034 (July 2011), p. 034. DOI: 10.1088/1475-7516/2011/07/034. arXiv: 1104.2933 [astro-ph.CO].

[49] Diego Blas et al. "Structure formation with massive neutrinos: going beyond linear theory". In: *JCAP* 2014.11, 039 (Nov. 2014), p. 039. DOI: 10.1088/1475-7516/2014/11/039. arXiv: 1408.2995 [astro-ph.CO].

[50] Diego Blas et al. "Time-sliced perturbation theory II: baryon acoustic oscillations and infrared resummation". In: *JCAP* 2016.7, 028 (July 2016), p. 028. DOI: 10.1088/1475-7516/2016/07/028. arXiv: 1605.02149 [astro-ph.CO].

[51] Jonathan A. Blazek, Joseph E. McEwen, and Christopher M. Hirata. "Streaming Velocities and the Baryon Acoustic Oscillation Scale". In: *Phys. Rev. Lett.* 116.12, 121303 (Mar. 2016), p. 121303. DOI: 10.1103/PhysRevLett.116.121303. arXiv: 1510.03554 [astro-ph.CO].

[52] J. R. Bond et al. "Excursion Set Mass Functions for Hierarchical Gaussian Fluctuations". In: *ApJ* 379 (Oct. 1991), p. 440. DOI: 10.1086/170520.

[53] Josh Borrow, Daniel Anglés-Alcázar, and Romeel Davé. "Cosmological baryon transfer in the SIMBA simulations". In: *MNRAS* 491.4 (Feb. 2020), pp. 6102–6119. DOI: 10.1093/mnras/stz3428. arXiv: 1910.00594 [astro-ph.GA].

[54] T. Buchert. "A class of solutions in Newtonian cosmology and the pancake theory". In: *A&A* 223.1-2 (Oct. 1989), pp. 9–24.

[55] A. Burden, W. J. Percival, and C. Howlett. "Reconstruction in Fourier space". In: *MNRAS* 453.1 (Oct. 2015), pp. 456–468. DOI: 10.1093/mnras/stv1581. arXiv: 1504.02591 [astro-ph.CO].

[56] Giovanni Cabass and Fabian Schmidt. "A new scale in the bias expansion". In: *JCAP* 2019.5, 031 (May 2019), p. 031. DOI: 10.1088/1475-7516/2019/05/031. arXiv: 1812.02731 [astro-ph.CO].

[57] Duncan Campbell et al. "The galaxy clustering crisis in abundance matching". In: *MNRAS* 477.1 (June 2018), pp. 359–383. DOI: 10.1093/mnras/sty495. arXiv: 1705.06347 [astro-ph.GA].

[58] Jordan Carlson, Beth Reid, and Martin White. "Convolution Lagrangian perturbation theory for biased tracers". In: *MNRAS* 429.2 (Feb. 2013), pp. 1674–1685. DOI: 10.1093/mnras/sts457. arXiv: 1209.0780 [astro-ph.CO].

[59] Jordan Carlson, Martin White, and Nikhil Padmanabhan. "Critical look at cosmological perturbation theory techniques". In: *Phys. Rev. D* 80.4, 043531 (Aug. 2009), p. 043531. DOI: 10.1103/PhysRevD.80.043531. arXiv: 0905.0479 [astro-ph.CO].

[60] John Joseph M. Carrasco, Mark P. Hertzberg, and Leonardo Senatore. "The effective field theory of cosmological large scale structures". In: *Journal of High Energy Physics* 2012, 82 (Sept. 2012), p. 82. DOI: 10.1007/JHEP09(2012)082. arXiv: 1206.2926 [astro-ph.CO].

[61] Paul Carter et al. "Low redshift baryon acoustic oscillation measurement from the reconstructed 6-degree field galaxy survey". In: *MNRAS* 481.2 (Dec. 2018), pp. 2371–2383. DOI: 10.1093/mnras/sty2405. arXiv: 1803.01746 [astro-ph.CO].

[62] Paul Carter et al. "The impact of the fiducial cosmology assumption on BAO distance scale measurements". In: *MNRAS* 494.2 (May 2020), pp. 2076–2089. DOI: 10.1093/mnras/staa761. arXiv: 1906.03035 [astro-ph.CO].

[63] Emanuele Castorina and Martin White. "Beyond the plane-parallel approximation for redshift surveys". In: *MNRAS* 476.4 (June 2018), pp. 4403–4417. DOI: 10.1093/mnras/sty410. arXiv: 1709.09730 [astro-ph.CO].

[64] Emanuele Castorina and Martin White. "The Zeldovich approximation and wide-angle redshift-space distortions". In: *MNRAS* 479.1 (Sept. 2018), pp. 741–752. DOI: 10.1093/mnras/sty1437. arXiv: 1803.08185 [astro-ph.CO].

[65] Emanuele Castorina et al. "Cosmology with massive neutrinos II: on the universality of the halo mass function and bias". In: *JCAP* 2014.2, 049 (Feb. 2014), p. 049. DOI: 10.1088/1475-7516/2014/02/049. arXiv: 1311.1212 [astro-ph.CO].

[66] Emanuele Castorina et al. "DEMNUni: the clustering of large-scale structures in the presence of massive neutrinos". In: *JCAP* 2015.7, 043 (July 2015), p. 043. DOI: 10.1088/1475-7516/2015/07/043. arXiv: 1505.07148 [astro-ph.CO].

[67] Emanuele Castorina et al. "Excursion set peaks: the role of shear". In: *arXiv e-prints*, arXiv:1611.03619 (Nov. 2016), arXiv:1611.03619. arXiv: 1611.03619 [astro-ph.CO].

[68] Paolo Catelan et al. "The bias field of dark matter haloes". In: *MNRAS* 297.3 (July 1998), pp. 692–712. DOI: 10.1046/j.1365-8711.1998.01455.x. arXiv: astro-ph/9708067 [astro-ph].

[69] Kwan Chuen Chan, Román Scoccimarro, and Ravi K. Sheth. "Gravity and large-scale nonlocal bias". In: *Phys. Rev. D* 85.8, 083509 (Apr. 2012), p. 083509. DOI: 10.1103/PhysRevD.85.083509. arXiv: 1201.3614 [astro-ph.CO].

[70] Shi-Fan Chen, Emanuele Castorina, and Martin White. "Biased tracers of two fluids in the Lagrangian picture". In: *JCAP* 2019.6, 006 (June 2019), p. 006. DOI: 10.1088/1475-7516/2019/06/006. arXiv: 1903.00437 [astro-ph.CO].

[71] Shi-Fan Chen, Emanuele Castorina, and Martin White. "Biased tracers of two fluids in the Lagrangian picture". In: *JCAP* 2019.6, 006 (June 2019), p. 006. DOI: 10.1088/1475-7516/2019/06/006. arXiv: 1903.00437 [astro-ph.CO].

[72] Shi-Fan Chen, Zvonimir Vlah, and Martin White. "A new analysis of galaxy 2-point functions in the BOSS survey, including full-shape information and post-reconstruction BAO". In: *JCAP* 2022.2, 008 (Feb. 2022), p. 008. DOI: 10.1088/1475-7516/2022/02/008. arXiv: 2110.05530 [astro-ph.CO].

[73] Shi-Fan Chen, Zvonimir Vlah, and Martin White. "A new analysis of galaxy 2-point functions in the BOSS survey, including full-shape information and post-reconstruction BAO". In: *JCAP* 2022.2, 008 (Feb. 2022), p. 008. DOI: 10.1088/1475-7516/2022/02/008. arXiv: 2110.05530 [astro-ph.CO].

[74] Shi-Fan Chen, Zvonimir Vlah, and Martin White. "Consistent modeling of velocity statistics and redshift-space distortions in one-loop perturbation theory". In: *JCAP* 2020.7, 062 (July 2020), p. 062. DOI: 10.1088/1475-7516/2020/07/062. arXiv: 2005.00523 [astro-ph.CO].

[75] Shi-Fan Chen, Zvonimir Vlah, and Martin White. "Consistent modeling of velocity statistics and redshift-space distortions in one-loop perturbation theory". In: *JCAP* 2020.7, 062 (July 2020), p. 062. DOI: 10.1088/1475-7516/2020/07/062. arXiv: 2005.00523 [astro-ph.CO].

[76] Shi-Fan Chen, Zvonimir Vlah, and Martin White. "Modeling features in the redshift-space halo power spectrum with perturbation theory". In: *JCAP* 2020.11, 035 (Nov. 2020), p. 035. DOI: 10.1088/1475-7516/2020/11/035. arXiv: 2007.00704 [astro-ph.CO].

[77] Shi-Fan Chen, Zvonimir Vlah, and Martin White. "Modeling features in the redshift-space halo power spectrum with perturbation theory". In: *JCAP* 2020.11, 035 (Nov. 2020), p. 035. DOI: 10.1088/1475-7516/2020/11/035. arXiv: 2007.00704 [astro-ph.CO].

[78] Shi-Fan Chen, Zvonimir Vlah, and Martin White. "The reconstructed power spectrum in the Zeldovich approximation". In: *JCAP* 2019.9, 017 (Sept. 2019), p. 017. DOI: 10.1088/1475-7516/2019/09/017. arXiv: 1907.00043 [astro-ph.CO].

[79] Shi-Fan Chen, Zvonimir Vlah, and Martin White. "The reconstructed power spectrum in the Zeldovich approximation". In: *JCAP* 2019.9, 017 (Sept. 2019), p. 017. DOI: 10.1088/1475-7516/2019/09/017. arXiv: 1907.00043 [astro-ph.CO].

[80] Shi-Fan Chen et al. "Cosmological Analysis of Three-Dimensional BOSS Galaxy Clustering and Planck CMB Lensing Cross Correlations via Lagrangian Perturbation Theory". In: *arXiv e-prints*, arXiv:2204.10392 (Apr. 2022), arXiv:2204.10392. arXiv: 2204.10392 [astro-ph.CO].

[81] Shi-Fan Chen et al. "Redshift-space distortions in Lagrangian perturbation theory". In: *JCAP* 2021.3, 100 (Mar. 2021), p. 100. DOI: 10.1088/1475-7516/2021/03/100. arXiv: 2012.04636 [astro-ph.CO].

[82] Shi-Fan Chen et al. "Redshift-space distortions in Lagrangian perturbation theory". In: *JCAP* 2021.3, 100 (Mar. 2021), p. 100. DOI: 10.1088/1475-7516/2021/03/100. arXiv: 2012.04636 [astro-ph.CO].

[83] Nora Elisa Chisari and Andrew Pontzen. "Unequal time correlators and the Zel'dovich approximation". In: *Phys. Rev. D* 100.2, 023543 (July 2019), p. 023543. DOI: 10.1103/PhysRevD.100.023543. arXiv: 1905.02078 [astro-ph.CO].

[84] Jens Chluba, Jan Hamann, and Subodh P. Patil. "Features and new physical scales in primordial observables: Theory and observation". In: *International Journal of Modern Physics D* 24.10, 1530023 (June 2015), p. 1530023. DOI: 10.1142/S0218271815300232. arXiv: 1505.01834 [astro-ph.CO].

[85] Anton Chudaykin and Mikhail M. Ivanov. "Measuring neutrino masses with large-scale structure: Euclid forecast with controlled theoretical error". In: *JCAP* 2019.11, 034 (Nov. 2019), p. 034. DOI: 10.1088/1475-7516/2019/11/034. arXiv: 1907.06666 [astro-ph.CO].

[86] Anton Chudaykin et al. "Nonlinear perturbation theory extension of the Boltzmann code CLASS". In: *Phys. Rev. D* 102.6, 063533 (Sept. 2020), p. 063533. DOI: 10.1103/PhysRevD.102.063533. arXiv: 2004.10607 [astro-ph.CO].

[87] J. D. Cohn et al. "Combining galaxy and 21-cm surveys". In: *MNRAS* 457.2 (Apr. 2016), pp. 2068–2077. DOI: 10.1093/mnras/stw108. arXiv: 1511.07377 [astro-ph.CO].

[88] Thomas Colas et al. "Efficient cosmological analysis of the SDSS/BOSS data from the Effective Field Theory of Large-Scale Structure". In: *JCAP* 2020.6, 001 (June 2020), p. 001. DOI: 10.1088/1475-7516/2020/06/001. arXiv: 1909.07951 [astro-ph.CO].

[89] Asantha Cooray and Ravi Sheth. "Halo models of large scale structure". In: *Phys. Rep.* 372.1 (Dec. 2002), pp. 1–129. DOI: 10.1016/S0370-1573(02)00276-4. arXiv: astro-ph/0206508 [astro-ph].

[90] Cosmic Visions 21 cm Collaboration et al. "Inflation and Early Dark Energy with a Stage II Hydrogen Intensity Mapping Experiment". In: *arXiv e-prints*, arXiv:1810.09572 (Oct. 2018), arXiv:1810.09572. arXiv: 1810.09572 [astro-ph.CO].

[91] Paolo Creminelli et al. "Single-field consistency relations of large scale structure". In: *JCAP* 2013.12, 025 (Dec. 2013), p. 025. DOI: 10.1088/1475-7516/2013/12/025. arXiv: 1309.3557 [astro-ph.CO].

[92] Martın Crocce and Román Scoccimarro. "Nonlinear evolution of baryon acoustic oscillations". In: *Phys. Rev. D* 77.2, 023533 (Jan. 2008), p. 023533. DOI: 10.1103/PhysRevD.77.023533. arXiv: 0704.2783 [astro-ph].

[93] Carolina Cuesta-Lazaro et al. "Towards a non-Gaussian model of redshift space distortions". In: *MNRAS* 498.1 (Oct. 2020), pp. 1175–1193. DOI: 10.1093/mnras/staa2249. arXiv: 2002.02683 [astro-ph.CO].

[94] Guido D'Amico, Leonardo Senatore, and Pierre Zhang. "Limits on wCDM from the EFTofLSS with the PyBird code". In: *JCAP* 2021.1, 006 (Jan. 2021), p. 006. DOI: 10.1088/1475-7516/2021/01/006. arXiv: 2003.07956 [astro-ph.CO].

[95] Guido D'Amico et al. "The Hubble tension in light of the Full-Shape analysis of Large-Scale Structure data". In: *JCAP* 2021.5, 072 (May 2021), p. 072. DOI: 10.1088/1475-7516/2021/05/072. arXiv: 2006.12420 [astro-ph.CO].

[96] Guido d'Amico et al. "The cosmological analysis of the SDSS/BOSS data from the Effective Field Theory of Large-Scale Structure". In: *JCAP* 2020.5, 005 (May 2020), p. 005. DOI: 10.1088/1475-7516/2020/05/005. arXiv: 1909.05271 [astro-ph.CO].

[97] Biwei Dai et al. "High mass and halo resolution from fast low resolution simulations". In: *JCAP* 2020.4, 002 (Apr. 2020), p. 002. DOI: 10.1088/1475-7516/2020/04/002. arXiv: 1908.05276 [astro-ph.CO].

[98] Neal Dalal, Ue-Li Pen, and Uroš Seljak. "Large-scale BAO signatures of the smallest galaxies". In: *JCAP* 2010.11, 007 (Nov. 2010), p. 007. DOI: 10.1088/1475-7516/2010/11/007. arXiv: 1009.4704 [astro-ph.CO].

[99] Neal Dalal et al. "Halo Assembly Bias in Hierarchical Structure Formation". In: *ApJ* 687.1 (Nov. 2008), pp. 12–21. DOI: 10.1086/591512. arXiv: 0803.3453 [astro-ph].

[100] Omar Darwish et al. "The Atacama Cosmology Telescope: a CMB lensing mass map over 2100 square degrees of sky and its cross-correlation with BOSS-CMASS galaxies". In: *MNRAS* 500.2 (Jan. 2021), pp. 2250–2263. DOI: 10.1093/mnras/staa3438. arXiv: 2004.01139 [astro-ph.CO].

[101] Kyle S. Dawson et al. "The Baryon Oscillation Spectroscopic Survey of SDSS-III". In: *AJ* 145.1, 10 (Jan. 2013), p. 10. DOI: 10.1088/0004-6256/145/1/10. arXiv: 1208.0022 [astro-ph.CO].

[102] Arnaud de Mattia et al. "The completed SDSS-IV extended Baryon Oscillation Spectroscopic Survey: measurement of the BAO and growth rate of structure of the emission line galaxy sample from the anisotropic power spectrum between redshift 0.6 and 1.1". In: *MNRAS* 501.4 (Mar. 2021), pp. 5616–5645. DOI: 10.1093/mnras/staa3891. arXiv: 2007.09008 [astro-ph.CO].

[103] J. DeRose et al. "Dark Energy Survey Year 3 results: cosmology from combined galaxy clustering and lensing – validation on cosmological simulations". In: *arXiv e-prints*, arXiv:2105.13547 (May 2021), arXiv:2105.13547. arXiv: 2105.13547 [astro-ph.CO].

[104] Joseph DeRose, Matthew R. Becker, and Risa H. Wechsler. "Modeling Redshift-Space Clustering with Abundance Matching". In: *arXiv e-prints*, arXiv:2105.12104 (May 2021), arXiv:2105.12104. arXiv: 2105.12104 [astro-ph.CO].

[105] Joseph DeRose et al. "Neural network acceleration of large-scale structure theory calculations". In: *JCAP* 2022.4, 056 (Apr. 2022), p. 056. DOI: 10.1088/1475-7516/2022/04/056. arXiv: 2112.05889 [astro-ph.CO].

[106] Joseph DeRose et al. "The AEMULUS Project. I. Numerical Simulations for Precision Cosmology". In: *ApJ* 875.1, 69 (Apr. 2019), p. 69. DOI: 10.3847/1538-4357/ab1085. arXiv: 1804.05865 [astro-ph.CO].

[107] Joseph DeRose et al. "The Buzzard Flock: Dark Energy Survey Synthetic Sky Catalogs". In: *arXiv e-prints*, arXiv:1901.02401 (Jan. 2019), arXiv:1901.02401. arXiv: 1901.02401 [astro-ph.CO].

[108] DESI Collaboration et al. "The DESI Experiment Part I: Science,Targeting, and Survey Design". In: *arXiv e-prints*, arXiv:1611.00036 (Oct. 2016), arXiv:1611.00036. arXiv: 1611.00036 [astro-ph.IM].

[109] Vincent Desjacques, Donghui Jeong, and Fabian Schmidt. "Large-scale galaxy bias". In: *Phys. Rep.* 733 (Feb. 2018), pp. 1–193. DOI: 10.1016/j.physrep.2017.12.002. arXiv: 1611.09787 [astro-ph.CO].

[110] Vincent Desjacques, Donghui Jeong, and Fabian Schmidt. "The galaxy power spectrum and bispectrum in redshift space". In: *JCAP* 2018.12, 035 (Dec. 2018), p. 035. DOI: 10.1088/1475-7516/2018/12/035. arXiv: 1806.04015 [astro-ph.CO].

[111] Vincent Desjacques et al. "Modeling scale-dependent bias on the baryonic acoustic scale with the statistics of peaks of Gaussian random fields". In: *Phys. Rev. D* 82.10, 103529 (Nov. 2010), p. 103529. DOI: 10.1103/PhysRevD.82.103529. arXiv: 1009.3449 [astro-ph.CO].

[112] Zhejie Ding et al. "Theoretical systematics of Future Baryon Acoustic Oscillation Surveys". In: *MNRAS* 479.1 (Sept. 2018), pp. 1021–1054. DOI: 10.1093/mnras/sty1413. arXiv: 1708.01297 [astro-ph.CO].

[113] Scott Dodelson. "Coherent Phase Argument for Inflation". In: *Neutrinos, Flavor Physics, and Precision Cosmology*. Ed. by José F. Nieves and Raymond R. Volkas. Vol. 689. American Institute of Physics Conference Series. Oct. 2003, pp. 184–196. DOI: 10.1063/1.1627736. arXiv: hep-ph/0309057 [hep-ph].

[114] Scott Dodelson and Fabian Schmidt. *Modern Cosmology*. 2020.

[115] Yaniv Donath and Leonardo Senatore. "Biased Tracers in Redshift Space in the EFTofLSS with exact time dependence". In: *JCAP* 10 (2020), p. 039. DOI: 10.1088/1475-7516/2020/10/039. arXiv: 2005.04805 [astro-ph.CO].

[116] Olivier Doré et al. "Cosmology with the SPHEREX All-Sky Spectral Survey". In: *arXiv e-prints*, arXiv:1412.4872 (Dec. 2014), arXiv:1412.4872. arXiv: 1412.4872 [astro-ph.CO].

[117] Olivier Doré et al. "WFIRST Science Investigation Team "Cosmology with the High Latitude Survey" Annual Report 2017". In: *arXiv e-prints*, arXiv:1804.03628 (Apr. 2018), arXiv:1804.03628. arXiv: 1804.03628 [astro-ph.CO].

[118] C. Doux et al. "Dark Energy Survey Year 3 results: cosmological constraints from the analysis of cosmic shear in harmonic space". In: *arXiv e-prints*, arXiv:2203.07128 (Mar. 2022), arXiv:2203.07128. arXiv: 2203.07128 [astro-ph.CO].

[119] Cyrille Doux et al. "Cosmological constraints from a joint analysis of cosmic microwave background and spectroscopic tracers of the large-scale structure". In: *MNRAS* 480.4 (Nov. 2018), pp. 5386–5411. DOI: 10.1093/mnras/sty2160. arXiv: 1706.04583 [astro-ph.CO].

[120] Daniel J. Eisenstein and Wayne Hu. "Baryonic Features in the Matter Transfer Function". In: *ApJ* 496.2 (Mar. 1998), pp. 605–614. DOI: 10.1086/305424. arXiv: astro-ph/9709112 [astro-ph].

[121] Daniel J. Eisenstein, Hee-Jong Seo, and Martin White. "On the Robustness of the Acoustic Scale in the Low-Redshift Clustering of Matter". In: *ApJ* 664.2 (Aug. 2007), pp. 660–674. DOI: 10.1086/518755. arXiv: astro-ph/0604361 [astro-ph].

[122] Daniel J. Eisenstein et al. "Improving Cosmological Distance Measurements by Reconstruction of the Baryon Acoustic Peak". In: *ApJ* 664.2 (Aug. 2007), pp. 675–679. DOI: 10.1086/518712. arXiv: astro-ph/0604362 [astro-ph].

[123] Daniel J. Eisenstein et al. "SDSS-III: Massive Spectroscopic Surveys of the Distant Universe, the Milky Way, and Extra-Solar Planetary Systems". In: *AJ* 142.3, 72 (Sept. 2011), p. 72. DOI: 10.1088/0004-6256/142/3/72. arXiv: 1101.1529 [astro-ph.IM].

[124] Willem Elbers et al. "Higher-order initial conditions with massive neutrinos". In: *arXiv e-prints*, arXiv:2202.00670 (Feb. 2022), arXiv:2202.00670. arXiv: 2202.00670 [astro-ph.CO].

[125] Richard Ellis and Kyle Dawson. "SpecTel: A 10-12 meter class Spectroscopic Survey Telescope". In: *Bulletin of the American Astronomical Society*. Vol. 51. Sept. 2019, 45, p. 45. arXiv: 1907.06797 [astro-ph.IM].

[126] Euclid Collaboration et al. "Euclid preparation: II. The EUCLIDEMULATOR - a tool to compute the cosmology dependence of the nonlinear matter power spectrum". In: *MNRAS* 484.4 (Apr. 2019), pp. 5509–5529. DOI: 10.1093/mnras/stz197. arXiv: 1809.04695 [astro-ph.CO].

[127] Xiao Fang et al. "FAST-PT II: an algorithm to calculate convolution integrals of general tensor quantities in cosmological perturbation theory". In: *JCAP* 2017.2, 030 (Feb. 2017), p. 030. DOI: 10.1088/1475-7516/2017/02/030. arXiv: 1609.05978 [astro-ph.CO].

[128] Matteo Fasiello and Zvonimir Vlah. "Nonlinear fields in generalized cosmologies". In: *Phys. Rev. D* 94.6, 063516 (Sept. 2016), p. 063516. DOI: 10.1103/PhysRevD.94.063516. arXiv: 1604.04612 [astro-ph.CO].

[129] G. Favole et al. "[O II] emitters in MultiDark-Galaxies and DEEP2". In: *MNRAS* 497.4 (Oct. 2020), pp. 5432–5453. DOI: 10.1093/mnras/staa2292. arXiv: 1908.05626 [astro-ph.GA].

[130] Ginevra Favole et al. "Galaxy clustering dependence on the [O II] emission line luminosity in the local Universe". In: *MNRAS* 472.1 (Nov. 2017), pp. 550–558. DOI: 10.1093/mnras/stx1980. arXiv: 1611.05457 [astro-ph.GA].

[131] Hume A. Feldman, Nick Kaiser, and John A. Peacock. "Power-Spectrum Analysis of Three-dimensional Redshift Surveys". In: *ApJ* 426 (May 1994), p. 23. DOI: 10.1086/174036. arXiv: astro-ph/9304022 [astro-ph].

[132] Yu Feng, Uroš Seljak, and Matias Zaldarriaga. "Exploring the posterior surface of the large scale structure reconstruction". In: *JCAP* 2018.7, 043 (July 2018), p. 043. DOI: 10.1088/1475-7516/2018/07/043. arXiv: 1804.09687 [astro-ph.CO].

[133] Yu Feng et al. "FASTPM: a new scheme for fast simulations of dark matter and haloes". In: *MNRAS* 463.3 (Dec. 2016), pp. 2273–2286. DOI: 10.1093/mnras/stw2123. arXiv: 1603.00476 [astro-ph.CO].

[134] Yu Feng et al. *FastPM: Scaling N-body Particle Mesh solver*. Astrophysics Source Code Library, record ascl:1905.010. May 2019. ascl: 1905.010.

[135] Simone Ferraro and Michael J. Wilson. "Inflation and Dark Energy from spectroscopy at z ¿ 2". In: 51.3, 72 (May 2019), p. 72. arXiv: 1903.09208 [astro-ph.CO].

[136] Christian Fidler, Nils Sujata, and Maria Archidiacono. "Relativistic bias in neutrino cosmologies". In: *JCAP* 06 (2019), p. 035. DOI: 10.1088/1475-7516/2019/06/035. arXiv: 1812.09266 [astro-ph.CO].

[137] Karl B. Fisher. "On the Validity of the Streaming Model for the Redshift-Space Correlation Function in the Linear Regime". In: *ApJ* 448 (Aug. 1995), p. 494. DOI: 10.1086/175980. arXiv: astro-ph/9412081 [astro-ph].

[138] Lucıa Fonseca de la Bella et al. "Impact of bias and redshift-space modelling for the halo power spectrum: testing the effective field theory of large-scale structure". In: *JCAP* 2020.7, 011 (July 2020), p. 011. DOI: 10.1088/1475-7516/2020/07/011. arXiv: 1805.12394 [astro-ph.CO].

[139] Tomohiro Fujita and Zvonimir Vlah. "Perturbative description of biased tracers using consistency relations of LSS". In: *JCAP* 10 (2020), p. 059. DOI: 10.1088/1475-7516/2020/10/059. arXiv: 2003.10114 [astro-ph.CO].

[140] Tomohiro Fujita et al. "Very massive tracers and higher derivative biases". In: *JCAP* 2020.1, 009 (Jan. 2020), p. 009. DOI: 10.1088/1475-7516/2020/01/009. arXiv: 1609.00717 [astro-ph.CO].

[141] Nicholas Galitzki et al. "The Simons Observatory: instrument overview". In: *Millimeter, Submillimeter, and Far-Infrared Detectors and Instrumentation for Astronomy IX*. Ed. by Jonas Zmuidzinas and Jian-Rong Gao. Vol. 10708. Society of Photo-Optical Instrumentation Engineers (SPIE) Conference Series. July 2018, 1070804, p. 1070804. DOI: 10.1117/12.2312985. arXiv: 1808.04493 [astro-ph.IM].

[142] Jorge Enrique Garcıa-Farieta et al. "Validating the methodology for constraining the linear growth rate from clustering anisotropies". In: *MNRAS* 494.2 (May 2020), pp. 1658–1674. DOI: 10.1093/mnras/staa791. arXiv: 1909.08016 [astro-ph.CO].

[143] Carlos Garcıa-Garcıa et al. "The growth of density perturbations in the last 10 billion years from tomographic large-scale structure data". In: *JCAP* 2021.10, 030 (Oct. 2021), p. 030. DOI: 10.1088/1475-7516/2021/10/030. arXiv: 2105.12108 [astro-ph.CO].

[144] Lehman H. Garrison et al. "The Abacus Cosmos: A Suite of Cosmological N-body Simulations". In: *ApJS* 236.2, 43 (June 2018), p. 43. DOI: 10.3847/1538-4365/aabfd3. arXiv: 1712.05768 [astro-ph.CO].

[145] Elena Giusarma et al. "Scale-dependent galaxy bias, CMB lensing-galaxy cross-correlation, and neutrino masses". In: *Phys. Rev. D* 98.12, 123526 (Dec. 2018), p. 123526. DOI: 10.1103/PhysRevD.98.123526. arXiv: 1802.08694 [astro-ph.CO].

[146] Jahmour J. Givans and Christopher M. Hirata. "Redshift-space streaming velocity effects on the Lyman-α forest baryon acoustic oscillation scale". In: *Phys. Rev. D* 102.2, 023515 (July 2020), p. 023515. DOI: 10.1103/PhysRevD.102.023515. arXiv: 2002.12296 [astro-ph.CO].

[147] Satya Gontcho A Gontcho, Jordi Miralda-Escudé, and Nicolás G. Busca. "On the effect of the ionizing background on the Lyα forest autocorrelation function". In: *MNRAS* 442.1 (July 2014), pp. 187–195. DOI: 10.1093/mnras/stu860. arXiv: 1404.7425 [astro-ph.CO].

[148] M. H. Goroff et al. "Coupling of modes of cosmological mass density fluctuations". In: *ApJ* 311 (Dec. 1986), pp. 6–14. DOI: 10.1086/164749.

[149] K. M. Górski et al. "HEALPix: A Framework for High-Resolution Discretization and Fast Analysis of Data Distributed on the Sphere". In: *ApJ* 622.2 (Apr. 2005), pp. 759–771. DOI: 10.1086/427976. arXiv: astro-ph/0409513 [astro-ph].

[150] R. Graziani et al. "Peculiar velocity cosmology with type Ia supernovae". In: *arXiv e-prints*, arXiv:2001.09095 (Jan. 2020), arXiv:2001.09095. arXiv: 2001.09095 [astro-ph.CO].

[151] Jan Niklas Grieb et al. "The clustering of galaxies in the completed SDSS-III Baryon Oscillation Spectroscopic Survey: Cosmological implications of the Fourier space wedges of the final sample". In: *MNRAS* 467.2 (May 2017), pp. 2085–2112. DOI: 10.1093/mnras/stw3384. arXiv: 1607.03143 [astro-ph.CO].

[152] Cameron Grove et al. "The DESI N-body Simulation Project I: Testing the Robustness of Simulations for the DESI Dark Time Survey". In: *arXiv e-prints*, arXiv:2112.09138 (Dec. 2021), arXiv:2112.09138. arXiv: 2112.09138 [astro-ph.CO].

[153] L. Guzzo et al. "A test of the nature of cosmic acceleration using galaxy redshift distortions". In: *Nature* 451 (2008), pp. 541–545. DOI: 10.1038/nature06555. arXiv: 0802.1944 [astro-ph].

[154] Salman Habib et al. "HACC: Simulating sky surveys on state-of-the-art supercomputing architectures". In: 42 (Jan. 2016), pp. 49–65. DOI: 10.1016/j.newast.2015.06.003. arXiv: 1410.2805 [astro-ph.IM].

[155] Ryuichiro Hada and Daniel J. Eisenstein. "An iterative reconstruction of cosmological initial density fields". In: *MNRAS* 478.2 (Aug. 2018), pp. 1866–1874. DOI: 10.1093/mnras/sty1203. arXiv: 1804.04738 [astro-ph.CO].

[156] Boryana Hadzhiyska et al. "Hefty enhancement of cosmological constraints from the DES Y1 data using a hybrid effective field theory approach to galaxy bias". In: *JCAP* 2021.9, 020 (Sept. 2021), p. 020. DOI: 10.1088/1475-7516/2021/09/020. arXiv: 2103.09820 [astro-ph.CO].

[157] Oliver Hahn et al. *MUSIC2-monofonIC: 3LPT initial condition generator*. Astrophysics Source Code Library, record ascl:2008.024. Aug. 2020. ascl: 2008.024.

[158] A. J. S. Hamilton. "Measuring Omega and the Real Correlation Function from the Redshift Correlation Function". In: *ApJL* 385 (Jan. 1992), p. L5. DOI: 10.1086/186264.

[159] A. J. S. Hamilton. "Uncorrelated modes of the non-linear power spectrum". In: *MNRAS* 312.2 (Feb. 2000), pp. 257–284. DOI: 10.1046/j.1365-8711.2000.03071.x. arXiv: astro-ph/9905191 [astro-ph].

[160] A. J. S. Hamilton et al. "Reconstructing the Primordial Spectrum of Fluctuations of the Universe from the Observed Nonlinear Clustering of Galaxies". In: *ApJL* 374 (June 1991), p. L1. DOI: 10.1086/186057.

[161] Nick Hand et al. "An optimal FFT-based anisotropic power spectrum estimator". In: *JCAP* 2017.7, 002 (July 2017), p. 002. DOI: 10.1088/1475-7516/2017/07/002. arXiv: 1704.02357 [astro-ph.CO].

[162] Nick Hand et al. "Extending the modeling of the anisotropic galaxy power spectrum to k = 0.4 hMpc^{-1}". In: *JCAP* 2017.10, 009 (Oct. 2017), p. 009. DOI: 10.1088/1475-7516/2017/10/009. arXiv: 1706.02362 [astro-ph.CO].

[163] Nick Hand et al. "nbodykit: An Open-source, Massively Parallel Toolkit for Large-scale Structure". In: *AJ* 156.4, 160 (Oct. 2018), p. 160. DOI: 10.3847/1538-3881/aadae0. arXiv: 1712.05834 [astro-ph.IM].

[164] J. Hartlap, P. Simon, and P. Schneider. "Why your model parameter confidences might be too optimistic. Unbiased estimation of the inverse covariance matrix". In: *A&A* 464.1 (Mar. 2007), pp. 399–404. DOI: 10.1051/0004-6361:20066170. arXiv: astro-ph/0608064 [astro-ph].

[165] Katrin Heitmann et al. "The cosmic code comparison project". In: *Computational Science and Discovery* 1.1, 015003 (Oct. 2008), p. 015003. DOI: 10.1088/1749-4699/1/1/015003. arXiv: 0706.1270 [astro-ph].

[166] Katrin Heitmann et al. "The Coyote Universe. I. Precision Determination of the Nonlinear Matter Power Spectrum". In: *ApJ* 715.1 (May 2010), pp. 104–121. DOI: 10.1088/0004-637X/715/1/104. arXiv: 0812.1052 [astro-ph].

[167] Katrin Heitmann et al. "The Coyote Universe. II. Cosmological Models and Precision Emulation of the Nonlinear Matter Power Spectrum". In: *ApJ* 705.1 (Nov. 2009), pp. 156–174. DOI: 10.1088/0004-637X/705/1/156. arXiv: 0902.0429 [astro-ph.CO].

[168] Catherine Heymans et al. "CFHTLenS tomographic weak lensing cosmological parameter constraints: Mitigating the impact of intrinsic galaxy alignments". In: *Mon. Not. Roy. Astron. Soc.* 432 (2013), p. 2433. DOI: 10.1093/mnras/stt601. arXiv: 1303.1808 [astro-ph.CO].

[169] Catherine Heymans et al. "KiDS-1000 Cosmology: Multi-probe weak gravitational lensing and spectroscopic galaxy clustering constraints". In: *A&A* 646, A140 (Feb. 2021), A140. DOI: 10.1051/0004-6361/202039063. arXiv: 2007.15632 [astro-ph.CO].

[170] Chiaki Hikage et al. "Cosmology from cosmic shear power spectra with Subaru Hyper Suprime-Cam first-year data". In: *Publ. Astron. Soc. Jap.* 71.2 (2019), p. 43. DOI: 10.1093/pasj/psz010. arXiv: 1809.09148 [astro-ph.CO].

[171] Chiaki Hikage, Kazuya Koyama, and Alan Heavens. "Perturbation theory for BAO reconstructed fields: One-loop results in the real-space matter density field". In: *Phys. Rev. D* 96.4, 043513 (Aug. 2017), p. 043513. DOI: 10.1103/PhysRevD.96.043513. arXiv: 1703.07878 [astro-ph.CO].

[172] Chiaki Hikage, Kazuya Koyama, and Ryuichi Takahashi. "Perturbation theory for the redshift-space matter power spectra after reconstruction". In: *Phys. Rev. D* 101.4, 043510 (Feb. 2020), p. 043510. DOI: 10.1103/PhysRevD.101.043510. arXiv: 1911.06461 [astro-ph.CO].

[173] G. J. Hill et al. "The Hobby-Eberly Telescope Dark Energy Experiment (HETDEX): Description and Early Pilot Survey Results". In: *Panoramic Views of Galaxy Formation and Evolution*. Ed. by T. Kodama, T. Yamada, and K. Aoki. Vol. 399. Astronomical Society of the Pacific Conference Series. Oct. 2008, p. 115. arXiv: 0806.0183 [astro-ph].

[174] J. Colin Hill et al. "Early dark energy does not restore cosmological concordance". In: *Phys. Rev. D* 102.4, 043507 (Aug. 2020), p. 043507. DOI: 10.1103/PhysRevD.102.043507. arXiv: 2003.07355 [astro-ph.CO].

[175] G. Hinshaw et al. "Nine-year Wilkinson Microwave Anisotropy Probe (WMAP) Observations: Cosmological Parameter Results". In: *ApJS* 208.2, 19 (Oct. 2013), p. 19. DOI: 10.1088/0067-0049/208/2/19. arXiv: 1212.5226 [astro-ph.CO].

[176] Christopher M. Hirata. "Tidal alignments as a contaminant of redshift space distortions". In: *MNRAS* 399.2 (Oct. 2009), pp. 1074–1087. DOI: 10.1111/j.1365-2966.2009.15353.x. arXiv: 0903.4929 [astro-ph.CO].

[177] E. Hivon et al. "Redshift distortions of clustering: a Lagrangian approach." In: *A&A* 298 (June 1995), p. 643. arXiv: astro-ph/9407049 [astro-ph].

[178] Eric Hivon et al. "MASTER of the Cosmic Microwave Background Anisotropy Power Spectrum: A Fast Method for Statistical Analysis of Large and Complex Cosmic Microwave Background Data Sets". In: *ApJ* 567.1 (Mar. 2002), pp. 2–17. DOI: 10.1086/338126. arXiv: astro-ph/0105302 [astro-ph].

[179] Bart Horn, Lam Hui, and Xiao Xiao. "Lagrangian space consistency relation for large scale structure". In: *JCAP* 2015.9, 068 (Sept. 2015), p. 068. DOI: 10.1088/1475-7516/2015/09/068. arXiv: 1502.06980 [hep-th].

[180] Bart Horn, Lam Hui, and Xiao Xiao. "Soft-Pion theorems for large scale structure". In: *JCAP* 2014.9, 044 (Sept. 2014), p. 044. DOI: 10.1088/1475-7516/2014/09/044. arXiv: 1406.0842 [hep-th].

[181] B. Horowitz and U. Seljak. "Cosmological constraints from thermal Sunyaev-Zeldovich power spectrum revisited". In: *MNRAS* 469.1 (July 2017), pp. 394–400. DOI: 10.1093/mnras/stx766. arXiv: 1609.01850 [astro-ph.CO].

[182] Cullan Howlett, Lister Staveley-Smith, and Chris Blake. "Cosmological forecasts for combined and next-generation peculiar velocity surveys". In: *MNRAS* 464.3 (Jan. 2017), pp. 2517–2544. DOI: 10.1093/mnras/stw2466. arXiv: 1609.08247 [astro-ph.CO].

[183] Wayne Hu and Martin White. "A New Test of Inflation". In: *Phys. Rev. Lett.* 77.9 (Aug. 1996), pp. 1687–1690. DOI: 10.1103/PhysRevLett.77.1687. arXiv: astro-ph/9602020 [astro-ph].

[184] Mikhail M. Ivanov. "Cosmological constraints from the power spectrum of eBOSS emission line galaxies". In: (June 2021). arXiv: 2106.12580 [astro-ph.CO].

[185] Mikhail M. Ivanov and Sergey Sibiryakov. "Infrared resummation for biased tracers in redshift space". In: *JCAP* 2018.7, 053 (July 2018), p. 053. DOI: 10.1088/1475-7516/2018/07/053. arXiv: 1804.05080 [astro-ph.CO].

[186] Mikhail M. Ivanov, Marko Simonović, and Matias Zaldarriaga. "Cosmological parameters from the BOSS galaxy power spectrum". In: *JCAP* 2020.5, 042 (May 2020), p. 042. DOI: 10.1088/1475-7516/2020/05/042. arXiv: 1909.05277 [astro-ph.CO].

[187] Mikhail M. Ivanov et al. "Constraining early dark energy with large-scale structure". In: *Phys. Rev. D* 102.10, 103502 (Nov. 2020), p. 103502. DOI: 10.1103/PhysRevD.102.103502. arXiv: 2006.11235 [astro-ph.CO].

[188] Mikhail M. Ivanov et al. "Cosmological constraints without nonlinear redshift-space distortions". In: *Phys. Rev. D* 105.4, 043531 (Feb. 2022), p. 043531. DOI: 10.1103/PhysRevD.105.043531. arXiv: 2110.00006 [astro-ph.CO].

[189] Mikhail M. Ivanov et al. "Precision analysis of the redshift-space galaxy bispectrum". In: *Phys. Rev. D* 105.6, 063512 (Mar. 2022), p. 063512. DOI: 10.1103/PhysRevD.105.063512. arXiv: 2110.10161 [astro-ph.CO].

[190] J. C. Jackson. "A critique of Rees's theory of primordial gravitational radiation". In: *MNRAS* 156 (Jan. 1972), 1P. DOI: 10.1093/mnras/156.1.1P. arXiv: 0810.3908 [astro-ph].

[191] Bhuvnesh Jain and Edmund Bertschinger. "Second-Order Power Spectrum and Nonlinear Evolution at High Redshift". In: *ApJ* 431 (Aug. 1994), p. 495. DOI: 10.1086/174502. arXiv: astro-ph/9311070 [astro-ph].

[192] Bhuvnesh Jain and Justin Khoury. "Cosmological tests of gravity". In: *Annals of Physics* 325.7 (July 2010), pp. 1479–1516. DOI: 10.1016/j.aop.2010.04.002. arXiv: 1004.3294 [astro-ph.CO].

[193] Austin Joyce, Lucas Lombriser, and Fabian Schmidt. "Dark Energy Versus Modified Gravity". In: *Annual Review of Nuclear and Particle Science* 66.1 (Oct. 2016), pp. 95–122. DOI: 10.1146/annurev-nucl-102115-044553. arXiv: 1601.06133 [astro-ph.CO].

[194] Austin Joyce et al. "Beyond the cosmological standard model". In: *Phys. Rep.* 568 (Mar. 2015), pp. 1–98. DOI: 10.1016/j.physrep.2014.12.002. arXiv: 1407.0059 [astro-ph.CO].

[195] R. Juszkiewicz. "On the evolution of cosmological adiabatic perturbations in the weakly non-linear regime". In: *MNRAS* 197 (Dec. 1981), pp. 931–940. DOI: 10.1093/mnras/197.4.931.

[196] Nick Kaiser. "Clustering in real space and in redshift space". In: *MNRAS* 227 (July 1987), pp. 1–21. DOI: 10.1093/mnras/227.1.1.

[197] Eyal A. Kazin et al. "The WiggleZ Dark Energy Survey: improved distance measurements to z = 1 with reconstruction of the baryonic acoustic feature". In: *MNRAS* 441.4 (July 2014), pp. 3524–3542. DOI: 10.1093/mnras/stu778. arXiv: 1401.0358 [astro-ph.CO].

[198] A. Kehagias and A. Riotto. "Symmetries and consistency relations in the large scale structure of the universe". In: *Nuclear Physics B* 873.3 (Aug. 2013), pp. 514–529. DOI: 10.1016/j.nuclphysb.2013.05.009. arXiv: 1302.0130 [astro-ph.CO].

[199] Hasti Khoraminezhad et al. "Quantifying the impact of baryon-CDM perturbations on halo clustering and baryon fraction". In: (Nov. 2020). arXiv: 2011.01037 [astro-ph.CO].

[200] Alex Kim et al. "Testing Gravity Using Type Ia Supernovae Discovered by Next-Generation Wide-Field Imaging Surveys". In: 51.3, 140 (May 2019), p. 140. arXiv: 1903.07652 [astro-ph.CO].

[201] Ellie Kitanidis and Martin White. "Cross-correlation of Planck CMB lensing with DESI-like LRGs". In: *MNRAS* 501.4 (Mar. 2021), pp. 6181–6198. DOI: 10.1093/mnras/staa3927. arXiv: 2010.04698 [astro-ph.CO].

[202] Francisco-Shu Kitaura et al. "The clustering of galaxies in the SDSS-III Baryon Oscillation Spectroscopic Survey: mock galaxy catalogues for the BOSS Final Data Release". In: *MNRAS* 456.4 (Mar. 2016), pp. 4156–4173. DOI: 10.1093/mnras/stv2826. arXiv: 1509.06400 [astro-ph.CO].

[203] Anatoly Klypin et al. "Clustering and halo abundances in early dark energy cosmological models". In: *MNRAS* 504.1 (June 2021), pp. 769–781. DOI: 10.1093/mnras/stab769. arXiv: 2006.14910 [astro-ph.CO].

[204] Yosuke Kobayashi et al. "Full-shape cosmology analysis of the SDSS-III BOSS galaxy power spectrum using an emulator-based halo model: A 5% determination of σ_8". In: *Phys. Rev. D* 105.8, 083517 (Apr. 2022), p. 083517. DOI: 10.1103/PhysRevD.105.083517. arXiv: 2110.06969 [astro-ph.CO].

[205] Nickolas Kokron et al. "Accurate predictions from small boxes: variance suppression via the Zel'dovich approximation". In: *arXiv e-prints*, arXiv:2205.15327 (May 2022), arXiv:2205.15327. arXiv: 2205.15327 [astro-ph.CO].

[206] Nickolas Kokron et al. "Priors on red galaxy stochasticity from hybrid effective field theory". In: *arXiv e-prints*, arXiv:2112.00012 (Nov. 2021), arXiv:2112.00012. arXiv: 2112.00012 [astro-ph.CO].

[207] Nickolas Kokron et al. "The cosmology dependence of galaxy clustering and lensing from a hybrid N-body-perturbation theory model". In: *MNRAS* 505.1 (July 2021), pp. 1422–1440. DOI: 10.1093/mnras/stab1358. arXiv: 2101.11014 [astro-ph.CO].

[208] Alex Krolewski, Simone Ferraro, and Martin White. "Cosmological constraints from unWISE and Planck CMB lensing tomography". In: *JCAP* 2021.12, 028 (Dec. 2021), p. 028. DOI: 10.1088/1475-7516/2021/12/028. arXiv: 2105.03421 [astro-ph.CO].

[209] Alex Krolewski et al. "unWISE tomography of Planck CMB lensing". In: *JCAP* 2020.5, 047 (May 2020), p. 047. DOI: 10.1088/1475-7516/2020/05/047. arXiv: 1909.07412 [astro-ph.CO].

[210] Johannes U. Lange et al. "Five per cent measurements of the growth rate from simulation-based modelling of redshift-space clustering in BOSS LOWZ". In: *MNRAS* 509.2 (Jan. 2022), pp. 1779–1804. DOI: 10.1093/mnras/stab3111. arXiv: 2101.12261 [astro-ph.CO].

[211] R. Laureijs et al. "Euclid Definition Study Report". In: *arXiv e-prints*, arXiv:1110.3193 (Oct. 2011), arXiv:1110.3193. arXiv: 1110.3193 [astro-ph.CO].

[212] Earl Lawrence et al. "The Coyote Universe. III. Simulation Suite and Precision Emulator for the Nonlinear Matter Power Spectrum". In: *ApJ* 713.2 (Apr. 2010), pp. 1322–1331. DOI: 10.1088/0004-637X/713/2/1322. arXiv: 0912.4490 [astro-ph.CO].

[213] Earl Lawrence et al. "The Mira-Titan Universe. II. Matter Power Spectrum Emulation". In: *ApJ* 847.1, 50 (Sept. 2017), p. 50. DOI: 10.3847/1538-4357/aa86a9. arXiv: 1705.03388 [astro-ph.CO].

[214] Titouan Lazeyras, Marcello Musso, and Vincent Desjacques. "Lagrangian bias of generic large-scale structure tracers". In: *Phys. Rev. D* 93.6, 063007 (Mar. 2016), p. 063007. DOI: 10.1103/PhysRevD.93.063007. arXiv: 1512.05283 [astro-ph.CO].

[215] Titouan Lazeyras and Fabian Schmidt. "Beyond LIMD bias: a measurement of the complete set of third-order halo bias parameters". In: *JCAP* 2018.9, 008 (Sept. 2018), p. 008. DOI: 10.1088/1475-7516/2018/09/008. arXiv: 1712.07531 [astro-ph.CO].

[216] Daniel Lenz, Brandon S. Hensley, and Olivier Doré. "A New, Large-scale Map of Interstellar Reddening Derived from H i Emission". In: *Astrophys. J.* 846.1 (2017), p. 38. DOI: 10.3847/1538-4357/aa84af. arXiv: 1706.00011 [astro-ph.GA].

[217] Matthew Lewandowski, Ashley Perko, and Leonardo Senatore. "Analytic prediction of baryonic effects from the EFT of large scale structures". In: *JCAP* 2015.5, 019 (May 2015), p. 019. DOI: 10.1088/1475-7516/2015/05/019. arXiv: 1412.5049 [astro-ph.CO].

[218] Matthew Lewandowski et al. "EFT of large scale structures in redshift space". In: *Phys. Rev. D* 97.6 (2018), p. 063526. DOI: 10.1103/PhysRevD.97.063526. arXiv: 1512.06831 [astro-ph.CO].

[219] Antony Lewis. "GetDist: a Python package for analysing Monte Carlo samples". In: (2019). arXiv: 1910.13970 [astro-ph.IM]. URL: https://getdist.readthedocs.io.

[220] Antony Lewis, Anthony Challinor, and Anthony Lasenby. "Efficient Computation of Cosmic Microwave Background Anisotropies in Closed Friedmann-Robertson-Walker Models". In: *ApJ* 538.2 (Aug. 2000), pp. 473–476. DOI: 10.1086/309179. arXiv: astro-ph/9911177 [astro-ph].

[221] D. Nelson Limber. "The Analysis of Counts of the Extragalactic Nebulae in Terms of a Fluctuating Density Field." In: *ApJ* 117 (Jan. 1953), p. 134. DOI: 10.1086/145672.

[222] Marilena LoVerde. "Halo bias in mixed dark matter cosmologies". In: *Phys. Rev. D* 90.8, 083530 (Oct. 2014), p. 083530. DOI: 10.1103/PhysRevD.90.083530. arXiv: 1405.4855 [astro-ph.CO].

[223] Marilena LoVerde and Niayesh Afshordi. "Extended Limber approximation". In: *Phys. Rev. D* 78.12, 123506 (Dec. 2008), p. 123506. DOI: 10.1103/PhysRevD.78.123506. arXiv: 0809.5112 [astro-ph].

[224] LSST Science Collaboration et al. "LSST Science Book, Version 2.0". In: *arXiv e-prints*, arXiv:0912.0201 (Dec. 2009), arXiv:0912.0201. arXiv: 0912.0201 [astro-ph.IM].

[225] Nobuyoshi Makino, Misao Sasaki, and Yasushi Suto. "Analytic approach to the perturbative expansion of nonlinear gravitational fluctuations in cosmological density and velocity fields". In: *Phys. Rev. D* 46.2 (July 1992), pp. 585–602. DOI: 10.1103/PhysRevD.46.585.

[226] Philip Mansfield and Andrey V. Kravtsov. "The three causes of low-mass assembly bias". In: *MNRAS* 493.4 (Apr. 2020), pp. 4763–4782. DOI: 10.1093/mnras/staa430. arXiv: 1902.00030 [astro-ph.CO].

[227] Daniel Martens et al. "A radial measurement of the galaxy tidal alignment magnitude with BOSS data". In: *MNRAS* 478.1 (July 2018), pp. 711–732. DOI: 10.1093/mnras/sty1100. arXiv: 1802.07708 [astro-ph.CO].

[228] Sabino Matarrese et al. "Redshift evolution of clustering". In: *MNRAS* 286.1 (Mar. 1997), pp. 115–132. DOI: 10.1093/mnras/286.1.115. arXiv: astro-ph/9608004 [astro-ph].

[229] Takahiko Matsubara. "Nonlinear perturbation theory with halo bias and redshift-space distortions via the Lagrangian picture". In: *Phys. Rev. D* 78.8, 083519 (Oct. 2008), p. 083519. DOI: 10.1103/PhysRevD.78.083519. arXiv: 0807.1733 [astro-ph].

[230] Takahiko Matsubara. "Recursive solutions of Lagrangian perturbation theory". In: *Phys. Rev. D* 92.2, 023534 (July 2015), p. 023534. DOI: 10.1103/PhysRevD.92.023534. arXiv: 1505.01481 [astro-ph.CO].

[231] Takahiko Matsubara. "Resumming cosmological perturbations via the Lagrangian picture: One-loop results in real space and in redshift space". In: *Phys. Rev. D* 77.6, 063530 (Mar. 2008), p. 063530. DOI: 10.1103/PhysRevD.77.063530. arXiv: 0711.2521 [astro-ph].

[232] Nuala McCullagh and Alexander S. Szalay. "Nonlinear Behavior of Baryon Acoustic Oscillations from the Zel'dovich Approximation Using a Non-Fourier Perturbation Approach". In: *ApJ* 752.1, 21 (June 2012), p. 21. DOI: 10.1088/0004-637X/752/1/21. arXiv: 1202.1306 [astro-ph.CO].

[233] Patrick McDonald. "Clustering of dark matter tracers: Renormalizing the bias parameters". In: *Phys. Rev. D* 74.10, 103512 (Nov. 2006), p. 103512. DOI: 10.1103/PhysRevD.74.103512. arXiv: astro-ph/0609413 [astro-ph].

[234] Patrick McDonald and Arabindo Roy. "Clustering of dark matter tracers: generalizing bias for the coming era of precision LSS". In: *JCAP* 2009.8, 020 (Aug. 2009), p. 020. DOI: 10.1088/1475-7516/2009/08/020. arXiv: 0902.0991 [astro-ph.CO].

[235] Matthew McQuinn and Martin White. "Cosmological perturbation theory in 1+1 dimensions". In: *JCAP* 2016.1, 043 (Jan. 2016), p. 043. DOI: 10.1088/1475-7516/2016/01/043. arXiv: 1502.07389 [astro-ph.CO].

[236] A. J. Mead et al. "Accurate halo-model matter power spectra with dark energy, massive neutrinos and modified gravitational forces". In: *MNRAS* 459.2 (June 2016), pp. 1468–1488. DOI: 10.1093/mnras/stw681. arXiv: 1602.02154 [astro-ph.CO].

[237] A. J. Mead et al. "An accurate halo model for fitting non-linear cosmological power spectra and baryonic feedback models". In: *MNRAS* 454.2 (Dec. 2015), pp. 1958–1975. DOI: 10.1093/mnras/stv2036. arXiv: 1505.07833 [astro-ph.CO].

[238] A. Meiksin, Martin White, and J. A. Peacock. "Baryonic signatures in large-scale structure". In: *MNRAS* 304.4 (Apr. 1999), pp. 851–864. DOI: 10.1046/j.1365-8711.1999.02369.x. arXiv: astro-ph/9812214 [astro-ph].

[239] Lorenzo Mercolli and Enrico Pajer. "On the velocity in the Effective Field Theory of Large Scale Structures". In: *JCAP* 2014.3, 006 (Mar. 2014), p. 006. DOI: 10.1088/1475-7516/2014/03/006. arXiv: 1307.3220 [astro-ph.CO].

[240] Thiago Mergulhão et al. "The effective field theory of large-scale structure and multi-tracer". In: *JCAP* 2022.4, 021 (Apr. 2022), p. 021. DOI: 10.1088/1475-7516/2022/04/021. arXiv: 2108.11363 [astro-ph.CO].

[241] Mehrdad Mirbabayi, Fabian Schmidt, and Matias Zaldarriaga. "Biased tracers and time evolution". In: *JCAP* 2015.7, 030 (July 2015), p. 030. DOI: 10.1088/1475-7516/2015/07/030. arXiv: 1412.5169 [astro-ph.CO].

[242] Chirag Modi, Emanuele Castorina, and Uroš Seljak. "Halo bias in Lagrangian space: estimators and theoretical predictions". In: *MNRAS* 472.4 (Dec. 2017), pp. 3959–3970. DOI: 10.1093/mnras/stx2148. arXiv: 1612.01621 [astro-ph.CO].

[243] Chirag Modi, Shi-Fan Chen, and Martin White. "Simulations and symmetries". In: *MNRAS* 492.4 (Mar. 2020), pp. 5754–5763. DOI: 10.1093/mnras/staa251. arXiv: 1910.07097 [astro-ph.CO].

[244] Chirag Modi, Shi-Fan Chen, and Martin White. "Simulations and symmetries". In: *MNRAS* 492.4 (Jan. 2020), pp. 5754–5763. DOI: 10.1093/mnras/staa251. URL: https://doi.org/10.1093%2Fmnras%2Fstaa251.

[245] Chirag Modi, Yu Feng, and Uroš Seljak. "Cosmological reconstruction from galaxy light: neural network based light-matter connection". In: *JCAP* 2018.10, 028 (Oct. 2018), p. 028. DOI: 10.1088/1475-7516/2018/10/028. arXiv: 1805.02247 [astro-ph.CO].

[246] Chirag Modi, Martin White, and Zvonimir Vlah. "Modeling CMB lensing cross correlations with CLEFT". In: *JCAP* 2017.8, 009 (Aug. 2017), p. 009. DOI: 10.1088/1475-7516/2017/08/009. arXiv: 1706.03173 [astro-ph.CO].

[247] Chirag Modi et al. "Intensity mapping with neutral hydrogen and the Hidden Valley simulations". In: *JCAP* 2019.9, 024 (Sept. 2019), p. 024. DOI: 10.1088/1475-7516/2019/09/024. arXiv: 1904.11923 [astro-ph.CO].

[248] Chirag Modi et al. "Reconstructing large-scale structure with neutral hydrogen surveys". In: *JCAP* 2019.11, 023 (Nov. 2019), p. 023. DOI: 10.1088/1475-7516/2019/11/023. arXiv: 1907.02330 [astro-ph.CO].

[249] F. G. Mohammad et al. "Group-galaxy correlations in redshift space as a probe of the growth of structure". In: *MNRAS* 458.2 (May 2016), pp. 1948–1963. DOI: 10.1093/mnras/stw411. arXiv: 1502.05045 [astro-ph.CO].

[250] F. Moutarde et al. "Precollapse Scale Invariance in Gravitational Instability". In: *ApJ* 382 (Dec. 1991), p. 377. DOI: 10.1086/170728.

[251] Emiliano Munari et al. "Testing approximate predictions of displacements of cosmological dark matter halos". In: *JCAP* 2017.7, 050 (July 2017), p. 050. DOI: 10.1088/1475-7516/2017/07/050. arXiv: 1704.00920 [astro-ph.CO].

[252] Julian B. Muñoz and Cora Dvorkin. "Efficient computation of galaxy bias with neutrinos and other relics". In: *Phys. Rev. D* 98.4, 043503 (Aug. 2018), p. 043503. DOI: 10.1103/PhysRevD.98.043503. arXiv: 1805.11623 [astro-ph.CO].

[253] Julio F. Navarro, Carlos S. Frenk, and Simon D. M. White. "A Universal Density Profile from Hierarchical Clustering". In: *ApJ* 490.2 (Dec. 1997), pp. 493–508. DOI: 10.1086/304888. arXiv: astro-ph/9611107 [astro-ph].

[254] Takahiro Nishimichi et al. "BAO extractor: bias and redshift space effects". In: *JCAP* 2018.1, 035 (Jan. 2018), p. 035. DOI: 10.1088/1475-7516/2018/01/035. arXiv: 1708.00375 [astro-ph.CO].

[255] Takahiro Nishimichi et al. "Blinded challenge for precision cosmology with large-scale structure: Results from effective field theory for the redshift-space galaxy power spectrum". In: *Phys. Rev. D* 102.12, 123541 (Dec. 2020), p. 123541. DOI: 10.1103/PhysRevD.102.123541. arXiv: 2003.08277 [astro-ph.CO].

[256] Eugenio Noda, Marco Peloso, and Massimo Pietroni. "A robust BAO extractor". In: *JCAP* 2017.8, 007 (Aug. 2017), p. 007. DOI: 10.1088/1475-7516/2017/08/007. arXiv: 1705.01475 [astro-ph.CO].

[257] Yookyung Noh, Martin White, and Nikhil Padmanabhan. "Reconstructing baryon oscillations". In: *Phys. Rev. D* 80.12, 123501 (Dec. 2009), p. 123501. DOI: 10.1103/PhysRevD.80.123501. arXiv: 0909.1802 [astro-ph.CO].

[258] Andrej Obuljen, Neal Dalal, and Will J. Percival. "Anisotropic halo assembly bias and redshift-space distortions". In: *JCAP* 2019.10, 020 (Oct. 2019), p. 020. DOI: 10.1088/1475-7516/2019/10/020. arXiv: 1906.11823 [astro-ph.CO].

[259] Andrej Obuljen, Will J. Percival, and Neal Dalal. "Detection of anisotropic galaxy assembly bias in BOSS DR12". In: *JCAP* 2020.10, 058 (Oct. 2020), p. 058. DOI: 10.1088/1475-7516/2020/10/058. arXiv: 2004.07240 [astro-ph.CO].

[260] Teppei Okumura, Uroš Seljak, and Vincent Desjacques. "Distribution function approach to redshift space distortions. Part III: halos and galaxies". In: *JCAP* 2012.11, 014 (Nov. 2012), p. 014. DOI: 10.1088/1475-7516/2012/11/014. arXiv: 1206.4070 [astro-ph.CO].

[261] Teppei Okumura et al. "Distribution function approach to redshift space distortions. Part II: N-body simulations". In: *JCAP* 2012.2, 010 (Feb. 2012), p. 010. DOI: 10.1088/1475-7516/2012/02/010. arXiv: 1109.1609 [astro-ph.CO].

[262] Stephen J. Osborne, Duncan Hanson, and Olivier Doré. "Extragalactic foreground contamination in temperature-based CMB lens reconstruction". In: *JCAP* 2014.3, 024 (Mar. 2014), p. 024. DOI: 10.1088/1475-7516/2014/03/024. arXiv: 1310.7547 [astro-ph.CO].

[263] J. P. Ostriker and Paul J. Steinhardt. "The observational case for a low-density Universe with a non-zero cosmological constant". In: *Nature* 377.6550 (Oct. 1995), pp. 600–602. DOI: 10.1038/377600a0.

[264] Nikhil Padmanabhan and Martin White. "Calibrating the baryon oscillation ruler for matter and halos". In: *Phys. Rev. D* 80.6, 063508 (Sept. 2009), p. 063508. DOI: 10.1103/PhysRevD.80.063508. arXiv: 0906.1198 [astro-ph.CO].

[265] Nikhil Padmanabhan and Martin White. "Constraining anisotropic baryon oscillations". In: *Phys. Rev. D* 77.12, 123540 (June 2008), p. 123540. DOI: 10.1103/PhysRevD.77.123540. arXiv: 0804.0799 [astro-ph].

[266] Nikhil Padmanabhan, Martin White, and J. D. Cohn. "Reconstructing baryon oscillations: A Lagrangian theory perspective". In: *Phys. Rev. D* 79.6, 063523 (Mar. 2009), p. 063523. DOI: 10.1103/PhysRevD.79.063523. arXiv: 0812.2905 [astro-ph].

[267] Nikhil Padmanabhan et al. "A 2 per cent distance to z = 0.35 by reconstructing baryon acoustic oscillations - I. Methods and application to the Sloan Digital Sky Survey". In: *MNRAS* 427.3 (Dec. 2012), pp. 2132–2145. DOI: 10.1111/j.1365-2966.2012.21888.x. arXiv: 1202.0090 [astro-ph.CO].

[268] Enrico Pajer and Matias Zaldarriaga. "On the renormalization of the effective field theory of large scale structures". In: *JCAP* 2013.8, 037 (Aug. 2013), p. 037. DOI: 10.1088/1475-7516/2013/08/037. arXiv: 1301.7182 [astro-ph.CO].

[269] S. Pandey et al. "Dark Energy Survey Year 3 Results: Constraints on cosmological parameters and galaxy bias models from galaxy clustering and galaxy-galaxy lensing using the redMaGiC sample". In: *arXiv e-prints*, arXiv:2105.13545 (May 2021), arXiv:2105.13545. arXiv: 2105.13545 [astro-ph.CO].

[270] Changbom Park et al. "Power Spectrum, Correlation Function, and Tests for Luminosity Bias in the CfA Redshift Survey". In: *ApJ* 431 (Aug. 1994), p. 569. DOI: 10.1086/174508.

[271] Particle Data Group et al. "Review of Particle Physics". In: *Progress of Theoretical and Experimental Physics* 2020.8, 083C01 (Aug. 2020), p. 083C01. DOI: 10.1093/ptep/ptaa104.

[272] J. A. Peacock. "Errors on the measurement of omega via cosmological dipoles." In: *MNRAS* 258 (Oct. 1992), pp. 581–586. DOI: 10.1093/mnras/258.3.581.

[273] J. A. Peacock and S. J. Dodds. "Non-linear evolution of cosmological power spectra". In: *MNRAS* 280.3 (June 1996), pp. L19–L26. DOI: 10.1093/mnras/280.3.L19. arXiv: astro-ph/9603031 [astro-ph].

[274] J. A. Peacock and S. J. Dodds. "Reconstructing the Linear Power Spectrum of Cosmological Mass Fluctuations". In: *MNRAS* 267 (Apr. 1994), p. 1020. DOI: 10.1093/mnras/267.4.1020. arXiv: astro-ph/9311057 [astro-ph].

[275] John A. Peacock. *Cosmological Physics*. 1999.

[276] P. J. E. Peebles. *The large-scale structure of the universe*. 1980.

[277] Marco Peloso and Massimo Pietroni. "Galilean invariance and the consistency relation for the nonlinear squeezed bispectrum of large scale structure". In: *JCAP* 2013.5, 031 (May 2013), p. 031. DOI: 10.1088/1475-7516/2013/05/031. arXiv: 1302.0223 [astro-ph.CO].

[278] Marco Peloso and Massimo Pietroni. "Galilean invariant resummation schemes of cosmological perturbations". In: *JCAP* 2017.1, 056 (Jan. 2017), p. 056. DOI: 10.1088/1475-7516/2017/01/056. arXiv: 1609.06624 [astro-ph.CO].

[279] Will J. Percival. "Large Scale Structure Observations". In: *arXiv e-prints*, arXiv:1312.5490 (Dec. 2013), arXiv:1312.5490. arXiv: 1312.5490 [astro-ph.CO].

[280] Ashley Perko et al. "Biased Tracers in Redshift Space in the EFT of Large-Scale Structure". In: *arXiv e-prints*, arXiv:1610.09321 (Oct. 2016), arXiv:1610.09321. arXiv: 1610.09321 [astro-ph.CO].

[281] S. Perlmutter et al. "Measurements of Ω and Λ from 42 High-Redshift Supernovae". In: *ApJ* 517.2 (June 1999), pp. 565–586. DOI: 10.1086/307221. arXiv: astro-ph/9812133 [astro-ph].

[282] Oliver H. E. Philcox and Mikhail M. Ivanov. "BOSS DR12 full-shape cosmology: ΛCDM constraints from the large-scale galaxy power spectrum and bispectrum monopole". In: *Phys. Rev. D* 105.4, 043517 (Feb. 2022), p. 043517. DOI: 10.1103/PhysRevD.105.043517. arXiv: 2112.04515 [astro-ph.CO].

[283] Oliver H. E. Philcox et al. "Combining full-shape and BAO analyses of galaxy power spectra: a 1.6% CMB-independent constraint on H_0". In: *JCAP* 2020.5, 032 (May 2020), p. 032. DOI: 10.1088/1475-7516/2020/05/032. arXiv: 2002.04035 [astro-ph.CO].

[284] Planck Collaboration et al. "Planck 2015 results. XIII. Cosmological parameters". In: *A&A* 594, A13 (Sept. 2016), A13. DOI: 10.1051/0004-6361/201525830. arXiv: 1502.01589 [astro-ph.CO].

[285] Planck Collaboration et al. "Planck 2018 results. I. Overview and the cosmological legacy of Planck". In: *A&A* 641, A1 (Sept. 2020), A1. DOI: 10.1051/0004-6361/201833880. arXiv: 1807.06205 [astro-ph.CO].

[286] Planck Collaboration et al. "Planck 2018 results. VI. Cosmological parameters". In: *A&A* 641, A6 (Sept. 2020), A6. DOI: 10.1051/0004-6361/201833910. arXiv: 1807.06209 [astro-ph.CO].

[287] Planck Collaboration et al. "Planck 2018 results. VIII. Gravitational lensing". In: *A&A* 641, A8 (Sept. 2020), A8. DOI: 10.1051/0004-6361/201833886. arXiv: 1807.06210 [astro-ph.CO].

[288] Planck Collaboration et al. "Planck 2018 results. X. Constraints on inflation". In: *A&A* 641, A10 (Sept. 2020), A10. DOI: 10.1051/0004-6361/201833887. arXiv: 1807.06211 [astro-ph.CO].

[289] Andrew Pontzen. "Scale-dependent bias in the baryonic-acoustic-oscillation-scale intergalactic neutral hydrogen". In: *Phys. Rev. D* 89 (8 Apr. 2014), p. 083010. DOI: 10.1103/PhysRevD.89.083010. URL: https://link.aps.org/doi/10.1103/PhysRevD.89.083010.

[290] Rafael A. Porto, Leonardo Senatore, and Matias Zaldarriaga. "The Lagrangian-space Effective Field Theory of large scale structures". In: *JCAP* 2014.5, 022 (May 2014), p. 022. DOI: 10.1088/1475-7516/2014/05/022. arXiv: 1311.2168 [astro-ph.CO].

[291] Vivian Poulin et al. "Early Dark Energy can Resolve the Hubble Tension". In: *Phys. Rev. Lett.* 122.22, 221301 (June 2019), p. 221301. DOI: 10.1103/PhysRevLett.122.221301. arXiv: 1811.04083 [astro-ph.CO].

[292] William H. Press and Paul Schechter. "Formation of Galaxies and Clusters of Galaxies by Self-Similar Gravitational Condensation". In: *ApJ* 187 (Feb. 1974), pp. 425–438. DOI: 10.1086/152650.

[293] Daniel Pryer et al. "The galaxy power spectrum on the lightcone: deep, wide-angle redshift surveys and the turnover scale". In: *arXiv e-prints*, arXiv:2111.01811 (Nov. 2021), arXiv:2111.01811. arXiv: 2111.01811 [astro-ph.CO].

[294] Anthony R. Pullen et al. "Constraining gravity at the largest scales through CMB lensing and galaxy velocities". In: *MNRAS* 460.4 (Aug. 2016), pp. 4098–4108. DOI: 10.1093/mnras/stw1249. arXiv: 1511.04457 [astro-ph.CO].

[295] Cornelius Rampf. "Cosmological Vlasov-Poisson equations for dark matter: Recent developments and connections to selected plasma problems". In: *arXiv e-prints*, arXiv:2110.06265 (Oct. 2021), arXiv:2110.06265. arXiv: 2110.06265 [astro-ph.CO].

[296] Cornelius Rampf. "The recursion relation in Lagrangian perturbation theory". In: *JCAP* 2012.12, 004 (Dec. 2012), p. 004. DOI: 10.1088/1475-7516/2012/12/004. arXiv: 1205.5274 [astro-ph.CO].

[297] Cornelius Rampf, Uriel Frisch, and Oliver Hahn. "Unveiling the singular dynamics in the cosmic large-scale structure". In: *arXiv e-prints*, arXiv:1912.00868 (Dec. 2019), arXiv:1912.00868. arXiv: 1912.00868 [astro-ph.CO].

[298] Cornelius Rampf, Cora Uhlemann, and Oliver Hahn. "Cosmological perturbations for two cold fluids in ΛCDM". In: *MNRAS* 503.1 (May 2021), pp. 406–425. DOI: 10.1093/mnras/staa3605. arXiv: 2008.09123 [astro-ph.CO].

[299] Cornelius Rampf, Barbara Villone, and Uriel Frisch. "How smooth are particle trajectories in a ΛCDM Universe?" In: *MNRAS* 452.2 (Sept. 2015), pp. 1421–1436. DOI: 10.1093/mnras/stv1365. arXiv: 1504.00032 [astro-ph.CO].

[300] Beth Reid et al. "SDSS-III Baryon Oscillation Spectroscopic Survey Data Release 12: galaxy target selection and large-scale structure catalogues". In: *MNRAS* 455.2 (Jan. 2016), pp. 1553–1573. DOI: 10.1093/mnras/stv2382. arXiv: 1509.06529 [astro-ph.CO].

[301] Beth A. Reid and Martin White. "Towards an accurate model of the redshift-space clustering of haloes in the quasi-linear regime". In: *MNRAS* 417.3 (Nov. 2011), pp. 1913–1927. DOI: 10.1111/j.1365-2966.2011.19379.x. arXiv: 1105.4165 [astro-ph.CO].

[302] Beth A. Reid et al. "A 2.5 per cent measurement of the growth rate from small-scale redshift space clustering of SDSS-III CMASS galaxies". In: *MNRAS* 444.1 (Oct. 2014), pp. 476–502. DOI: 10.1093/mnras/stu1391. arXiv: 1404.3742 [astro-ph.CO].

[303] Beth A. Reid et al. "The clustering of galaxies in the SDSS-III Baryon Oscillation Spectroscopic Survey: measurements of the growth of structure and expansion rate at z = 0.57 from anisotropic clustering". In: *MNRAS* 426.4 (Nov. 2012), pp. 2719–2737. DOI: 10.1111/j.1365-2966.2012.21779.x. arXiv: 1203.6641 [astro-ph.CO].

[304] Adam G. Riess et al. "A Comprehensive Measurement of the Local Value of the Hubble Constant with 1 km/s/Mpc Uncertainty from the Hubble Space Telescope and the SH0ES Team". In: *arXiv e-prints*, arXiv:2112.04510 (Dec. 2021), arXiv:2112.04510. arXiv: 2112.04510 [astro-ph.CO].

[305] Adam G. Riess et al. "Observational Evidence from Supernovae for an Accelerating Universe and a Cosmological Constant". In: *AJ* 116.3 (Sept. 1998), pp. 1009–1038. DOI: 10.1086/300499. arXiv: astro-ph/9805201 [astro-ph].

[306] Ashley J. Ross, Will J. Percival, and Marc Manera. "The information content of anisotropic Baryon Acoustic Oscillation scale measurements". In: *MNRAS* 451.2 (Aug. 2015), pp. 1331–1340. DOI: 10.1093/mnras/stv966. arXiv: 1501.05571 [astro-ph.CO].

[307] Ashley J. Ross et al. "The clustering of galaxies in the completed SDSS-III Baryon Oscillation Spectroscopic Survey: observational systematics and baryon acoustic oscillations in the correlation function". In: *MNRAS* 464.1 (Jan. 2017), pp. 1168–1191. DOI: 10.1093/mnras/stw2372. arXiv: 1607.03145 [astro-ph.CO].

[308] Noah Sailer et al. "Optimal multifrequency weighting for CMB lensing". In: *Phys. Rev. D* 104.12, 123514 (Dec. 2021), p. 123514. DOI: 10.1103/PhysRevD.104.123514. arXiv: 2108.01663 [astro-ph.CO].

[309] Shun Saito, Masahiro Takada, and Atsushi Taruya. "Nonlinear power spectrum in the presence of massive neutrinos: Perturbation theory approach, galaxy bias, and parameter forecasts". In: *Phys. Rev. D* 80.8, 083528 (Oct. 2009), p. 083528. DOI: 10.1103/PhysRevD.80.083528. arXiv: 0907.2922 [astro-ph.CO].

[310] Shun Saito et al. "Understanding higher-order nonlocal halo bias at large scales by combining the power spectrum with the bispectrum". In: *Phys. Rev. D* 90.12, 123522 (Dec. 2014), p. 123522. DOI: 10.1103/PhysRevD.90.123522. arXiv: 1405.1447 [astro-ph.CO].

[311] Lado Samushia et al. "The clustering of galaxies in the SDSS-III Baryon Oscillation Spectroscopic Survey: measuring growth rate and geometry with anisotropic clustering". In: *MNRAS* 439.4 (Apr. 2014), pp. 3504–3519. DOI: 10.1093/mnras/stu197. arXiv: 1312.4899 [astro-ph.CO].

[312] Siddharth Satpathy et al. "The clustering of galaxies in the completed SDSS-III Baryon Oscillation Spectroscopic Survey: on the measurement of growth rate using galaxy correlation functions". In: *MNRAS* 469.2 (Aug. 2017), pp. 1369–1382. DOI: 10.1093/mnras/stx883. arXiv: 1607.03148 [astro-ph.CO].

[313] Emmanuel Schaan and Martin White. "Multi-tracer intensity mapping: cross-correlations, line noise & decorrelation". In: *JCAP* 2021.5, 068 (May 2021), p. 068. DOI: 10.1088/1475-7516/2021/05/068. arXiv: 2103.01964 [astro-ph.CO].

[314] David Schlegel, Juna A. Kollmeier, and Simone Ferraro. "The MegaMapper: a z¿2 spectroscopic instrument for the study of Inflation and Dark Energy". In: *Bulletin of the American Astronomical Society*. Vol. 51. Sept. 2019, 229, p. 229. arXiv: 1907.11171 [astro-ph.IM].

[315] David J. Schlegel, Douglas P. Finkbeiner, and Marc Davis. "Maps of Dust Infrared Emission for Use in Estimation of Reddening and Cosmic Microwave Background Radiation Foregrounds". In: *ApJ* 500.2 (June 1998), pp. 525–553. DOI: 10.1086/305772. arXiv: astro-ph/9710327 [astro-ph].

[316] Fabian Schmidt. "Effect of relative velocity and density perturbations between baryons and dark matter on the clustering of galaxies". In: *Phys. Rev. D* 94.6, 063508 (Sept. 2016), p. 063508. DOI: 10.1103/PhysRevD.94.063508. arXiv: 1602.09059 [astro-ph.CO].

[317] Fabian Schmidt and Florian Beutler. "Imprints of reionization in galaxy clustering". In: *Phys. Rev. D* 96.8, 083533 (Oct. 2017), p. 083533. DOI: 10.1103/PhysRevD.96.083533. arXiv: 1705.07843 [astro-ph.CO].

[318] Marcel Schmittfull, Tobias Baldauf, and Matias Zaldarriaga. "Iterative initial condition reconstruction". In: *Phys. Rev. D* 96.2, 023505 (July 2017), p. 023505. DOI: 10.1103/PhysRevD.96.023505. arXiv: 1704.06634 [astro-ph.CO].

[319] Marcel Schmittfull and Zvonimir Vlah. "Reducing the two-loop large-scale structure power spectrum to low-dimensional, radial integrals". In: *Phys. Rev. D* 94.10, 103530 (Nov. 2016), p. 103530. DOI: 10.1103/PhysRevD.94.103530. arXiv: 1609.00349 [astro-ph.CO].

[320] Marcel Schmittfull, Zvonimir Vlah, and Patrick McDonald. "Fast large scale structure perturbation theory using one-dimensional fast Fourier transforms". In: *Phys. Rev. D* 93.10, 103528 (May 2016), p. 103528. DOI: 10.1103/PhysRevD.93.103528. arXiv: 1603.04405 [astro-ph.CO].

[321] Marcel Schmittfull et al. "Eulerian BAO reconstructions and N -point statistics". In: *Phys. Rev. D* 92.12, 123522 (Dec. 2015), p. 123522. DOI: 10.1103/PhysRevD.92.123522. arXiv: 1508.06972 [astro-ph.CO].

[322] Marcel Schmittfull et al. "Modeling biased tracers at the field level". In: *Phys. Rev. D* 100.4, 043514 (Aug. 2019), p. 043514. DOI: 10.1103/PhysRevD.100.043514. arXiv: 1811.10640 [astro-ph.CO].

[323] Marcel Schmittfull et al. "Modeling galaxies in redshift space at the field level". In: *JCAP* 2021.5, 059 (May 2021), p. 059. DOI: 10.1088/1475-7516/2021/05/059. arXiv: 2012.03334 [astro-ph.CO].

[324] Aurel Schneider et al. "Matter power spectrum and the challenge of percent accuracy". In: *JCAP* 2016.4, 047 (Apr. 2016), p. 047. DOI: 10.1088/1475-7516/2016/04/047. arXiv: 1503.05920 [astro-ph.CO].

[325] Román Scoccimarro. "Fast estimators for redshift-space clustering". In: *Phys. Rev. D* 92.8, 083532 (Oct. 2015), p. 083532. DOI: 10.1103/PhysRevD.92.083532. arXiv: 1506.02729 [astro-ph.CO].

[326] Roman Scoccimarro and Joshua Frieman. "Loop Corrections in Nonlinear Cosmological Perturbation Theory". In: *ApJS* 105 (July 1996), p. 37. DOI: 10.1086/192306. arXiv: astro-ph/9509047 [astro-ph].

[327] L. F. Secco et al. "Dark Energy Survey Year 3 results: Cosmology from cosmic shear and robustness to modeling uncertainty". In: *Phys. Rev. D* 105.2, 023515 (Jan. 2022), p. 023515. DOI: 10.1103/PhysRevD.105.023515. arXiv: 2105.13544 [astro-ph.CO].

[328] Uroš Seljak and Patrick McDonald. "Distribution function approach to redshift space distortions". In: *JCAP* 2011.11, 039 (Nov. 2011), p. 039. DOI: 10.1088/1475-7516/2011/11/039. arXiv: 1109.1888 [astro-ph.CO].

[329] Uroš Seljak, Ue-Li Pen, and Neil Turok. "Polarization of the Microwave Background in Defect Models". In: *Phys. Rev. Lett.* 79.9 (Sept. 1997), pp. 1615–1618. DOI: 10.1103/PhysRevLett.79.1615. arXiv: astro-ph/9704231 [astro-ph].

[330] Uroš Seljak and Zvonimir Vlah. "Halo Zel'dovich model and perturbation theory: Dark matter power spectrum and correlation function". In: *Phys. Rev. D* 91.12, 123516 (June 2015), p. 123516. DOI: 10.1103/PhysRevD.91.123516. arXiv: 1501.07512 [astro-ph.CO].

[331] Agne Semenaite et al. "Cosmological implications of the full shape of anisotropic clustering measurements in BOSS and eBOSS". In: *MNRAS* 512.4 (June 2022), pp. 5657–5670. DOI: 10.1093/mnras/stac829. arXiv: 2111.03156 [astro-ph.CO].

[332] Leonardo Senatore. "Bias in the effective field theory of large scale structures". In: *JCAP* 2015.11, 007 (Nov. 2015), p. 007. DOI: 10.1088/1475-7516/2015/11/007. arXiv: 1406.7843 [astro-ph.CO].

[333] Leonardo Senatore and Gabriele Trevisan. "On the IR-resummation in the EFTofLSS". In: *JCAP* 2018.5, 019 (May 2018), p. 019. DOI: 10.1088/1475-7516/2018/05/019. arXiv: 1710.02178 [astro-ph.CO].

[334] Leonardo Senatore and Matias Zaldarriaga. "The Effective Field Theory of Large-Scale Structure in the presence of Massive Neutrinos". In: *arXiv e-prints*, arXiv:1707.04698 (July 2017), arXiv:1707.04698. arXiv: 1707.04698 [astro-ph.CO].

[335] Leonardo Senatore and Matias Zaldarriaga. "The IR-resummed Effective Field Theory of Large Scale Structures". In: *JCAP* 2015.2, 013 (Feb. 2015), p. 013. DOI: 10.1088/1475-7516/2015/02/013. arXiv: 1404.5954 [astro-ph.CO].

[336] Hee-Jong Seo and Daniel J. Eisenstein. "Baryonic Acoustic Oscillations in Simulated Galaxy Redshift Surveys". In: *ApJ* 633.2 (Nov. 2005), pp. 575–588. DOI: 10.1086/491599. arXiv: astro-ph/0507338 [astro-ph].

[337] Hee-Jong Seo and Daniel J. Eisenstein. "Improved Forecasts for the Baryon Acoustic Oscillations and Cosmological Distance Scale". In: *ApJ* 665.1 (Aug. 2007), pp. 14–24. DOI: 10.1086/519549. arXiv: astro-ph/0701079 [astro-ph].

[338] Hee-Jong Seo et al. "Modeling the reconstructed BAO in Fourier space". In: *MNRAS* 460.3 (Aug. 2016), pp. 2453–2471. DOI: 10.1093/mnras/stw1138. arXiv: 1511.00663 [astro-ph.CO].

[339] Blake D. Sherwin and Martin White. "The impact of wrong assumptions in BAO reconstruction". In: *JCAP* 2019.2, 027 (Feb. 2019), p. 027. DOI: 10.1088/1475-7516/2019/02/027. arXiv: 1808.04384 [astro-ph.CO].

[340] Blake D. Sherwin and Matias Zaldarriaga. "Shift of the baryon acoustic oscillation scale: A simple physical picture". In: *Phys. Rev. D* 85.10, 103523 (May 2012), p. 103523. DOI: 10.1103/PhysRevD.85.103523. arXiv: 1202.3998 [astro-ph.CO].

[341] Ravi K. Sheth, H. J. Mo, and Giuseppe Tormen. "Ellipsoidal collapse and an improved model for the number and spatial distribution of dark matter haloes". In: *MNRAS* 323.1 (May 2001), pp. 1–12. DOI: 10.1046/j.1365-8711.2001.04006.x. arXiv: astro-ph/9907024 [astro-ph].

[342] Ravi K. Sheth and Giuseppe Tormen. "Large-scale bias and the peak background split". In: *MNRAS* 308.1 (Sept. 1999), pp. 119–126. DOI: 10.1046/j.1365-8711.1999.02692.x. arXiv: astro-ph/9901122 [astro-ph].

[343] Masatoshi Shoji and Eiichiro Komatsu. "Erratum: Massive neutrinos in cosmology: Analytic solutions and fluid approximation [Phys. Rev. D 81, 123516 (2010)]". In: *Phys. Rev. D* 82.8, 089901 (Oct. 2010), p. 089901. DOI: 10.1103/PhysRevD.82.089901. arXiv: 1003.0942 [astro-ph.CO].

[344] Marko Simonović et al. "Cosmological perturbation theory using the FFTLog: formalism and connection to QFT loop integrals". In: *JCAP* 2018.4, 030 (Apr. 2018), p. 030. DOI: 10.1088/1475-7516/2018/04/030. arXiv: 1708.08130 [astro-ph.CO].

[345] S. Singh. "improved MASTER for the LSS: fast and accurate analysis of the two-point power spectra and correlation functions." In: *MNRAS* 508 (Jan. 2021), pp. 1632–1651. arXiv: 2105.04548 [astro-ph.CO].

[346] Sukhdeep Singh, Rachel Mandelbaum, and Joel R. Brownstein. "Cross-correlating Planck CMB lensing with SDSS: lensing-lensing and galaxy-lensing cross-correlations". In: *MNRAS* 464.2 (Jan. 2017), pp. 2120–2138. DOI: 10.1093/mnras/stw2482. arXiv: 1606.08841 [astro-ph.CO].

[347] Sukhdeep Singh et al. "Cosmological constraints from galaxy-lensing cross-correlations using BOSS galaxies with SDSS and CMB lensing". In: *MNRAS* 491.1 (Jan. 2020), pp. 51–68. DOI: 10.1093/mnras/stz2922. arXiv: 1811.06499 [astro-ph.CO].

[348] Sukhdeep Singh et al. "Probing gravity with a joint analysis of galaxy and CMB lensing and SDSS spectroscopy". In: *MNRAS* 482.1 (Jan. 2019), pp. 785–806. DOI: 10.1093/mnras/sty2681. arXiv: 1803.08915 [astro-ph.CO].

[349] Manodeep Sinha and Lehman H. Garrison. "CORRFUNC - a suite of blazing fast correlation functions on the CPU". In: *MNRAS* 491.2 (Jan. 2020), pp. 3022–3041. DOI: 10.1093/mnras/stz3157. arXiv: 1911.03545 [astro-ph.CO].

[350] Samuel W. Skillman et al. "Dark Sky Simulations: Early Data Release". In: *arXiv e-prints*, arXiv:1407.2600 (July 2014), arXiv:1407.2600. arXiv: 1407.2600 [astro-ph.CO].

[351] Zachary Slepian et al. "Constraining the baryon-dark matter relative velocity with the large-scale three-point correlation function of the SDSS BOSS DR12 CMASS galaxies". In: *MNRAS* 474.2 (Feb. 2018), pp. 2109–2115. DOI: 10.1093/mnras/stx2723. arXiv: 1607.06098 [astro-ph.CO].

[352] Anze Slosar et al. "Packed Ultra-wideband Mapping Array (PUMA): A Radio Telescope for Cosmology and Transients". In: *Bulletin of the American Astronomical Society*. Vol. 51. Sept. 2019, 53, p. 53. arXiv: 1907.12559 [astro-ph.IM].

[353] Anze Slosar et al. "Scratches from the Past: Inflationary Archaeology through Features in the Power Spectrum of Primordial Fluctuations". In: 51.3, 98 (May 2019), p. 98. arXiv: 1903.09883 [astro-ph.CO].

[354] R. E. Smith et al. "Stable clustering, the halo model and non-linear cosmological power spectra". In: *MNRAS* 341.4 (June 2003), pp. 1311–1332. DOI: 10.1046/j.1365-8711.2003.06503.x. arXiv: astro-ph/0207664 [astro-ph].

[355] Tristan L. Smith, Vivian Poulin, and Mustafa A. Amin. "Oscillating scalar fields and the Hubble tension: A resolution with novel signatures". In: *Phys. Rev. D* 101.6, 063523 (Mar. 2020), p. 063523. DOI: 10.1103/PhysRevD.101.063523. arXiv: 1908.06995 [astro-ph.CO].

[356] Gábor Somogyi and Robert E. Smith. "Cosmological perturbation theory for baryons and dark matter: One-loop corrections in the renormalized perturbation theory framework". In: *Phys. Rev. D* 81.2, 023524 (Jan. 2010), p. 023524. DOI: 10.1103/PhysRevD.81.023524. arXiv: 0910.5220 [astro-ph.CO].

[357] Volker Springel. "The cosmological simulation code GADGET-2". In: *MNRAS* 364.4 (Dec. 2005), pp. 1105–1134. DOI: 10.1111/j.1365-2966.2005.09655.x. arXiv: astro-ph/0505010 [astro-ph].

[358] Naonori S. Sugiyama, Teppei Okumura, and David N. Spergel. "Understanding redshift space distortions in density-weighted peculiar velocity". In: *JCAP* 2016.7, 001 (July 2016), p. 001. DOI: 10.1088/1475-7516/2016/07/001. arXiv: 1509.08232 [astro-ph.CO].

[359] Tomomi Sunayama et al. "Efficient construction of mock catalogs for baryon acoustic oscillation surveys". In: *JCAP* 2016.5, 051 (May 2016), p. 051. DOI: 10.1088/1475-7516/2016/05/051. arXiv: 1510.06665 [astro-ph.CO].

[360] R. A. Sunyaev and Ya. B. Zeldovich. "The Observations of Relic Radiation as a Test of the Nature of X-Ray Radiation from the Clusters of Galaxies". In: *Comments on Astrophysics and Space Physics* 4 (Nov. 1972), p. 173.

[361] Ryuichi Takahashi. "Third-Order Density Perturbation and One-Loop Power Spectrum in Dark-Energy-Dominated Universe". In: *Progress of Theoretical Physics* 120.3 (Sept. 2008), pp. 549–559. DOI: 10.1143/PTP.120.549. arXiv: 0806.1437 [astro-ph].

[362] Ryuichi Takahashi et al. "Revising the Halofit Model for the Nonlinear Matter Power Spectrum". In: *ApJ* 761.2, 152 (Dec. 2012), p. 152. DOI: 10.1088/0004-637X/761/2/152. arXiv: 1208.2701 [astro-ph.CO].

[363] Amélie Tamone et al. "The completed SDSS-IV extended baryon oscillation spectroscopic survey: growth rate of structure measurement from anisotropic clustering analysis in configuration space between redshift 0.6 and 1.1 for the emission-line galaxy sample". In: *MNRAS* 499.4 (Dec. 2020), pp. 5527–5546. DOI: 10.1093/mnras/staa3050. arXiv: 2007.09009 [astro-ph.CO].

[364] M. Tanabashi et al. "Review of Particle Physics*". In: *Phys. Rev. D* 98.3, 030001 (Aug. 2018), p. 030001. DOI: 10.1103/PhysRevD.98.030001.

[365] Atsushi Taruya and Stéphane Colombi. "Post-collapse perturbation theory in 1D cosmology - beyond shell-crossing". In: *MNRAS* 470.4 (Oct. 2017), pp. 4858–4884. DOI: 10.1093/mnras/stx1501. arXiv: 1701.09088 [astro-ph.CO].

[366] Atsushi Taruya, Takahiro Nishimichi, and Shun Saito. "Baryon acoustic oscillations in 2D: Modeling redshift-space power spectrum from perturbation theory". In: *Phys. Rev. D* 82.6, 063522 (Sept. 2010), p. 063522. DOI: 10.1103/PhysRevD.82.063522. arXiv: 1006.0699 [astro-ph.CO].

[367] Atsushi Taruya et al. "Wide-angle redshift-space distortions at quasi-linear scales: cross-correlation functions from Zel'dovich approximation". In: *Mon. Not. Roy. Astron. Soc.* 491.3 (2020), pp. 4162–4179. DOI: 10.1093/mnras/stz3272. arXiv: 1908.03854 [astro-ph.CO].

[368] Svetlin Tassev and Matias Zaldarriaga. "Towards an optimal reconstruction of baryon oscillations". In: *JCAP* 2012.10, 006 (Oct. 2012), p. 006. DOI: 10.1088/1475-7516/2012/10/006. arXiv: 1203.6066 [astro-ph.CO].

[369] A. N. Taylor and A. J. S. Hamilton. "Non-linear cosmological power spectra in real and redshift space". In: *MNRAS* 282.3 (Oct. 1996), pp. 767–778. DOI: 10.1093/mnras/282.3.767. arXiv: astro-ph/9604020 [astro-ph].

[370] A. N. Taylor et al. "Probing dark energy with the shear-ratio geometric test". In: *MNRAS* 374.4 (Feb. 2007), pp. 1377–1403. DOI: 10.1111/j.1365-2966.2006.11257.x. arXiv: astro-ph/0606416 [astro-ph].

[371] Peter L. Taylor and Katarina Markovič. "The Covariance of Photometric and Spectroscopic Two-Point Statistics: Implications for Cosmological Parameter Inference". In: *arXiv e-prints*, arXiv:2205.14167 (May 2022), arXiv:2205.14167. arXiv: 2205.14167 [astro-ph.CO].

[372] Max Tegmark. "Measuring Cosmological Parameters with Galaxy Surveys". In: *Phys. Rev. Lett.* 79.20 (Nov. 1997), pp. 3806–3809. DOI: 10.1103/PhysRevLett.79.3806. arXiv: astro-ph/9706198 [astro-ph].

[373] The MSE Science Team et al. "The Detailed Science Case for the Maunakea Spectroscopic Explorer, 2019 edition". In: *arXiv e-prints*, arXiv:1904.04907 (Apr. 2019), arXiv:1904.04907. arXiv: 1904.04907 [astro-ph.IM].

[374] R. J. Thornton et al. "The Atacama Cosmology Telescope: The Polarization-sensitive ACTPol Instrument". In: *ApJS* 227.2, 21 (Dec. 2016), p. 21. DOI: 10.3847/1538-4365/227/2/21. arXiv: 1605.06569 [astro-ph.IM].

[375] Jeremy Tinker et al. "Toward a Halo Mass Function for Precision Cosmology: The Limits of Universality". In: *ApJ* 688.2 (Dec. 2008), pp. 709–728. DOI: 10.1086/591439. arXiv: 0803.2706 [astro-ph].

[376] Chun-Hao To et al. "Combination of cluster number counts and two-point correlations: validation on mock Dark Energy Survey". In: *MNRAS* 502.3 (Apr. 2021), pp. 4093–4111. DOI: 10.1093/mnras/stab239. arXiv: 2008.10757 [astro-ph.CO].

[377] Joseph Tomlinson, Henry S. Grasshorn Gebhardt, and Donghui Jeong. "Fast calculation of the nonlinear redshift-space galaxy power spectrum including selection bias". In: *Phys. Rev. D* 101.10, 103528 (May 2020), p. 103528. DOI: 10.1103/PhysRevD.101.103528. arXiv: 2004.03629 [astro-ph.CO].

[378] Jesús Torrado and Antony Lewis. *Cobaya: Bayesian analysis in cosmology*. Astrophysics Source Code Library, record ascl:1910.019. Oct. 2019. ascl: 1910.019.

[379] Jesús Torrado and Antony Lewis. "Cobaya: code for Bayesian analysis of hierarchical physical models". In: *JCAP* 2021.5, 057 (May 2021), p. 057. DOI: 10.1088/1475-7516/2021/05/057. arXiv: 2005.05290 [astro-ph.IM].

[380] Dmitriy Tseliakhovich and Christopher Hirata. "Relative velocity of dark matter and baryonic fluids and the formation of the first structures". In: *Phys. Rev. D* 82.8, 083520 (Oct. 2010), p. 083520. DOI: 10.1103/PhysRevD.82.083520. arXiv: 1005.2416 [astro-ph.CO].

[381] Cora Uhlemann, Michael Kopp, and Thomas Haugg. "Edgeworth streaming model for redshift space distortions". In: *Phys. Rev. D* 92.6, 063004 (Sept. 2015), p. 063004. DOI: 10.1103/PhysRevD.92.063004. arXiv: 1503.08837 [astro-ph.CO].

[382] Phoebe Upton Sanderbeck et al. "Estimates for the impact of ultraviolet background fluctuations on galaxy clustering measurements". In: *MNRAS* 485.4 (June 2019), pp. 5059–5072. DOI: 10.1093/mnras/stz741. arXiv: 1810.12321 [astro-ph.CO].

[383] Georgios Valogiannis, Rachel Bean, and Alejandro Aviles. "An accurate perturbative approach to redshift space clustering of biased tracers in modified gravity". In: *JCAP* 01 (2020), p. 055. DOI: 10.1088/1475-7516/2020/01/055. arXiv: 1909.05261 [astro-ph.CO].

[384] Marcel P. van Daalen, Ian G. McCarthy, and Joop Schaye. "Exploring the effects of galaxy formation on matter clustering through a library of simulation power spectra". In: *MNRAS* 491.2 (Jan. 2020), pp. 2424–2446. DOI: 10.1093/mnras/stz3199. arXiv: 1906.00968 [astro-ph.CO].

[385] Frank C. van den Bosch et al. "Disruption of dark matter substructure: fact or fiction?" In: *MNRAS* 474.3 (Mar. 2018), pp. 3043–3066. DOI: 10.1093/mnras/stx2956. arXiv: 1711.05276 [astro-ph.GA].

[386] J. L. van den Busch et al. "KiDS-1000: cosmic shear with enhanced redshift calibration". In: *arXiv e-prints*, arXiv:2204.02396 (Apr. 2022), arXiv:2204.02396. arXiv: 2204.02396 [astro-ph.CO].

[387] A. van Engelen et al. "CMB Lensing Power Spectrum Biases from Galaxies and Clusters Using High-angular Resolution Temperature Maps". In: *ApJ* 786.1, 13 (May 2014), p. 13. DOI: 10.1088/0004-637X/786/1/13. arXiv: 1310.7023 [astro-ph.CO].

[388] Mariana Vargas-Magaña et al. "The clustering of galaxies in the completed SDSS-III Baryon Oscillation Spectroscopic Survey: theoretical systematics and Baryon Acoustic Oscillations in the galaxy correlation function". In: *MNRAS* 477.1 (June 2018), pp. 1153–1188. DOI: 10.1093/mnras/sty571. arXiv: 1610.03506 [astro-ph.CO].

[389] Mariana Vargas-Magaña et al. "The clustering of Galaxies in the SDSS-III Baryon Oscillation Spectroscopic Survey: potential systematics in fitting of baryon acoustic feature". In: *MNRAS* 445.1 (Nov. 2014), pp. 2–28. DOI: 10.1093/mnras/stu1681.

[390] Anagha Vasudevan et al. "Time-sliced perturbation theory with primordial non-Gaussianity and effects of large bulk flows on inflationary oscillating features". In: *JCAP* 2019.9, 037 (Sept. 2019), p. 037. DOI: 10.1088/1475-7516/2019/09/037. arXiv: 1906.08697 [astro-ph.CO].

[391] Francisco Villaescusa-Navarro et al. "Cosmology with massive neutrinos I: towards a realistic modeling of the relation between matter, haloes and galaxies". In: *JCAP* 03 (2014), p. 011. DOI: 10.1088/1475-7516/2014/03/011. arXiv: 1311.0866 [astro-ph.CO].

[392] Francisco Villaescusa-Navarro et al. "Ingredients for 21 cm Intensity Mapping". In: *ApJ* 866.2, 135 (Oct. 2018), p. 135. DOI: 10.3847/1538-4357/aadba0. arXiv: 1804.09180 [astro-ph.CO].

[393] Francisco Villaescusa-Navarro et al. "The imprint of neutrinos on clustering in redshift-space". In: *Astrophys. J.* 861.1 (2018), p. 53. DOI: 10.3847/1538-4357/aac6bf. arXiv: 1708.01154 [astro-ph.CO].

[394] Francisco Villaescusa-Navarro et al. "The Quijote Simulations". In: *ApJS* 250.1, 2 (Sept. 2020), p. 2. DOI: 10.3847/1538-4365/ab9d82. arXiv: 1909.05273 [astro-ph.CO].

[395] E. T. Vishniac. "Why weakly non-linear effects are small in a zero-pressure cosmology". In: *MNRAS* 203 (Apr. 1983), pp. 345–349. DOI: 10.1093/mnras/203.2.345.

[396] Zvonimir Vlah, Emanuele Castorina, and Martin White. "The Gaussian streaming model and convolution Lagrangian effective field theory". In: *JCAP* 2016.12, 007 (Dec. 2016), p. 007. DOI: 10.1088/1475-7516/2016/12/007. arXiv: 1609.02908 [astro-ph.CO].

[397] Zvonimir Vlah, Uroš Seljak, and Tobias Baldauf. "Lagrangian perturbation theory at one loop order: Successes, failures, and improvements". In: *Phys. Rev. D* 91.2, 023508 (Jan. 2015), p. 023508. DOI: 10.1103/PhysRevD.91.023508. arXiv: 1410.1617 [astro-ph.CO].

[398] Zvonimir Vlah and Martin White. "Exploring redshift-space distortions in large-scale structure". In: *JCAP* 2019.3, 007 (Mar. 2019), p. 007. DOI: 10.1088/1475-7516/2019/03/007. arXiv: 1812.02775 [astro-ph.CO].

[399] Zvonimir Vlah, Martin White, and Alejandro Aviles. "A Lagrangian effective field theory". In: *JCAP* 2015.9, 014 (Sept. 2015), p. 014. DOI: 10.1088/1475-7516/2015/09/014. arXiv: 1506.05264 [astro-ph.CO].

[400] Zvonimir Vlah et al. "Distribution function approach to redshift space distortions. Part IV: perturbation theory applied to dark matter". In: *JCAP* 2012.11, 009 (Nov. 2012), p. 009. DOI: 10.1088/1475-7516/2012/11/009. arXiv: 1207.0839 [astro-ph.CO].

[401] Zvonimir Vlah et al. "Distribution function approach to redshift space distortions. Part V: perturbation theory applied to dark matter halos". In: *JCAP* 2013.10, 053 (Oct. 2013), p. 053. DOI: 10.1088/1475-7516/2013/10/053. arXiv: 1308.6294 [astro-ph.CO].

[402] Zvonimir Vlah et al. "Perturbation theory, effective field theory, and oscillations in the power spectrum". In: *JCAP* 2016.3, 057 (Mar. 2016), p. 057. DOI: 10.1088/1475-7516/2016/03/057. arXiv: 1509.02120 [astro-ph.CO].

[403] Maximilian von Wietersheim-Kramsta et al. "Magnification bias in galaxy surveys with complex sample selection functions". In: *MNRAS* 504.1 (June 2021), pp. 1452–1465. DOI: 10.1093/mnras/stab1000. arXiv: 2101.05261 [astro-ph.CO].

[404] Digvijay Wadekar and Román Scoccimarro. "Galaxy power spectrum multipoles covariance in perturbation theory". In: *Phys. Rev. D* 102.12, 123517 (Dec. 2020), p. 123517. DOI: 10.1103/PhysRevD.102.123517. arXiv: 1910.02914 [astro-ph.CO].

[405] Lile Wang, Beth Reid, and Martin White. "An analytic model for redshift-space distortions". In: *MNRAS* 437.1 (Jan. 2014), pp. 588–599. DOI: 10.1093/mnras/stt1916. arXiv: 1306.1804 [astro-ph.CO].

[406] Michael S. Warren. "2HOT: An Improved Parallel Hashed Oct-Tree N-Body Algorithm for Cosmological Simulation". In: *arXiv e-prints*, arXiv:1310.4502 (Oct. 2013), arXiv:1310.4502. arXiv: 1310.4502 [astro-ph.IM].

[407] G. N. Watson. *A Treatise on the Theory of Bessel Functions, 2nd ed.* Ed. by Cambridge University Press. 1995.

[408] Risa H. Wechsler and Jeremy L. Tinker. "The Connection Between Galaxies and Their Dark Matter Halos". In: *Ann. Rev. Astron.& Astrophys.* 56 (Sept. 2018), pp. 435–487. DOI: 10.1146/annurev-astro-081817-051756. arXiv: 1804.03097 [astro-ph.GA].

[409] Risa H. Wechsler et al. "ADDGALS: Simulated Sky Catalogs for Wide Field Galaxy Surveys". In: *arXiv e-prints*, arXiv:2105.12105 (May 2021), arXiv:2105.12105. arXiv: 2105.12105 [astro-ph.CO].

[410] David H. Weinberg et al. "Observational probes of cosmic acceleration". In: *Phys. Rep.* 530.2 (Sept. 2013), pp. 87–255. DOI: 10.1016/j.physrep.2013.05.001. arXiv: 1201.2434 [astro-ph.CO].

[411] Kim F. Werner and Cristiano Porciani. "Renormalization of linear halo bias in N-body simulations". In: *MNRAS* 492.2 (Feb. 2020), pp. 1614–1633. DOI: 10.1093/mnras/stz3469. arXiv: 1907.03774 [astro-ph.CO].

[412] M. White. "The mass of a halo". In: *A&A* 367 (Feb. 2001), pp. 27–32. DOI: 10.1051/0004-6361:20000357. arXiv: astro-ph/0011495 [astro-ph].

[413] Martin White. "Baryon oscillations". In: *Astroparticle Physics* 24.4-5 (Dec. 2005), pp. 334–344. DOI: 10.1016/j.astropartphys.2005.07.007. arXiv: astro-ph/0507307 [astro-ph].

[414] Martin White. "Reconstruction within the Zeldovich approximation". In: *MNRAS* 450.4 (July 2015), pp. 3822–3828. DOI: 10.1093/mnras/stv842. arXiv: 1504.03677 [astro-ph.CO].

[415] Martin White. "The Zel'dovich approximation". In: *MNRAS* 439.4 (Apr. 2014), pp. 3630–3640. DOI: 10.1093/mnras/stu209. arXiv: 1401.5466 [astro-ph.CO].

[416] Martin White, Paul Martini, and J. D. Cohn. "Constraints on the correlation between QSO luminosity and host halo mass from high-redshift quasar clustering". In: *MNRAS* 390.3 (Nov. 2008), pp. 1179–1184. DOI: 10.1111/j.1365-2966.2008.13817.x. arXiv: 0711.4109 [astro-ph].

[417] Martin White et al. "Cosmological constraints from the tomographic cross-correlation of DESI Luminous Red Galaxies and Planck CMB lensing". In: *JCAP* 2022.2, 007 (Feb. 2022), p. 007. DOI: 10.1088/1475-7516/2022/02/007. arXiv: 2111.09898 [astro-ph.CO].

[418] Martin White et al. "Tests of redshift-space distortions models in configuration space for the analysis of the BOSS final data release". In: *MNRAS* 447.1 (Feb. 2015), pp. 234–245. DOI: 10.1093/mnras/stu2460. arXiv: 1408.5435 [astro-ph.CO].

[419] Martin White et al. "The clustering of intermediate-redshift quasars as measured by the Baryon Oscillation Spectroscopic Survey". In: *MNRAS* 424.2 (Aug. 2012), pp. 933–950. DOI: 10.1111/j.1365-2966.2012.21251.x. arXiv: 1203.5306 [astro-ph.CO].

[420] Benjamin D. Wibking et al. "Cosmology with galaxy-galaxy lensing on non-perturbative scales: emulation method and application to BOSS LOWZ". In: *MNRAS* 492.2 (Feb. 2020), pp. 2872–2896. DOI: 10.1093/mnras/stz3423. arXiv: 1907.06293 [astro-ph.CO].

[421] M. J. Wilson and Martin White. "Cosmology with dropout selection: straw-man surveys & CMB lensing". In: *JCAP* 2019.10, 015 (Oct. 2019), p. 015. DOI: 10.1088/1475-7516/2019/10/015. arXiv: 1904.13378 [astro-ph.CO].

[422] M. J. Wilson et al. "Rapid modelling of the redshift-space power spectrum multipoles for a masked density field". In: *MNRAS* 464.3 (Jan. 2017), pp. 3121–3130. DOI: 10.1093/mnras/stw2576. arXiv: 1511.07799 [astro-ph.CO].

[423] X. Xu et al. "A New Statistic for Analyzing Baryon Acoustic Oscillations". In: *ApJ* 718.2 (Aug. 2010), pp. 1224–1234. DOI: 10.1088/0004-637X/718/2/1224. arXiv: 1001.2324 [astro-ph.CO].

[424] Xiaoying Xu et al. "A 2 per cent distance to z = 0.35 by reconstructing baryon acoustic oscillations - II. Fitting techniques". In: *MNRAS* 427.3 (Dec. 2012), pp. 2146–2167. DOI: 10.1111/j.1365-2966.2012.21573.x. arXiv: 1202.0091 [astro-ph.CO].

[425] Kazuhiro Yahata et al. "The effect of FIR emission from SDSS galaxies on the SFD Galactic extinction map". In: *Publ. Astron. Soc. Jap.* 59 (2007), pp. 205–219. DOI: 10.1093/pasj/59.1.205. arXiv: astro-ph/0607098.

[426] Kazuhiro Yamamoto et al. "A Measurement of the Quadrupole Power Spectrum in the Clustering of the 2dF QSO Survey". In: *PASJ* 58 (Feb. 2006), pp. 93–102. DOI: 10.1093/pasj/58.1.93. arXiv: astro-ph/0505115 [astro-ph].

[427] Jaiyul Yoo, Neal Dalal, and Uroš Seljak. "Supersonic relative velocity effect on the baryonic acoustic oscillation measurements". In: *JCAP* 2011.7, 018 (July 2011), p. 018. DOI: 10.1088/1475-7516/2011/07/018. arXiv: 1105.3732 [astro-ph.CO].

[428] Byeonghee Yu et al. "Towards Neutrino Mass from Cosmology without Optical Depth Information". In: *arXiv e-prints*, arXiv:1809.02120 (Sept. 2018), arXiv:1809.02120. arXiv: 1809.02120 [astro-ph.CO].

[429] Yu Yu, Hong-Ming Zhu, and Ue-Li Pen. "Halo Nonlinear Reconstruction". In: *ApJ* 847.2, 110 (Oct. 2017), p. 110. DOI: 10.3847/1538-4357/aa89e7. arXiv: 1703.08301 [astro-ph.CO].

[430] Sihan Yuan et al. "Stringent σ_8 constraints from small-scale galaxy clustering using a hybrid MCMC+emulator framework". In: *arXiv e-prints*, arXiv:2203.11963 (Mar. 2022), arXiv:2203.11963. arXiv: 2203.11963 [astro-ph.CO].

[431] Ya. B. Zel'dovich. "Gravitational instability: An approximate theory for large density perturbations." In: *A&A* 5 (Mar. 1970), pp. 84–89.

[432] Matteo Zennaro et al. "The BACCO simulation project: biased tracers in real space". In: *arXiv e-prints*, arXiv:2101.12187 (Jan. 2021), arXiv:2101.12187. arXiv: 2101.12187 [astro-ph.CO].

[433] Andrew R. Zentner et al. "Constraints on assembly bias from galaxy clustering". In: *MNRAS* 485.1 (May 2019), pp. 1196–1209. DOI: 10.1093/mnras/stz470. arXiv: 1606.07817 [astro-ph.GA].

[434] Zhongxu Zhai et al. "The Aemulus Project V: Cosmological constraint from small-scale clustering of BOSS galaxies". In: *arXiv e-prints*, arXiv:2203.08999 (Mar. 2022), arXiv:2203.08999. arXiv: 2203.08999 [astro-ph.CO].

[435] Zhongxu Zhai et al. "The Aemulus Project. III. Emulation of the Galaxy Correlation Function". In: *ApJ* 874.1, 95 (Mar. 2019), p. 95. DOI: 10.3847/1538-4357/ab0d7b. arXiv: 1804.05867 [astro-ph.CO].

[436] Zhongxu Zhai et al. "The Clustering of Luminous Red Galaxies at z $\sim$ 0.7 from EBOSS and BOSS Data". In: *ApJ* 848.2, 76 (Oct. 2017), p. 76. DOI: 10.3847/1538-4357/aa8eee. arXiv: 1607.05383 [astro-ph.CO].

[437] Pengjie Zhang et al. "Probing Gravity at Cosmological Scales by Measurements which Test the Relationship between Gravitational Lensing and Matter Overdensity". In: *Phys. Rev. Lett.* 99.14, 141302 (Oct. 2007), p. 141302. DOI: 10.1103/PhysRevLett.99.141302. arXiv: 0704.1932 [astro-ph].

[438] Pierre Zhang et al. "BOSS Correlation Function analysis from the Effective Field Theory of Large-Scale Structure". In: *JCAP* 2022.2, 036 (Feb. 2022), p. 036. DOI: 10.1088/1475-7516/2022/02/036. arXiv: 2110.07539 [astro-ph.CO].

[439] Yucheng Zhang et al. "Testing general relativity on cosmological scales at redshift z $\sim$ 1.5 with quasar and CMB lensing". In: *MNRAS* 501.1 (Feb. 2021), pp. 1013–1027. DOI: 10.1093/mnras/staa3672. arXiv: 2007.12607 [astro-ph.CO].

[440] Vladislav Zheligovsky and Uriel Frisch. "Time-analyticity of Lagrangian particle trajectories in ideal fluid flow". In: *Journal of Fluid Mechanics* 749 (June 2014), pp. 404–430. DOI: 10.1017/jfm.2014.221. arXiv: 1312.6320 [math.AP].

[441] Zheng Zheng et al. "Theoretical Models of the Halo Occupation Distribution: Separating Central and Satellite Galaxies". In: *ApJ* 633.2 (Nov. 2005), pp. 791–809. DOI: 10.1086/466510. arXiv: astro-ph/0408564 [astro-ph].

[442] Fangzhou Zhu, Nikhil Padmanabhan, and Martin White. "Optimal redshift weighting for baryon acoustic oscillations". In: *MNRAS* 451.1 (July 2015), pp. 236–243. DOI: 10.1093/mnras/stv964. arXiv: 1411.1424 [astro-ph.CO].

[443] Hong-Ming Zhu, Yu Yu, and Ue-Li Pen. "Nonlinear reconstruction of redshift space distortions". In: *Phys. Rev. D* 97.4 (2018), p. 043502. DOI: 10.1103/PhysRevD.97.043502. arXiv: 1711.03218 [astro-ph.CO].